PHYSIK - DEPARTMENT

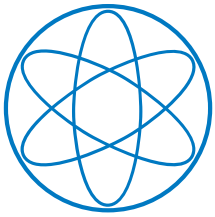

Artificial Neural Network Based Pulse-Shape Analysis for Cryogenic Detectors Operated in CRESST-II

DISSERTATION

VON

ANDREAS JOSEF ZÖLLER

TECHNISCHE UNIVERSITÄT MÜNCHEN

TECHNISCHE UNIVERSITÄT MÜNCHEN
Physik-Department
Lehrstuhl für Experimentalphysik und Astroteilchenphysik
Univ.-Prof. Dr. Stefan Schönert

Artificial Neural Network Based Pulse-Shape Analysis for Cryogenic Detectors Operated in CRESST-II

Andreas Josef Zöller

Vollständiger Abdruck der von der Fakultät für Physik der Technischen Universität München zur Erlangung des akademischen Grades eines

Doktors der Naturwissenschaften (Dr. rer. nat.)

genehmigten Dissertation.

Vorsitzender:	Univ.-Prof. Dr. Björn Garbrecht
Prüfer der Dissertation:	
	1. Univ.-Prof. Dr. Lothar Oberauer
	2. Hon.-Prof. Allen Caldwell, Ph.D.

Die Dissertation wurde am 28.04.2016 bei der Technischen Universität München eingereicht und durch die Fakultät für Physik am 25.07.2016 angenommen.

Abstract

The puzzle of Dark Matter remains one of the biggest challenges of modern physics. Several astronomical observations at different length and time scales in the universe hint towards the existence of Dark Matter (see chapter 1). Due to the precise measurement of the cosmic microwave background, in particular by the Planck satellite, it is known that the universe is literally dark: $\sim 68.5\,\%$ of the energy content in the universe is made up by the totally unknown Dark Energy, $\sim 26.6\,\%$ by cold Dark Matter and only $\sim 4.9\,\%$ by the well-known baryonic matter. In the standard model (SM) of particle physics there exists no particle which fulfills all the requirements for a Dark Matter candidate. Therefore, the astronomical observations are hints towards physics beyond the standard model.

Weakly Interacting Massive Particles (WIMPs) are a well-motivated Dark Matter candidate which arises from several theories. A well-known theory predicting the existence of WIMPs is the supersymmetric extension of the SM. WIMPs gained large interest due to the *WIMP miracle*, i.e. the fact that the expected relic density of a particle with a mass of $\gtrsim 30\,\mathrm{GeV}/c^2$ and a cross section in the order of the electroweak scale is very well compatible with the observations. However, in other theories more generic WIMP-like Dark Matter particles with masses in the $\mathcal{O}\left(1\mathrm{GeV}/c^2\right)$ are proposed.

The present work is performed in a direct detection experiment searching for WIMP-like Dark Matter. WIMPs are expected to scatter off nuclei and, thereby, transfer a tiny amount of energy ($\mathcal{O}(\mathrm{keV})$) to the nucleus (see chapter 2). The expected recoil-energy spectrum is featureless and exponentially decaying. Large experimental efforts are required to be able to observe these tiny recoil energies.

The Cryogenic Rare Event Search with Superconducting Thermometers (CRESST-II) experiment aims to detect Dark Matter via nuclear recoils in scintillating $CaWO_4$ crystals (see chapter 3). In a particle interaction a large fraction of the energy deposited in the crystal is converted into heat which is recorded by a sensitive thermometer. Simultaneously, a small amount of energy is converted into scintillation light, whereby the ratio of light to heat – the light yield – depends on the kind of interacting particle. This light is detected by a separate detector and allows to discriminate signal (nuclear recoils) from background (electron recoils) on an event-by-event basis. Thus, each event consists of the collection of both, a pulse in the phonon detector (heat) and in the light detector (scintillation light).

For five modules the data collected during the ~ 2 years of CRESST-II phase 2 are analysed starting from the raw pulses. The steps required to analyse the recorded pulses and to extract the energy information via a template fit are discussed in chapter 4. All pulses where one or both of the detectors were not fully operational or where this fit algorithm fails, have to be removed. The parameters and methods applied to remove invalid events are discussed in chapter 5. For the most generic cut based on the RMS parameter of the template fit a new automatic data-driven method is developed and applied in the present work.

Pulses which feature a shape different from the one expected for interactions in the absorber crystal are another type of background. To be able to remove these events efficiently down to

the energy threshold of the detector artificial neural networks (ANN) are applied (see chapter 6). Thereby, a weighted non-linear sum of several input parameters is calculated to output a decision parameter. In order to result in a meaningful output the ANN has to be trained with pulses of known type. A pulse simulation method is developed and applied within the present work. The combination of two ANNs trained slightly differently allows to efficiently discriminate the different pulse classes in both, simulation and data. Thus, for the first time machine-learning algorithms have successfully been applied for a pulse-shape analysis in the cryogenic detectors of CRESST.

The results of the raw-data analysis are further processed in the high-level analysis to obtain information about the WIMP-nucleon cross section. Therefore, first the region where nuclear recoils are expected to show up has to be identified (see chapter 7). In the light yield - energy plane different horizontal bands are observed and this information is used to define an acceptance region, where a high signal and, simultaneously, a low background contribution is expected. Based on the observed number of events inside this region of interest an exclusion limit on the WIMP-nucleon cross section is obtained by Yellin's one dimensional optimum interval method (see chapter 8).

The results of the five modules analysed are presented and discussed in chapter 9. For three modules an excess of events with low light yield is observed, which is most probably caused by an unknown background contribution related to the phonon-detector design (see section 9.6). However, for the two modules TUM40/Michael and Lise/Enrico exclusion limits are obtained from low-threshold analyses. In particular, the excellent performance of the latter module leads to a sensitivity down to Dark Matter particle masses of $0.5\,\mathrm{GeV}/c^2$, which is a novelty in the direct Dark Matter search community. Simultaneously, for Dark Matter particle masses smaller than $\sim 1.7\,\mathrm{GeV}/c^2$ a world leading exclusion limit is obtained, showing the great potential of low-threshold detectors for low-mass Dark Matter searches.

Zusammenfassung

Die Suche nach dem Ursprung der Dunklen Materie ist eine der bedeutendsten Herausforderungen der modernen Physik. Von mehreren astronomischen Beobachtungen gibt es Hinweise darauf, dass Dunkle Materie zu allen Zeiten und auf allen Längenskalen des Universums vorhanden war und ist (siehe Kapitel 1). Seit der exakten Messung der kosmischen Hintergrundstrahlung durch das Satellitenexperiment Planck ist bekannt, dass das Universum buchstäblich dunkel ist: $\sim 68.5\,\%$ des gesamten Energieinhalts des Universums sind als die sogenannte "Dunkle Energie" vorhanden, weitere $\sim 26.6\,\%$ als kalte Dunkle Materie und nur $\sim 4.9\,\%$ als die uns bekannte Form von baryonischer Materie. Interessanterweise erfüllt kein Teilchen aus dem Standardmodell der Teilchenphysik (SM) alle Voraussetzungen für einen Kandidaten der Dunkle Materie. Daher sind alle oben erwähnten astronomischen Beobachtungen ein Hinweis auf Physik jenseits des SM.

Sogenannte "WIMPs" (Weakly Interacting Massive Particles) sind ein gut motivierter Kandidat für Dunkle Materie, der von mehreren Theorien vorhergesagt wird. Die bekannteste Klasse davon sind die supersymmetrischen Erweiterungen des SM. Durch das sogenannte "WIMP-Wunder", d.h. die Tatsache, dass die Restdichte für ein thermisch erzeugtes schwachwechselwirkendes Teilchen mit einer Masse von $\gtrsim 30\,\mathrm{GeV}/c^2$ in der Größenordnung der beobachteten Dunkle Materie Dichte liegt, haben diese Teilchenkandidaten große Beachtung bekommen. Zusätzlich sagen weitere Theorien auch WIMP-ähnliche Teilchen mit Massen in der Größenordnung von $\mathcal{O}\left(1\mathrm{GeV}/c^2\right)$ voraus.

Die vorliegende Arbeit wurde im Rahmen eines Experiments zur direkten Suche nach Dunkler Materie durchgeführt. Dabei wird angenommen, dass das WIMP an einem Kern streut und einen Teil seiner Energie (im niedrigen keV-Bereich) auf selbigen überträgt. Das erwartete Rückstoßspektrum weist neben einem exponentiellen Abklingen mit ansteigender Energie keine signifikante Strukturen auf (siehe Kapitel 2). Um diese kleinen Rückstoßenergien messen zu können, sind große experimentelle Anstrengungen notwendig.

Das CRESST-Experiment benutzt für den Nachweis von Kernrückstößen szintillierende $CaWO_4$-Kristalle (siehe Kapitel 3). Während einer Teilchen-Wechselwirkung wird der größte Teil der im Kristall deponierten Energie in Wärme (Phononen) umgewandelt, die durch ein sehr sensitives Thermometer nachgewiesen werden. Gleichzeitig entsteht auch eine kleine Menge an Szintillationslicht, das mit einem separaten Lichtdetektor gemessen wird. Das genaue Verhältnis von Licht zu Wärme – der sogenannte "Light Yield" – hängt dabei von der Art des wechselwirkenden Teilchens ab. Auf Basis des Lichtsignals ist es möglich, für jedes einzelne Ereignis zu bestimmen, ob es ein Untergrund- (Stoß an der Elektronenhülle) oder ein mögliches Signalereignis (Kernrückstoß) ist. Daher wird für jede Wechselwirkung sowohl das Wärme- als auch das Lichtsignal für die nachfolgende Datenanalyse gemeinsam gespeichert.

In der vorliegenden Arbeit werden die Daten von fünf Modulen, die in den zwei Jahren Laufzeit von CRESST-II Phase 2 betrieben wurden, analysiert. Dabei startet die Analyse mit den aufgezeichneten Rohpulsen. Die verschiedenen Schritte der Rohdaten-Analyse und insbesondere die Methode zur Bestimmung der Energieinformation sind in Kapitel 4 erklärt. Letztere erfolgt über das Anpassen eines Musterpulses an die gemessene Signalkurve. Pulse,

die in einer Zeitperiode aufgezeichnet wurden, in der einer oder sogar beide Detektoren nicht voll funktionstüchtig waren oder für die die Bestimmung der Energieinformation fehlgeschlagen ist, müssen für die weitere Analyse aussortiert werden. Die dafür benutzten Parameter und die auf ihnen basierenden Methoden sind in Kapitel 5 näher erklärt. Dabei wurde im Rahmen der vorliegenden Arbeit das allgemeinste Selektionskriterium, basierend auf der Abweichung von gefitteter und gemessener Pulsform, entwickelt und auf die untersuchten Detektoren angewandt.

Auch jene Pulse, die eine andere Form aufweisen als die für eine Wechselwirkung im Absorberkristall erwartete, müssen vom Datenset entfernt werden. Dies soll dabei möglichst effizient auch bis zur Energieschwelle des jeweiligen Detektors erfolgen. Daher werden künstliche neuronale Netze eingesetzt (siehe Kapitel 6). Diese Netze berechnen auf nicht-lineare Weise aus mehreren Eingangsparametern eine gewichtete Summe und geben diese aus. Damit diese Entscheidungsvariable sinnvoll für eine Pulsformanalyse genutzt werden kann, müssen die neuronalen Netze vorher mit Pulsen bekannter Art trainiert werden. Im Rahmen der vorliegenden Arbeit wurde eine Simulationstechnik entwickelt und angewandt, um diese Pulse zu erzeugen. Die Kombination von zwei dieser Netze ermöglich es sowohl in simulierten als auch gemessenen Daten eine effiziente Bestimmung der Pulsklasse durchzuführen. Damit wurden zum ersten Mal Maschinenlernalgorithmen erfolgreich für eine Pulsformanalyse in den kryogenen CRESST-Detektoren angewandt.

Die Ergebnisse der Rohdatenanalyse werden in einer weiterführenden Analyse benutzt, um die Wechselwirkungsstärke von WIMPs mit Kernen zu bestimmen oder einzuschränken. Dafür muss allerdings zuerst die Region, in der Kernrückstöße erwartet werden, bestimmt werden (siehe Kapitel 7). Wenn der "Light Yield" gegen die Rückstoßenergie aufgetragen wird, werden nahezu horizontale Bänder für die verschiedenen wechselwirkenden Teilchen beobachtet. Basierend auf diesem Wissen wird die Akzeptanzregion so definiert, dass in ihr nur eine kleine Anzahl an Untergrundereignissen erwartet wird und gleichzeitig möglichst viel der erwarteten Signalregion abgedeckt wird. Anschließend wird die Anzahl der tatsächlich beobachteten Ereignisse in dieser Akzeptanzregion bestimmt und mit der eindimensionalen Interval-Methode von Yellin statistisch ausgewertet, um eine obere Grenze für die Wechselwirkungsstärke von WIMPs und Kernen zu erhalten (siehe Kapitel 8).

Die Ergebnisse der fünf analysierten Detektormodule werden in Kapitel 9 dargelegt. Für drei dieser Module wird ein Überschuss an Ereignissen in der Akzeptanzregion festgestellt. Dieser Überschuss ist allerdings höchstwahrscheinlich durch einen noch unbekannten Untergrundprozess hervorgerufen, der von dem Detektordesign der drei untersuchten Module abzuhängen scheint (siehe Abschnitt 9.6). In den verbleibenden zwei Modulen TUM40/Michael und Lise/Enrico hingegen ist kein solcher Überschuss feststellbar, und deshalb können obere Grenzen von dezidierten Niederschwellenanalysen angegeben werden. Die hervorragende untere Detektorschwelle von 0.3 keV im Phonondetektor Lise ermöglicht es, eine Sensitivität bis zu Teilchenmassen von $0.5\,\mathrm{GeV}/c^2$ der Dunklen Materie zu erzielen, was eine Neuheit für Experimente zur direkten Suche nach Dunkler Materie darstellt. Gleichzeitig wird für Teilchenmassen der Dunklen Materie unterhalb von $\sim 1.7\,\mathrm{GeV}/c^2$ mit diesem Ergebnis eine neue weltweit führende Ausschlussgrenze erreicht, was das großartige Potential derartiger Detektoren für Niederschwellenanalysen zur Suche nach leichter Dunkle Materie bestärkt.

Contents

I Hunting Dark Matter with CRESST

II Raw Data Analysis

III High Level Analysis

Part I

Hunting Dark Matter with CRESST

1 Evidence and Candidates for Dark Matter

In 1933 Fritz Zwicky published his famous paper "Die Rotverschiebung von extragalaktischen Nebeln" where he explained, for the first time, a phenomenon by a possible existence of *Dark Matter* [1]. Zwicky observed in the Coma cluster that the mean matter density must be at least 400 times bigger than the expectation from the luminous matter to describe the measured velocity distribution. Thus, he was among the first to indicate that luminous matter only contributes a minor part to the total matter density whereas a large fraction of it consists of Dark Matter which cannot be detected via emission, absorption, or reflection of electromagnetic waves. The term Dark Matter was already introduced by Jacobus Kapteyn in 1922 for matter only observable through the kinematics of celestial bodies [2].

1.1 Evidence for Dark Matter

Today there is overwhelming evidence for the existence of Dark Matter based on several astrophysical observations discovered in the years after Zwicky's proposal. On all time scales in our universe, beginning with the primordial nucleosynthesis to the moment of the last electron-photon scattering when the *Cosmic Microwave Background* (CMB) radiation was released ($\sim 380\,000$ years after the Big Bang) up to our present universe, Dark Matter is necessary to explain the observed effects. Simultaneously, hints for Dark Matter exist on all astronomical length scales, starting with individual galaxies up to the largest scales of our universe visible in the CMB.

1.1.1 Rotation Curves of Galaxies

On small cosmological scales evidence for Dark Matter can already be found within an individual galaxy. With the measurement of the Doppler shift of, e.g. the 21 cm hydrogen line it is possible to derive the orbital velocity of stars as a function of the distance to the respective galactic center. According to newtonian dynamics the distance dependent velocity $v_{\mathrm{rot}}(r)$ is given by

$$v_{\mathrm{rot}}(r) = \sqrt{\frac{GM(r)}{r}}, \tag{1.1}$$

where r is the radial distance and G the gravitational constant. $M(r)$ is the total mass contained inside the orbit of the observed object at radius r since masses outside of this orbit do not contribute to the gravitational force. In general, the Virial Theorem can be used to infer the

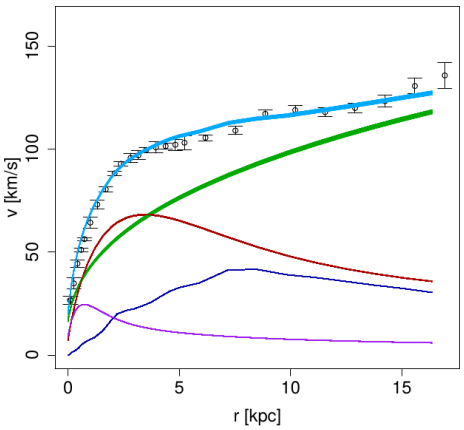

(a) *Rotation curve of M33 taken from [4].*

(b) *Optical image of M33 taken from [5].*

Figure 1.1: *The circular velocity distribution of the Triangulum Galaxy (M33) is measured up to radii r of ~ 16 kpc as depicted in (a). This measurement (black data points) is compared with proposed rotation curves of the major mass components of M33 [4]. It is observed, that for large r an almost constant velocity value is measured, which, however, is not explainable solely with baryonic mass components. The expected circular velocity contribution of the inner (purple) and outer (red) stellar components as well as the contribution of the gas (dark blue) are included. The discrepancy between measured and expected curve is only resolved when a Dark Matter halo (green line) is added. In this case, the quadratic sum of all expectations (light blue line) describe the measured data points well. In (b) an optical image of the stellar halo of the spiral galaxy M33, which is part of the Local Group and located at ~ 850 kpc distance, is shown.*

potential energy from the kinetic energy of a system. Furthermore, depending on the galaxy type, $M(r)$ can be estimated with known empirical correlations between mass and luminosity, e.g. the Tully-Fisher relation for spiral galaxies [3].

The measured rotation curves of galaxies, which describe the orbital velocity $v_{\mathrm{rot}}(r)$ as a function of the distance r to the galactic center, show discrepancies with respect to the expectations solely based on the observed luminous matter distribution. In spiral galaxies (e.g. M33) typically the majority of the luminous matter is clustered in the center (bulge) region with a radius R_0. Therefore, the expectation for the rotation curve is a rise of the velocities up to distances of R_0 due to the increase of the total mass. According to equation 1.1 a decrease $v_{rot}(r) \propto 1/\sqrt{r}$ is expected for objects with larger radii $r > R_0$. However, observations of many galaxies show that $v_{rot}(r)$ is roughly constant for large distances.

As an example, in figure 1.1a the measured rotation curve (black data points) of the Triangulum Galaxy (M33) is shown [4, 6]. For radii r starting from ~ 5 kpc up to ~ 16 kpc an almost constant (or even slightly increasing) circular velocity value is observed. Additionally, an optical image of the stellar halo of the spiral galaxy M33, which is part of the Local Group and located at a distance of ~ 850 kpc [7], is depicted in figure 1.1b. Since the major linear diameter of the stellar halo of M33 is 16.09 kpc [7] a decrease proportional to $1/\sqrt{r}$ is expected for $r \gtrsim 8$ kpc. Thus, the observation of an almost constant velocity at higher radii r is a hint

for Dark Matter.

In [4] the velocity data is decomposed into four different major mass components potentially contributing to the total mass of the galaxy and also included in figure 1.1a. First, the expected velocity contributions of the inner (purple) and outer (red) stellar components as well as of the intergalactic gas (dark blue) are drawn. Only when a Dark Matter halo (green) is included, the data points are described well by the combined model (light blue). Thereby, the circular velocity contribution of each component is added in quadrature to obtain the proposed combined rotation curve. In particular the measured behaviour of constant or slightly increasing velocities at large radii ($r \gtrsim 5\,\mathrm{kpc}$) are explained with the proposed components. Thus, the total mass of the galaxy consists of more than the luminous matter, i.e. Dark Matter. The fraction of Dark Matter in the galaxy is increasing with distances and dominates at larger scales since luminous matter clusters at small distances.

Another attempt to describe the observed rotation curves of galaxies are *MOdified Newton Dynamics* (MOND) theories [8]. These theories suggest that the well-known newtonian dynamics are at large scales not valid anymore and have to be modified to explain the observation. Since large scales correspond to low accelerations, the idea of these theories is the introduction of a new physical constant a_0 with the dimension of acceleration to explain the observed rotation curves without Dark Matter. For accelerations lower than a_0 new MOND physics has to be applied while for larger accelerations the well-known physics are approximately restored. Thus, the constant a_0 marks the borderline between newtonian dynamics and new physics, similarly to $\hbar$ or c in quantum physics or relativity theory.

1.1.2 Mass Density in Galaxy Clusters

Galaxy clusters consist of thousands of galaxies that are gravitationally bound to each other as, e.g. our galaxy, the Milky Way, is part of the Local Group. Also in galaxy clusters hints for the existence of Dark Matter are found.

According to Albert Einstein's general relativity theory, the presence of mass distorts space and, therefore, the path of a light beam. A massive object, e.g. a galaxy cluster, in the line of sight between the earth and distant objects can deflect the light from these objects in the background. Thus, the mass density profile in galaxy clusters can be calculated using this effect. After the postulation of general relativity in 1916 the gravitational lensing effect was observed for the first time during a solar eclipse in 1919 [9]. Meanwhile, it became clear, that there exist three classes of gravitational lensing namely the strong lensing, the weak lensing and the microlensing effect.

As depicted in figure 1.2 the strong gravitational lensing effect creates Einstein rings, i.e. arc-shaped images of the same object [11]. The bright objects in the foreground are galaxies gravitationally bound inside the galaxy cluster "Abell 2218". However, the light of the objects behind the cluster is bent due to the large mass of the cluster acting as gravitational lens.

In the case of the weak gravitational lensing effect the distortions of the background sources are much smaller. Therefore, they can only be observed statistically when analysing a large number of objects. Without gravitational lensing the shapes and orientations of galaxies follow a certain distribution. If there is a massive object in the line of sight, the measured distribution deviates from the former one revealing the existence of a lens.

Figure 1.2: *Image of the galaxy cluster "Abell 2218" taken by the Hubble space telescope [10]. The bright objects in the foreground are galaxies gravitationally bound inside the cluster. The arc-shaped structures are images of objects behind the cluster distorted by the large mass acting as strong gravitational lens. Credit: NASA, ESA, A. Fruchter and the ERO Team (STScI, ST-ECF)*

For the microlensing effect the distortions are even fainter and no single observation can confirm that microlensing is occurring. Instead, a measurement campaign has to be carried out, where the light curve of different objects is monitored over long time periods. A rise and fall of a source brightness over time is the signature of the microlensing effect.

Additionally, with lensing effects the mass profile and the gravitational mass of the massive object can be obtained. These results solely achieved by gravitational observations are compared to estimations based on the luminosity. Also lensing in galaxy clusters shows a discrepancy between luminous and gravitational mass and, thus, is another hint for Dark Matter.

Strong evidence for Dark Matter is found in the Bullet Cluster [12, 13]. It was discovered that the observed galaxy cluster is an active merger of two smaller clusters. During the collision the two main components of the clusters – stars and interstellar gas clouds – were separated. The stars hardly interact with each other while the interstellar medium experiences a friction. Therefore, the stars leave the center of the system faster than the gas which explains the observed separation. In addition, due to the friction the gas heats up, which leads to an emission of X-rays. The separation can be seen in figure 1.3, where an image taken in the visible spectrum (left) is compared to one obtained by an X-ray satellite (right). In a galaxy cluster the interstellar gas contributes much more to the total mass than the individual stars [14]. Thus, one would expect that the matter distributions measured by gravitational lensing (green overlay in figure 1.3) are peaking where the gas resides and not in the outer regions containing the stars. The measured mass distribution is in contrast to this expectation and shows that the majority of the matter was not affected by the collision.

Therefore, it becomes clear that Dark Matter significantly contributes to the total mass of the galaxy cluster. Furthermore, the observation of the Bullet Cluster strongly disfavors MOND theories, since these theories cannot explain such a behaviour [12].

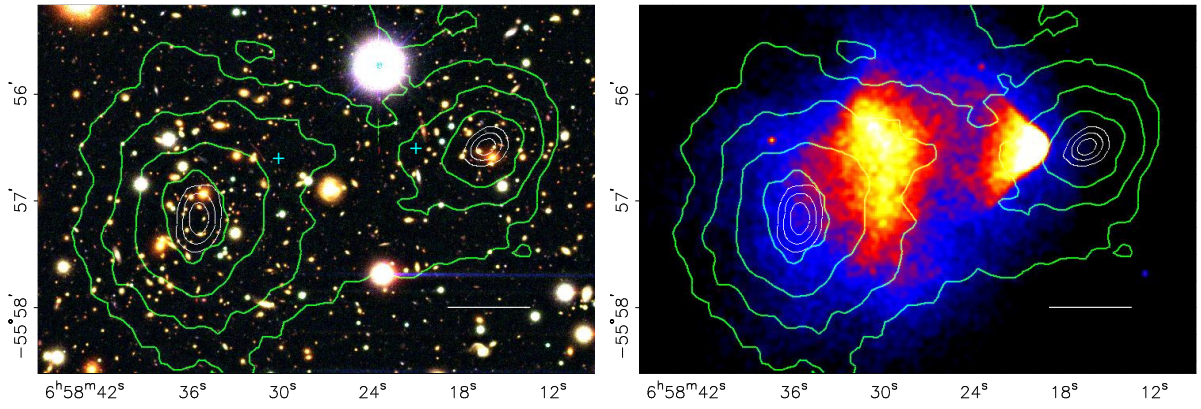

(a) Visible spectrum *(b) X-ray spectrum*

Figure 1.3: *Images of the Bullet Cluster in the visible (left) and X-ray (right) spectrum. The X-rays are emitted by the interstellar plasma heated up during the collision of the two merging clusters. Overlaid in both pictures are the contour lines of the gravitational potential (measured by weak gravitational lensing). It can be seen that there are two distinct gravitational centers, which do not locally coincide with the two centers of the plasma. This is seen as a "direct" observation of Dark Matter. Image taken from [12].*

Since the discovery of the Bullet Cluster several other galaxy mergers have been found (see, e.g. [15] and references therein). For some time there were controversial results in one of these clusters called "Abell 520" which seems not to be explainable with the standard cosmological model containing Dark Matter [16]. Further investigations with longer exposure and different instruments were performed and in the end no evidence that Abell 520 contradicts the collisionless Dark Matter scenario was found in these studies [15]. In summary, all observations in galaxy mergers hint again towards Dark Matter and furthermore can be used to limit the self-interaction cross section of Dark Matter [15].

1.1.3 Cosmic Microwave Background

In 1964 Penzias and Wilson discovered the Cosmic Microwave Background (CMB) radiation, which exhibits the best black body spectrum ever measured [17]. The temperature of this radiation is measured to be $T = 2.725\,\mathrm{K}$ and it was found that it penetrates the universe isotropically. Imprinted in the temperature spectrum are tiny fluctuations ($\frac{\Delta T}{T} \approx 10^{-5}$) which are correlated with cosmological parameters.

In figure 1.4 an all-sky map of these temperature fluctuations as measured by the Planck satellite experiment is depicted [18]. The color-coding visualizes the tiny temperature fluctuations ($\frac{\Delta T}{T} \approx 10^{-5}$) of the different regions in the sky. From these temperature fluctuations all relevant parameters of the standard cosmological ΛCDM model can be derived precisely[1]. In 2014 the Planck Collaboration published their first results which stated that the Cold Dark

[1] In this model the dark energy (Λ) and Cold Dark Matter (CDM) contributions dominate the energy content of the universe. Thereby, cold means Dark Matter particles, that were non-relativistic during their respective freeze-out.

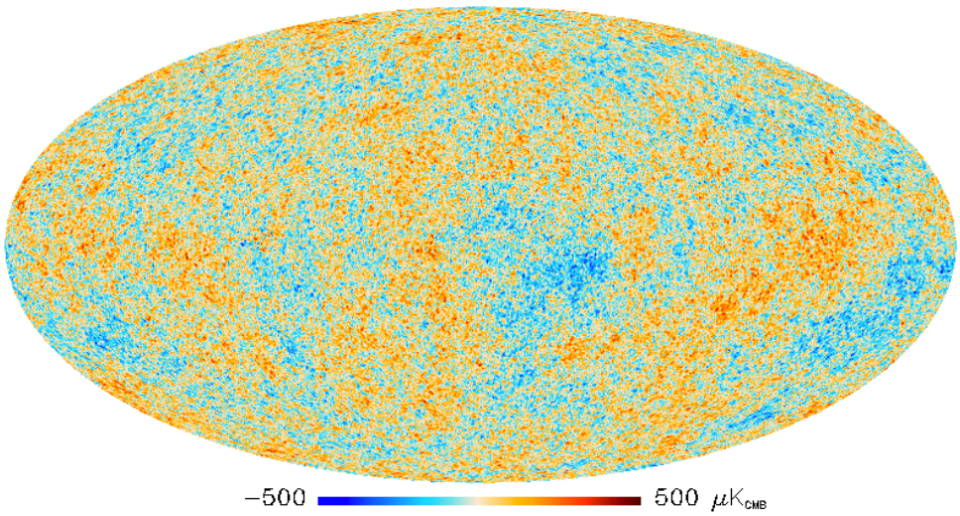

Figure 1.4: *All-sky CMB image measured by the satellite experiment Planck [18]. Color-coded are the tiny temperature fluctuations ($\frac{\Delta T}{T} \approx 10^{-5}$). These fluctuations are correlated to cosmological parameters and yield a cold Dark Matter density of ∼26.6 % of the total energy in the universe [19]. Therefore, Planck results show that Dark Matter is the dominant matter contribution in our universe today. Image taken from [18].*

Matter (CDM) density today is ∼26.6 % of the total energy in the universe [19]. Furthermore, the Planck results show, that only ∼4.9 % of the total energy in the universe is made up of baryonic matter, meaning that Dark Matter accounts for five times more energy than the known baryonic matter. The remaining ∼68.5 % are due to the totally unknown Dark Energy leading to the conclusion that most of our universe is literally dark and still unexplained.

1.1.4 Cosmological Structure Formation

Today the observed matter distribution of visible matter and thereby the large scale structure of our universe can be measured for instance with the *Sloan Digital Sky Survey* (SDSS) [20]. These observations lead to the conclusion that we live in a so-called hierarchical universe, in which small structures merge to form larger and larger structures [21]. The seed of all these structures were the tiny disturbances in the Cosmic Microwave Background still visible today. During the evolution of the universe the disturbances evolved and finally led to the observed structures.

Large computer simulations (e.g. *MultiDark Simulation* [22] or *Bolshoi* [23][2]) are the only way to model this time evolution and compare the output with the observed universe. It is found, that baryonic matter is not sufficient to reproduce the observed structure due to the interaction with photons. The latter leads to a photon pressure resulting in a repulsive force hindering the creation of large structures and washing out tiny distortions in the CMB. Thus, a dark component (without interaction with photons) is needed to clump and form structures earlier than baryonic matter. Baryonic matter flows into the gravitational potential of the Dark

[2] The results of these simulations are available in a dedicated database [24].

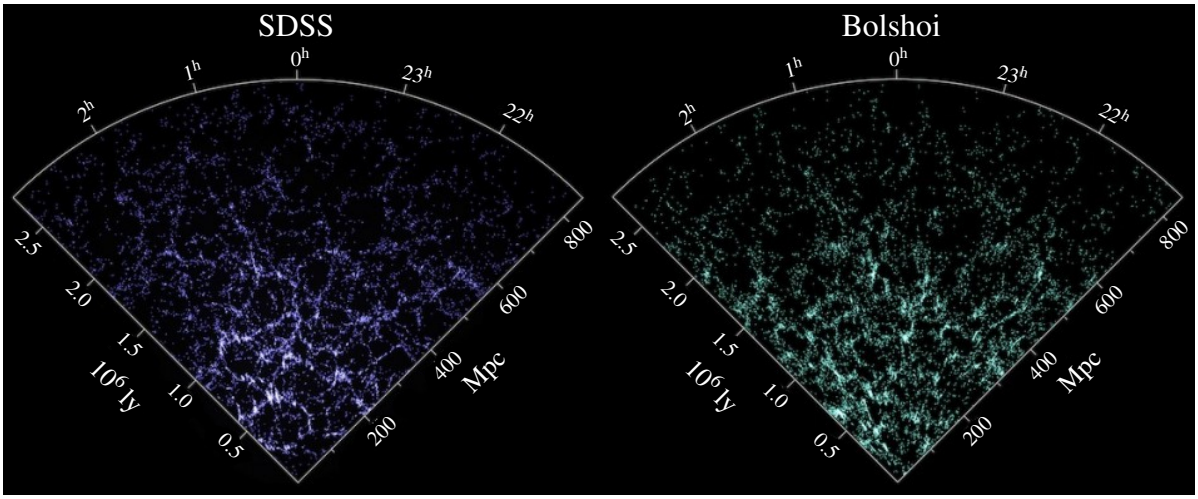

Figure 1.5: *On the left-hand side of the image the matter distribution observed by the Sloan Digital Sky Survey (SDSS) is depicted [20]. On the right-hand side a comparable section of a universe calculated by a computer simulation is drawn [23]. Both matter distributions are statistically similar which supports the model of cold non-baryonic Dark Matter as dominant matter contribution. Image adapted from [25].*

Matter and can clump and create the observed structure. Indeed, the computer simulations predict realistic structures when an amount of Dark Matter in the range of the observed fraction is included.

In figure 1.5 the observed structure determined by SDSS (left) is compared to an output of the Bolshoi simulation (right). Both observed and simulated matter distributions are statistically similar supporting the model that cold non-baryonic Dark Matter is the dominant matter contribution in the observed universe.

In conclusion, from the smallest scales of single galaxies up to the largest scales in the CMB and throughout all times in our universe there is evidence that Dark Matter exists. This naturally raises the question for particle candidates for Dark Matter.

1.2 Dark Matter Candidates

Since the first evidences for Dark Matter were found, ideas exist to explain them by the existence of non-luminous ordinary baryonic matter. Indeed, so-called *Massive Astrophysical Compact Halo Objects* (e.g. brown dwarfs, neutron stars or black holes) are such "dark" baryonic candidates, which were observed among others by the MACHO project [26]. However, it was shown that the total mass of these objects is too low to explain Dark Matter solely [27]. Furthermore, the CMB results of Planck and also structure formation simulations require that the largest fraction of Dark Matter has to be non-baryonic. Thus, in the following, we focus only on this unknown matter form and their particle candidates. Thereby we concentrate on candidates which are well motivated and could be detected directly in an experiment. For a more comprehensive list of Dark Matter candidates refer, e.g., to [28, 29].

1.2.1 Requirements for Dark Matter Candidates

A particle has to fulfill certain requirements to be a valid Dark Matter candidate:

- The Dark Matter particle has to be stable or at least has to have a life time of the order of the time scale of the universe. Otherwise it could not have had an influence at early times (CMB) and could not be still present today (galaxies).
- The particle has to be electronically neutral, otherwise it would interact via electromagnetic interaction and would not be dark. It should not interact via the strong force, which requires that it is color-neutral. The particle has to be massive and it might interact via the weak force or a new force with a similar interaction strength.
- The interaction cross section between the Dark Matter particle and baryonic matter has to be small. Otherwise it would already have been observed. Furthermore, it should be compatible with the current bounds from different searches (e.g. collider or direct).
- The Dark Matter particles had to be non-relativistic and, thus, Cold Dark Matter at the time of the structure formation, otherwise the hierarchical observed universe would not have formed. Hot Dark Matter is expected to wash out the tiny fluctuations in the CMB and, therefore, hinders the creation of anisotropies.
- The existence and the properties of the Dark Matter particle have to be in agreement with the primordial nucleosynthesis and the observed relic abundances of primordial elements. Also the alternations calculated in stellar evolution models have to be smaller than those observed today.

1.2.2 Neutrinos

The Standard Model (SM) of particle physics contains only one particle type that fulfills at least partly the previous requirements for Dark Matter candidates, namely the neutrino. Since the observation of neutrino oscillations it is clear that neutrinos have non-zero masses and since then they were considered as Dark Matter candidates. The current upper limit for the sum of all neutrino masses is set by the Planck collaboration to be $\sum m_\nu \leq 0.23\,\mathrm{eV}$ [19]. Thereby also the energy density Ω_ν of neutrinos is limited, since it is directly related to the mass limit [29]:

$$\Omega_\nu = \frac{\sum m_\nu}{47\,\mathrm{eV}} \lesssim 0.005. \tag{1.2}$$

Despite their huge number, the energy density of neutrinos is much too small too account for the whole Dark Matter energy density ($\Omega_c \approx 0.27$). Furthermore, neutrinos were relativistic (i.e. hot Dark Matter) when they decoupled from other matter and, thus, cannot be the dominant part of Dark Matter.

Both facts taken together exclude SM neutrinos as the main Dark Matter component and as a direct consequence all evidence for Dark Matter has to be considered as indications for physics beyond the Standard Model of particle physics.

One Dark Matter candidate beyond the SM are so-called sterile neutrinos, which have been proposed to solve the problem of neutrino masses [29]. In the SM only left-handed neutrinos have a coupling to the gauge bosons of the electroweak force. By introducing right-handed sterile (i.e., without electroweak interaction) neutrinos, also the masses of neutrinos can be explained by the same mechanism that generates the masses for the quarks and charged leptons. Sterile neutrinos might be good (warm) Dark Matter candidates if their mass is not too big ($m_{\nu_s} \approx \mathcal{O}$ (10 keV)). However, most of the allowed parameter space for sterile neutrinos as Dark Matter candidates has already been excluded mainly by non-observations in indirect searches and astrophysical signals [29]. In a recent article a comprehensive review of keV-scale sterile neutrino Dark Matter is presented [30].

1.2.3 Axions

Many extensions of the Standard Model exist that propose particles, which are viable Dark Matter candidates. Among these are the so-called axions, which where postulated to solve the strong CP-problem [29]. Quantum chromodynamics predicts that the electric dipole moment of a neutron d_n should be $|d_\mathrm{n}| \sim 10^{-16}\,\mathrm{e}\cdot\mathrm{cm}$. However, up to now nobody measured this quantity directly and the current upper limits are almost ten orders of magnitude better ($|d_\mathrm{n}| < 2.9\cdot 10^{-26}\,\mathrm{e}\cdot\mathrm{cm}$ [31]) than the theoretical expectations. Peccei and Quinn introduced an additional symmetry to solve this problem and to explain the required fine tuning [32]. Since this symmetry could not be observed, they concluded that it has to be spontaneously broken. The respective Nambu-Goldstone boson is called axion, a perfectly valid Dark Matter candidate with masses in the range of 1 – 100 μeV/c^2 [29].

1.2.4 Weakly Interacting Massive Particles

Another well motivated Dark Matter candidate is the Weakly Interacting Massive Particle (WIMP). As the name suggests, these particles should be massive ($\gtrsim 1\,\mathrm{GeV}/c^2$) and have an interaction cross section that is typically in the range of the electroweak interaction. The most exciting fact about WIMPs is, that they were postulated to solve problems not related to Dark Matter at all but would have the relic density consistent with that required for Dark Matter. This fact is also called *WIMP miracle* and is explained together with several WIMP candidates in this section.

WIMP Miracle

Similar to baryonic matter, Dark Matter may be produced as a thermal relic of the Big Bang [33]. The evolution of a thermal relic's number density is shown in figure 1.6. Initially all different particles are in thermal equilibrium as the universe is dense and hot. With time evolving the universe cools down to temperatures T. At some point the temperature falls below the Dark Matter particle's mass m_χ. Therefore, the number density of WIMPs becomes Boltzmann suppressed, i.e. drops exponentially with $e^{-m_\chi/T}$. Due to the annihilation with its antiparticle the number of Dark Matter particles would drop to zero (dashed line). In addition to cooling the universe is expanding and, therefore, the Dark Matter density is decreasing. At some point the

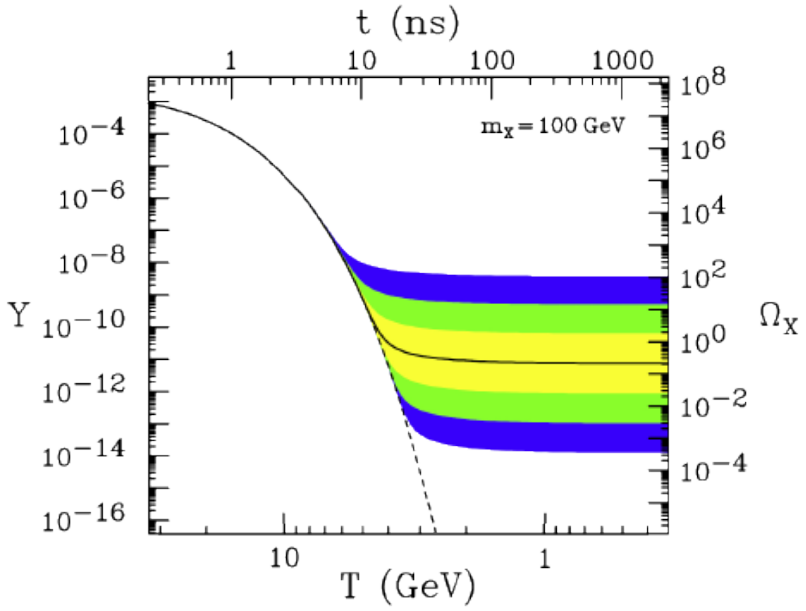

Figure 1.6: *Temperature (x-axis bottom) and time (x-axis top) evolution of the comoving number density Y (y-axis left) and the resulting thermal relic density (y-axis right) for a* 100 *GeV/c^2 WIMP particle. The solid line is for an annihilation cross section that yields the correct relic density, while the dashed line is valid for a particle remaining in thermal equilibrium. The shaded areas are for cross sections differing by a factor of* 10 *(yellow),* 10^2 *(green) and* 10^3 *(blue) from the correct value. Image taken from [29].*

Dark Matter particle gas is so diluted, that the probability for annihilation vanishes and these particles freeze out. The number density of Dark Matter particles asymptotically approaches a constant, i.e. the thermal relic density. The WIMP miracle is now that particles with typical masses $m_\chi \gtrsim 30\,\mathrm{GeV}/c^2$ and cross sections of the electroweak scale ($< 10^{-38}\,\mathrm{cm}^2$) would give the correct relic density observed today.

WIMP Candidates

In supersymmetric extensions of the standard model the well-known set of standard model particles is extended by a set of particles, which have a spin difference of $1/2$ (the supersymmetric partner of a fermion is a boson and vice versa). In most of these theories, due to the so-called R-parity conservation, there exists a lightest stable particle (LSP) which is a good candidate for a WIMP [33].

Not only from supersymmetry, but also from other theories, particles with WIMP properties can arise. For example in models with extra spatial dimensions so-called *Kaluza-Klein states* manifest and the lightest of them would be another appealing WIMP candidate. If the mass of these particles is large enough, it could be able to explain the total amount of Dark Matter in our universe [29].

1.2.5 Asymmetric Dark Matter

In recent years light Dark Matter has gained more and more interest. The Lee-Weinberg bound excludes (thermal) WIMPs lighter than $\sim 2\,\mathrm{GeV}/c^2$ since they would lead to an overclosure of the universe [34]. As explained before, the thermal freeze-out of a particle is directly connected to the particle mass. Lighter particles have a lower annihilation cross section and, therefore, a higher relic density. At $\sim 2\,\mathrm{GeV}/c^2$ the resulting Dark Matter relic density would lead to such a high total density that the universe could never attain its present age.

Asymmetric Dark Matter (ADM) models are a viable option for light Dark Matter candidates typically, though not exclusively, with masses in the range of 1–15 GeV/c^2 [35]. Such models gained much interest when it was observed that the amount of Dark Matter and the amount of baryonic matter only differ by the small factor of five. According to ADM this similarity might be a hint for a strong connection between baryons and Dark Matter. The main idea is that, similar to the baryonic sector where an asymmetry between particles and antiparticles is observed, the present Dark Matter density might be due to a Dark Matter particle-antiparticle asymmetry [35].

Like WIMPs, ADM particles might interact with baryonic matter and, therefore, be detectable in, e.g., a direct detection experiment. ADM models propose the interaction with nucleons via the exchange of a new mediator. If the interaction length is short, which is the case for a heavy mediator, there is no experimental difference between ADM particles and WIMPs, i.e., the usual WIMP analysis and bounds can be applied also for these models [35].

2 Direct Detection of WIMP Dark Matter

A confirmation of the WIMP Dark Matter scenario would be the third evidence supporting the hot big bang cosmology besides the observation of the CMB and big bang nucleosynthesis. There exist different complementary strategies to enlighten the mystery of WIMP Dark Matter.

Figure 2.1 depicts the three different schemes to probe Dark Matter particles. It is assumed that there is some a-priori unknown interaction between Dark Matter particles χ and well-known Standard Model (SM) particles. Dependent on the time direction (arrows) the three different schemes can be depicted in one generic Feynman diagram.

The first approach are collider based searches for Dark Matter, where Dark Matter particles should be produced in a collision of a pair of standard model particles. Unfortunately direct production of WIMP pairs is not observable, as the cross section of Dark Matter is expected to be tiny and, thus, an interaction in the detectors surrounding the beam interaction points is not expected. Therefore, either the simultaneous production of another signal, e.g. a jet, is required to trigger the detector or only indirect production, e.g. via the decay of a heavier particle, can be investigated. The existence of these different production channels leads to a huge variety of possible signatures. In general the signature of Dark Matter at colliders would be events with missing energy in the range of the mass of the new particle. Indeed, e.g. ATLAS and CMS located at the LHC can set upper limits on the WIMP-nucleon scattering cross section, which are especially in the low WIMP mass regions compatible or even better compared to direct Dark Matter searches [36, 37].However, the collider results strongly depend on the particular models, predicting the coupling constants of Dark Matter and standard model particles.

Even the discovery of a new heavy particle at a collider alone is still not a proof that the observed Dark Matter consists of this newly discovered particle. First of all it has to be investigated if the life time of this new particle is stable on the time scale of the universe ($\tau \gtrsim 10^{17}$ s), which is not feasible with collider searches alone. One approach would be a precise measurement of the properties of this hypothetical particle at a collider, which can determine the candidate's relic density [29] . This result has to be compared to the cosmologically observed densities and only if both values agree one could be confident that Dark Matter is made of the particles produced at the collider. Alternatively if the mass of the hypothetical particle would fit to an observed excess in either indirect or direct searches the combination of both might also solve this problem.

The second approach for the detection of Dark Matter are indirect search experiments, which aim to detect secondary standard model particles produced in the annihilation or decay of Dark Matter particles. After the thermal freeze-out the pair annihilation rate is strongly suppressed and, thus, has only negligible impact on the relic density. Nonetheless the process still continues and it might be possible that two WIMPs annihilate into two Standard Model

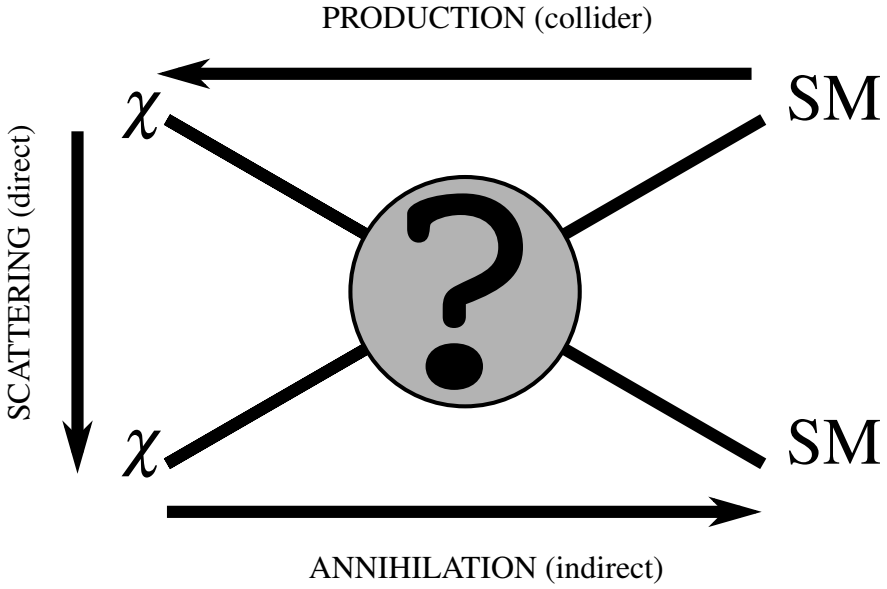

Figure 2.1: *The three different scenarios for the detection of Dark Matter particles χ. The first approach is the* ***production*** *of Dark Matter particles via the collision of Standard Model (SM) particles at colliders. The signature of these events would be a missing energy in the range of the WIMP mass. The second approach is the indirect detection via the* ***annihilation*** *of Dark Matter particles in SM ones. Finally, direct detection experiments aim to detect the* ***scattering*** *recoils of Dark Matter and SM particles.*

particles (see figure 2.1). Another possibility is that Dark Matter particles have a long but still finite lifetime compared to the age of the universe and, thus, could decay into standard model particles.

From an experimental point of view the most crucial and at the same time most difficult task for indirect searches is to exclude that the observed secondary particles have an astrophysical source. The most promising particles to detect with indirect experiments are photons, neutrinos and charged anti-particles like positrons and anti-protons. Photons and neutrinos have the advantage that they are not influenced by magnetic fields inside the galaxies and, thus, would directly point towards the source. This information is used by observing regions where either a large Dark Matter density is expected and/or the expected background contribution is low. Typical search regions are massive and dense objects like the center of galaxy clusters, the galactic center or even the sun as well as dwarf galaxies, which might be dominated by Dark Matter [38]. Due to the deflection inside the strong magnetic fields of our galaxy the source information is lost for charged (anti-)particles.

The advantage of the low interaction rate for neutrinos is simultaneously a drawback, since the detection of this particles is more difficult compared to e.g. γ-rays. Huge Čerenkov detectors located underground (or under-ice or under-water) are necessary to detect the secondary particles, created during an interaction in the material inside the instrumented volume or in the surroundings [38]. The charged secondaries, in particular muons, emit Čerenkov light which in turn can be recorded by the experiments. This light enables them to determine the energy and direction of the secondary particles. Thereby, also the energy and the direction

of the parent neutrino are obtained, since these quantities are directly connected. Interestingly, the non-observation of neutrino fluxes from the sun constrained the scattering cross section of Dark Matter particles with nuclei, which is directly comparable with direct detection searches [39–41].

A compact review about the different indirect detection fields and experiments including recent results can be found e.g. in [42].

The third approach of Dark Matter searches is via the direct detection of scattering recoils of WIMPs with Standard Model particles in the experimental target. This approach is explained in the remaining part of this chapter by first discussing the expected count rates in direct detection experiments in section 2.1. In section 2.2 a generic overview of the different experimental approaches used in this field is given.

The three different detection scenarios provide complementary information about Dark Matter [43]. Colliders can uniquely investigate the interaction with standard model particles, while direct detection provides information about the local density and the velocity distribution of Dark Matter particles. Finally, indirect searches based on astrophysical observations could contribute by tracing the Dark Matter distribution in the sky. The finding of Dark Matter would be a major breakthrough in modern physics and would solve a long lasting mystery.

2.1 Expected Count Rates in Direct Detection Experiments

As far as we know, the Milky Way is an ordinary barred spiral galaxy and, thus, it is valid to assume that our galaxy includes also a halo consisting of Dark Matter particles. This hypothesis is also supported by the measured rotational curve of the galaxy, which is in good agreement with the expectations including Dark Matter. Despite the weak interaction rate of WIMPs, it might happen that a detectable fraction of WIMPs scatter off the nuclei inside the target of a direct detection experiment.

Depending on the mass m_χ of the Dark Matter particle, its relative velocity v with respect to the target and the local Dark Matter density ρ_χ the Dark Matter flux Φ can be calculated as

$$\Phi = \frac{\rho_\chi}{m_\chi} v. \tag{2.1}$$

In a detector this leads to a detection rate R_{det} depending on the number density of target nuclei n_{target} and the WIMP-nucleus cross section $\sigma(v)$:

$$R_{\text{det}} = \Phi \cdot n_{\text{target}} \cdot \sigma(v). \tag{2.2}$$

The number density $n_{\text{target}} = \frac{M_{\text{target}}}{m_N}$ depends on the total target mass M_{target} and the mass of one nucleon m_N. In order to compare different experiments the total expected rate R is normalized by the detector mass and given as

$$R = \frac{R_{\text{det}}}{M_{\text{target}}} = \frac{\rho_\chi}{m_N m_\chi} v \cdot \sigma(v). \tag{2.3}$$

The typical velocity in galaxies is $v \sim 10^{-3}$ c and, therefore, the scattering process can be described by non-relativistic kinematics. WIMPs with such low energies do not probe the substructure of the target nucleus but instead do mainly interact coherently with the complete nucleus. This simplifies the expression of the recoil energy E_R that is transferred to a target nucleus in the center of mass frame. It is given by

$$E_R = \frac{\mu_N^2 v^2}{m_N} (1 - \cos\theta), \tag{2.4}$$

where θ is the scattering angle between the WIMP and the recoiling nucleus and μ_N the reduced mass. The latter is defined as

$$\mu_N := \frac{m_\chi m_N}{m_\chi + m_N}. \tag{2.5}$$

According to equation 2.4 the recoil energy is maximal in the case of $m_\chi = m_N$ and $\theta = \pi$ resulting in

$$E_{R,\max} = \frac{2\mu_N^2 v^2}{m_N} = \frac{1}{2} m_\chi v^2 \approx \frac{1}{2} \left(\frac{m_\chi}{\mathrm{GeV}/c^2} \right) \mathrm{keV}. \tag{2.6}$$

Since the angular distribution is isotropic at low velocities the recoil energy varies between zero and $E_{R,\max} \sim \mathcal{O}(10\,\mathrm{keV})$ for $m_\chi \sim \mathcal{O}(20\,\mathrm{GeV}/c^2)$. Experimentally it is a big challenge to detect such small recoil energies especially in the case of light WIMPs.

2.1.1 Differential Recoil Spectrum

Rather than the total rate (see equation 2.3) the differential recoil spectrum is typically the quantity of interest for Dark Matter searches. Usually it is expressed in terms of counts per kilogram of target material, days of exposure and keV of recoil energy and describes the expected spectral shape of the event distribution.

The differential recoil spectrum can be calculated by differentiation of equation 2.3 with respect to the recoil energy E_R. Up to now it was assumed that all Dark Matter particles have the same velocity v but this simplification is released. A more realistic velocity distribution $f(\vec{v})$ which has to be integrated is considered and, thus, the differential rate is given as

$$\frac{dR}{dE_R} = \frac{\rho_\chi}{m_N m_\chi} \int_{v_{\min}}^{\infty} d^3v\, f(\vec{v}) \cdot v \cdot \frac{d\sigma(\vec{v}, E_R)}{dE_R}. \tag{2.7}$$

The lowest speed $v_{\min}$ of a WIMP that can induce a nuclear recoil of energy E_R can be calculated by

$$v_{\min} = \sqrt{\frac{E_R m_N}{2\mu_N^2}}. \tag{2.8}$$

Formally the upper limit of the velocity integral is infinity but high energetic WIMPs could not be gravitationally bound inside the galaxy leading to a vanishing density. This effect is taken into account later by truncating the integral at the galactic escape velocity v_{esc}.

In part II of the present work methods to efficiently reject background events are presented resulting in a spectrum of nuclear recoil events. This measured spectrum acts in part III as the left hand side of equation 2.7 to gain information about the Dark Matter particle properties. Right now, however, the right hand side of equation 2.7 requires additional inputs, in particular from particle, nuclear and astrophysics, to evaluate the differential rate further.

Particle and Nuclear Physics Inputs

The majority of the particle and nuclear physics inputs are condensed in the differential WIMP-nucleus cross section $\frac{d\sigma}{dE_R}$. Starting from theoretical considerations concerning the microscopic description of the WIMP-quark interaction in the model considered, the final WIMP-nucleus scattering cross section has to be derived. In general, the latter can be separated into two contributions

$$\frac{d\sigma}{dE_R} = \left(\frac{d\sigma}{dE_R}\right)_{\mathrm{SI}} + \left(\frac{d\sigma}{dE_R}\right)_{\mathrm{SD}}. \tag{2.9}$$

The spin independent (SI) term summarizes the scalar interactions, whereas the spin dependent (SD) interaction describes a possible coupling of the Dark Matter particle with the net spin of the target nucleus. For target nuclei with no or only a small net spin, e.g. $CaWO_4$ – the target material of CRESST-II – the spin dependent term can be neglected.

For most models the couplings of WIMPs to neutrons and protons is similar leading to the following form of the spin independent cross section [28]

$$\left(\frac{d\sigma}{dE_R}\right)_{\mathrm{SI}} = \frac{2\,m_N A^2 f_p^2}{\pi v^2} \cdot F^2(q)\,, \tag{2.10}$$

where f_p describes the interaction strength of WIMPs and protons. As a consequence of the coherent scattering where the individual scattering amplitudes of all A nucleons add up in phase the cross section has an A^2 dependency leading to an increasing interaction probability for heavy target nuclei.

The function $F(q)$ is the so-called *form factor*, which describes the influence of the nuclear substructure especially for high momentum transfers $q \equiv \sqrt{|\vec{q}|^2} = \sqrt{2\,m_N E_R}$. For these high energies the corresponding wavelength of the WIMP is of the order of the nuclear radius inducing a partial loss of coherence and, therefore, a decrease in the interaction probability. The form factor is the Fourier transformation of the spatial density distribution of the scattering partners in the nuclei. Different models to calculate form factors for various nuclei exist, but usually – due to its analytical form – the Helm parametrisation is chosen [46, 47]. One disadvantage of this parametrisation is the simplicity of the model so that it might be inappropriate in describing the nuclear density especially for the more complex substructure of heavy elements. Furthermore, the model parameters are often obtained by a fit to many nuclei and, thus, describe various elements with different precision. Therefore, in the present work exactly as in [44] a different parametrisation based on model independent form factors for oxygen and calcium and a Woods-Saxon form factor for tungsten are used.

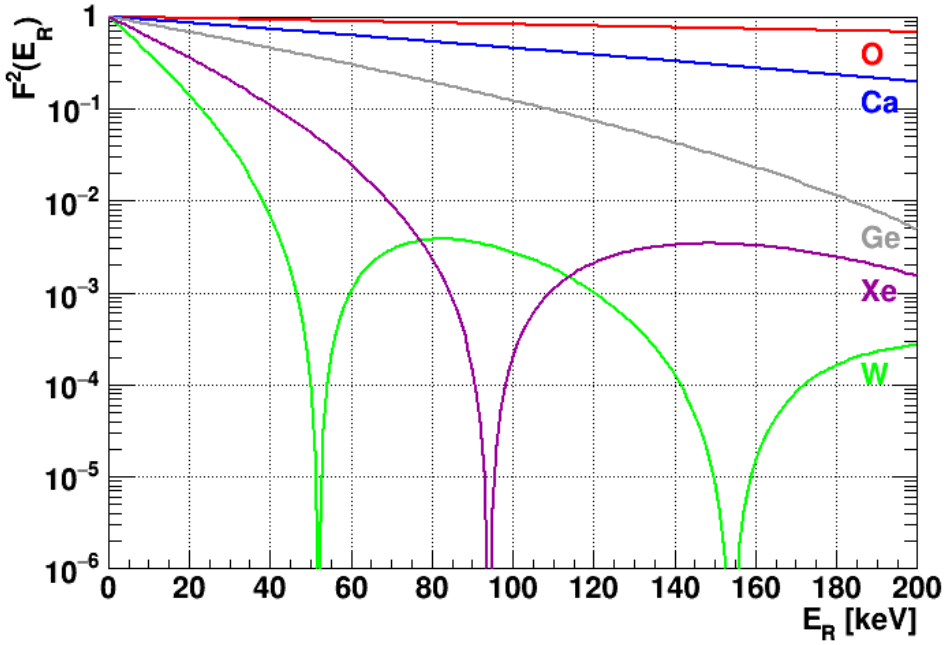

Figure 2.2: *Squared form factor $F^2(E_R)$ for various Dark Matter target materials as a function of the recoil energy E_R. Exactly as in [44] model independent form factors are used for oxygen and calcium, while for tungsten a Woods-Saxon form factor is calculated. For the other target materials the Helm form factor as introduced by Lewin and Smith is applied [45]. For light elements only an exponential decrease of the squared form factor with increasing energy is observed. However, for the heavy elements tungsten and xenon steep drops at distinct energies are observed.*

In figure 2.2 squared form factors $F^2(E_R)$ for various target materials used in direct Dark Matter search experiments are shown as a function of the recoil energy E_R. For oxygen, calcium and tungsten the previously described parametrisation is applied, for all other materials a slightly modified Helm form factor is depicted [45]. For the recoil-energy range shown in figure 2.2 the influence of the form factor is modest for light elements but for heavy elements like xenon or tungsten steep drops at discrete energies are observed.

We can define the total point-like WIMP-nucleus cross section σ_0 by using the result of equation 2.6 and write for the spin independent cross section

$$\left(\frac{d\sigma}{dE_R}\right)_{\mathrm{SI}} =: \frac{\sigma_0}{E_{R,\max}} \cdot F^2(q)\,. \tag{2.11}$$

Obviously the complete influence of the target nucleus (especially the number of nucleons A) is contained in this quantity σ_0 which disqualifies it for comparison between different experiments. Instead, a target-independent normalized *WIMP-nucleon cross section* is defined as [48]

$$\sigma_{\mathrm{WN}} := \left(\frac{1+m_\chi/m_N}{1+m_\chi/m_p}\right)^2 \frac{\sigma_0}{A^2}, \tag{2.12}$$

where m_p denotes the proton mass.

All results reported in the framework of Dark Matter searches are either upper limits on σ_{WN} or allowed parameter regions for a certain Dark Matter mass and cross section combination.

Making use of all the previously discussed particle physics inputs the differential rate defined in equation 2.7 can be rewritten as

$$\frac{dR}{dE_R} = \frac{\rho_\chi}{2 m_\chi \mu_N^2} \cdot \sigma_0 \cdot F^2(E_R) \cdot \int_{v_{\min}}^{\infty} d^3v \frac{f(\vec{v})}{v}. \tag{2.13}$$

Astrophysics Inputs

In the following the integral of the velocity distribution $I(v_{\min}) := \int_{v_{\min}}^{\infty} d^3v \frac{f(\vec{v})}{v}$ is investigated in more detail, since almost all astrophysical inputs are related to this integral.

Starting with the velocity distribution $f(\vec{v})$ of Dark Matter particles, the simplest model assumes that the Dark Matter particles are thermalized. In this case they follow a Maxwell-Boltzmann distribution in the galactic rest frame [48]

$$f_G(\vec{v_G}) = \frac{1}{N} \left(\frac{3}{2\pi w^2} \right)^{3/2} \exp\left(-\frac{3 v_G^2}{2 w^2} \right), \tag{2.14}$$

where $\vec{v_G}$ is the Dark Matter particle velocity in the galactic rest frame, w the root mean square velocity of these particles and N a normalization factor.

For a stationary earth with respect to the galaxy and for WIMP velocities up to infinity the velocity distribution $f_G(\vec{v_G})$ would be exactly the one to use for the evaluation of equation 2.13. Using the definition of the minimal velocity $v_{\min}$ yields for the velocity integral $I(v_{\min})$

$$I(v_{\min}) \propto \exp\left(-\frac{v_{\min}^2}{w^2} \right) \propto \exp(-E_R). \tag{2.15}$$

The evaluation of the velocity integral $I(v_{\min})$ under these oversimplified assumptions gives a rough idea about the spectral shape of the differential rate as function of the recoil energy: Essentially it is the product of the (energy dependent) form factor and an exponentially decaying function.

Two additional effects have to be taken into account to derive a more realistic Dark Matter velocity distribution. As already mentioned earlier the distribution has to be truncated at the escape velocity v_{esc} of the Milky Way, since particles with higher velocities are not gravitationally bound inside the galaxy. By introducing the galactic escape velocity v_{esc} as upper limit of the integration also the normalization constant N has to change. The modified normalization factor is of the form [48]

$$N = \mathrm{erf}(z) - \frac{2}{\sqrt{\pi}} z \exp\left(-z^2\right), \tag{2.16}$$

with

$$z^2 := \frac{3 v_{\mathrm{esc}}^2}{2 w^2}. \tag{2.17}$$

The second correction arises from the revolution of the earth around the sun and the movement of the solar system through the galaxy creating a considerable speed $v_\oplus$ with respect to

the galactic rest frame. For the calculation of the velocity distribution this effect is taken into account by a Galilei transformation [33]

$$v_{\oplus}(t) = v_0 \cdot \left[1.05 + 0.07 \cdot \cos\left(\frac{2\pi\,(t-t_0)}{1\mathrm{yr}}\right)\right], \tag{2.18}$$

where v_0 is the asymptotic value of the rotational velocity of the solar system orbiting around the galactic center ($v_0 \sim 220\,\mathrm{km/s}$ [49]) and t_0 the phase corresponding to June $2^{\mathrm{nd}} \pm 1.3$ days [33]. Thus, the observed WIMP velocity with respect to Earth is the superposition $v_G + v_{\oplus}$.

In [48] it is shown that using these two corrections leads to a velocity integral I of the form

$$I(v_{\mathrm{min}}) = \frac{1}{N\eta} \cdot \left(\frac{3}{2\pi w^2}\right)^{1/2} \cdot \left[\frac{\sqrt{\pi}}{2} \cdot \left[\mathrm{erf}\,(x_{\mathrm{min}} - \eta) - \mathrm{erf}\,(x_{\mathrm{min}} + \eta)\right] - 2\eta \exp\left(-z^2\right)\right], \tag{2.19}$$

where N and z are still defined as before (see equation 2.16 and equation 2.17, respectively). The new quantities η and x_{min} are defined as follows:

$$\eta^2 := \frac{3v_{\oplus}^2}{2w^2} \quad \text{and} \quad x_{\mathrm{min}}^2 := \frac{3v_{\mathrm{min}}^2}{2w^2} = \frac{3m_N E_R}{4\mu_N^2 w^2}. \tag{2.20}$$

Taking all effects together, the complete differential rate can finally be derived:

$$\frac{dR}{dE_R} = \frac{\rho_\chi}{2\,m_\chi\,\mu_N^2} \cdot \sigma_0 \cdot F^2\,(E_R) \cdot I(v_{\mathrm{min}}). \tag{2.21}$$

Additionally, some astrophysical constants are inputs into the differential rate equation. As described earlier, the simplest case of an isothermal spherical halo model for the Dark Matter particles is assumed. This leads to a connection (see e.g. [48]) between the root mean square velocity w of Dark Matter particles and the rotational velocity of the solar system v_0:

$$w = \sqrt{\frac{3}{2}} \cdot v_0 = 270\,\mathrm{km/s}. \tag{2.22}$$

For the galactic escape velocity the conventional value of the direct Dark Matter community of $v_{\mathrm{esc}} = 544\,\mathrm{km/s}$ is assumed in the present work [50].

Also the value of the local Dark Matter density ρ_χ is required for the calculation of the expected spectra. There exist different methods to determine this quantity [51] and, among others, the choice of the Dark Matter halo profile affects the expected density [52]. For reasons of simplicity, i.e. mainly for easy comparison of different experiments, the direct Dark Matter search community conventionally assumes an average value of $\rho_\chi := 0.3 \frac{\mathrm{GeV/c^2}}{\mathrm{cm^3}}$ [53].

Expected Differential Rate

Finally, the expected differential rate of WIMPs scattering off various target nuclei and different masses can be calculated.

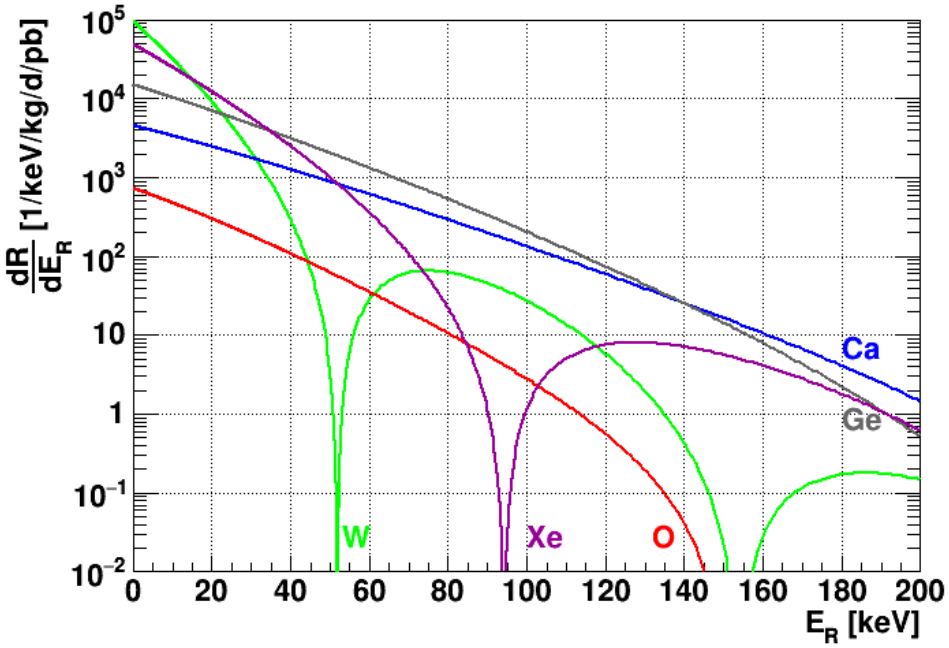

Figure 2.3: *Expected differential event rate of a 100 GeV/c^2 WIMP scattering elastically off nuclei in various target materials. Thereby, an ideal detector without energy threshold and perfect energy resolution as well as a WIMP-nucleon cross section of 1 pb are assumed. The influence of the form factor leads to the drastic drop of the event rate for heavy elements like tungsten and xenon. At small energies the rate increases with the mass squared of the target nucleus, due to the assumed A^2 enhancement of the cross section.*

The expected spectra of a 100 GeV/c^2 WIMP for various target materials are depicted in figure 2.3. The given rates correspond to a WIMP-nucleon cross section of 1 pb and assume an ideal detector without an energy threshold and perfect energy resolution.

At small energies the expected differential rate increases with the mass squared of the target nucleus, due to the assumed A^2 enhancement of the cross section. For the heavy elements xenon and tungsten the shape is completely dominated by the form factor leading to a sharp suppression of the rate at the same distinct energies as observed for the form factor (see figure 2.2). Together with the exponential decay of the rate this limits the energy range of interest to small low energetic regions – e.g. < 40 keV for tungsten – where the expected spectra are featureless.

In figure 2.4 the influence of the WIMP mass on the expected differential recoil spectra of tungsten (solid lines) and oxygen (dashed lines) is shown in the energy range from 0 – 55 keV. Again a WIMP-nucleon scattering cross section of 1 pb and an ideal detector are assumed.

At small recoil energies the expected differential rate in tungsten ($A \approx 184$) is ~ 2 orders of magnitude higher than the one in oxygen ($A \approx 16$). Since this is due to the expected A^2-enhancement of the WIMP-nucleon cross section, it is independent of the given WIMP mass.

For a WIMP mass of 300 GeV/c^2 the expected curve drops towards ~ 50 keV since the form factor plays the dominant role at high recoil energies. Thus, the spectral shape is comparable with the one for 100 GeV/c^2, whereas the total rate is smaller due to the reduced number

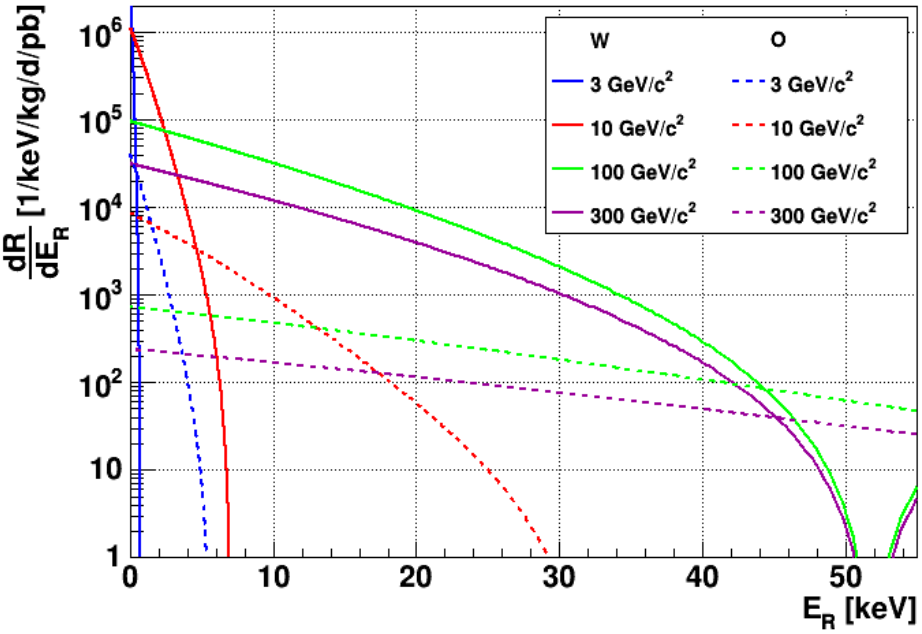

Figure 2.4: *Expected differential spectra for tungsten (solid lines) and oxygen (dashed lines) for different WIMP masses. For high WIMP masses the spectral shape is dominated by the form factor but for lower masses the spectra become steeper and no influence of the form factor is visible. The velocity integral $I(v_{\mathrm{min}})$ as well as the maximum recoil energy $E_{R,max}$ are decreasing with decreasing WIMP mass.*

density. For lighter WIMPs the influence of the form factor strongly decreases since already the decreasing velocity integral $I(v_{\mathrm{min}})$ leads to a strong confinement of the expected recoil energies. The maximal expected recoil energy is strongly affected by the reduction of the WIMP mass and the target material. While for a 10 GeV/c^2 WIMP scattering off tungsten recoil energies of ~ 7 keV are expected, it is only ~ 0.7 keV for a 3 GeV/c^2 WIMP. For oxygen the expected recoil energies are slightly higher, namely ~ 28 keV for a 10 GeV/c^2 WIMP and ~ 5 keV for a 3 GeV/c^2 WIMP. Simultaneously, with decreasing WIMP masses the spectra become steeper and, thus, a higher fraction of the spectra are located in the low energy region.

2.1.2 Detector Effects

Up to now an ideal detector consisting of a single element has been considered for the calculation of the differential rate. This simplification is dropped in this section and the effects induced by a realistic detector are explained.

Multi-Element Target

For a multi-material target, e.g. $CaWO_4$ in CRESST, the total differential rate has to be calculated as the weighted sum of the constituents, where the weights are defined by the mass fractions in the target compound. In figure 2.5 the expected differential rate in a $CaWO_4$

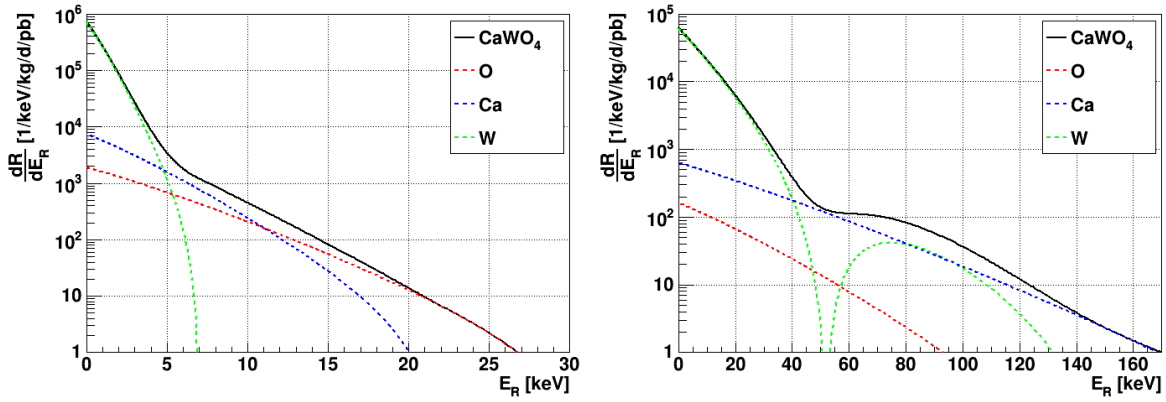

(a) 10 GeV/c^2 WIMP *(b)* 100 GeV/c^2 WIMP

Figure 2.5: *Differential spectrum of $CaWO_4$ and its three components oxygen, calcium and tungsten for two different WIMP masses. In both cases the rate of the single elements is scaled to match the respective mass fraction in $CaWO_4$. Please note the different scaling of x and y-axes in the two subfigures. For a 100 GeV/c^2 WIMP (b) the total spectrum is dominated by scatterings off tungsten while for a 10 GeV/c^2 WIMP (a) the total spectrum is confined to a smaller energy region. Additionally, all three elements contribute: tungsten still dominates the differential rate at low energies whereas calcium and oxygen are important at higher energies. Nonetheless, for both WIMP masses the total spectra drop almost exponentially with increasing energy.*

target is depicted for two different WIMP masses. Also shown are the rates of the single components of $CaWO_4$ but calculated for the respective mass fraction in the compound. For the 100 GeV/c^2 WIMP (b) the total spectrum is dominated by scatterings off tungsten. Only when the form factor plays an important role ($\gtrsim 40$ keV), the calcium fraction becomes relevant. However, at these high energies only a negligible contribution of the spectrum is expected. The situation changes completely for a 10 GeV/c^2 WIMP (a). Here, the total spectrum is confined in a smaller energy region. In addition there are three different energy regions where the different elements contribute. Tungsten still dominates the differential rate but due to its steep drop at ~ 5 keV calcium takes over. At even higher recoil energies ($\gtrsim 11$ keV) oxygen plays the most important role. Nonetheless for both WIMP masses the total spectra drop almost exponentially with increasing energy.

Energy Detection Efficiency

The absolute amount of energy recognized in the detector does not necessarily equal the total amount of energy deposited but may be only a certain fraction of it. In addition, this fraction can depend on the type of the interacting particle. For Dark Matter experiments the energy calibration is often performed with sources inducing electron recoils, e.g. γ-sources, and, thus, the energy scale is denoted as *electron equivalent* energies E_{ee}.

Consequently, for electron recoils the true energy which has been deposited is directly measured ($E_{\mathrm{ee}} = E_R$), while for other particles the measured value is just proportional to the true

recoil energy E_R

$$E_{\mathrm{ee}} = QF_p \cdot E_R. \tag{2.23}$$

The proportionality constant QF_p is called *quenching factor* and depends on the particle type p.

It is shown in the next chapter that in particular for CRESST this efficiency effect is negligible. In the *phonon channel*, used to set the energy scale, the amount of detected energy is hardly particle dependent and, thus, it is valid to assume $QF_p \approx 1$. The clean notation involving E_{ee} is used here but later the distinction between E_{ee} and E_R is dropped.

Energy Resolution and Threshold

Any real detector has a finite energy resolution ΔE which, in general, is dependent on the observed energy E_{ee}. This has to be taken into account by a convolution of the expected recoil spectrum $\frac{dR}{dE_R}$ with $\Delta E(E)$. Here, a Gaussian error of the measured energy is assumed leading to

$$\left.\frac{dR}{dE_{\mathrm{ee}}}\right|_{\mathrm{obs}} = \frac{C}{\Delta E\left(E_{\mathrm{ee}}\right)} \int_0^{\infty} \frac{dR}{dE_R} \exp\left(-\frac{\left(E_{\mathrm{ee}} - E_R\right)^2}{2\Delta E^2\left(E_{\mathrm{ee}}\right)}\right) dE_R. \tag{2.24}$$

The normalization constant C is given by:

$$C = \sqrt{\frac{2}{\pi}} \left(1 + \mathrm{erf}\left(\frac{E_{\mathrm{ee}}}{\sqrt{2}\Delta E\left(E_{\mathrm{ee}}\right)}\right)\right)^{-1}. \tag{2.25}$$

A real detector has a certain energy dependent fraction of events $A\left(E_R\right)$, lying between zero and one, that are accepted. One example is a lower energy threshold E_{th}, below which the deposited amount of energy can not be registered anymore, implying an acceptance $A\left(E_R\right)$ of the form:

$$A\left(E_R\right) = \begin{cases} 0 & E_R < E_{\mathrm{th}} \\ 1 & E_R \geq E_{\mathrm{th}} \end{cases}. \tag{2.26}$$

The accepted differential event rate is, thus, defined as

$$\left.\frac{dR}{dE_R}\right|_{\mathrm{acc}} = A\left(E_R\right) \cdot \left.\frac{dR}{dE_R}\right|_{\mathrm{obs}}. \tag{2.27}$$

The expected event rate R above a given energy threshold E_{th} is obtained via integration of the differential event rate spectra (see figure 2.3) from E_{th} to infinity. In figure 2.6 the event rate R is depicted as function of E_{th} for a $100\,\mathrm{GeV}/c^2$ WIMP and for various materials. Independent of the target material a reduced (i.e. improved) energy threshold leads to an exponential increase of the expected rate. Thus, already a small reduction of the energy threshold results in an appreciable improvement of the expected sensitivity for WIMPs. In particular, a low energy threshold and a good energy resolution are essential for light WIMP searches, since the expected spectrum is steep and, simultaneously, the maximum recoil energy is small.

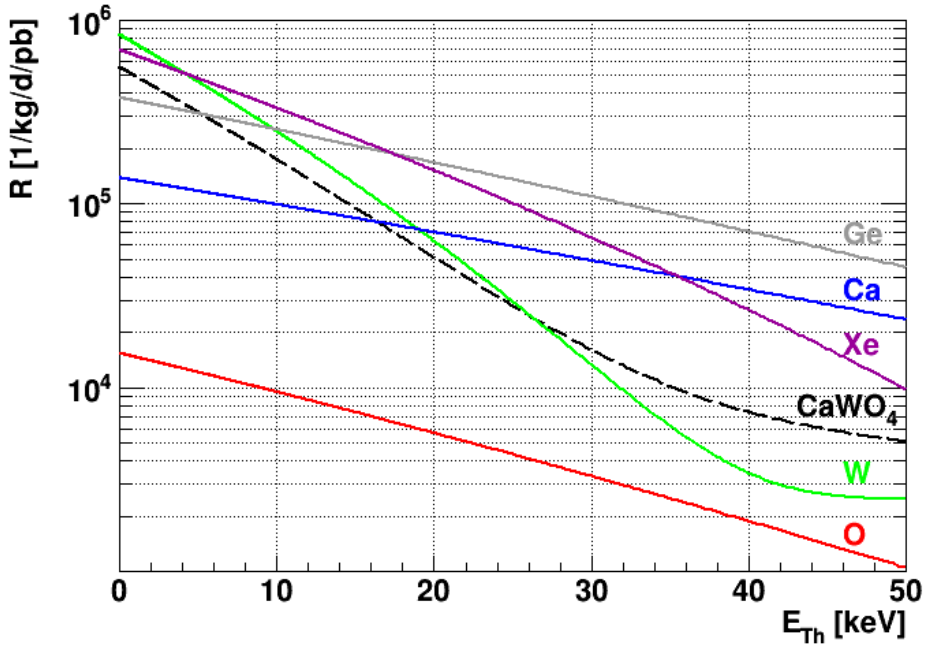

Figure 2.6: *Expected event rate R above a given energy threshold E_{th} of a 100 GeV/c^2 WIMP for different target materials. The rate is obtained via integration of the differential spectra depicted in figure 2.3 from threshold up to infinity. A WIMP-nucleon cross section of 1 pb and a perfect energy resolution are assumed. Independent of the target material a reduced energy threshold leads to an exponential increase of the expected rate.*

2.1.3 Experimental Requirements and Signatures for WIMP Searches

Finally, the main properties of the WIMP interaction rate and the resulting experimental requirements are discussed. Also the different WIMP signatures which might be observable by some of the experiments are explained.

Experimental Requirements

In the last section it is shown, that for WIMPs scattering elastically off nuclei only very low recoil energies of $\mathcal{O}(10\,\text{keV})$ are expected. In addition, the spectrum of recoil energies decreases exponentially with increasing energy and, thus, sensitive detectors with low energy threshold and good energy resolution are a key feature. This is especially important for experiments searching directly for light Dark Matter.

In the last decade a large step in the sensitivity of direct Dark Matter search experiments was achieved. Since none of these experiments found indisputable evidence for Dark Matter, the expected interaction rate must be very low. The exclusion limits on the WIMP-nucleon cross section depend on the expected WIMP mass. Currently the leading exclusion limit is in the order of $\sigma_{\text{WN}} < 10^{-9}\,\text{pb}$ at $\sim 30\,\text{GeV}/c^2$ [54]. Thus, the expected event rate is lower than $R \lesssim 0.001\,\text{kg}^{-1}\,\text{d}^{-1}$, which is only detectable in experiments with a very low background. For

lighter WIMPs the limits are not that stringent but nonetheless the expected event rate is still small.

Especially for high WIMP masses the smallness of the expected rate requires a high total target mass and long measurement times. Furthermore, a careful material selection has to be carried out to prevent radioactive contaminations inside or near the target volume. Additionally, good passive and active background suppression techniques are necessary to be able to detect the sought-for nuclear recoils.

Finally, for coherent spin-independent scattering an A^2-enhancement of the scattering rate is expected. Therefore, in general heavy target materials are beneficial and also in compound targets WIMPs mainly scatter off the nuclei of the heaviest element. However, the maximal recoil energy depends on the reduced target mass and, therefore, for light WIMPs only small amounts of energy might be transferred to the heavy element. Thus, a considerable fraction of the recoil spectrum of the heavy element might not be detectable due to the finite energy threshold of the detector. In such a case also the scattering off lighter target elements might be non-negligible. However, a low energy threshold increases the total expected rate in the detector exponentially and, thus, is a key requirement for low WIMP mass searches.

Signatures of WIMPs

As outlined before WIMPs create a featureless exponential energy spectrum near the energy threshold of the detector. This experimental signature alone is not sufficient to claim the observation of WIMPs if an excess is observed. Typically the background is not very well understood at the low energies and rates in question and, thus, might also contribute to or even completely explain the observed events. Therefore, it is important to define specific signatures to identify true WIMP interactions.

First of all the potential WIMP signal could be detected using more than one target nucleus. This is either possible by more than one experiment with different target materials or with a single experiment employing a compound material (as it is the case for CRESST). In both cases, due to the expected rate and energy spectrum being dependent on the target nucleus, it can be checked whether the potential signal events are consistent with the A^2 expectation of WIMPs or not. In contrast, background sources should hardly feature the same dependency on the target element and the experimental site.

For Dark Matter particles a seasonal variation of the event rate in the detector is expected [56, 57]. The solar system is orbiting around the galactic center leading to a movement towards the constellation Cygnus. Since it is assumed that the WIMP halo is not rotating at all, this motion of the sun and earth together leads to a WIMP wind with a relative velocity of $v_0 \sim 220\,\mathrm{km/s}$ [55]. At the same time the earth is revolving around the sun in a plane tilted by 60° with respect to the galactic plane. The relative velocity of the earth with respect to the WIMP wind will be maximal (minimal) in June (December), when the parallel component of the velocity $v_{||}$ with respect to the solar system's motion is maximal (minimal) (see figure 2.7). This velocity modulation is directly converted into a seasonal rate change due to the integration of the velocity distribution $I(v_{\mathrm{min}})$. However, the modulation amplitude is expected to be small ($\simeq 7\,\%$ [58]) and, thus, high exposures, i.e. high target mass and/or long measurement times, and/or good background suppression methods are required. Under the assumption of

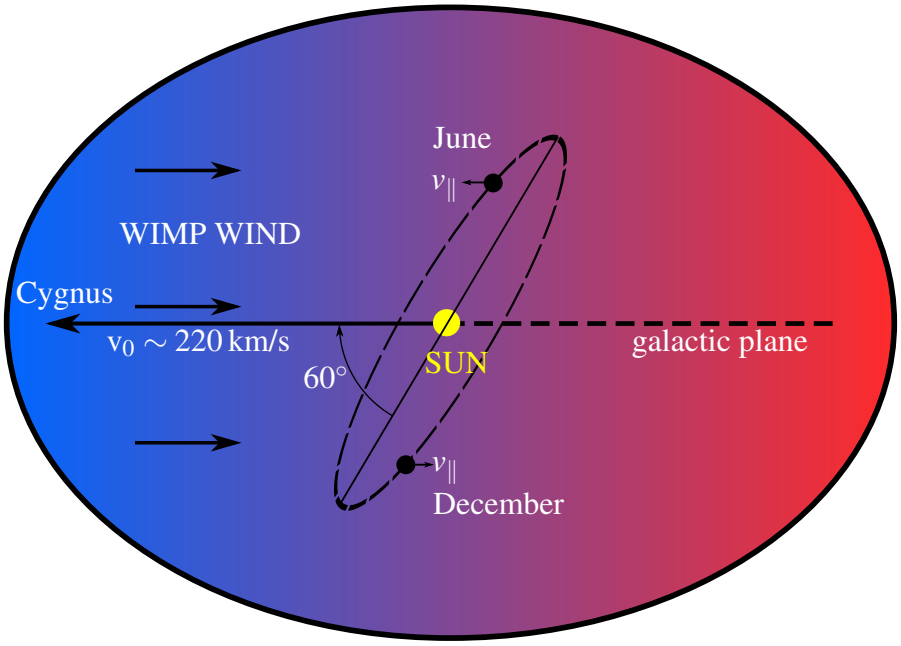

Figure 2.7: *A signature for a Dark Matter particle would be the seasonal variation of the event rate due to the terrestrial rotation around the sun. The solar system orbits around the galactic center moving into the direction of Cygnus with a velocity of $v_0 \sim 220$ km/s [55]. For objects, which move towards (away from) the solar system a blue (red) shift is observed. The rotation plane of the earth around the sun is tilted by $\sim 60^\circ$ with respect to the galactic plane. The maximum rate is expected beginning of June when the anti-parallel velocity component $v_{\parallel}$ of the earth with respect to the WIMP wind is maximal, while the minimum rate should occur in December.*

a non-rotating WIMP halo the expected event rate exhibits a maximum (minimum) in June (December).

Finally, in detectors capable of detecting the direction of the recoiling nucleus, a third possibility arises. As for the rate modulation, due to the motion of the solar system and in particular by the revolution of the Earth a (time dependent) preferred direction for WIMPs is introduced. Therefore, for signal events the recoiling nucleus should point in the direction of the WIMP wind as seen from the laboratory frame. Due to the additional rotation of the earth around its axis, the preferred direction will vary on a 24 h time scale. This specific signal pattern is not expected for background events, which should exhibit a uniformly distributed directionality. Thus, observing such a correlation between the measured recoil direction and the theoretical expectations based on the Earth's motion would be a powerful tool for discriminating WIMP signals from terrestrial background.

2.2 Experimental Approaches for Direct Detection of WIMPs

Three different kinds of signals are used to record recoils in direct detection experiments, namely scintillation, ionization and heat (phonons). If the target material is a scintillator the light created from a particle interaction inside the target can be recorded with photo-sensors. In (semi-)conductors an interaction creates charged carriers (electron-hole pairs) and, thus, the ionization channel is an alternative possibility to observe recoils. The heat signal in the form of phonons can be used in cryogenic detectors as another detection channel.

Some experiments only exploit one of these three effects to record recoils, but the combination of two of these three channels allows to discriminate electron from sought-for nuclear recoil events. This discrimination capability is crucial since in the majority of the experiments electron recoils are the main background source.

In the following several direct detection techniques and experiments are explained.

2.2.1 Liquid Noble Gas Detectors

Liquid noble gases like xenon and argon are widely used target materials for Dark Matter experiments. The main detection channel is the scintillation light produced by an interaction in the target volume, typically detected by an array of photomultiplier tubes (PMT). Some experiments also have a gaseous phase above the liquid one and drift the created electrons with strong electric fields towards the surface of the liquid. There the electrons are extracted out of the liquid into the gas due to the high electric field applied and, thus, create – via the ionization of the gas – a second light signal proportional to the total extracted charge. This signal is recorded by additional PMTs and used for the discrimination of electron and sought-for nuclear recoils.

Detectors which only exploit scintillation light and are solely made of liquid noble gases are called single phase detectors. Examples for experiments using this technique are DEAP [59], MiniCLEAN [60] and XMASS [61]. For the discrimination of electron and nuclear recoil events these detectors totally rely on pulse shape discrimination.

The detectors which record both ionization and scintillation signals are called double phase time projection chambers (TPC). DarkSide [62], LUX [63], PandaX [64] and XENON [65] are examples for this type of liquid noble gas detector.

This technique provides a rather easy scalability of target masses even up to the ton scale and, simultaneously, a good radiopurity. The latter is mainly achieved by a fiducial volume and self shielding, since the innermost volume is protected against radioactivity by the outer volume. Furthermore the possibility of a constant purification of the target liquid reduces the backgrounds further. Due to the large target mass and the low background liquid noble gas detectors play nowadays the leading role in the direct Dark Matter search for high WIMP masses ($\gtrsim 10\,\mathrm{GeV}/c^2$).

Nonetheless, at lower WIMP masses the reachable sensitivity is limited resulting in a steep rise of the obtained exclusion limits. This limitation is mainly caused by the worse energy resolution together with the high energy threshold compared to, e.g., cryogenic detectors.

Additionally, these limitations might hinder a precise measurement of the parameters of a possible WIMP signal.

2.2.2 Cryogenic Detectors

Both the CDMS experiment [66] and the EDELWEISS experiment [67] utilize diodes to search directly for WIMP interactions. Typically these diodes are made of germanium, but also silicon is investigated as target material. In all cases electrodes on the surfaces are used to apply an electric field and, thus, drift charge carriers inside the detectors. Surface events can be vetoed due to the electronic layout of the electrodes leading to a fiducial detector mass (e.g. $\sim 600\,\mathrm{g}$ fiducial mass for a 800 g EDELWEISS detector [68]).

The combination of ionization and heat signal, measured by a sensitive thermometer, allows to discriminate signal events (nuclear recoils) from backgrounds (electron recoils). For the operation of these thermometers cryogenic temperatures are necessary and provided in both experiments by a cryostat.

CDEX [69, 70] and CoGeNT [71] operate p-type point contact germanium detectors[3] to search for Dark Matter particles. In contrast to the germanium diodes explained previously, for these detectors only the ionization signal is read out. Surface events, microphonics and partial charge collection events can be vetoed by pulse shape discrimination leading to a fiducial mass of $\sim$ 330 g for CoGeNT [71] and 994 g for CDEX [70]. However, these detectors are characterized by a low readout capacity and, thus, can achieve low energy thresholds. Consequentially, both experiments are mainly sensitive for light Dark Matter particles with masses below $10\,\mathrm{GeV}/c^2$. While CoGeNT reported on the observation of an annual modulation signal of events near threshold [72] this scenario is clearly excluded by the CDEX results [70]. A more recent re-analysis of the CoGeNT data by a subset of the collaboration also ascribes part of the observed excess events to a surface contamination [73].

CRESST uses scintillating $CaWO_4$ single crystals cooled down to cryogenic temperatures as target material for the direct Dark Matter search. The experiment is explained in detail in the next chapter, which is mainly dedicated to the setup and the detection technique.

All cryogenic experiments are typically characterized by a precise energy scale, an excellent energy resolution and a low energy threshold and, thus, can perfectly explore the low WIMP mass region. Consequently, below $\sim 6\,\mathrm{GeV}/c^2$ cryogenic detectors obtained the world-leading exclusion limits.

A drawback of all cryogenic experiments is the small mass of an individual detector unit ($m \lesssim 1\,\mathrm{kg}$). To get the target mass for a ton-scale experiment a huge number of units has to be combined which also leads to a huge number of readout channels. This will introduce an enormous heat load to the cryostat and has to be considered in the construction phase. Furthermore, data analysis of such large experiments might be time consuming and sophisticated. Therefore, cryogenic experiments are not the first choice to explore the parameter space in the high WIMP mass region. However, if a hint for Dark Matter has been observed by, e.g., a liquid noble gas detector the cryogenic experiments are well suited to clarify and determine

[3] CANBERRA Industries labels their line of p-type point contact germanium detectors BEGe, for **B**road **E**nergy **Ge**rmanium diode.

precisely the properties of this WIMP candidate.

2.2.3 Bubble Chambers

In direct Dark Matter searches bubble chambers had a revival after having been used successfully for decades in accelerator experiments. There have been two collaborations, namely COUPP [74] and PICASSO [75], that tried to detect WIMPs with these chambers filled with superheated liquids. The efforts of both experiments have been merged and form now the PICO collaboration operating such a device in the SNOLAB underground laboratory [76]. An energy deposition inside the target volume leads to a local nucleation of a bubble at the interaction site. Video cameras placed around the detector are triggered by the pressure spike induced by the bubble formation and record the event. The bubble formation process does not allow to determine the amount of energy deposited and, therefore, only the total integrated interaction rate above an energy threshold can be measured. However, since the energy threshold depends on the operating temperature and pressure, it is possible to determine statistically an energy distribution of the interactions [77].

An important property of these detectors is the discrimination ability of the dominant e^-/γ-background and sought-for nuclear recoils. Also the energy loss per unit path length $\frac{dE}{dx}$ required to nucleate a bubble is strongly dependent on the pressure and temperature of the liquid. Thus, it is possible to adjust these operation parameters in such a way that electron recoils – in contrast to nuclear recoils – can not nucleate bubbles and are, therefore, simply not visible [78]. Furthermore, the α-background which is dangerous for bubble chambers can be discriminated via the acoustic emission from bubbles [79].

2.2.4 Novel Experimental Approaches

The field of direct Dark Matter search is very vital and several novel experimental approaches have been discussed and studied. Here only one of these novel techniques is mentioned explicitly: The DAMIC experiment is the first experiment that uses thick, fully depleted Charge-Coupled Devices (CCDs) with an active mass of 0.5 g [80]. In these silicon devices a detection threshold of $40\,\mathrm{eV_{ee}}$ has been achieved. The CCDs are installed in an underground site and after a certain exposure they are read out (in [80] every 40 000 s). X-rays and nuclear recoils are expected to deposit their charge in point like events in the detector, while other particles (e.g. muons, α-particles) produce long tracks. The discrimination between X-rays and nuclear recoils is accomplished basically by a fiducial volume cut, since unlike nuclear recoils low-energetic X-rays are only able to penetrate a few microns into the detector [80].

2.2.5 Seasonal Modulation Search with DAMA/LIBRA

The DAMA/LIBRA experiment [81] uses 25 titanium doped NaI(Ti) crystal scintillators to search for annual modulations of the event rate. Each of these crystals has a mass of 9.7 kg and is read out by two low-background photomultiplier tubes (PMTs) [81]. In total DAMA/LIBRA and its predecessor experiment DAMA/NaI collected an exposure of 1.33 ton years, corresponding to 14 annual cycles.

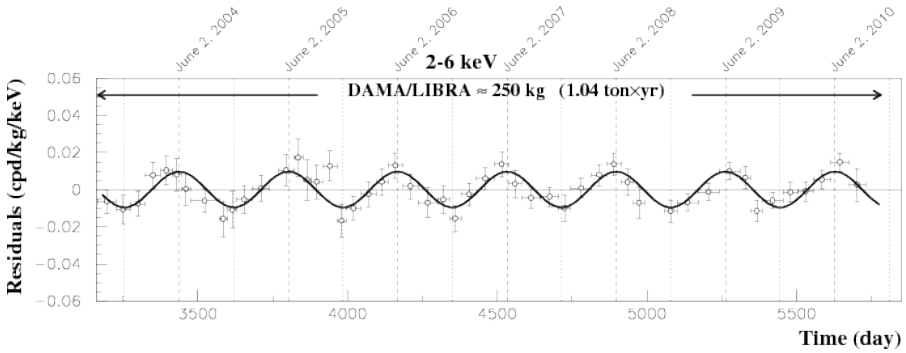

Figure 2.8: *Experimental residual rate of the single-hit scintillation events measured by DAMA/LIBRA-phase1 in the energy range of 2 – 6 keV. Superimposed is a cosinusoidal function $A \cdot \cos(\omega \cdot (t - t_0))$ with a fixed period of $T = \frac{2\pi}{\omega} = 1$ yr and a fixed phase $t_0 = 152.5$ day (June 2nd). The values obtained with an unconstrained fit are given in the text. The dashed vertical lines correspond to the maximum expected Dark Matter signal, while the dotted vertical lines corresponds to the minimum. Image taken from [81].*

In figure 2.8 the measured residual rate (after subtracting the constant background) for the energy region from 2 – 6 keV is shown. The solid black line corresponds to a cosinusoidal function $A \cdot \cos(\omega \cdot (t - t_0))$ with a fixed period of $T_{exp.} = 1$ yr and fixed phase $t_{0,exp.} = 152.5$ day (June 2nd) according to the expectations for Dark Matter. The modulation amplitude A is the central value obtained by best fit on the complete data set. For energies above 6 keV the measured energy spectrum is flat and no annual modulation is observed.

The best fit values of the unconstrained fit yield a period of $T = \frac{2\pi}{\omega} = (0.998 \pm 0.002)$ yr and a phase $t_0 = (144 \pm 7)$ day [81]. The modulation amplitude is determined to be $A = (0.0112 \pm 0.0012)$ counts/ (keV kg day). The statistical significance of this modulation in the combined data set of the two phases is $9.3\,\sigma$.

The modulation parameters obtained by DAMA/LIBRA are in good agreement with the expectations for a WIMP signal. However, under standard assumptions the claimed signal region is clearly excluded by several other direct search experiments. Despite numerous ideas for the observed modulation no conclusive alternative explanation has been found up to now. The null results obtained from CsI crystals deployed as target material by the KIMS collaboration reject the possibility to explain the DAMA signal via WIMP-Iodine nuclei interaction [82]. To confirm or reject the modulation signal unambiguously in a model independent way, several programs are currently ongoing [83–87]. Since the NaI(Ti) crystals with excellent radiopurity, which are used in DAMA/LIBRA, are not available for other experimental groups, it seems to be the biggest challenge for these programs to achieve this radiopurity [86].

3 Cryogenic Rare Event Search with Superconducting Thermometers

Cryogenic Rare Event Search with Superconducting Thermometers (CRESST) is a direct Dark Matter search experiment located in the "Laboratori Nazionali del Gran Sasso" (LNGS) underneath the Gran Sasso mountains in Italy. Due to the low expected signal event rates (see section 2.1) it is necessary to shield external radiation from the innermost part of the setup (the experimental volume, where the detectors are located) to reduce backgrounds. Therefore, an active and passive shielding concept is realized in CRESST-II[4], which is described as part of the experimental setup in section 3.1.

In section 3.2 the detector technology as well as the basic concepts of detector operation and data taking are presented. The electronics and the data acquisition system are described in section 3.3. The main results of the previous CRESST-II phase 1 are given in section 3.4 to understand the motivation of the different measures taken for phase 2 (section 3.5). This last section is mainly dedicated to the new active background discriminating detector module designs.

3.1 Experimental Setup

A schematic drawing of the whole CRESST-II setup is depicted in figure 3.1. In the following the different parts of the experimental setup are explained.

3.1.1 Cryostat and Experimental Volume

The cryogenic detectors of CRESST-II need to be cooled down to $\sim 10\,\mathrm{mK}$. To achieve these low temperatures a commercial $^3\mathrm{He}/^4\mathrm{He}$ dilution refrigerator is used. All parts of the cryostat and the dewars for liquid nitrogen and helium are depicted in the upper half of figure 3.1. Since the cryostat is a commercial product, not all materials are suited for a low background experiment. Therefore, the setup has been designed to separate the cryostat from the experimental volume, where the actual detector modules are mounted inside a copper support structure. The mechanical and thermal connection is provided by a longish copper rod, the so-called cold finger, which transfers the cooling power from the mixing chamber of the cryostat to the experimental volume.

In the current stage the CRESST-II setup has 66 readout channels, which correspond to 33 mounted detector modules with one phonon and one light detector each. Thus, the support

[4] CRESST-I used non-scintillating sapphire crystals as target material. In contrast, the current stage of CRESST – denoted CRESST-II – changed the target to scintillating $CaWO_4$ crystals and the phonon-light technique.

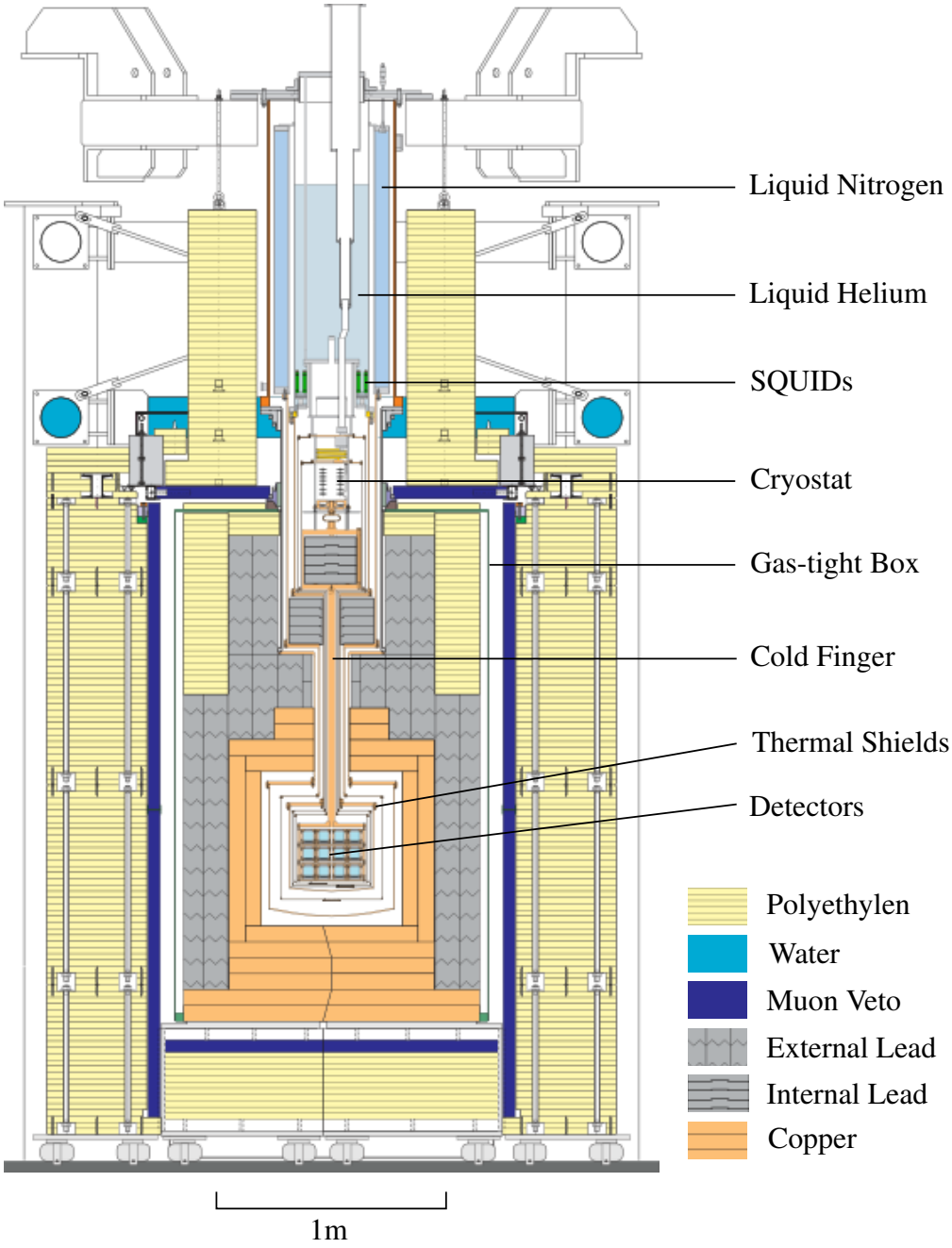

Figure 3.1: *Schematic drawing of the CRESST-II experimental setup. Most of the volume is used by the various shieldings made of polyethylene (yellow), lead (gray), and copper (orange) to reduce external backgrounds. At some places, which are hardly accessible, water filled structures are mounted to prevent neutrons from entering the experimental setup. Additionally, a muon veto system (dark blue) consisting of 20 plastic scintillator panels is installed. The gas-tight radon box is constantly flushed with gaseous nitrogen to prevent radon from penetrating to the inner setup. A cryostat provides the low temperatures required for the detector operation and is located in the upper part of the setup. The detectors themselves are mounted in a small volume in the innermost part at the center of the setup and are surrounded by thermal shields.*

structure is designed to house the same amount of modules, which are individually accessible. Since the experimental volume is inside all shieldings and contains the actual detectors, a careful selection of only radio-clean materials is necessary. In addition, the materials must be able to be cooled down to mK temperatures without loosing their mechanical properties. Therefore, most parts are made of a specially selected, radio-clean copper with a reduced hydrogen content[5].

Since the operated detectors are very sensitive to mechanical vibrations (e.g. caused by the cryogenic facility) the whole cryostat rests on air dampers and does not touch the surrounding shielding. To prevent electromagnetic radiation from external sources to interfere with the sensitive readout electronics, the complete setup depicted in figure 3.1 is located inside a Faraday cage. Furthermore, the lower part of the setup is installed in a clean-room environment to allow for detector mounting under clean conditions.

3.1.2 Background Reduction

The CRESST-II setup and in particular the experimental volume are surrounded by different layers which suppress the main backgrounds.

Muons

Muons are constantly produced by cosmic rays in the atmosphere of the earth. Due to their low interaction cross section with matter they are very penetrating. The underground laboratory is built next to a highway tunnel and has an overburden of 1400 m rock which corresponds to an average depth of ~ 3600 m water equivalent [88]. Therefore, in the LNGS the hadronic component of the natural radiation vanished but muons are still detectable. The remaining muon flux was measured to be $2\,\mathrm{h}^{-1}\mathrm{m}^{-2}$, which is a reduction by about six orders of magnitude in comparison to the surface flux [89]. Thus, even in underground laboratories muons can still induce background events either by directly depositing energy in the target crystals or via the production of secondary particles (e.g. electrons, γ-rays, neutrons or even nuclei) inside the surrounding materials. These secondaries can be very high-energetic and, thus, are able to penetrate the shieldings. Alternatively, they can be directly produced in the vicinity of the experimental volume. In all cases they introduce muon-related background events when they hit the detectors.

To be able to detect and tag the primary muons, the CRESST-II experiment is surrounded by a muon veto (dark blue in figure 3.1). The veto consists of 20 individual plastic scintillator panels with a thickness of 5 cm each. Each of them is read out with a single photomultiplier tube (PMT). The veto covers 98.7 % of the solid angle around the detectors. The remaining area cannot be covered, because there has to be a hole for the cryostat.

Every interaction in the plastic scintillator panels produces a finite amount of light, which can be detected by the corresponding PMT. These PMT signals are then converted by a QDC

[5] Hydrogen molecules can cause a so-called *heat leak* which prevents the sufficient cooling of the material. It is well known that hydrogen molecules show a spin excitation between their ortho and para states. The de-excitation after cooldown can release heat over a long time period.

module into a single charge value and stored for offline analysis[6]. Furthermore, the analog sum of all channels is built and treated as another independent channel. Thus, a trigger in the muon veto results in 21 stored QDC values. This information is used during the analysis to decide whether a cryogenic event was coincident with a signal in the muon veto and, thus, that it was most likely muon induced.

γ-Rays

As already stated before, the rock of the Gran Sasso mountains shields the hadronic component of the cosmic rays and reduces the muon flux by $\sim$ six orders of magnitude. Therefore, in the CRESST-II setup the most dominant backgrounds are introduced by γ-rays and electrons. The γ-rays are produced mainly in the natural decay chains of ^{238}U and ^{232}Th with energies up to 2.61 MeV [90]. Furthermore, the isotope ^{40}K with a natural abundance of only 0.0117 % is a prominent source of γ-background [91]. To minimize these backgrounds a pre-selection of the materials surrounding the detectors and of the detectors themselves in terms of their internal radioactive contamination is necessary.

To prevent γ-rays of the surroundings (e.g. the rock) from entering the experimental volume, the cryostat is enclosed by a layer of lead with a thickness of 20 cm and a weight of 24 t (see figure 3.1, gray). On the one hand, lead provides a good stopping power for γ-radiation due to its high mass number and density. On the other hand, the intrinsic radioactive contamination of lead is very high, due to the unstable isotope ^{210}Pb, which is part of the uranium decay chain. With a half life of $t_{1/2}$ =22.3 a ^{210}Pb decays over several steps to the stable isotope ^{206}Pb [90]. Throughout this decay chain α, β and γ-radiation is emitted which could contribute to the background. A measure taken against this background is the installation of a copper shield with a thickness of 14 cm and a weight of 10 t placed inside the lead shield (see figure 3.1, orange). Copper can be produced with very low intrinsic radioactive contamination and, hence, it is a suitable material in the vicinity of the detectors.

Therefore, CRESST-II uses copper not only for the shielding but also for all support structures in the experimental volume. For technical reasons it is not always possible to avoid lead close to the detectors. In that case specially selected lead bricks with a reduced intrinsic contamination of ^{210}Pb are used in these positions. To allow access to the experimental volume the lead and copper shieldings are mounted together on movable wagons.

Radon

Another source of natural radioactivity is the noble gas ^{222}Rn, another member of the ^{238}U decay chain. Since radon is a noble gas it penetrates all materials easily and, thus, special measures have to be carried out to avoid a radon contamination. At LNGS radon mainly emanates from the surrounding rock and concrete of the walls of the experimental hall. The corresponding activity due to radon was measured to be $\sim$ 50 Bq per cubic meter of air [92].

[6] Analog to an ADC (Analog-to-Digital Converter) a QDC converts a charge Q to a digital number. Therefore, the signal is integrated for a pre-defined time interval to collect the charge Q and then converted to a digital number.

Therefore, a gas-tight box enclosing the inner parts of the setup (called *radon box* - see figure 3.1, green box) is kept under slight overpressure and constantly flushed with pure nitrogen gas.

Furthermore, ^{222}Rn atoms can be adsorbed on surfaces and after decay, the daughter nuclei might be implanted in the material. Thus, it is important to either veto surface events or to remove the surface layers of all parts in the vicinity of the detectors. In the latter case the materials have to be stored afterwards in, e.g. nitrogen-flushed storage areas, since otherwise all surfaces can introduce background events related to radon and its daughters.

Neutrons

The ultimate background for all direct Dark Matter search experiments are neutrons since they scatter off nuclei much as expected for WIMPS. Therefore, neutrons cannot be discriminated from signal events in the offline analysis and have to be avoided by all means. Neutrons are produced by muons in the surrounding rock or shielding materials, by (α, n) reactions on light elements or by fission of heavy nuclei. The total neutron flux in hall A in the LNGS was measured and also confirmed by simulations to be $(3.81 \pm 0.11) \cdot 10^{-6}\,\mathrm{s}^{-1}\,\mathrm{cm}^{-2}$ [93, 94].

To prevent neutrons from reaching the experimental volume a polyethylene (PE) shield with a thickness of $\sim 50\,\mathrm{cm}$ encloses the whole setup (yellow in figure 3.1). Since polyethylene has a high content of hydrogen atoms it is a good moderator for neutrons, which leads to either neutrons being stopped inside the shielding or being moderated to thermal energies of $\mathcal{O}(\mathrm{meV})$. Recoils introduced by these thermal neutrons produce a signal well below the energy threshold of the detectors and, therefore, are no relevant source of background. Some regions of the setup are hardly accessible and, thus, mounting of a sufficient PE shielding was not possible. These areas are covered by structures containing either water or PE granulate. Just like the lead and copper shield, also the neutron shield is mounted mainly on movable wagons to allow access to the experimental volume.

3.2 Detection Principle

To detect the low energies of $\mathcal{O}(10\,\mathrm{keV})$ which are expected for WIMP-induced nuclear recoils (see section 2.1) very sensitive detectors are required. In this section, the CRESST detection principle to recognize such events and determine their properties is described. Furthermore, the key feature exploited mainly for background discrimination is explained.

3.2.1 Phonon and Light Detector

CRESST-II uses $CaWO_4$ single crystals as target material for the direct Dark Matter search. A particle interaction in the crystals mainly produces phonons (heat) and to detect them the crystal is equipped with a sensitive thermometer. The combination of crystal and thermometer forms the so-called *phonon detector*.

Additional to the phonons scintillation light is produced in the crystal ($\lesssim 9\,\%$ of the deposited energy [95]). The light escaping the crystal can hit the *light detector*, which is a thin

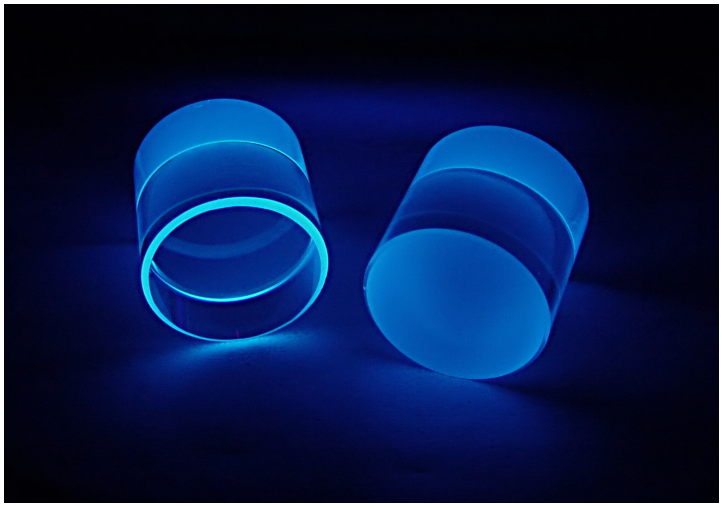

Figure 3.2: *Two cylindrically shaped $CaWO_4$ crystals ($\oslash = h = 40$ mm, $m = 300$ g) are irradiated with UV light. The plane surface of the right crystal facing the observer is roughened to increase the probability for scintillation light escaping the crystal. Furthermore, the light output is more homogeneous than for the crystal with the polished surface (left), where it is concentrated at the baffled edges.*

substrate – usually made of silicon on sapphire (SOS) – also equipped with a thermometer. In the substrate photons are absorbed and converted into phonons, which are measured with the light detector thermometer. Since the amount of created light is depending on the interacting particle this allows to discriminate the main background sources inducing electron recoils from sought-for nuclear recoils.

In figure 3.2 two $CaWO_4$ crystals of cylindrical shape with a height and diameter of 40 mm and a mass of 300 g are depicted. The crystals are irradiated with UV light and, thus, the blue scintillation light with a peak emission at ~ 420 nm can be observed [96]. The plane facing the observer is optically polished for the left crystal and roughened for the crystal on the right. Roughening increases the amount of escaping scintillation light and in addition, the light output is more homogeneous [97]. The latter effect can be observed (see figure 3.2) for the roughened crystal in comparison to the polished one, where the light is concentrated at the baffled edges.

3.2.2 Transition Edge Sensor

The basic measurement principle of the CRESST detectors, which are operated as cryogenic calorimeters, is that an energy deposition ΔE in the absorber leads to a temperature rise ΔT in the absorber and the sensitive thermometer. The relation between both quantities is given by:

$$\Delta T = \frac{\Delta E}{C}, \tag{3.1}$$

where C is the heat capacity of the absorber. It is crucial to reduce the heat capacity C as much as possible to be able to measure the small energies deposited by WIMP interactions

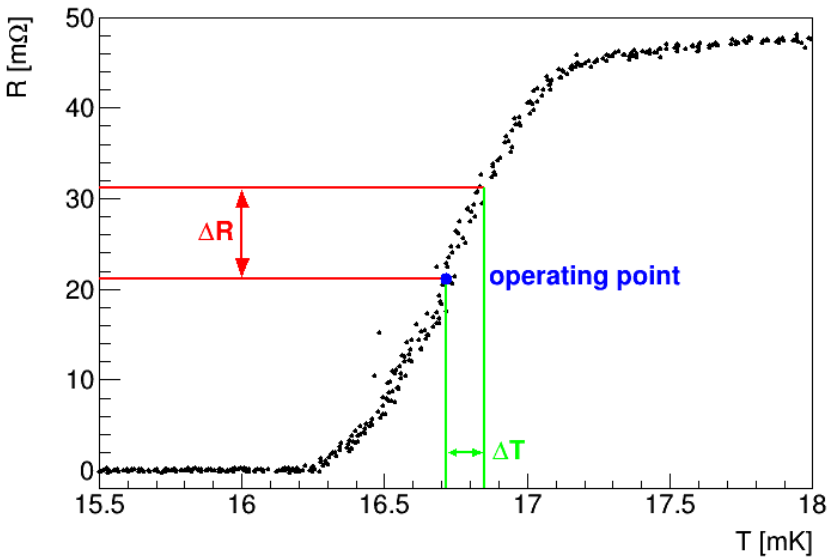

Figure 3.3: *A typical TES transition curve with a critical temperature $T_c \approx 16.8\,\mathrm{mK}$. The detector is stabilized by the heater current at its specific operating point (blue dot). Due to the steep rise of the resistance in the transition region between normal and superconducting phase a small temperature change ΔT ($\mathcal{O}(\mu\mathrm{K})$, [98]) translates to a measurable resistance rise ΔR of $\mathcal{O}(\mu\Omega)$. Data provided by [99].*

($\mathcal{O}(10\,\mathrm{keV})$). Thus, in CRESST the crystals are cooled down to cryogenic temperatures of $\sim 10\,\mathrm{mK}$ to meet this requirement. For dielectric materials at low temperatures the following relation applies: $C \propto \left(\frac{T}{\theta_D}\right)^3$ (with Debye temperature θ_D). This means, by cooling down to mK temperatures the heat capacity C is reduced by 13 orders of magnitude compared to room temperature, but nevertheless the temperature change ΔT to be detected is still of $\mathcal{O}(\mu\mathrm{K})$ [98].

Thus, in addition to the small heat capacity, a very sensitive thermometer is necessary to detect such small temperature changes. Such a thermometer is a Transition Edge Sensor (TES), which is a thin superconducting film operated in the transition between normal and superconducting phase. In CRESST-II TESs made of thin tungsten films are used to measure both signals (phonon and light). In figure 3.3 a typical transition curve of such a TES is depicted. The steep rise of the electrical resistance allows to detect tiny temperature rises introduced by e.g. a particle interaction in the absorber. A small temperature change ΔT ($\mathcal{O}(\mu\mathrm{K})$) is converted to a measurable resistance rise ΔR ($\mathcal{O}(\mu\Omega)$). Typically, for low-energetic events the induced temperature rise is smaller than the width of the transition region and, thus, a linear relation between temperature ΔT and resistance change ΔR is obtained. After an energy deposition the temperature relaxes back to equilibrium via a thermal coupling – a gold contact – to the heat bath. Furthermore, the thermometer is equipped with a heater to be able to thermally stabilize the TES in the specific operating point (blue dot in figure 3.3) via regulation of the heater current. A more quantitative model that is able to describe the observed properties of CRESST signal pulses can be found in [98].

In case of the light detector the TES is directly evaporated onto the absorber substrate. For

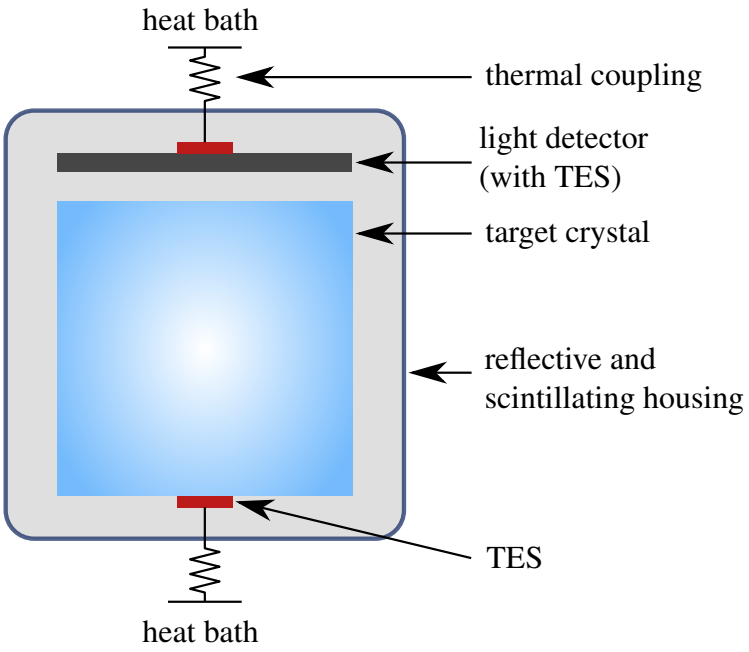

Figure 3.4: *Schematic drawing of a conventional CRESST-II detector module. A particle interaction in the target crystal produces phonons and scintillation light. The phonon and light detector are both equipped with a TES weakly coupled to the heat bath to measure both signals simultaneously. The detectors are paired in a detector module and mounted together in a reflective and scintillating housing.*

the phonon detector, different possibilities exist to equip the crystal with a TES. Firstly, like for the light detector the TES can be directly evaporated onto the target crystal. However, it was observed that due to the high temperature necessary for the evaporation process ($\sim 450\,^{\circ}\mathrm{C}$) an oxygen deficiency is created in the scintillating target crystal [100]. This deficiency leads to a reduced light output for the crystal resulting in a worse background discrimination. To face this, a composite detector design was developed, in which the TES is evaporated onto a small (usually $20 \times 10 \times 1\,\mathrm{mm}^3$) separated $CaWO_4$ crystal called TES-carrier [101, 102], which in turn is glued onto the target crystal with a small epoxy glue spot. Due to the different thermal coupling to the TES, events in the TES-carrier can be distinguished from absorber events via pulse-shape analysis (see chapter 6).

3.2.3 Detector Module

In CRESST-II typically one phonon detector is paired with one light detector to form a so-called *detector module*.

A schematic drawing of a conventional detector module is depicted in figure 3.4. As explained above, the target crystal as well as the light absorber are equipped with a TES, which is weakly coupled to the heat bath. Both detectors are surrounded by a reflective and scintillating foil (VM2002) to increase the amount of light absorbed by the light detector and, thus, improving the discrimination capabilities of the module.

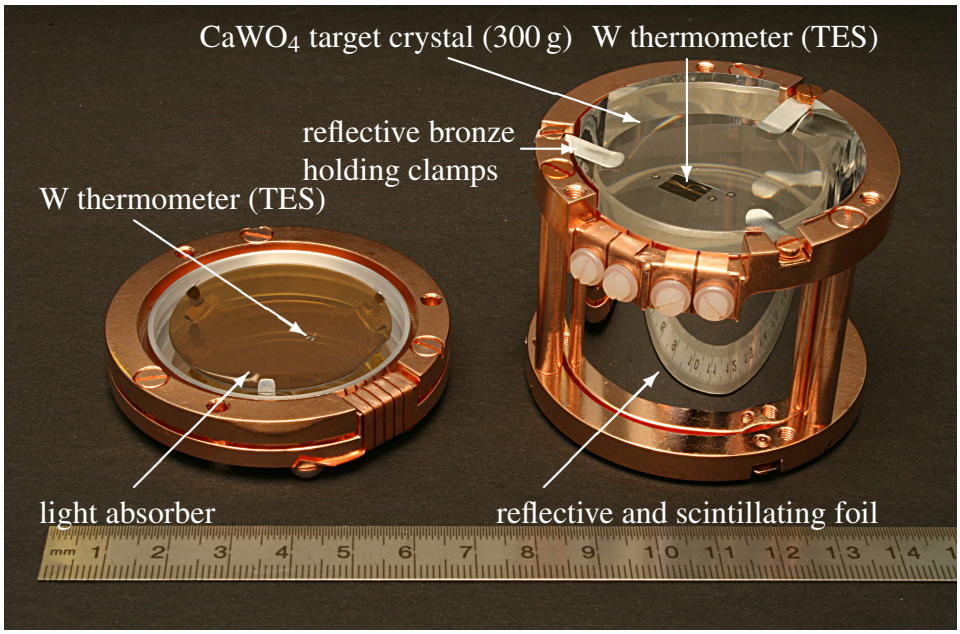

Figure 3.5: *Picture of an opened conventional CRESST-II detector module. The cylindrical $CaWO_4$ single crystal ($m \sim 300$ g, right) is mounted in the reflective and scintillating housing. The target crystal is held in place with reflective but non-scintillating bronze clamps. On the left the light absorber made of silicon on sapphire (SOS) mounted in its copper holder is depicted. Both, crystal and light detector, are equipped with a thermometer (TES) made of tungsten. The module is closed by mounting the light detector on top of the crystal.*

The actual realization of a conventional detector module can be seen in figure 3.5. On the left side of the picture the light detector mounted in its copper holder is shown. It is made of a silicon on sapphire (SOS) disc equipped with a tungsten TES. The cylindrically shaped $CaWO_4$ crystal mounted in its copper holder and surrounded by the reflective and scintillating VM2002 foil is depicted on the right. The additional light created in this foil helps to discriminate signal from background events (see section 4.5). On top of the crystal a directly evaporated tungsten thermometer is visible. The crystal is held in place by six pairs of bronze clamps. In the depicted module of conventional type the holding clamps are coated with aluminum and, thus, are only reflective but not scintillating.

3.2.4 Particle Discrimination

CRESST exploits the fact that different particles produce different amounts of scintillation light. Thus, the light signal is used for particle discrimination. The discrimination parameter defined in CRESST-II is the so-called *light yield*, i.e. the fraction of energy deposited in the light and in the phonon detector (see section 4.5). A schematic drawing of the light yield - energy plane observed by CRESST detectors is depicted in figure 3.6. The bands with different colors mark the light yield regions, where the central 80 % of the respective events are expected. In the energy calibration the light yield is set to one for a 122 keV γ-event. Thus,

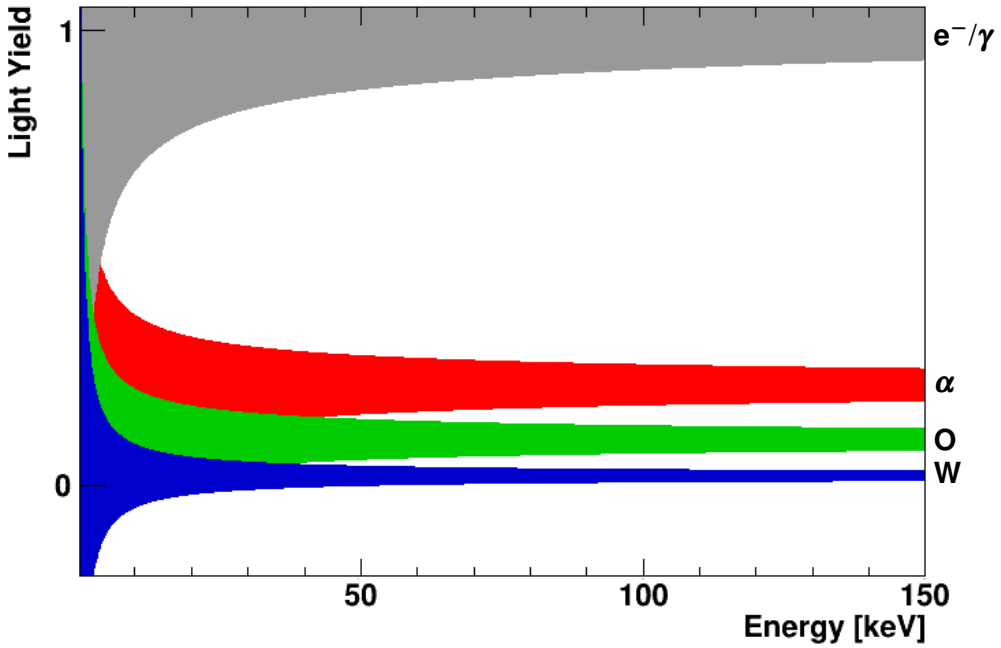

Figure 3.6: *Schematic drawing of the light-yield energy-plane of a CRESST-II module. By calibration, the light yield of electron recoils is set to* ~ 1*. All other event types, in particular nuclear recoils, show a reduced light output and, thus, are centered at lower light yields.*

all electron recoils which are caused by electrons and γ-rays show up at a light yield of ~ 1 (gray). All other event types show bands at lower light yields since the light output is reduced by quenching (α-events in the red band, oxygen and tungsten in the green and blue regions, respectively). The exact quenching factors used in the present work are listed in section 4.5. The calcium band is located between the oxygen and tungsten bands but is not shown for reasons of clarity. Since WIMPs are expected to scatter off nuclei they would induce events in the nuclear recoil bands. Thus, the light yield is an excellent parameter to discriminate a possible signal contribution from backgrounds.

3.3 Electronics and Data Acquisition

Up to now it has only been described how an energy deposition in one detector leads to a resistance change of the thermometer film. The present section focuses on the readout of the signals and explains the main electronic components required for the operation of the detectors [103]. In addition, the stabilization scheme of the detectors, as well as some details of the trigger and readout scheme with relevance for the data analysis performed in the present work are described.

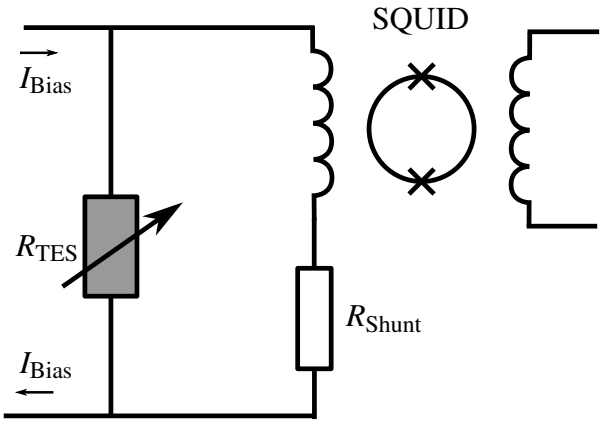

Figure 3.7: *Schematic drawing of the SQUID based readout circuit of a TES. A constant bias current I_{Bias} is applied to the parallel circuit. It contains in one branch the input coil of the SQUID and a shunt resistor R_{Shunt} and in the other branch the TES. A resistance change in the TES changes the branching of the total current and, thus, the current measured by the SQUID. The SQUID outputs a voltage signal proportional to the current in the input coil.*

3.3.1 Electronic Readout

In figure 3.7 the parallel circuit used to measure the film resistance R_{TES} is shown. One branch of the circuit contains solely the TES, while in the other branch a shunt resistor and the input coil of a SQUID (Superconducting Quantum Interference Device) are connected in series [104, 105]. A SQUID is a device which provides a very sensitive measurement of the magnetic field [106].

The parallel circuit is constantly biased with a current I_{Bias} (typically $\mathcal{O}(\mu\text{A})$). As explained before a temperature rise leads to a rise of R_{TES} in the thermometer. Therefore, the branching of the total current and as a consequence the current in the input coil of the SQUID changes. Hence, the magnetic field created by the coil and measured by the SQUID varies. Finally the SQUID outputs a voltage proportional to the current in the input coil.

In summary, a temperature rise created by an interacting particle ultimately leads to a voltage pulse that can be recorded and stored on disk for the offline analysis.

3.3.2 Data Acquisition

In figure 3.8 a simplified diagram of all electronic components needed either for the readout (blue) or the operation (bias highlighted in black, heater in red) of a single detector are depicted. The various components are operated at different temperature stages, ranging from room temperature to the mK stage. In the following the different components and their purpose are described in detail.

The constant bias current for the parallel circuit is provided by a controllable current source located at room temperature. The detectors and the shunt resistors are cooled to the base temperature of the cryostat ($\lesssim 10\,\text{mK}$), while the SQUIDs are mounted in the liquid helium reservoir (4 K). The SQUID can be controlled with the SQUID electronics, which also pro-

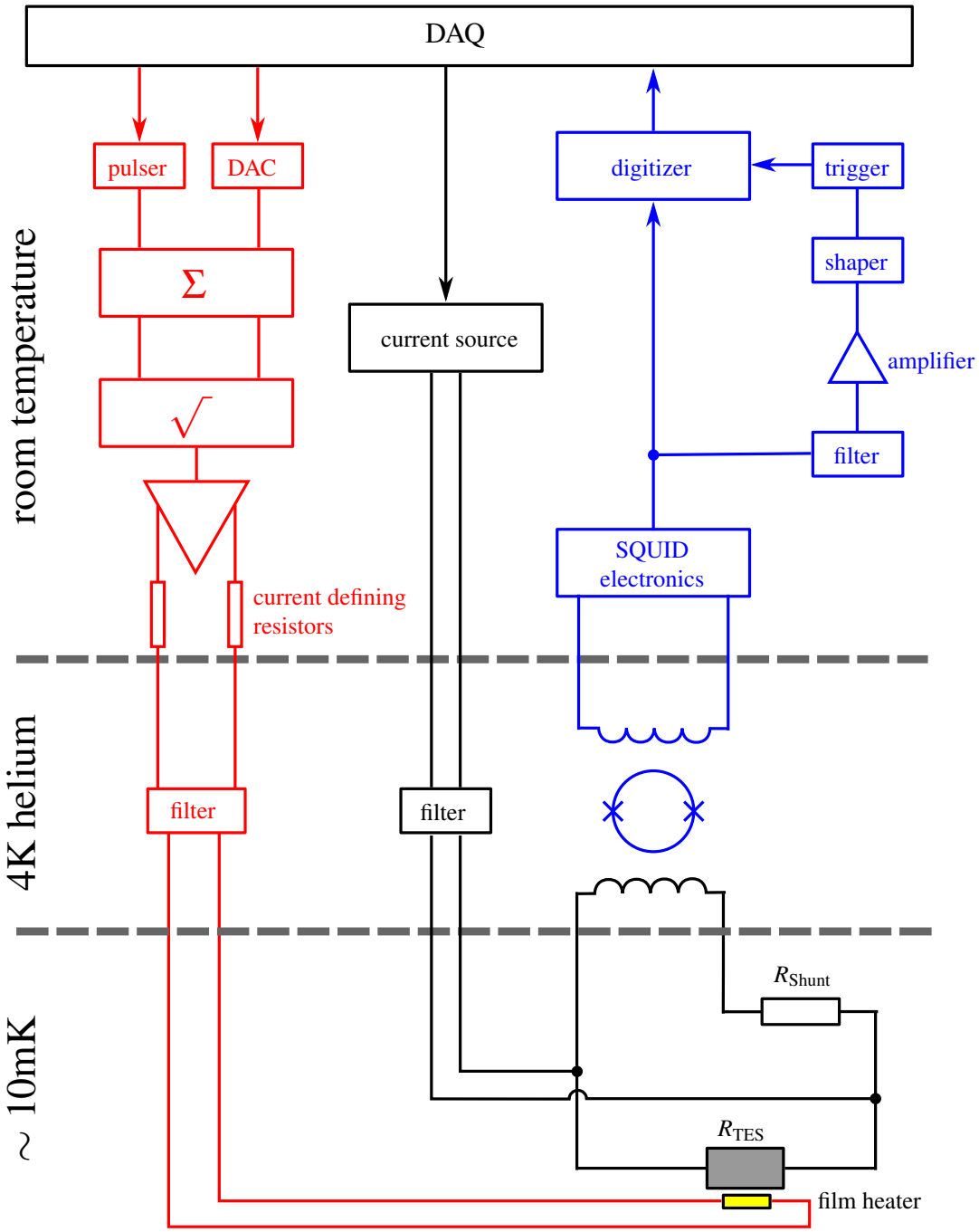

Figure 3.8: *Simplified diagram of the CRESST-II electronic components required for the operation and readout of a single detector. The right half of the diagram (blue) shows the SQUID readout electronic chain, while the bias circuit is marked in black. The heater electronics providing the heater current is depicted on the left side of the diagram (red). For more details see text. Figure adapted from [103].*

vides the output voltage.

The output signal is transferred out of the cryostat and split into two branches. One branch is directly fed into a 16 bit digitizer module, while the other branch is further processed to create a trigger signal. This part of the signal is filtered and amplified leading to a shaping of the signal. The shaped signal is processed in a trigger unit which sends a pulse to the digitizer when it recognizes a change of the signal level above an adjustable threshold.

The digitizer module constantly samples the signal with a sampling rate of 25 kHz (i.e. one sample every 40 µs). When a trigger is received, the digitizer saves 8192 samples, which are read out by the Data Acquisition (DAQ) software and finally saved to hard disk. The first quarter of this pulse is called *pre-trigger region* since the samples contain information obtained before the signal triggered. These samples are used to determine the baseline level before the signal occurred. The actual pulse information is contained in the remaining three quarters of the samples, which are hence denoted as *post-trigger region*.

Each digitizer unit can handle up to eight detectors simultaneously and, therefore, at maximum eight pulses can be read out together. When a certain digitizer channel triggered, the partner channel of that specific detector is also read out, so that phonon and light detector signals are always stored together.

Furthermore, after a trigger in one channel, the remaining seven channels of that digitizer unit can still trigger in a certain time window (half the post-trigger time with respect to the first trigger). Afterwards all channels of that unit are blocked for further triggering. After the complete post trigger time has passed all triggered channels are finally read out and stored for offline analysis. During this pulse procession the trigger of these channels is still blocked. For all channels which were read out, triggering is additionally blocked for a complete pre-trigger time to ensure that the pre-trigger region of the next pulse is valid. The total dead-time introduced is calculated for each channel and stored as accumulated dead-time in the header information of each pulse (see section 4.2).

3.3.3 Detector Operation and Stabilization

In order to operate and stabilize the detectors more components besides the readout electronics are necessary. On the left side of figure 3.8 the main components of the heater system are depicted in red. The electronics provide a heater current, which is fed into the film heater[7].

For each detector the heater current is made up of two contributions: On the one hand there is a constant current to stabilize the TES in its operating point. On the other hand, heater pulses with a pulse shape similar to particle pulses are injected in regular time steps for control purposes.

A digital-to-analog converter (DAC) outputs an adjustable voltage which is proportional to the desired constant heating current. Additionally, an arbitrary waveform generator (pulser) outputs a voltage signal in form of the desired heater pulses. Both voltages are summed up, send through an analog square rooter and finally converted to the total heating current by a pair of resistors. This heating current is fed into the cryostat and driven through the detector heater.

[7] For the phonon detectors the heater is electrically connected to the TES. On (almost) all light detectors the heater is separated and placed next to the TES.

The purpose of the square rooter is to decouple both signals from each other. The heating power dissipated in the detector is proportional to the square of the heating current. Thus, the total heating power is the sum of the constant current and the heater pulses. Therefore, the injected energy via a heater pulse is always the same independent of the constant current, which might change with time.

Control Pulses

One application of the heater pulses is to control the operating point of a detector via so-called *control pulses* which are injected every five seconds. Since the temperature changes induced by a particle interaction are of $\mathcal{O}(\mu\mathrm{K})$ also the stabilization has to be at least at this precision level. Control pulses are high energetic pulses, which drive the detector out of the transition to the normalconducting state.

The pulse height (i.e. the maximum sample of a running average filtered pulse) of the detector response to a control pulse is a measure of the distance to the top of the superconducting transition. Therefore, this quantity is determined online by the DAQ and used as input into a PID (Proportional-Integral-Differential) control loop. The loop regulates the constant heating power in order to keep the height of the control pulse (i.e. the operating point) at the predefined value. Furthermore, the determined pulse height is stored for offline analysis. Both, the control loop and the pulse height evaluation, are software implemented.

Test Pulses

The second application of the heater pulses are so-called *test pulses*. Additionally to the control pulses low energetic pulses with several different pulse heights are injected every $\sim 30\,\mathrm{s}$. The purpose of test pulses is to monitor the time-dependent detector response. In the offline analysis they are used for the energy calibration (see section 4.4). Furthermore, the very low energetic test pulses serve to directly measure the trigger efficiency of the respective detector (see section 5.4).

3.4 Results and Background Discussion of CRESST-II Phase 1

The first extended physics run of CRESST-II lasted from 2009 until 2011[8]. During phase 1 eight detector modules were fully functional and a net exposure of 730 kg days was collected and analysed [107]. In the following the main results of this analysis are listed and explained.

Figure 3.9 shows the typical plot used to depict CRESST-II data. The total energy deposited (x-axis) can be precisely measured (up to a few percent) with the phonon detector. The region of interest (ROI), i.e. the area where nuclear recoil events induced by WIMPs are expected to be measured, is shown in orange. Furthermore, all accepted events inside the ROI, are

[8] To distinguish the different data taking periods of CRESST-II the terms *phase 1* (2009–2011) and *phase 2* (2013–2015) are used.

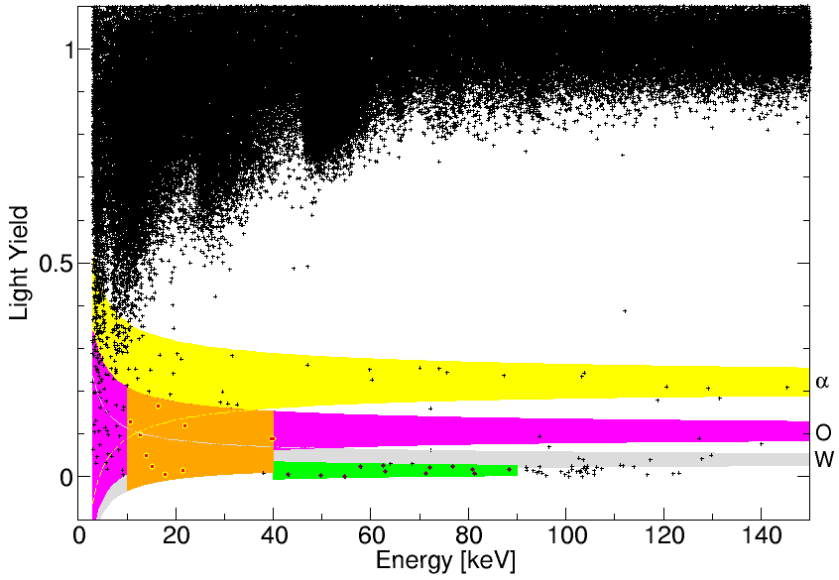

Figure 3.9: *Typical light-yield plot of a single detector module operated during CRESST-II phase 1 [107]. e^-/γ-events have per definition a light yield (LY) of ~ 1, while all other particles have a lower mean light yield ($LY_\alpha \sim 0.22$ (yellow), $LY_O \sim 0.1$ (magenta), $LY_W \sim 0.02$ (gray)). The lower energy analysis threshold of the region of interest (ROI, orange area) is chosen individually for each detector module based on the e^-/γ-background (here: 10.2 keV). In the whole data set only a single event is allowed to leak into the ROI for each module. All accepted events in the ROI are additional highlighted in red. Furthermore, a population of events below the tungsten band caused by ^{206}Pb recoils was observed (see text for more details). Figure taken from [107].*

highlighted in red. In phase 1 the ROI included all nuclear recoil bands in the light-yield parameter. The upper energy boundary was set to 40 keV since no significant WIMP contribution is expected at higher energies. The lower energy boundary was chosen for each detector individually according to the e^-/γ-leakage. This boundary is set to the energy where the expected e^-/γ-background in the ROI for the whole data set analysed, is a single event. In figure 3.9 data of one module operated in phase 1 is shown. For this module the lower energy boundary of the ROI is set to 10.2 keV [107]. In all eight detectors analysed in CRESST-II phase 1 in total 67 accepted events are observed [107].

3.4.1 Background Induced by Lead Recoils

In figure 3.9 several events are observed in the lead band right below the tungsten band (gray band), which are most probably caused by ^{206}Pb recoils. These recoiling nuclei are created during the decay of ^{210}Po with a half-life of $\tau = 138.4$ days [90]:

$$^{210}\text{Po} \rightarrow {}^{206}\text{Pb}(103\,\text{keV}) + \alpha(5.3\,\text{MeV}). \tag{3.2}$$

Thereby, the recoiling nucleus with an energy of 103 keV and the α-particle with an energy of 5.3 MeV are emitted in diametrical directions in the rest frame.

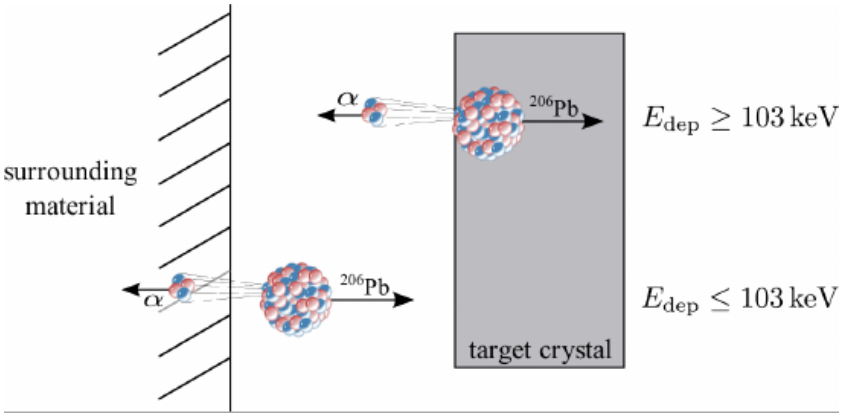

Figure 3.10: *The two decay scenarios inside a CRESST-II module leading to ^{206}Pb recoil events. In case the ^{210}Po decay happens on a crystal surface (upper part) at least the recoil energy of the ^{206}Pb daughter nucleus of 103 keV is observed in the phonon channel. In contrast the decay can also happen on a surrounding surface (lower part). While the recoiling nucleus might escape the material but lose part of its energy, the α-particle is stopped therein. Thus the ^{206}Pb nucleus deposits only its remaining energy of $\leq$ 103 keV in the crystal. Figure taken from [107].*

^{210}Po in turn is a decay product of ^{210}Pb which is the first long-lived daughter nucleus of gaseous ^{222}Rn in the natural ^{238}U decay chain with a half-life of τ =22.3 a [90]. As the noble gas is present in ambient air, ^{210}Po can be found on all surfaces but also adsorbed and implanted in the outermost layers of all materials.

In figure 3.10 the two possible decay scenarios inside a CRESST-II detector module leading to ^{206}Pb recoil events are depicted. If the ^{210}Po decay happens on a crystal surface (upper part of figure 3.10) the whole recoil energy of the ^{206}Pb daughter nucleus of 103 keV is measured in the phonon detector. Furthermore, the corresponding α-particle can deposit also part of its energy while leaving the crystal. Therefore, events with energies $\geq$ 103 keV in the phonon detector are observed. Depending on the material, in which the α-particle is stopped, these events are located in different regions of the light yield - energy plane. In case of being stopped in a scintillating material the additional light created shifts these events out of the nuclear recoil band. However, in the second case of a non-scintillating surface the events show up in the lead recoil band located just below the tungsten band. Neither of these two cases is problematic for the Dark Matter search since the minimal energy deposited is 103 keV and, thus, well above the upper limit of the ROI.

In contrast to the former situation, the ^{210}Po decay can also happen on a surrounding surface (lower part of figure 3.10). This time, the α-particle is stopped inside the surrounding material while the recoiling nucleus might escape. During the escape process the nucleus can loose part of its energy and, thus, can deposit energies $\leq$ 103 keV in the phonon detector. If the decay happens inside a scintillating material, the additional light created by the α-particle shifts this kind of events with energies $\leq$ 103 keV out of the nuclear recoil bands. As before, if the material is non-scintillating no additional light is created and these events are located just below the tungsten band. Such events are very problematic for WIMP searches since the

tungsten band and the lead band overlap in particular at low energies. Consequently, these events have almost no light-yield difference with respect to WIMP-induced events and, thus, might appear inside the ROI.

During the decay of ^{210}Po an α-particle is produced and might hit the target crystal. The maximum energy of this particle is 5.3 MeV and, thus, well above the energy region for WIMP searches. However, the particle might have lost most of its energy while escaping the surrounding material. If such a *degraded α-particle* hits the $CaWO_4$ crystal it deposits its remaining energy. Thus, it might show up in the α-band (highlighted in yellow in figure 3.9). The same is true for all external α-particles penetrating the detector housing while losing part of their energy.

In CRESST-II the detector housing is made of scintillating VM2002 foil to reduce the non-scintillating surfaces in the vicinity of the detectors. The only non-scintillating material inside the housing of the conventional module were the holding bronze clamps of both detectors, in particular the six pairs holding the phonon detector (see figure 3.5). Thus, the events slightly below the tungsten band are due to ^{210}Po contamination in the holding clamps.

There were several attempts to cover the bronze clamps with plastic scintillator. However, all of them resulted in phonon events without corresponding light emission so called *phonon-only* events [108]. Whenever plastic is in contact with $CaWO_4$ and cooled to mK temperatures phonon-only events with disturbed pulse shapes are observed. Stress might be introduced inside the plastic due to the different thermal expansion coefficients of the materials in contact. These stress relaxations are released by the creation of microcracks and phonons inside the plastic over long time periods. Due to the slow phonon-propagation properties of plastic and the necessary transportation into the absorber crystal a different pulse shape is expected and observed. However, at low energies the discrimination becomes at least challenging if not impossible. An additional source of phonon-only events are micro-fractures of the crystal leading to events with the same pulse shape as for particle-induced events. This kind of events might be created by a too tight holding of the crystal and is obviously not related to a contact between plastic and $CaWO_4$. Regardless of the origin of phonon-only events, they are a dangerous background for WIMP searches, since their energy distribution peaks at low energies, where also for WIMP-induced events almost no light emission is expected.

3.4.2 Results of the Likelihood Analysis

As stated before in CRESST-II phase 1 in total 67 accepted events are observed. A likelihood analysis was performed to estimate the unknown parameters of the background contributions. The α- and Pb-background contributions are constrained with the help of reference regions, where no WIMP signal is expected. For the lead background the reference region is depicted as green shaded area in figure 3.9. An additional possible signal contribution is also included in the total likelihood. The used likelihood functions for all the different contributions can be found in [107]. Here only the result of this maximum likelihood analysis is depicted in table 3.1.

The maximum likelihood fit results in two maxima M1 and M2. In both cases only $\sim 50\,\%$ of the observed events in the region of interest can be explained by known backgrounds. For both solutions the observed statistical significance is well above 3σ. The remaining events

	M1	M2
e^-/γ-events	8.00 ± 0.05	8.00 ± 0.05
α-events	$11.5^{+2.6}_{-2.3}$	$11.2^{+2.5}_{-2.3}$
neutron events	$7.5^{+6.3}_{-5.5}$	$9.7^{+6.1}_{-5.1}$
Pb recoils	$15.0^{+5.2}_{-5.1}$	$18.7^{+4.9}_{-4.7}$
signal events	$29.4^{+8.6}_{-7.7}$	$24.2^{+8.1}_{-7.2}$
m_χ [GeV]	25.3	11.6
σ_{WN} [pb]	$1.6 \cdot 10^{-6}$	$3.7 \cdot 10^{-5}$
statistical significance	$4.7\,\sigma$	$4.2\,\sigma$

Table 3.1: *Two maxima M1 and M2 are found as result of the maximum likelihood fit of CRESST-II phase 1 [107]. For both cases not all of the 67 accepted events are explained by the background contributions leading to an excess of signal events. An interpretation as positive WIMP signal with mass m_χ and WIMP-nucleon cross section σ_{WN} is possible. However, due to the high background level large uncertainties are observed.*

might either be explained by an unknown background contribution or a possible WIMP signal with a mass of either 25.3 GeV or 11.6 GeV [107]. However, due to the high background level observed also the resulting parameters have large uncertainties.

Since CRESST-II uses a multi-material target the ambiguity in the likelihood function can be understood. Due to the limited light detector resolution and the energy threshold of the detectors it is impossible to distinguish between a light WIMP mainly interacting with oxygen nuclei (M2) or a heavier WIMP mainly interacting with tungsten (M1).

Shortly after the release of the results of phase 1 another explanation of the excess events was published [109]. Simulations showed that the energy spectrum of the radon-induced background events can have a steep rise at low energies due to sputtering in the surrounding materials when the surface roughness of the material is not neglected. This behavior is in contrast to the simulation-based model of a flat energy distribution used in [107].

However, the exact shape of the energy spectrum of these background events is strongly dependent on the surface roughness of the holding clamps. Furthermore, it is hard to exactly model this roughness precisely in simulations and even harder to validate the result. Last but not least it is important to mention, that based on the data set it is not possible to decide which of the two scenarios is true. This has a strong influence on the results since all events which could not be explained by a background contribution are assigned to a possible WIMP signal by the likelihood analysis. Thus, an underestimation of Pb recoils leads to an increased WIMP contribution and vice versa. To clarify the origin of the excess events experimentally a significant reduction of all background contributions is necessary. In particular the lead recoil background has to be removed to avoid the observed ambiguity in the background model. The different measures which were taken against all observed backgrounds in phase 1 are described in the next section.

3.5 Background Rejection Measures for CRESST-II Phase 2

Phase 2 of CRESST-II started in May 2013 with the cooldown of the main cryostat and lasted until August 2015. The physical aim of phase 2 is to either validate or disproof the signal excess observed in phase 1 and, thus, a considerable reduction of all observed background sources is required. The different measures to achieve this prerequisite are explained in this section.

3.5.1 Neutron Background

Out of the 67 accepted events observed in CRESST-II phase 1 at least ~ 8 are ascribed to neutrons by the likelihood fit (see table 3.1). Two different production mechanisms for free neutrons are considered in [107]. Firstly, in radioactive decays, in particular during spontaneous fission of heavy elements or (α,n)-reactions on light elements, free neutrons can be emitted. Typical energies of these neutrons range up to a few MeV and, thus, they are efficiently moderated by the PE-shielding if produced in the rock outside. However, these processes can also occur inside the shielding and contribute to the background budget. The resulting neutron background was estimated by Monte Carlo simulations to be at a negligible level of 10^{-5} events/kg/day from the rock [94] and 10^{-3} events/kg/day from inside the shielding [110].

Secondly, neutrons can be produced by muons either in the surrounding rock or inside the Pb/Cu-shielding. The latter case should be vetoed by the muon veto. However, due to the hole required for the cryostat there is a small probability that a muon is missed. A neutron shower inside the PE shield may be created by such a muon and, thus, neutrons might reach the experimental volume and the detectors. In addition, high energetic neutrons from outside might penetrate the PE-shield and scatter inelastically inside the Pb/Cu parts. In this way, secondary neutrons and γ-rays could be created. The event characteristics of these secondaries is very similar to the case when muons create neutrons inside the shielding.

Muon Veto

To encounter the neutron background a well performing muon veto is required. The functionality of all scintillation panels and of the mounted photomultiplier tubes (PMTs) was checked during the preparations for phase 2. Simultaneously, the panels were calibrated with a thorium source by adjusting the gain of the PMTs such that the resulting peak observed in the QDC module is centered around the same mean value. More details about this calibration can be found in appendix A.

Inner Neutron Shield

Detailed simulations showed that an additional layer of polyethylene inside the lead and copper shielding reduces the remaining neutron flux by one order of magnitude [111]. Furthermore, it was investigated how much radioactive contamination is tolerable in the direct vicinity

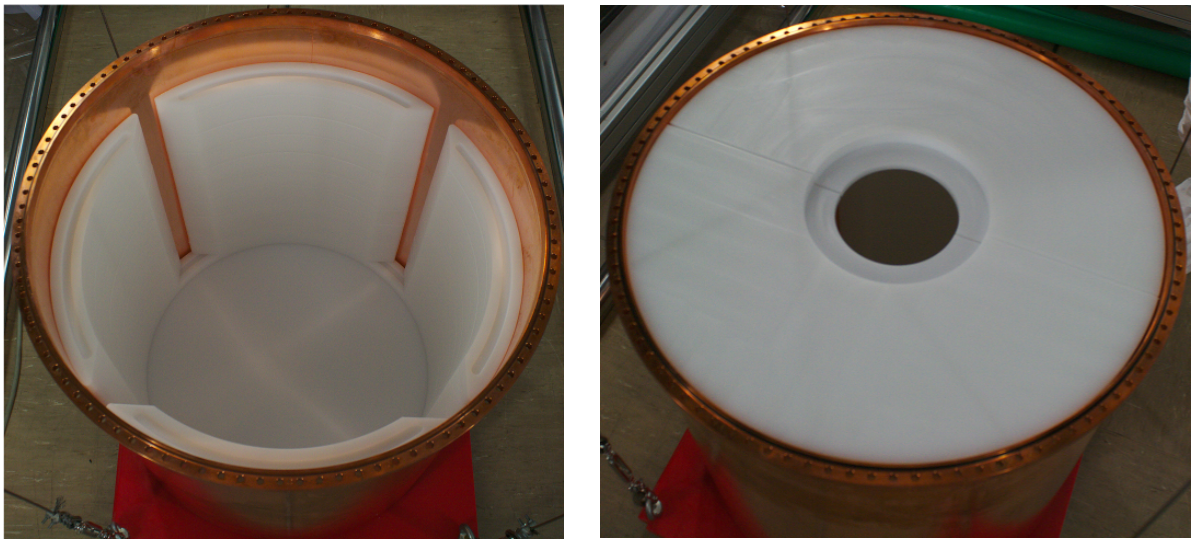

Figure 3.11: *Newly installed inner neutron shield made of radioclean polyethylene (PE) with a thickness of 3.5 cm. The two slits visible in the left picture are necessary to be able to calibrate the detectors from outside with neutron and γ-sources with a sufficient event rate. The two top plates also made of PE (right picture) complete the neutron shielding on the top and are put in place when the cryostat is closed. The hole in the middle of the top plate is the feed through for the different pumping rods of the inner chambers and the cold finger.*

of the experimental volume. A careful material selection process was carried out to find a production batch, which fulfills all requirements set by these simulations.

In figure 3.11 the outer vacuum chamber of the cryostat made of copper is depicted. Inside the chamber parts of the newly deployed inner neutron shield, made of polyethylene pieces with a thickness of 3.5 cm is depicted [112]. The four slits (two are clearly visible in figure 3.11) are necessary to be able to expose the detectors to different calibration sources from outside, in particular an AmBe-source for neutron calibrations. At these positions additional polyethylene pieces are mounted outside of the vacuum chamber to enlarge the neutron shielding accordingly.

Inside the outer vacuum chamber there are four more copper pots of which the innermost encloses the experimental volume. During closing of the cryostat the two PE half plates (figure 3.11, right) are put in place on top of the neutron-shield parts previously shown and, thus complete the polyethylene shielding. The hole in the middle of the PE top plate is the feedthrough for the cold finger and the pumping rods of the different vacuum chambers.

3.5.2 Intrinsic Background Reduction - TUM-Grown Crystals

Since 2008 $CaWO_4$ crystals have been produced in a dedicated furnace in the crystal laboratory of the Technische Universität München (TUM) [113, 114]. The aim of this effort is to gain more control over growth parameters resulting in the same or even better crystal properties compared to commercially available ones. In particular the radioactive contamination of the TUM-grown crystals should be reduced by using the radiopurest raw materials. Therefore,

dedicated screening campaigns were performed to find the best raw materials [97]. Moreover, several crystal production steps were investigated to determine their influence on the achievable radiopurity and optical quality.

In dedicated test measurements the radiopurity of two of these TUM-grown crystals was determined. It was shown, that the radiopurity of the TUM-grown crystal was among the best ones compared to the commercial crystals operated in phase 1 [115]. However, the observed optical quality, especially the light output of the TUM-grown crystals is not yet compatible with the best commercial ones [97].

Nevertheless, since the radiopurity of the TUM-grown crystals is so high (i.e. they have a low contamination with radioactive isotopes), four TUM-grown crystals are used in phase 2 in alternative module designs to investigate the radiopurity and optical properties further [116].

3.5.3 Radon-Induced Backgrounds

Since the majority of the observed background events in CRESST-II phase 1 was radon induced, extraordinary efforts were carried out to reduce this background. A two-stage approach during assembling and mounting of the modules was developed and performed. The assembling took place in a newly built clean room environment installed on the top floor of the CRESST-II hut in the LNGS. To minimize the exposure to radon the clean room was constantly flushed with radon-depleted air, which was supplied by the neighboring experiment CUORE [88]. In addition, the modules were stored in nitrogen-flushed containers. During the mounting of the assembled modules into the experimental volume the radon-depleted air was led into the clean room surrounding the cryostat. Despite the fact that the radon activity in the radon-depleted air was measured to be below the experimental sensitivity of the radon monitor (≤ 3 Bq/m^3), for both locations the quantity was constantly monitored and no positive signal was observed. In addition to the radon prevention during mounting, new clamps made of carefully selected radioclean material were produced and installed in the conventional module design [108]. Thus, the surface contamination caused in particular by radon as well as the intrinsic α-contamination are reduced.

The second stage of the approach was the development of alternative module designs which are presented in the following in more detail.

3.5.4 Alternative Module Designs

Up to now only modules containing cylindrically shaped $CaWO_4$ crystals, which are held by non-scintillating bronze clamps, were described. To be able to distinguish between the different designs this type is called *conventional module design* in the present work. Three alternative designs were developed for phase 2 to veto efficiently all surface-related background events.

Crystal with Big Carrier

The first alternative design uses - like the conventional design - a cylindrically shaped $CaWO_4$ crystal and a standard light detector as depicted in figure 3.12. The main difference with

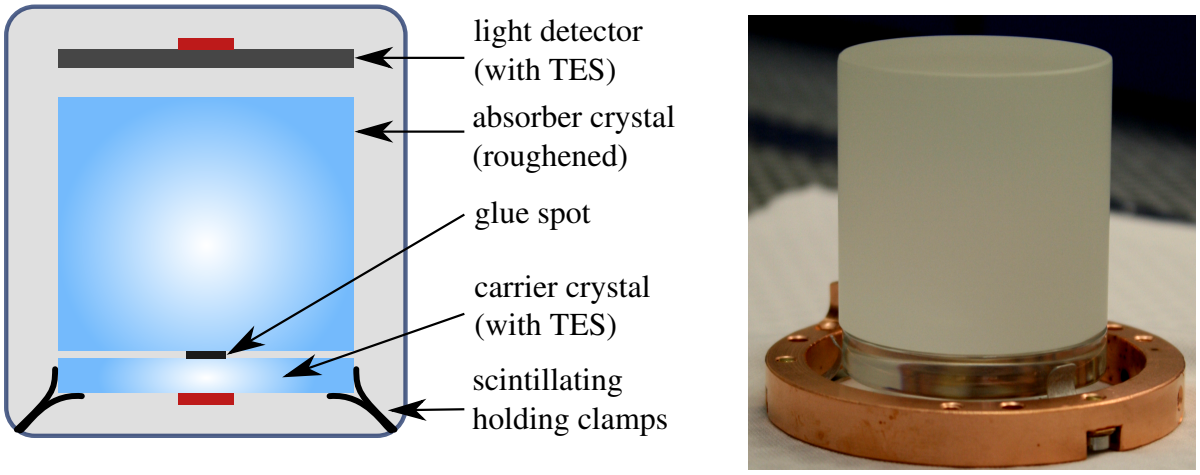

Figure 3.12: *Schematic drawing (left) and realization (right) of the first alternative module design with a big carrier crystal. As in the composite detector design the TES is evaporated onto a TES-carrier. This time the latter is an optically polished big $CaWO_4$ disk glued to the roughened absorber crystal. Solely the TES-carrier crystal is held by scintillating clamps and, thus, all surfaces inside the scintillating housing are either active or scintillating. The phonon detector is mounted together with a standard light detector in a conventional module housing.*

respect to the conventional design is a big TES-carrier slice with the same diameter as the absorber crystal which is glued onto the latter. Only this $CaWO_4$ slice is held by scintillating holding clamps and, thus, the unavoidable phonon-only events are solely introduced in the TES-carrier. This can be accepted since a pulse shape difference between absorber and carrier crystal allows to discriminate all events inside the carrier (see chapter 6).

Due to the modifications of this alternative design all materials inside the module housing are either scintillating or active. Concerning the radon-induced background this ensures that the additional light produced by the α-particle of the corresponding ^{210}Po decay (see section 3.4.1) shifts these events to higher light yields out of the nuclear recoil bands. Thus, these events can be efficiently vetoed.

The right part of figure 3.12 shows the actual realization of the phonon detector of this alternative design. All surfaces of the absorber crystal (except the one facing the carrier) are roughened to increase the amount of escaping scintillating light and to remove local dependencies of the light output [97]. Since the big carrier is optically polished it can clearly be distinguished by eye from the roughened absorber crystal in figure 3.12. The crystal is mounted together with a standard light detector in a standard reflective and scintillating housing.

Crystal with Silicon Beaker Light Detector

The second alternative design is a further development of the first approach with a novel type of light detector. Again a big $CaWO_4$ carrier crystal equipped with a TES is glued onto the absorber crystal. The latter is hanged inside a beaker made of silicon used as light detector. Therefore, the beaker is equipped with a TES and, thus, the whole surface of the beaker is

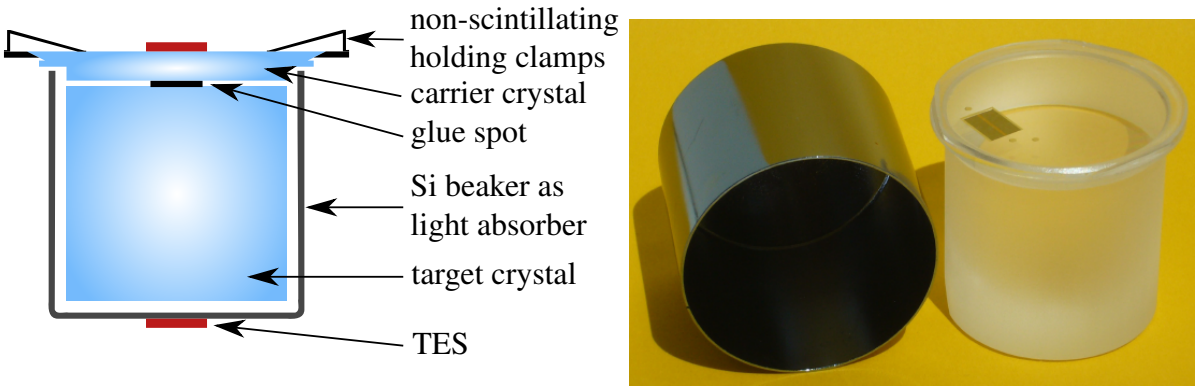

Figure 3.13: *Schematic drawing (left) and realization (right) of the second alternative design with a beaker light detector made of silicon. Just as in the first alternative design the main absorber is glued to a big carrier crystal. In this design the carrier can be held by non-scintillating bronze clamps since there is no direct line of sight to the main absorber. The absorber crystal is hanging inside the beaker made of silicon, which increases the solid angle covered by the light detector and, therefore, the amount of detected light.*

active and sensitive to light. The solid angle covered by the light detector drastically increases compared to all other available designs leading to an enhancement of the amount of detected scintillation light. A schematic drawing of this alternative design as well as a picture of the silicon beaker and the corresponding crystal for such a module are depicted in figure 3.13.

This design allows to hold the carrier by non-scintillating clamps since there is no direct line of sight between the absorber crystal and the clamps when assembled together with the beaker. Events in the clamps can either hit the carrier or have to penetrate the light detector to reach the main absorber. As in the first alternative design, events in the carrier can be distinguished from absorber events via pulse shape analysis. In order to fit into a standard module housing the main absorber crystal has reduced dimensions with a total mass of $\sim 200\,\mathrm{g}$ compared to $\sim 300\,\mathrm{g}$ in a conventional module.

Crystal Held with $CaWO_4$ Sticks

Figure 3.14 shows a schematic drawing of the third alternative design (left) and a picture of the absorber crystal (right). Since the block-shaped crystal is held in place by in total nine $CaWO_4$ sticks [117], it is also called *stick design*. The eight side sticks are pressed onto the crystal by bronze clamps mounted outside of the module housing, while the thicker bottom stick is placed inside a hole in the bottom plate.

The dimensions of the absorber crystal are adjusted to maximize the target mass but still fit into a conventional cylindrical housing. Thus, the block-shaped crystal has an edge length of 32 mm and a height of 40 mm corresponding to a mass of $\sim 250\,\mathrm{g}$. This is slightly lighter than a target crystal of 300 g for a conventional module. The crystal is roughened on all sides except for the bottom surface where the small TES-carrier is glued onto the absorber. Additionally, the contact areas of the sticks are polished to prevent stress relaxation events. Both modifications, i.e. crystal shape and surface roughness, should increase the total amount of

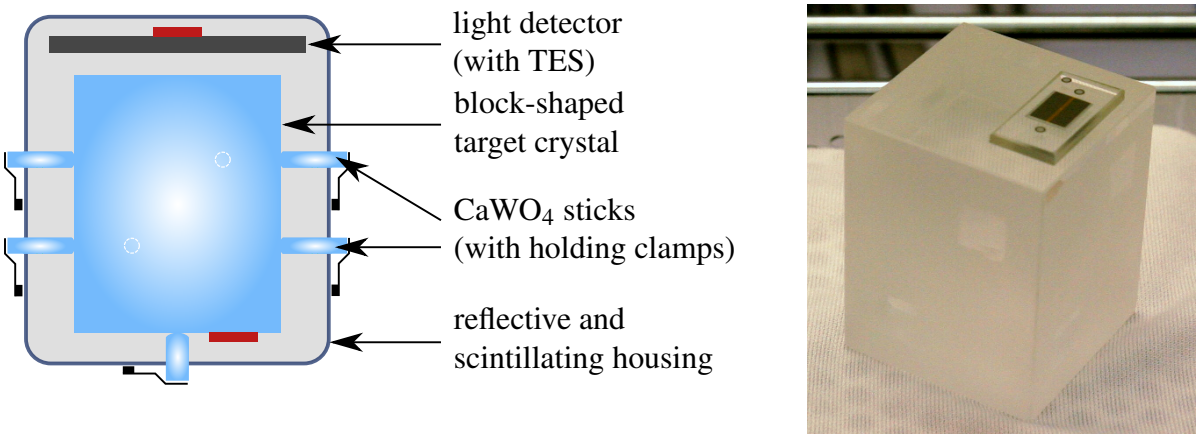

Figure 3.14: *Schematic drawing (left) and image of the phonon detector (right) of the alternative design with $CaWO_4$ sticks. The crystal is held in place by in total 9 $CaWO_4$ sticks. Thus, only scintillating or active surfaces are present inside the housing. Furthermore, the target crystal is block-shaped and has a mass of ~ 250 g. All surfaces of the crystal are roughened, except the bottom surface where the TES-carrier is glued onto the crystal. In addition, also the areas where the sticks are pressed to the crystal are polished.*

light emitting from the crystal as well as reduce position dependencies of the light output [97].

Like in the other alternative designs all surfaces inside the housing are either scintillating (absorber crystal, sticks and foil) or active (light detector). Radon-induced ^{210}Po events are shifted out of the nuclear recoil band by additional light leading to an efficient veto. A detailed description of this module design and first results can be found in [112].

3.5.5 Detector Ensemble in CRESST-II Phase 2

A picture of all assembled modules ready for mounting inside the cryostat is depicted in figure 3.15. While phonon detectors have either female names or a series of characters and numbers describing their supplier (e.g. TUM40), light detectors have a male name by convention. In summary, 18 modules are installed and their name is preceded by the readout channel number. The two modules without a number are the spare ones. In total a target mass of ~ 5 kg of $CaWO_4$ was installed in CRESST-II phase 2. In figure 3.16 an image of all modules mounted in the experimental volume is depicted. Twelve modules are of conventional design and additionally, for each of the three alternative designs two modules are installed. Four of the six crystals in the alternative designs are TUM-grown crystals, namely TUM29, TUM38, TUM40 and TUM45.

During the cooldown of the cryostat all 36 mounted detectors (18 phonon and 18 corresponding light detectors) had a transition to the superconducting state. While setting up the individual detectors it became clear, that one light detector of a conventional module could not be operated properly. A small heater current in this detector heats up the whole carousel driving all other detectors out of their transition. Since simultaneously the connection to the dedicated carousel heater was lost during cooldown of the cryostat, it was decided to sacrifice

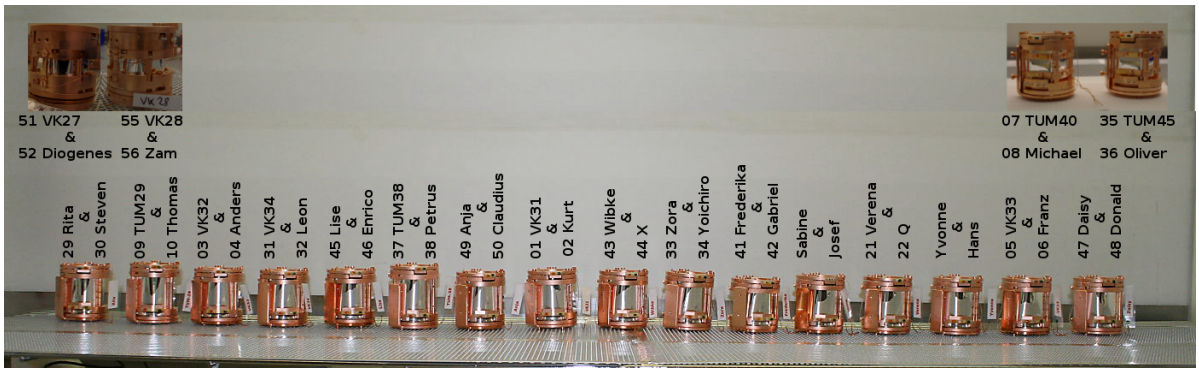

Figure 3.15: *Collage of all assembled modules right before mounting in the cryostat. In total 18 modules are installed corresponding to a target mass of ~ 5 kg $CaWO_4$. The numbers are the respective readout channels, while the labels are the corresponding names of the detectors. Light detectors have a male name, whereas phonon detectors have either a female name or a series of characters and numbers describing their supplier.*

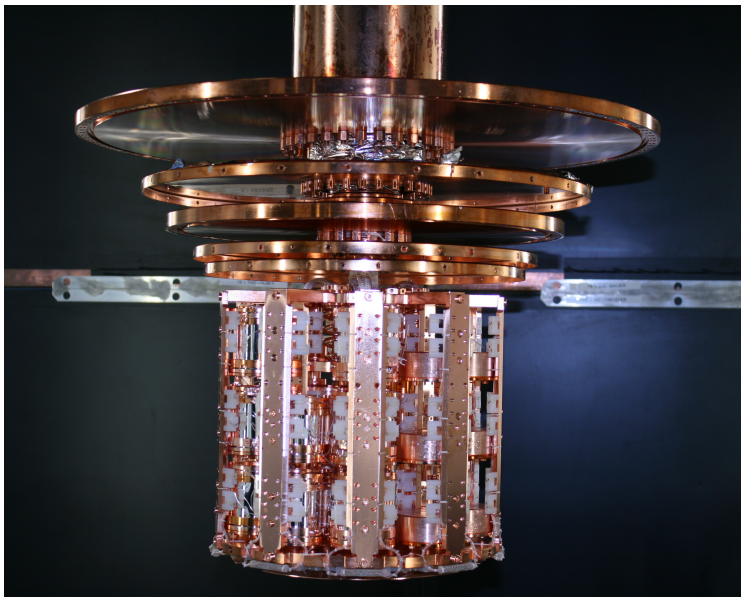

Figure 3.16: *Image of the experimental volume equipped with all modules mounted for CRESST-II phase 2.*

this non-fully functional light detector and re-use it as heater to improve the overall performance of the remaining detectors. The data of the remaining 35 detectors was recorded for more than two years and is available for analysis.

Part II

Raw Data Analysis

4 Data Preparation

Before the analysis of the collected data can start, some preparatory steps have to be performed. In this chapter, first the analysis software is briefly introduced in section 4.1. Thereafter, in section 4.2 all applied methods to derive the pulse parameters, which are of special interest for the analyses are described. Furthermore, the technique to properly determine the pulse height of the recorded pulses is discussed in section 4.3. Thereafter, the time dependent energy calibration (section 4.4) and the important light-yield parameter (section 4.5) are described. The anti-correlation of heat and light signal and the measure to correct for this effect and, thus, obtain the event type independent total energy are explained in section 4.6. In section 4.7 the accuracy of the energy calibration and the obtained energy resolution are discussed. At the end of this chapter, the trigger threshold measurement method is explained for one example and cross-checked with an alternative method in section 4.8.

4.1 Analysis Software

The backbone of every analysis is the software package used for it. In the present work a program called *OxRop* [118, 119], based on the ROOT analysis framework [120], is used to analyse the data. OxRop is a collection of classes to read, visualize and analyse in particular all binary data produced by the CRESST DAQ system. In addition, it also provides a graphical user interface to steer the whole analysis. The biggest advantage of OxRop, besides providing standard methods for data handling and analysis, is that it is easily extendible due to an interface for loading user-written macros and libraries. This allows to access all parts of the analysis and even develop and implement new features.

4.2 Pulse Parameters

In figure 4.1 a typical pulse recorded by a typical CRESST-II detector is shown. In the present work also the term *record* is used to describe obtained data. However, in contrast to the generic term *record* the term *pulse* implies a physical interaction recorded in the time window. For all the data sets analysed here, the records are sampled with a time base of 40 µs (i.e. 25 kHz sampling rate). One record consists of 8192 samples, hence lasting 327.68 ms. As described earlier (see section 3.3.2) the first quarter (2048 samples) of the pulse is called *pre-trigger region* and is mainly used for evaluation of the baseline parameters. The remaining three quarters of the pulse are denoted *post-trigger region* accordingly. Since the information of the absolute value of the baseline level is usually not used in the present work, all pulses are

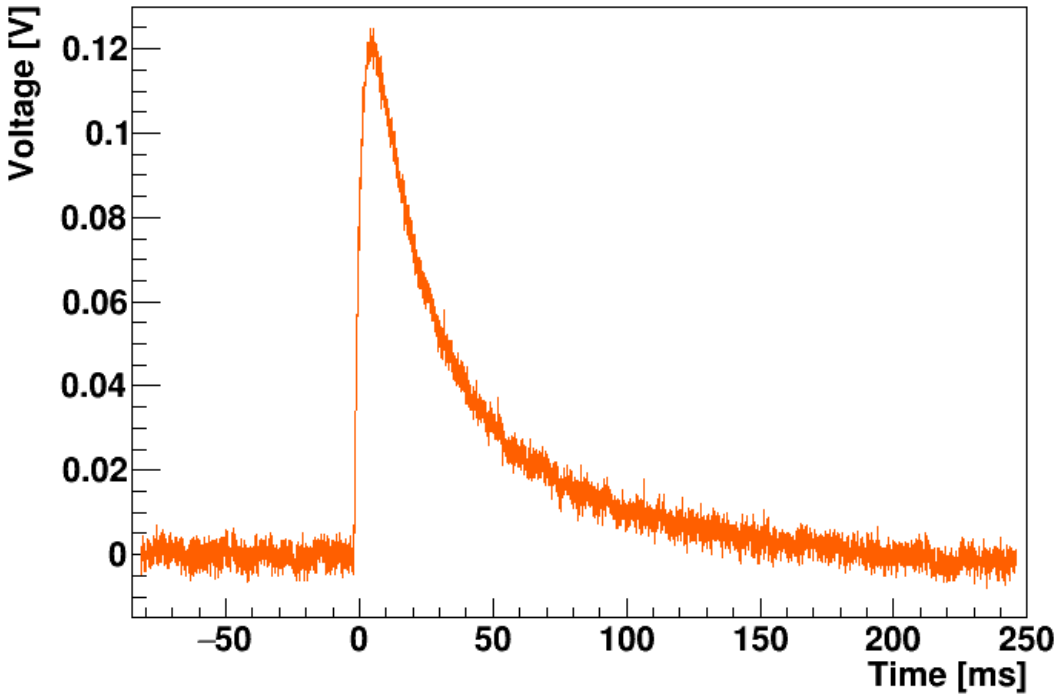

Figure 4.1: *A typical pulse recorded by a CRESST-II phonon detector – here TUM40 – with an energy of* ~ 13 *keV. The time base of the Data Acquisition (DAQ) system is 40* μ*s and 8192 samples are recorded at once. Hence, all pulses last for 327.68 ms, whereas the point in time when the trigger happened is set to zero. For each pulse the baseline offset is determined within the pre-trigger range and is afterwards subtracted from each sample of the pulse to center the baseline around zero.*

shown with a subtracted baseline offset, i.e. the samples of the pre-trigger region are centered around zero.

4.2.1 Main Pulse Parameters

For the analysis a set of parameters (called main parameters) is assigned to each pulse, which is partially already done online during the data taking by the DAQ system. The first step of the offline analysis is the calculation of an additional set of fast and robust parameters to describe the main features of each pulse [118]. Parameters which are determined online and stored on disk in the raw data file include:

Time The time of each trigger since the beginning of the respective data file in microseconds is saved. Together with the start time of the data file this information can be used to calculate the absolute time stamp of the event.

Trigger Delay This parameter is 0 for the first trigger of a given digitizer module. Other channels of the same module which trigger later (but before the digitizer module is read out) get assigned the time difference to the first trigger.

Test Pulse Amplitude For test and control pulses this parameter contains the actual amplitude of the injected artificial test pulse (in Volts). Control pulses usually have a test pulse amplitude ≥ 10 V, while particle pulses have per definition a test pulse amplitude of 0 V. Empty baselines, i.e. random triggers, recorded periodically throughout the whole data taking period, are also flagged by this parameter as test pulses with a negative amplitude.

Live and Dead Time These parameters store the cumulative live and dead time of the respective channel (as determined by the DAQ system), given at the time when the pulse occurred. When a new data file is started by the DAQ system, these values are reset to zero.

In addition to these online parameters also offline parameters are calculated for each pulse. Therefore, as a first step each record is shaped by a moving average filter with a width of 50 samples to reduce the influence of the noise[9].

Unless stated otherwise the offline parameters are determined from these shaped pulses. The most important ones are described here in detail:

Baseline Offset This parameter is the average of the absolute level of the first 95 % of the samples in the pre-trigger range. In the present work pulses are typically shown with their baseline centered around zero, which means that this parameter is subtracted from each sample of the record.

FWHM of Baseline This parameter is calculated using the standard deviation of the first 95 % of the samples in the pre-trigger range and assuming a Gaussian distribution of the samples.

Pulse Height This parameter is the maximum of the record minus the **baseline offset**. Therefore, it is a first estimator of the real pulse height of the pulse but biased due to the noise. In section 4.3 a more sophisticated method to determine the real pulse height of a pulse is explained.

Peak Position The position of the sample with the maximum signal height in the record (used for the **pulse height** parameter) is stored in this parameter.

Pulse Onset Going from the peak position backwards in time, the pulse onset is the point, where the signal height relaxes in the noise of the baseline. It is the first sample in the averaged record, which is smaller than the sum of the baseline level and the **FWHM of baseline** parameter value.

[9] A moving average filter calculates for each data point the average of a fixed number of samples. For the calculation of the next point the set of points is modified by a one-sample shift, i.e. the first element is replaced by the next sample, previously not included in the set. Special treatment is necessary for the absolute beginning and end of the pulse where not enough samples are recorded previous or subsequent to the respective data point. Thus, the high-frequent components (mainly noise contributions) are suppressed, while the slow components are highlighted.

Rise and Decay Time Two rise time parameters are stored to describe how much time is required for the plain record, i.e. the samples without averaging, to rise from 10 % to 50 % or 70 %, respectively. Furthermore, the time necessary to decay from the maximal sample to $1/e$ of the total **pulse height** is calculated.

Right−Left Baseline This parameter describes the difference between the average of the last (right) and the first 50 (left) samples of the plain record.

Delta Voltage/RMS Some pulses show negative delta peak like distortions (see, e.g. figure 5.1b) most probably caused by external electronic disturbances [121]. To tag these pulses, a loop over all samples of the plain record is performed and, thereby, the largest voltage drop between adjacent and next-to-adjacent samples is calculated. To relate the voltage drop with the observed baseline noise at the time of the pulse, the quantity is normalized to the root mean square (RMS) deviation of the baseline.

4.2.2 DAQ Live and Dead Time

The exposure of a detector is the product of the target mass times the live time, i.e. the time when the detector was able to recognize an event. Hence, the live time is simply the difference of the real time minus the dead time, i.e. the time when no trigger can occur. As mentioned beforehand, each pulse carries two additional cumulative parameters, **dead time** and **live time**, which are only reset at the beginning of a new data file.

After each trigger, further triggering is blocked for a complete pre-trigger range (81.92 µs) to ensure a valid pre-trigger region for the next record. Each pulse introduces a dead time and, thus, the DAQ increments the Dead Time parameter of the respective channel accordingly. Furthermore, the time required for the read out of the records is also added to the dead time parameter of the respective channels. After a trigger in at least one detector, all channels on the same transient recorder (8 channels) are allowed to trigger only half of the post-trigger length (= 122.88 ms). Thus, for the channels which do not trigger in the digitizer module, this time value is added to the dead time parameter. The live time parameter on the other hand is set to the real time minus the dead time value.

Also heater pulses, regardless whether control or test pulses, introduce additional dead time since they get flagged by the DAQ accordingly and, thus, are not considered as Dark Matter data[10]. To increase the probability that the control pulse height is determined correctly the control pulse is only shot if a time corresponding to the pre-trigger range is trigger free in all detectors. Therefore, control pulses that are fired after a free pre-trigger range, only add the post-trigger range of $3/4 \cdot 8192 \cdot 40\,\mu s = 245.76$ ms to the dead time parameter of all detectors. However, to ensure a proper operation of the detector, after a certain number of skipped trials, the control pulse is shot regardless if the pre-trigger range is trigger free or not. The latter procedure is the default always applied for test pulses. Thus, for both cases, where it is not checked whether a trigger occurred in the pre-trigger range, the dead time is increased by a value of 327.68 ms, corresponding to the complete record length.

[10] In the present work, data obtained without a radioactive source mounted next to the cryostat is denoted with this term, since it can be used for the search for Dark Matter.

4.3 Pulse Height Determination

As stated before the **pulse height** parameter is only a rough estimator of the actual true pulse height of the record. First of all, the pulse height is biased since it is determined as the pure maximum of the record. Therefore, the probability for choosing a sample with positive noise fluctuation is higher than choosing one with negative fluctuation. This leads to a tendency to overestimate this parameter compared to the true pulse height.

In addition, the determined pulse height is only a valid measure for the energy deposited as long as the pulse shape is the same for all recorded pulses of a specific pulse class[11]. For small pulses which probe only a small region in the transition this condition is fulfilled. However, due to the finite transition region from the super to the normal-conducting state this is not always true for larger pulses. The extreme case of a large pulse, driving the TES completely to the normal-conducting state, results in a record, where the uppermost part is almost flat since the resistance is almost constant above the transition region. However, due to non-linearities in the transition the pulse shape of larger pulses is already changing before this point.

These two facts rise the need of a more accurate method to determine the energy deposited, hence the real pulse height of the pulse. Additionally, this method should be less influenced by noise and non-linearity effects, in particular compared to the pulse height method.

4.3.1 Template Fit

The so-called *template fit* (also denoted *standard pulse fit*) fulfills all the previous specifications. Thereby, a template describing the measured pulse shape for particle induced events is fitted to all recorded pulses and a robust estimate of the actual pulse height is gained.

By averaging pulses of a sufficiently large data set (usually a few hundred pulses) a template for this pulse class is created. To avoid the effect of the trigger walk[12] only pulses from a narrow energy window are selected. In practice, mostly mono-energetic lines within the background spectrum or from the calibration data are used to generate templates. The selected pulses have to be sufficiently small so that they are part of the linear transition region of the respective detector. Furthermore, very strict quality cuts are applied to select only proper pulses with a clean pulse shape typical for this pulse class. Following this procedure the resulting template describes the typical pulse shape of a pulse of the respective pulse class from the linear transition region. In addition, due to the averaging over several pulses a reduced noise contribution compared to a single pulse is achieved.

The template pulse is then fitted to all recorded pulses (see figure 4.2 for an example) by minimizing the Root Mean Square (RMS) deviation of the fitted function and the recorded data points. There are three free parameters, namely the baseline offset (1), the shift of the pulse in time (2) and finally a scaling factor of the pulse height, the sought-for amplitude (3). These three parameters are stored together with the RMS of the fit for later use in the analysis.

[11] As long it is ensured that with a larger amount of energy deposited also a large pulse height parameter is obtained, it is reasonable to compare pulses of different pulse classes. In that case a larger pulse height results in a larger energy value in each class.

[12] The term trigger walk denotes an influence of the trigger time (relative to the true onset of the pulse) on the pulse height.

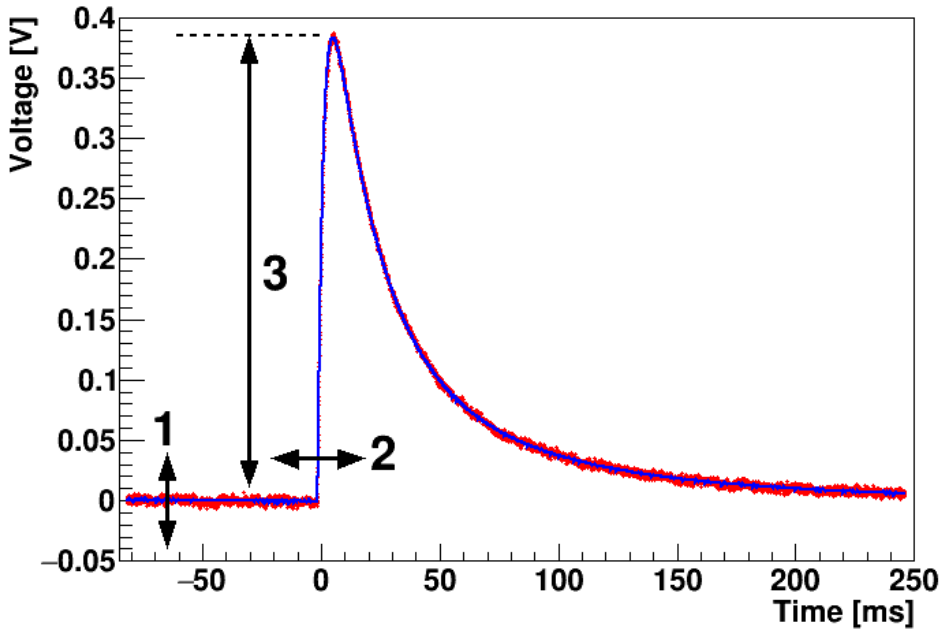

Figure 4.2: *Example of a recorded pulse (red data points) fitted with a template pulse (blue solid line) of the respective detector (here: TUM40). During the fit the three free parameters are the baseline offset (1), the time shift (2) and the amplitude (3) of the template.*

The resulting amplitude is the desired measure for the real pulse height of the pulse. The present work sticks to the term *amplitude* for this quantity to distinguish it from the simple pulse height parameter described earlier.

4.3.2 Truncated Template Fit

The fit method described up to now only works well for pulses in the linear region of the respective detector. Typically this region reaches up to 100 keV and is large enough for our standard Dark Matter search. However, it is desirable to be able to analyse also pulses with high energies (e.g. α-events in the MeV range).

The recorded pulse shape maps the transition curve of the respective TES. However, in particular for higher energies, it is not valid to describe the shape of the transition only by a constant slope. Thus, for the unmodified fit (see figure 4.3a) the RMS distribution is clearly rising for higher amplitudes. In conclusion, it is shown that the simple template fit only yields a valid amplitude for pulses of the linear region and that the linear template is not able to extract the amplitude of high-energetic events.

Nevertheless, even for large pulses parts of the pulse information, in particular the samples below the specific amplitude, are well described by the linear template. Hence, the template fit method is slightly modified to truncate the pulse at a certain level (the so-called *truncation limit*). During the fit all samples with a larger signal height with respect to this limit are neglected in the fit, in particular in the RMS calculation (see figure 4.4). Thus, only the linear parts of the pulse are fitted leading to an amplitude, which is effectively obtained by an

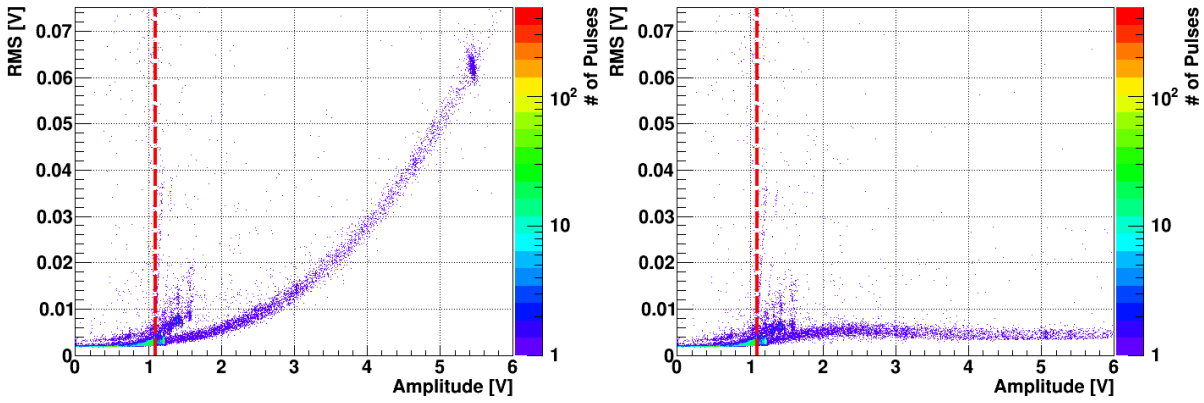

(a) *Template fit* **(b)** *Truncated template fit*

Figure 4.3: *Comparison of the RMS distribution as function of the fitted amplitude of a standard (a) and a truncated template fit (b). Pulses with large amplitudes exceed the linear region of the transition curve (to the left of the vertical dashed line) and, thus, the resulting pulse shape is distorted. For the unmodified template fit, this leads to an increasing RMS deviation starting at a certain amplitude above the linear region (a). However, the samples of such pulses, which probe the linear region, are well described by the template. Thus, in the truncated fit all samples above the linear region, i.e. above the truncation limit, are neglected. This results in a nearly constant RMS deviation even for large amplitudes (b). For the shown detector the truncation limit is set to 1.1 V (red dashed line).*

extrapolation of the linear pulse shape to the non-linear regime. Indeed, this method linearizes the detector response up to energies of, e.g. α-particles ($\mathcal{O}$(MeV)) (see figure 4.3b), which allows for detailed studies even of the high-energetic background contribution in CRESST-II detectors [115].

4.3.3 Correlated Template Fit

Only $\lesssim 9\,\%$ of the energy deposited in the target crystal is converted into scintillation light [95]. In particular for nuclear recoils at low energies, this leads to pulses in the light detector, which are hardly separable from baseline fluctuations. However, there is additional information which could be used to solve this task, namely the timing between phonon and light channel. Since most of the energy of a particle event is usually detected in the phonon channel it is easier to determine the position of its pulse. Thus, the position of the pulse is known also for the light detector and one free parameter in the fit is restricted by this external information. A correlated (truncated) template fit is performed, whereas the templates of the phonon and light channel are fitted simultaneously to the respective pulses with a common shift parameter. With this modification, a clear pulse onset in one of these channels (typically in the phonon channel) helps to improve the fit in the other channel.

One essential requirement for the proper functionality of this correlated fit method is that the templates of the phonon and light channel must have the correct relative timing. This can be ensured by using exactly the same set of pulses and in particular events from a small energy

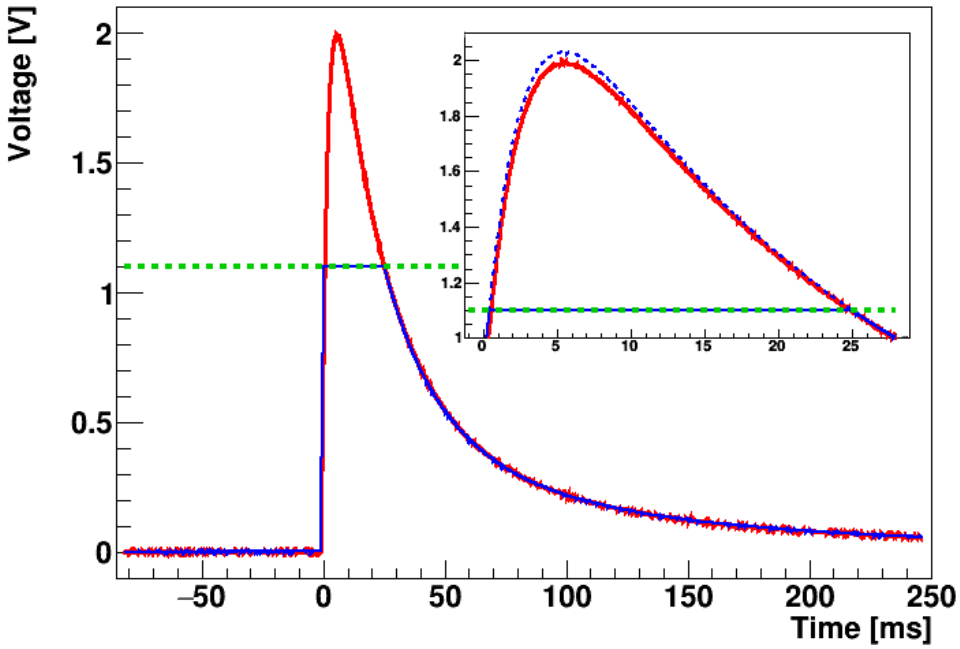

Figure 4.4: *Example of a truncated template fit (solid blue line) and the respective pulse samples (red data points). In this case the truncation limit (green dashed line) is set to 1.1V (compare figure 4.3). All samples with a signal height above the truncation limit are neglected in the fit to remove non-linearity effects. Therefore, the resulting reconstructed amplitude (here: 2.03 V) is an extrapolation of the linear template. This is also visible in the inlay which shows a zoom into the region of the pulse maximum. Again the actual pulse is drawn in red, while the extrapolated pulse template is depicted as blue dashed line.*

region for the creation of both templates (phonon and light), so that the relative timing is not affected by a trigger walk effect.

4.3.4 Pile-up and Noise

To account for pile-up events and low-frequency noise another slight modification of the template fit is possible. This is necessary, when either the previous pulse is not completely decayed or when the baseline is not flat due to low-frequency noise. In both cases this results in a tilted baseline, which might drastically deviate from the baseline of the template (see figure 4.5). One possibility to correct for this effect is fitting the sum of the template and a specific baseline model to the pulse. In OxRop either a polynomial model ranging from order zero to three or an exponentially decaying function can be used for this task. The results of template fits with different baseline models are compared later in section 4.7.2.

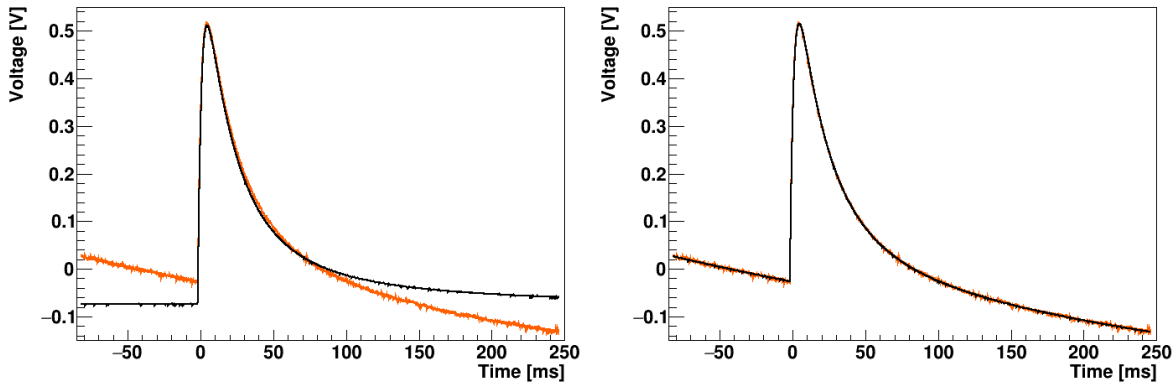

(a) *Fit with template only*

(b) *Fit with a cubic baseline model*

Figure 4.5: *Example of a pulse with tilted baseline, once fitted with the bare template (a) and once allowing for a tilted baseline by fitting the sum of the template and a cubic baseline model (b).*

4.4 Energy Calibration

After the amplitude of each pulse has been determined by the template fit, the resulting amplitude has to be converted into physical energy deposited. In this section the different steps of the energy calibration process are described in detail.

4.4.1 Cobalt-57 Calibration

First of all, the detectors have to be irradiated at least once in the beginning of the data taking campaign with a radioactive source with known (mono-energetic) lines or spectral features. In CRESST, typically a ^{57}Co-source is used, which has prominent γ-lines at 122.1 keV and (with reduced intensity) at 136.5 keV [90]. Both γ-rays are energetic enough to penetrate several layers of copper, e.g. the vacuum cans and thermal shields surrounding the experimental volume. Thus, the source is placed outside of the cryostat but inside the massive shielding next to the outermost vacuum can.

In figure 4.6 the measured energy spectrum of a ^{57}Co source is depicted for a phonon (black) and the corresponding light detector (red). While the phonon detector is able to resolve the main emission lines of the radioactive source at 122.1 keV and 136.5 keV this is not the case for the light detector. The different spectral features besides the already mentioned main γ-lines are explained in section 4.7. The energy deposited in the target crystal is shared between the creation of phonons and scintillation light. For γ-events $\gtrsim 91\,\%$ of the energy is converted into phonons measurable in the phonon channel and only $\lesssim 9\,\%$ into scintillation light [95]. For nuclear recoil events even less light is produced and, thus, due to energy conservation the phonon signal is slightly enhanced. This means, that for a fixed energy deposition in the target crystal, the detected phonon signal is almost independent of the interacting particle type. Therefore, the energy scale of the phonon channel determined with the ^{57}Co-source is a good estimator for the total-energy scale regardless of the incident particle. In contrast to the

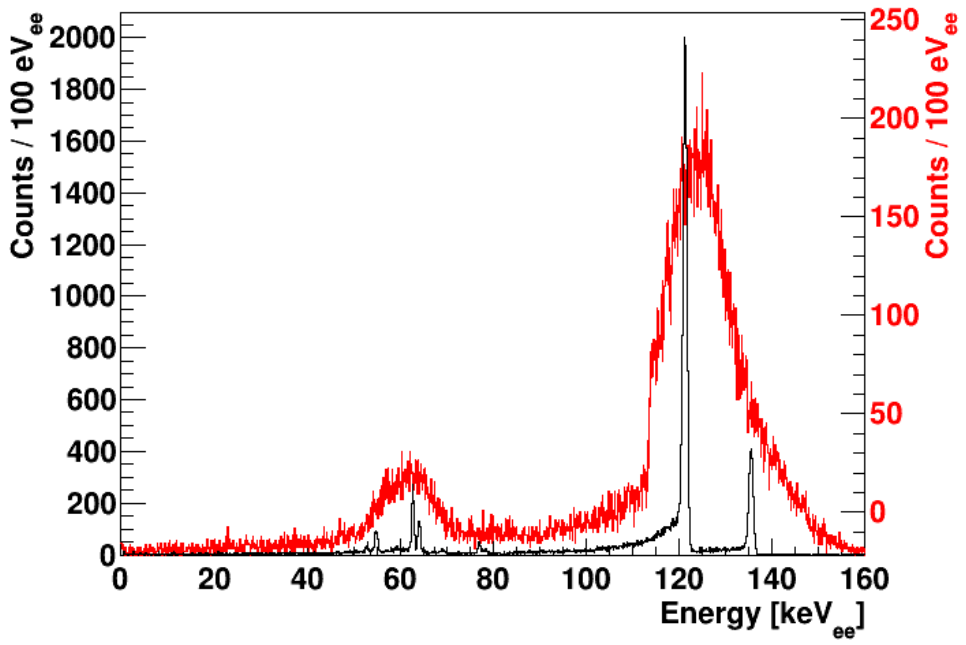

Figure 4.6: *Measured energy spectra during the ^{57}Co calibration with a phonon (black, TUM40) and the corresponding light detector (red, Michael). The resulting energy scale of this energy calibration is denoted as electron equivalent and, thus, labeled with the subscript ee. The light channel cannot resolve the two main emission lines of the radioactive source at 122.1 keV$_{ee}$ and 136.5 keV$_{ee}$. The lines observed around 60 keV$_{ee}$ are tungsten escape peaks (see section 4.7).*

phonon channel, the amount of energy deposited in the light channel is strongly dependent of the interacting particle. Hence, the scale set by the ^{57}Co-calibration only yields the true energy deposited for γ-events. More strictly speaking it is only true for events, which have the energy of the γ-source (here 122.1 keV). Other particles (e.g. nuclei) interacting with the scintillating crystal produce less light when depositing the same amount of total energy, resulting in lower energy values measured in the light detector. Since the calibration is performed with γ-rays inducing electron recoils, this effect is formally taken into account by denoting the energy scale (especially of the light channel) as electron equivalent with the typical unit keV$_{ee}$. Strictly speaking this is required for both detector channels, but for the phonon channel the subscript "ee" is usually skipped since the energy response in this channel is almost independent of the particle used for the calibration.

4.4.2 Test Pulse Calibration

The ^{57}Co-calibration probes the detector response for 122.1 keV γ-events at the time when the calibration takes place. To monitor the detector response for a wider energy range and, in particular, at different times throughout the data taking period, CRESST relies on the usage of test pulses. These pulses are injected at a constant rate and with different amplitudes, which are similar in shape to particle pulses. They serve two distinct purposes: firstly they

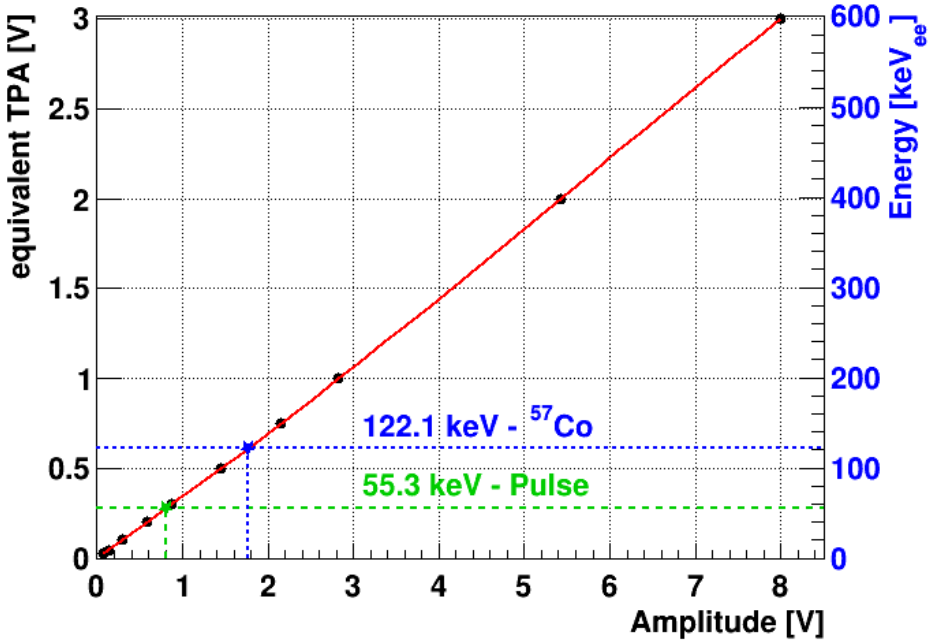

Figure 4.7: *Example of the energy calibration of a single particle pulse. The data points (black dots) are the response to injected heater pulses with dedicated test pulse amplitudes evaluated at the time of the particle pulse. To model the detector response, describing the relation between reconstructed amplitude and injected test pulse amplitude, a polynomial of low order is fitted to these data points (red solid line). By evaluating this fit function at the measured amplitude of the particle pulse, the amplitude is first converted to an equivalent test pulse amplitude (TPA, left y-axis). Since the absolute energy scale is fixed typically at 122.1 keV during the calibration with a ^{57}Co-source, a linear transformation of the (equivalent) test pulse amplitude yields the amount of energy measured (right y-axis).*

help to transfer the detector response down to the lowest energies of interest and, secondly, probe potential time dependencies in the detector response. Thus, it is possible to correct for detector-response drifts in the offline analysis, leading to an almost time independent energy reconstruction combined with an excellent energy resolution.

In a purely ohmic heater circuit the injected energy E is proportional to the square of the injected heater voltage U [13]. For the power P and the current I the following relations hold: $P = U \cdot I$, $I = U/R$, so that finally $E \propto P = U^2/R$. The heater voltage is sent through an analog square root circuit to linearize the output. Hence, for a linear thermometer a linear dependence of the reconstructed amplitude on the injected voltage is expected. Like in the case of particle pulses, the amplitude of a test pulse is evaluated applying the truncated template fit method (see section 4.3.2) utilizing a dedicated template for (low-energetic) test pulses.

In figure 4.7 the relation between injected test pulse voltage and the reconstructed amplitude is depicted for all test pulses with different injected amplitudes evaluated at the time of

[13] The naming convention in CRESST for the injected voltage amplitude is “test pulse amplitude”. Therefore this name is used throughout the present work.

a certain particle event. As expected, the dependency between injected and reconstructed amplitude seems to be rather linear, especially for small test pulse. Thus, a low-order polynomial (typically between order 3 and 5) is fitted to the data points to model the transfer function between injected test pulse amplitude and reconstructed amplitude. This detector response can now be evaluated also for a particle pulse to transfer the reconstructed amplitude (x-axis) to an equivalent test pulse amplitude (left y-axis).

As described before, the absolute energy scale is fixed at a single point during the calibration of the heater with radioactive sources. This step connects the injected test pulse amplitude (left y-axis in figure 4.7) and the equivalent particle energy (right y-axis in figure 4.7) via a linear relation. The latter is the (electron equivalent) energy that a particle has to deposit in the target crystal to create the same signal amplitude (response) in the detector as a heater pulse. Thereby, the only parameter required is the linear conversion factor, also called *CPE-factor* (see also appendix B). The value of this parameter is obtained, by first identifying the two test pulses which create amplitudes next to the measured amplitude of a γ-ray of the calibration source interacting in the target crystal. In the next step the injected heater amplitudes of the identified test pulses are used to perform a linear interpolation and evaluate the interpolation function at the measured amplitude of the calibration source. As explained earlier, in CRESST-II typically the 122.1 keV line of a ^{57}Co-source is used for this calibration.

4.4.3 Correction for Time Variations

If the detector response to test pulses is known at all times, the previously described calibration scheme allows to correct also for time dependencies in the detector response. Since test pulses are fired with a fixed rate and, thus, at distinct times, a proper interpolation method is required to track time variations and achieve the best energy resolution.

In figure 4.8 the reconstructed amplitude of heater pulses with a test-pulse amplitude of 0.1 V (black data points) is depicted as a function of the (real) measurement time. Small fluctuations of the amplitude are observable and since the functional form of these time variations is not known a method called *smoothing spline* is used to model this behavior [122]. One example of such a smoothing spline is also shown in figure 4.8 as solid red line. The most important parameter in this method is the so-called *smoothing factor* p which needs to be set a-priori. Depending on the parameter value of p in the allowed interval $[0,1]$ the behavior of the smoothing spline changes. In the extreme case of no smoothing at all ($p = 0$), the smoothing spline method converges to a spline interpolation while in the other extreme case of $p = 1$ the smoothing spline is exactly a linear least squares estimate [122].

During the refilling procedure of the cryostat, data taking is stopped since usually all detectors are non-functional due to the increased temperature induced by mechanical vibrations. By the time when all detectors are fully functional again, data taking is continued. This leads to time periods between the two data files were no test-pulse response is recorded (red shaded areas in figure 4.8). Thus, in the present work the whole measuring time is split into numerous small data sets for the energy calibration[14]. For each of these data sets and in addition for

[14] Usually, the size of these data sets corresponds to at least two days which is the time of one cryostat fill cycle. Technically, a new spline is determined, whenever no test pulse was recorded for more than 30 minutes.

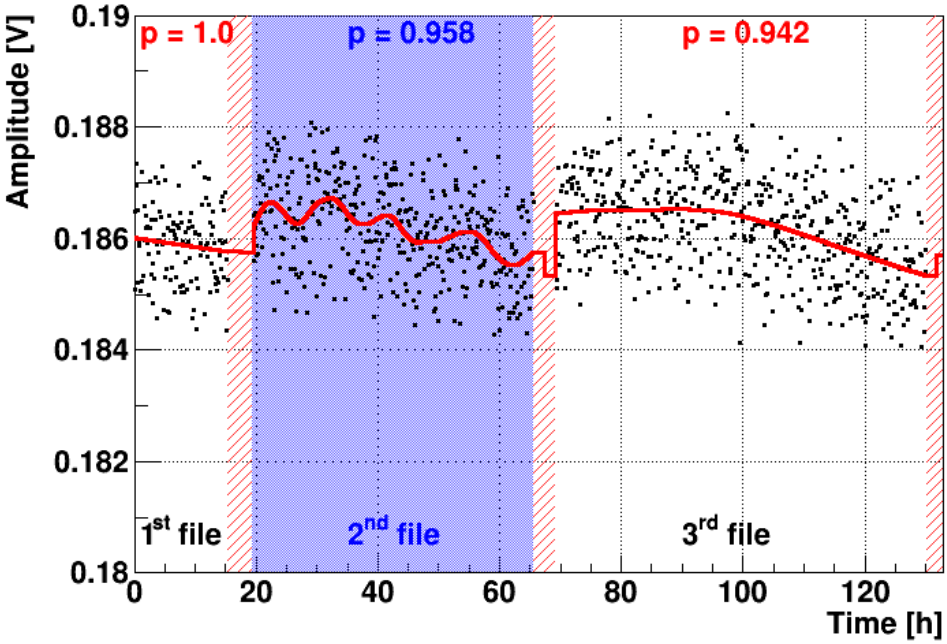

Figure 4.8: *Reconstructed amplitude of 0.1 V test pulses as a function of time. As for particle pulses, the amplitude is reconstructed with a truncated template fit (see section 4.3.2) but with a dedicated test pulse template. For the refilling procedure of the cryostat the data taking is stopped and, thus, no test pulses are recorded between the different files (red shaded areas). The functional form of the time variations is unknown and unpredictable. Therefore, a smoothing spline (red solid line) is adjusted to the data points to model the time dependency. The automatically chosen smoothing factor p for the respective files is also given. During the energy calibration these splines are evaluated to get the approximate detector response at all times. See text for a more detailed explanation.*

the different test-pulse amplitudes smoothing splines have to be adjusted leading to a huge number of smoothing parameters. This might lead to discontinuities between two consecutive splines as observable in figure 4.8.

In contrast to previous works, where the spline parameter was fixed to a specific value, a new method (so-called adaptive method) was implemented in close collaboration with [123] to determine the smoothing factor p automatically. Therefore, the data points for each smoothing spline are split into a training and a test data set and p is varied in the allowed range of $[0, 1]$. For a given value of p the smoothing spline algorithm is only performed for the training set, while the RMS deviation of the resulting function and the data points is calculated for the test set. The optimum value of p is determined such that the calculated RMS is minimal.

After fitting[15] the splines to all test pulse amplitudes the energy of a particle pulse is derived as described in the previous section. The only difference is that the polynomial transfer function is now fitted to the values of the different splines, evaluated at the time of the particle

[15] In the present work the smoothing parameter is limited to the interval $[0.5, 1]$ and, therefore, the spline behaves more like a fit and less like a spline.

smoothing factor	^{55}Fe 6.2 keV	Cu K$_\alpha$ 8.0 keV	^{57}Co–W K$_\beta$ 54.0 keV	^{57}Co–W K$_\alpha$ 63.5 keV	^{57}Co 122.1 keV	^{57}Co 136.1 keV
	Energy resolution [eV]					
adaptive	112±9	121±15	445±15	421±7	706±3	745±7
fixed	115±9	125±16	449±15	421±7	703±3	746±7

(a) Lise

smoothing factor	Cu K$_\alpha$ 8.0 keV	^{57}Co–W K$_\beta$ 54.0 keV	^{57}Co–W K$_\alpha$ 63.5 keV	^{57}Co 122.1 keV	^{57}Co 136.1 keV
	Energy resolution [eV]				
adaptive	100±28	401±21	362±9	625±4	596±8
fixed	106±31	394±22	362±9	612±4	592±8

(b) TUM40

Table 4.1: *Energy resolutions of different spectral lines obtained with the two different smoothing methods (adaptive and fixed) for the detectors Lise (a) and TUM40 (b). In all cases the test pulse set is pre-cleaned by limiting the allowed amplitude range. For the fixed method the smoothing factor is set to $p = 0.98$, while for the adaptive method the newly developed algorithm is carried out. Independent of the module, almost no differences for the obtained energy resolutions of both methods are observed. However, for the adaptive algorithm the handling of the numerous splines is much easier due to the higher degree of automation.*

pulse (see figure 4.7).

In order to select only test pulses with proper amplitudes two cuts are applied. First of all, the range of the reconstructed amplitude for each injected test pulse amplitude is limited by removing all test pulses which are located outside an allowed region. In a second step a smoothing spline with a pre-defined fixed smoothing factor (usually $p = 0.98$ for phonon detectors and $p = 0.95$ for light detectors) is calculated right before the automatic determination of the smoothing parameter. Based on the reconstructed amplitude and the distance to the spline function, test pulses which show too great a deviation from the mean population are rejected [124]. Thereby, the limiting deviation factor, which is given in units of the observed width of the distribution, and the maximal allowed fraction of rejected events (typically $\lesssim 20\,\%$) have to be specified. If a higher fraction of events should be removed by this automatic method the user is informed and can manually check the specific spline. Thus, together with the automatic smoothing the amount of splines which have to be investigated is drastically reduced.

In table 4.1 the obtained energy resolutions at different energies for the newly developed adaptive method are listed. Additionally, the energy resolutions for a fixed smoothing param-

eter of $p = 0.98$ are included for comparison. Almost no difference in the obtained energy resolutions is observed between both methods. However, as already described above the handling of the numerous splines is much easier for the adaptive method (due to the higher degree of automation) than for the fixed method.

4.4.4 Energy Calibration in a Nutshell

In summary, the energy of a particle pulse is reconstructed in the following way:

- First, the response function of the respective detector is determined by fitting a low-order polynomial to the heater-pulse amplitudes. To correct for time dependencies of the detector response, these data points are the results of smoothing splines evaluated at the time of the particle pulse.
- Since the detector heater is calibrated using a ^{57}Co-source, this response function provides a direct relation between the reconstructed amplitude and the (electron equivalent) particle energy.
- The response function is evaluated for the reconstructed amplitude of the particle pulse and the resulting energy is stored for later use.

In appendix B the derived values for the energy calibration obtained for all analysed detectors are listed.

4.5 Light Quenching and Light Yield

In a particle interaction the total amount of energy deposited splits up between the phonon and the light channel, but typically most of the energy is detected in the phonon detector. The remaining energy creates scintillation photons and the exact sharing depends on the incident particle. While for electron recoils $\lesssim 9\,\%$ of the energy deposited is converted into scintillation light it is even less for nuclear recoils [95]. This effect is called quenching and is exploited in CRESST-II to distinguish the different interaction types.

As already explained in section 3.2.4, events are visualized in the light yield - energy plane, where the different event populations form roughly horizontal bands (see figure 3.6). Thereby, the light yield LY is a dimensionless quantity defined as the ratio of the energy detected in the light channel L to the energy in the phonon channel E_P:

$$LY := \frac{L}{E_P}. \tag{4.1}$$

The energy values are assigned to both pulses of an event during the energy calibration as described in section 4.4. The e^-/γ-band is centered around a light yield of 1 since the energy scale in both detectors is determined with a γ-source. To be more precise, typically the energy calibration is performed with 122 keV γ-rays of a ^{57}Co source and, thus, the light yield is by definition 1 at exactly this energy.

The other bands have a reduced mean in the light yield parameter according to the respective quenching factors QF_x of the corresponding particle x. These quenching factors were measured with unprecedented accuracy in a dedicated campaign at the Maier Leibnitz Laboratorium (MLL) in Garching [117, 125]. Thereby, the tungsten quenching factor was determined precisely for the first time to be $QF_W = 0.0196 \pm 0.0022$. In addition, an energy dependence of the quenching factors of oxygen and calcium was observed, while for tungsten this effect turned out to be very small and was not measurable with the given light detector resolution. The empirical model to describe the energy dependence of the quenching factors of the two nuclei oxygen and calcium is discussed in [117, 125] with the final result:

$$QF_x(E_R) = LY_x^{\infty} \cdot (1 + f_x \cdot \exp(-(E_R/\lambda_x))), \tag{4.2}$$

where E_R denotes the recoil energy and LY_x^{∞} is the light yield at infinite recoil energy ($E_R = \infty$). LY_x^{∞} was determined together with the fraction f_x of the energy-dependent component and the exponential decay constant λ_x from a simultaneous likelihood fit to the data points at different energies. In table 4.2 the obtained fit parameters of the dedicated measurement for oxygen and calcium are listed. In addition, also the energy independent quenching factor of tungsten is included. For an easier comparison the respective light yield at 10 keV is shown in the last column. In [123] it is explained, how these parameters are implemented in the high-level analysis software and in this way they are also used in the present work.

particle x	LY_x^{∞}	f_x	λ_x	$LY_x^{10\,\mathrm{keV}}$
O	0.07908	0.7088	567.1	0.1342
Ca	0.05949	0.1887	801.3	0.0706
W	0.0196	-		0.0196

Table 4.2: *Energy dependent (for O, Ca) and energy independent (for W) quenching factors of $CaWO_4$ determined in a dedicated measurement at the MLL in Garching [117, 125]. The three parameters necessary for the evaluation of equation 4.2 for oxygen and calcium are listed. No energy dependency could be measured for tungsten with the obtained energy resolution of the light detector. For comparison also the LYs evaluated at 10 keV are included in the last column.*

4.6 Event Type Independent Total Energy

Due to the light quenching the amount of produced scintillation light depends on the interacting particle. Energy conservation implies that also the amount of energy detected in the phonon channel is slightly particle dependent. Due to this anti-correlation of heat and light signal the measured line widths in the phonon detector are increased compared to the actual energy resolution of the detector [126].

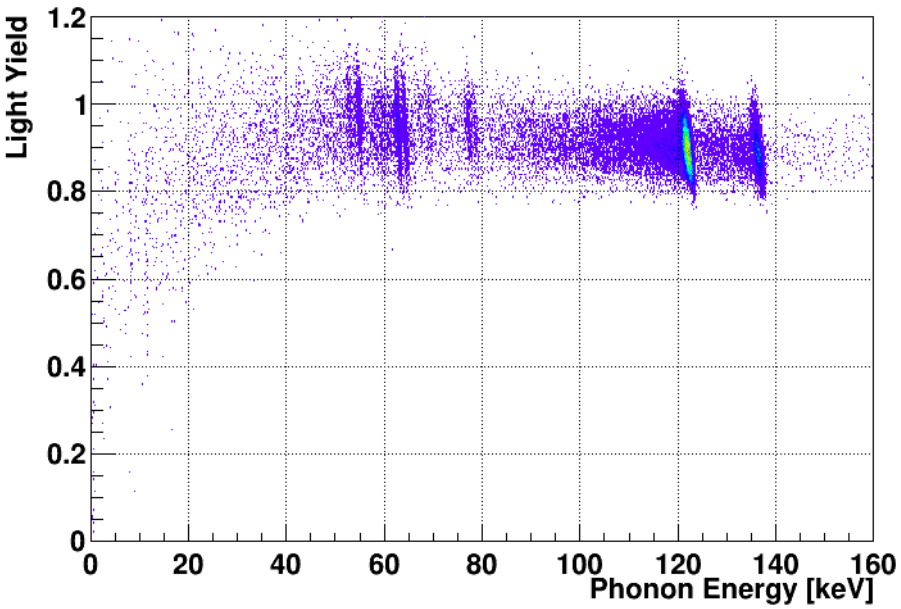

(a) *No correction applied*

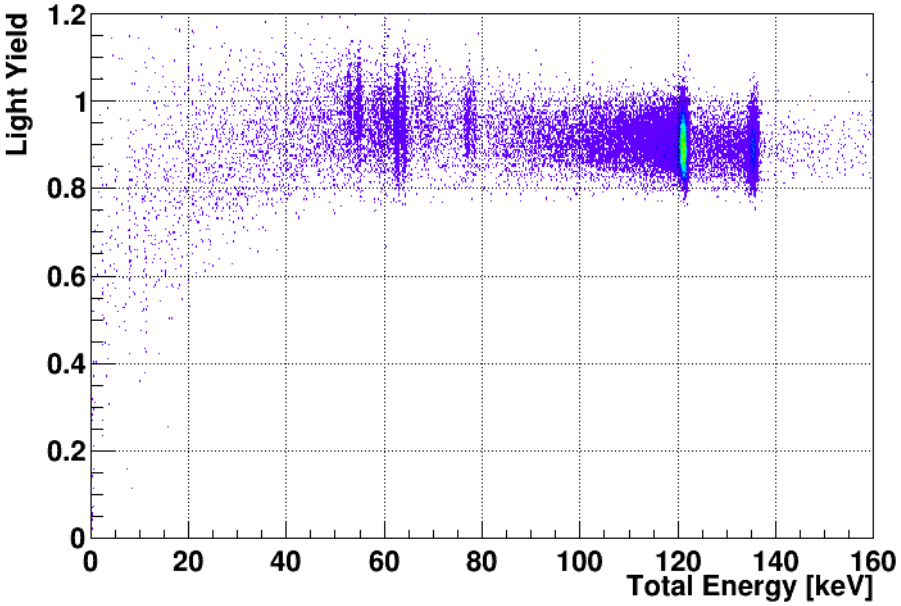

(b) *Anti-correlation correction applied*

Figure 4.9: *Due to energy conservation the particle dependent light signal results in a slightly particle dependent signal in the phonon detector. This is visible as tilted γ-lines in the light yield - energy plane of TUM40 (a). Applying a correction for this anti-correlation (see equation 4.3) results in straight vertical lines (b) and the event type independent total energy E_{total}. The scintillation efficiency of the (individual) $CaWO_4$ crystal (here: 6.6 %) is the only parameter in this algorithm.*

In figure 4.9a the light yield - energy plane of TUM40 is depicted. For almost all γ-lines a slight tilt is visible, leading to a non-optimal energy resolution in the phonon detector.

The tilt can be removed by applying the following formula [126, 127], resulting in the event type independent total energy E_{total}:

$$E_{\text{total}} = (1 - \eta\,(1 - LY)) \cdot E_P, \tag{4.3}$$

where E_P is the uncorrected energy measured in the phonon channel and LY is the measured light yield of this event. The amount of produced scintillation light η is in general crystal dependent. Using several different methods it is found to be $\sim$6.6 % for the crystal TUM40[16] [127]. This means that $\sim$6.6 % of the total energy deposited in the absorber crystal is converted into scintillation light. The resulting light yield - energy plot after applying the anti-correlation correction is shown in figure 4.9b. The tilt of the γ-lines observed in TUM40 vanished, leading to a better energy resolution of up to $\sim$ 31 % as summarized in table 4.3 for different γ-energies.

correction	**Cu K$_\alpha$** 8.0 keV	**^{57}Co–W K$_\beta$** 54.0 keV	**^{57}Co–W K$_\alpha$** 63.5 keV	**^{57}Co** 122.1 keV	**^{57}Co** 136.1 keV
	Energy resolution [eV]				
not applied	100±28	401±21	362±8	625±3	596±8
applied	78±14	305±16	251±6	438±3	463±7
improvement [%]	22.0	23.9	30.7	29.9	22.3

Table 4.3: *Improvement of the energy resolution of TUM40 due to the application of the anti-correlation correction.*

In section 2.1 the recoil energy is defined (see equation 2.4) as the amount of energy transferred to the target nucleus and, thus, recoil energy and the above-defined total energy are equivalent. In the remaining part of the present work, to separate the different available energy quantities the terms *phonon energy* as well as *light energy* always refer to the pure result of the energy calibration of the respective detector, while the phrase *recoil energy* is used for the event type independent total energy.

However, for the module consisting of the phonon detector Lise and the light detector Enrico this correction is not applied[17]. Enrico shows an unusual performance with a small signal height and a low signal to noise ratio. This results in a worse energy resolution (see table 7.1), which leads to extremely broad bands in the light yield - energy plane (see figure 7.5). The spread is clearly dominated by the worse energy resolution of the light detector and not by the

[16] In all cases when the anti-correlation correction is applied in the present work, the same scintillation efficiency of $\sim$6.6 % is used independent of the crystal [128].

[17] Thus, for the module Lise/Enrico only the energy measured in the phonon detector is available. However, due to the small size of the anti-correlation correction, this parameter is still a very good estimator for the event-type independent total energy deposited and, thus, for the recoil energy.

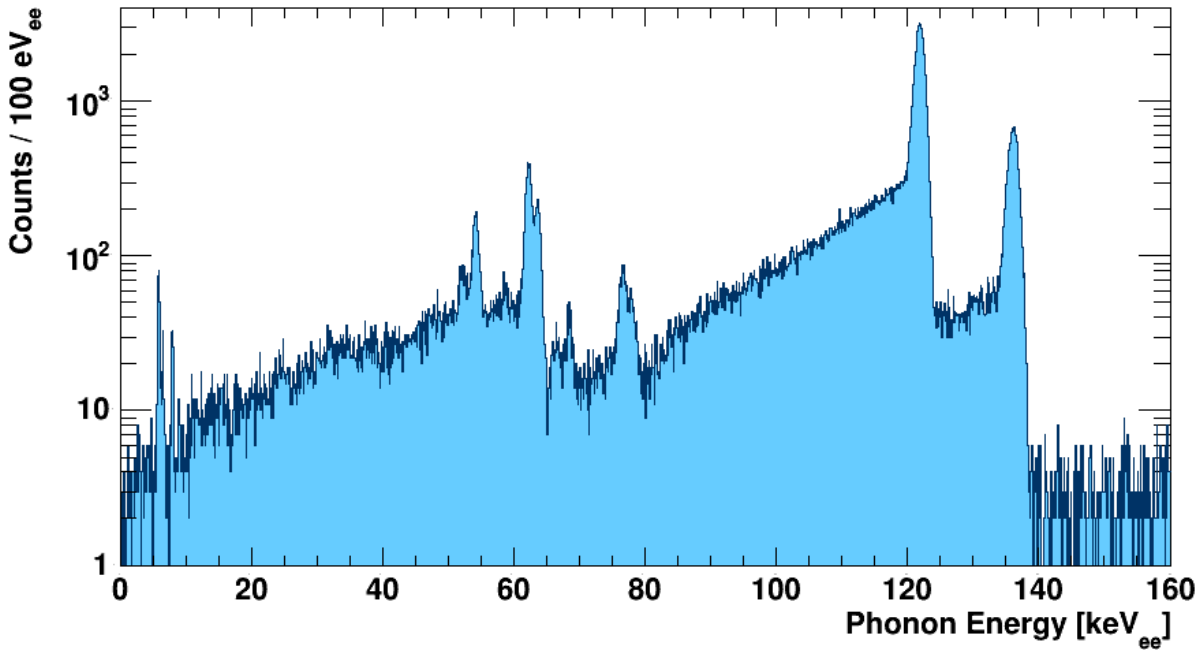

Figure 4.10: *Energy spectrum measured during the ^{57}Co calibration in the detector Lise. At 122.1 keV and 136.5 keV the main emission lines of the radioactive source are visible. At lower energies ($\sim$ 60 keV) tungsten escape lines are observed (compare table 4.4). See main text for more details on the observed spectral features.*

slightly different amount of produced light. However, since the measured light yield *LY* is a direct input parameter for the correction it is not valid to apply it in this case.

4.7 Validity Check of the Energy Calibration

Several checks are performed to show the excellent performance and the unique feature of cryogenic detectors in reconstructing the amount of energy deposited precisely.

The energy spectrum measured with the detector Lise during the irradiation with a ^{57}Co-source is depicted in figure 4.10. The two prominent lines at 122.1 keV and 136.5 keV are the main emission lines of the radioactive source. Due to the photoelectric effect a γ-particle of the ^{57}Co-source can excite a photoelectron and, simultaneously, create an excited atom. By emitting an X-ray the atom returns to the ground state. If the interaction of both particles is fully contained in the sensitive volume the energy detected equals the total energy of the original γ-ray. However, it is possible that only one of the two particles deposits its energy while the other one escapes without loosing energy in the detector. For the first case when the electron escapes, a line at the released X-ray energy is measured. However, since the interaction probability of electrons is higher with respect to a γ-particle, the second case of an escaping γ-particle, results in more pronounced so-called *escape lines* at the energy difference between the line energy and the energy of the released X-ray. In table 4.4 the X-ray energies of tungsten and the corresponding escape lines visible in a ^{57}Co calibration measurement are

line type	Origin	Energy [keV]
X-ray line	W $K_{\alpha 1}$	59.318
	W $K_{\alpha 2}$	57.981
	W $K_{\beta 1}$	67.244
	W $K_{\beta 2}$	69.067
Escape line	^{57}Co(122.1 keV)−W $K_{\alpha 1}$	62.743
	^{57}Co(122.1 keV)−W $K_{\alpha 2}$	64.080
	^{57}Co(122.1 keV)−W $K_{\beta 1}$	54.817
	^{57}Co(122.1 keV)−W $K_{\beta 2}$	52.994
Escape line	^{57}Co(136.5 keV)−W $K_{\alpha 1}$	77.156
	^{57}Co(136.5 keV)−W $K_{\alpha 2}$	78.493
	^{57}Co(136.5 keV)−W $K_{\beta 1}$	69.230
	^{57}Co(136.5 keV)−W $K_{\beta 2}$	67.407

Table 4.4: *Literature energy values of tungsten X-ray lines and the corresponding calculated ^{57}Co 122.1 keV and 136.5 keV escape lines [90].*

listed.

Due to low statistics only the tungsten escape lines of the ^{57}Co 122.1 keV line are clearly observable in figure 4.10. At $\sim$ 78 keV both K_α escape peaks of the 136.5 keV line overlap due to low statistics and the finite energy resolution. Since the X-ray lines are less pronounced with respect to the escape lines, only small peaks at the corresponding energies of $\sim$ 58 keV and $\sim$ 68 keV exist.

In addition to the spectral features introduced by the ^{57}Co-source additional lines are observed. Lise is accidentally illuminated by a ^{55}Fe-source mounted on a neighboring module for absolute light-detector calibration. ^{55}Fe decays by electron capture to ^{55}Mn and, thus, in Lise the K_α and K_β line of ^{55}Mn are observed at 5.9 keV and 6.5 keV, respectively [90]. At slightly higher energies (8.0 keV) the copper fluorescence line is also visible.

Throughout the remaining part of this section, the observed peaks (see, e.g. figure 4.10) are fitted in several small energy regions to obtain the energy dependent energy resolution as well as the mean position of the mono-energetic γ-lines. For a single peak in the spectrum a Gaussian function and a linear background contribution are fitted to the data. In case of two lines close ($\lesssim$ 5 keV) in energy – which is true for most of the spectral features – the fitted model consists of a linear background contribution and two Gaussian functions. Typically, the energy resolution of the detector is good enough to separate both lines. However, to improve the performance of the fit and in particular to enhance the convergence, it is assumed that in

the small energy range of the two nearby lines the energy resolution is not changing drastically and, thus, only a combined width parameter is introduced.

4.7.1 Precision of the Energy Reconstruction

The energies of the different γ-lines determined by the fit are compared with literature values taken from [90] and summarized in table 4.5. If lines of different origin overlap within the energy resolution σ of the detector, the given literature values are weighted means. In table 4.5a the fitted mean energies of the two main emission lines of the calibration source are listed. The more intensive line at 122.061 keV is used during the energy calibration to set the absolute scale. Furthermore, the observed tungsten escape lines related to the used radioactive source are listed in table 4.5b. Finally, table 4.5c lists the spectral features observed in Lise and TUM40, which are not induced by the ^{57}Co-source. In both detectors investigated here (Lise and TUM40) the copper fluorescence line at 8.041 keV is observed, while Lise additionally exhibits the two ^{55}Mn lines originating from a nearby ^{55}Fe-source.

Regardless of the detector, an excellent agreement between the reconstructed energies and the literature values is observed. For the module Lise the mean deviation is as low as 0.62 % while for TUM40 an even lower value of 0.37 % is found. This shows convincingly that the energy reconstruction is at no means an issue for cryogenic detectors and, thus, one advantage with respect to other direct detection techniques like liquid noble gas detectors. In addition, the values given in table 4.5 show that an excellent energy resolution is achieved in cryogenic detectors.

4.7.2 Baseline Model

In order to find the best baseline model describing the observed noise situation (see section 4.3.4) polynomials of different orders ranging from zero to three are used in the template fit. A fit with a zero-order polynomial baseline is identical to a bare template fit, since the constant offset is already a free parameter in the fit. For each baseline model, all pulses of the ^{57}Co energy calibration data are fitted and an energy calibration is performed. For this study the small anti-correlation correction of the phonon energy of TUM40 (see section 4.6) is not applied, since it requires the measured light yield as input. Hence, the measured energy in the phonon channel is required in order to calculate the light yield, whereas the reconstructed energy varies depending on the baseline model. Despite the fact that the correction results in a clear improvement of the energy resolution it is assumed that this improvement does not drastically depend on the baseline model. Thus, only a small influence on the conclusion from the investigation of the baseline model is expected.

The resulting energy resolutions at several energies are listed in table 4.6 for the two detectors Lise (a) and TUM40 (b). In case of a single line the stated energy corresponds to the literature value while in case of two nearby lines the mean value of both lines is given, yielding a proxy of the respective energy range.

When a baseline model is included in the template fit (polynomial order ≥ 1), a clear improvement of the energy resolution is observed with respect to the bare template fit in both detectors. As an example, due to the low statistics and the broadening caused by the worse

module	**origin**	^{57}**Co**	^{57}**Co**
	$\mathbf{E_{lit}}$ **[keV]**	**122.061**	**136.474**
Lise	$\mathbf{E_{fit}}$ **[keV]**	121.830±0.003	136.105±0.008
	$\frac{\mathbf{E_{fit}-E_{lit}}}{\mathbf{E_{lit}}}$ **[%]**	-0.19	-0.27
	$\boldsymbol{\sigma}$ **[eV]**	706±3	745±7
TUM40	$\mathbf{E_{fit}}$ **[keV]**	121.217±0.004	135.415±0.008
	$\frac{\mathbf{E_{fit}-E_{lit}}}{\mathbf{E_{lit}}}$ **[%]**	-0.69	-0.78
	$\boldsymbol{\sigma}$ **[eV]**	438±3	463±7

(a) *Main emission lines of the ^{57}Co-source.*

module	**origin**	^{57}**Co−W K$_{\beta 2}$**	^{57}**Co−W K$_{\beta 1}$**	^{57}**Co−W K$_{\alpha 1}$**	^{57}**Co−W K$_{\alpha 2}$**
	$\mathbf{E_{lit}}$ **[keV]**	**52.994**	**54.817**	**62.743**	**64.080**
Lise	$\mathbf{E_{fit}}$ **[keV]**	52.255±0.043	54.179±0.016	62.223±0.009	63.596±0.015
	$\frac{\mathbf{E_{fit}-E_{lit}}}{\mathbf{E_{lit}}}$ **[%]**	-1.40	-1.17	-0.76	-0.83
	$\boldsymbol{\sigma}$ **[eV]**	445±15		421±7	
TUM40	$\mathbf{E_{fit}}$ **[keV]**	52.839±0.034	54.817±0.016	62.731±0.008	64.069±0.011
	$\frac{\mathbf{E_{fit}-E_{lit}}}{\mathbf{E_{lit}}}$ **[%]**	-0.29	0.00	-0.02	-0.02
	$\boldsymbol{\sigma}$ **[eV]**	305±16		251±6	

(b) *Observed tungsten escape lines induced by the 122.1 keV γ-line of the ^{57}Co-source.*

module	**Lise**			**TUM40**
origin	**Mn K$_{\alpha}$**	**Mn K$_{\beta}$**	**Cu K$_{\alpha}$**	**Cu K$_{\alpha}$**
$\mathbf{E_{lit}}$ **[keV]**	**5.895**	**6.490**	**8.041**	**8.041**
$\mathbf{E_{fit}}$ **[keV]**	5.924±0.009	6.515±0.022	8.051±0.016	8.106±0.018
$\frac{\mathbf{E_{fit}-E_{lit}}}{\mathbf{E_{lit}}}$ **[%]**	0.49	0.39	0.12	0.81
$\boldsymbol{\sigma}$ **[eV]**	116±8		121±15	78±14

(c) *Low energetic γ-lines not related to the ^{57}Co-source.*

Table 4.5: *Fitted mean energy of the main emission lines of the ^{57}Co-source (a) and the tungsten escape lines (b) measured with Lise and TUM40. Table (c) lists the observed low energetic peaks. For comparison the literature values taken from [90] and weighted for intensity, if needed, are included. Finally, also the resulting energy resolutions σ at the given energies are contained for all γ-lines observed in both detectors.*

polynomial order	^{55}Fe 6.2 keV	Cu K$_\alpha$ 8.0 keV	^{57}Co–W K$_\beta$ 54.0 keV	^{57}Co–W K$_\alpha$ 63.5 keV	^{57}Co 122.1 keV	^{57}Co 136.1 keV
	Energy resolution [eV]					
0	230±49	n.A.	430±26	502±10	766±3	804±8
1	130±9	126±29	441±15	425±7	696±3	729±7
2	160±7	139±22	439±15	420±7	697±3	735±7
3	112±9	121±15	445±15	421±7	706±3	745±7

(a) Lise

polynomial order	Cu K$_\alpha$ 8.0 keV	^{57}Co–W K$_\beta$ 54.0 keV	^{57}Co–W K$_\alpha$ 63.5 keV	^{57}Co 122.1 keV	^{57}Co 136.1 keV
	Energy resolution [eV]				
0	-	567±32	480±16	721±4	674±11
1	182±36	422±22	385±9	619±4	600±9
2	202±73	416±21	371±9	616±4	601±8
3	100±28	401±21	362±8	625±3	596±7

(b) TUM40

Table 4.6: *Energy resolution in eV for different spectral features observed in Lise (a) and TUM40 (b) using ^{57}Co calibration data. All recorded pulses were fitted with the sum of the respective template and polynomials of given order to model the baseline. With increasing order of the polynomial the energy resolution improves since the observed noise contribution is modelled better. In case of two nearby lines ($\lesssim$ 5 keV) the given energy values are the mean values of the spectral features.*

resolution, no copper fluorescence line at 8.0 keV is observed in both detectors for a bare template fit (polynomial of order zero). However, for all fits including a particular baseline model the line could be fitted.

For the cases where a baseline model is included in the fit, at high energies almost no difference in the obtained resolutions is visible. This is expected, since the influence of the baseline noise is decreasing due to the higher signal-to-noise ratio for larger pulses. However, at lower energies relevant deviations are observed between the different models. The best result was achieved in both investigated detectors with a baseline model of a polynomial of order three. An improvement of maximal 51 % is observed for both detectors at 8.0 keV.

For the energy resolution of the two main emission of TUM40 a peculiar result is observed that with increasing energy the resolution improves. Although this effect is small it is systematically observed for all investigated polynomial orders. As explained above the anti-correlation correction is not applied in this study and when this correction is performed (see table 4.5) the resulting resolutions σ are increasing with increasing energy as expected. Thus, the small systematic effect here is due to the fact, that the scintillation efficiency η is energy

dependent (see table 4.3), as already observed in [126, 129].

In conclusion, in the present work the chosen baseline model for all detectors is a polynomial of order three, introducing four additional free baseline parameters in the fit[18]. As shown, this modification improves the energy reconstruction since the fit describes the observed data better, leading to an improved energy resolution.

4.7.3 Long-Term Stability of the Energy Reconstruction

As explained earlier, the module Lise is accidentally illuminated by a ^{55}Fe-source leading to two dominant lines in the low-energy region. In contrast to, e.g. the ^{57}Co-source, the low energetic radioactive source has to be mounted inside the experimental volume next to the respective detector, since it is unable to penetrate the several shielding layers of the cryostat. Thus, the spectral features induced by this source are observed throughout the whole data taking period. This allows to perform a long-term stability check of the energy calibration at energies inside the region of interest for Dark Matter searches.

For this analysis only events in the energy window of 5.5 keV–7.0 keV are considered. In total, data collected in a live time of ~ 4100 h, corresponding to ~ 171 live days, is analysed and depicted in figure 4.11. The fit function (red line) is the sum of two Gaussian functions with a combined width parameter modelling the two mono-energetic ^{55}Mn K lines, and a linear function for the observed background. Also in the Dark Matter data set the fit yields good agreement between the two means of the lines and the respective literature values.

In figure 4.12 all events in the relevant energy window throughout the data taking period are shown as gray points. As an overlay, the resulting mean positions together with the statistical errors of the Mn K_α (blue) and the Mn K_β (magenta) lines obtained in individual fits of 7 live day time slices are also shown. Almost no deviations from the fitted mean of the whole data set (cyan and violet solid lines) are observed for the mean positions, confirming the long-term stability of the applied energy reconstruction.

The time evolution of the energy resolution obtained from individual fits is depicted in figure 4.13. Due to low statistics in the individual time slices the resulting fit error in the width parameter is rather large. However, the red line shows the energy resolution determined in the whole data set and is in good agreement with the individual fit results. Thus, it is shown that also the resolution is rather stable for long time periods.

4.8 Trigger Threshold Determination

Another application of test pulses is the direct measurement of the trigger threshold of a detector. Therefore, in a dedicated measurement low energetic test pulses with discrete energies are

[18] The best choice to model the pile-up effect is an exponential decay with the decay constant of the template. In [123] also a test of the influence of the baseline model on the resulting energy resolution is performed, similar to the one presented here. One baseline model tested in [123] is the sum of an exponential decay and a polynomial of order two. However, it is shown, that the best resolution is still achieved by a template fit including a polynomial of order three as baseline model.

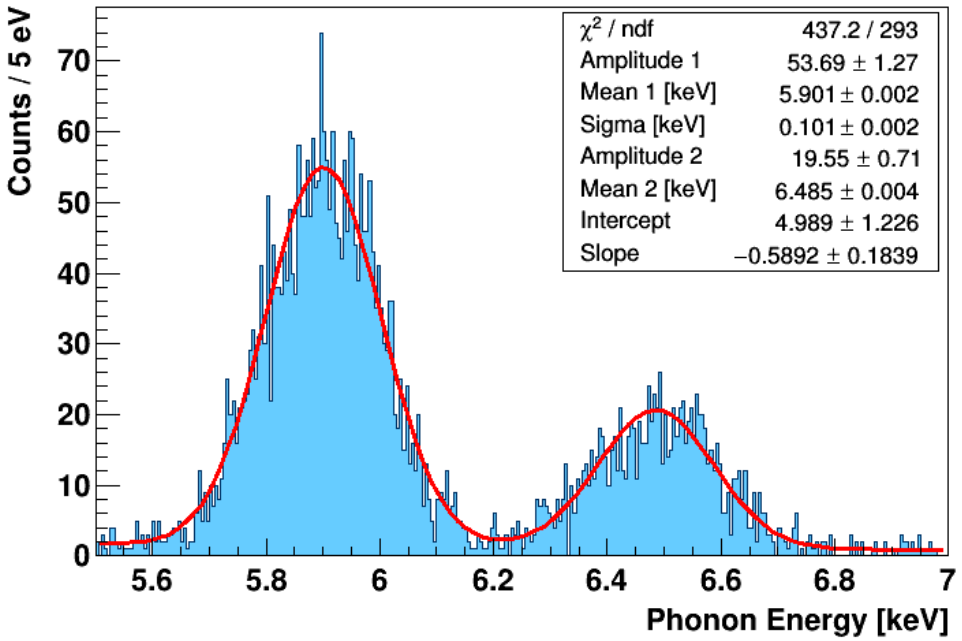

Figure 4.11: *Measured energy spectrum between 5.5 keV and 7.0 keV in the whole Dark Matter data set of Lise. In total a live time of* $\sim 4100\,h$ *has been collected. The* ^{55}Mn K_α *(5.90 keV) and* K_β *(6.49 keV) lines are induced by a* ^{55}Fe*-source mounted at a neighboring light detector accidentally illuminating Lise. The fit function is the sum of two Gaussian functions with a combined width parameter and a linear background (intercept and slope parameter).*

injected with exactly the same rate as in the Dark Matter data set to ensure the same stability conditions.

For the threshold determination, no cuts are applied on the test pulses. By simply counting the fraction of test pulses causing a trigger, the energy dependent acceptance is obtained as depicted in figure 4.14 for the example of the phonon detector Lise. Due to the finite baseline noise a deviation from an ideal step function for the trigger threshold is observed. The solid curve (red) is the function $f(E_{\text{inj}})$ describing the probability of a test pulse with a given energy E_{inj} to cause a trigger:

$$f(E_{\text{inj}}) = \frac{1 - p_{\text{pile-up}}}{2} \cdot \left[1 + \text{erf}\left(\frac{E_{\text{inj}} - E_{\text{th}}}{\sqrt{2}\sigma}\right)\right] + p_{\text{pile-up}}, \tag{4.4}$$

where erf denotes the Gaussian error function describing the convolution of the ideal step function and the baseline noise modelled by a Gaussian with width σ. The pile-up probability $p_{\text{pile-up}}$ (blue dashed line) accounts for random coincidences with any trigger. Pile-up events can cause triggers independent of the injected energy E_{inj} even well below the actual threshold of the detector resulting in a constant pedestal visible at low energies. The fit of $f(E_{\text{inj}})$ to the data points obtained for the detector Lise results in a value of $p_{\text{pile-up}} = (5.57 \pm 1.16)\,\%$, which is compatible with expectations based on the trigger rate in this module and the respective coincident time window. For the energy threshold, which is defined to be at 50 % acceptance,

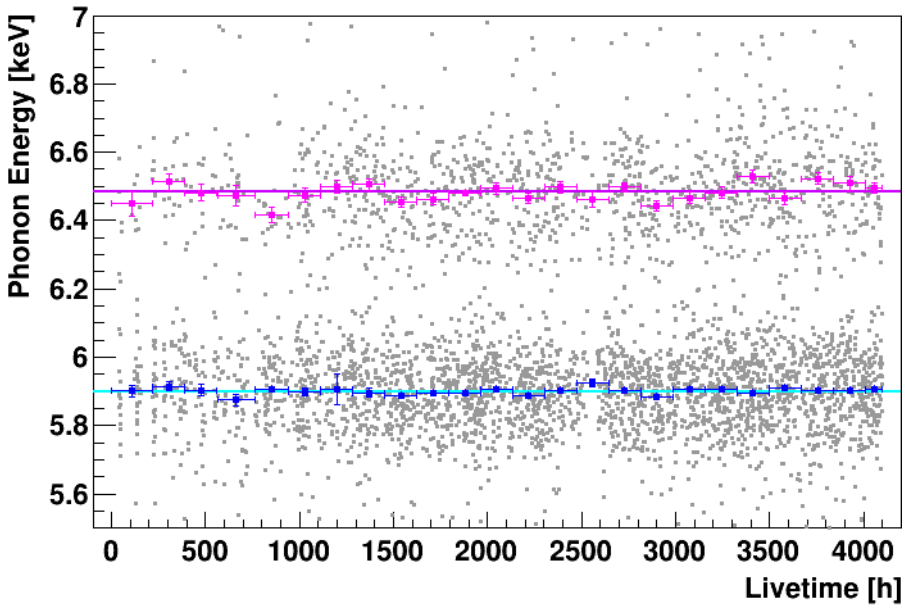

Figure 4.12: *Long-term stability of the applied energy calibration for the ^{55}Fe-source induced Mn K_α (blue) and Mn K_β (magenta) lines. No significant deviation from the fitted mean of the lines in the whole data set (cyan and violet solid lines) is observed. The gray data points show the spread of all events in the respective energy region. From the spread it is concluded, that also the energy resolution is stable over long time periods.*

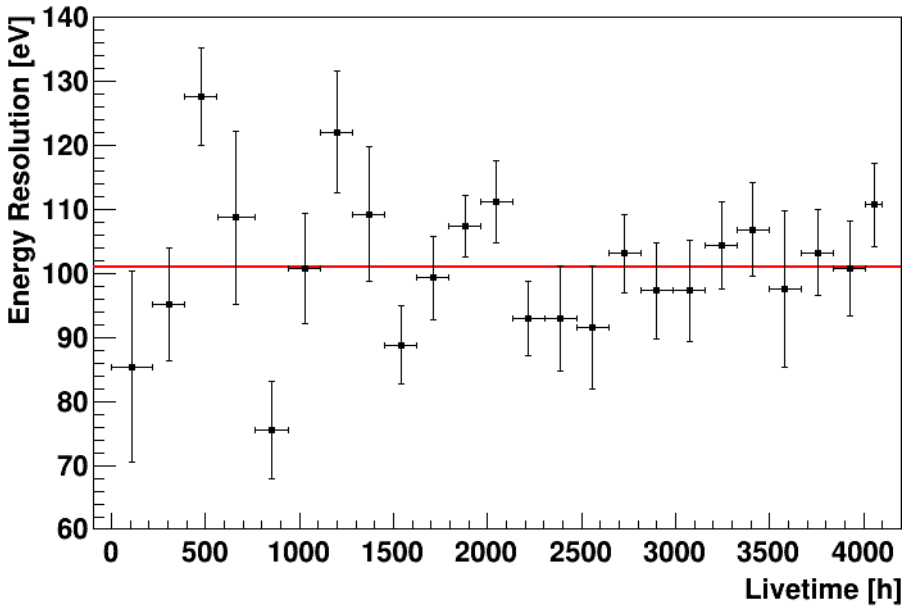

Figure 4.13: *Time dependent energy resolution obtained from a combined fit of the ^{55}Mn lines in several time slices. Due to low statistics in the individual slices the resulting fit error is rather large. The red line is the fitted resolution of the whole data set and is in good agreement with the individual fit results.*

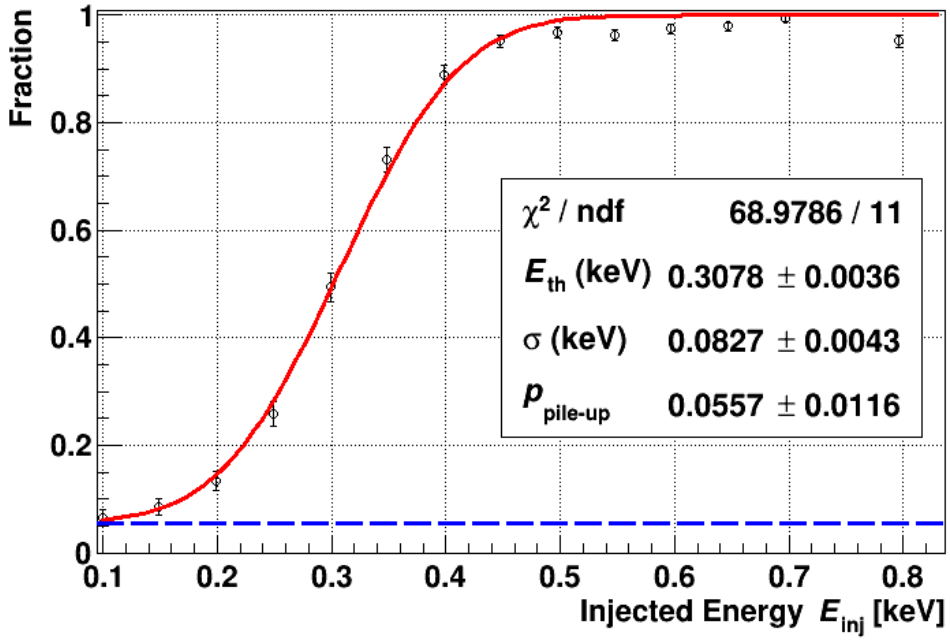

Figure 4.14: *Energy dependent acceptance measured with low-energetic test pulses at the trigger threshold of the phonon detector Lise. The fit (red solid line) yields an excellent energy threshold of* $E_{th} = (307.8 \pm 3.6)\,\text{eV}$ *(50 % acceptance) and a width of* $\sigma = (82.7 \pm 4.3)\,\text{eV}$*. For more details see text.*

the fit yields an excellent value of $E_{\text{th}} = (307.8 \pm 3.6)\,\text{eV}$ and a width of $\sigma = (82.7 \pm 4.3)\,\text{eV}$. Compared with the resolution of low-energetic γ-lines observed in Lise (see table 4.5c) the result shows that the energy resolution at low energies is dominated by the baseline noise contribution.

One possibility to cross-check the determined energy threshold is given by the fact, that both detectors are able to trigger separately. As explained earlier, in light-only events due to a direct interaction only the light detector triggered and, thus, it is expected that no significant signal in the phonon detector is recorded. In other words, for energies where the phonon detector triggers with 100 % efficiency no light-only event is expected. In contrast to the direct measurement of the energy threshold, for the cross-check it is important that the energy reconstruction of all investigated events is valid. However, too tight cuts might remove events which indeed suffer from an invalid energy reconstruction due to artifacts (e.g. pile up) but would be still relevant, because the true energy is above the trigger threshold. Thus, as a compromise for this cross-check, only a small set of loose selection criteria is applied to remove only extreme cases. In total 31236 of the 33545 light-only candidates survive all cuts, which corresponds to an acceptance of 93 %.

In figure 4.15 the resulting energy spectrum in the phonon detector Lise of the surviving light-only events is depicted. The dashed red vertical line indicates the measured energy threshold via test pulses where the trigger efficiency is 50 %. As expected the majority of the events are pure baselines without a pulse contribution and, thus, they have Gaussian distributed pulse heights centered around zero. Only 9 events are observed above the red vertical dashed

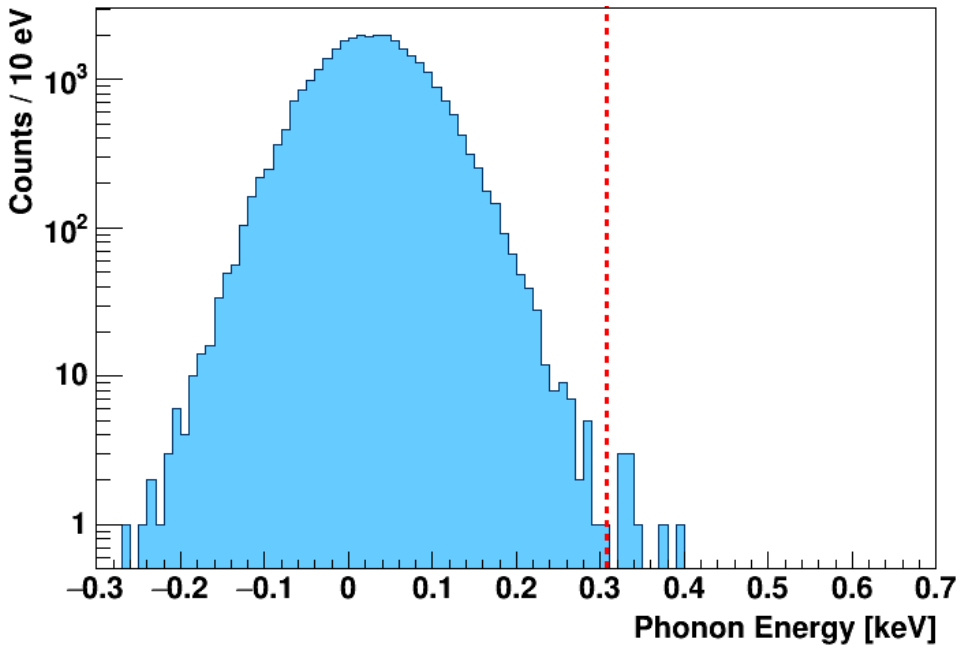

Figure 4.15: *Energy spectrum of light-only events in Lise and the energy threshold determined by test pulse events (red vertical dashed line). For energies where the trigger efficiency is 100 % no light-only events are expected. Since only a few events are observed above the energy threshold this method confirms the direct measurement of the energy threshold via test pulses.*

line, confirming the threshold determined by the test pulse method. Furthermore, at higher energies where the trigger efficiency is approaching 100 % ($\gtrsim$ 0.45 keV) no light-only event is observed. However, with the shown cross-check method the threshold can not be determined precisely, while the test-pulses method has this advantage.

5 Data Selection

During the data acquisition it can happen that besides valid physical events also invalid records are observed, which e.g. do not allow a precise determination of the deposited energy. These records as well as the chosen analysis scheme require a selection of data. In section 5.1 the applied blinding scheme as well as the analysed detectors and the available data sets are described. Examples of invalid records and pulses are shown and discussed in section 5.2. The applied selection criteria, which are based on the parameters described in the previous chapter 4, are listed in section 5.3. Finally, the method to determine the survival probability for signal events is explained in section 5.4.

5.1 Analysis Scheme and Data Sets

In the present work data of CRESST-II phase 2, obtained between end of June 2013 and mid of August 2015, are analysed. Most of the acquired data are background-only data which can be used for Dark Matter searches and, hence, called Dark Matter data set. Additionally, calibrations with low energetic γ-rays (^{57}Co-source), high energetic γ-rays (^{232}Th-source) and twice with neutrons (AmBe-source, inside and outside of the outer shielding) were performed. In this section the blind analysis scheme and the data sets for the different modules analysed are explained.

5.1.1 Blind Analysis Scheme

In modern physics, experiments become more and more complex and expensive, such that it is not always possible to cross-check obtained results with an independent setup. Thus, it becomes more and more important to reduce or at best eliminate all biases induced by the human being dealing with the measurement and in particular the data analysis. However, bias in data analysis is by far not limited to physics but rather present in all modern sciences. Phrases like “placebo effect” and “double-blind analysis” are widely known outside the bio-medical research community where they originate from.

A *blind analysis* is the optimal way to avoid the possibility of experimenters biasing their result towards their own preconceptions by preventing them from knowing the answer until the analysis is complete [130]. In particular in the search for rare processes a subtle bias scenario is due to the fact that the result may unintendedly be influenced towards either detection or elimination of a signal. Whether one event is discarded by a cut or not might strongly influence the physical outcome, since these types of experiments are searching for small signals at the edge of the detectability in statistics or above backgrounds. Thus, it has to be avoided that the cut values could be set such that individual events are rejected. By hiding some aspects

of the data or the result, a blind analysis guarantees the latter point. However, there is not a distinct blind analysis technique, usable in all different experiments. Instead, the applied scheme is strongly dependent on the actual experiment and has to match, in particular, the analysis techniques involved [130]. Several different methods and their successful application are explained in detail in [130]. Here only two concepts which are used in the Dark Matter search community are discussed.

One commonly used blinding method is called *hidden box method* [130]. A certain region in a suitable parameter space, where the signal events are expected, is defined a-priori. Whenever an event falls into this region it is hidden from the analyst as long as the analysis is not finalized and in particular the selection criteria are not yet fixed. The whole analysis has to be developed without exactly knowing its influence on the possibly observed signal. Only when the fixed selection criteria and methods are applied to the whole data set – without changing anything – the final result is obtained. Hence, this last step is called *un-blinding*.

One prerequisite for the hidden box method is, that the signal characteristics and location in the relevant parameter space must be known. In addition, the experiment must be able to independently estimate the background contribution in the signal box. While the first requirement is true for CRESST-II, the second one is not fulfilled up to now. In particular, in the prototype modules new and a-priori unknown background types might appear. Furthermore, the different detectors operated in CRESST-II show individual behaviors (e.g. detector-specific quenching factors) leading to a complication of the blinding scheme. Finally, up to now no Monte Carlo simulation describing the observed background completely is available. However, by using data obtained with a module operated in CRESST-II phase 2 great progress has been made in this subject lately [131].

Consequently, for CRESST a more suited blinding scheme has to be carried out and is explained in the following (called *data prescaling* in [130]). It has to be mentioned, that this blinding scheme only avoids statistical bias, i.e. the tuning of cuts to enhance statistical fluctuations [130]. First of all, a statistically insignificant part ($\lesssim 30\,\%$) of the complete Dark Matter data is defined as training set. All data preparation methods and especially all data selections cuts are defined and checked solely by the training set data. In particular, it is allowed to check the influence of the cuts on the result, e.g. the light yield - energy plot, and use this information to determine the actual cut values. This makes it possible to develop new cut algorithms including training and testing on real data. Thereby, either the actual cut values are fixed, based only on the training set data or an algorithm defining the cut limit has to be fixed before un-blinding. For the latter case, the method is allowed to operate on the complete data set, i.e. including the blinded data, to determine the cut value, however, the final cut limit is unknown when the method is fixed. Ideally, also the region of interest is defined solely based on training set data and in advance of un-blinding.

For the previously given reasons, all Dark Matter analyses performed in the present work are carried out as blind analyses if not stated otherwise.

5.1.2 Analysed Modules and Data Sets

As stated earlier, CRESST-II phase 2 lasted for more than 2 years until August 2015. Unfortunately, already in the training set data of several detectors of conventional design, nuclear-

recoil events most probably induced by α-decays on non-scintillating surfaces inside the module housing are observed.

However, most of the prototype detectors were working as expected and already in 2014 first results of the best overall performing detector module were published [127]. With a (prototype) module of the stick design called TUM40, a non-blind analysis of the training set data showed for the first time, that CRESST-II detectors provide reliable data down to the threshold of 0.6 keV. Afterwards, the trigger thresholds of all modules were carefully revised and could be lowered for several modules. The lowest threshold of 0.3 keV is achieved with the conventional module Lise while the one of TUM40 was lowered to 0.4 keV.

Detector	**mass [g]**	**exposure [kg · days]**	**data set type**	E_{th} **[eV]**
Lise (composite)	306	35.59	high-threshold training set	901
		6.98	low-threshold supplement	308
		52.24	blind data set	
TUM40 (stick)	248	29.40	high-threshold training set	609
		45.06	blind data set 1	
		2.52	low-threshold supplement	409
		52.93	blind data set 2	
TUM38 (big carrier)	299	35.23	training set	$< 3\,000$
		123.64	blind data set	
VK27 (beaker)	197	22.66	training set	11 250
		79.70	blind data set	
VK28 (beaker)	194	22.28	training set	$< 2\,000$
		78.37	blind data set	

Table 5.1: *Data sets for the different detector modules analysed. Also included is the crystal mass, the raw exposure and the trigger threshold E_{th} of the phonon detector. Concerning the plots of the measurement of the trigger thresholds see appendix D.*

In table 5.1 the data sets used for the different modules considered in the present work, their respective exposure before cuts and the type are listed. Additionally, the mass of the absorber crystal of the respective module and the energy threshold E_{th} of the phonon detector are included. The plots of the measurement of the trigger thresholds are depicted in appendix D. For TUM40 two blind data sets are obtained, where in one set a trigger threshold of 609 eV and in the other one the lower value of 409 eV is achieved. To obtain a larger amount of exposure both subsets are typically combined to form one blind data set with an analysis threshold of 609 eV and a summed exposure before cuts of 97.99 kg days.

In the present work no conventional module except Lise is analysed, since all of them show background events induced by surface α-decays at ~ 100 keV, whereby the actual contamination is dependent on the module. Since it can not be excluded that these events also leak

down to lower energies and, thus, into the region of interest for Dark Matter searches, all conventional modules are discarded from the analysis searching for heavy Dark Matter particles. However, for low-mass Dark Matter searches, background events related to α-decays on inner surfaces are not that crucial anymore for two reasons: Firstly, they leak into the region of interest (ROI) from the high energetic side, while light Dark Matter particles should induce mainly low energetic events. Secondly, in a low-threshold analysis searching for light Dark Matter particles the background separation typically worsens leading to a higher total background rate. Thus, the small amount of surface α-decay related background events leaking into the ROI for Dark Matter searches typically does not limit the expected sensitivity drastically.

The decisive parameter for this kind of analysis is the energy threshold of the phonon detector. For this reason the module Lise/Enrico, which uses the phonon detector with the lowest threshold is analysed. Next to Lise, only TUM40 has a low enough trigger threshold to be included in a dedicated low-mass Dark Matter analysis. For both modules, a supplement of the training set with data obtained with lower trigger thresholds is required, to check the correct performance of the template fit of the low-energetic pulses. However, for this check only a few days of data are required and, thus, the exposure of the supplementary data sets is $\lesssim 7\,\mathrm{kg}$ days[19]. Some small changes of the fit algorithm implementation in OxRop have been necessary to ensure a proper energy determination down to the lowest energies. These modifications have been tested not only during the present work but also in [123], where they are described in detail.

Of the six prototype modules only four are suited for an analysis searching for heavy Dark Matter particles. Among these four are both modules of the silicon beaker design (VK27, VK28), one module of the $CaWO_4$-stick design (TUM40) and one module with a big carrier crystal (TUM38). In the two discarded prototype modules, the phonon detector had an electronic issue resulting in pulses with abnormally small signal heights. In addition, one of these two phonon detectors could not be set up despite several attempts and, thus, it was not possible to operate it reliably until ~ 1 year after the start of phase 2. Thus, data of these two modules – one of the stick design (TUM45) and one of the big carrier design (TUM29) – are not considered in the present work.

5.2 Classes of Invalid Records and Pulses

One reason for the non-blind training set is to identify the different classes of invalid pulses and to develop cuts to remove such events. This is especially important for all modules of the newly developed prototype designs, where new previously unknown classes of events can occur. In this section the known classes of invalid pulses are described while section 5.3 focuses on the developed selection criteria to remove such events.

The foremost requirement of a valid event is that both, phonon and light detector of one detector module are working properly at the time of the event. However, even with this requirement fulfilled invalid pulses can occur and have to be removed for the further analysis. In

[19] As the reduction of the threshold is quite significant for Lise (factor ~ 3 smaller threshold), a larger exposure compared to TUM40 is used for the supplement training set. Thus, in principle this low-threshold supplement is used as a completely new training set for Lise.

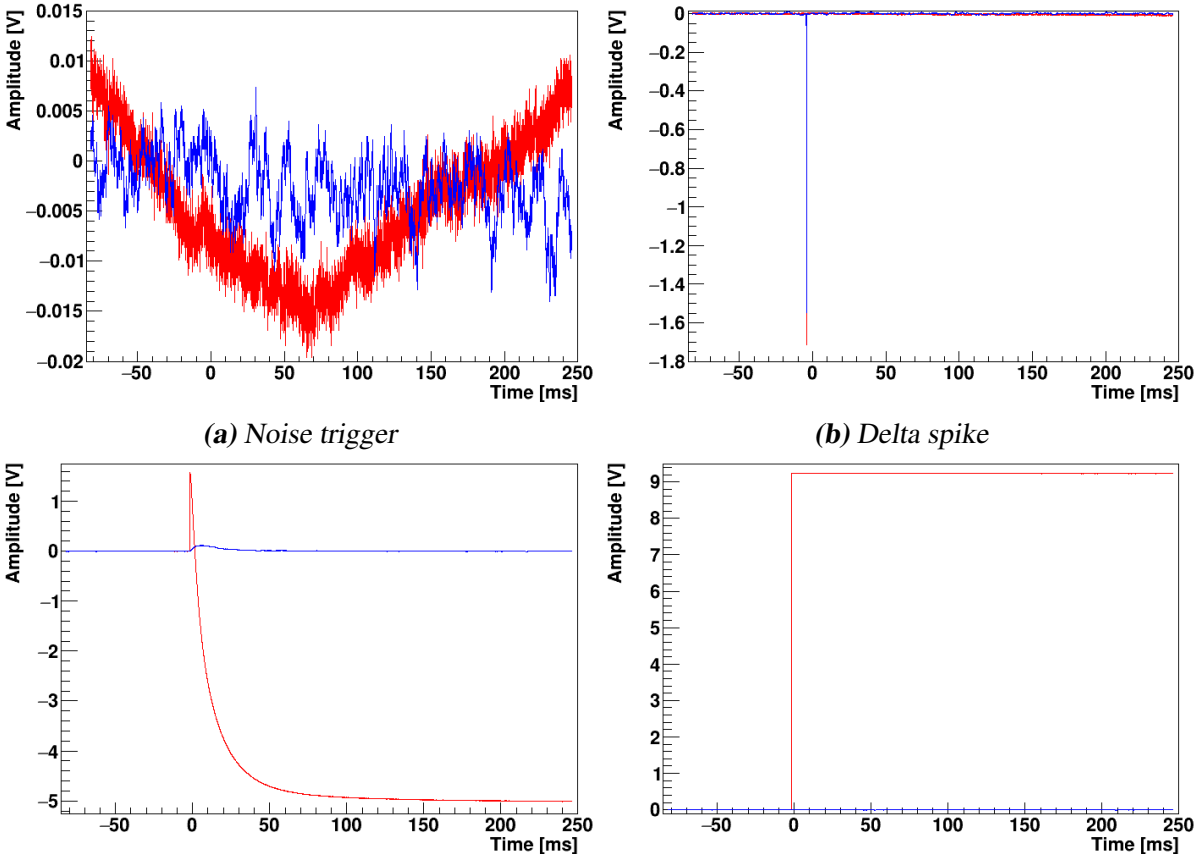

(a) *Noise trigger*

(b) *Delta spike*

(c) *Flux quantum loss*

(d) *SQUID reset*

Figure 5.1: *Examples for pathological pulses not created by a particle induced interaction but caused by a disturbance (noise trigger (a), delta spike (b) and SQUID reset (d)). Also during an actual interaction these interferences can occur as shown in case of the flux quantum loss record (c). The red pulse is recorded by the phonon detector Lise, while the pulse in the corresponding light detector Enrico is depicted in blue.*

this section, the more general term *record* rather than the term *pulse* is often used to emphasize the difference between both. While the term *pulse* implies a physical event, the term *record* just reflects that data with or without a physical event was recorded and stored on disk.

5.2.1 Pathological Records

On the one hand, there are records caused by a disturbance leading to a trigger, which do not correspond to a real particle interaction in the detector. On the other hand, these disturbances can also occur during a real interaction leading to an unusual record. In the present work both cases are grouped together and called *pathological records*. Regardless of the type and origin, these records have to be removed from the data set since either no physical information is contained in them or the energy reconstruction is possibly spoiled. In figure 5.1 examples for the different possibilities of this invalid record class are depicted.

First of all, figure 5.1a shows a record, where the noise was temporarily enhanced and, thus, above the trigger threshold. Typically, this increase is caused by vibrations originating in- or outside the experimental setup and recognized by the sensitive detectors. Consequently, such records and in particular noise periods are typically observed in more than one detector module simultaneously.

In a few records a sudden decrease of the bin values for a short time period (typically not more than ~ 10 samples) is observed, most probably caused by external electronic disturbances [121]. This results in negative spikes in the pulse trace – so-called *delta spikes* – as depicted in figure 5.1b. Just like noise triggers this disturbance is typically observed in more than one detector module simultaneously.

Another type of an invalid record related with the SQUID electronics is a flux quantum loss, which is depicted in figure 5.1c. For records with very large signals the SQUID might not be able to follow the resulting current change leading to a loss of an integer amount of flux quanta, which finally results in a lower baseline level than measured before. For these records the applied amplitude reconstruction fails since information is lost in the rising part of the pulse. In principle, it might be possible to reconstruct also these pulses because the baseline level is shifted by a discrete amount directly related to the number of flux quanta lost. However, due to the low number of records of this type the effort is not elaborated, in particular since this effect is typically only observed at high energies well above the region of interest for Dark Matter searches [132].

Subsequent to a flux quantum loss often a so-called *SQUID reset* causes a trigger as depicted in figure 5.1d. The SQUID electronic resets the baseline level whenever the output value reaches the boundaries of the readout electronics (absolute signal level of about $\pm 10\,\mathrm{V}$). Typically, this happens at the lower boundary of the electronics and, thus, the observed record is a positive step function resulting in a trigger.

5.2.2 Incomplete and Pile-Up Pulses

Also during a particle interaction invalid records can be created, in particular when two interactions are observed in the same detector. If the two interactions are within a short time period it might happen, that after the first event the respective detector is not yet back in its initial state, when the second one occurs. While the resulting records of the four possible cases depicted in figure 5.2 are well distinguished, the difference between all these cases is in principle just the time interval between the two interactions.

In figure 5.2a a classical pile-up record is shown, where for each detector two pulses in the same digitizer record are visible. Although it might be possible to reconstruct both pulses separately, this is not done here and, thus, such events have to be rejected. Due to the low total trigger rate of 7 Hz in all modules ignoring these events introduces only negligible dead time.

As discussed in section 3.3.2, after a trigger further triggering is deactivated for a certain time window in order to allow for the readout of the record and to ensure a valid pre-trigger range for the next pulse. However, especially for high energetic events it can happen, that the signal level is still above the trigger threshold, when triggering is re-activated. In this case two different classes of records are observed: Most of the time no further interaction is detected and, thus, only the decaying tail of the previous pulse is recorded as depicted in figure 5.2b.

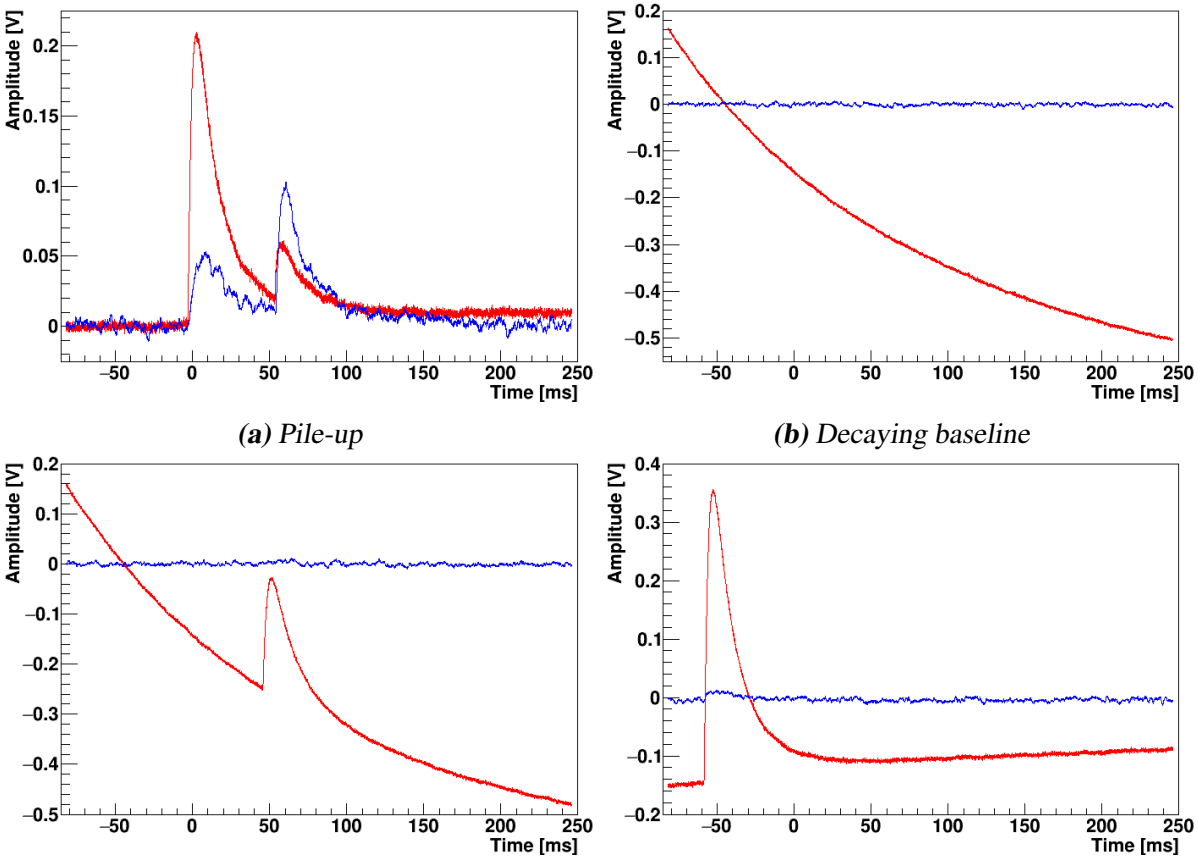

(a) *Pile-up*

(b) *Decaying baseline*

(c) *Strongly tilted baseline*

(d) *Early pulse*

Figure 5.2: *Examples for incomplete and pile-up pulses in one detector module. During a pile-up pulse (a) two interactions happened in a short time period of one record length. Thus, in both channels of the module two pulses are recorded in one time window. After a trigger in one detector, further triggering in this module is blocked for a specific time. However, in particular after high energetic events it happens that the signal level is still above the threshold when triggering is reactivated. Then either a decaying baseline (b) or a record with strongly tilted baseline (c) in case of a second interaction is observed. Whenever a second interaction happens while triggering in the respective channel is blocked, an early pulse (d) is recorded. The red pulse is recorded by the phonon detector Lise, while the pulse in the corresponding light detector Enrico is depicted in blue.*

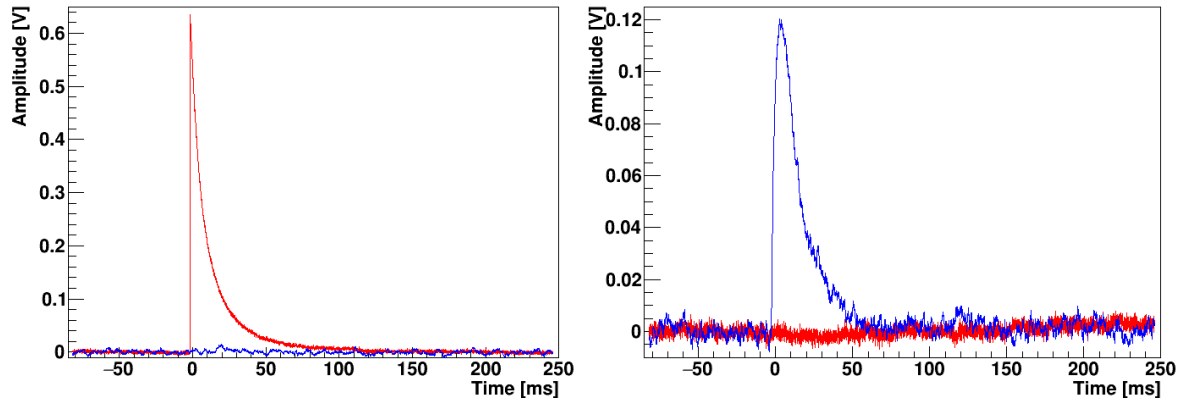

(a) TES-carrier pulse *(b) Light-only event*

Figure 5.3: *Examples for physical events, which create pulses with different shapes compared to absorber events. When an interaction in the TES-carrier happens (a), the resulting pulse exhibits a faster rise and decay time compared to an absorber pulse. A direct hit in the light detector (b) typically creates only a pulse in this channel and no signal at all in the phonon detector. Hence, these events are called light-only events and compared to scintillation pulses a different shape in the light detector signal is observed. The red pulse is recorded by the phonon detector Lise, while the pulse in the corresponding light detector Enrico is depicted in blue.*

Since there is no physical pulse information in this record, these events have to be removed from the data set. However, it can also happen that another interaction is happening, leading to a pile-up pulse simply on top of the decaying tail of the previous high energetic event. One example of this type is shown in figure 5.2c. As described previously in section 4.3 the template fit can account for this effect to some extend by the free baseline model. However, if the baseline is tilted too strongly the energy reconstruction is inaccurate and, thus, also these events have to be rejected.

Finally, it might also happen, that an interaction occurs during the time interval when the trigger is blocked. When the trigger is reactivated the signal level is still above the threshold and the record is stored. However, due to the blocking time the timing of the pulse is misaligned and the complete pulse is shifted towards earlier samples. Hence, this type of invalid pulses is called *early pulses* and an example is shown in figure 5.2d. Due to the limited baseline information a correct pulse height evaluation is doubtful and, thus, this kind of events is dismissed.

5.2.3 Records with Different Pulse Shape

The last class of invalid records is not induced by a particle interaction in the target crystal but rather somewhere else. Thus, the resulting pulse shape observed in both channels of the module can be different to the one introduced by interactions in the target crystal. In chapter 6 various methods to tag pulses with different pulse shapes and their respective discrimination power are presented in detail. Here, only the different interaction classes are explained and

evaluated according to their consequences for direct Dark Matter searches.

In all modules equipped with a TES-carrier, i.e. all modules of the composite design as well as of all the prototype designs, events can happen in the separated $CaWO_4$ crystal carrying the TES. In figure 5.3a an example of such a pulse is depicted. The resulting record exhibits a faster rise and decay time compared to absorber pulses (see figure 6.1b) and has to be removed for two reasons: Firstly, due to the different pulse shape the fit will not extract the correct energy for these events. Secondly, it is not ensured that the relative light output is the same as for events in the target crystal. Both facts taken together are problematic, since it can lead to background events misleadingly and accidentally showing up in the signal region.

Another, very similar eventuality for records with a different pulse shape is an energy deposition directly in the tungsten thermometer itself, which can happen in all detectors. However, due to the small area covered by the TES, in particular compared to the TES-carrier or the target crystal, it is a rare process. Nonetheless, due to the long measurement time this still might lead to records with even faster rise and decay times compared to TES-carrier pulses and in particular absorber pulses, but eventually not even accompanied by scintillation light.

In the stick-design another class of records with distorted pulse shape is observed, caused by a particle interaction taking place in one of the holding sticks. The sticks are pressed with bronze clamps onto the target crystal and, thus, phonons can be transferred into the main absorber. This transportation is not efficient, leading to a decreased phonon signal with distorted shape observed in the phonon detector. Simultaneously, the complete amount of the created scintillation light can be detected by the light detector. Thus, these events are typically located at high light yields ($\gtrsim 10$) due to the degeneration of the phonon signal. However, if part of the light is not detected these events can accidentally populate the signal region.

In particular in modules where the light detector is equipped with an ^{55}Fe-source, records with a different shape in the light detector are observed. One example is depicted in figure 5.3b. The pulse shape of a direct hit in the light detector is different from a scintillation event due to the finite scintillation time constants of $CaWO_4$. While the direct interaction is happening instantly (at least on the time base scale of the digitizer unit), the scintillation event has an increased rise and decay time, due to the long time components of the scintillation process. The radioactive source is mounted such, that it cannot directly shine onto the respective phonon detector, since it is only installed for an absolute energy calibration of the light detector. Typically, the pulse in the light detector is not accompanied by a signal in the phonon channel and, hence, this invalid event type is called *light-only events*. In contrast to the other invalid classes this type of records is not problematic but irrelevant for Dark Matter searches and, thus, they are removed from the data set for convenience.

5.3 Selection Criteria

In this section the different selection criteria (also called cuts) to remove the invalid events are explained. The aim of all cuts applied is either to ensure that the detector response to an amount of deposited energy is always the same (stability cuts) or that the energy reconstruction – in particular the template fit – yields a valid result (data quality cuts). Finally, also coincident cuts are applied since for Dark Matter particles only a single interaction in one detector module

is expected. To keep the discussion simple here the cuts are described only qualitatively, while the actual detector dependent cut values are listed in appendix D. As already stated above, these cut values are determined solely based on data of the training set and are applied blindly to all recorded pulses of the final analysis. In the following the different cuts are explained and the corresponding parameter distribution in the training set is shown. Thereby, if not stated otherwise all cuts explained prior to the current one are performed consecutively to remove all kinds of different invalid events.

5.3.1 Detector Stability

As described in section 3.3.3 control pulses are sent into the detector heater periodically throughout the complete data taking period. The pulse height of the corresponding detector response is a measure for the operating point of the detector. This parameter is determined online by the DAQ software and fed into a PID controller to stabilize the detector in its operating point via controlling the heater current. For control pulses only the pulse height and a small set of additional parameters are stored on disk for the offline analysis. A perfect PID controller would stabilize the detector instantly and, thus, the recorded pulse height would always be the same corresponding to the set point of the controller. However, in reality the pulse height fluctuates around this set value due to imperfect regulation. During some (short) time periods external influences (e.g. mechanical vibrations introduced by the cryogenic facility heating up the whole cryostat) drive the detector out of its desired operating point. The controller detects these deviations and adjusts the heating current accordingly. An example of the pulse height spectrum for all control pulses recorded during the training set of one detector is shown in figure 5.4. The fact that the distribution peaks at the set point (vertical blue dashed line) shows that the regulation works very well even over long time periods.

The aim of the stability cut is to detect and tag unstable time periods in one detector module. All events – not only control pulses but in particular particle and test pulses – recorded during these unstable periods are discarded and not considered for the analysis [44, 133]. In this work, the respective pulse height distribution is fitted by a Gaussian function (limited to the central part of the distribution) to estimate the width of the distribution. This information is used to determine the $3\,\sigma$ bounds (vertical red long-dashed lines in figure 5.4) which are used as allowed range of pulse heights around the nominal set point. It is assumed that the energy calibration of particle pulses is still applicable, when the detector is operated in this range. For times where the control pulse height is not contained inside this region the detector response to a defined amount of energy might deviate too strongly from the expectation and, thus, these control pulses are considered as invalid.

Unstable time periods begin with the first invalid control pulse and end when the first valid control pulse is recorded again. These periods are determined for the phonon and light detector of a module separately and combined afterwards to ensure that the module itself is stable throughout all times. Thus, it is guaranteed that both detectors were fully functional at all recorded event times, in particular that the detector response to a defined amount of energy is always the same.

The stability cut should remove all time periods were the detectors where unstable but it should not be too conservative and remove unnecessarily too much data-taking time. Thus,

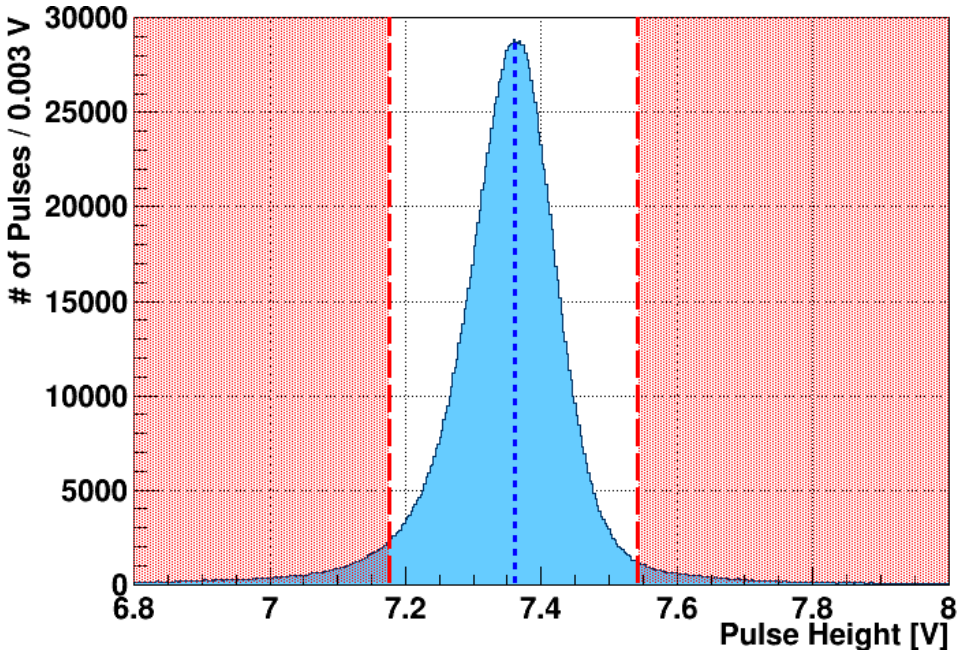

Figure 5.4: *Example of the pulse height distribution for all control pulses of the phonon detector Lise. In the vicinity of the set point (7.36 V, blue dashed line) the distribution is fitted with a Gaussian function to determine the width. All control pulses outside the 3 σ bounds (vertical red long-dashed lines) are considered as unstable.*

the previously explained method is slightly modified by applying the following two criteria.

The time difference between sending the control pulse into the heater and the resulting trigger in this detector is determined online by the DAQ and stored as an additional parameter. Only control pulses which are recorded in a narrow time window with respect to the known injection time of the control pulse are tagged as valid. For a time difference outside the allowed range it is very likely that either a particle pulse was misidentified as a control pulse or a pile-up of two or more pulses is recorded. The determined pulse height, i.e. the pure maximum of the pulse, might not correspond solely to the injected control pulse leading to incorrect conclusions about the stability of the detector. Thus, these events are neglected, in particular they can not begin or end unstable time periods.

Real excursions of the detector out of the nominal operating point typically extend over at least a few control pulses and, thus, a long time period with respect to the control pulse rate (typically 0.16 Hz) is invalid. Therefore, single outliers preceded and succeeded by a valid control pulse are ignored and are not allowed to start an unstable time period. Otherwise unnecessarily long times would be rejected by the stability cut. These single outliers are for example caused by a pile-up of a control and particle pulse.

A particular situation needs special treatment: It might happen that over long time periods no (valid) control pulse is recorded. This might happen, because the detector is driven out of the superconducting transition and, thus, it is unable to record any pulse. It was observed

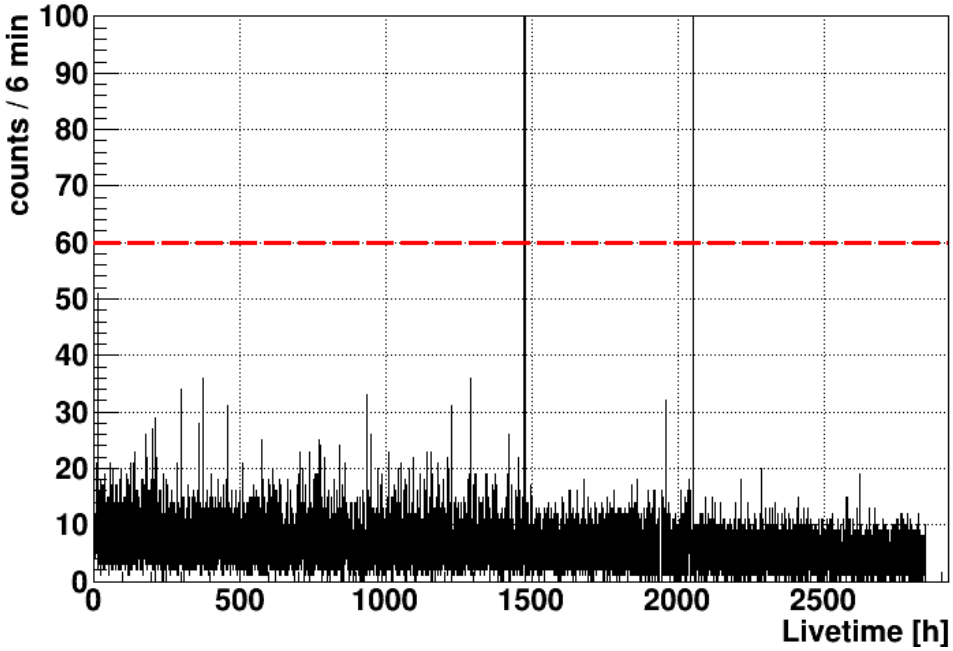

Figure 5.5: *Number of trigger counts per 6 minutes time intervals for the detector TUM40*[21]*. The y-axis is truncated at a value of 100 counts per 6 minutes for clarity reasons. Due to high noise conditions or mechanical vibrations introduced by the cryogenic facility some time bins show an abnormally high trigger rate. Time periods with rates above the cut limit (here: 60 counts/6 minutes, horizontal red dashed line) are removed from the data set.*

that these large disturbances appear so suddenly[20] that the last control pulse is still valid and cannot introduce an unstable time period. Nevertheless, the whole time period without control pulses must be removed, of course. Therefore, the stability cut demands that at least every 15 s a valid control pulse is recorded, otherwise the whole time period – starting with the last valid control pulse before the period and ending with the first one afterwards – is removed.

5.3.2 Trigger Rate

In a module the rate of all records, whether they are signal or background, is usually roughly constant over time. However, periods of unquiet running conditions may lead to an in average increased trigger rate. Due to high noise conditions or mechanical vibrations, e.g. introduced by the cryogenic facility, a huge amount of records, even without a physical pulse, are observed. Obviously, such time periods have to be removed from the analysis which is the aim of this cut.

The number of triggers per (defined) time period is calculated for each detector. In figure 5.5 for the detector TUM40, for example, the trigger rate in 6 minutes intervals is depicted[21]. A limit for the trigger rate is defined based on the average rate in this detector and data set such

[20] An example are the frequent weak earthquakes in the Gran Sasso region.

[21] During the training set of Lise the trigger rate was constant and, thus, no rate cut is applied. Thus, before un-blinding the data set of Lise the trigger rate was calculated and a cut limit defined.

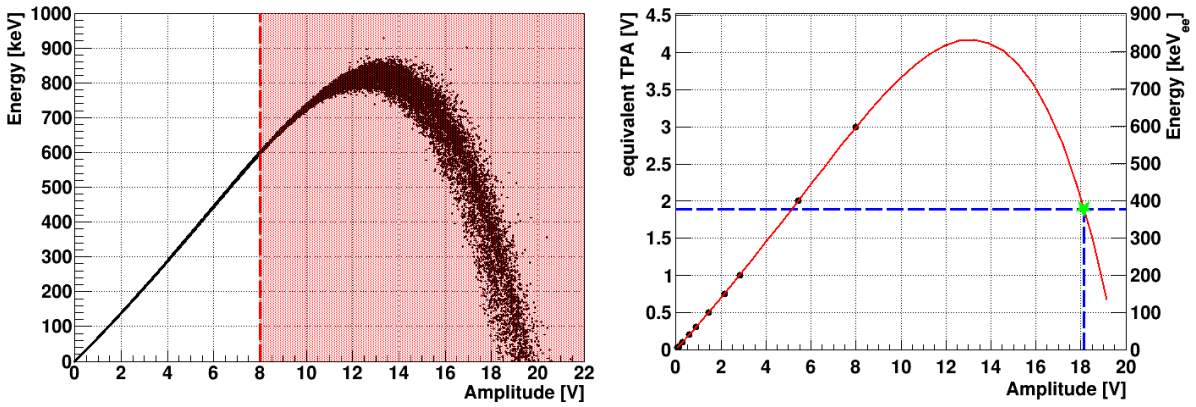

(a) Reconstructed energy-amplitude distribution. *(b) Drop in the fitted detector response.*

Figure 5.6: *The reconstructed energy against the amplitude of all pulses in the training set of Lise is depicted in (a). At an amplitude of 8 V (corresponding to $\sim$ 600 keV, dashed red line) the response function of this detector begins to drop which leads to an energy ambiguity. Pulses with a large amplitude are mistakenly assigned to low energy values and, thus, these events might end up in the region of interest for the Dark Matter search. All records with an amplitude larger than the cut limit are removed from the Dark Matter data set by a simple amplitude cut (red shaded area). An example of such a drop in the detector response is shown in (b). The high energetic pulse with a reconstructed amplitude of $\sim$ 18.2 V gets mistakenly the same energy assigned as a hypothetical pulse with a smaller amplitude of $\sim$ 5.16 V.*

that all severe spikes in the rate are removed (in the case shown 60 counts per 6 minutes, horizontal red dashed line). The time bins with rates above the cut limit are tagged and all events recorded in the respective time periods are removed from the data set.

Technically this cut is realized by removing only the control pulses in these time periods and apply the stability cut afterwards. Thus, the latter treats these periods as unstable periods and removes all records obtained during this time.

5.3.3 Amplitude

While the stability cut and the trigger rate cut are criteria which aim to ensure the detector stability, the measures described in the following are data quality cuts which should ensure a proper energy reconstruction.

One interesting feature of cryogenic detectors is the wide accessible energy range. While for Dark Matter particles the expected amount of deposited energy in the $CaWO_4$ crystal is $\leq$ 40 keV, most of the backgrounds can lead to much higher energies deposited. For example α-events have typically energies in the MeV range and are in principle still detectable in the CRESST-II detectors [131, 132].

On the one hand, it is very interesting to extent the accessible dynamic range even up to these high energies but, on the other hand, this causes spurious low energetic events. An example of the reconstructed energy-amplitude distribution is depicted in figure 5.6a. As a reminder, for the energy calibration procedure described in section 4.4 the detector response

is fitted to test pulses by a low-order polynomial function. This polynomial may drop or oscillate above the range where it is well defined by the injected test pulses as depicted in figure 5.6b. Due to this unphysical behavior high-energetic events are mistakenly assigned to too low energies during the energy calibration[22]. For the case shown in figure 5.6b the high energetic pulse ($\gtrsim 1\,\mathrm{MeV}$) with an amplitude of $\sim 18.2\,\mathrm{V}$ gets mistakenly the same energy assigned by the calibration ($\sim 376\,\mathrm{keV}$) as a hypothetical pulse with an amplitude of $\sim 5.16\,\mathrm{V}$. However, these wrongly energy calibrated pulses have a high amplitude and this information is used to tag them. To remove such events, simply an upper amplitude limit is defined in the training set at the point slightly below the start of the ambiguity. For Lise the upper cut limit is set to 8 V (dashed red line in figure 5.6a), which corresponds to an energy of $\sim 600\,\mathrm{keV}$.

While in phonon detectors also a lower amplitude limit (not shown here) is used to remove noise triggers, i.e. records with energies below the trigger threshold, this is not done in light detectors since for nuclear recoils only a small amount of scintillation light is emitted and, thus, it is not ensured that a positive signal is recorded in the light detector.

5.3.4 Trigger Delay

The **trigger delay** parameter is used to remove light-only events (see figure 5.3b), i.e. events where only the light detector in a module has triggered. If any detector is read out without invoking a trigger, the trigger delay parameter of this record is set to an artificial value of $-2499\,\mathrm{ms}$ by the DAQ. Hence, by removing all records with this value from the data set it is ensured that the specific detector has triggered during the event. For the same reasons as for the lower amplitude cut limit, also the trigger delay cut is only applied to phonon detectors, since it is not valid to assume that during a nuclear recoil event induced by a possible Dark Matter particle the light detector triggers at all.

5.3.5 Peak Position and Shift

Events which happened too early or too late in the recorded time window to ensure a correct amplitude reconstruction have to be removed, since either baseline information is missing or most of the decaying part of the pulse might not be recorded. In the latter case, the fit has to rely on the few samples of the steeply rising part, leading to a systematic uncertainty of the result. Furthermore, it is not clear if the pulse decays to the same baseline level as before since, e.g. flux quantum losses or pile up might occur outside the recorded time window.

In figure 5.7 the distribution of the two parameters used to determine and, thus, to reject this kind of events are depicted. The **peak position** of a pulse is shown in 5.7a while the **shift** parameter of the template fit is depicted in 5.7b. In both figures the cut values are shown as vertical red dashed lines and all pulses outside of the allowed region are rejected.

Since both parameters are usually strongly correlated the event distributions are very similar. Only for e.g. pile-up records the maximum of the pulse (peak position) and the fitted shift might differ. Thus, in both figures the same subset of recorded pulses is used to obtain the

[22] There is the possibility to extent the energy calibration into the α-region by using a linear function as detector response (see e.g. [132]). This has the advantage that the mono-energetic lines of the α-contamination can be identified and used for a dedicated energy calibration. The disadvantage is an error at low energies due to the assumption of a linear detector behavior.

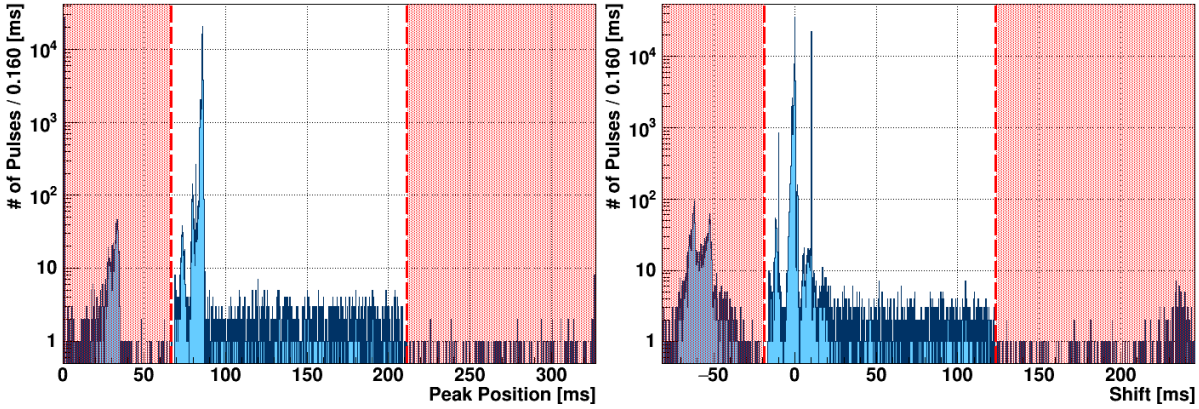

(a) Peak Position *(b) Shift*

Figure 5.7: *Peak position (a) and shift (b) parameter distribution of the training set data of Lise. Typically both parameters are strongly correlated and usually both cuts remove the same events. Only for pile-up pulses the peak position and the fitted shift might differ. Therefore, the same data set is used to generate both plots. In early pulses, baseline information is missing and, thus, they are rejected. Late pulses are dismissed, since they might not decay inside the recorded time window. The actual cut values are marked as vertical red dashed lines.*

distributions. The majority of the removed events is tagged by both cuts, while only a few events are removed either by one or the other.

5.3.6 Delta Voltage

Although the exact origin of the delta spikes (see figure 5.1b) is not clear they are most probably caused by external disturbances coupled into the readout electronics [121]. However, it is obvious that such events have to be removed. The **Delta Voltage/RMS** parameter is used to discriminate such events. In figure 5.8 one example of the obtained parameter distribution is depicted. The lower, i.e. more negative, the parameter value is the more pronounced is the delta spike. Thus, a limit is defined (vertical red dashed line) and all records with a parameter value below are rejected. For technical reasons also an upper limit (not shown in figure 5.8) must be defined and is set to a value well above the observed maximum in the training set.

5.3.7 Right−Left Baseline

Another cut which can remove pulses from a lot of different unwanted populations is based on the **right−left baseline** parameter. Whenever the difference between the two averaged sample values at the beginning and end of the record is too big, the corresponding record must be removed from the data set. This mainly addresses records with flux quantum losses and SQUID resets, since their baseline difference is abnormally high. Furthermore decaying baselines are also effectively removed by this cut. In figure 5.9 the parameter distribution for the detector Lise is shown together with the chosen cut limits (vertical red dashed line). Typically, almost all problematic events which might be tackled by this cut are already removed earlier by other

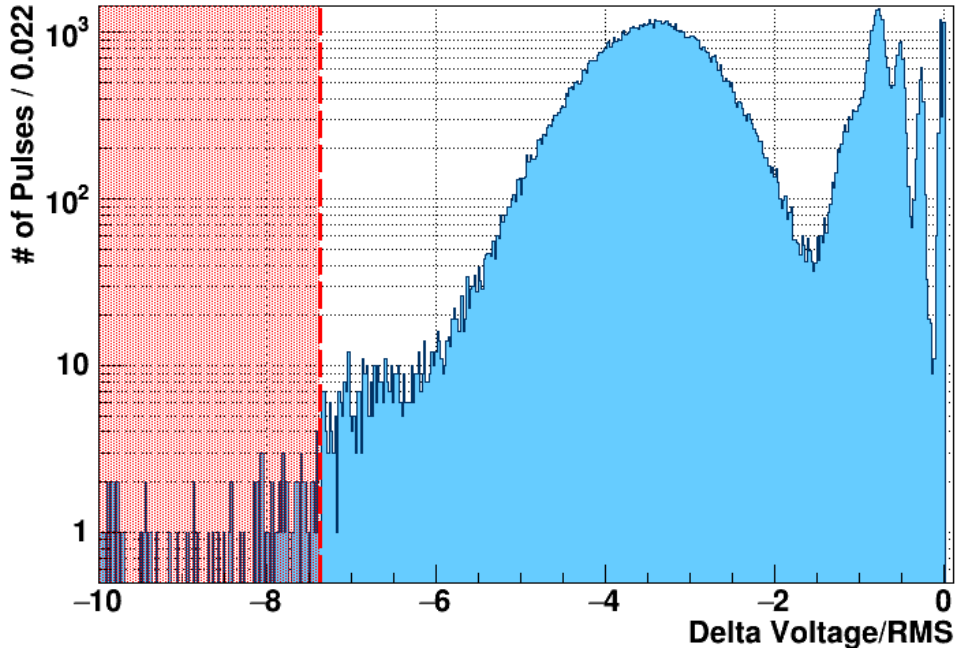

Figure 5.8: *Delta Voltage/RMS parameter distribution of training set data of Lise. The lower, i.e. more negative, the parameter value is, the more pronounced is the voltage drop. Records with a value below the shown limit (vertical red dashed line) are removed from the data set.*

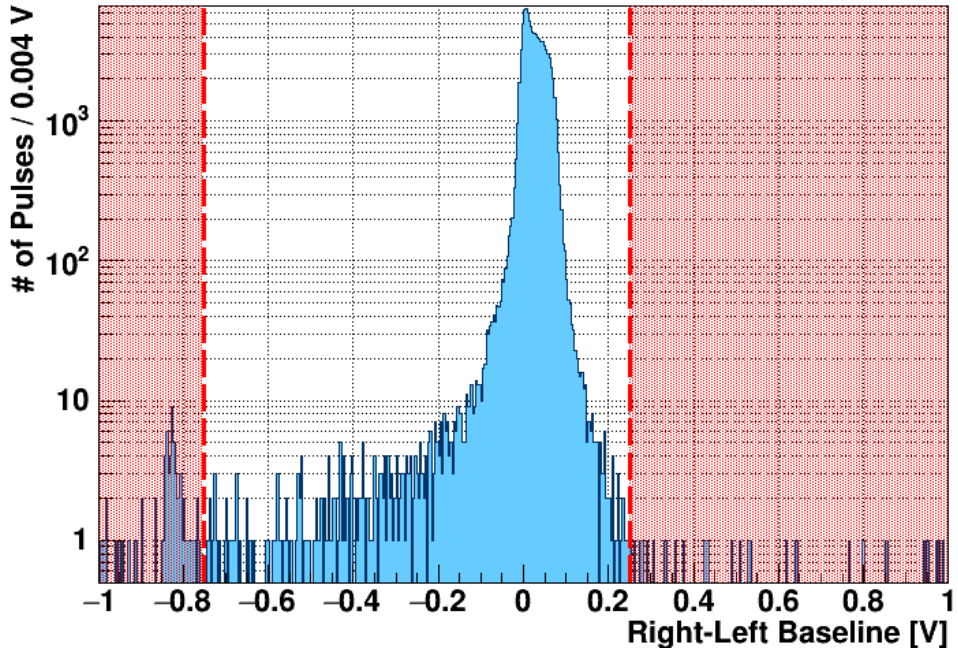

Figure 5.9: *Right−left baseline parameter distribution for the training set data of Lise. Loose cut limits (red dashed vertical lines) are chosen to remove mainly records with flux quantum losses or SQUID resets, which were not yet removed by previous criteria.*

criteria. Thus, for this parameter rather loose cut limits are chosen, whereby the upper limit is more stringent than the lower one. This prevents records with a modest tilted baseline, where the energy information is extractable, from being removed.

If high-energetic events are of interest (e.g. α-particles), special care has to be taken while choosing the cut limit at the positive side to not remove too many events which did not completely decay in the recorded time window. However, all records where the last sample is still above the respective truncation limit of the detector must be removed, since the template fit does not work properly for these records. Thus, the positive cut limit must be set at maximum to the truncation limit.

Since no assumption about an actual pulse in the record is required for the calculation of this parameter, the cut is applied to the phonon detector as well as to the light detector.

5.3.8 Template Fit Quality

In the cryogenic detectors operated in CRESST-II the shape of particle-induced pulses is almost independent of the amount of energy deposited. This allows us the usage of the template fit method to extract the relevant amplitude and, thus, energy information. As described earlier, the template fit calculates, minimizes and finally stores the Root Mean Square (RMS) deviation of the fitted curve from the measured pulse samples. Already tiny deviations from the template pulse shape might be a hint that the energy reconstruction failed and lead to an increased RMS value. The fitted curve might not describe the measured samples properly - either because the measured pulse features an artifact (e.g. pile-up or SQUID reset), the observed pulse shape is not compatible with the template (e.g. TES-carrier pulse) or unusually high noise conditions disturbed the record. Thus, a cut on the template fit quality is a generic measure to remove all different kinds of invalid records in a simple way.

However, small differences between the pulse shape of electron and nuclear recoils are expected. Therefore, first of all it has to be checked with, e.g. a dedicated neutron calibration, that the RMS cut is insensitive to these differences between electron and nuclear recoils and, thus, can not separate both populations. Ideally, the RMS cut ensures that for each event class, the same fraction of pulses is removed. A detailed study concerning this point is shown in section 7.3.

It has to be pointed out – again – that the template fit quality cut is a crucial and powerful but also potentially dangerous selection criterion. On the one hand it can remove almost all types of invalid pulses due to the different pulse shapes of such records. On the other hand, however, it is known, that nuclear recoils have a slightly different pulse shape than electron recoils. A careful cut must be designed, to be able to separate between different pulse shapes and, simultaneously, not to remove the desired nuclear recoils. In the present work an improved algorithm to determine the cut value automatically based on the observed data has been applied and is described in the following. This algorithm is a further development of an already available method discussed in [124].

As already shown in figure 4.3 even after linearization of the detector response by truncating the template, the RMS distribution of the template fit usually exhibits a slight energy dependency. The strength of this deviation is detector specific and has to be taken into account, when a stringent cut limit should be used. Therefore, the whole energy range is split

into several energy slices of an almost constant width[23]. In each slice the RMS distribution is individually fitted with an empirical model described later in this section. Based on the fit result a cut limit is determined for each slice. Finally, all individual cuts are combined to form the final cut.

In general, for phonon detectors three different parameters are available as proxy for the energy:

Amplitude The fitted amplitude is directly related to the RMS value, since both parameters are obtained in the same template fit.

Reconstructed Energy The energy measured by the phonon detector is the result of the energy calibration when the small correction of the heat - light anti-correlation is not yet applied. One advantage of this quantity compared to the amplitude is the better comparability of different detectors. However, the direct relation with the RMS value might be weaker than for the amplitude due to the non-linear relation of amplitude and energy.

Recoil Energy The event type independent total energy can also be used (see section 4.6). To obtain this parameter the small anti-correlation correction is applied. This energy proxy is most similar to the simulated energy of the signal survival probability method explained later in section 5.4.1.

For light detectors only the amplitude as well as the reconstructed energy parameter are available.

All three different choices are justified and in the end it is only important, that the chosen parameter is used consistently. In the present work, the cut is designed and performed as a function of the reconstructed energy both in the phonon and light detector.

It has to be noted, that the RMS cut does not implicitly cut on the energy of the records, i.e. it does not remove all events below a specific energy limit. In records with a pulse height of the order of the baseline noise, it might happen, that the template is fitted to a negative fluctuation and, thus, the resulting energy is negative. This effect is only observable in records where the noise contribution dominates and, thus, should equally result in positive or negative low-energy values. In order to also determine the RMS cut limit for slices containing records with negative energies these slices are merged with the first slice containing also positive energies[24]. The fit as well as the cut limit calculation are performed for the merged slice and applied to all pulses in the given range.

Figure 5.10 depicts histograms of the observed RMS distribution in two energy slices of Lise. In red the empirical fit function is shown and independent of the energy the respective

[23] For the creation of the energy slices a constant width is used up to a predefined energy. Above this limit the slice width is doubled and an adaptive algorithm checks if the statistics inside a slice is high enough to ensure a proper fit. Otherwise several slices are combined until the number of pulses inside the newly created slice is above a predefined limit of pulses.

[24] This combination of slices is, for example, required for the blind data set of Lise/Enrico due to noise fluctuations, which were not observed in the training set as well as in the low threshold supplement. Unfortunately, this was just observed after un-blinding the final data of Lise/Enrico and, thus, for both detectors this modification is performed in a non-blind manner.

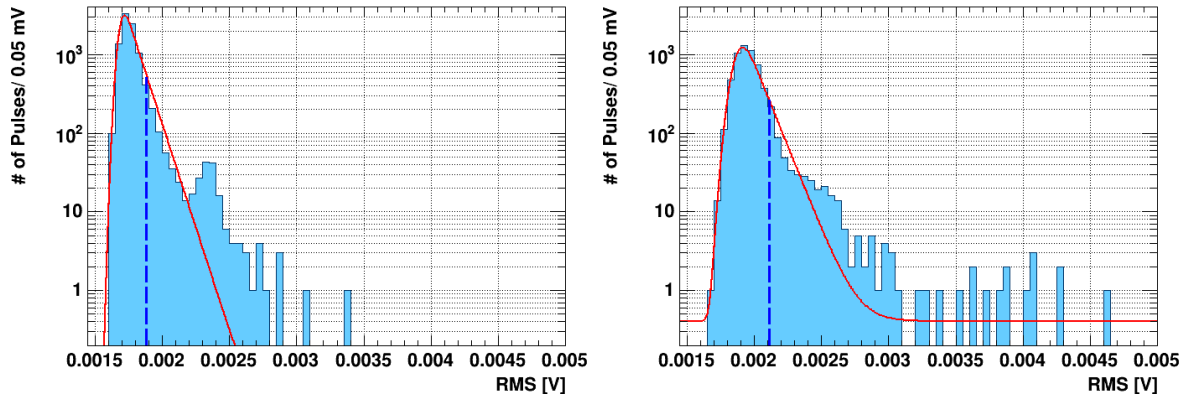

(a) *Energy Slice:* $0 \pm 10\,keV$ **(b)** *Energy Slice:* $60 \pm 10\,keV$

Figure 5.10: *Measured RMS distributions in two energy slices fitted with an empirical model (red line). In both slices the model consisting of the sum of a Gaussian function convoluted with an exponential and a linear function describes the observed distribution well. The obtained cut limit (RMS_{cut}) in both slices is depicted as vertical blue-dashed line. In (a) and to a lesser extend also in (b) a tiny peak centered around ~ 0.0024 V is observed and not explained by the empirical model. Most probably this is a short time period where either the noise contribution was different or the detector was in a slightly different operating point. See text for more details.*

model function describes the observed distribution well. In the case of white noise, i.e. serially uncorrelated random samples with zero mean and finite variance, the expected RMS distribution of the template fit is a χ^2 distribution. However, for large degrees of freedom (denoted k in the following) the χ^2 distribution converges to the normal distribution. For many practical purposes the differences between the two distributions are negligible when $k > 50$ [134], which is definitely fulfilled here where $k > 8000$. However, in the observed RMS distributions also non-Gaussian features are visible especially at the right side of the populations (see figure 5.10). This deviation is expected as there is no pure white noise distribution due to the influence of e.g. pile-up pulses or noise induced by the cryogenic facility. Thus, an empirical fit function is determined consisting of a convolution of an exponential and a Gaussian function to model the main part of the distribution. In addition, also a linear function is added to describe the contribution up to the high RMS values observed. During the template fit the RMS difference of the scaled template and the actual record is minimized and, thus, well fitted pulses have a low RMS value. While these pulses contribute to the main part of the distribution, in all other cases the template fit yields a higher RMS value. When the empirical model is fitted to the observed distribution (see figure 5.10), in total 6 free parameters are constrained.

After fitting the model to the distributions in each slice the cut values (vertical blue-dashed lines) are determined independently. Therefore, in each slice only the convolution of the exponential and the Gaussian function is integrated from 0 to an adjustable value RMS_{cut}. The percentage of records below this limit is determined and the value of RMS_{cut} is constantly increased. The previous step is iterated until the desired percentage of records of the main

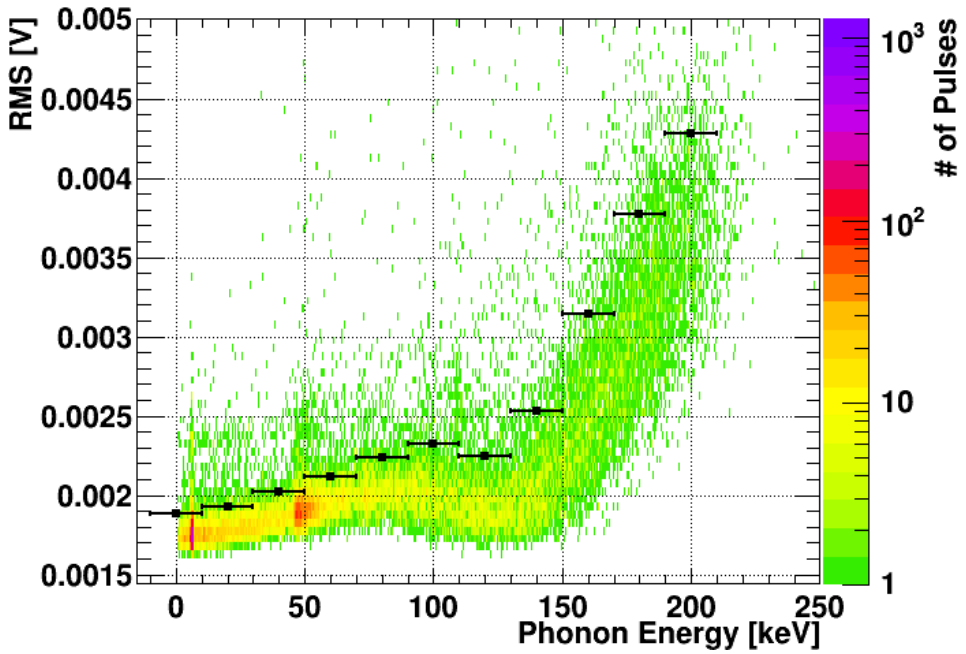

Figure 5.11: *RMS distribution observed in Lise as function of the measured phonon energy. The black data points are the individual cut values for the different energy slices of the given width (error bars, see table D.2c in the appendix for the numerical values). In each slice the observed RMS distribution is fitted by an empirical model and parts of the fit function are integrated to obtain the cut limit. All records below these lines survive the cut. Two prominent features are observable in the distribution: The peak at* $\sim 6\,keV$ *is caused by an accidental illumination of Lise with a radioactive* ^{55}*Fe-source, while the feature at* $\sim 46\,keV$ *originates from a* ^{210}*Pb contamination of the absorber crystal.*

distribution survives (here 90 %, see figure 5.10)[25].

In figure 5.11 the RMS distribution as a function of the recoil energy is depicted for the phonon detector Lise. The large population of pulses at $\sim 46\,\mathrm{keV}$ is a ^{210}Pb contamination observed in the crystal. The peak at $\sim 6\,\mathrm{keV}$ is due to the accidental illumination of Lise with a radioactive ^{55}Fe-source. The black data points are the obtained cut values in the respective energy slice, whereby the energy width of the slice is represented by the error bars. Thus, in each slice 90 % of the records of the main distribution are below this line. The complete cut is obtained by simply combining the cut limits of the individual slices.

Since the RMS cut is able to remove generically all different kinds of invalid records, in the present work this aspect is exploited. For all other criteria besides the RMS cut, loose cut limits are defined to remove the worst cases and to enable the described fit method. The remaining invalid records are removed by a proper choice of the fraction of surviving records

[25] On the one hand a higher fraction of surviving pulses is desired. On the other hand increasing the cut limit $\mathrm{RMS}_{\mathrm{cut}}$ might increase the number of pulses where the template fit was distorted due to some feature observed in the record. Thus, here a fixed amount of pulses of the main part of the distribution should survive. In principle, a method which optimises the cut limit based on the observed distribution and the empirical fit model might be used.

of the RMS cut.

For the Dark Matter analyses typically long data taking periods are required and during these it might be possible that the running conditions slightly change resulting in different noise conditions. For example, in the data set analysed in [124] two distinct running conditions were observed in several modules, resulting in periods with either a high or a low noise contribution. In contrast to that data set, no different phases of noise conditions are observed in the recorded data analysed here. However, if required it is possible to use the developed method of [124] to separate the different times and noise states and apply the new algorithm to both subsets independently.

5.3.9 Time Coincidences

As already explained in chapter 2, the interaction cross section for Dark Matter particles is so low that it is highly unlikely for a Dark Matter particle to scatter twice in the experimental setup of CRESST. Thus, all events of a specific module which are coincident in time with either a signal in the muon veto or in a cryogenic detector of another module are rejected. Therefore, a reliable method to determine the exact interaction time of a cryogenic event is required. For the threshold trigger used, the time when the trigger occurred depends on the actual height of the pulse (this effect is the so-called *trigger walk*). Thus, the time stamp of the DAQ which is based on this trigger time gives only a first hint where the pulse is located in the record. Therefore, in the present work, the shift parameter obtained by the template fit is used to determine the interaction time with better accuracy. In [124] it is shown that using this parameter improves the achievable time resolution and, thus, smaller coincident time windows are possible. In contrast to the other selection criteria where the cut parameters are set for each detector individually, for the coincident cuts common timing parameters are used for all modules.

Muons can introduce particle events in the cryogenic detectors which might mimic signal events (e.g. a neutron can hit the phonon detector). However, a muon hitting either the detector itself or the vicinity of the experimental volume is most probably detected in the muon veto. All cryogenic events that exhibit a signal in the muon veto system within a time window of ± 2 ms around the determined interaction time are discarded[26].

Coincidences in more than one cryogenic detector of different modules are removed from the data set by searching for a record in another module ± 5 ms around the interaction time of the event in question[27].

[26] In principle it is possible to use the individual 21 QDC channel values of the muon veto and apply some selection criteria on these records to disentangle at least to some extent muon from background (e^-/γ-events) induced veto events. However, due to the low trigger rate ($\lesssim 25$ Hz) and the stringent coincident window (± 2 ms) only a small fraction of dead time (~ 9 %) is introduced, when all muon veto records are conservatively considered as muons.

[27] The only requirement for discarding the event in question is a trigger in another module inside the time range and not a valid event, i.e. an actual particle induced event. This conservative scheme is possible, since the trigger rate in the whole setup is low ($\lesssim 7$ Hz) and, thus, the amount of random coincidences is negligible.

5.3.10 Energy Cut

There is a slight difference between the amplitude observed by the trigger unit and the energy reconstructed by the template fit method. As explained in section 3.3.2 the signal is shaped before it is fed into the hardware trigger. However, the energy reconstruction is based on the template fit which leads to a different shaping of the pulse and, thus, it is possible that the energy is reconstructed below the trigger threshold measured. A cut on the reconstructed energy in the phonon detector is performed to remove such events. For the signal survival probability method described later this cut is absolutely necessary to model the cut-off of the trigger unit.

5.3.11 Sequence of Cuts

To conclude this section about the different selection criteria a typical cut sequence performed in the present work for a detector module is listed. The different criteria are applied consecutively and if a record is discarded by a specific cut the whole event, consisting of the phonon and the light detector record, is removed from the data set. The stability cuts and the two coincidence cuts are performed for the whole detector module while the data quality cuts are performed for individual detectors. In the following, the phonon detector is abbreviated by PD, while LD denotes the respective light detector.

Stability Cuts

1. Trigger Rate Cut
2. Stability Cut

Data Quality Cuts

3. Amplitude Cut PD
4. Trigger Delay Cut PD
5. Delta Voltage Cut PD
6. Peak Position Cut PD
7. Template Shift Cut PD
8. Right−Left Baseline Cut PD
9. Amplitude Cut LD
10. Delta Voltage Cut LD
11. Right−Left Baseline Cut LD
12. Pulse Shape Cuts PD (see chapter 6 for more details)
13. RMS Cut PD
14. RMS Cut LD
15. Energy Cut PD

16. Muon Veto Coincidence Cut
17. Cryogenic Coincidence Cut
} **Coincidence Cuts**

5.4 Artificial Pulse Simulation and Signal Survival Probability

In an ideal world all applied cuts would remove only background events while simultaneously all signal events survive. Since this is not true in reality, a method to determine the probability for a signal event to survive a specific cut is required. While for most of the cuts the fraction of surviving events does not depend on the energy of the record, this is by construction not true for the amplitude and, in particular, for some of the pulse shape cuts (see chapter 6). Thus, the resulting survival probability and consequently the exposure are energy dependent. In this section first the data-driven pulse simulation method used to generate mock-up signal pulses is explained. Afterwards these artificial pulses are used to determine the survival probability and finally the result is cross checked with neutron calibration data.

5.4.1 Data-Driven Pulse Simulation

A cryogenic pulse consists of the noise conditions present at the time of the interaction and the pulse shape specific for the interaction type. To simulate a pulse, samples of both constituents are required. As already mentioned, the template, which is generated for the fit and required to extract the amplitude, describes the shape of an absorber pulse in an (almost) energy independent way. For the noise conditions in this simulation empty baselines, i.e. random triggers recorded periodically throughout the whole data taking period, are used. By superimposing the particle template of the respective detector on the obtained baselines artificial pulses are created. As described in chapter 4, the amplitude of a pulse and the energy deposited in an interaction are strongly correlated, indeed there is a one-to-one relation. In the range of interest the relation is linear in very good approximation. Thus, to simulate pulses with any energies the template is scaled before superimposing. In total 45 different phonon energies ranging from 0.1 keV up to 40 keV with different energy spacings are used.

To generate an artificial event the procedure is performed for the phonon as well as for the light detector. Like cryogenic pulses recorded by the DAQ these events are saved to disk and, thus, are indistinguishable for the analysis software. Since for the Dark Matter search the expected signals are nuclear recoil events light quenching must also be considered in the simulation. To keep the simulation simple, only tungsten events are created, since no strong dependency on the recoiling nucleus and, thus, the actual light yield position is expected. This is done by considering the energy independent quenching factor of tungsten $\mathrm{QF_W} = 0.0196$ [117, 125] for the energy expected of the light detector.

One minor drawback of this simulation method is, that during the creation of the artificial pulses no time shift can be introduced since the record lengths of the empty baseline and of

the template are the same. Therefore, the amount of events which are removed at earlier or later times than the "standard" event time can not be determined. One solution would be to sample empty baselines with a longer record length with respect to particle pulses. However, since for the majority of all records the pulse is located in a small time window next to the trigger point (see figure 5.7) this effect is negligible.

5.4.2 Signal Survival Probability

Since the artificial records are indistinguishable from real records for the data analysis software the usual data analysis chain is applied to the artificial data set. To determine the survival probability of an individual cut the fraction of pulses surviving the given selection criterion is determined. By applying a subset or the whole cut sequence the signal survival probability of the combination of different cuts is determined.

It is important to know the functional form of this quantity, since it is an input for the limit calculation and allows to determine the expected recoil spectrum. The latter is required for comparison with the observed event distribution to constrain the allowed interaction cross section.

In the real data set, in particular during the development of the cuts in the training set, the sequence of cuts is important, since otherwise some features in parameter distributions might be hidden or covered by records which are removed by another cut. However, in the simulation the sequence of cuts is not relevant, only the fact that all cuts are finally applied is requested. Thus, for the cross-check the cuts are re-ordered so that the coincident cuts are applied directly after the stability cuts. Furthermore, the pulse shape cuts are applied after all other cuts to highlight their influence on the signal survival probability.

In figure 5.12 an exemplary signal survival probability after successive application of different selection criteria is depicted. The combined survival probability of rate and stability cut is drawn as solid purple line, while the one of the coincidence cuts is shown in blue. The fraction of removed events is dominated by random coincidences and, thus, as expected no energy dependency is observed for these first two cuts. The red solid line is the resulting probability after application of all the different data quality cuts, whereby the majority of records is removed by the RMS cut. The artificial pulses are simulated with different discrete energy values starting slightly below the energy threshold of 0.3 keV (data points). As can be seen, also the spacing in energy between the various pulses differs. Since the probability is in particular of importance at low energies more pulses are generated in this energy region. Due to the pulse shape cuts (see chapter 6) at low energies a considerable fraction of signal events is removed and the final signal survival probability (black line) is obtained. The distinct shape of the curve of the pulse-shape cuts is discussed together with the details concerning the different cuts involved in the next chapter.

As can be seen in figure 5.12 the data quality cuts (red line) introduce an energy dependency visible as a drop of the survival probability at low energies ($\lesssim$ 1 keV). This drop is mainly caused by two different effects: The sharp drop at $\sim$ 0.3 keV is due to the trigger threshold (compare figure 4.14). Additionally, for decaying or rising baselines the maximum of the record is found in the first or last few samples, respectively. The peak-position parameter corresponds to the position of the maximum of the record and by cutting on this parameter a

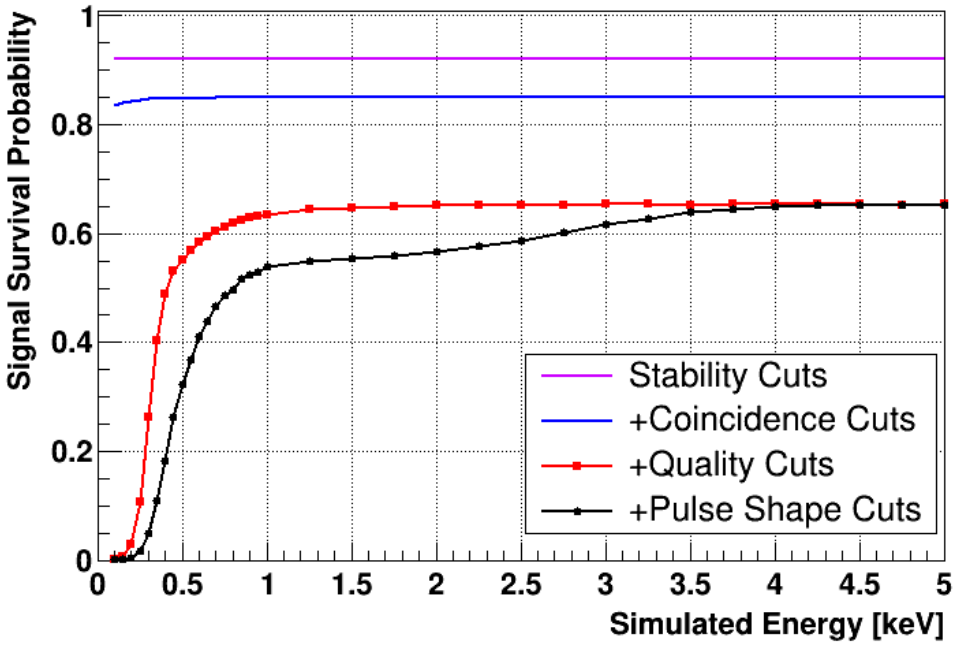

Figure 5.12: *Exemplary signal survival probability of Lise after successive application of different selection criteria. The simulated artificial nuclear recoil events are created at discrete energies starting from the threshold of 0.3 keV (data points).*

slight energy dependency is introduced (from ~ 0.5 keV to ~ 1.5 keV). While for pulses with large amplitudes a strongly tilted baseline is required to result in a rejection of the record, for pulses with smaller amplitudes already modestly tilted baselines may have their maximum outside the allowed parameter range. Thus, by selecting only a subset of the possible peak positions the additional slight energy dependency from ~ 0.5 keV up to ~ 1.2 keV of the red curve in figure 5.12 is explained. For the future, it might be beneficial to use only the shift parameter obtained from the template fit to reject early and late pulses and to avoid a cut on the peak-position parameter.

5.4.3 Cross Check of the Signal Survival Probability

To cross check the obtained survival probabilities of the template-based simulation method, data with a large amount of nuclear recoils is required. In CRESST-II phase 2 a calibration with neutrons from an AmBe-source was performed two times. However, since the energy spectrum of the used source is not known precisely enough also the expected energy spectrum induced by nuclear recoils is not available. Thus, it is not possible to validate the final survival probability, however, a cross check of the influence of a subset of cuts is performed. In Lise this is done for the pulse-shape cuts, since they introduce the biggest energy dependency on the resulting signal survival probability (see figure 5.12).

Figure 5.13 shows the combined survival probability of the pulse shape cuts in Lise for nuclear recoil events (signal) in blue as well as for electron recoils (background) in red. Due to the energy resolution in both detectors of a module, the different bands overlap in particular

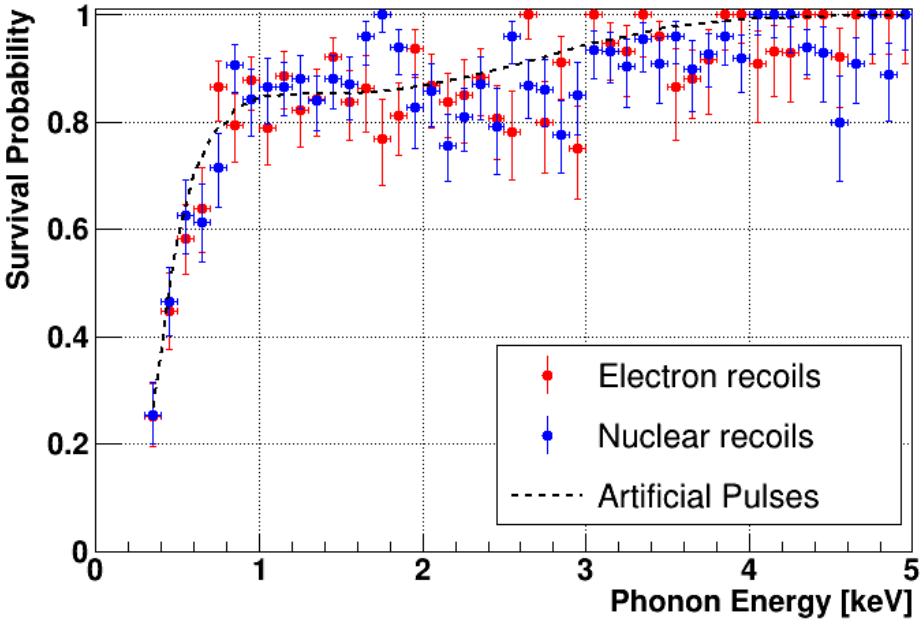

Figure 5.13: *Signal survival probability of Lise obtained with the template based method creating artificial pulses (black dashed line). The result is confirmed within the error bars by data obtained during a neutron calibration with an AmBe-source introducing nuclear recoil events (blue data points). The resulting survival probability of electron recoils is also included (red data points) and shows no significant difference compared to nuclear recoils.*

at low energies. Hence, for this cross-check all events which have a light yield ranging from 0.5 to 1.5 are considered as electron recoils, while nuclear recoils are events with a light yield of -0.5 to 0.5.

As expected, no drastic difference between these two event populations is observed. For the cross check, also the signal survival probability estimated by the template-based method is shown as black dashed line. Within the statistical error bars good agreement is observed between both methods for the estimation of the signal survival probability. However, due to the larger available statistics the template-based method results in a more constrained functional shape and, thus, is used in the following.

6 Artificial Neural Network based Pulse-Shape Analysis

In CRESST-II phase 2 two alternative module designs rely on pulse-shape analysis to efficiently veto radon induced surface background events resulting in dangerous ^{206}Pb-recoil events (see section 3.5.4). These modules are equipped with a large $CaWO_4$ crystal disk carrying the W-TES and only this TES-carrier is in contact with the holding clamps. The observed pulse-shape difference between events induced in the absorber and events induced in the carrier allows to cover the clamps with plastic scintillator which is not possible in the conventional design (see section 3.4.1). Moreover, almost all other modules are of the composite design and, thus, small TES-carriers are present.

In the present work only differences in the shape of phonon-detector pulses are investigated although for some event types also for light-detector pulses a distorted pulse shape is observed (e.g. direct hits of the light detector). These events are typically not considered as crucial background for the Dark Matter search and, thus, are neglected here. However, in general, all techniques described are also applicable to light-detector pulses.

Figure 6.1a shows a picture of the phonon detector TUM40, consisting of the cuboidal-shaped absorber crystal, which is equipped with a small TES-carrier substrate. Events in the latter exhibit a different pulse shape observed in the phonon channel compared to absorber events. In figure 6.1b the templates for an absorber (black line) and a TES-carrier pulse (red line) of the phonon detector TUM40 are depicted. Due to the better coupling to the TES, TES-carrier pulses exhibit much faster rise and decay times in the phonon detector compared to absorber pulses. Since both, the absorber as well as the TES-carrier, are made of $CaWO_4$, no differences are expected and observed in the shape of the respective light-detector pulse. However, due to the high evaporation temperatures (leading to a lower light output [100]) and geometric effects, for most of the TES-carrier events no or only a small light-detector signal is detected.

TES-carrier pulses are problematic in terms of light output as well as energy calibration. This might lead to events reconstructed in the nuclear-recoil band and, thus, for direct Dark Matter searches these events have to be removed. The differences in the pulse shape observed in the phonon detector can be used to characterize each event in one of the two categories and, thus, remove TES-carrier events. However, the discrimination power is strongly energy dependent, since for larger pulses it is much easier to distinguish both classes than for pulses with energies close to the threshold of the detector.

In the present work, Artificial Neural Networks (ANNs) are used to efficiently discriminate the two pulse classes observed in phonon detectors. The first part of this chapter presents the basic concepts of ANNs (section 6.1) as well as the pulse simulation used for the creation of artificial pulses of known type (section 6.2). These simulated pulses are essential for the train-

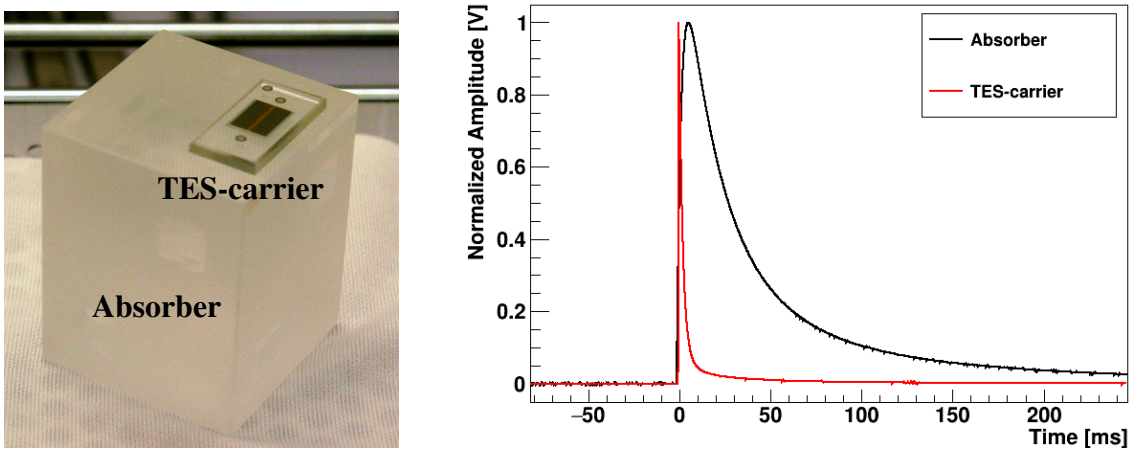

(a) Phonon detector TUM40 *(b) Templates for both pulse classes*

Figure 6.1: *The phonon detector TUM40, consisting of the cuboidal-shaped absorber and the small TES-carrier crystal glued onto it, is shown in (a). In (b) the two templates of the phonon detector TUM40 for absorber (black line) and TES-carrier (red line) pulses are depicted. Due to the better coupling to the TES, TES-carrier pulses exhibit a much faster rise and decay time in the phonon channel compared to absorber pulses. These differences are exploitable in a pulse-shape analysis to distinguish both pulse classes.*

ing of the ANN and required to compare the output with the expected values. The different available pulse shape parameters and their discrimination power evaluated with simulated data are discussed in section 6.3. In section 6.4 the two utilized training algorithms are explained and the discrimination performance for a single detector is studied in detail with simulated data. This performance is checked with real CRESST-II phase 2 data in section 6.5. Using the measured data set leads to the idea to use the combination of the two ANNs as decisive parameter at low energies, which is presented and discussed in section 6.6. In section 6.7 the final cut sequence of all criteria forming together the pulse-shape cut is summarized and the resulting signal survival probability is shown. Last but not least ANNs are applied to different phonon detectors and the respective performance is shown in section 6.8.

6.1 Artificial Neural Networks

An Artificial Neural Network (ANN) is a machine learning algorithm, which offers the possibility for a non-linear combination of several input parameters to obtain a decisive output variable. The term *neural network* originates from the first attempts to model and describe information processing in biological systems [135]. However, in the present work only the practical application of neural networks as pattern recognition algorithms is imported and, thus, the constraints induced by biological realism are neglected. The basis functions of the network are given in parametric form which allows to obtain the actual parameter values suited for the specific problem during the so-called *training* of the network [135]. Substantial computational resources are required to determine a compact model during the training phase of the network.

However, after the training of the network, the model is fast at processing new data. In the context of pattern recognition the most successful ANNs are so-called *multilayer perceptrons* (MLPs). They are the only type of ANNs considered in the present work and are discussed in the following. The subsequent discussion about the layout and properties of MLPs follows mainly the description given in [135]. Several reviews of the recent development in the field of machine intelligence and learning can be found in [136].

6.1.1 Multilayer Perceptron

Like in biological systems, also an artificial neural network is basically made up of two components, namely *neurons* and *synapses*. Neurons (also known as units) can have several inputs but only one output value, which is a non-linear combination of its inputs via the so-called activation function f_{act}. Synapses connect two neurons and transfer the information from one to the other, while the strength of the connection is adjustable by a weight parameter.

A schematic drawing of a neural network layout with four input parameters is depicted in figure 6.2. As can be seen, the neurons depicted by the nodes are arranged in several layers (here three) and totally interconnected with each other via the synapses (black arrows). This means, that all possible connections between the nodes of adjacent layers are present. There are three types of neurons in an ANN, the input unit (yellow nodes, denoted by x_i), the hidden unit (green nodes, denoted by z_j) and the output unit (blue nodes, denoted by y_k), which act slightly differently and are discussed in more detail later in this section. The first layer is the so-called *input layer*, since here each variable enters the neural network via an input unit. In the next layer, the hidden units are located, which transform the input variables and propagate their information to the last layer, the so-called *output layer*. There, an output neuron processes all information and results in a value for the output variable. In principle, it is possible to have several outputs but for the classification task described here, where only two pulse classes should be distinguished, a single output neuron is enough. Another generalization of the network architecture is the consideration of additional layers containing hidden units. However, to keep the shown example simple, here the number is limited to the minimum and, thus, only one hidden layer is drawn.

In literature, there is no consensus about the terminology for counting the number of layers of a network [135]. Thus, the network depicted in figure 6.2 may be denoted as a 3-layer network by simply counting the number of layers containing units, whereby the inputs are counted also as units. Another alternative is to specify the drawn network as a single-hidden-layer network, since only one layer of hidden units is present. However, following the recommendation given in [135] in the present work this network is described as a 2-layer network, because this is the number of layers with adaptive weights and only these weights are important for the properties of the network.

Multilayer Perceptrons (MLP) are so-called *feed-forward* networks, where the information is only transferred in one direction from the inputs through the neural network to the output unit [135]. No closed loops or back-propagation are allowed, and, thus, all arrows point in the direction of the output layer. In this way, it is ensured that the outputs are deterministic functions of the inputs.

In figure 6.3 a schematic drawing of the j-th neuron (n_j, green node) in the hidden layer

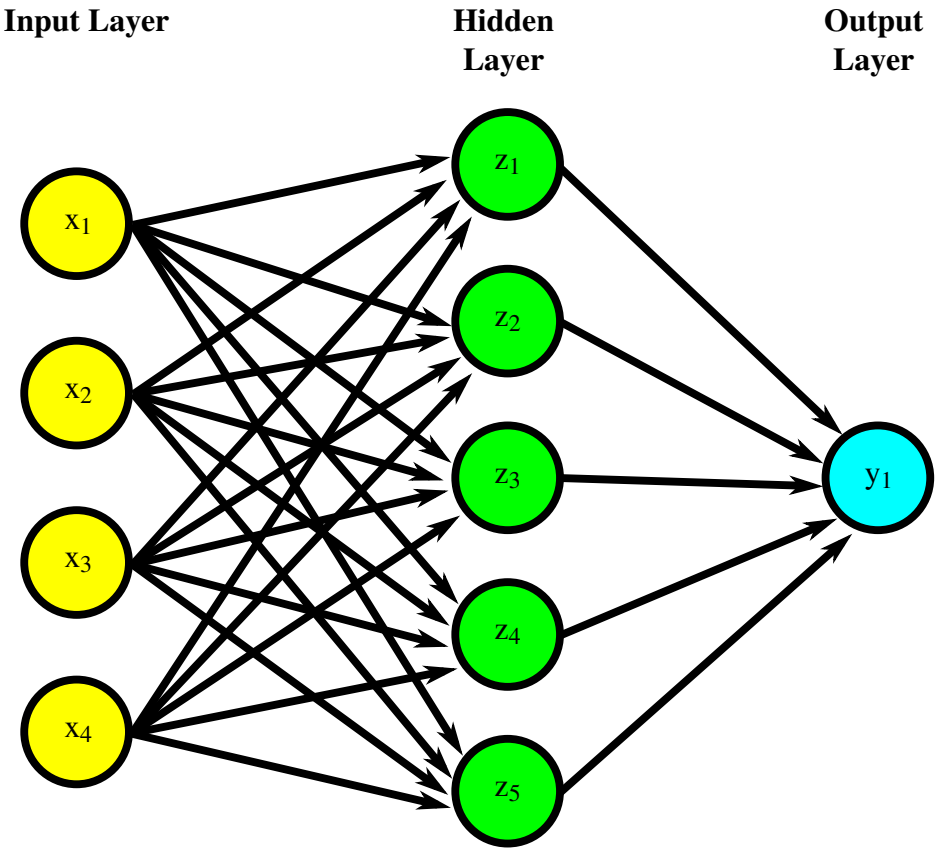

Figure 6.2: *Schematic drawing of an artificial neural network (ANN) with four input parameters and ten neurons in total. In the present work only multilayer perceptrons (MLPs), i.e. a special kind of a feed-forward network, are used. All neurons (nodes) located in adjacent layers are connected via synapses (arrows) with each other. The units of the input layer also called input neurons (yellow nodes) are connected to the hidden units (green nodes) in the hidden layer. In the example shown the outputs of the hidden units are directly connected to the single output neuron (blue node), but in general also a series of hidden layers is possible. Each individual synapse and also the neurons have a weight which is adjusted to the specific problem by training of the network.*

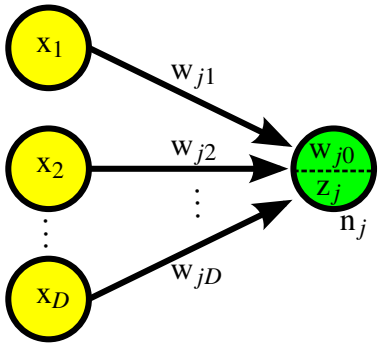

Figure 6.3: *Schematic drawing of a subset of an artificial neural network with, in total, D input parameters x_i ($i = 1,\ldots,D$) and a single hidden neuron n_j. The input parameters are connected with the neuron via D synapses with weights w_{ji} while the bias of the neuron is denoted by w_{j0}. The activation a_j of the neuron n_j is calculated as weighted sum of all inputs (see equation 6.1). The sigmoid activation function $f_{\text{act}}(a_j)$ given in equation 6.4 transforms the activation and results in the output value z_j of the hidden neuron.*

is shown. It is connected to, in total, D input variables (x_i, yellow node) via synapses (black arrows). The synapse connecting the i-th input variable with the neuron n_j is mathematically described by an individual weight w_{ji}. Furthermore, also the neuron itself has an adjustable weight, called the bias and denoted by w_{j0}. The activation a_j of the neuron n_j is the weighted sum of the inputs and the bias parameter and, thus, is given by:

$$a_j = \sum_{i=1}^{D} w_{ji}^{(1)} \cdot x_i + w_{j0}, \tag{6.1}$$

where the superscript (1) denotes that the corresponding parameters are in the first layer of the network.

By defining another input variable x_0 with a clamped value of $x_0 = 1$ the bias parameter w_{j0} can be absorbed into the weight parameters [135]:

$$a_j = \sum_{i=0}^{D} w_{ji}^{(1)} \cdot x_i. \tag{6.2}$$

The activation a_j is transformed via the activation function $\boldsymbol{h}$ to form the output z_j

$$z_j = \boldsymbol{h}\left(a_j\right) = \boldsymbol{h}\left(\sum_i w_{ji} \cdot x_i\right), \tag{6.3}$$

where the sum runs over all input units i connected to the hidden unit j.

Generally, the activation functions f_{act} of the hidden units are chosen to be sigmoids [135]. In the present work the logistic sigmoid function is used

$$\boldsymbol{h}\left(a\right) \equiv f_{\text{act}}\left(a\right) = \frac{1}{1+e^{-a}}, \tag{6.4}$$

where a is the activation of the neuron.

Analogously to the hidden units in the first layer the activation and outputs z_k of all units in the following layers are evaluated, whereby the outputs of the hidden units in the previous layer (z_j) become the inputs of the current units

$$z_k = \boldsymbol{h}(a_k) = \boldsymbol{h}\left(\sum_j w_{kj} \cdot z_j\right). \tag{6.5}$$

The iterative application of equation 6.5 allows to evaluate all the activations in the network including those of the output units. Please note that in general the activation function of the output neurons (denoted by $\boldsymbol{\sigma}$ thereafter) can differ from the sigmoidal activation function $\boldsymbol{h}$ used for the hidden units. Depending on the type of the specific problem, there are several possibilities for that choice. In the present work the identity is used but in general also logistic sigmoids or softmax functions are possible [135].

In summary, mathematically each hidden unit is described by the adjustable bias parameter w_{k0}. The activation a of the neuron is calculated as the weighted sum of all inputs of the neuron, whereby the bias parameter is treated as a further synapse connecting the neuron with an input fixed at a value of one. The activation of the neuron is transformed via the sigmoidal activation function $\boldsymbol{h}(a)$ to form the output z_j of the neuron. These outputs become the new input values that feed the neurons in the next layer. This process is repeated through all layers until the output layer is reached and the output variable is determined. In general, the activation function $\boldsymbol{\sigma}$ of the output neurons can differ from the sigmoidal activation function $\boldsymbol{h}$ used for the hidden units.

For a 2-layer feed-forward neural network as depicted in figure 6.2 with D input variables, and M neurons in a single hidden layer the overall network function $y_k(\vec{\boldsymbol{x}_n}, \vec{\boldsymbol{w}})$ is given by:

$$y_k(\vec{\boldsymbol{x}_n}, \vec{\boldsymbol{w}}) = \boldsymbol{\sigma}\left(\sum_{j=0}^{M} w_{kj}^{(2)} \cdot \boldsymbol{h}\left(\sum_{i=0}^{D} w_{ji}^{(1)} \cdot x_i\right)\right), \tag{6.6}$$

where all weight and bias parameters are grouped together in the weight vector $\vec{\boldsymbol{w}}$, while the input parameters are given as input vector $\vec{\boldsymbol{x}_n}$. In general y_k is the output value of the k-th output neuron of the neural network. Despite the above-mentioned fact, that in the present work only one output neuron is considered and, thus, $k = 1$, the subscript k is not dropped to be formally correct.

It can be shown, that feed-forward neural networks are *universal approximators* [135]. This means, that any continuous function can be uniformly approximated to arbitrary accuracy by a two-layer neural network provided the network has a sufficiently large number of neurons. How to find suitable parameter values for the adaptive weights during the training with a given set of data remains the key issue, in practice.

6.1.2 Neural Network Training

The aim of the training of the neural network is to reach a state, where the network can be used to predict the type of pulses not processed before. For a classification task, the network

has ideally learned all characteristic differences in the input parameters of the different classes to disentangle them.

As mentioned above each neuron and each synapse are mathematically described by adjustable weights and biases grouped together in the vector $\vec{\boldsymbol{w}}$. To get a more useful network it has to be trained with samples (denoted $\vec{\boldsymbol{x}}_{\boldsymbol{n}}$, where $n = 1, \ldots, N$) with known properties, in particular the target type $\vec{\boldsymbol{t}}_{\boldsymbol{n}}$ has to be known for each input sample. These samples are processed by the neural network and the respective value y_{nk} of the k-th output neuron is compared with its target value t_{nk}. Thus, the error of an individual training sample is given by:

$$E_n(\vec{\boldsymbol{w}}) = \frac{1}{2} \sum_k (y_{nk} - t_{nk})^2 , \tag{6.7}$$

where $y_{nk} \coloneqq y_k(\vec{\boldsymbol{x}}_{\boldsymbol{n}}, \vec{\boldsymbol{w}})$.

Based on this equation the weights are adjusted either directly after a single input sample is processed (*on-line methods*) or after a complete training epoch, where all input samples are processed at once before the weights are updated (*batch training*). For the latter the total error function of the neural network is calculated as the sum of all individual errors

$$E(\vec{\boldsymbol{w}}) = \sum_{n=1}^{N} E_n(\vec{\boldsymbol{w}}). \tag{6.8}$$

However, here we only evaluate a single term $E_n(\vec{\boldsymbol{w}})$ of the total error function $E(\vec{\boldsymbol{w}})$.

As mentioned above, for the training a set of inputs with known properties is required and, thus, the algorithms discussed here are part of the *supervised training algorithms*. It is at least not easy to extract clean samples of both pulse types from the experimental data. In particular in the present work for the interesting energy range near the threshold of the detector this is a crucial task. In addition, the number of pulses clearly identifiable as proxy for one of the two classes might be limited and, thus, the training might be not optimal due to limited statistics.

To counter these two limitations at least to some extend the simulation method presented earlier (see section 5.4.1) is adapted. The actual implementation is explained in section 6.2, since here it is only important that clean data sets for both pulse classes are available. Another alternative approach are *unsupervised learning algorithms*, which try to find regularities and patterns in unlabeled data [135] but those are not discussed here.

Since the error function is in general a highly non-linear function of the weights and biases, there might be several local minima and only a single global minimum in the weight space. However, for a successful application of the neural network it might not be required to reach the global minimum during training but it might be necessary to compare several local minima in order to find a sufficiently good solution[28] [135].

Most training algorithms involve an iterative procedure to find the best solution which minimizes the error function $E(\vec{w})$, i.e. finding a weight vector $\vec{\boldsymbol{w}}$ such that $\nabla E_n(\vec{\boldsymbol{w}}) = 0$. As the training of a neural network is equivalent to the minimization of the non-linear error function a huge variety of algorithms to solve this task is available.

[28] In general it is not known whether the global minimum has been reached and, thus, comparing different solutions is the only choice.

Typically the first step of the iterative algorithms is the initialization of the weight vector $\vec{\boldsymbol{w}}^{(0)}$ and then this vector is adjusted in a succession of steps of the form

$$\vec{\boldsymbol{w}}^{(\tau+1)} = \vec{\boldsymbol{w}}^{(\tau)} + \Delta\vec{\boldsymbol{w}}^{(\tau)} \tag{6.9}$$

where τ labels the corresponding iterative step.

Two distinct stages are present at each step of this iteration: In the first stage, the steepest gradient $\nabla E_n(\vec{\boldsymbol{w}})$ of the error function of the neural network with respect to the weights has to be computed. The so-called *backward propagation of errors*, or simply *backpropagation of errors*, provides thereby, a computationally efficient method for evaluating the derivatives and is discussed in more detail later in this section. These derivatives are used in the second stage of each step, where the training algorithm proposes the weight updates $\Delta\vec{\boldsymbol{w}}^{(\tau)}$ to improve the error of the network.

The *gradient descent* method is the simplest approach of such a training algorithm using the gradient information of the error function. In equation 6.9 the weight update $\Delta\vec{\boldsymbol{w}}^{(\tau)}$ is chosen such that it comprises a small step in the direction of the negative gradient

$$\vec{\boldsymbol{w}}^{(\tau+1)} = \vec{\boldsymbol{w}}^{(\tau)} - \eta\nabla E_n\left(\vec{\boldsymbol{w}}^{(\tau)}\right), \tag{6.10}$$

where η is the so-called *learning rate*. After each step the gradient is re-evaluated and the process is repeated. In section 6.4 the training algorithms actually used in the present work are described in more detail.

Error Backpropagation

Suppose a ANN-training set of data contains N samples with input parameters $\vec{\boldsymbol{x}}_{\boldsymbol{n}}$, where $n = 1,\ldots,N$ [29]. Also for each sample the target value t_{nk} for the k-th output of a general network is known. In case of a general feed-forward network, the activation a_j of each unit is computed as the weighted sum of its inputs of the form

$$a_j = \sum_i w_{ji} \cdot z_i, \tag{6.11}$$

where z_i is the output of a unit sending information over a connection with weight w_{ji}. This unit could be either an input unit or a hidden unit which is not of importance here. As mentioned above the bias of the neuron is absorbed in the weights by introducing an extra unit with fixed value of $z_0 = 1$. The activation a_j is transformed via the activation function $\boldsymbol{h}$ to give the output z_j of the unit

$$z_j = \boldsymbol{h}\left(a_j\right) = \boldsymbol{h}\left(\sum_i w_{ji} \cdot z_i\right). \tag{6.12}$$

For the following discussion it is supposed that an input vector $\vec{\boldsymbol{x}}_{\boldsymbol{n}}$ is supplied to the neural network and that all activations are calculated by recursive application of equation 6.12. As a

[29] To not confuse the training set used for the training of the neural network with the training set used for the determination of the cut limits, the former is denoted ANN-training set hereafter.

reminder this process is also called *forward propagation* since the information flows from the input through the network to the output.

The quantity of interest for the training is the gradient of the error function in the weight space. In particular the partial derivative of E_n with respect to the weight w_{ji} is important. The error $E_n(\vec{\boldsymbol{w}})$ depends on the weight w_{ji} via its dependency on the activation a_j. Thus, the application of the chain rule for partial derivatives results in

$$\frac{\partial E_n}{\partial w_{ji}} = \frac{\partial E_n}{\partial a_j} \cdot \frac{\partial a_j}{\partial w_{ji}} = \delta_j \cdot z_i, \tag{6.13}$$

whereby a new quantity δ_j often referred to as *error* is introduced [135]

$$\delta_j \equiv \frac{\partial E_n}{\partial a_j}. \tag{6.14}$$

Equation 6.13 states, that the sought-for partial derivative of the error function E_n with respect to the weight w_{ji} is obtained simply by multiplying the error δ_j with the input z_i.

This new quantity δ_j is investigated further by applying the chain rule for partial derivatives a second time:

$$\delta_j \equiv \frac{\partial E_n}{\partial a_j} = \sum_k \frac{\partial E_n}{\partial a_k} \cdot \frac{\partial a_k}{\partial a_j}, \tag{6.15}$$

where the sum runs over all units k which are connected to unit j. This could be either other hidden units or output units. Variations in a_j affect the error function only via variations in a_k and, thus, the error of the units k is backpropagated to the unit j and, hence, the name of the method.

From the combination of equation 6.11 and equation 6.12 it follows that the partial derivative $\frac{\partial a_k}{\partial a_j}$ is:

$$\frac{\partial a_k}{\partial a_j} = w_{kj} \cdot h'(a_j). \tag{6.16}$$

Finally, by putting everything together, the backpropagation formula is obtained:

$$\delta_j = h'(a_j) \cdot \sum_k w_{kj} \cdot \delta_k, \tag{6.17}$$

where the sum runs over the first index of w_{kj} corresponding to a propagation of information backwards through the network. This is in contrast to equation 6.12, where the sum iterates over the second index and, thus, propagates information in the forward direction.

Basically, equation 6.17 states, that the error δ for a particular hidden unit is obtained via propagation of the δ's for the units higher up in the network, i.e. units closer to the output neuron. Thus, all δ's can be recursively calculated if δ is known for the output neurons. For the latter the activation function $\boldsymbol{\sigma}$ corresponds to the identity in the present work and, thus, $y_{nk} = a_k$. Therefore, it follows from equation 6.7 that the sought-for error δ_k simply is

$$\delta_k \equiv \frac{\partial E_n}{\partial a_k} = y_{nk} - t_{nk}. \tag{6.18}$$

The recursive application of equation 6.17 allows to obtain all required information for all hidden units in a feed forward network, regardless of its topology [135].

The procedure of the error backpropagation is summarized as follows:

1. Evaluate the activation a_j of all units and, thus, the output of the network y_{nk} for an input vector $\vec{x_n}$.
2. Compute the partial derivatives $\frac{\partial E_n}{\partial a_k}$ and, thus, the error δ_k for all output units by using equation 6.18.
3. Apply recursively the backpropagation formula given in equation 6.17 to obtain δ_j for all hidden units in the network .
4. Calculate the required derivatives $\frac{\partial E_n}{\partial w_{ji}}$ according to equation 6.13.

As explained above the derivatives $\frac{\partial E_n}{\partial w_{ji}}$ together form the gradient $\nabla E_n(\vec{w})$ in the weight space, which in turn is used by the training algorithm to find a weight update $\Delta\vec{w}$ improving the total error $E_n(\vec{w})$ of the network output.

Overtraining

Whenever all data samples with known outcome that are available for training of the neural network are processed a so-called *training epoch* is finished. In the present work, the aim of the training of the network is to reach a state, where the ANN is able to distinguish between the two pulse classes. A first naive thought leads to the idea that as many training epochs as possible are desired to reach the optimal separation for the given problem. However, due to the so-called *overtraining* the number of training cycles has to be limited. Overtraining is an effect commonly observed during supervised training, in particular if training is performed for too many epochs and/or not enough data samples are available for training.

To illustrate the effect of overtraining a very simple example in a two-dimensional parameter space $\vec{X} = (X_1, X_2)$ is considered: In the following it is assumed, that there are two separate populations which both are distributed linearly in this parameter space. Due to some noise effects modelled by a Gaussian distribution with constant width, the obtained samples from both populations slightly overlap. In figure 6.4 several events sampled from these two populations are depicted. Since the shown events belong to the ANN-training set and are created artificially it is known which event belongs to which population and, thus, they are marked with red triangles or blue dots, respectively. Based on the functions used to generate these events the theoretically best possible and most general separation between both populations is calculated and also shown as black dashed line in figure 6.4. Furthermore an ANN is trained with these samples, whereby the target value of the one population is set to zero and of the other population to one. Also depicted as green line in figure 6.4 are the points in the weight space where the ANN has an output value of 0.5.

In figure 6.4a the ANN training is stopped after 15 epochs. The separation line of the ANN is close to the optimum value calculated from the distributions used to generate both data sets. As in real applications, these distributions are not known to the ANN and only the samples

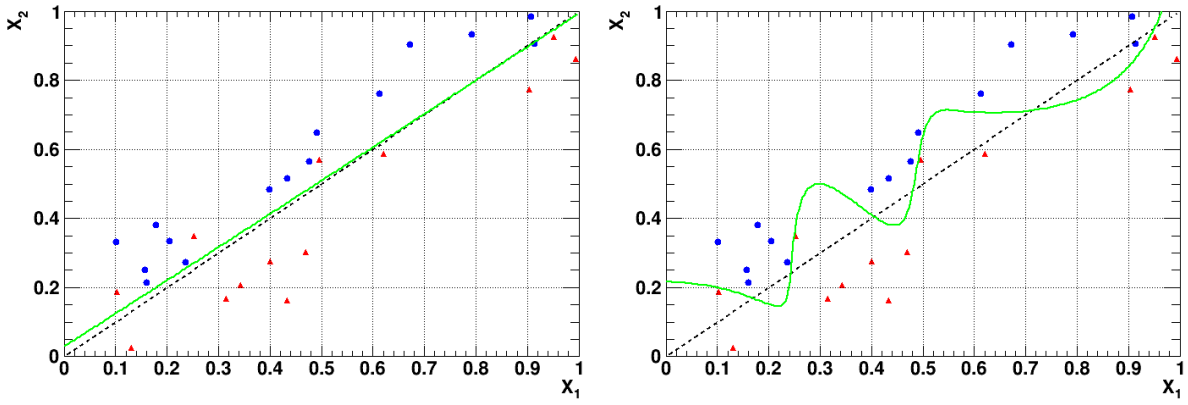

(a) ANN trained for 15 epochs *(b) ANN trained for 200 epochs*

Figure 6.4: *Illustrative example of overtraining of an ANN. The red triangles and the blue dots are samples of two distinct populations which are slightly overlapping due to the influence of noise. The network is trained such, that the output value is* 0 *for one population and* 1 *for the other population. The optimum separation line is drawn as black dashed line and is determined from the theoretical distributions used to generate the respective samples. Also depicted as green line are the points, where the ANN has an output value of* 0.5*. In (a) the training of the ANN is stopped after 15 epochs. The resulting equipotential line is close to the optimum line and, thus, shows the great separation potential of this network. In (b) the ANN is trained further for in total* 200 *epochs and overtraining occurred. While all the data samples of the set are perfectly classified the ability of generalizing the network to previously not processed data is lost.*

with known type are used for the training. It is expected, that a good performance is achieved when this network is applied to data not seen before.

In figure 6.4b the network is trained further for 185 epochs and, thus, in total 200 training epochs are performed. Due to this high number of training epochs, the network learned very special random features of the data samples of the ANN-training set, which are not related to the target function. Thus, overtraining occurred and the equipotential line describes perfectly the data points of the ANN-training set but for the expense of generalization. In that case, the performance on an independent data set from the same populations would be rather poor.

To be able to recognize overtraining, the simulated data set is split into two parts the *training set* and the *test set*. The ANN-training set is actually used to adjust the weights and, thus, train the neural network for the specific problem. However, the purpose of the test set is only to check the total error and no feedback into the ANN (i.e. no update of the weights) is provided for this part of the data. Thus, in each training epoch the pulses of the test set can be considered as previously unprocessed data and are used to recognize overtraining as illustrated in figure 6.5. While the error of the ANN-training data set (red line) is constantly decreasing with increasing training epoch number, this might in general not be true for the error determined with an independent data set called validation or test set. At the beginning of the training the error of the test set (blue line) also decreases but at some point it might rise again due to overtraining.

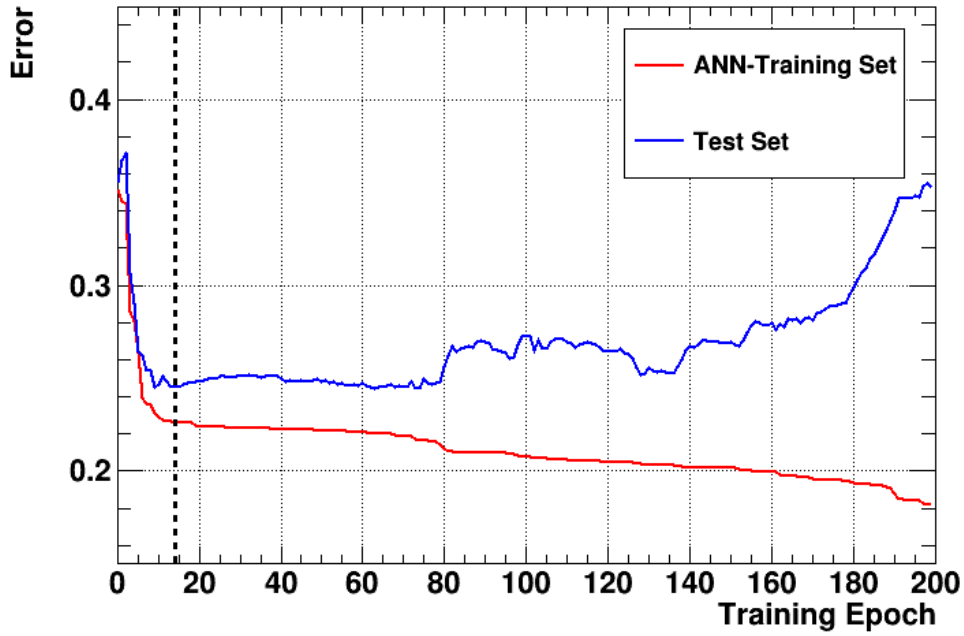

Figure 6.5: *Total error of the training (red line) and of the test set (blue line) as function of the number of training epoch. The network shown in figure 6.4 is trained. While the error of the ANN-training set is constantly decreasing with increasing epoch number this is not the case for the test set. All samples of the ANN-training set are constantly processed by the network and used to update the weight vector. In contrast, the samples of the test set are only used to determine the error but do not influence the weights in the ANN. When the test set error is increasing this is a hint that the network concentrates on special features observed only in the particular samples of the ANN-training set and which are not representative for the whole distribution. At this point the network starts to become overtrained and training should be stopped. When the training is stopped after 15 epochs (vertical black-dashed line) the network, the performance of which is depicted in figure 6.4a, is obtained*[30].

Thus, in order to obtain the network with the best generalization performance training should be stopped directly at the point where the test-set error starts to rise. This procedure is denoted *early stopping* in [135]. In case of the ANN shown in figure 6.4a training is stopped after 15 epochs[30] which is marked by the vertical black-dashed line in figure 6.5.

6.2 Artificial Pulse Simulation

For the creation of artificial pulses of the different classes the data-driven pulse simulation, which is explained earlier in section 5.4.1, is adopted. For the analysis here only differences in the shape of phonon detector pulses are considered and, thus, no artificial signal events, i.e. events consisting of a set of a phonon and a light detector pulse, are required. Hence, the simulation generates only pulses for the respective phonon detector.

[30] Please note that the first training epoch of the ANN-training set has a training number of zero.

To create clean absorber and TES-carrier samples empty baselines are superimposed with the respective template. Pulses with different energies are created by scaling the template with different amplitudes. For the phonon detector TUM40, which is discussed here, in total 10 different energies are simulated ranging from slightly below the trigger threshold of $\sim 0.4\,\mathrm{keV}$ up to $\sim 10\,\mathrm{keV}$[31]. The spacing between the discrete energy values varies, whereby the majority is concentrated at low energy values near the energy threshold of the detector. The resulting pulses are stored for the offline analysis and treated like actually recorded CRESST data.

Due to the fast rise and decay times of the TES-carrier template of TUM40 the reconstructed pulse height is lower than the desired amplitude. The pulse height is determined in a running-average filtered pulse, whereby 50 samples are averaged to reduce the influence of the noise (see section 4.3). In case the TES-carrier pulse rises faster than these 50 samples only an averaged and, thus, reduced value for the pulse-height parameter is determined. Therefore, in a first test artificial pulses with ten different amplitudes of both classes are simulated based on a subset of all empty baselines available. The resulting peaks in the pulse-height spectrum are fitted by a Gaussian function to infer the reconstructed pulse height $\mathrm{PH_{rec}}$ and compare it with the injected pulse height $\mathrm{PH_{inj}}$. While for the absorber set no systematic deviation is observed, the following equation holds for almost all energies in the TES-carrier set[32]:

$$\mathrm{PH_{rec}} = 0.75 \cdot \mathrm{PH_{inj}}. \tag{6.19}$$

Thus, for the final simulation the desired amplitude of all TES-carrier pulses is scaled to correct for this effect and ensure in average the same pulse-height distribution for both pulse classes.

In the present work the same empty baselines are used for the absorber as well as for the TES-carrier data set. However, the final artificial data sets for each pulse type are achieved by randomly selecting one specific energy for each baseline in each data set. Thus, each baseline is only represented once in each set and most likely the amplitudes of the artificial pulses of the same baseline are different in both sets.

Examples of a simulated pulse for each class are depicted in figure 6.6. The same empty baseline is superimposed with both templates to obtain an absorber (a) as well as a TES-carrier (b) pulse. The absorber pulse corresponds to an energy deposition of $\sim 1\,\mathrm{keV}$ while for the TES-carrier pulse no energy calibration is available. Both pulses are simulated such, that the means of the reconstructed pulse-height distributions are equal.

As explained earlier, empty baselines are obtained by manually enforce the read out of the digitizer at regular time intervals. Although usually no interaction is observed, it might happen that coincidentally a valid pulse is recorded in the respective time window. In contrast to the simulation of the signal survival probability (see section 5.4.1), where it is important to also keep these events, this time such pulses have to be removed, since it is not always clear to which class the recorded pulse belongs. Therefore, several cuts including the pulse height,

[31] For most of the detectors considered pulses with a height corresponding to 10 keV can be assigned to the respective pulse type using simpler methods based on the parameters described in section 6.3.

[32] Only for small injected pulse heights, where the baseline noise dominates the resulting pulse, no difference between both data sets is observed. There the reconstructed pulse height is independent of the injected pulse height.

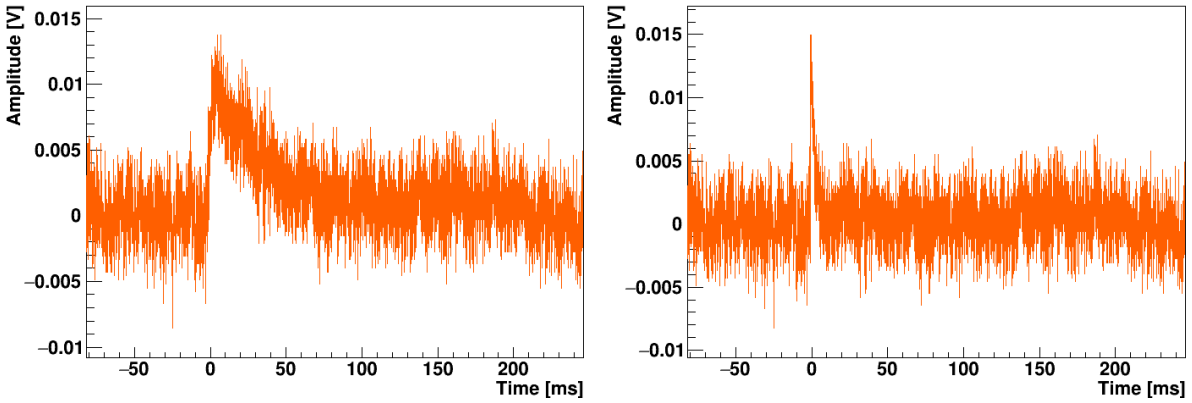

(a) *Simulated absorber pulse* ***(b)*** *Simulated TES-carrier pulse*

Figure 6.6: *Example of a simulated absorber (a) and a TES-carrier (b) pulse of TUM40. The pulses are simulated such, that the reconstructed pulse heights of both pulses are equal in average. For the absorber type the shown pulse corresponds to an energy deposition of* $\sim 1\,keV$.

amplitude and RMS of the fit are performed in order to remove all baselines spoiled with actual pulses and select only real empty baselines. It is important to note, that these cuts do not completely ensure that all remaining records are empty baselines completely free of any pulse. It still might happen that small pulses, with a signal height below the trigger threshold, are present and are hidden inside the baseline fluctuations. Such records might lead to artificial pulses where the pulse shape is disturbed compared to the respective template. A solution for this problem would be the simulation of artificial baselines, which are created with the same properties as observed for empty baselines in the data. However, this has not been possible up to now due to some limitations in the used algorithms (for more information see appendix E).

For each data set, in total 466 560 pulses with ten different energies are simulated. For each baseline of a data set an amplitude is randomly chosen, while the other nine pulses are not considered anymore. Thus, in total 46 656 simulated pulses are contained in each data set.

The aim of this pulse-shape analysis is to only separate absorber and TES-carrier pulses, while records with features already rejected by another cut should not be considered. Thus, all different cuts which are applied to the actual data set are also applied to the artificial data set. If possible, the same cut limits are used but in some cases this was not possible (e.g. RMS cut). In that case a new cut is designed in the simulation and applied to the absorber as well as to the TES-carrier data set.

In table 6.1 the resulting number and the corresponding fraction of pulses surviving the cuts are depicted for each simulated energy. While for the absorber data set only the numbers of pulses surviving all cuts are shown, for the TES-carrier data set the numbers of surviving pulses before and after the RMS cut are given. Interestingly at high energies ($\gtrsim 2\,keV$) all simulated TES-carrier pulses differ drastically in the RMS distribution and, thus, are already rejected by the applied RMS cut. Since it might be important for the training of the ANN to also have TES-carrier pulses with large amplitudes available, both TES-carrier data sets before and after application of the RMS cut are usable for training. For the simulation here,

Simulated Energy [keV]	Absorber Data Set		TES-Carrier Data Set			
			before RMS Cut		RMS Cut applied	
	pulses	%	pulses	%	pulses	%
0.10	135	2.89	63	1.35	62	1.33
0.25	1 315	28.19	105	2.25	105	2.25
0.50	3 109	66.64	605	12.97	601	12.88
0.75	3 518	75.40	1 904	40.81	1 890	40.51
1.00	4 028	86.33	3 300	70.73	3 263	69.94
1.50	4 260	91.31	4 319	92.57	4 232	90.71
2.00	4 389	94.07	4 440	95.16	4 139	88.71
5.00	4 444	95.25	4 377	93.81	0	0
7.50	4 362	93.49	4 392	94.14	0	0
10.00	4 472	95.85	4 548	97.48	0	0
Σ	**34 032**	**72.94**	**28 053**	**60.13**	**14 292**	**30.63**

Table 6.1: *Number of pulses for all simulated energies (first column) in the different data sets available for the training of ANNs. Also given is the surviving fraction (%) of pulses reduced by the different selection criteria. For absorber pulses only one data set is available. For TES-carrier pulses two data sets are available, one before the RMS cut and one after the RMS cut is applied. This is reasonable, since the RMS-cut removes all TES-carrier pulses at energies* ≥ 5 *keV.*

no energy cut is applied and, thus, also pulses below the energy threshold of TUM40 (409 eV or 609 eV depending on the data set) are present.

To validate the simulation, parameter distributions of simulated and measured pulses are compared. In figure 6.7 as an example the rise-time distributions of simulated (a) and measured (b) pulses of TUM40 are depicted. Despite the fact that in the simulation pulses with discrete energies are generated while in reality a continuous energy spectrum is observed both distributions seem to be similar and, thus, validate the used pulse simulation.

In the simulation the different energy spacing of the (in total) 10 different amplitudes leads to an overlapping region below 3 keV (7 amplitudes) while at higher energies distinct peaks, simulated with three different amplitudes, are observed. The energy resolution in the simulation is solely caused by the noise contribution of the measured baseline while in reality also other effects, e.g. charge carrier statistics, are important (see section 7.1.2 for more details). With the help of the simulation the expectation that TES-carrier pulses (gray scale) have a lower mean rise time compared to absorber pulses (color scale) is confirmed. Since a huge number of pulses is observed at lower rise times in the training set of TUM40 (figure 6.7b), this is an indication that the majority of pulses observed in TUM40 are of the TES-carrier type.

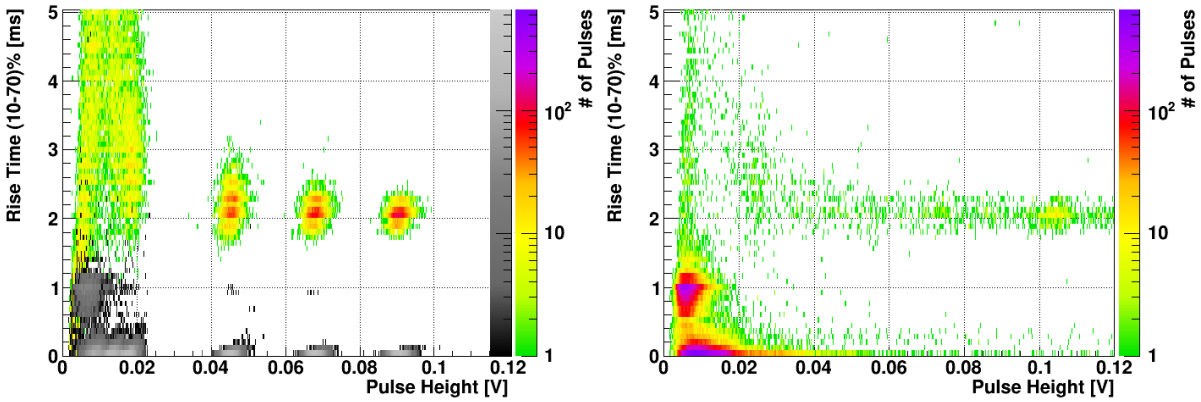

(a) Simulated pulses *(b) Measured pulses*

Figure 6.7: *Comparison of the rise time distributions of simulated (a) and measured (b) pulses of TUM40. For the simulation the color scale applies for absorber pulses, while TES-carrier pulses are depicted in gray scale. In the simulation pulses with discrete amplitudes are created and, thus, distinct peaks are observed. However, in the measurement a continuous energy spectrum is observed. Beside this effect, the simulation agrees well with the measurement hinting towards a large number of TES-carrier pulses in the respective detector.*

6.3 Input Parameters and their Discrimination Power

In this section the different parameters suitable for the pulse-shape analysis in cryogenic detectors are explained. Furthermore, the discrimination power of each individual parameter is defined and shown for different energy ranges. In section 6.4 the individual discrimination powers presented here are compared to the discrimination power of the multilayer perceptrons (MLPs).

Whenever pulses of the two different classes (absorber and TES-carrier) are compared to each other in this chapter, the pulse height is depicted on the x-axis. This is the only parameter related to the energy of the pulses whose determination does not depend on the actual pulse class. As explained in section 4.4, the energy reconstruction depends on the template fit and, therefore, on the template used to determine the amplitude of a pulse. Thus, both parameters, the amplitude obtained from the fit with the absorber template as well as the reconstructed energy based on this fit, are not suited as estimator for the energy deposited in a TES-carrier pulse due to the different pulse shape in the phonon detector. It has not been possible to energy-calibrate a TES-carrier up to now and, thus, no energy information is available for this pulse class. However, to get an impression which energy scale the pulse-height range corresponds to, for absorber pulses also the simulated energy is shown on an additional x-axis. Furthermore, in the discussion in the main text also the energy values are mainly used since the energy is a much more intuitive physical quantity compared to the pulse height. In order to be able to see differences between absorber and TES-carrier pulses over the complete simulated energy range, the TES-carrier pulses of the data set before application of the RMS cut, are used to create all plots shown in the current section.

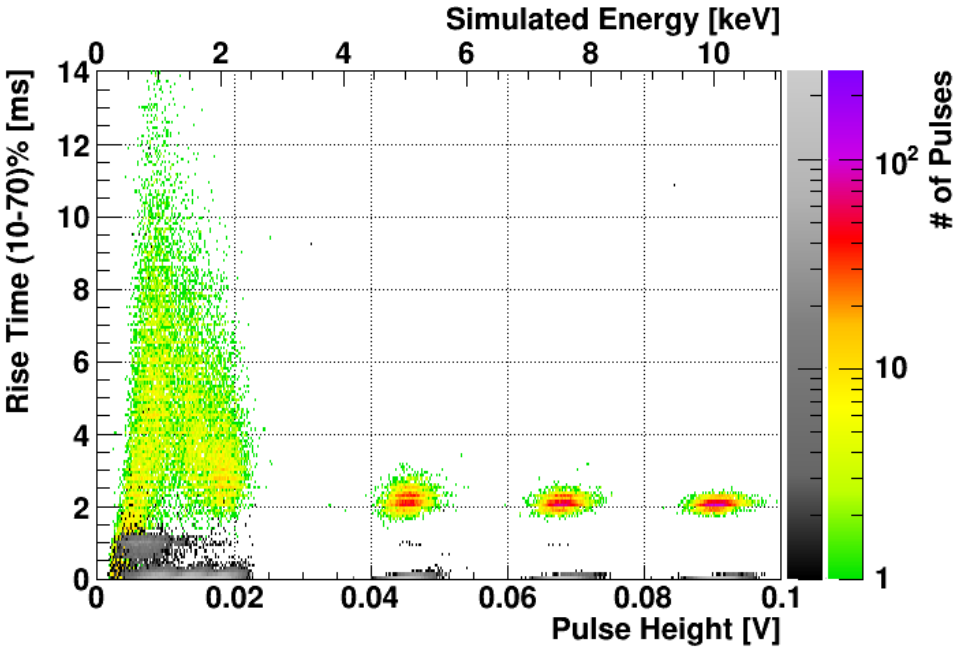

Figure 6.8: *Energy dependent distribution of the rise time 10–70% parameter for simulated absorber (color scale) and TES-carrier (gray scale) pulses. At energies $\gtrsim 3$ keV both distributions are clearly separable. Due to the noise it is hard to determine this parameter precisely for small pulses and, thus, a broadening is observed. Furthermore, for TES-carrier pulses at low energies a new population shows up centered around a rise time value of ~ 1 ms. Both facts together result in a bad separation performance of this parameter at low energies.*

6.3.1 Rise Time

In OxRop, rise-time parameters for different start-to-end levels in the pulse trace are calculated by default (see section 4.2). Firstly, there is the **rise time 10–70%** parameter, which is the time a pulse needs to rise from 10 % to 70 % of its pulse height. Secondly, also the parameter **peak position−onset** is calculated, which is the time difference between peak position and pulse onset. Thereby, the peak position is the time of the maximal sample, while the onset is the first sample above the baseline noise. Here both rise-time parameters are discussed regarding their potential discrimination power since it is a-priori not clear which one shows better results.

Rise Time 10–70%

In figure 6.8 the parameter distributions of the **rise time 10–70%** (henceforth simply denoted by rise time) for the simulated absorber (color scale) and TES-carrier (gray scale) data set are shown as a function of the simulated energy.

In the simulation the mean value of the rise-time parameter for the detector TUM40 is ~ 2 ms for the absorber events, whereas it is only ~ 0.1 ms for the TES-carrier events. Since the sampling frequency is 40 µs this corresponds to ~ 50 and ~ 2.5 samples, respectively. At low energies ($\lesssim 3$ keV) the influence of the noise increases and, thus, a precise determination

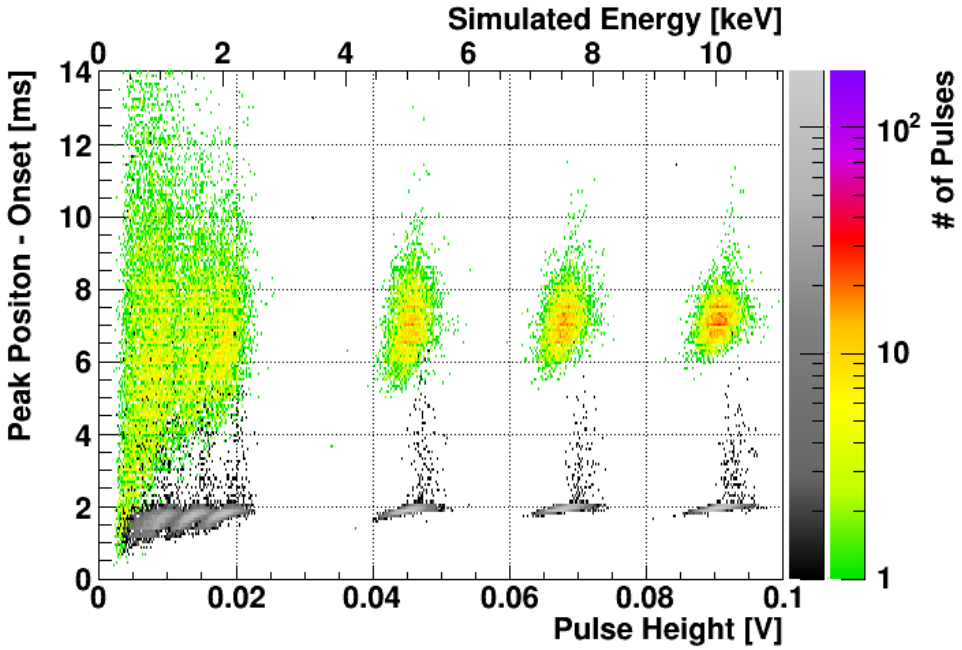

Figure 6.9: *Peak position−onset parameter distribution for simulated absorber (color scale) and TES-carrier (gray scale) pulses. Only at high energies ($\gtrsim 3$ keV) the separation power is good enough to discriminate both populations. For some TES-carrier pulses most probably the pulse onset determination suffers from the influence of the noise and the onset is determined at an earlier sample. Thus, independent of the energy an increased parameter value is observed for some pulses, spoiling the region between both populations. At low energies these pulses overlap with the absorber distribution and, thus, no sufficient discrimination is possible anymore.*

of the rise time is not possible anymore. Consequently, a broader distribution is observed at lower energies compared to the width at high energies. When going down in energy the mean rise time of the absorber pulses increases before it drops towards zero in the vicinity of the energy threshold (0.61 keV). For low-energetic TES-carrier pulses a second population at higher rise times (mean $\sim$ 1 ms) shows up.

In conclusion, the rise time parameter is suited to discriminate absorber and TES-carrier pulses at high energies ($\gtrsim 3$ keV). However, this separation becomes almost impossible at low energies due to the broader distributions and the second population for TES-carrier pulses.

Peak Position - Onset

In figure 6.9 the simulated event distributions of the **peak position−onset** parameter are shown for the absorber (color scale) and TES-carrier (gray scale) data set as a function of the simulated energy. Compared to the rise-time distribution the results do not drastically differ. The mean distributions are well separated in particular at high energies while separation becomes harder at low energies. At all simulated energies several outliers in the TES-carrier data set leaking up towards the absorber population are observed. Most probably the pulse

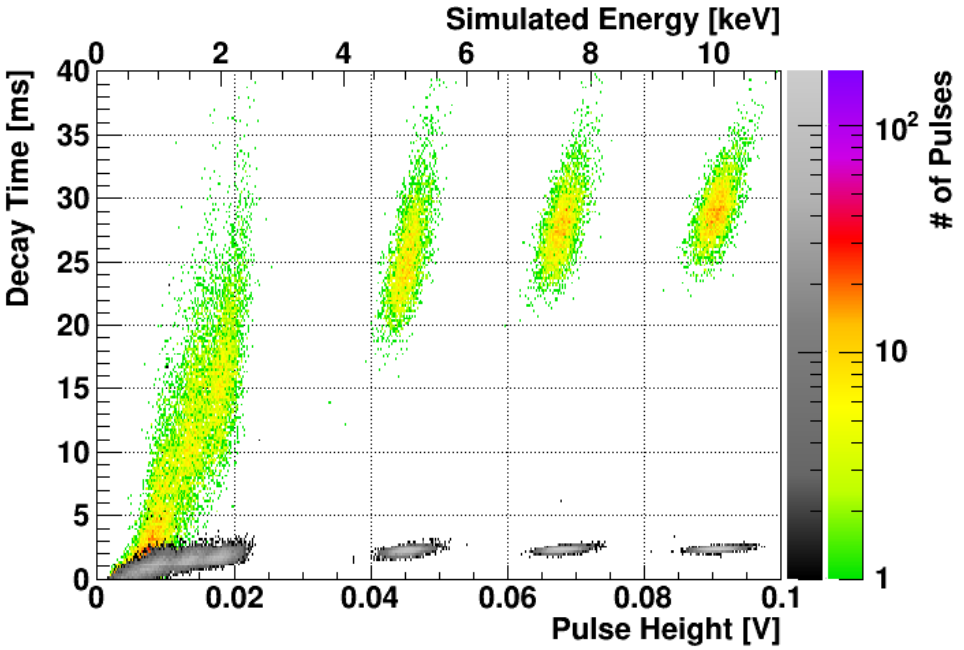

Figure 6.10: *Decay-time distribution for simulated absorber (color scale) and TES-carrier (gray scale) pulses. At high energies ($\gtrsim 3$ keV) both distributions are clearly separated and almost no outlier spoils the parameter space in between. However, at lower energies ($\lesssim 3$ keV) the mean determined decay time of absorber pulses decreases and, thus, both populations approach each other. At energies $\lesssim 1.5$ keV both populations considerably overlap and no clear separation is possible anymore.*

onset determination suffers from the influence of the noise and compared to a mean TES-carrier pulse the onset point is determined in these cases at an earlier sample in the pulse trace. Consequently, the calculated time difference between maximum and onset increases and, thus, these events spoil the discrimination power of this parameter.

6.3.2 Decay Time

The **decay time** is the time difference between the peak position and the sample, where the pulse has decayed to $1/e$ of its pulse height. For the TES-carrier template not only a faster rise time but also a more rapid decay is observed compared to the absorber template (see figure 6.1b). Thus, for both pulse classes a difference can be observed in figure 6.10, where the distributions of the decay-time parameter of simulated absorber pulses (color scale) as well as of TES-carrier pulses (gray scale) are depicted. Again, at high energies ($\gtrsim 3$ keV) the two main populations are clearly separated. There, the mean decay time for absorber events is ~ 28 ms, while it is only ~ 2 ms for TES-carrier pulses. Almost no outlier is observed between both main populations and, thus, a good separation between both distributions is achieved. However, at lower energies ($\lesssim 3$ keV) the mean of the determined decay time decreases for absorber pulses and approaches the distribution of TES-carrier pulses. At energies $\lesssim 1.5$ keV both populations overlap considerably and no clear separation is possible anymore.

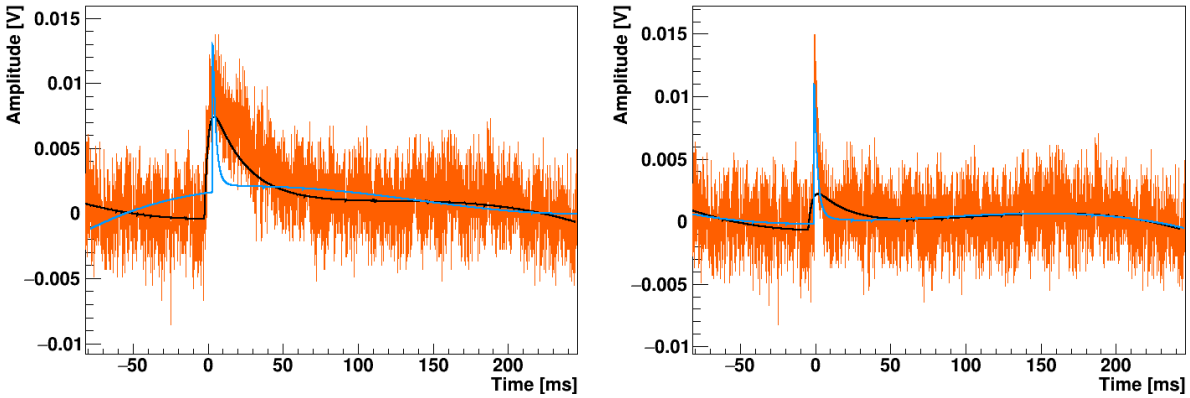

(a) *Absorber pulse* ***(b)*** *TES-carrier pulse*

Figure 6.11: *Example of a simulated absorber pulse (a) and a simulated TES-carrier (b) pulse, both fitted with the absorber (black) as well as the TES-carrier (blue) template. While the fit of the absorber pulse (a) with the absorber template (black) yields as expected a reasonable amplitude value, the fit with the TES-carrier template (blue) results in an amplitude, which is too large compared to the observed pulse height. However, the TES-carrier pulse (b) is fitted well with the TES-carrier template (blue) but an amplitude which is too small is obtained from the fit with the absorber template (black). Therefore, the ratio between both amplitudes is another parameter to discriminate between both pulse classes.*

6.3.3 Amplitude Ratio

As mentioned in chapter 4 all records are fitted with the absorber template to extract the amplitude of the pulse and, thus, to reconstruct the amount of energy deposited. In addition, for all pulses a second template fit with the TES-carrier template of the respective detector is performed.

In figure 6.11 examples of a simulated absorber pulse (a) and a TES-carrier pulse (b) are shown. For the fit of the absorber pulse (a) with the absorber template (black) a reasonable result is obtained, while the fit with the TES-carrier template (blue) leads to an overestimation of the amplitude. However, the situation is completely different when the TES-carrier pulse (b) is fitted. The fit with the TES-carrier template (blue) describing the proper pulse shape results in a reasonable value, while the resulting amplitude of the fit with the absorber template (black) is too small. While the underestimation of the amplitude of the TES-carrier pulse fitted with the absorber template is clearly observable in figure 6.11b, the overestimation of the amplitude in case of the absorber pulse fitted with the TES-carrier template is hardly visible in figure 6.11a due to the strongly tilted baseline. The ratio of the two amplitudes obtained by the template fits – denoted by **amplitude ratio** hereafter – is another parameter to separate both pulse classes and is defined as

$$\text{Amplitude Ratio} = \frac{\text{A}_{\text{Absorber}}}{\text{A}_{\text{TES-carrier}}}, \tag{6.20}$$

where A is the amplitude obtained from the respective fit.

Parameter	Absorber Pulse	TES-carrier Pulse
Pulse Height [V]	0.0104	0.0099
A_{Absorber} [V]	0.0101	0.0035
$A_{\text{TES-carrier}}$ [V]	0.0145	0.0142
Amplitude Ratio	0.6989	0.2495
RMS_{Absorber} [V]	0.0020	0.0021
$RMS_{\text{TES-carrier}}$ [V]	0.0025	0.0020
RMS Ratio	0.1057	-0.0297

Table 6.2: *Template fit results for the absorber and TES-carrier pulses depicted in figure 6.11. Both simulated pulses are fitted with both templates and the respective parameters (amplitude and RMS) are given. The obtained (reconstructed) pulse-height parameter is also listed for both pulses. Also the amplitude ratio as well as the RMS ratio are calculated and included. As expected, the simulated pulses show different values for both parameters. Thus, it might be possible to distinguish both pulse classes by using – among others – these two quantities.*

Table 6.2 lists the values of the relevant parameters for the two simulated pulses depicted in figure 6.11. The determined pulse height as well as the two amplitudes yielded by the respective template fit are given. Additionally, the Root Mean Square (RMS) deviation of the respective template fits are included. Also included are the amplitude ratio as defined in equation 6.20 as well as the RMS Ratio, which is another discrimination quantity explained later in this section (see equation 6.21).

As expected, for the simulated absorber pulse the pulse height and the amplitude obtained from the fit with the absorber template do not differ significantly. The fit of this pulse with the TES-carrier template yields a larger amplitude compared to the pulse height. Thus, a value of ~ 0.70 is determined for the amplitude ratio.

The situation changes for the simulated TES-carrier pulse. As explained in section 6.2, the pulse height for TES-carrier pulses is determined systematically too low due to the time window of the running average filter, which is very long (~ 50 samples) compared to the rise and decay times of the corresponding template. In particular the fast rise time of TES-carrier pulses with a mean value of ~ 2.5 samples is problematic. Consequently, a large difference between the obtained amplitude of the fit with the TES-carrier template and the (reconstructed) pulse height is observed. Taking this effect into account (see equation 6.19 in section 6.2) leads to an injected pulse height value of 0.0132 V, which is comparable with the observed amplitude of 0.0142 V yielded by the fit with the TES-carrier template. Compared to the latter value the amplitude obtained by the fit of the TES-carrier pulse with the absorber template is lower which results in an amplitude ratio of ~ 0.25. Therefore, whenever a TES-carrier pulse is not recognized by the pulse-shape analysis the reconstructed energy is even smaller compared to the estimation based on the respective pulse-height value. This means, that regardless of their actual energy deposited, TES-carrier pulses are in any case reconstructed at low energies due to the pulse-shape difference.

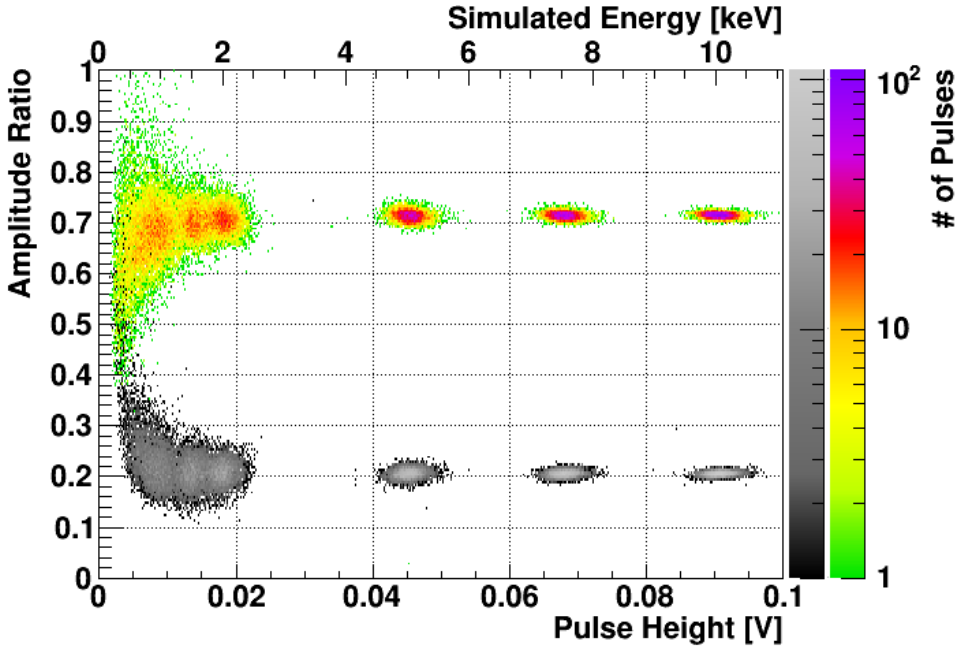

Figure 6.12: *Parameter distribution of the amplitude ratio of simulated absorber (color scale) and TES-carrier (gray scale) pulses. As the name suggests, the amplitude ratio is defined as the ratio of the amplitude obtained from the fit with the absorber template and the amplitude yielded by the fit with the TES-carrier template (see equation 6.20). Except for a few pulses at the lowest energies ($\lesssim 1$ keV) a clear separation between both populations is observed.*

The parameter distributions of the amplitude ratio for simulated absorber (color scheme) and TES-carrier (gray scale) pulses are depicted in figure 6.12. The absorber population is centered around ~ 0.7 while the TES-carrier population is located around ~ 0.2. A clear separation of the main populations almost down to the energy threshold is visible. However, at the lowest energies ($\lesssim 1\,\mathrm{keV}$) several TES-carrier pulses start to leak into the main region of the absorber pulses hindering an absolutely efficient discrimination of both pulse classes there.

6.3.4 RMS Ratio

In the template fit the Root Mean Square (RMS) deviation between data and fitted template is minimized and, thus, it is a quantity describing the fit quality. The lower the RMS value the better the accuracy between data and fit and, thus, for a perfect fit the RMS tends towards zero. One feature of this fit method is that the RMS values of both fits differ and the fit with the proper template has a lower RMS value (see table 6.2).

This information is utilized when the **normalized RMS ratio** (henceforth simply denoted by RMS ratio) for a recorded pulse is calculated. This parameter is defined as

$$\text{RMS ratio} = \frac{\text{RMS}_{\text{TES-carrier}} - \text{RMS}_{\text{Absorber}}}{\text{RMS}_{\text{TES-carrier}} + \text{RMS}_{\text{Absorber}}}, \tag{6.21}$$

where $\text{RMS}_{\text{TES-carrier}}$ and $\text{RMS}_{\text{Absorber}}$ are the RMS values of the respective template fits.

According to this definition the RMS-ratio parameter is typically positive for absorber pulses, whereas it is negative for TES-carrier pulses. In case of a perfect fit, i.e. the respective RMS value equals zero, the RMS-ratio parameter value becomes ± 1, respectively. In figure 6.13 the distribution of the RMS-ratio parameter is depicted for the simulated absorber (color scale) and the TES-carrier (gray scale) data set as a function of the simulated energy. Compared to all other plots, obviously this parameter shows together with the amplitude ratio the best separation ability since in both cases both populations only partly overlap in the low energetic region ($\lesssim 1\,\mathrm{keV}$). This discrimination power is investigated further in the remaining part of this section where the discrimination power is defined and determined.

6.3.5 Discrimination Power

To judge quantitatively which of the presented discrimination parameters separates both populations best the discrimination power has to be determined. Suppose, that the simulated data set contains in total N_a absorber pulses and N_c TES-carrier pulses, respectively. After the application of a cut on a certain discrimination parameter at a distinct cut limit, n_a absorber pulses and n_c TES-carrier pulses survive the cut. The *TES-carrier cut efficiency* ε_c is the fraction of TES-carrier pulses removed by this specific cut and, thus, is calculated by

$$\varepsilon_c = \frac{N_c - n_c}{N_c} = 1 - \frac{n_c}{N_c}. \tag{6.22}$$

Simultaneously, with a high TES-carrier cut efficiency a good cut is characterized by a low *absorber rejection* η_a, which is the fraction of absorber pulses unintentionally removed by this

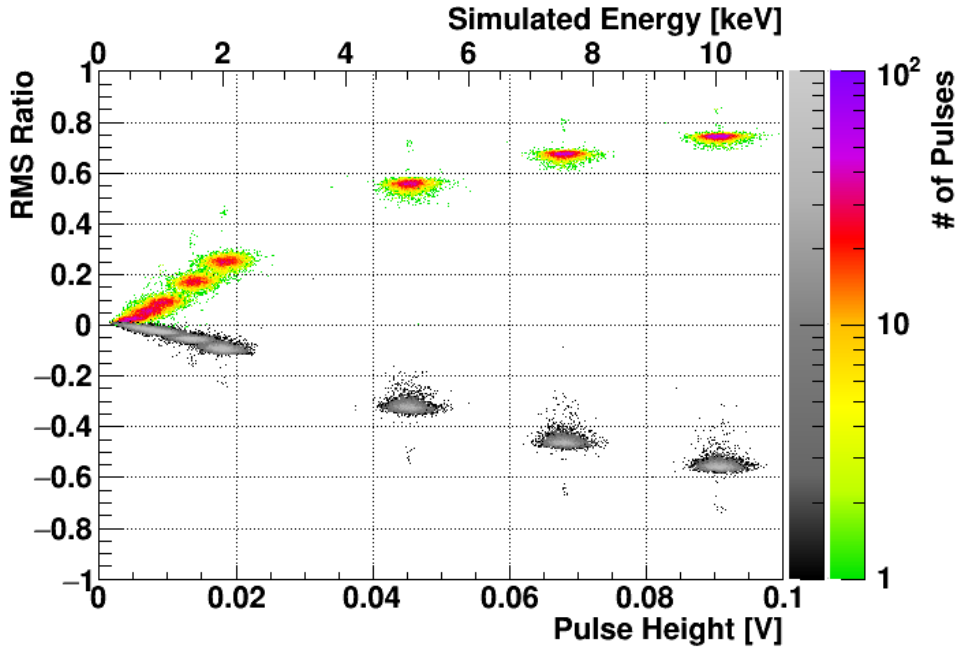

Figure 6.13: *Energy dependent RMS-ratio distribution for simulated absorber (color scale) and TES-carrier (gray scale) pulses. The parameter definition is given in equation 6.21. Typically, absorber pulses exhibit a positive parameter value while it is negative for TES-carrier pulses. In the case of a perfect fit the parameter approaches* ± 1*, respectively. A clear separation between both populations is observed except for energies* $\lesssim 1\,keV$*, where both distributions partly overlap. However, this discrimination parameter is the best single parameter available for the discrimination of the two pulse classes.*

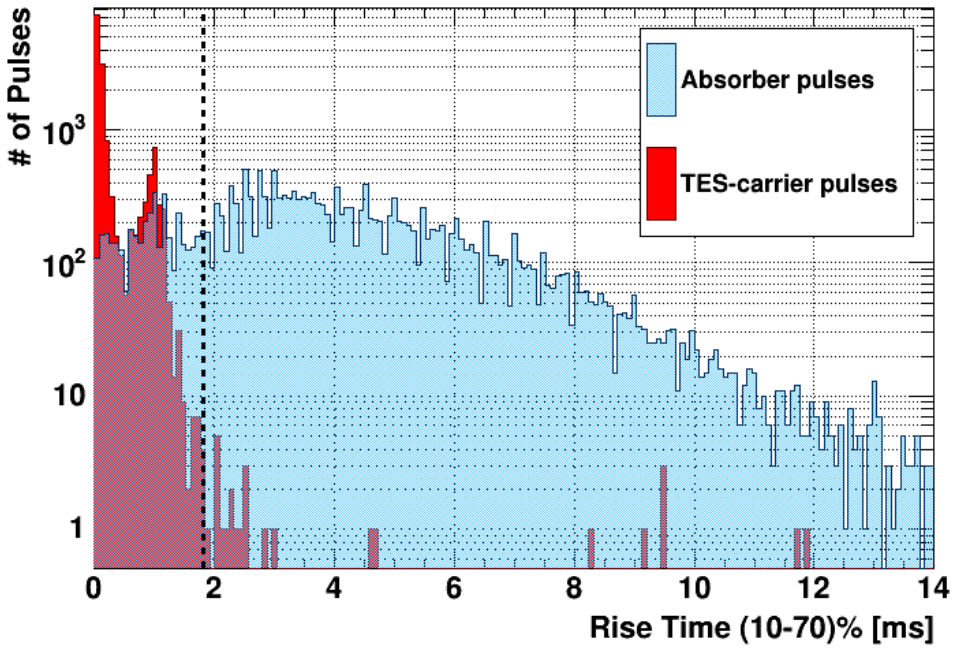

Figure 6.14: *One-dimensional discrimination parameter distribution of simulated absorber (blue) and TES-carrier pulses (red). Also depicted as vertical-dashed line is a possible cut limit whereby all pulses above this line survive this pulse shape cut. By varying the cut limit the TES-carrier cut efficiency ε_c, i.e. the fraction of TES-carrier pulses removed by this cut, is determined. Simultaneously, the absorber rejection η_a, i.e. the fraction of absorber pulses removed by this cut, is also probed. A better discrimination parameter will result in a lower value for η_a at a given TES-carrier cut efficiency ε_c.*

cut. Thus, it is given by

$$\eta_a = 1 - \frac{n_a}{N_a}. \tag{6.23}$$

To determine these two quantities the simulated data set is utilized and the one-dimensional simulated distributions of the discrimination parameters are constructed. However, for higher cut efficiencies close to unity, outliers (which might be randomly distributed in the parameter space) in the data set become more and more important . Thus, for an objective discussion whether one or another discrimination parameter performs better, the absorber rejection η_a should be compared at a fixed TES-carrier cut efficiency $\varepsilon_c \neq 1$.

As an example the rise-time distributions of the simulated absorber (red) and TES-carrier (blue) pulses are depicted in figure 6.14. A possible cut limit is also drawn as vertical-dashed line and all pulses above this line survive, independent of their type. Thus, typically, for a high TES-carrier cut efficiency ε_c a high cut limit is desired, while simultaneously for a low absorber rejection η_a a lower limit is required. By varying the value of the cut limit certain fractions of TES-carrier and absorber pulses are removed and, thus, the respective efficiencies are determined.

A commonly used plot to compare the efficiency of the different discrimination parameters is depicted in figure 6.15. There the absorber rejection η_a, i.e. the fraction of absorber pulses

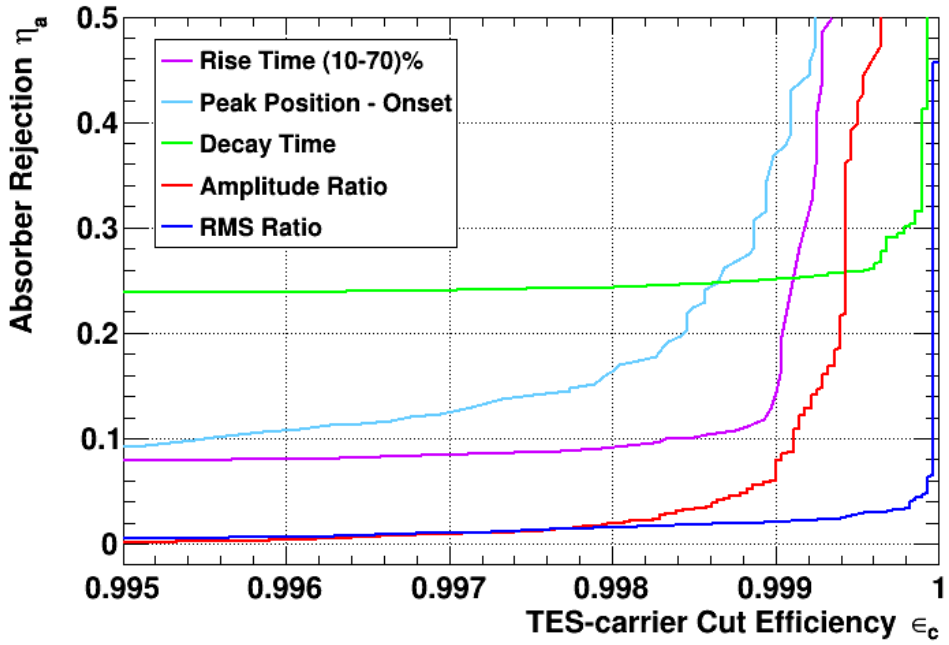

Figure 6.15: *Efficiency curve for the discrimination parameters previously explained in this section. Here, the overall performance for the complete energy range is drawn. The more a curve approaches the lower right corner of the plot (high TES-carrier cut efficiency and simultaneously low absorber rejection) the better the parameter can discriminate both pulse classes. All parameters show a good efficiency without removing too many absorber pulses. The best performance is obtained by the RMS-ratio parameter.*

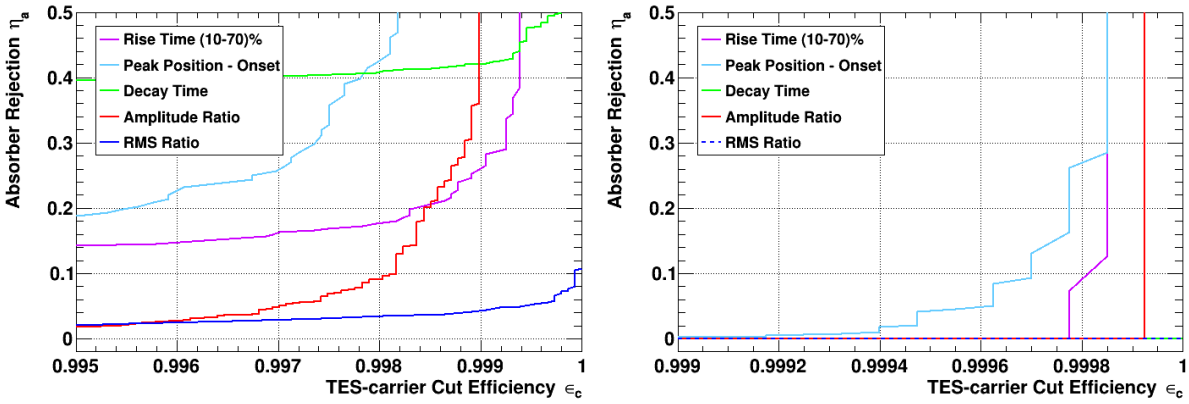

(a) *Energies ≤ 3 keV* ***(b)*** *Energies > 3 keV*

Figure 6.16: *Efficiency curves of the discrimination parameters discussed in this section for two energy intervals. In (a) the performance at energies ≤ 3 keV is depicted, while (b) shows the discrimination for pulses with energies > 3 keV. As expected from the two-dimensional parameter distributions concerning the performance of the different parameters, in case of high energies the discrimination power is better compared to the overall performance depicted in figure 6.15 while it is worse in case of low energies. Nonetheless, in all cases the best separation is achieved with the RMS-ratio parameter.*

removed by a cut, is drawn against the TES-carrier cut efficiency ε_c, i.e. the fraction of TES-carrier pulses removed by a cut. The more a curve of a specific parameter approaches the lower right corner of the plot, the better the discrimination power of this parameter. There as many of the unwanted TES-carrier pulses as possible are removed (large ε_c) and, simultaneously, the number of absorber pulses dismissed (low η_a) is minimized.

Figure 6.15 compares the overall performance of the different parameters. Thereby, all pulses are included independent of the reconstructed energy and for the TES-carrier sample no RMS cut is applied. For most of the described parameters, a high value for ε_c is achieved without loosing too much signal. Except for the decay time (green line in figure 6.15), 99.50 % of all TES-carriers could be rejected with loosing $\lesssim 10$ % of the absorber pulses. If a better TES-carrier cut efficiency is required typically also more signal pulses are removed. By far the best overall performance is achieved by the RMS-ratio parameter (dark blue line), where it is possible to remove 99.90 % of all TES-carrier pulses with only removing ~ 2.16 % of the absorber pulses. Interestingly, the decay time parameter shows a rather flat behavior with increasing values of ε_c and, thus, for $\varepsilon_c \gtrsim 99.95$ % it is the second best parameter to discriminate the two pulse classes.

However, as observed earlier in this section the discrimination power is dependent on the energy of the pulse and, thus, in figure 6.16 two efficiency plots for energies $\lesssim 3$ keV and $\gtrsim 3$ keV are depicted in (a) and in (b), respectively. As expected in case of low energies (a) all methods perform worse compared to the overall performance shown in figure 6.15. Again the RMS-ratio parameter shows by far the best capability to discriminate the two populations. Based on this parameter all simulated TES-carrier pulses could be removed ($\varepsilon_c = 1$) while simultaneously only ~ 10.8 % of the absorber pulses are dismissed. All parameters are well suited to discriminate both pulse classes at high energies. The shown lower limit in (b) starts at

99.90 % since all different parameters are able to separate both pulse classes for the simulated data set up to that point. The RMS ratio as well as the decay-time parameter are able to discriminate the two pulse classes perfectly up to a TES-carrier cut efficiency of one.

6.4 Multilayer Perceptron (MLP) Performance with Simulated Pulses

In this section the results of an ANN based pulse-shape analysis for simulated data sets of TUM40 are shown. The main idea of using an artificial neural network for this task is, that the combination of the different pulse parameters might disentangle both classes better than a single parameter. Assume the case of a pulse with a value for a certain discrimination parameter lying outside the main population but not well enough separated to be sufficient for a clear decision. If this is the case in several or even all discrimination parameters, it can imply that this pulse is rather a TES-carrier sample than an absorber pulse. The idea is, that the used MLPs are able to process this information and to decide more efficiently whether or not the suspicious pulse belongs to the TES-carrier class.

In this section first the architecture of the used MLPs is described and afterwards the actually used training algorithms are explained in detail. Finally, an example of a network applied to the simulated data set is shown and the idea of the combination of two or more neural networks to increase the performance is explained.

6.4.1 MLP Structure

Before the performance of the MLP can be studied in detail the network has to be constructed. As explained earlier in section 4.1 OxRop is based in the ROOT framework [120] and, thus, the multilayer perceptron class of ROOT could be used. Additionally, since the TMVA package (Toolkit for Multivariate Data Analysis) [137] is included in ROOT, its implementations of neural networks are also available. Both implementations were tested during the present work as well as in an accompanying master thesis [138]. TMVA features a better training utility and shows an enhanced performance during training compared to the standard ROOT implementation. Since it is also possible to train the ROOT class with TMVA, this framework is always used to train the neural networks constructed in the present work.

The following eight OxRop parameters are used as inputs of the MLP:

- Rise time 10–70 % [ms]
- Decay time [ms]
- Amplitude of fit with the absorber template (A_{Absorber} [V])
- RMS of fit with the absorber template (RMS_{Absorber} [V])
- Amplitude of fit with the TES-carrier template ($A_{\text{TES-carrier}}$ [V])
- RMS of fit with the TES-carrier template ($RMS_{\text{TES-carrier}}$ [V])

- Amplitude ratio
- RMS ratio

The architecture of the MLPs is a three-layer network with two hidden layers consisting of eight and seven neurons respectively and a single neuron in the output layer. Thus, in total 143 weight parameters (127 synapses and 16 biases) have to be adjusted during training.

6.4.2 Training of the MLP

For all detectors a simulated data set with TES-carrier and absorber pulses is created and used to train the respective networks. The target value of the ANN for absorber pulses is set to one, while for TES-carrier pulses it is set to zero.

Usually the first step of the training is to reset all weights in the network to random values. The input values of the neural network have to be normalized, i.e. the output value x_i of the input neuron i is given by:

$$x_i = \frac{p_i - \mu_i}{R_i}, \tag{6.24}$$

where p_i is the parameter value, μ_i and R_i are the corresponding mean and root mean square deviation of this parameter[33]. The normalization constants μ_i and R_i for each input parameter are determined during training of the network. For reasons of numerical stability this is especially important if the numerical values of the inputs are different by several orders of magnitude.

Unfortunately, no automatic early stopping algorithm is included in the used framework and, thus, in the present work the maximum number of training epochs has to be limited manually. Therefore, the available combined artificial data set including absorber and TES-carrier pulses is split into two not necessarily equally sized sets, namely the ANN-training set and the test set. While the ANN-training set is actually used for the training of the ANN the purpose of the test set is to check the total error and recognize when overtraining occurs (see figure 6.5). Firstly, the neural networks are trained without limiting the maximum number of epochs and the epoch when the error of the test set increases is determined. In the next step, training with a limited number of epochs set to the previously determined value is started and the errors of both sets are determined. If there is a clear hint for overtraining, the last step is iterated otherwise training is finished and the performance of this network is compared with other ones.

In ROOT a variety of different training algorithms exists, but all have in common that they adopt the weightings in a predictable way in order to minimize the total error, i.e. for classification to reduce the number of wrongly recognized pulses. The general concept of training and error backpropagation is discussed earlier in section 6.1 and, thus, here only the actually used algorithms are listed and briefly explained.

Two training algorithms were ultimately used for the training of all MLPs and were selected after showing (subjectively) the best overall performance during testing of all available algorithm. A more objective and detailed analysis of the influence of the training algorithm

[33] Not to be confused with the RMS parameter obtained in the template fit.

especially on the achievable separation power is performed in an accompanying master thesis [138]. Both analyses conclude on the best performing algorithms, namely *stochastic minimization* and the *BFGS method*.

Typically the training methods are based on multidimensional minimization algorithm, since training of a network is equivalent to root finding of a non-computational function. The total error of the network corresponds to the function to minimize, while the different weightings describing the performance of the network are its adjustable parameters. However, the algorithm has to be able to deal with the situation where only noisy observations of the data points are available.

The first training algorithm (stochastic minimization) used in the present work is related to the *gradient descent* method (see section 6.1). It is an application of a stochastic approximation method based on the Robbins-Monro-Algorithm [139]. During the minimization the weights are updated directly after each sample (on-line learning) according to the following rule:

$$w_{ji}(t+1) = w_{ji}(t) + \Delta w_{ji}(t), \tag{6.25}$$

$$\text{with} \quad \Delta w_{ji}(t) = -\eta \cdot \left(\frac{\partial E_n}{\partial w_{ji}} + \delta \right) + \varepsilon \cdot \Delta w_{ji}(t-1). \tag{6.26}$$

The parameters are the learning rate η, a constant drift δ and a momentum value ε. They can be set by the user, whereby in the present work for all three parameters the default values of ROOT are used, i.e. $\eta = 0.1$, $\delta = \varepsilon = 0$. In general it is also possible to reduce η after each training epoch, i.e. a full cycle of all training events, but this batch-training option is not used in the present work. That case would correspond to the gradient descent method explained already in section 6.1 which turned out to be a poor algorithm in practice [135, 138]. With the update formula the steps are calculated using the gradient of the total error and ultimately the algorithm should converge towards the optimum.

The second training method is based on the Broyden-Fletcher-Goldfarb-Shanno (BFGS) algorithm [140], the most popular quasi newton method designed to solve nonlinear optimizations problems iteratively [141]. A detailed description including derivation and properties studies can e.g. be found in [141]. This method has the property that the error function always decreases at each iteration unless a (global or local) minimum is reached [135]. Theoretically convergence is not guaranteed for the BFGS algorithm; however, in practical problems this method has shown its superlinear convergence, i.e. a fast convergence towards the optimum [141].

In the ROOT implementation the search direction is reset to the one of the steepest descent gradient after a settable number of epochs. Also another parameter τ (used in the line search algorithm as a step size parameter) can be set by the user. Again the default values of ROOT are used leading to a reset of the search direction after 50 epochs and a value of $\tau = 3$.

6.4.3 Application to Simulated Data

For both previously explained training algorithms (stochastic minimization and BFGS method) separate MLPs are trained. Thereby, different data sets are used for the training. While

the network trained with the stochastic minimization algorithm is trained with samples of the energy range from the lowest energies up to $\sim 12\,\mathrm{keV}$, the data used to train a network with the BFGS method are restricted to the most problematic region below $\sim 3\,\mathrm{keV}$. However, in both cases the data set after application of the RMS cut is used and, thus, in case of the stochastic minimization method still no TES-carrier pulse is available for energies $\gtrsim 3\,\mathrm{keV}$. During training the described measures to avoid overtraining are applied leading to 150 and 250 training epochs, respectively[34]. The resulting MLPs are applied to the complete simulated data set (including training and test data set) to get a first glance on the performance of both methods.

In figure 6.17 the energy dependent output of a MLP trained with the stochastic minimization algorithm is depicted. In both plots absorber pulses (color scale) as well as TES-carrier pulses (gray scale) are shown. In figure 6.17a the complete simulated energy range is included. As expected the main population of the absorber pulses is located around one, while TES-carrier pulses are expected around zero. For low energies ($\lesssim 7\,\mathrm{keV}$) this corresponds to the observed mean output value, while at higher energies a slightly larger mean value (~ 0.1) is obtained. This is due to the fact that in this energy range no TES-carrier pulse is available for the training of the network and is discussed in more detail in the next section. Nonetheless, a clear separation between both pulse classes down to $\lesssim 1\,\mathrm{keV}$ with almost no outlier is achieved. However, for smaller energies pulses exist in both data sets, where the MLP yields lower/higher output values than expected for the respective pulse class. In most cases this might be caused by the imperfect separation probability of the MLP at low energies. Due to the usage of measured empty baselines a second scenario is possible. In some cases it might happen, that the empty baseline is spoiled by a pulse with a pulse height in the order of the respective baseline fluctuation[35]. If the spoiling pulse is of the same pulse class as the superimposed template or if the height of the superimposed template dominates, the pulse shape of the resulting pulse is well defined and correctly assigned. However, if the pulse classes differ and, simultaneously, a pulse with small pulse height is created this results in a mixed pulse shape. This might lead to problematic samples for the network training, since the resulting pulse is flagged by one specific class but also exhibits typical features of the other class. For a specific baseline it can not be judged which of the two scenarios is true and, thus, it has to be assumed that the pulse class assignment is performed perfectly.

In figure 6.17b a zoom into the expected output region for absorber pulses with energy values $\lesssim 3\,\mathrm{keV}$ is depicted. As can be seen, the majority of the absorber pulses exhibits a MLP output value of ~ 1 and, thus, these pulses are assigned to the correct class. However, also a few TES-carrier pulses result in an output value in the drawn parameter range and have to be rejected. Therefore, the shown performance of the MLP trained with stochastic minimization does not allow to completely remove the TES-carrier pulses without simultaneously loosing a significant amount of absorber pulses.

In figure 6.18 the energy dependent output of a MLP trained with the BFGS method is

[34] For TUM40 the network trained with the BFGS method and finally applied to the blind data set is supplied by [138].

[35] As mentioned above, different selection criteria are applied to remove pulses which are mistakenly tagged as empty baselines by the DAQ. However, for pulses with low pulse heights such an identification is hardly possible.

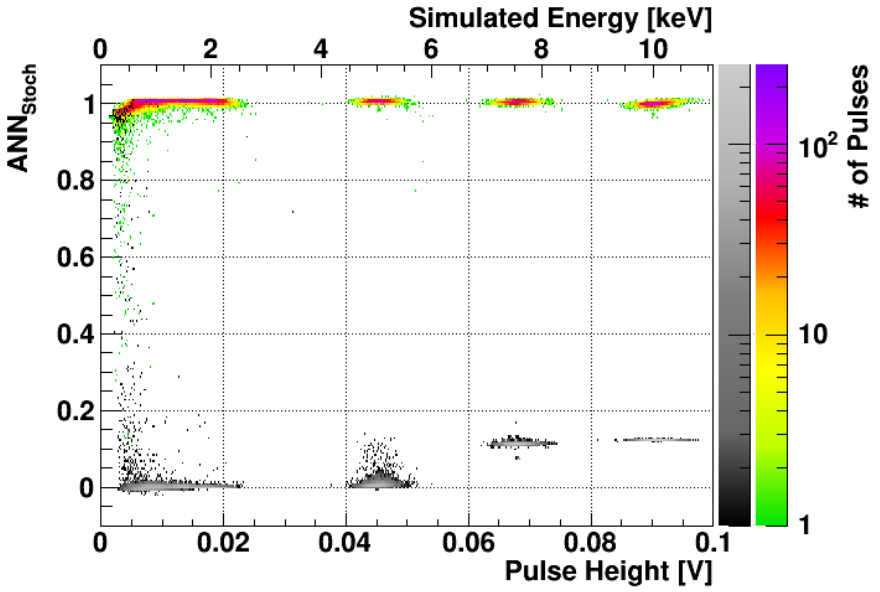

(a) Full MLP-output range

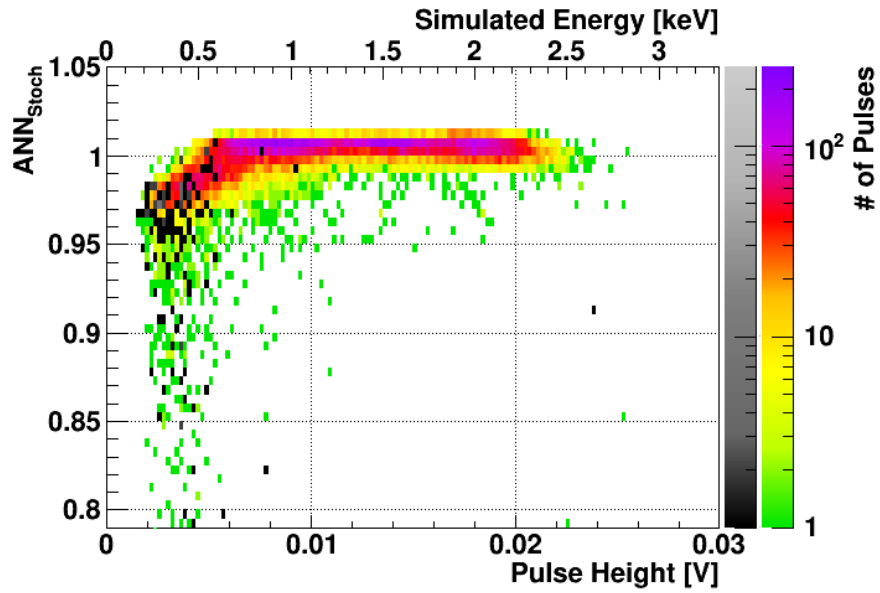

(b) Zoom into the output region expected for low-energetic absorber pulses ($\lesssim 3$ keV).

Figure 6.17: *Energy dependent output of a MLP trained with the stochastic minimization training algorithm. The full output-value and energy range is depicted in (a), where the target value of all simulated absorber pulses (color scale) is set to one, while it is zero for TES-carrier pulses (gray scale). The majority of the pulses is correctly assigned to the respective pulse class and almost no outliers are observed. In this simulation, output values between both main populations are observed only for low energies ($\lesssim 1$ keV). In (b) a zoom into the low energetic output region for absorber pulses is shown. While the majority of all TES-carrier pulses, which are visible in this zoom-in, is located slightly below the main population of absorber pulses, the distance is rather small. Thus, even for the MLP a few pulses are indeed indistinguishable.*

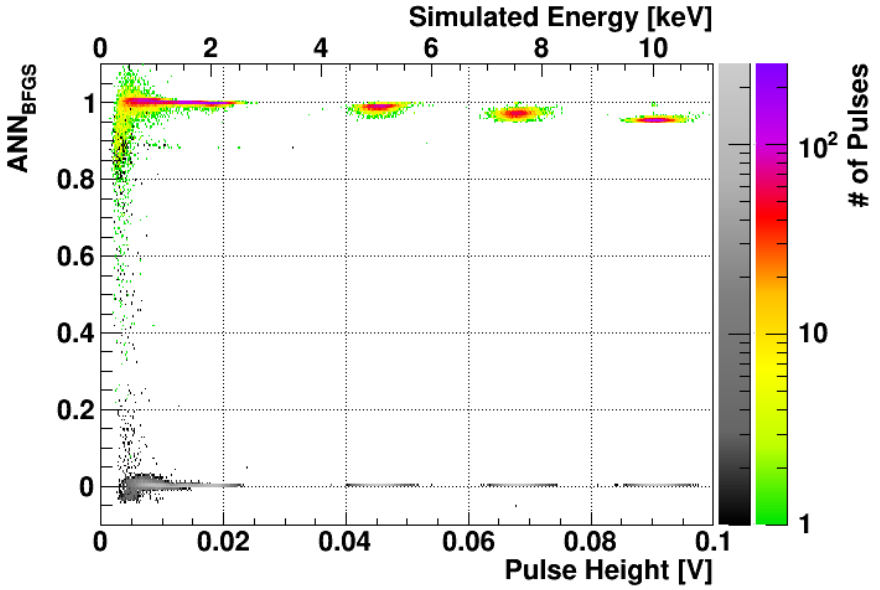

(a) Full MLP-output range

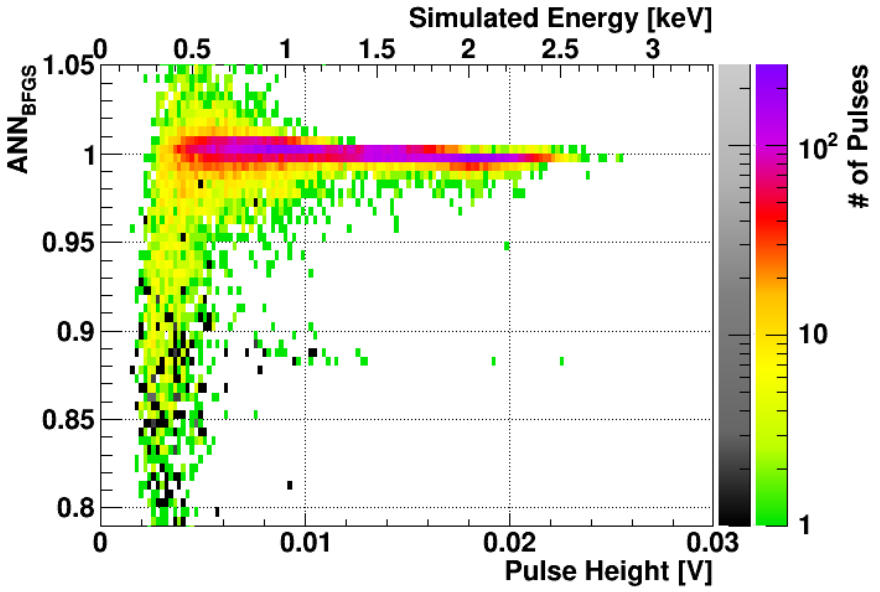

(b) Zoom into the output region expected for low-energetic absorber pulses ($\lesssim 3$ keV).

Figure 6.18: *Energy dependent output of a MLP trained with the BFGS training algorithm. The target value of all simulated absorber pulses (color scale) is set to one, while it is zero for TES-carrier pulses (gray scale). While (a) shows the full energy and output-value range, in (b) a zoom into the low energetic output region expected for absorber pulses is depicted. The majority of all TES-carrier pulses in the vicinity of the output region of absorber pulses are separated well enough. Thus, compared to the MLP depicted in figure 6.17 a better separation is achieved.*

depicted. As explained above, for the training of this neural network the data are limited to the energy region below $\lesssim 3\,\mathrm{keV}$. However, in figure 6.18a the output values for all pulses of the absorber data set (color scale) and the TES-carrier set (gray scale) are still depicted for energies up to $\sim 12\,\mathrm{keV}$. The output of the resulting network seems to have no significant difference for TES-carrier pulses with higher energies compared to the output in the training range. However, for absorber pulses a slight decrease of the mean output value is observed; but due to the high separation between both populations this has no significant impact on the discrimination power. Compared to the performance of the first MLP, this one shows clearly a better separation. This is in particular observable in figure 6.18b where a zoom into the parameter region below $\lesssim 3\,\mathrm{keV}$ and above an output value of ~ 0.8 is depicted. The majority of the visible TES-carrier pulses are located around an output value of ~ 0.9. Only a few TES-carrier pulses exhibit higher values directly approaching the main region of the absorber pulses and, thus, an efficient discrimination without loosing a huge fraction of absorber pulses is possible in this simulation.

6.4.4 Validation Data Set

As mentioned before, the data set used for the training of the MLPs is included in the complete simulated data set and, thus, here no plots of the discrimination power obtained in the training data set are produced. The achieved performance there might not be general but very specific due to this fact. However, there is another simulated data set available to perform this task, which has not been used up to now[36]. Therefore, the efficiency obtained in this distinct *validation data set* is discussed in the following.

After cuts this new data set contains 35 717 empty baselines, which are superimposed with the respective templates. As for the simulated data set used for the training of the network, in total 10 different energy values are simulated and for each baseline the actual energy is chosen randomly in a second step. In this simulation the same cuts as before are applied whereby also the RMS cut is performed. In the most interesting energy region ($\lesssim 3\,\mathrm{keV}$) 16 911 absorber and 11 929 TES-carrier pulses survive the cut.

In figure 6.19 and figure 6.20 the output plots for the MLP trained with the stochastic minimization algorithm and the MLP trained with the BFGS method are depicted, respectively. Thereby, only the most interesting energy region $\lesssim 3\,\mathrm{keV}$ is shown for simulated absorber (color scale) as well as TES-carrier (gray scale) pulses. In the validation data set very similar results are obtained compared to the ANN-training set and a good separation between both pulse classes is achieved. However, due to some outliers of the TES-carrier population neither the MLP trained with the stochastic minimization algorithm nor the MLP trained with the BFGS method are able to perfectly disentangle both populations with a simple one-dimensional cut without loosing a significant fraction of the absorber population.

Based on the data of this validation data set, discrimination curves are obtained for all different available parameters as depicted in figure 6.21. Again only pulses in the low energetic part ($\lesssim 3\,\mathrm{keV}$) are considered and, thus, this plot has to be compared with the one shown in

[36] For this task empty baselines of TUM40 are extracted from data files, which are part of the respective blind data set, without violating the blinding scheme. These baselines are used for the artificial pulse simulation.

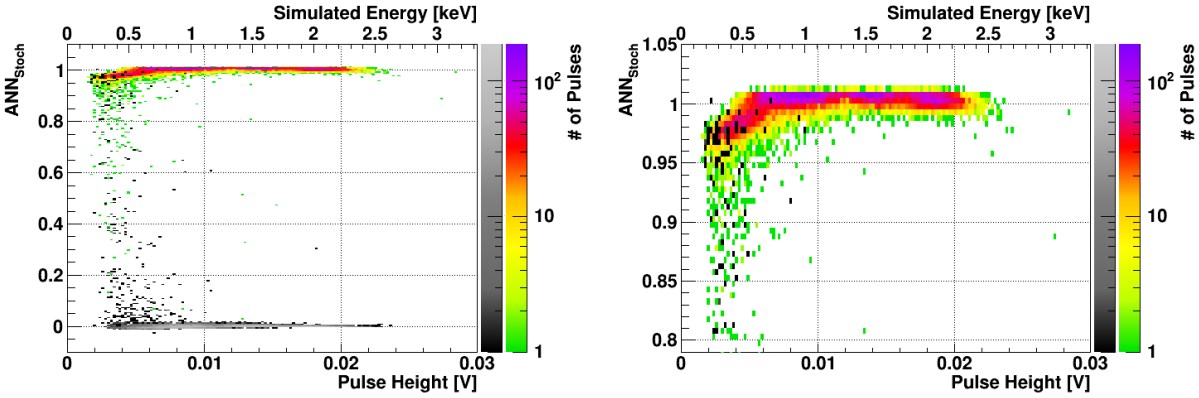

(a) Full MLP-output range *(b) Output region expected for absorber pulses*

Figure 6.19: *Network output of the MLP trained with the stochastic minimization algorithm for simulated absorber (color scale) as well as TES-carrier (gray scale) pulses of the validation data set. Compared to the plots obtained from the ANN-training set (see figure 6.17) no significant difference is observed. A good separation between both populations is achieved, whereby several outliers of the TES-carrier populations are close to the main absorber populations at the lowest energies.*

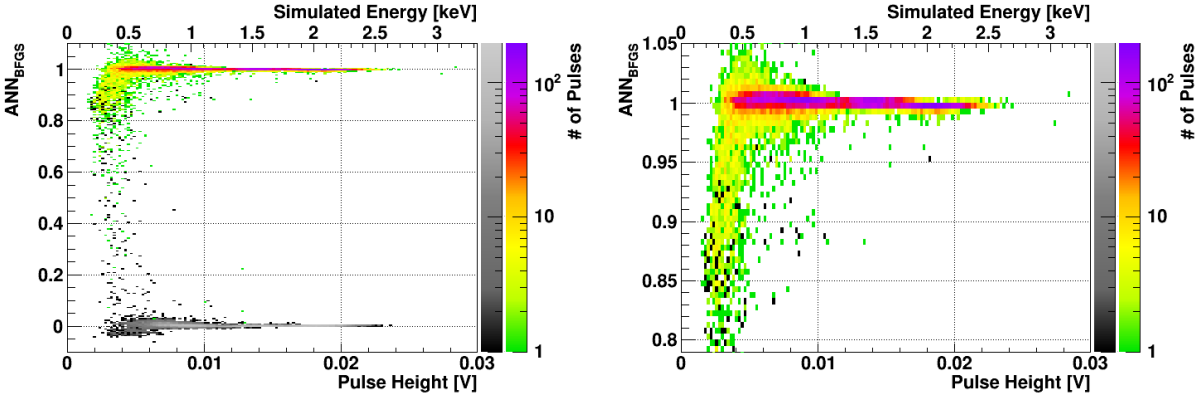

(a) Full MLP-output range *(b) Output region expected for absorber pulses*

Figure 6.20: *Network output of the MLP trained with the BFGS method for simulated absorber (color scale) as well as TES-carrier (gray scale) pulses of the validation data set. Also for this network no notable deviation between both simulated data sets, i.e. ANN-training and validation set, is observable. A good separation between both populations is achieved, whereby a single outlier of the TES-carrier population hinders the perfect discrimination of the two classes without losing a significant amount of absorber pulses.*

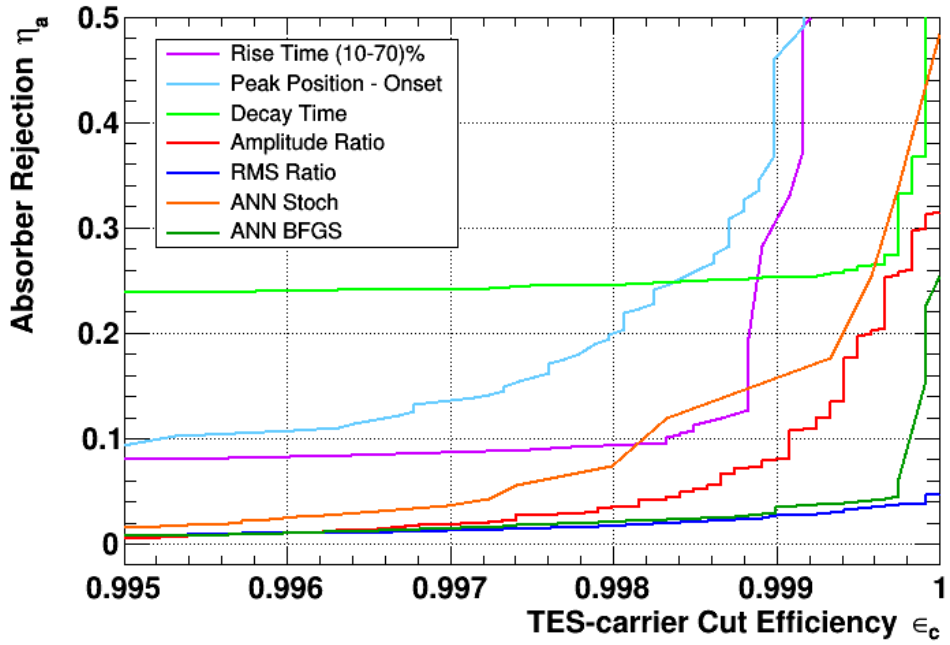

Figure 6.21: *Discrimination curves of all available parameters obtained in the validation set for all pulses with energies $\lesssim 3$ keV. The more a curve approaches the lower right corner, the better is the discrimination achieved with this parameter: A high amount of TES-carrier pulses is rejected (large ε_c) and, simultaneously, the unwanted rejection η_a of absorber pulses is minimized. In the shown case, the RMS-ratio parameter (dark-blue curve) performs best, while the MLP trained with the BFGS method (dark-green curve) follows closely. Despite the fact that it is not only trained for this low energetic region, the MLP trained with the stochastic minimization (orange curve) achieves still a good performance.*

figure 6.16a. Also in the validation set the majority of the parameters results in an exceptionally good performance, whereby the two neural networks (orange and dark-green curves), the amplitude-ratio parameter (red curve) and the RMS-ratio parameter (dark-blue curve) achieve the best results. Of these four parameters, the MLP trained with the stochastic minimization algorithm shows the worst performance but this can be expected as the training of this network was not concentrated only on this low energetic region. For most of the pulses the MLP trained with the BFGS method and the RMS-ratio parameter are equivalent, but for the highest TES-carrier cut efficiencies ε_c the RMS-ratio parameter shows a better performance. Thus, for the latter, an almost perfect separation between both pulse classes ($\varepsilon_c \approx 1$) is achieved in the validation data set with loosing only $\sim 4.8\,\%$ of the absorber pulses. To remove indeed all simulated TES-carrier pulses a slightly higher cut limit is required and, thereby, a fraction of $\sim 8.0\,\%$ of all absorber pulses is rejected.

6.5 Application of MLPs to Training Set Data

After having shown good performances for the simulated data sets the neural networks are applied to real data mainly to check if the output is comparable with the simulation. All cuts which are listed in section 5.3.11 after the pulse-shape cut are not applied while all other selection criteria are performed. Thus, the two RMS-cuts for both the phonon and the light detector, the energy cut and the two coincidence cuts are not performed.

For the MLP trained with the stochastic minimization algorithm the respective output for all pulses of the training data set is depicted in figure 6.22. In this plot a lot of pulses with low MLP-output values are observed, leading to the conclusion, that in TUM40 a large number of TES-carrier pulses is observed. This fact is discussed in more detail in section 9.2.2.

As already observed in the simulation (see figure 6.17) also in the measurement the output value for TES-carrier pulses slightly increases starting at pulse heights of $\sim 0.05\,\mathrm{V}$. However, with increasing pulse heights the number density of TES-carrier pulses clearly decreases and, thus, as expected the majority of TES-carrier pulses exhibits a low pulse height $\lesssim 0.04\,\mathrm{V}$. Furthermore, this increase of the output value does not have a significant influence on the final result since the separation between both pulse classes is still very pronounced.

Nonetheless, in a dedicated study the origin for this slight increase of the MLP-output value is investigated. As mentioned above both RMS values of the two fits with the respective template are input parameters for the neural network. In figure 6.23 the RMS distribution of all pulses (black dots) with a pulse height lower than $0.1\,\mathrm{V}$ is depicted as a function of the respective pulse height. Thereby, the RMS value yielded by the fit with the absorber template is shown. Highlighted in red are all pulses where the MLP trained with the stochastic minimization algorithm yields an output value lower than 0.25. Thus, these pulses are most probably of TES-carrier type. While the distribution for absorber and TES-carrier pulses clearly overlaps at low pulse heights, the RMS parameter alone is already able to distinguish both pulse classes for pulses that are large enough ($\gtrsim 0.03\,\mathrm{V}$). Therefore, in the simulation these pulses are already removed by the applied RMS cut before training and, thus, this feature of an increasing parameter value is totally unknown to the network. For each input parameter the mean μ and rms deviation R of the discrimination parameter are determined based on the data of the ANN-training set and the network inputs are normalized (see equation 6.24).

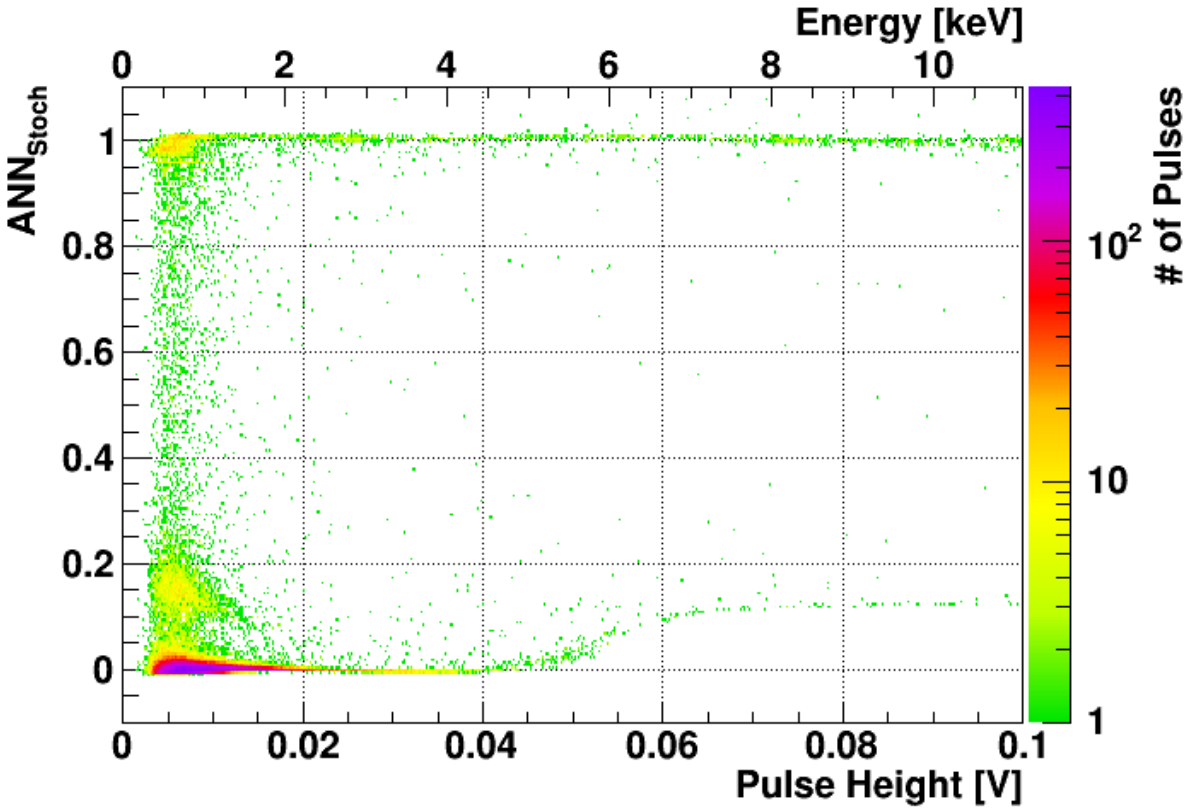

Figure 6.22: *Energy dependent output of the MLP trained with the stochastic minimization algorithm for all pulses of the TUM40 training data set. In general there is good agreement between simulation (see figure 6.17) and the data set of measurement shown here. A large number of pulses is observed with low output values leading to the conclusion, that in the training set of TUM40 the majority of the pulses measured are of the TES-carrier type. The different features observed in this plot are explained in the main text.*

However, as in the simulated data set only TES-carrier pulses with pulse heights smaller than $\sim 0.03\,\mathrm{V}$ are available these two normalization parameters do not correspond to the actual mean and rms values of the measured data set. For pulses with larger pulse heights this leads to a systematic increase of the output of the respective input neuron, which results in the slight enhancement of the output value of this specific MLP. Therefore, for the future it might be more convenient to train the neural network either only with low energetic pulses as in the case of the BFGS training algorithm or to include also TES-carrier pulses with high pulse heights which are actually removed by another cut in the ANN-training set.

The most striking difference between simulation and measurement is the larger number of pulses with output values located between the two expected populations. In particular in the low energetic region ($\lesssim 2\,\mathrm{keV}$) at output values of $\mathrm{ANN_{Stoch}} \lesssim 0.25$ a population, not observed in the simulation, shows up.

As mentioned in section 6.4.1 also the two amplitudes of both template fits are inputs for the neural network. In figure 6.24a a scatter plot of the two amplitudes ($\mathrm{A_{Absorber}}$ vs. $\mathrm{A_{TES\text{-}carrier}}$) yielded by the fit with the respective template is depicted for all pulses in the relevant energy

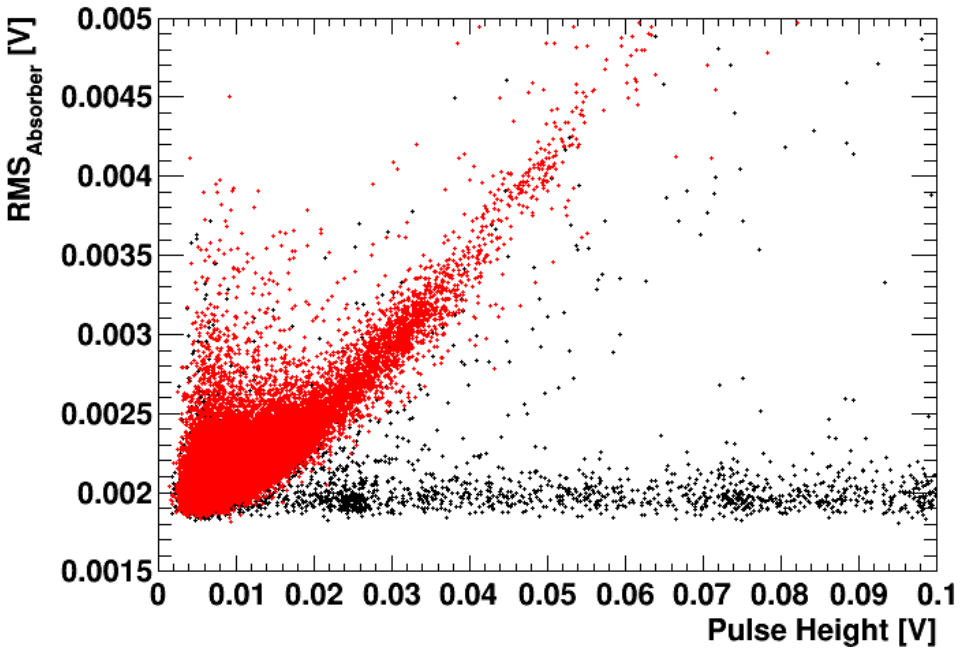

Figure 6.23: *RMS distribution as a function of the pulse height for all pulses of the training set, whereby the RMS value is obtained by the fit of the pulse with the absorber template. Highlighted in red are the pulses where the output value of the MLP trained with the stochastic minimization algorithm is below* 0.25*. Thus, most likely these pulses are of TES-carrier type. In the simulated data set used for the training of the MLP the observable increase of the RMS for pulses with large pulse heights (*$\gtrsim$ 0.03 V*) leads to a rejection of all TES-carrier pulses above the corresponding energy of* $\sim$ 3 keV *already by the RMS cut (see section 6.2). Thus, for the training of the network no TES-carrier pulses with a large pulse height are available. This ultimately explains the rise of the output value* ANN_{Stoch} *for TES-carrier pulses observed in the simulation (see figure 6.17) as well as in the measurement (see figure 6.22). For more details see text.*

region. As can be seen in this plot, there are different populations: Firstly, the population marked in red, where a negative amplitude $A_{Absorber}$ is obtained in the fit with the absorber template and, simultaneously, the amplitude $A_{TES\text{-}carrier}$ yielded by the fit with the TES-carrier template is positive. Secondly, marked in green are the pulses which exhibit a parameter value in $A_{TES\text{-}carrier}$ that is lower than that of the majority of the pulses and, thus, are separated from the black population. Finally, the remaining pulses (marked in black) are located mainly in two linear bands, which overlap in the low-amplitude region. TES-carrier pulses are found mainly in the band with a larger slope while absorber pulses are in the band with the lower gradient.

These populations are visible in different regions in figure 6.24b, where the output value of the MLP trained with the stochastic minimization algorithm is depicted. Thereby, the considered pulses are highlighted by the same color as in (a). Thus, the particular population (red) observed at output values slightly above the TES-carrier main population is caused by pulses, where the amplitude $A_{Absorber}$ yielded by the fit with the absorber template is negative,

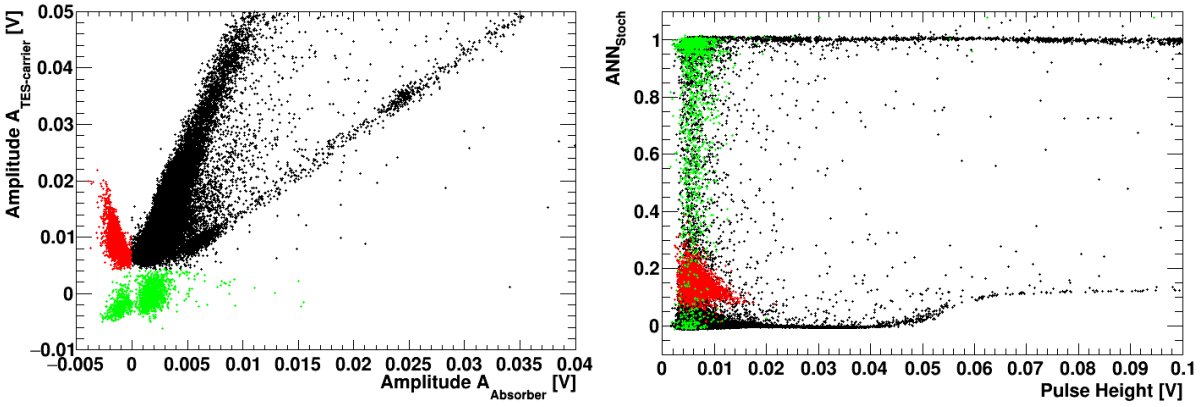

(a) *Amplitude scatter plot* ***(b)*** *Pulse height dependent MLP output*

Figure 6.24: *In (a) a scatter plot of the two amplitudes $A_{Absorber}$ and $A_{TES\text{-}carrier}$ obtained by the fits with the two templates is depicted for all the pulses of the training set of TUM40 in the relevant energy region. The amplitude obtained by the fit with the absorber template ($A_{Absorber}$) is depicted on the x-axis, while the y-axis shows the amplitude yielded by the fit with the TES-carrier template ($A_{TES\text{-}carrier}$). The output of the MLP trained with the stochastic minimization algorithm is shown in (b). In both plots different populations of pulses are highlighted by the same color. The red population slightly above the main population for TES-carrier pulses in (b), which is only observed in the measurement but not in the simulated data sets, consists of pulses which have a negative amplitude value yielded by the fit with the absorber template whereas simultaneously a positive value for $A_{TES\text{-}carrier}$ is obtained by the fit. For more details see text.*

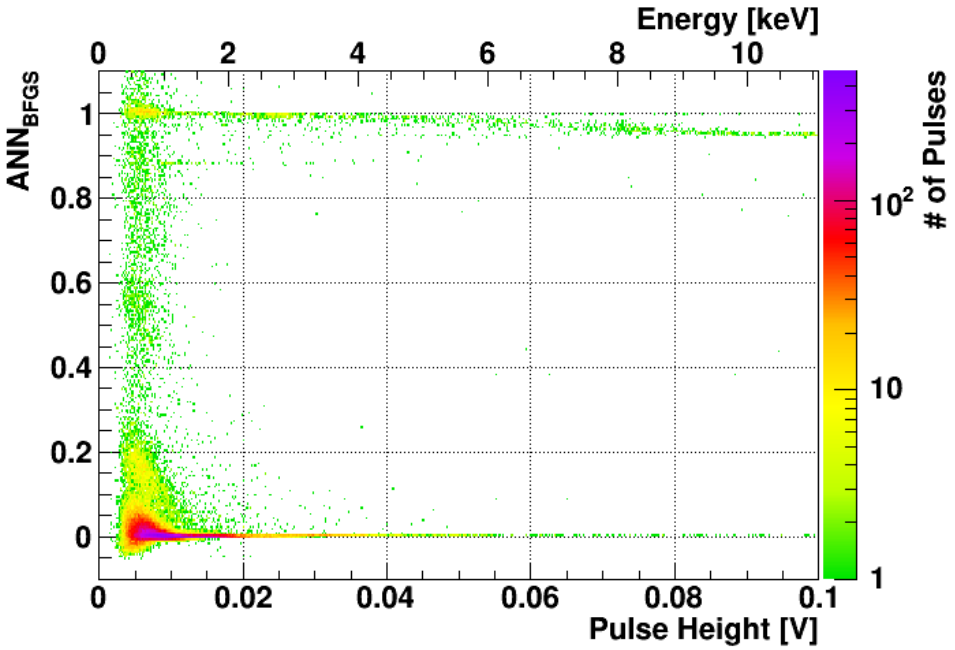

Figure 6.25: *Energy dependent output of the MLP trained with the BFGS method for all pulses of the TUM40 training data set. Also for this network there is good agreement between the measurement depicted here and the simulation shown in figure 6.18a. For example the slight decrease of the output value ANN_{BFGS} for absorber pulses with pulse heights larger than 0.06 V is predicted by the simulation. It is caused by the fact, that for the training only low-energetic pulses ($\lesssim$ 3 keV corresponding to $\lesssim$ 0.03 V) are used for the training of this network.*

while the fit with the TES-carrier template results in a positive value. Since, these pulses are assigned to negative energies in the energy calibration they are removed by the energy cut applied later anyway.

As the pulses marked in green in figure 6.24 are only separated in the amplitude obtained from the fit with the TES-carrier template it is per se not clear whether or not they have to be removed. Also in the MLP-output plot these pulses do not form a special population since they are located in the complete parameter range. Thus, most likely TES-carrier pulses as well as absorber pulses are part of this group and no special treatment is performed to remove them.

In figure 6.25 the output value of the MLP trained with the BFGS method is depicted as a function of the pulse height. Also in this case the pulses with a negative amplitude ratio are observed slightly above ($ANN_{BFGS} \sim 0.2$) the main population of the TES-carrier pulses centered around zero. As for the simulation (see figure 6.18) also for the measured data set a slight decrease of the network output for absorber pulses with large pulse heights ($\gtrsim 0.06$ V) is observed. This effect is most probably due to the fact that this network is only trained with smaller pulses.

In the result of both networks, there is a visible fraction of pulses with output values between the two main populations of clear absorber or TES-carrier pulses. These are most likely pulses, where it is hard to decide whether or not they are TES-carrier pulses due to their small signal heights. However, in case of a MLP where the target value of an absorber pulse is set to

one during training, the output of this network can be interpreted as a parameter, which is proportional to the probability of being an absorber pulse. Thus, the higher the output value the more likely it is, that the respective pulse contains an absorber pulse while for a lower value it is more likely a TES-carrier pulse. Thus, by selecting very strictly only pulses close to one the probability of missing a TES-carrier pulse should be small. However, this comes with the cost of loosing a certain amount of absorber pulses.

Neither a cut on the output value of the MLP trained with the BFGS method nor a cut on the output value of the MLP trained with the stochastic minimization algorithm is able to remove all TES-carrier pulses in the measured data set. Thus, in the next section a combination of both MLPs is used to achieve this goal.

6.6 Combination of MLPs

The main idea for the combination of MLPs is that despite the neural networks are trained with the same data sets the actual weighting of the eight input parameters is different for all trained instances. Thereby, the fact is used that the expected signal shape is well described by the template of absorber pulses for all relevant energy values. Thus, both neural networks trained in the present work know very well how an absorber pulse looks like but might result in slightly different output values for all other types of pulses.

6.6.1 Simulated Data Set

In figure 6.26 a scatter plot of the two MLP output values for the simulated absorber (color scale) as well as the TES-carrier (gray scale) data sets are depicted. The output of the MLP trained with the stochastic minimization algorithm ($\mathrm{ANN_{Stoch}}$) is shown on the x-axis, while the output of the MLP trained with the BFGS method ($\mathrm{ANN_{BFGS}}$) is given on the y-axis. For the majority of all pulses the MLP outputs are similar resulting in a linear correlation between both parameters. However, in particular in the region of large output values (both output values $\gtrsim 0.8$) exploitable differences between both networks are obtained.

Therefore, a two-step cut is performed, whereby the cut limits are chosen solely based on the parameter values observed in the simulation as depicted in figure 6.27. First (figure (a)) a cut on the output value of the MLP trained with the stochastic minimization algorithm is performed such that not too many absorber pulses are removed. A constant cut limit (red dashed line) is defined right below the absorber populations at higher pulse heights (~ 0.03 V – 0.08 V) and also applied to lower pulse heights. As the mean output value for absorber pulses slightly decreases with increasing pulse heights, for pulses with a pulse height $\gtrsim 0.08$ V a marginally lower cut value is used. This should be completely unproblematic, since in this region the two populations are clearly separated and no large number of outliers nearby is observed in the simulation. For pulses with a pulse height ≥ 0.1 V it is assumed that the performance of the RMS-ratio parameter is good enough to discriminate both pulse classes. The output value of the MLP trained with the BFGS method for the surviving pulses is depicted in (b). In the next step a cut on this parameter (horizontal red-dashed line) is performed, whereby the cut limit is chosen such that all remaining TES-carrier pulses are rejected (red

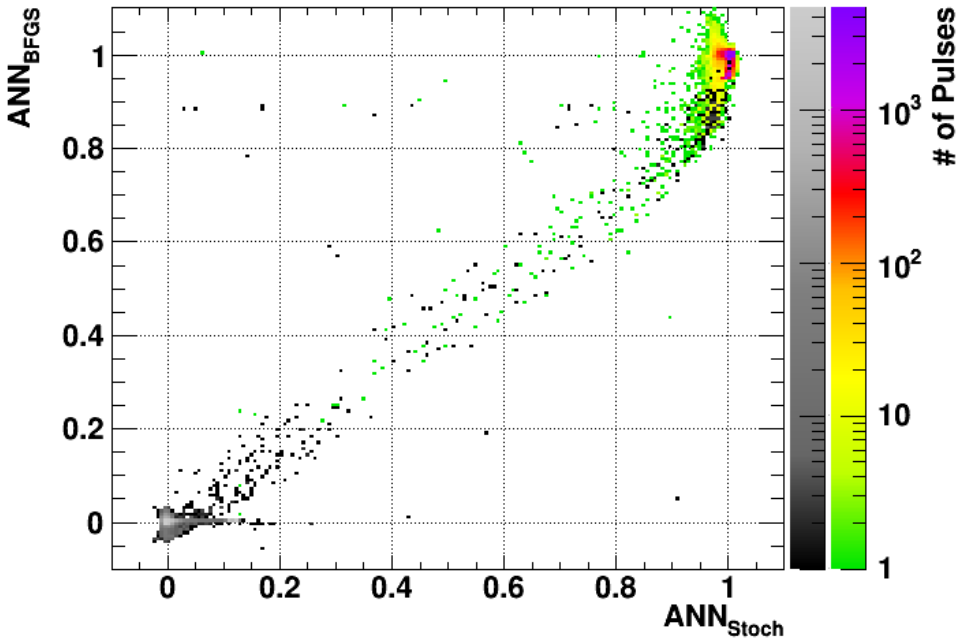

Figure 6.26: *Scatter plot of the two ANN output values. The x-axis shows the output of the network trained with the stochastic minimization algorithm (ANN_{Stoch}) and the y-axis the output of the network trained by the BFGS method (ANN_{BFGS}). For the majority of all pulses both networks result in similar output values and, thus, for these pulses a linear correlation is observed. However, in particular in the region where absorber pulses are expected (both ANN values larger than ~ 0.8) exploitable differences in both output values are obtained. By a successive application of cuts on both network outputs it is possible to remove all TES-carrier pulses in the simulation.*

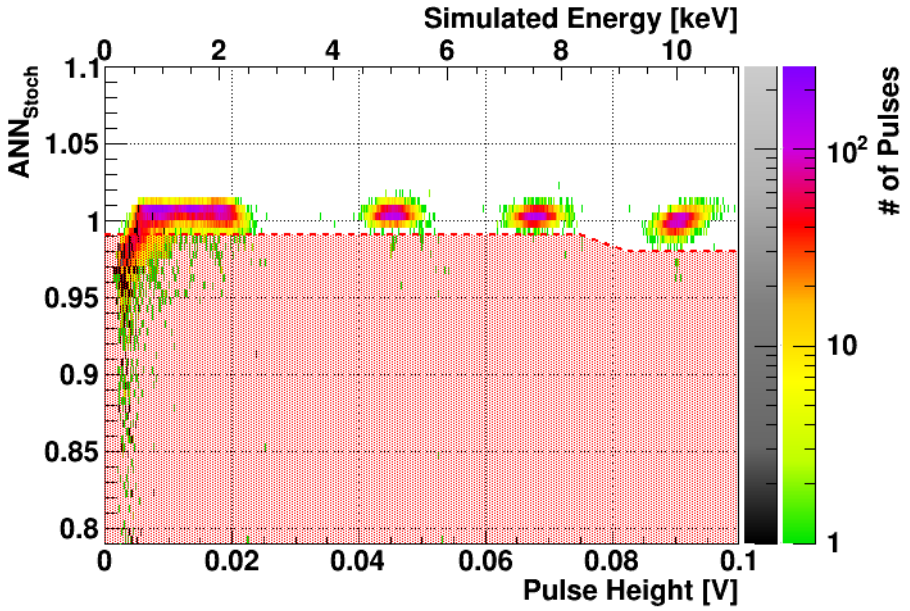

(a) MLP trained with the stochastic minimization algorithm

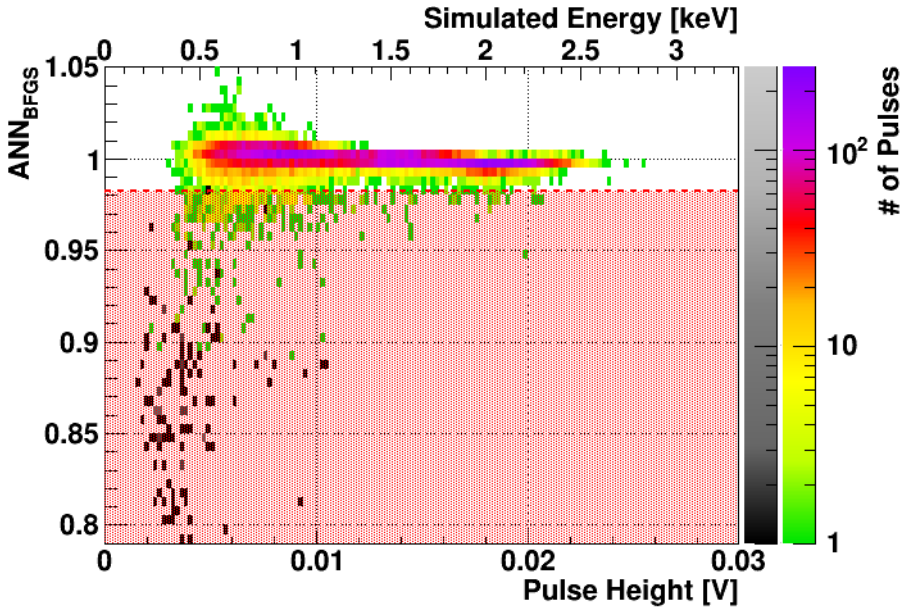

(b) MLP trained with the BFGS method

Figure 6.27: *Illustrative description of the determination method for the cut limit. The cut limits in the combined cut are set by a two-step approach. First, in (a) the cut value used for the output of the MLP trained with the stochastic minimization algorithm is set in such a way that not too many absorber pulses are removed (dashed-red line). All pulses with a pulse height ≤ 0.1 V featuring a lower output value than the cut limit are removed (red shaded area). For the resulting pulses, as depicted in (b), the cut limit on the output value of the MLP trained with the BFGS method is set such that in the simulation all TES-carrier pulses are rejected. Thereby, a small safety margin (smaller than the shown bin width) is applied, such that a small upward fluctuation of the output value does not immediately result in a pulse surviving the cut.*

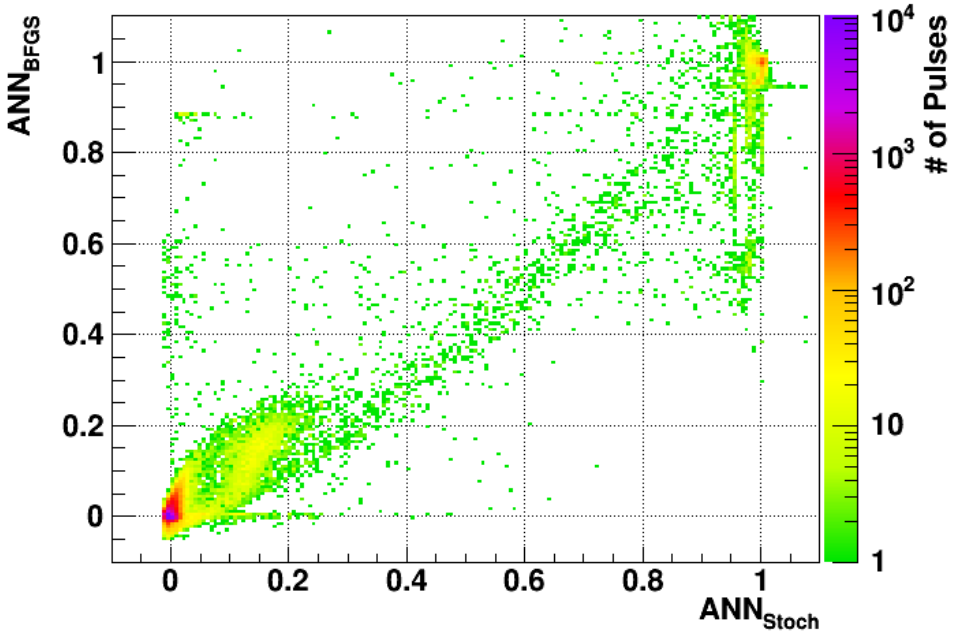

Figure 6.28: *Scatter plot of the two MLP output values for all pulses of the training set of TUM40, which have a pulse height smaller than* 0.1 *V. The x-axis shows the output value of the MLP trained with the stochastic minimization algorithm, while the y-axis depicts the output of the network trained with the BFGS method. The combination of the two MLP-output values allows to dismiss pulses which are only assigned to a certain pulse class by one of the two networks. Only when both networks agree that a certain pulse is of the absorber type it should survive the pulse-shape cut.*

shaded area). Thereby, a safety margin is used such that a small deviation to higher output values does not immediately lead to a TES-carrier pulse which survives this cut[37]. In the simulation, all the remaining TES-carrier pulses feature a pulse height well below ~ 0.03 V and, thus, the second cut is only applied for pulses with smaller pulse heights. When these two ANN-based cuts are applied to the simulated pulses of the independent validation data set a perfect removal of TES-carrier pulses is achieved within the given statistics. Thus, also an excellent performance for the real measured data set is expected.

6.6.2 Measured Data Set

In figure 6.28 the scatter plot of the two MLP output parameters is depicted for all pulses of the training set of TUM40, which have a pulse height smaller than 0.1 V. As it was already the case for the energy-dependent MLP-output plots, also the scatter plot of this measurement shows results similar to the simulation (see figure 6.26). For the majority of all pulses both networks result in comparable output values and, thus, confirm the fact that most of the pulses observed in the training set of TUM40 are of TES-carrier type.

[37] Due to the binning of the histogram this is not visible in figure 6.27b.

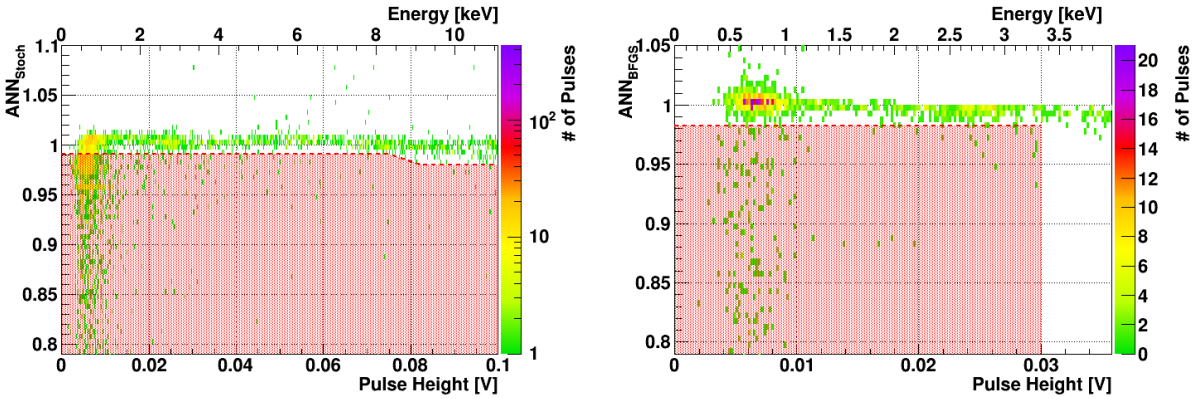

(a) MLP trained with the stochastic minimization algorithm

(b) MLP trained with the BFGS method

Figure 6.29: *Application of the ANN based cuts to the measured pulses with low pulse heights of the training set of TUM40. In (a) the output of the MLP trained with the stochastic minimization algorithm is depicted. Due to the good agreement between simulation and measurement, at least at higher pulse heights the majority of all pulses shown (which are most probably absorber pulses) survives the cut (red dashed line). The output of the MLP trained with the BFGS method for the surviving pulses is depicted in (b). Again the red dashed line shows the corresponding cut limit. As in the simulated data set, the cut is only applied to pulses with a pulse height* ≤ 0.03 *V.*

As intended by the combination of the network outputs it is possible to identify pulses wrongly assigned of a single network. For example, there are a few pulses located at high $\mathrm{ANN_{BFGS}}$ parameter values while simultaneously a low $\mathrm{ANN_{Stoch}}$ parameter value is obtained. Due to the different weighting of the input parameters for one network (here the MLP trained with the BFGS method) these pulses look similarly to absorber pulses while for the other one (here the MLP trained with the stochastic minimization algorithm) these pulses are clearly of TES-carrier type. In particular when both output values are large ($\gtrsim 0.8$) a larger spread of the output values is observed.

In figure 6.29 the application of the two ANN-based cuts to the measured low energetic pulses of the training set of TUM40 is depicted. While (a) shows the output value of the MLP trained with the stochastic minimization algorithm ($\mathrm{ANN_{Stoch}}$), the output value of the MLP trained with the BFGS method ($\mathrm{ANN_{BFGS}}$) is depicted in (b) for the surviving pulses. The red-dashed lines are the respective cut limits, whereby the first cut on $\mathrm{ANN_{Stoch}}$ is only applied to pulses with a pulse height ≤ 0.1 V. As in the simulation the cut on $\mathrm{ANN_{BFGS}}$ is only performed for even smaller pulses with a pulse height ≤ 0.03 V. As can be seen, the majority of potential absorber pulses survives the combination of both cuts on the respective MLP-output value. The resulting signal survival probability plots are discussed in the next section.

All low energetic pulses ($\lesssim 1$ keV) of TUM40, which are recorded in the training set and survive all cuts, are checked by eye if there are unrecognized TES-carrier pulses. In total 1 553 records are checked and thereby, only one record is found to contain a TES-carrier pulse. In figure 6.30 this record is depicted and it seems that first a TES-carrier pulse triggered the

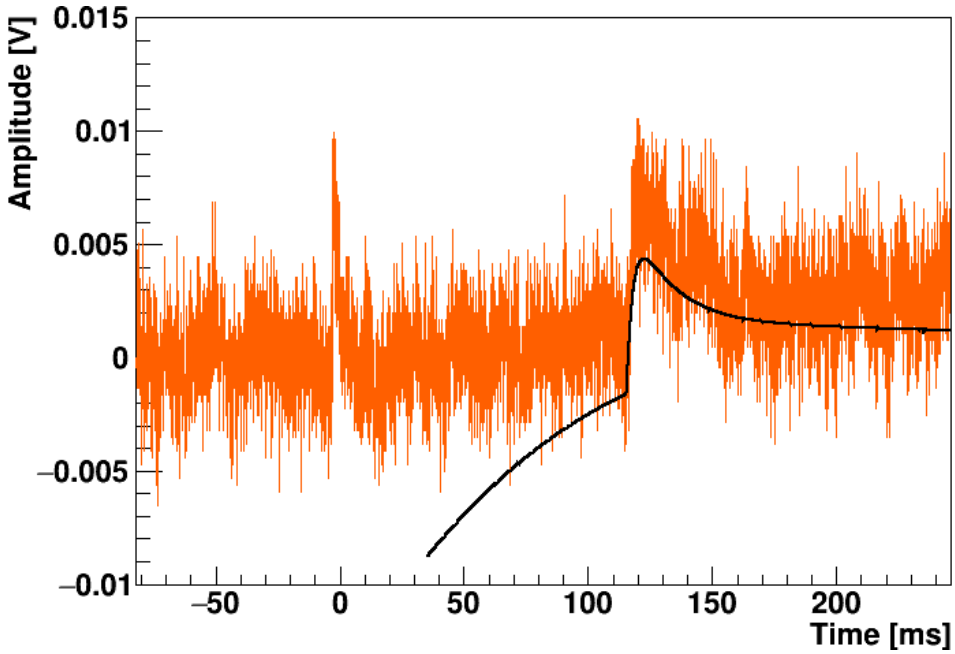

Figure 6.30: *Pile-up of a TES-carrier pulse (peak position $\sim$ 0 ms) and a low energetic absorber pulse (peak position $\sim$ 120 ms) observed in the training set of TUM40. Also shown as black solid line is the fit with the absorber template. This record was found manually while for all low energetic pulses ($\lesssim$ 1 keV) of TUM40 it was checked by eye, whether a TES-carrier pulse is visible. The TES-carrier pulse is contained in the record but it is completely ignored in the template fit and, thus, does not influence the energy reconstruction.*

readout (peak position $\sim$ 0 ms) and in the post trigger region a pile-up of an absorber pulse occurred (peak position $\sim$ 120 ms). The black line corresponds to the result of the fit with the absorber template. As the record survives the shift-difference cut also the TES-carrier template is fitted to this part of the record. Therefore, it is clear that this record survives all pulse-shape cuts, since both fits neglect all samples earlier than $\sim$ 30 ms, where the TES-carrier pulse occurred. Furthermore, as the absorber pulse is fitted in this record and is not disturbed by the TES-carrier pulse happening early it is valid that this pulse survives all cuts.

6.7 Pulse-Shape Cut

In the previous section the ANN based pulse shape cuts applied to low energetic pulses are explained in detail. However, also at higher pulse heights TES-carrier pulses have to be identified and rejected. In the present section different cuts are grouped together to form the *pulse-shape cut* sequence. The respective signal survival probabilities of the individual pulse-shape cuts are shown here based on the signal simulation explained in section 5.4. The aim of the pulse-shape cut is to remove ideally all TES-carrier pulses without removing more signal pulses than necessary to achieve this goal. The cut is designed to remove all simulated TES-carrier pulses without considering the absorber pulses in a first step.

6.7.1 Pulse-Shape Cuts and Related Cuts

In the present work, this aim could not be achieved by a single pulse-shape cut performing all the required steps at once. However, it is fulfilled when a sequence of cuts is applied to remove all pulses with different pulse shapes. Here this sequence is listed and explained in more detail.

Due to the exceptional good performance observed in the simulated data set (see section 6.3) the RMS-ratio parameter is used to easily and efficiently remove all pulses with deviating pulse-shapes at reconstructed energies $\gtrsim 10\,\mathrm{keV}$. The actual cut value is set based on the lowest parameter value observed in the simulated data set for an absorber pulse with low pulse height.

As explained in section 4.3.1 the shift parameter of the template fit describes the time shift in the record and is also stored for later use. To be well defined, the RMS-ratio parameter relies on the fact that the two template fits are fitted to the same "pulse" in the record and, thus, exhibit a comparable shift parameter. Typically, this is ensured for records where a pulse is clearly visible but when the energy approaches the threshold this is not guaranteed anymore. Thus, by comparing the difference of both shift parameters (obtained from the fit with absorber and TES-carrier template) it can be judged whether or not the same time region is considered. The difference of both parameter values is denoted by *shift difference* hereafter. For pulses with an amplitude above the respective truncation limit (see section 4.3.2) this parameter calculation is not robust anymore and, thus, it is not applied. However, as already observed in the simulated data set, for high energetic pulses the RMS values significantly differ for both classes. For smaller pulses a limit on the allowed shift difference is defined and pulses which exhibit a larger parameter value are dismissed from the data set.

As explained in section 6.6, for the ANN based pulse-shape cut a combination of two differently trained networks is used. Furthermore, in the training set a few pulses are observed which have a faster rise time than the mean population but which are not removed by this ANN-based cuts. Thus, finally also a rise time cut is applied to remove these pulses efficiently. To summarize the previous discussion the different pulse-shape cuts and the related cuts are listed in the following:

- Shift-difference cut (if required) to ensure a proper RMS-ratio parameter
- Rise-time cut
- RMS-ratio cut
- ANN trained with stochastic minimization algorithm for pulses with reconstructed energies $\lesssim 10\,\mathrm{keV}$
- ANN trained with BFGS method for pulses with reconstructed energies $\lesssim 3\,\mathrm{keV}$

6.7.2 Signal Survival Probability

In figure 6.31 the signal survival probability obtained for TUM40 after successive application of the different pulse-shape cuts is depicted. Starting from the signal survival probability after application of the quality cuts (red line, see section 5.4) the first two pulse shape cuts

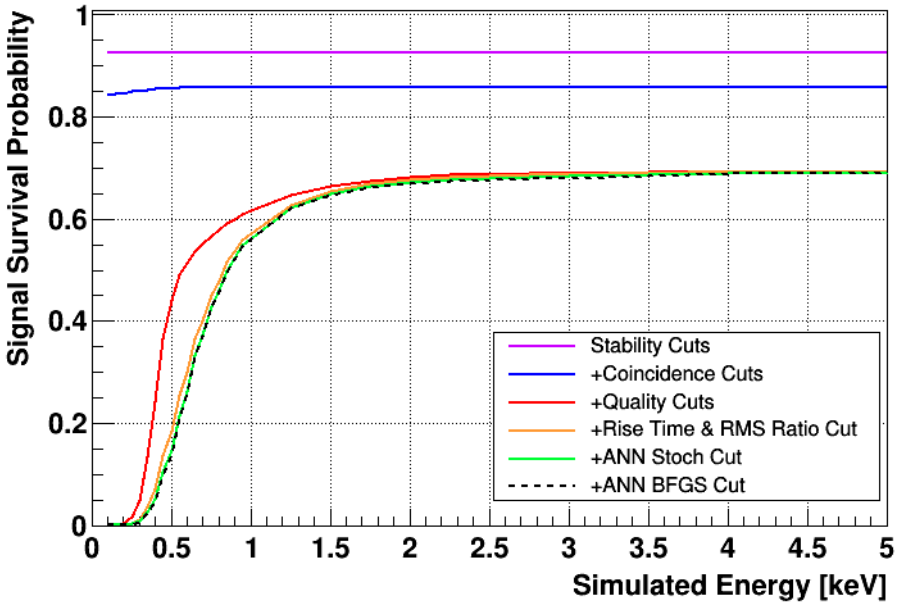

Figure 6.31: *Signal survival probability of TUM40 after successive application of the different pulse-shape cuts. Starting from the quality cuts (red line), already by the first two pulse-shape cuts on the rise-time and RMS-ratio parameter (orange line) the majority of the signal pulses is removed. The successive application of the neural networks removes only a small fraction of signal pulses resulting in the final signal survival probability depicted as black dashed line.*

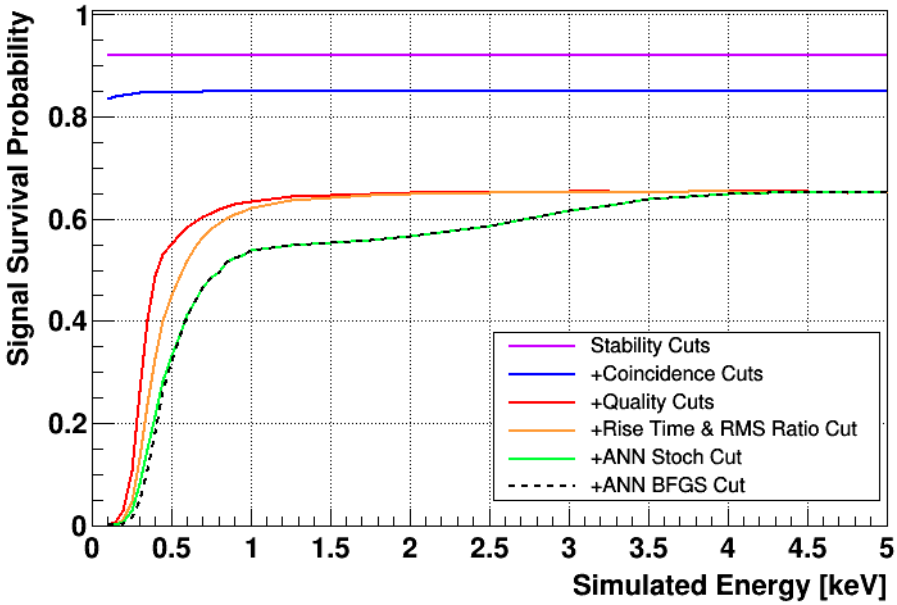

Figure 6.32: *Signal survival probability of Lise after successive application of the different pulse-shape cuts. Also for Lise the first simple cuts on the rise-time and RMS-ratio parameter (orange curve) remove a significant signal fraction, in particular at energies $\lesssim 1.5$ keV. However, in this case the ANN based pulse-shape cuts are responsible for the peculiar shape of the final curve (black dashed line).*

based on the rise time and the RMS-ratio parameter (orange line) remove the majority of all signal pulses at low energies. The cuts on the neural-network parameters remove only a non-significant fraction resulting in the final signal survival cut efficiency (black dashed line). Please note, that for TUM40 the majority of all pulses rejected by the complete sequence of pulse-shape cuts are removed by the neural network based cuts as well as the rise-time selection criterion. Depending on the ordering of the criteria the one which is performed first removes the largest fraction of absorber pulses. In the case shown first the simple cut on the rise-time parameter is performed. However, this does not imply, that this criterion is removing a larger fraction of absorber pulses than required. If the ordering of the cuts is changed, such that first an ANN-based cut is performed, the latter one removes a similarly large fraction of absorber pulses while the influence of the subsequent rise-time cut on the absorber pulses is almost not visible in this plot.

A similar plot is depicted in figure 6.32 for the detector Lise, where also the signal survival probability after successive application of different selection criteria is shown. In that case, still an observable fraction of signal events at energies $\lesssim 1.5\,\mathrm{keV}$ is removed by the first pulse-shape cuts. However, the criterion based on the MLP trained with the stochastic minimization algorithm (green curve) removes pulses in particular at energies $\lesssim 3\,\mathrm{keV}$ while the second MLP only removes a relevant part next to the energy threshold of 0.3 keV. Thus, for Lise the ANN based pulse-shape analysis is responsible for the peculiar shape of the final curve (black dashed line in figure 6.32).

6.8 Application to Different Detectors

Up to now mostly results of the MLPs used for the pulse-shape analysis of TUM40 have been shown in this chapter. However, also with the other alternative modules as well as with the module Lise, which is of the conventional design, pulse-shape differences are observed. Similarly to the situation in TUM40 also there TES-carrier pulses are recorded which have to be rejected as efficiently as possible.

In figure 6.33 the templates of the two pulse classes are shown for the respective detectors analysed. Lise is equipped with a small TES-carrier like TUM40, while the other three modules feature a larger TES-carrier. TUM38 is of the module design with a big carrier crystal (see figure 3.12 on page 56). VK27 and VK28 are the two modules each with a silicon beaker as light detector depicted in figure 3.13 on page 57.

As can be seen in figure 6.33 the absorber template (black) as well as the TES-carrier template (red) are very specific for each detector. As explained earlier in section 4.3.1 the template pulse describes the pulse shape of the respective pulse class with reduced noise and, thus, specific networks have to be trained for each phonon detector. Compared to the templates of TUM40 depicted in figure 6.1b, for the detectors shown in figure 6.33 the TES-carrier pulses are more similar to absorber pulses, i.e. the difference between both populations is not as distinct as in TUM40. Thus, it might be even harder to disentangle both pulse classes in these detectors.

For each detector simulated pulses of both types are created in the relevant energy range starting from the energy threshold of the respective detector. Based on these simulated data

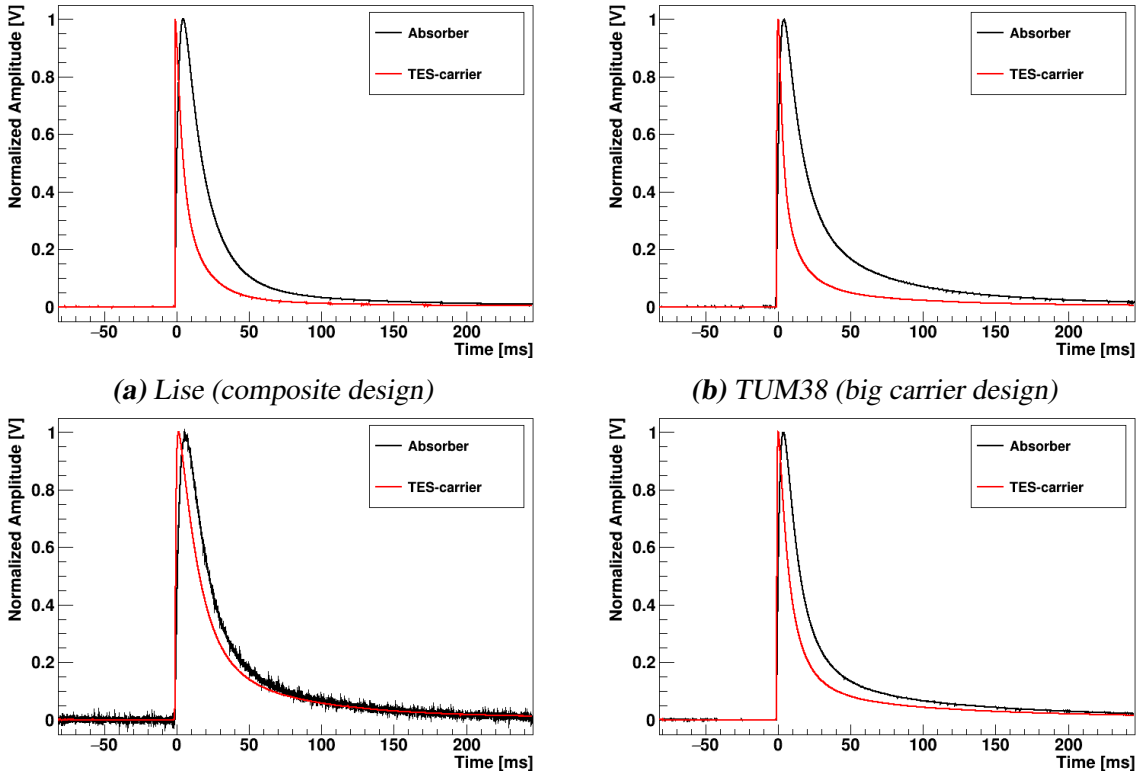

(a) *Lise (composite design)*

(b) *TUM38 (big carrier design)*

(c) *VK27 (silicon beaker design)*

(d) *VK28 (silicon beaker design)*

Figure 6.33: *Comparison of the absorber (black) and TES-carrier (red) templates of several detectors. Lise is a module of the composite design and, thus, is equipped with a small TES-carrier substrate similar to TUM40. The other three modules feature a considerably larger carrier crystal. All the different module designs are explained in more detail in chapter 3. The actual pulse shape observed in each detector depends on several parameters and is strongly detector specific. Thus, for each detector, separate MLPs have to be trained in order to perform an efficient pulse-shape cut. However, for the detectors depicted here, the TES-carrier template is more similar to the absorber template than in the case of TUM40 (see figure 6.1).*

for each detector two MLPs are trained, one with the stochastic minimization algorithm and one with the BFGS method. To determine the cut limits for all four modules, it is tried to find a combination, where all simulated TES-carrier pulses are rejected without removing the complete absorber data. Therefore, some procedures similar to the ones applied in TUM40 are required to achieve this goal (e.g. different energy ranges used for the training of the two MLPs). For Lise, TUM38 and VK28 it is possible to find neural networks and corresponding cut limits that fulfill this requirement. The results of VK27 are discussed in more detail later in this section.

The outputs of the MLPs trained with the stochastic minimization method (left column) and of the MLPs trained with the BFGS method (right column) are depicted in figure 6.34 for all low-energetic pulses measured in the training sets of the detectors Lise (a), TUM38 (b) and VK28 (c). Thereby, for both plots the same subset of pulses is depicted to show comparable results for both MLPs. However, for the final cut sequence again the combination of both

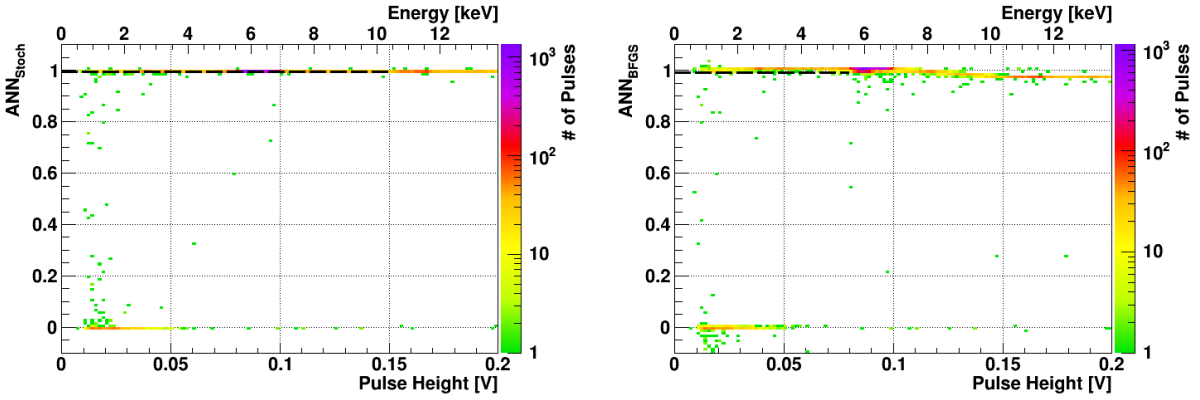

(a) Lise

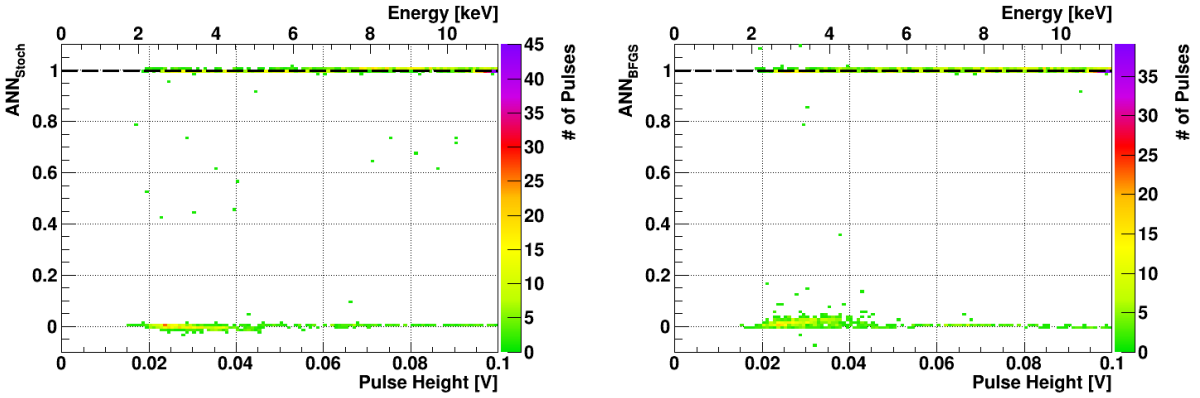

(b) TUM38

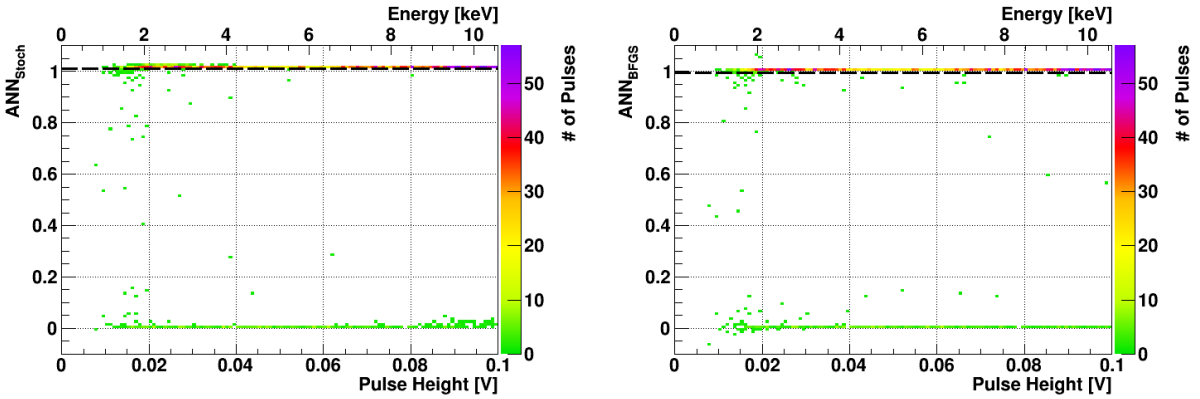

(c) VK28

Figure 6.34: *Pulse-height dependent output of the MLP trained with the stochastic minimization method (left column) and of the MLP trained with the BFGS method (right column) for all low-energetic pulses of the training sets of the detectors Lise (a), TUM38 (b) and VK28 (c). Please note that the same pulses are used for both plots and that no cut restricting one MLP output is performed. The respective cut limits applied in the depicted pulse-height range are drawn as black dashed lines, whereby all pulses below this line are removed by the cut. The cut limits are set based on the respective simulation data set such that all TES-carrier pulses are rejected. This procedure leads to the rather stringent cut limits applied here.*

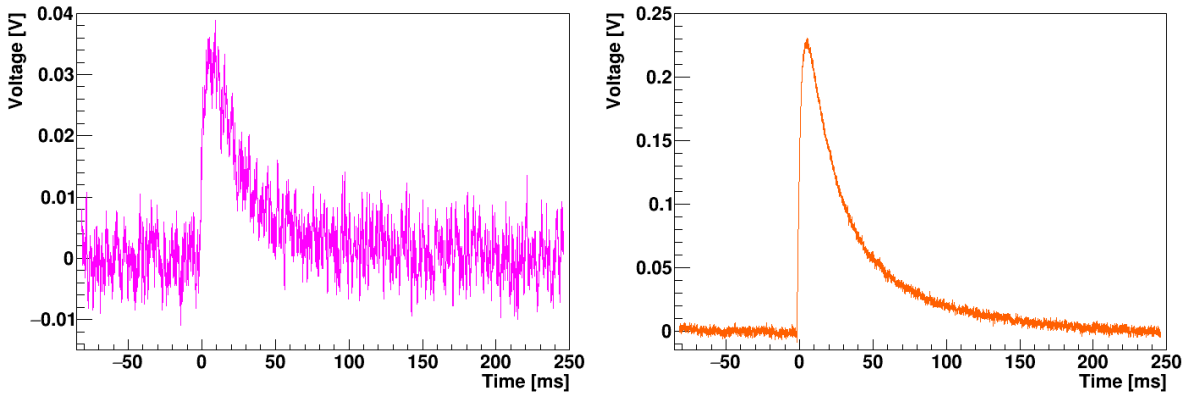

(a) VK27 *(b) TUM40*

Figure 6.35: *Example of the resulting pulse for an energy deposition of $\sim 25\,keV$ in the detector VK27 (a) and TUM40 (b). The resulting signal height is much larger in TUM40 compared to VK27. Thus, due to the worse signal-to-noise ratio in VK27 a large trigger threshold of only $\sim 11\,keV$ is achieved. Due to these effects obtaining MLPs with satisfactory performance is difficult.*

MLPs is used to reject all TES-carrier pulses. The second x-axis on the top of each plot shows the corresponding energy, valid only for absorber pulses. In each plot, the black dashed line marks the cut limit applied and all pulses below this line are dismissed from the data set[38]. As for TUM40 also for these detectors not only the two cuts based on the MLP outputs are applied but also a rise-time cut as well as a cut on the RMS ratio. Thus, it is expected that the majority of the TES-carrier pulses is rejected by this cut sequence.

Compared to the result of TUM40 (see figure 6.22 and figure 6.25) some differences are visible in the plots depicted in figure 6.34. First of all, in all three detectors only a few TES-carrier pulses are observed. This is in contrast to TUM40, where pulses of the TES-carrier type seem to be the majority of all pulses recorded. As for TUM40 also in Lise, the majority of the TES-carrier pulses exhibit a low pulse height ($\lesssim 0.1\,V$). However, in the modules featuring a big carrier crystal a continuous spectrum up to large pulse heights is observed.

For almost all pulses of Lise, TUM38 and VK28 the pulse type is rather clear for the respective MLP and, thus, only a few pulses result in output values between the two main populations. In this light, the cut limits obtained (black dashed lines) seem to be almost too strict. However, one has to keep in mind that they are defined on the expectation based on the simulated data set. By doing so, a stringent rejection of (almost) all TES-carrier pulses can probably also be achieved in the complete data set.

For VK27 the situation is slightly more complicated due to the worse detector performance, compared to standard CRESST phonon detectors. This worse performance is caused by a problem in the cabling of the detector and not by the TES-sensor itself [142]. This results in small signal heights for all pulses but a normal absolute noise level. Therefore, a worse signal-to-noise ratio and a rather high trigger threshold of only $\sim 11\,keV$ compared to other CRESST-II phonon detectors is achieved. In figure 6.35 a pulse corresponding to an energy

[38] The numerical values are given in table D.4 in the appendix.

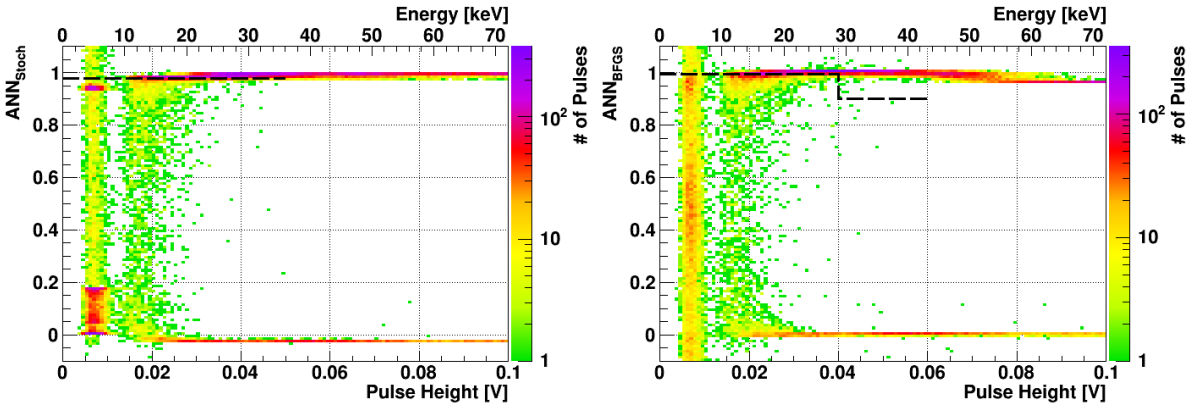

(a) MLP trained with the stochastic minimization algorithm

(b) MLP trained with the BFGS method

Figure 6.36: *Pulse-height dependent output of the two MLPs (ANN_{Stoch} in (a) and ANN_{BFGS} in (b)) for all measured pulses of the training set for the detector VK27. Due to the small signal-to-noise ratio training of the network is challenging. Nonetheless, after several tries a combination of two networks is found, which allows to reject all pulses of TES-carrier type without rejecting all absorber pulses in the simulated data set. When these cut limits (black dashed lines) are applied to the measured pulses, the ones located in the red shaded area are rejected. A decrease of the MLP output of the MLP trained with the BFGS method (see (b)) results in a slightly lower cut limit for pulse heights ≥ 0.04 V.*

deposition of ~ 25 keV is depicted for the phonon detectors VK27 (a) and for comparison also for TUM40 (b). While the signal height is smaller in VK27 compared to that of TUM40 the absolute noise level is almost the same. Therefore, a worse signal-to-noise ratio is obtained in VK27 which affects also the separation capability in this detector.

Nonetheless, the two simulated data sets for absorber and TES-carrier pulses are created with 17 different amplitudes corresponding to energies ranging from ~ 5 keV to ~ 40 keV. After application of the cuts for the ANN-training set, 24 728 and 24 206 simulated pulses of absorber and TES-carrier type survive, respectively. These pulses are used for the training of two MLPs. One remarkable difference in VK27 is, that even for the largest numbers of training epochs (~ 5000) no overtraining effect is visible. For the other detectors it is only possible to train the networks for a few hundred epochs before overtraining is occurring. Simultaneously, the error of the training set (as well as the control set) only decreases significantly in the beginning of the training and becomes rather flat afterwards. However, finally also for VK27 a combination of two MLPs is found, that results in a perfect separation of all simulated TES-carrier pulses without loosing the complete absorber population.

In figure 6.36 the resulting outputs of the MLP trained with the stochastic minimization algorithm (a) as well as the MLP trained with the BFGS method (b) are depicted for all pulses of the training set of VK27. The pulses with corresponding energies (for absorber pulses) below ~ 10 keV are due to noise triggers and are removed by the selection criteria on the energy deposited, applied later. Most probably due to the worse detector performance, at low pulse heights a considerable fraction of pulses is located between the two main populations of

clearly identified absorber and TES-carrier pulses. The black dashed line marks the applied cut limit and all pulses below are removed by the respective cut. Since the output of the MLP trained with the BFGS method decreases for large pulse heights in the simulation (not visible in the measured data set depicted in figure 6.36b) a lower cut limit is applied above 0.04 V.

Part III

High Level Analysis

7 Light Yield Bands

In the previous part of the present work all steps required to derive the energy from particle pulses are explained. Furthermore, different types of invalid records are described together with the selection criteria to remove them. Additionally, a pulse shape analysis based on artificial neural networks is performed to remove events with different pulse shapes compared to particle induced pulses. Finally, the raw data analysis results in light yield - energy plots of all valid events acquired with several detectors.

The high-level analysis, which is described in this part, starts with the determination of regions, where the different event populations are located in this parameter space. In particular, the region where the sought-for nuclear recoils are expected must be defined. This chapter focuses on the mathematical description of these regions, which roughly form horizontal bands in the light yield - energy plane. The bands are completely described by only two functions, the mean and the width depending on the energy. The mean describes the average amount of light produced by the particle interactions and is correlated with the respective quenching factor. The energy dependent width of the bands is mainly dominated by the finite energy resolution of the light detector. In the present work exactly the same procedure and algorithms as outlined in [44] are used to define these bands and, thus, here only a brief explanation is given.

In section 7.1 the e^-/γ-band model is explained and the results of the likelihood fits, to obtain the respective parameters for the different modules, are presented. The method to calculate the nuclear recoil bands based on the e^-/γ-band model is explained in section 7.2. In section 7.3 a validation of this method with data of dedicated neutron calibrations is performed.

7.1 e^-/γ-Band

The e^-/γ-background events are located in a band centered at a light yield of ~ 1 as depicted in figure 7.1. Since this type is the dominant source of background in CRESST-II it is highly populated by a large number of events. Thus, it is most suited to extract the detector specific parameters of the band model by a likelihood fit. The result of such a fit is also depicted in figure 7.1 where the central 80 % band of e^-/γ-events is shown as red lines. The red dashed line is the energy dependent mean of the band, while the red solid lines are the lower and upper 90 % boundaries of the e^-/γ-distribution.

Although the data are usually displayed in the light yield - energy plane the fit is conventionally performed in the light - energy parameter space, where the energy detected in the light detector is plotted against the recoil energy (see section 4.6). Thus, in the following the given equations are all defined for the conventional case of a light-energy plot.

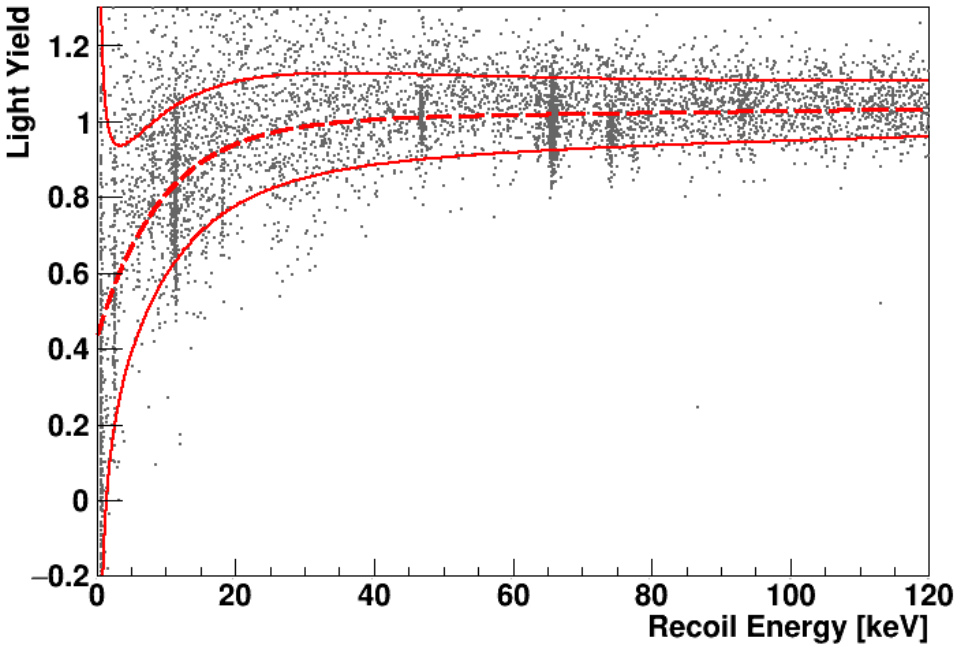

Figure 7.1: *Light yield - energy plot of the training set data of TUM40. Also depicted are the upper and lower 90 % boundaries of the e^-/γ-distribution (red solid lines) and, thus, the central 80 % band is drawn. The mean function of this band is shown as red dashed line.*

7.1.1 Mean Light

In the light-energy plane the mean line of the e^-/γ-band is described by the following function:

$$L^{e^-/\gamma}(E_R) = (L_0 E_R + L_1 E_R^2) \cdot \left[1 - L_2 \cdot \exp\left(-\frac{E_R}{L_3}\right)\right], \tag{7.1}$$

where E_R denotes the total energy deposited in the absorber (recoil energy).

The leading term $L_0 E_R$ of the first factor of equation 7.1 describes a linear scintillator while a deviation from linearity is taken into account by the second summand $L_1 E_R^2$. In first approximation the $CaWO_4$ crystals are linear scintillators, and, thus, usually L_1 is found to be small with respect to L_0. As mentioned earlier, during the energy calibration of both detectors the light yield is set to 1 at 122 keV for γ-events, resulting in a value of $L_0 \sim 1$. The deviation from linearity is typically only observed at higher energies and, thus, only plays a non-negligible role if a fit is performed for large energy ranges spanning more than ~ 100 keV.

At small energies a detector dependent drop of the mean light yield is observed, which has to be considered in the band model. This so-called *non-proportionality effect* is a commonly observed effect in scintillators [143, 144], which is taken into account by the second factor in equation 7.1, where L_2 describes the magnitude of this effect and L_3 corresponds to the typical energy scale on which the non-proportionality effect is important.

In [145] a comprehensive microscopic model of the scintillation mechanism in $CaWO_4$ is developed and therein, also the non-proportionality effect is discussed. During an interaction in the scintillating crystal so-called *self-trapped excitons* (STE) – consisting of a bound

electron-hole pair – are created. There are four different recombination possibilities for these quasiparticles, whereof only two are important here in the case of mK temperatures. Firstly, STEs can recombine radiatively via emittance of (scintillation) light. Secondly, besides two other non-radiative recombination possibilities which are negligible at such low temperatures, two STEs can interact with each other via the exchange of a virtual photon. Thereby, one STE recombines non-radiatively and, thus, is lost for the creation of scintillation light. Via the latter decay channel of STEs light quenching is obtained, since less light than expected from the total amount of STEs created is produced. Thereby, the total amount of STEs created depends on both the particle type interacting and the amount of energy deposited [145]. The recombination channel depends on the distance between two STEs, where the non-radiative recombination is dominating at distances smaller than the so-called Förster radius [146].

The non-proportionality effect observed for low energies in the mean light yield can be explained by closely located STEs. The stopping power dE/dx of electrons in $CaWO_4$ increases for low energies [147]. Thus, low-energetic electrons produce STEs more closely, i.e. within a smaller volume, resulting in a more pronounced light quenching effect. Hence, the mean light output for a smaller amount of energy deposited is decreasing, leading to the observed drop of the band. Furthermore, this model also explains the observed quenching effect in $CaWO_4$. Compared to an electron recoil, a nuclear recoil creates a lower amount of STEs for the same amount of energy deposited. In addition, for nuclear recoils the energy is more densely deposited than for electron recoils and due to the non-radiative recombination of the STEs less light is produced. Both facts together explain the observed quenching behavior, that describes the effect that for nuclear recoils a lower amount of energy is released as light compared to electron recoils.

7.1.2 Width of the Band

The finite resolutions of phonon and light detector have a strong influence on the width of the observed bands. Since the amount of created scintillation light is only a small fraction of the total absorbed energy ($\lesssim 9\,\%$), typically the phonon detector resolution is much better than the one of the light detector, i.e. smaller line widths are observed. Thus, it is convenient to model the width σ of the band as a function of the detected light energy L and not of the total deposited energy E_R. In general, the width observed in the light detector is influenced by two contributions: firstly the baseline noise typically modelled by a Gaussian function and secondly the counting statistics of the detected photons. At low energies the baseline noise dominates and, thus, a Gaussian shape of the band is expected. At high energies a large number of photons is observed, and, thus, the Poisson statistics can be approximated by the normal distribution resulting finally also in a Gaussian shape of the band. Only in the transition region where none of the contributions clearly dominates Poisson statistics is required. Nonetheless, mainly for computational reasons in [44] a Gaussian shape of the band is assumed leading to the following form for the energy dependent width of the e^-/γ-band:

$$\sigma^{e^-/\gamma}(L) = \sqrt{S_0 + S_1 L + S_2 L^2}. \tag{7.2}$$

In case the phonon detector resolution is good, i.e. small line widths are observed, it is valid to assume that $\sigma^{e^-/\gamma}(L)$ is solely the resolution of the light detector. By doing so, the three

parameters S_i can be interpreted as the different effects causing a broadening of the amount of measured light: The parameter S_0 describes the influence of the baseline noise of the light detector and, thus, is independent of the light energy L. The additional uncertainty caused by statistical fluctuation of the number of produced photons is expected to be proportional to $\sqrt{L}$ and described by S_1. The third parameter S_2 accounts for other effects directly proportional to the amount of detected light L. Examples are position dependencies of the emitted light in the absorber crystal due to defects in the crystal structure [97] or local dependencies in the light detector [148].

In general, the observed width of the bands is also influenced by the energy uncertainty in the phonon detector. The true amount of energy deposited might be different to the reconstructed recoil energy E_R of an event due to the finite phonon detector resolution $\sigma_{\mathrm{P}}(E_R)$. For e^-/γ-events the uncertainty in the phonon channel transfers to a fluctuation in the produced scintillation light of the same amount, since the quenching factor $\mathrm{QF}_{\mathrm{e}^-/\gamma}$ for these events is ~ 1. During the measurement of the scintillation light additional uncertainties occur due to the light detector resolution σ_{L}. Approximately, the measurement uncertainties of the light detector are statistically independent of the fluctuation in the light production and, thus, the following equation holds:

$$\sigma^{\mathrm{e}^-/\gamma}(L) = \sqrt{\sigma_{\mathrm{L}}^2(L) + \left[\mathrm{QF}_{\mathrm{e}^-/\gamma} \cdot \sigma_{\mathrm{P}}(E(L))\right]^2}. \tag{7.3}$$

The resolution of the phonon detector σ_{P} has to be evaluated at an energy $E(L)$ where the mean of the band is at a light energy L. However, since the consideration of the phonon detector resolution is usually only a small correction, the energy dependency is dropped. This results in a constant width for the phonon detector corresponding to the resolution at zero energy $\sigma_{\mathrm{P},0}$.

In principle, the three parameters S_0, S_1 and S_2 can be determined by the likelihood fit. However, for the baseline noise parameter S_0 additional information is available. As already explained earlier, test pulses with various distinct amplitudes are periodically injected into the detector heater to monitor the time dependency of the detector response. The test pulses have a fixed amount of energy and, thus, the observed finite resolutions of low energetic test pulses are dominated by the baseline noise and only slightly influenced by the other effects. Hence, the observed widths of low energetic test pulses in the respective detector are a good estimator for the width at zero energy $\sigma_{\mathrm{x},0}$, where x denotes either the phonon or light detector [44].

However, the best conclusion about the influence of the baseline noise S_0 on the energy resolution can be obtained from the artificial pulse simulation explained earlier in section 5.4.1. The events are generated with different but distinct energies and, thus, several peaks are observed after energy reconstruction. These peaks are fitted individually with Gaussian functions to obtain the energy independent width. To derive a statistically robust value for $\sigma_{\mathrm{x},0}$ the different values are averaged. Thereby, peaks at small energies are neglected due to an observed asymmetry caused by the energy dependent signal survival probability: events with lower energies (left flank of the Gaussian peak) are removed more likely than events on the right side.

In case of test or artificial pulses the influence of S_1 and S_2 on the measured width is negligible and, thus, by comparing equation 7.2 and equation 7.3 it follows that $S_0 = \sigma_{\mathrm{P},0}^2 + \sigma_{\mathrm{L},0}^2$.

Therefore, in the present work typically S_0 is fixed to this calculated value and only S_1 and S_2 are free parameters in the likelihood fit. Fixing S_0 considerably improves the convergence of the likelihood fit [44].

Often it is important to also know the width of the bands in the light yield - energy plane. Therefore, the light energy L has to be divided by the phonon energy E_P to obtain the light yield (see equation 4.1). As previously explained, the determined width $\sigma^{e^-/\gamma}(L)$ already contains the uncertainty of the phonon channel. Thus, it must not be considered a second time when the Gaussian width function is transformed to the light yield - energy form by the following equation:

$$\sigma_{\text{yield}}(E_P) = \frac{1}{E_P} \cdot \sigma^{e^-/\gamma}(L). \tag{7.4}$$

7.1.3 Excess Light Events

In almost all modules another event population influences the likelihood fit of the e^-/γ-band and, thus, must be modelled properly. Events of this population are mainly observed at low energies deposited in the phonon detector and, simultaneously, characterized by an excess of light with respect to the total amount of energy deposition in the absorber crystal. Thus, these events show a higher light yield compared to e^-/γ-events and, hence, are called *excess light events*. Due to this class the e^-/γ-band seems to be asymmetric, with more events above the mean of the band. If this population is not considered in the fit, the fitted centroid of the e^-/γ-band would be shifted to higher light yields. Simultaneously, a broader width of the band than appropriate for the detector resolution would be obtained, i.e. larger values for S_1 and S_2.

Based on the explained characteristics a purely empirical model to describe this population was developed in [44]. Three new parameters are introduced to the fit and are described briefly in the following. First of all, the parameter X_{el} describes the fraction of all events at zero energy observed as excess light events. With increasing total energy this fraction exponentially decreases with a typical decay energy $E_{\text{el}}^{\text{decay}}$. For higher light energies and in turn higher light yields less excess events are observed. This observation is modelled by an additional exponential decay with a typical decay energy $L_{\text{el}}^{\text{decay}}$ in the light channel. This second exponential must be convoluted with the energy resolution of the light detector, since otherwise it would only describe the distribution as seen by an ideal detector [44].

One possible explanation for the origin of such events are particles (e.g. electrons) which only deposit part of their energy in the absorber crystal. Another part of their energy is either lost before or afterwards in the scintillating surrounding or the light detector directly. In this case the resulting amount of energy observed in the light detector is larger than for the scintillation of the absorber crystal alone. This explanation is supported by the fact, that a pulse shape difference between excess and normal light events has been reported in [103]. Additionally, the non-observation of these events in the two silicon beaker prototype designs implies that they are created from particles, which penetrate the scintillating foil which is in all the other module designs surrounding the crystal.

Despite the observed pulse-shape difference, no efficient discrimination method has been found up to now. Removing these events only partly, might worsen the problem since then it might be difficult or almost impossible to describe the influence of these events on the

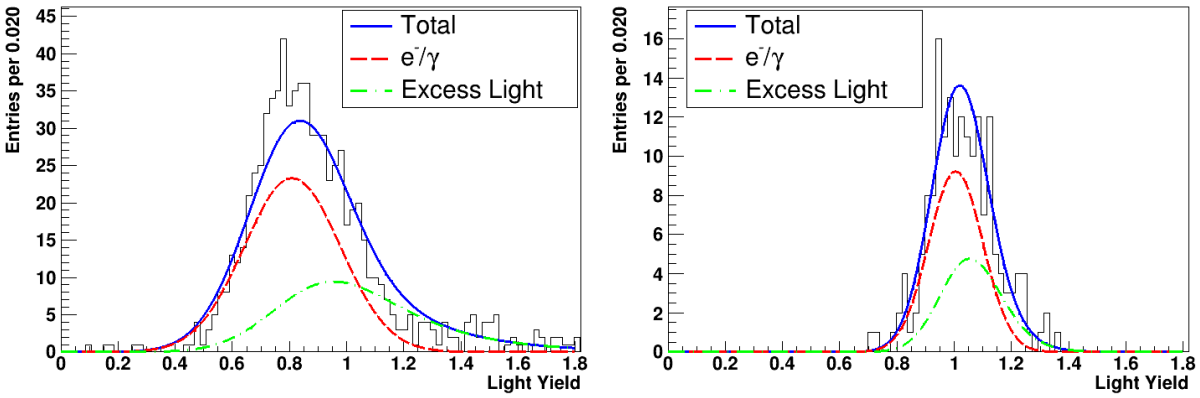

(a) *Energy bin* 10 ± 2.5 *keV*

(b) *Energy bin* 40 ± 2.5 *keV*

Figure 7.2: *Light-yield distributions of events from the training set data of TUM40 for two different energy slices. The result of the fit is shown as blue line and describes in both cases the observed distribution well. While the normal e^-/γ-population[41] as inferred from the fit is depicted as red dashed line, the excess light distribution is shown as green dashed line. Due to the non-proportionality effect the mean of the band is shifted from 1.00 at 40 keV in (b) towards lower light yield values of 0.81 at 10 keV in (a).*

likelihood fit properly. Thus, the complete population is included in the fit and no cut attempt is performed. However, this scenario might be another interesting application of neural network based pulse-shape analysis in cryogenic detectors.

7.1.4 Likelihood Fit Results

The resulting total likelihood as well as a short introduction to the unbinned likelihood fit method are given in [44]. Here only the results of the performed fits are presented and discussed. In order to stick to the blind analysis scheme (see section 5.1), the likelihood fits are performed on data of the training set. The energy range of the fit is constrained from 1 keV up to 120 keV to achieve appropriate results in the relevant region for Dark Matter search[39]. Furthermore, to reduce the influence of outliers, first a fit describing the e^-/γ-band roughly is performed. Typically, all events which are located more than 5 σ above or 3 σ below the mean of this estimated band are not considered in the final likelihood fit[40]. For the two modules of the silicon beaker design, unphysical values (< 0) for S_2 are obtained, if S_2 is a free parameter in the fit. Since this parameter is typically very small and only important at higher energies it is fixed to zero, since it is not possible to constrain this parameter in the fitted energy range for these modules.

In figure 7.2 histograms of the light-yield distribution in two energy slices are depicted. The Gaussian shaped e^-/γ-population with normal light yields[41] as inferred from the fit is drawn

[39] The threshold of the phonon detector VK27 is $\sim$ 11 keV and, thus, for this module the fitted energy region ranges from threshold to 120 keV.

[40] In the module Lise/Enrico this cut is not performed, due to the worse light detector resolution of this module.

[41] These are all e^-/γ-events, where no excess in the light channel is observed compared to the energy deposited

as red dashed line, while the excess light event population is included as green dashed line. As explained earlier both contributions sum up to the total event distribution (blue solid line), which in both cases matches well with the observations.

The likelihood fit results of all modules analysed in the present work are presented in table 7.1. As expected for an approximately linear scintillator, the parameter value obtained for L_0 is close to unity in all cases. At the same time, the non-linearity correction required at large energies is only very small ($L_1 \ll 1$).

In particular in the TUM-grown crystals, the non-proportionality effect is very pronounced in comparison to the results obtained in [44] and for the commercial crystals VK27 and VK28. Thereby, pronounced implies that the parameter describing the magnitude of this effect (L_2) is large and, simultaneously, the typical energy scale (L_3) is small (see section 7.1.1). The magnitude observed in TUM40 is about twice as large as for the maximal value of CRESST-II phase 1. Furthermore, due to the small typical energy range the drop is constrained to a smaller energy region. For Lise the obtained parameter values are more similar to the TUM-grown than to the other commercial crystals, however due to the bad light detector resolution no definite conclusion is possible[42].

Due to the different signal-to-noise ratios in the different detectors the parameter S_0 strongly differs between the modules. The resolutions of the phonon ($\sigma_{P,0}$) as well as of the light ($\sigma_{L,0}$) detector are inferred from the respective artificial data set (see section 5.4.1) and are also included in table 7.1. The observed light detector resolution $\sigma_{L,0}$ shows a superior performance of the silicon beakers (Diogenes, Zam) with respect to standard light detectors.

As already mentioned earlier, for the two modules of the silicon beaker design (VK27/Diogenes, VK28/Zam) no excess light event population is observed. Thus, for the likelihood fits of these modules the fraction X_{el} is fixed to zero. In contrast to the observations made in [44], for the two modules containing TUM-grown crystals (TUM38, TUM40) the fraction of excess light events seems to be constant, resulting in a huge decay length E_{el}^{decay}. Simultaneously, the fraction X_{el} itself is also rather high compared to the previous observations with commercial crystals.

7.2 Nuclear Recoil Bands

As explained in chapter 2, Dark Matter particles are expected to scatter off nuclei and, thus, they would show up in the nuclear recoil band. In $CaWO_4$ this band consists of the three sub-bands of oxygen, calcium and tungsten, which are to some extent separated from each other due to the finite width. Based on the parameters determined by the likelihood fit of the e^-/γ-band, the mean and the width of the quenched bands are calculated [44]. As is shown in the following, the only prerequisite for this step is the knowledge of the respective energy dependent quenching factor[43].

in the phonon channel.

[42] For TUM40 in [123] comparable values are obtained in the likelihood fit. However, for Lise in particular for the non-proportionality effect (L_2 and L_3) considerably different values are found.

[43] The actual implementation of the energy dependency in the existing limit calculation software package is described in [123].

Module	L_0	L_1 [keV^{-1}]	L_2	L_3 [keV]
Lise/Enrico	0.949	$1.156 \cdot 10^{-3}$	0.549	5.127
TUM38/Petrus	0.931	$0.742 \cdot 10^{-3}$	0.476	11.387
TUM40/Michael	1.003	$0.245 \cdot 10^{-3}$	0.570	9.362
VK27/Diogenes	1.156	0 *	0.317	39.415
VK28/Zam	1.132	$-0.257 \cdot 10^{-3}$	0.354	34.736

Module	S_0 [keV$^2_{ee}$]	S_1 [keV$_{ee}$]	S_2	$\sigma_{P,0}$[keV]	$\sigma_{L,0}$[keV$_{ee}$]
Lise/Enrico	17.4842	0.506	$0.985 \cdot 10^{-3}$	0.0603	4.305
TUM38/Petrus	0.1344 *	0.358	$0.883 \cdot 10^{-3}$	0.1110	0.3494
TUM40/Michael	0.0703 *	0.336	$0.357 \cdot 10^{-3}$	0.0733	0.2549
VK27/Diogenes	0.9907 *	0.384	0*	0.9718	0.2153
VK28/Zam	0.0485 *	0.311	0 *	0.1224	0.1831

Module	X_{el}	E_{el}^{decay} [keV]	L_{el}^{decay} [keV$_{ee}$]
Lise/Enrico	0.028	77.997	20.240
TUM38/Petrus	0.293	$1.486 \cdot 10^8$	3.967
TUM40/Michael	0.383	$5.118 \cdot 10^6$	2.421
VK27/Diogenes	0 *	-	-
VK28/Zam	0 *	-	-

Table 7.1: *Likelihood fit results of the e^-/γ-band for the investigated modules. All values marked with * are fixed in the likelihood fit. In case S_0 is fixed the given value is determined by the artificial pulse simulation $\left(S_0 = \sigma_{P,0}^2 + \sigma_{L,0}^2\right)$. For the silicon beaker modules VK27/Diogenes and VK28/Zam no excess light events are observed and, thus, for both modules X_{el} is fixed to zero. Furthermore, for these modules also S_2 is fixed to zero, since the fitted energy range is too small to constrain this parameter well. In VK27 also L_1 is fixed to zero, since otherwise no convergence of the fit is achieved.*

7.2.1 Mean Light

Since the scintillator non-proportionality effect was not observed for nuclear recoil bands up to now, the following simplified definition for the mean light function of a quenched band is used:

$$L^{\mathrm{QF}}(E_R) = \mathrm{QF}^{*}_{x,i}(E_R) \cdot \left(L_0\, E_R + L_1\, E_R^2\right). \tag{7.5}$$

The parameters L_0 and L_1 are the ones fixed by the e^-/γ-band description. Also required is the crystal and energy dependent quenching factor $\mathrm{QF}^{*}_{x,i}(E_R)$ for the nucleus x. The model to describe the energy dependency is explained in section 4.5. For different crystals a variation of $\mathcal{O}(10\,\%)$ of the quenching factor value is observed [117, 125]. To account for this effect, a scaling factor ε_i is defined, such that the quenching factor of the respective module is simply the product of ε_i and the quenching factor $\mathrm{QF}_{x,i}(E_R)$, the latter having been obtained in a dedicated campaign at a neutron-scattering facility [117, 125]:

$$\mathrm{QF}^{*}_{x,i}(E_R) = \varepsilon_i \cdot \mathrm{QF}_{x,i}(E_R). \tag{7.6}$$

Following the proposed method in [117, 125], the different scaling factor values of all modules analysed are obtained and given in table 7.2.

module	$\boldsymbol{\varepsilon_i}$
Lise/Enrico	0.941
TUM38/Petrus	0.962
TUM40/Michael	0.893
VK27/Diogenes	0.827
VK28/Zam	0.818

Table 7.2: *Crystal dependent scaling factors ε_i for the quenching factor calculation.*

As already observed for the crystals operated in CRESST-II phase 1, also in phase 2 lower quenching factor values are found compared to the reference crystal operated in the dedicated external measurement campaign [117, 125]. Thus, all values of ε_i are smaller than one with a mean value of $\bar{\varepsilon} = 0.888$. This value is comparable to the one determined for CRESST-II phase 1, where $\bar{\varepsilon} = 0.880$ has been obtained [117, 125].

7.2.2 Band Width

Similar to the band width of the e^-/γ-band (see equation 7.3) the width of the quenched band is defined:

$$\sigma^{\mathrm{QF}}(L^{\mathrm{QF}}) = \sqrt{\sigma_L^2\left(L^{\mathrm{QF}}\right) + \left[\mathrm{QF}\left(E\left(L\right)\right) \cdot \sigma_P\left(E_R\right)\right]^2}, \tag{7.7}$$

where $L^{\mathrm{QF}} \simeq \mathrm{QF}(E_R) \cdot E_R$. Compared to equation 7.3 the influence of the phonon detector resolution σ_P on the observed band width is further reduced in the quenched band due to the

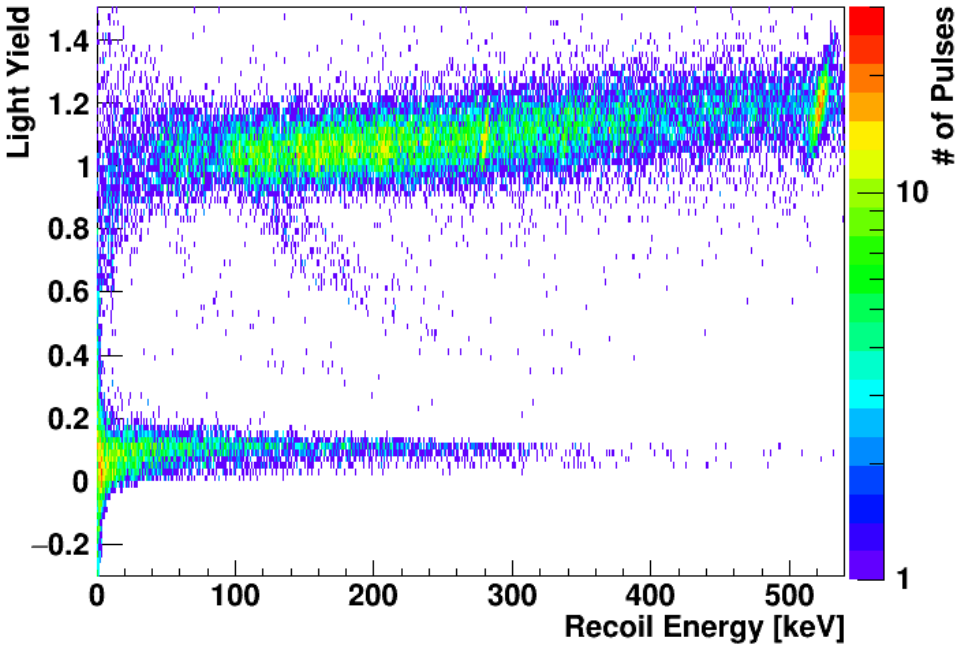

Figure 7.3: *Two-dimensional histogram of the light yield - energy data of TUM40 obtained during the neutron calibration with an AmBe-source in CRESST-II phase 2. The neutrons scatter off nuclei and, thus, these events are observed with a lower light yield ($\lesssim 0.2$) with respect to electron recoils centered around one. Due to inelastic scattering of neutrons off tungsten a curved band is observed between the electron and the nuclear recoil band. The data are used for a cross check of the method to calculate the nuclear-recoil bands based on the likelihood fit result of the e^-/γ-band.*

energy dependent quenching factor with values smaller than one. Again in practice the energy dependence of the phonon detector resolution σ_P is dropped but included in the equations to be formally correct. The function $\sigma_L(L^{\mathrm{QF}})$ is already known from the likelihood fit of the e^-/γ-band and, thus, the quenched width can be easily calculated.

7.3 Validation with Neutron Calibration Data

In order to validate the described procedure for the calculation of the mean and the width of the quenched bands, dedicated neutron calibrations were performed two times during CRESST-II phase 2. The two distinct data sets are merged and analysed in combination. As expected for Dark Matter particles, neutrons scatter off nuclei and, thus, are a perfect candidate for this validation task. However, in contrast to WIMPs which are expected to preferably scatter off heavy elements, neutrons mainly scatter off the lightest nuclei, which is oxygen in case of $CaWO_4$. To ensure a reasonable rate in the cryogenic detectors, the used AmBe neutron source is placed inside the outer shielding next to the experimental volume of the setup (see figure 3.1).

In figure 7.3 a two-dimensional histogram of the light yield - energy data of TUM40 ob-

tained during the neutron calibration is depicted. The different histogram entries are color coded and allow to observe various features. First of all, the electron-recoil (e^-/γ) band centered around a light yield of one is highly populated up to the maximal shown energies of 540 keV[44]. Due to the large energy range shown, the slight increase of the mean of the e^-/γ-band is visible (described by L_1 in equation 7.1) Besides the intended neutrons the AmBe-source also produces a high amount of γ-rays. Via pair-production, high energetic γ-particles can create electron-positron pairs, which might in turn annihilate to two 511 keV photons. The peak observed at this energy in figure 7.3 is due to such single photons, which are detected in the phonon detector.

Below the electron-recoil band for light yields (LY) of $0.2 \lesssim LY \lesssim 0.8$ several events are observed populating curved bands. These events are due to inelastic scattering of neutrons on tungsten where an excited W-recoil and, simultaneously, a γ-particle from the de-excitation of an excited W-energy level to the ground state are observed [117, 149]. The most prominent excited levels of the relevant tungsten isotopes cluster between 100 keV and 120 keV but further levels exist with lower intensity at higher as well as at lower energies. Most probably due to these excited levels also the γ-background is enhanced between ~ 50 keV and ~ 400 keV.

The neutrons generated in the AmBe-source induce nuclear recoils and, thus, are located at lower light yields ($\lesssim 0.2$) compared to the e^-/γ-band. In contrast to the latter, for nuclear recoils the mean of the band does not rise with increasing energy due to the light quenching (see equation 7.5) and, thus, a horizontal band is observed. Several events are visible up to the maximal shown energies of 540 keV, however the population thins out with increasing energy. Due to kinematic reasons the energy transferred to the nucleus is higher for lighter elements. Thus, at high energies mainly oxygen recoils are observed, while at the low energies that are of interest for Dark Matter search all three constituents of $CaWO_4$ contribute. Therefore, the collected data set is predestined for the validation of the above-described procedure to calculate the nuclear recoil bands.

7.3.1 Validation of the Quenching Factor

In figure 7.4 again the data of the neutron calibration of TUM40 are shown for energies below 300 keV in a similar way as for the training set data depicted in figure 7.1. Depicted in red is the expected 80 % band for e^-/γ-recoils, as determined by the training set data. Despite the fact that the likelihood fit is only performed for energies between 1 keV and 120 keV, the band description of TUM40 can be extrapolated up to the maximal shown energies without introducing a large error.

The calculated quenched nuclear recoil band is drawn in dark blue in figure 7.4. The boundaries correspond to the 90 % upper limit of the oxygen band and the 90 % lower limit of tungsten and, thus, the majority of all nuclear recoil events is expected to be inside these lines. However, the exact amount depends on the scattering nucleus and is therefore, not stated here. Furthermore, also the 90 % lower limit of oxygen (green) and the 90 % upper limit of the tungsten band (cyan) are shown. It can be observed in figure 7.4 that the calculated nuclear recoil band contains the majority of all neutron induced events and, thus, the previously described

[44] This is the maximum energy which is accessible with the applied energy calibration of TUM40 and Michael.

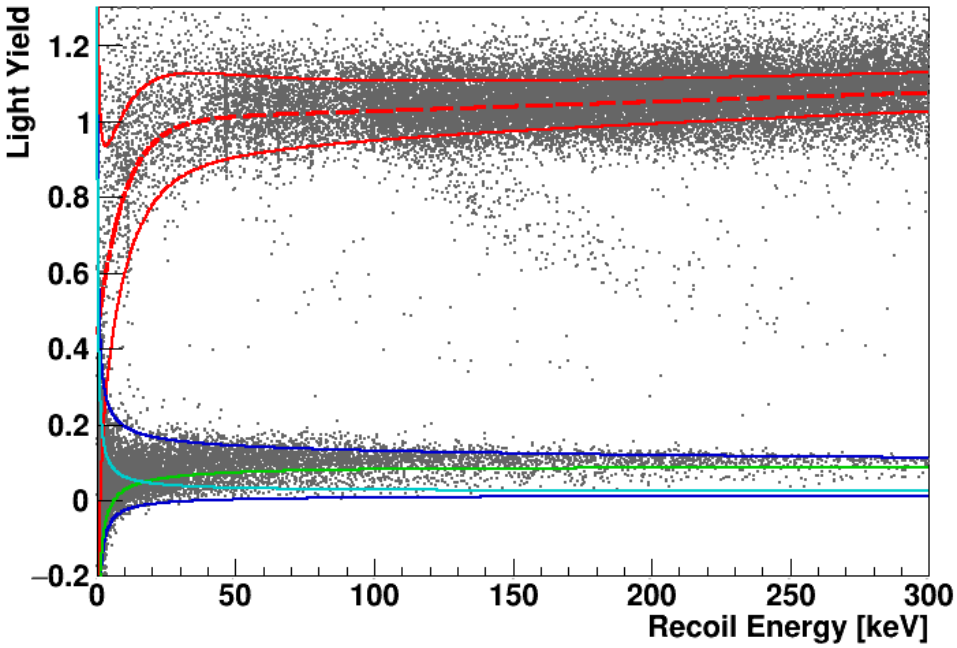

Figure 7.4: *Light yield - energy plot of the neutron calibration data set of TUM40. The red band is the model describing the e^-/γ-background as explained in the text. Nuclear recoils are expected to be located inside the dark blue band limited by the 90 % upper limit of the oxygen band and the 90 % lower limit of the tungsten band. Also drawn are the 90 % lower limit of the oxygen band (green) and the 90 % upper limit of the tungsten band (cyan). At higher energies ($\gtrsim$ 150 keV) neutrons mainly scatter off the lighter elements oxygen and calcium and, thus, the tungsten band is diluted.*

method is validated by this neutron calibration data set.

In figure 7.5 a zoom of the light yield - energy plot into the energy region below 50 keV is depicted for TUM40 (a) and Lise (b). In both plots the respective e^-/γ-band (red) and the nuclear-recoil band (blue) are included. Due to the different scaling of the y-axes visibly it seems that the bands of TUM40 are broader compared to Lise but indeed, it is the other way around. This is mainly caused by the bad energy resolution of the light detector Enrico. Therefore, the bands overlap in Lise more strongly but nonetheless, in both modules the obtained band model describes the data well.

7.3.2 Event-Type Dependent Template-Fit RMS Distribution

As already explained in section 5.3.8 there is a slight pulse-shape difference expected between pulses induced by electron and nuclear recoils. Since the template is created from electron recoils, an enhanced RMS value might be observed for nuclear recoils. In addition, the applied RMS cut is based on the observed distribution of the RMS parameter, where the majority of all pulses are created by electron recoils. Thus, it might be possible to unintentionally remove a large fraction of nuclear recoil events. This section focuses on the RMS difference of electron and nuclear recoils and its influence on Dark Matter searches.

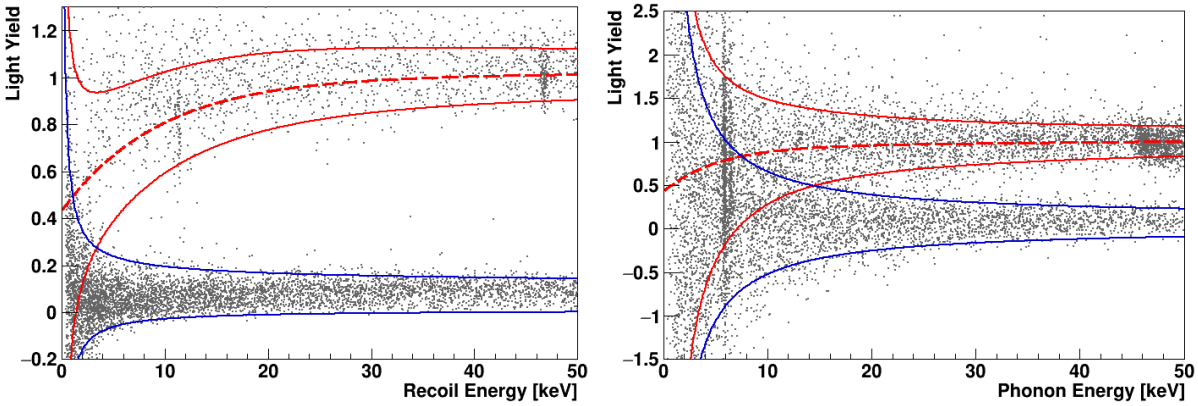

(a) TUM40 *(b) Lise*

Figure 7.5: *Light yield - energy plots of TUM40 (a) and Lise (b) for energies below 50 keV (see footnote 17 on page 80). Also depicted are the respective e^-/γ-bands in red, and the nuclear-recoil bands in blue. Please note the different scales of the two y-axis and that the band width of Lise is broader compared to TUM40. Consequently, the two bands intersect at considerably higher energies ($\sim$ 14.5 keV) for Lise compared to TUM40, where this point is at $\sim$ 3.5 keV.*

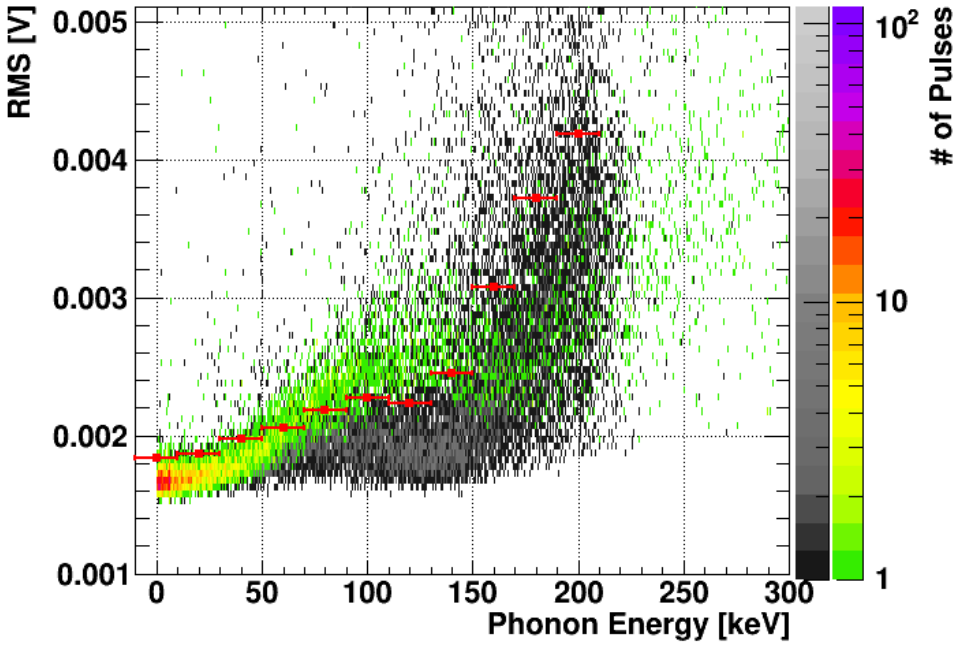

Figure 7.6: *RMS distribution of nuclear-recoil (color scale) and electron-recoil (gray scale) candidates for the neutron calibration data set of Lise. Also depicted is the cut limit determined in the blind data set (red data points with error bars, see also table D.3c in the appendix). Starting at $\sim$ 50 keV the mean value of the RMS distribution of nuclear recoils increases. At $\sim$ 100 keV the majority of all nuclear recoils are above the cut limit and, thus, are removed.*

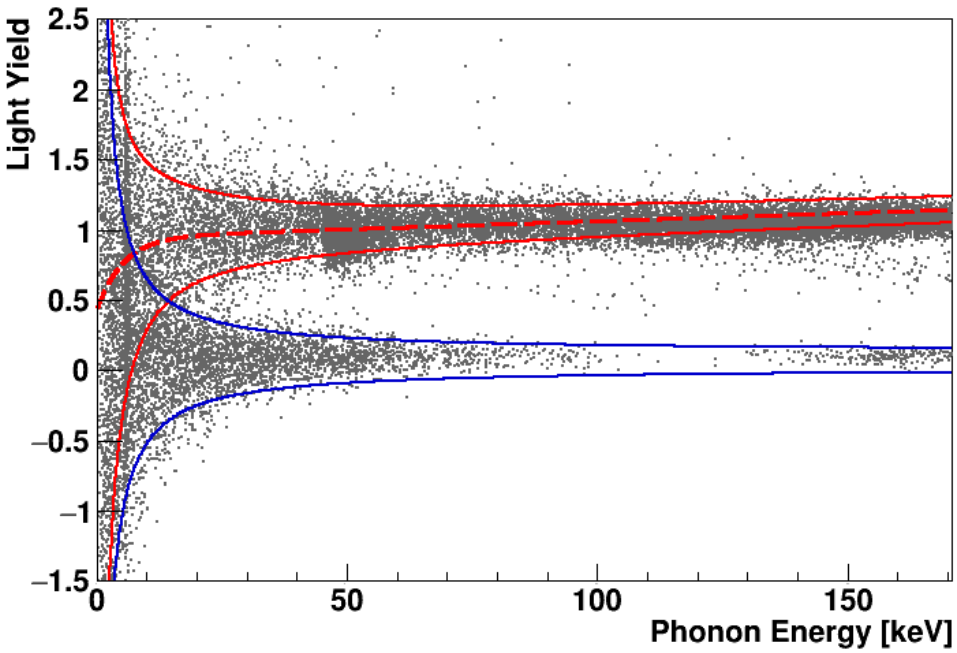

Figure 7.7: *Light yield - energy plot of the neutron calibration data of Lise (see footnote 17 on page 80). The red band is the model describing the e^-/γ-background while the nuclear-recoil band is drawn in blue. The increased RMS value for nuclear recoils (see figure 7.6) results for energies between $\sim$ 100 keV and $\sim$ 140 keV in a observable decrease of the number of events in the nuclear-recoil band. Due to an intrinsic ^{210}Pb-contamination in Lise at $\sim$ 46 keV a peak is observed in the e^-/γ-band, while at higher energies the background is enhanced due to the used AmBe-source (see figure 7.3).*

In figure 7.6 the RMS distributions for e^-/γ-events (gray scale) and neutron induced events (color scale) observed in the neutron calibration data of the detector Lise are depicted. A simple light-yield cut is applied to separate the two different event populations. In this simple analysis, events with a light yield ≤ 0.5 are considered as neutron candidates, while events with light yield > 0.5 are tagged as candidates for electron recoils. Indeed, a difference between both populations is observed but is not completely understood up to now. Starting at energies of $\sim$ 50 keV the mean RMS value of nuclear recoils increases more strongly compared to that of electron recoils. However, at $\sim$ 150 keV the difference relaxes back to the observed distribution for electron-recoil candidates.

Also depicted as red data points (with error bars) in figure 7.6 are the cut values automatically determined in the blind data set of Lise (see section 5.3.8 and table D.3c in the appendix). In the energy range below 170 keV in total 24 869 γ-candidates and 8 694 neutron-candidates are observed before the cut is applied and thereof 20 399 and 5 892 events survive, respectively. Thus, the energy independent surviving fraction is 82.03 % for γ-candidates and only 67.77 % for neutron candidates. For energies between $\sim$ 100 keV and $\sim$ 140 keV the majority of the neutron induced events is removed by the RMS cut.

As depicted in figure 7.7 this results in an observable decrease of the number of events up to a complete removal of the nuclear recoil population, while in the same energy region electron

recoils are not strongly affected. This is discussed in more detail in the remaining part of this section. As for TUM40, also for Lise the calculated nuclear recoil band (blue) describes the measured location of neutron induced events well.

It has to be noted, that this "removal effect" is not caused by the newly developed cut-limit-determination method but is an effect of the detector and the template fit. It is also present in other analyses of Lise [150, 151] and, furthermore, also in the detector TUM38. For TUM40 nothing comparable is observed (see figure 7.3) and also VK27 and VK28 are not affected.

There are several ways to deal with this observation: firstly, the cut limit can be released to not remove the nuclear recoil events at high energies. While this solution is easy to implement for a manually chosen cut limit it is hardly possible with the automatic determination method since the RMS distributions of both populations in Lise seem to be very different for energies between $\sim 50\,\mathrm{keV}$ and $\sim 150\,\mathrm{keV}$ (see figure 7.6).

However, at the low energies of interest for Dark Matter searches no large deviation between both populations is observed in figure 7.6. Thus, a cross-check of the fraction surviving the RMS cut for both populations is performed and the result is depicted in figure 7.8. While the fraction of nuclear recoils surviving the cut is depicted as blue data points, electron recoils are marked in red. As already described before, starting at $\sim 50\,\mathrm{keV}$ a large fraction of nuclear recoil events is removed by the RMS cut. In the energy bin ranging from 110 keV to 130 keV a minimal surviving probability for the RMS cut of only $\sim 1.3\,\%$ for neutron candidates is observed. Also for electron recoils a slight decrease of the surviving probability with increasing energy is observed. However, in the energy range relevant for Dark Matter searches ($< 40\,\mathrm{keV}$) only a negligible difference of a few percent is observed between both populations.

In figure 7.9 the corresponding plot for the neutron calibration data of TUM38 is depicted. Again, for electron-recoil candidates depicted in red a modest drop with increasing energy is observed. Similar to the situation in Lise starting at $\sim 65\,\mathrm{keV}$ a large fraction of nuclear-recoil candidates (blue) is removed from the RMS cut. The minimum surviving probability of $\sim 2.3\,\%$ is achieved in the energy bin around $\sim 140\,\mathrm{keV}$ Interestingly, the surviving probability increases again and at higher energies $\sim 92.4\,\%$ of all nuclear-recoil candidates survive.

However, as for Lise also for TUM38 for the relevant energy range for Dark Matter search ($\lesssim 40\,\mathrm{keV}$) no significant difference between both populations is observed. In conclusion, despite the removal of high-energetic nuclear recoil events it is valid to apply the RMS cut to the Dark Matter data set of Lise and TUM38.

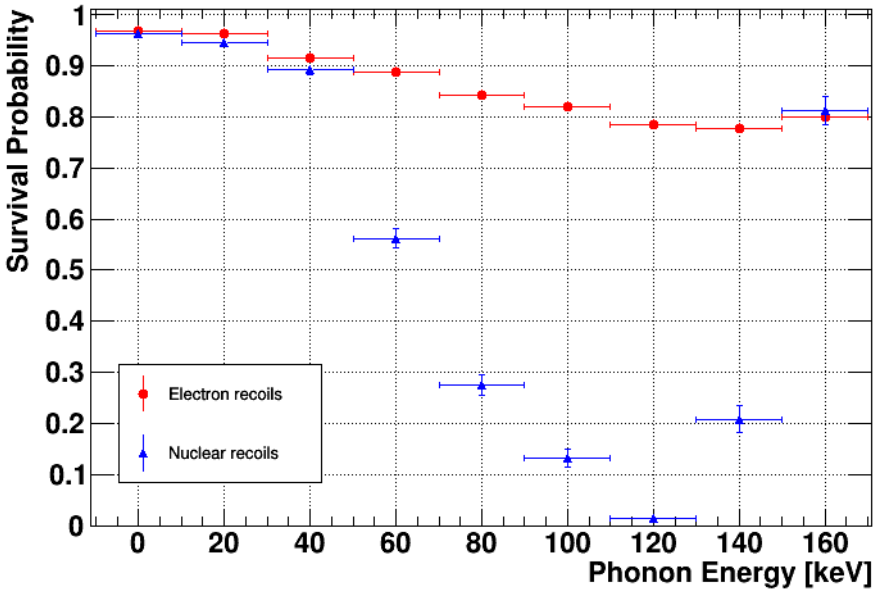

Figure 7.8: *Survival probability of the RMS cut of Lise (values determined based on data of the blind data set) for neutron (blue) and electron (red) recoils. For electron recoils a slight decrease with increasing energy is observed. Starting at $\sim 50\,keV$ a large fraction of nuclear recoils is removed by the RMS cut. However, in the energy range relevant for Dark Matter searches ($< 40\,keV$) no strong deviation between both event populations is observed.*

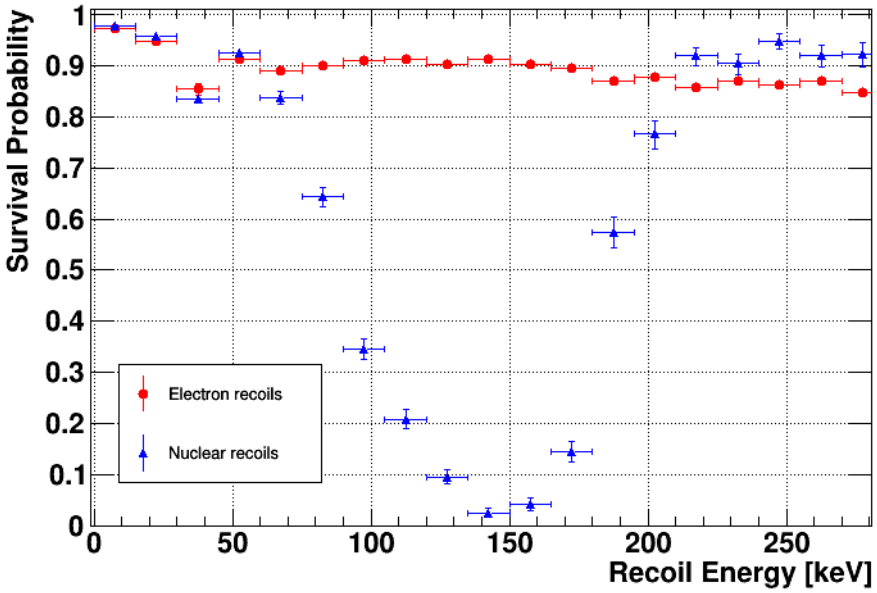

Figure 7.9: *Survival probability of the RMS cut of TUM38 for neutron (blue) and electron (red) recoils. As for Lise also for electron recoils of TUM38 a modest decrease with increasing energy is observed. Starting at $\sim 65\,keV$ a large fraction of nuclear recoils is removed by the RMS cut. However, as for Lise also in TUM38 in the energy range relevant for Dark Matter searches ($< 40\,keV$) no strong deviation between both event populations is observed.*

8 Exclusion Limits

As long as no clear signal of Dark Matter particles is observed in the data set of an experiment, only upper limits constraining the possible WIMP-nucleon cross section σ_{WN} (see section 2.1) can be obtained. Thereby, the observed number of events in the given exposure, i.e. the product of measurement time and detector mass, is an important input. The less events are observed the stronger is the limit, i.e. the lower is the allowed cross section. These limits are the figure of merit when the performances of different (direct) Dark Matter search experiments are compared. Thus, the main topic of the high level analysis performed in the present work is the calculation of exclusion limits restricting the allowed parameter space in WIMP mass and WIMP-nucleon cross section for possible Dark Matter particles based on the obtained data.

In section 8.1 the statistical methods used by the direct Dark Matter community are briefly presented. Furthermore, the influence of changing several detector parameters on a generic limit is discussed. The actually used one-dimensional method to calculate an optimal limit in case of the presence of an unknown background is explained in more detail in section 8.2. Finally, in section 8.3 the acceptance region and the method to calculate the expectations are briefly described.

8.1 Statistical Methods and Generic Limit

The following discussion about the used statistical methods and the generic results of a direct detection experiment is mainly based on [152] and references therein. Various statistical methods are used in direct Dark Matter experiments to derive upper limits on the WIMP-nucleon cross section as a function of the Dark Matter mass or to claim a detection of Dark Matter. Thereby, the analysis has to consider two contributions, the Poisson distribution of the signal and the detector response together with its uncertainties due to unavoidable backgrounds. A detailed description of various statistical methods used in the Dark Matter community can be found in [153].

The first intuitive method used in experiments featuring a discrimination between different types of particles is the selection of a signal region, where the expected signal-to-background ratio is high. If the background distribution is known, e.g. from Monte Carlo simulations or by using calibration data, the expected background contribution can be calculated. By using a method developed by Feldman and Cousins, which is based on the likelihood ratio of Poisson distributions, either an exclusion limit (one sided confidence interval) or an interval representing the uncertainties on a possible signal (two sided confidence interval) can be computed [154].

However, if the background contribution is unknown or the uncertainty is too large Yellin's method to calculate an optimum limit can be used [155]. In the next section this method is

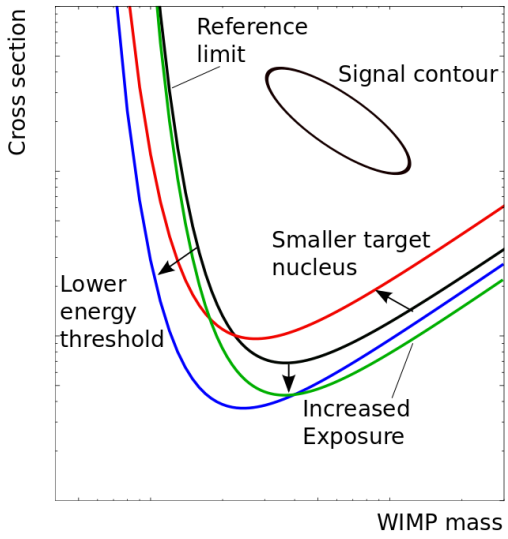

Figure 8.1: *Illustration of generic results of direct Dark Matter search experiments. If an excess of events is observed a signal contour (black closed curve), enclosing the constrained parameter space, is drawn. However, typically no or only a few events, comparable with the background expectation, are observed. Thus, only upper limits (open curves) constraining the WIMP-nucleon cross section as a function of the WIMP mass are obtained. While the black line shows the reference limit, the colored lines illustrate the effect on the achievable sensitivity of variations of the detector design or properties. Image taken from [152].*

explained in more detail, while here it is only important that the difference between expected signal shape and observed event distribution is exploited to obtain conservative results. However, by construction using this method always results in an upper limit (one-sided confidence interval) and, therefore, no signal discovery is possible.

Finally, when the full knowledge of the signal and the background distributions is available a maximum likelihood estimator could be used to obtain statistical conclusions (see e.g. [156]). Using a profile likelihood method it is possible to include systematic uncertainties of nuisance parameters, which are not of direct interest for the analysis. One advantage of this kind of method is the natural transition between the calculation of a limit (one-sided confidence interval) and a possible signal (two-sided confidence interval).

Independent of which method is used to calculate an upper limit on the WIMP-nucleon cross section or to obtain the allowed parameter space of a possible signal the result is commonly depicted as function of the WIMP mass. Figure 8.1 illustrates the parameter space and also contains an example of a generic signal contour (black closed curve), which encloses the allowed parameter space obtained from the calculation method. Furthermore, different upper limits are drawn in figure 8.1, where all points lying in the parameter space above the respective open curve are excluded. Three different typical regions are observable for all drawn limits. Due to the energy threshold of the detector the sensitivity is reduced at low WIMP masses. The minimum of the exclusion curve is defined by the kinematics of the scattering

process, and, thus, it depends on the target nucleus. The local Dark Matter density ρ_χ is a constant (see section 2.1) and, therefore, a lower overall number of particles must exist if the individual particles become heavier. Thus, the event rate scales overall with $1/m_\chi$, where m_χ is the Dark Matter particle mass. This explains the reduction of the sensitivity at large WIMP masses.

Two factors typically limit the achievable sensitivity: the exposure, which is the product of the target mass and the measurement time, and the observed background therein. Performing longer measurements or increasing the available target mass results in an increased exposure. However, compared to the reference limit (black line in figure 8.1) an increased exposure (green line) leads only to an improved sensitivity if the background does not scale up simultaneously. Therefore, typically better background reduction techniques are required when an experiment upgrades its target mass.

As explained in section 2.1 for the WIMP-nucleon scattering the event rate is expected to be proportional to the square of the nucleon number (A^2). However, using a lighter element also modifies the kinematics of the scattering process as well as it reduces the probable minimum velocity v_{min}. Thus, for an experiment with a lighter target nucleus (red line in figure 8.1), compared to the target material used to obtain the reference limit (black line), a shift of the maximum sensitivity to lighter WIMP masses is observed, while simultaneously, the overall sensitivity is reduced due to the lower event rate.

Finally, lowering the energy threshold of the detector would not only make it possible to extend the sensitivity to lighter WIMP masses but also to probe a lower minimum velocity v_{min}. Thus, the observed limit (blue line) is shifted towards smaller cross sections as well as to lower WIMP masses compared to the reference limit (black line). Simultaneously, due to the exponential rise of the expected recoil-energy spectrum a higher rate and, thus, a lower limit is observed for all WIMP masses. However, reducing the energy threshold of a real detector is – if at all possible – not an easy task.

8.2 Yellin's Statistical Methods

In this section the above-mentioned statistical methods developed by Yellin and used in the present work are explained in more detail. As a first step, in the relevant parameter space of discrimination parameter and energy deposited a signal region is defined and all events therein are considered as potential signal. This allowed region is designated as *acceptance region* and the actually chosen boundaries are explained in section 8.3. Here it is only important that the events considered are used to calculate an upper limit on the WIMP-nucleon cross section. The basic idea behind this limit calculation is, that for a given Dark Matter particle mass in the obtained exposure a certain cross section leads to a certain amount of events in the acceptance region. This expectation is statistically compared to the observed number of events. Cross sections which lead to a number of events that is too high are ruled out with a certain confidence, if the expectation is above the number of observed events at this confidence level (C.L.).

Conventionally, for Dark Matter searches a confidence level of 90 % is chosen. Thereby, *frequentist statistics* (as opposed to a Bayesian interpretation) have to be applied and in this

statistic framework the meaning of an upper limit at a confidence interval of 90 % is the following: Imagine a large set of independent experiments, all identical to the single one actually performed in reality. For the outcome of each imaginary experiment a limit is calculated with a certain method. If for 90 % of these limits the true value of the cross section is below the actual limit the method provides a 90 % confidence level. Thus, the frequency of possible outcomes is stated and hence, the name of the framework. In contrast, Bayesian credible intervals are a statement about the degree of belief of the tested hypothesis inferred from Bayes' theorem. Consequently, only Bayesian statistics allow to compute the probability for a theoretical model to be true based on the observed data. A review about Bayesian analysis of several dark matter experiments is given in [157]. However, this is still less common for direct Dark Matter experiments.

By using Poissonian probabilities such a (frequentist) 90 % C.L. upper limit could be calculated based on the comparison between the expected and the observed numbers of events. However, usually not only signal events are observed in the acceptance region but, due to imperfect separation, also backgrounds may contribute. Thus, the total number of observed events is the sum of a potential signal and background events. In case the rate of background events is not known precisely no background subtraction is possible and the resulting limit based on the total number of events might be too conservative.

Yellin developed statistical methods to calculate an upper limit for such a situation where an unknown background is present in the data [155]. These methods are nowadays used by several direct detection experiments [152] like SuperCDMS, CRESST and PICO. These methods have in common, that in addition to the number of events they also take the distribution of all accepted events in a certain parameter (e.g. the recoil energy) into account and exploit the absence or low density of events in regions where a high signal contribution is expected. Thus, these methods can yield stronger limits than a procedure where only the total number of events is considered. Without loss of generality in the following it is assumed that the relevant parameter is the recoil energy for simplicity reasons.

In figure 8.2 a schematic example is depicted to visualize the basic concepts of these methods. A set of observed events with different recoil energies (blue histogram) is drawn together with the expected recoil-energy spectrum $\left.\frac{dR}{dE_R}\right|_{\text{exp}}$ for a certain Dark Matter mass and cross section (black solid line). Apparently, there is a difference in the observed and expected recoil-energy spectrum. Most likely the high-energetic events are induced by backgrounds and Yellin's methods, explained in the following, take this kind of information into account.

8.2.1 Maximum Gap Method

The first method is the so-called *maximum gap method* since it utilizes the maximum gap in the recoil energy between the different events. For a given set of N observed events with recoil energies E_i $(i = 1, \ldots, N)$ and the lower and upper boundary of the acceptance region (E_0 and E_{N+1}, respectively) the gaps (in energy) between any two adjacent events are searched. If the expected energy spectrum of the signal $\left.\frac{dR}{dE_R}\right|_{\text{exp}}$ is scaled by the measured exposure, for a given value of the WIMP-nucleon cross section σ_{WN} the "size" of the gap is equivalent to

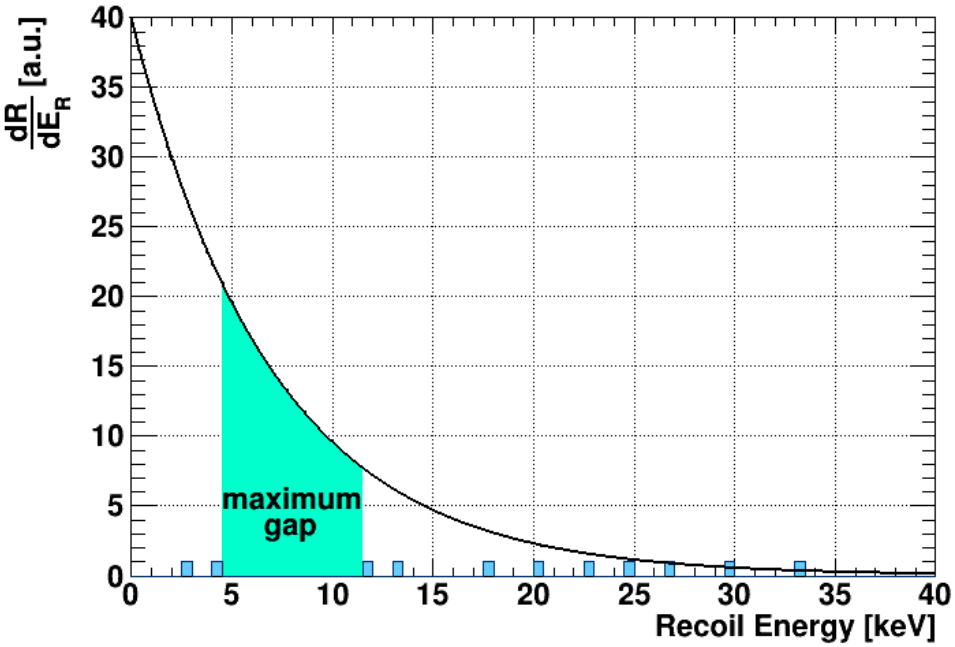

Figure 8.2: *Illustration of Yellin's maximum gap method [155]. Shown is the observed event distribution as a function of the recoil energy (blue histogram) and the expected signal spectrum* $\left.\frac{dR}{dE_R}\right|_{exp}$ *(black solid line). The maximum gap (shaded area) is the interval between two adjacent events, where the integral of the signal expectation (also denoted size) is maximal. Based on the non-observation of signal events in the maximum gap an upper limit is set. The method exploits the spectral difference between signal and background distribution and, thus, results in upper limits not too badly weakened by a large unknown background contribution [155].*

the number of expected events in the respective gap. The number of events is given by the following integration:

$$x_i \equiv x_i(\sigma_{\mathrm{WN}}) \coloneqq \int_{E_i}^{E_{i+1}} \left.\frac{dR(E_R,\sigma_{\mathrm{WN}})}{dE_R}\right|_{\mathrm{exp}} dE_R, \quad i = 0,\ldots,N. \tag{8.1}$$

The gap with the maximal size (the so-called *maximum gap*) is denoted by $\hat{x}$ in the following and is used to set the upper limit.

The maximum gap method exploits the observed difference between the spectral shapes of signal and background and, thus, is robust against unexpected background events as long as the observed background is distributed differently than the signal expectation. The maximum gap used to set the limit is preferably found in regions where the number of expected signal events is large but simultaneously only a few events are observed. On the contrary, in densely populated regions which are probably spoiled by a large number of background events, the maximum gap is only found when the signal expectation is very high as well.

The total number of expected events μ is defined as:

$$\mu \equiv \mu\left(\sigma_{\mathrm{WN}}\right) \coloneqq \int_{E_0}^{E_{N+1}} \left.\frac{dR(E_R, \sigma_{\mathrm{WN}})}{dE_R}\right|_{\mathrm{exp}} dE_R. \tag{8.2}$$

In [155] it is shown that the probability of the maximum gap being smaller than a particular value $\hat{x}$ is only a function of $\hat{x}$ and μ and given by

$$C_0(\hat{x}, \mu) = \sum_{k=0}^{m} \frac{(k\hat{x} - \mu)^k \, e^{(-k\hat{x})}}{k!} \cdot \left(1 + \frac{k}{\mu - k\hat{x}}\right), \tag{8.3}$$

where m is the greatest integer $\leq \mu/\hat{x}$.

The expected energy spectrum of the signal $\left.\frac{dR}{dE_R}\right|_{\mathrm{exp}}$ is directly proportional to the assumed cross section σ_{WN} and, thus, increasing the latter results in a larger value for $\hat{x}$ and μ. Therefore, at some point, $C_0(\hat{x}, \mu)$ reaches the value 0.9 and the respective value of σ_{WN} is then the desired upper limit σ_{90} at a 90 % confidence level. No Monte Carlo simulation is required to compute the confidence level, since the same analytical function for C_0 applies independently of the expected shape of the signal distribution [155].

8.2.2 Optimum Interval Method

The *optimum interval method* is a generalization of the maximum gap method for the case of a relatively high density of events in the data [155]. The difference is, that instead of searching only for the largest interval with $n = 0$ events inside (maximum gap method) also the largest intervals with $n = 1, 2, \ldots, N$ events inside are determined. Similar to the maximum gap method also here the "sizes" of the intervals correspond to the number of events expected therein and are denoted by $\hat{x}_n$. Out of these intervals the one which gives the most stringent result is used to set the upper limit.

Technically, this new approach requires new functions $C_n(\hat{x}_n, \mu)$, which describe, analogously to equation 8.3, the probability that the largest interval with n events inside has a size $\leq \hat{x}_n$. These functions can no longer be calculated analytically but have to be computed and tabulated with a Monte Carlo program [155]. Out of the set of intervals $\hat{x}_n$ there exists one with the largest value $C_{\mathrm{max}} \coloneqq \max\, C_n(\hat{x}_n, \mu)$ and this interval is used to set the upper limit.

Similar to the maximum gap method, also here the desired upper limit is the smallest cross section, for which the value of C_{max} is above a certain probability. However, a statistical penalty has to be paid for being allowed to determine C_{max} as the maximum of all $C_n(\hat{x}_n, \mu)$ a posteriori. Thus, for a 90 % confidence level it is not sufficient to increase the cross section until a value of 0.9 has been reached. Instead, C_{max} has to reach a value $\bar{C}(\mu) \geq 0.9$, whereby the values of the function $\bar{C}(\mu)$ are either tabulated with a Monte Carlo program (low statistics) or in case of high statistics an analytical approximation exists [155, 158]. In figure 8.3 the required values of $\bar{C}(\mu)$ are shown. In [155] and in [123] it is checked and confirmed that for the resulting limit, obtained by the method itself as well as the actual implementation used in the present work, the confidence level is truly 90 %.

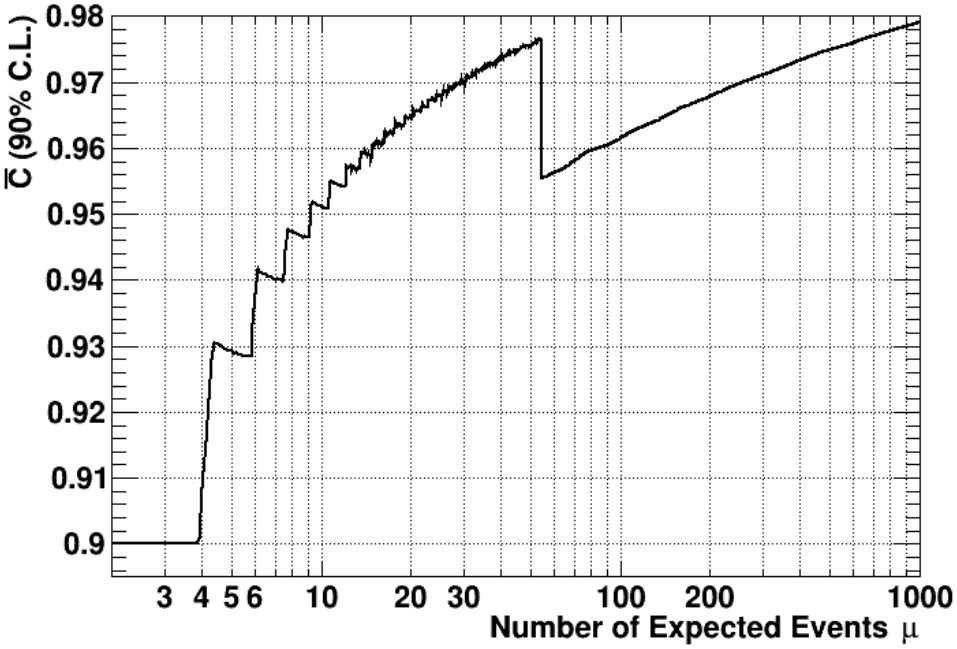

Figure 8.3: *Plot of $\bar{C}(\mu)$ used by Yellin's optimum interval method as a function of the total number of expected events μ. The values are either obtained by a Monte Carlo simulation (low statistics) or in case of high statistics by an analytical approximation [155, 158]. For the limit calculation the cross section σ_{WN} is increased until the value of C_{max} reaches the drawn value of $\bar{C}(\mu)$. Then, the cross section is the desired upper limit at a 90 % confidence level.*

In [155] the performance of the two different methods is compared to each other. On average the performance of the optimum interval method results in stronger limits than the maximum gap method, in particular for a larger number of observed events. However, this depends on the particular data set and in some cases also the maximum gap method might result in stronger limits. For the analysis performed in the present work, the optimum interval method is chosen a priori, since in all detectors analysed a relatively large number of events is observed.

To conclude this section about the two Yellin methods the main advantages of these methods are summarized:

- There is no influence caused by binning of the data, since the unbinned data set is handled by the algorithms.
- Both algorithms are relatively insensitive to small changes in the accepted energy range since this will only change the maximum gap/optimum interval if the latter extends to the lower or upper energy threshold of the accepted range.
- A difference in the spectral shape of signal and background distributions is inherently exploited by Yellin's methods. Therefore, background events, which are distributed differently than the expected signal distribution, weaken the upper limit less compared to methods, where only the total number of observed events is considered.

8.3 Acceptance Region and Signal Expectation

In section 2.1 it is explained how the expected recoil spectrum for a given WIMP mass is calculated. It is discussed, that for high transferred energies the influence of the form factor dominates and that several other detector effects, like e.g. energy resolution and energy threshold, have to be taken into account when a real detector is considered. In the present section, this theoretical spectrum is used as an input for the generation of an expected spectrum $\left.\frac{dR}{dE_R}\right|_{\text{exp}}$ which is then in turn used in Yellin's optimum interval method and compared to the observed recoil energy distribution. An additional aspect, which is explained below, is how the three nuclei of $CaWO_4$ and their different light yield distributions are considered in the one-dimensional Yellin methods.

8.3.1 Acceptance Region

As a first step the *acceptance region*, where a high number of signal events and, simultaneously, a low background contribution are expected, has to be defined. In CRESST-II the light yield is the discrimination parameter between sought-for nuclear recoils and the dominant backgrounds inducing electron recoils. Thus, the acceptance region is defined in the light yield - energy plane. In principle, the complete nuclear recoil band, consisting of the three bands for oxygen, calcium and tungsten is the region, where events induced by Dark Matter particles are expected to show up. Thus, it is desired to include as much as possible of this region to be able to detect as much as possible of the low event rate expected for Dark Matter particles.

However, due to the finite detector resolution of both phonon and light detectors the observed bands have a finite width whereby the bands are broader at lower energies (see chapter 7). Therefore, at the low energies of interest for Dark Matter searches ($\lesssim 40\,\text{keV}$) the nuclear recoil band overlaps to some extent with the e^-/γ-band. Thus, it is expected that with increasing light yield more and more e^-/γ-events leak into the nuclear recoil band. This overlap strongly depends on the module and, in particular, on the respective detector performance.

In order to reduce the leakage from the e^-/γ-band, in [127, 159] the upper limit of the acceptance region is set to the mean line of the oxygen band. The lower boundary of the acceptance region is set to the 90 % lower boundary of the tungsten band. Thus, only $\sim 50\,\%$ of the recoils scattering off oxygen are expected to be located in the acceptance region. For the two other constituents the fraction is higher but dependent on the recoil energy and the mass of the Dark Matter particle.

Based on the data of the training set of TUM40, for different acceptance regions exclusion limits were computed, whereby the above-mentioned choice results in the best, i.e. lowest, upper limit [127]. The influence of the choice, which definition for the acceptance region is used, on the final results has been studied in [123]. For reasons of comparability, in the present work for the calculation of the exclusion limits of all detectors analysed the above-defined acceptance region is used.

8.3.2 Expected Recoil-Energy Spectrum Observed in a Real Detector

As a first step towards the expected recoil-energy spectrum observed in a real detector, the expected (WIMP-mass dependent) distribution of WIMP-induced events in the light yield (LY) - energy plane can be defined. Therefore, the two-dimensional density function $\rho\,(E_R, LY)$ is used

$$\rho\,(E_R, LY) \equiv \frac{\partial^2 R(E_R, LY)}{\partial E_R\,\partial LY}. \tag{8.4}$$

Within the observed exposure X (given in units of kg d) of the respective detector the number of expected events in a small two-dimensional bin $(E_R; E_R + dE_R)/(LY; LY + dLY)$ should be given by $\rho\,(E_R, LY)\,dE_R\,dLY$. Both ingredients required for the construction of such a function have already been introduced for the case of a single type of target nuclei. The differential rate $\left.\frac{dR}{dE_R}\right|_{\text{acc}}$, which already contains the effects caused by the finite energy resolution and energy threshold, is defined by equation 2.27. In addition, it is discussed in chapter 7 that nuclear recoils are observed in a roughly horizontal band, whereby the mean $LY\,(E_R)$ and width $\sigma\,(E_R)$ are energy and nucleus dependent. Under the assumption that the events of a certain type are Gaussian distributed in the light yield around the calculated mean of the band the desired distribution function takes the following form:

$$\rho^{\text{QF}}\,(E_R, LY) = X \cdot \left.\frac{dR(E_R)}{dE_R}\right|_{\text{acc}} \cdot \frac{1}{\sqrt{2\pi}\;\sigma^{\text{QF}}_{\text{yield}}(E_R)}\;\exp\left(-\frac{\left(LY - LY^{\text{QF}}(E_R)\right)^2}{2\left(\sigma^{\text{QF}}_{\text{yield}}(E_R)\right)^2}\right). \tag{8.5}$$

Thereby, $LY^{\text{QF}}(E_R)$ is the mean line and $\sigma^{\text{QF}}_{\text{yield}}$ is the width of the quenched band in the light yield - energy plane as discussed in detail in chapter 7. Please note, that in general also the quenching factor $\text{QF}_x\,(E_R)$ of the particle x is energy dependent (see section 4.5), but in the notation this dependency is dropped for simplicity reasons. Conventionally, the differential rate $\frac{dR(E_R)}{dE_R}$ is given in units of the exposure X. However, the density function $\rho^{\text{QF}}\,(E_R, LY)$ as defined here includes the exposure X for reasons of convenience.

The generalization of this approach to define $\rho^{\text{QF}}\,(E_R, LY)$ for a target material made of in total M different constituents is straightforward. Each element m makes up a certain mass fraction x_m of the total mass and hence, of the total exposure. Also the energy dependent quenching factor $\text{QF}_m\,(E)$ is different for each constituent. However, the number of expected events in a certain bin in the light yield - energy plane is just the sum of the different event numbers expected in this region for the constituents. Thus, the total expected density distribution is given by

$$\rho\,(E_R, LY) = \sum_{m=1}^{M} x_m \cdot \rho^{\text{QF}_m}\,(E_R, LY)\,, \tag{8.6}$$

where the partial densities $\rho^{QF_m}\,(E_R, LY)$ are defined by equation 8.5 and calculated for the total obtained exposure. The different interaction probabilities expected for WIMPs scattering off target nuclei are automatically taken into account by using the expected energy spectrum

$\frac{dR(E_R)}{dE_R}$ of the respective nucleus for the evaluation of the partial densities. Via the differential rate, the expected signal density $\rho(E_R, LY)$ depends linearly on the WIMP-nucleon cross section σ_{WN}:

$$\rho(E_R, LY) = \sigma_{\mathrm{WN}} \cdot \rho^{1\mathrm{pb}}(E_R, LY), \tag{8.7}$$

where $\rho^{1\mathrm{pb}}(E_R, LY)$ is the expected density for a reference cross section of 1 pb.

In $CaWO_4$, which consists of the three nuclei oxygen (O), calcium (Ca) and tungsten (W), the mass fractions are:

$$x_{\mathrm{Ca}} = 0.1392, \quad x_{\mathrm{O}} = 0.2223, \quad x_{\mathrm{W}} = 0.6385. \tag{8.8}$$

An image of the expected total signal density as well as the partial densities for a WIMP scattering off $CaWO_4$ is given in [44].

For the two previously explained one-dimensional Yellin's methods the expected energy spectrum and not the signal density is required as an input. Thus, the signal density has to be integrated over the light yield, whereby the integration boundaries are given by the light yield boundaries of the acceptance region. Finally, the obtained energy spectrum has to be multiplied by the signal survival probability to derive $\left.\frac{dR}{dE_R}\right|_{\mathrm{exp}}$, which is then compared by Yellin's methods to the observed energy spectrum of all accepted events.

The software to compute exclusion limits based on Yellin's statistical methods has been developed mainly during the works described in [44, 103, 123, 124]. In the present work, it is used to calculate the upper limits based on the data of the detectors analysed and the results are shown in chapter 9.

9 Results and Discussion

In the present chapter the results for all five modules analysed are presented and discussed. In several detectors it was required to adjust some minor issues of the analysis in particular to ensure a proper fit of the RMS distribution also in the complete data set. To reestablish the convergence of the fit in most detectors, it is sufficient to enlarge the energy-limit parameter. As a reminder, above this limit the bin width is doubled compared to the low energetic region (for more details see section 5.3.8). As this limit is set far above the energy region relevant for the Dark Matter search this is typically not discussed further. However, in the case of the module TUM38/Petrus further adjustments are required which are discussed in detail in section 9.3.

The chapter is structured in the following way: First, in section 9.1 the results of the analysis performed in the present work for Lise/Enrico is shown and compared to the published result of this module [159]. In section 9.2 the results of the overall best performing module TUM40/Michael are presented and the exclusion limit of the low-threshold analysis is compared to other limits obtained by CRESST. In the sections 9.3 – 9.5 the results of the three modules TUM38/Petrus, VK27/Diogenes and VK28/Zam, respectively, are discussed. In particular, in these three modules an excess of events in the acceptance region is observed. Therefore, in section 9.6 possible sources for these low light-yield events are discussed. The radioactive contamination observed in the TUM-grown crystals TUM38 and TUM40 are compared in section 9.7. Finally, to summarize this chapter the parameter space containing recent results of various direct Dark Matter searches is shown in section 9.8.

9.1 Module Lise/Enrico

The module Lise/Enrico, where Lise is the phonon detector and Enrico the corresponding light detector, is of conventional design (see section 3.2). In this design not all parts inside the module housing are scintillating or active (e.g. the holding clamps, see section 3.4.1). Thus, a surface α-contamination can potentially lead to background events, which mimic WIMP recoils. Therefore, all detectors of the conventional design are excluded from the high mass Dark Matter analysis ($\gtrsim 10\,\mathrm{GeV}$), where a background free region of interest (ROI) is favored. However, due to the finite resolution of the detectors (in particular of the light detectors) the different bands in the light yield - energy plane overlap at low energies. Thus, an increased background contribution is anyhow expected at low energies. Therefore, whenever a dedicated low-threshold analysis is performed the request of an almost background-free ROI is relaxed. In this case it is beneficial to include modules of conventional design if the threshold of these modules is considerably lower than the one of the alternative designs. As mentioned in section 5.1, Lise features the lowest trigger threshold (308 eV) of all phonon

detectors operated in CRESST-II phase 2 and, thus, is analysed in a dedicated low-threshold analysis.

Beginning of 2016 the CRESST collaboration published a low-threshold analysis solely based on this single module [159]. The present analysis is one of four independent analyses performed to cross-check and validate the complete analysis process starting from raw data to the final result. Based on the results of the training set of Lise, one analysis has been chosen a-priori, i.e. before un-blinding, to be used for the final publication. It has to be explicitly mentioned, that all analyses yield consistent results in the training set as well as in the final blind data set. Data collected during an exposure of in total 52 kg days are analysed and the results are presented in the following.

9.1.1 Signal Survival Probability

As explained in chapter 5, several cuts are performed to remove all kinds of invalid pulses from the data set and in particular to ensure that the energy reconstruction of all pulses is valid. The method to obtain the signal survival probability, i.e. the probability for a nuclear recoil event to survive the complete cut sequence, is discussed in section 5.4. There, one example of Lise is shown and cross-checked with neutron calibration data, whereby good agreement between both methods is found.

In figure 9.1 the signal survival probabilities for the blind data set of Lise are depicted. The different curves are the resulting signal survival probabilities after successive application of the different selection criteria. Firstly, the combination of rate and stability cut (purple solid line) removes all periods of the data taking, where one or even both detectors of the respective module were not fully functional. As all pulses recorded during these time periods are removed, no energy dependency is expected and observed. The same is valid for the coincidence cuts (blue solid line), which remove all events which are coincident with another detector (cryogenic module or muon veto). For the majority of these events random coincidences are removed and, thus, no energy dependency is expected. The largest fraction of events is removed by the data quality cuts (red solid curve), which introduce a slight energy dependency at low energies ($\lesssim 1\,\text{keV}$)[45]. There the determination of some pulse parameters is already limited due to the low signal-to-noise ratio, resulting in a larger fraction of removed events compared to higher energies (see section 5.4.1). The final signal survival probability is obtained after application of the pulse shape cuts (black curve). This last cut sequence removes another considerable fraction of signal events at low energies ($\lesssim 4\,\text{keV}$). As explained in section 6.6 stringent cuts are applied to remove all TES-carrier pulses. At low energies, these cuts are mainly based on the performance of multilayer perceptrons (MLPs), trained with simulated pulses. The peculiar shape of the curve is explained in section 6.7 and is basically caused by the application of these two MLP based cuts. At the threshold energy of 308 eV of Lise only $\sim 6\,\%$ of all signal events survive the complete cut sequence, which is half the value of 12 % reported in [159].

[45] The steep drop of the signal survival probability starting at $\sim 0.4\,\text{keV}$ is due to the trigger threshold of the detector.

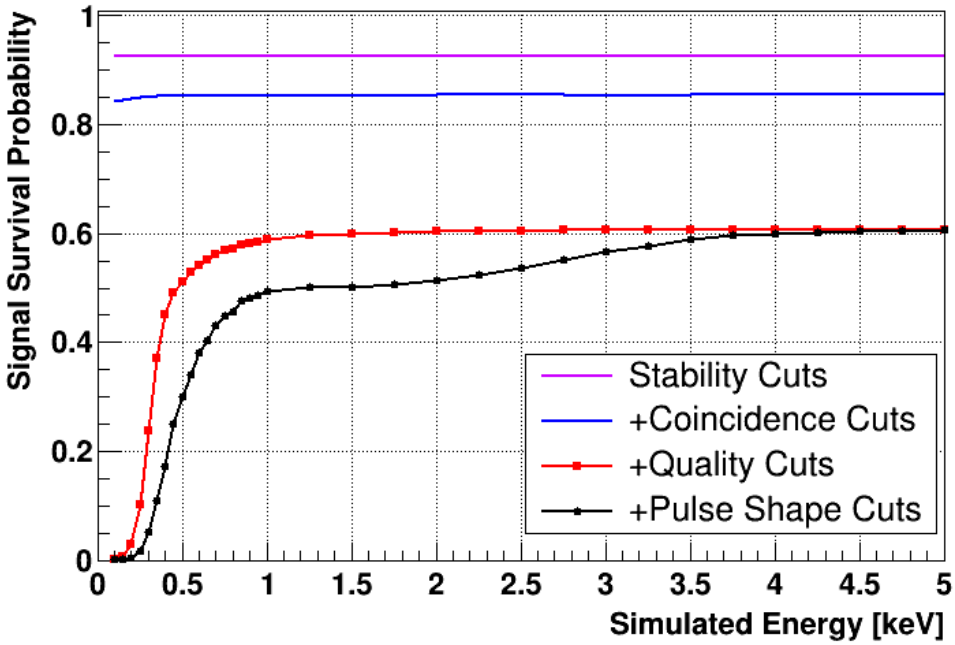

Figure 9.1: *Signal survival probabilities for the blind data-set of the module Lise/Enrico after successive application of different selection criteria. The stability cuts (purple curve) and the coincidence cuts (blue curve) remove a fraction of events independent of the energy. The biggest fraction of events is removed by the data quality cuts (red curve). Besides the drop off at the trigger threshold of* 308 eV *a slightly larger fraction of events is removed by the data quality cuts at low energies. The final cut efficiency is obtained after application of the pulse shape cuts (black curve), which removes a significant fraction of events at low energies. At the threshold a final cut acceptance of only* ~ 6 *% survives the complete cut sequence. In section 5.4 the method to determine these probability curves is explained and also cross-checked with neutron calibration data.*

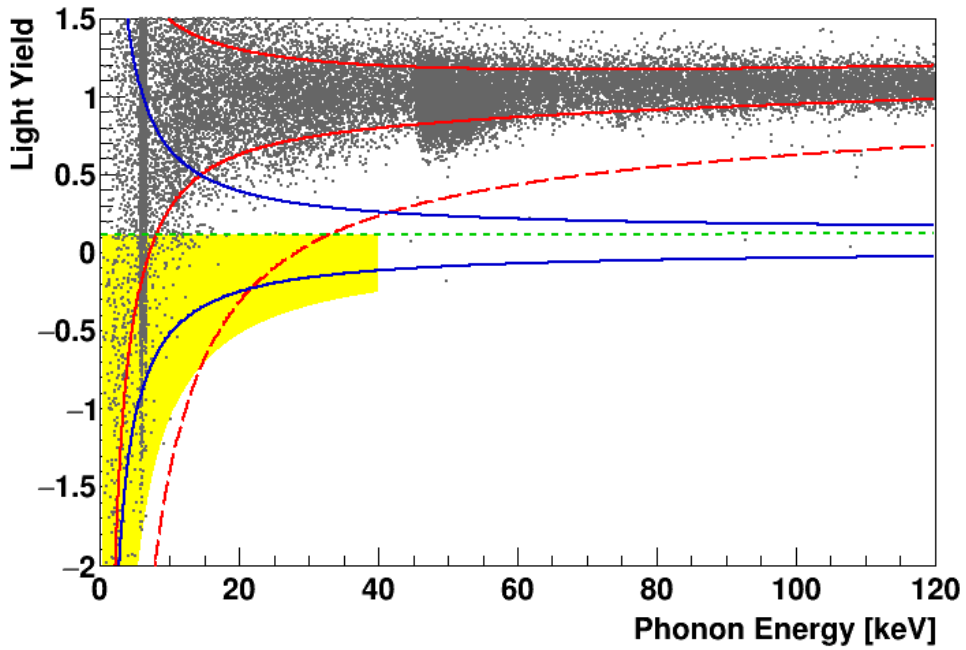

Figure 9.2: *Light yield - energy plot of the blind data set of Lise. In red different limits of the e^-/γ-band are drawn: The solid lines restrict the central 80 % e^-/γ-band and correspond to its 90 % upper and lower limit, while the red dashed line is its lower 5 σ boundary. The blue solid lines mark the nuclear recoil band, where the upper line is the 90 % upper limit of the oxygen band and the lower line the lower 90 % limit of the tungsten band. The region of interest used for the Dark Matter analysis is highlighted in yellow. In energy it ranges from the energy threshold of 308 eV up to 40 keV. In the light yield coordinate it is restricted from the mean of the oxygen band (green dashed line) down to the lower 99.5 % line of the tungsten band. All events in this region are considered as potential WIMP events in the one-dimensional Yellin optimum interval method applied.*

9.1.2 Light Yield - Energy Plot

In figure 9.2 the light yield - energy plot for the blind data set of Lise (after application of all cuts) is depicted. Additionally, also different lines mark different limits of the expected bands (see chapter 7). The red solid lines restrict the central 80 % e^-/γ-band and correspond to its 90 % upper and lower limit, respectively. The red dashed line corresponds to the 5 σ lower limit of the e^-/γ-band below which no significant leakage is expected.

The nuclear recoil band is marked in blue, where the upper line corresponds to the upper 90 % limit of the oxygen band and the lower line to the 90 % lower limit of the tungsten band. Highlighted in yellow is the ROI used for the Dark Matter analysis. In energy it expands from the threshold of the detector (308 eV) up to an analysis threshold of 40 keV. Above this energy no significant Dark Matter contribution is expected anymore due to the strong influence of the form factor (see section 2.1). In the light-yield coordinate the ROI ranges from the center of the oxygen band (green dashed line) down to the 99.5 % lower limit of the tungsten band.

There are a few events below the 5 σ lower limit of the e^-/γ-band (red dashed line) indicat-

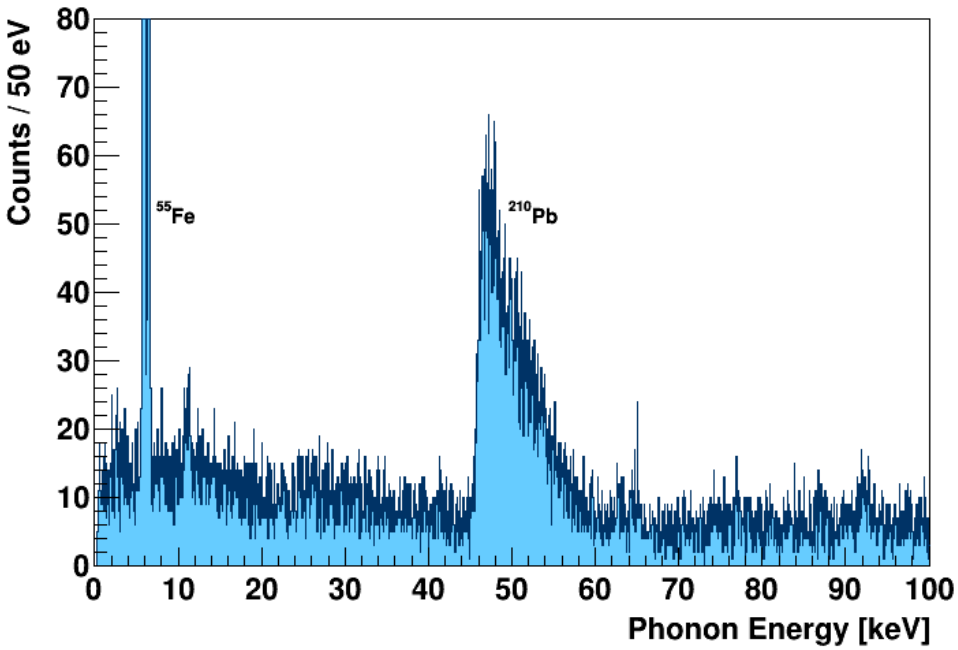

Figure 9.3: *Energy spectrum of Lise below* 100 *keV and truncated at* 80 *counts / 50 eV for clarity. Two prominent features are visible: Firstly, the* β*-spectrum of an intrinsic* ^{210}*Pb contamination ranging from* $\sim$ 46.5 *keV up to 63.5 keV is measured. Secondly, the two X-ray lines of* ^{55}*Mn at* 5.9 *keV and* 6.5 *keV are observable. They are caused by a* ^{55}*Fe-source, mounted in a near-by module, accidentally illuminating the absorber crystal of Lise. The total count rate in the energy region from 1 keV up to 40 keV is* 10.53 ± 0.09 *counts/(keV kg day). When the accidental illumination with the* ^{55}*Fe-source is excluded a value of only* 7.04 ± 0.08 *counts/(keV kg day) is obtained for the overall background level.*

ing the presence of an additional background source. As explained in section 3.4.1 due to a surface α-contamination events are induced with recoil energies of $\sim$ 103 keV. If the recoiling nucleus looses part of its energy before hitting the absorber crystal events with lower recoil energies are observable. For some events also the corresponding α-particle or light produced in the scintillating surroundings is detected resulting in a population of events near the $5\,\sigma$ limit of the e^-/γ-band. However, the four events above 40 keV and below the central line of the oxygen band are most probably due to background events where no additional light of the α-particle is observed.

Two prominent features are observable in the e^-/γ-band of Lise in figure 9.2 as well as in the energy spectrum below 100 keV, as depicted in figure 9.3. Firstly, there is an intrinsic contamination of the crystal with ^{210}Pb resulting in the large event population around $\sim$ 46.5 keV. ^{210}Pb is part of the natural decay chain of ^{238}U and decays under emission of a β-particle with a half-life of 22.3 a into ^{210}Bi [90]. In 84 % of the decays the resulting daughter nucleus is in an excited state and relaxes within less than 3 ns by emission of a $\sim$ 46.5 keV γ-ray. If the electron of the β-decay is not detected only the γ-line is observed, otherwise the endpoint of the resulting β-spectrum is at 63.5 keV. The observation of this additional high-energetic tail in Lise supports the assumption of an internal contamination, since for an external contamination

only the γ-line would be observed.

The second spectral feature visible in figure 9.2 and more clearly in figure 9.3 is a prominent line at ~ 6 keV. A detailed zoom into this energy region reveals a double-peak structure at the K_α and K_β X-ray energies of ^{55}Mn caused by the accidental illumination of the absorber crystal by a near-by ^{55}Fe-source[46]. Via electron capture ^{55}Fe decays into ^{55}Mn and the resulting vacancy in the electron shell is filled via emission of a characteristic X-ray [90]. In section 4.7.3 these two lines are used to monitor the long-term stability of the energy calibration.

There are a few other features in the e^-/γ-band (e.g. the Cu fluorescence line at ~ 8 keV), which are hardly visible in figure 9.3 due to the low activity and are of no particular interest here. The overall e^-/γ-background level in the energy region from 1 keV up to 40 keV is determined to be 10.53 ± 0.09 counts/(keV kg day). When the contribution of the accidental illumination with the ^{55}Fe-source is excluded a value of 7.04 ± 0.08 counts/(keV kg day) is obtained for the overall background level. Compared to the result obtained in [159] of 13.0 counts/(keV kg day) and 8.5 counts/(keV kg day), respectively, the values achieved in the present work are significantly lower.

9.1.3 Exclusion Limit of the Blind Data Set

As mentioned earlier (see section 7.1) the light detector Enrico has a worse performance compared to a standard light detector operated in CRESST-II and, thus, a large leakage into the ROI is observed. In the blind data set, in total 1318 events are located in the ROI for Dark Matter search (yellow region in figure 9.2). The corresponding energy spectrum is depicted in figure 9.4 and also shows the two characteristic lines caused by the ^{55}Fe-source. As explained in section 8.2 all accepted events are considered as WIMP events for the calculation of the one-dimensional Yellin's optimum interval exclusion limit. This results in a conservative exclusion curve, since also the considerable leakage, e.g., of the two ^{55}Mn X-ray lines, is treated as signal events.

In figure 9.5 the resulting 90 % C.L. exclusion limit on the WIMP-nucleon cross-section is shown for the present analysis as black solid line and compared to other results of CRESST-II. The published result of the blind data set of Lise is shown as red solid line, while the corresponding 1σ sensitivity expectation is the light red band [159]. To obtain this band 10000 Monte Carlo sets are created from an empirical model describing the observed background. For each of these mock-up data sets an exclusion limit is calculated and the region where ~ 68 % are located is marked by the band (for more details see [123]). The impact of the choice of reasonable light-yield boundaries on the resulting exclusion limits is in the order of these expected statistical fluctuations [123, 159]. In section 8.3 the actual choice for the light-yield boundaries of the acceptance region are discussed.

The exclusion limit obtained from the training set of TUM40 is drawn as red long-dashed line [127], while the re-analysis of the commissioning run of CRESST-II results in the red

[46] These radioactive sources are placed next to the light detectors of a few modules to be able to absolutely energy calibrate the respective detector. Typically, they are mounted such, that no X-ray can escape the module housing and, thus, they only irradiate the respective light detector. However, this does not seem to be the case for a module located close-by to Lise/Enrico.

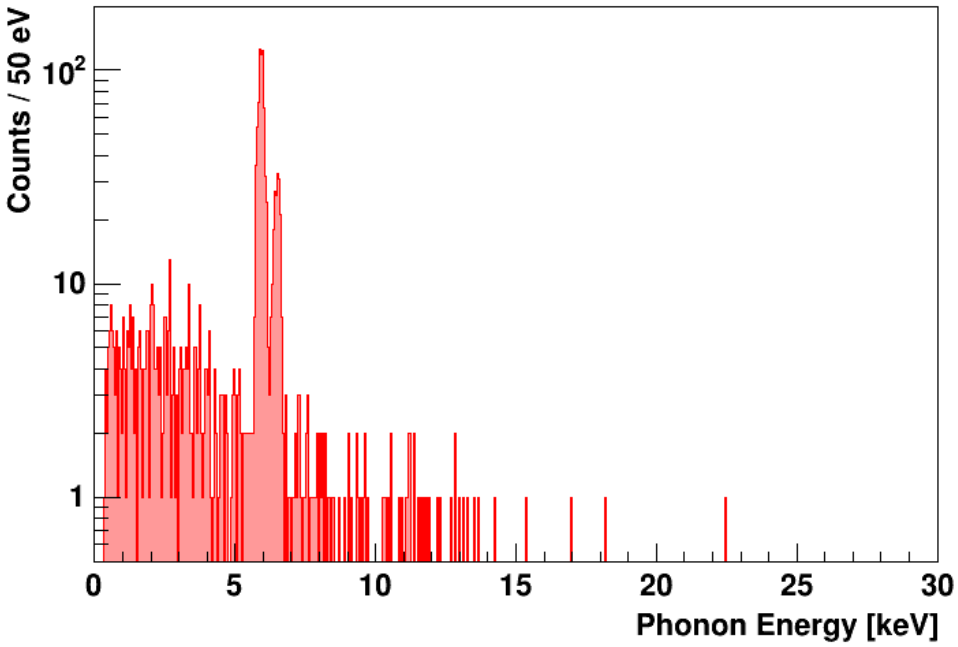

Figure 9.4: *Energy spectrum of all* 1 318 *events located in the ROI of Lise. Due to the worse light detector resolution of Enrico compared to a standard CRESST light detector a large fraction of leakage events from the e^-/γ-band is observed. Therefore, also in the energy spectrum of the accepted events the characteristic ^{55}Mn X-ray lines are visible at $\sim$ 5.9 keV and $\sim$ 6.5 keV. To be able to see more details the y-axis is drawn in a logarithmic scale. In the one-dimensional Yellin's optimum interval method, all accepted events are treated conservatively as signal events for the calculation of the 90 % C.L. exclusion limit on the WIMP-nucleon cross-section.*

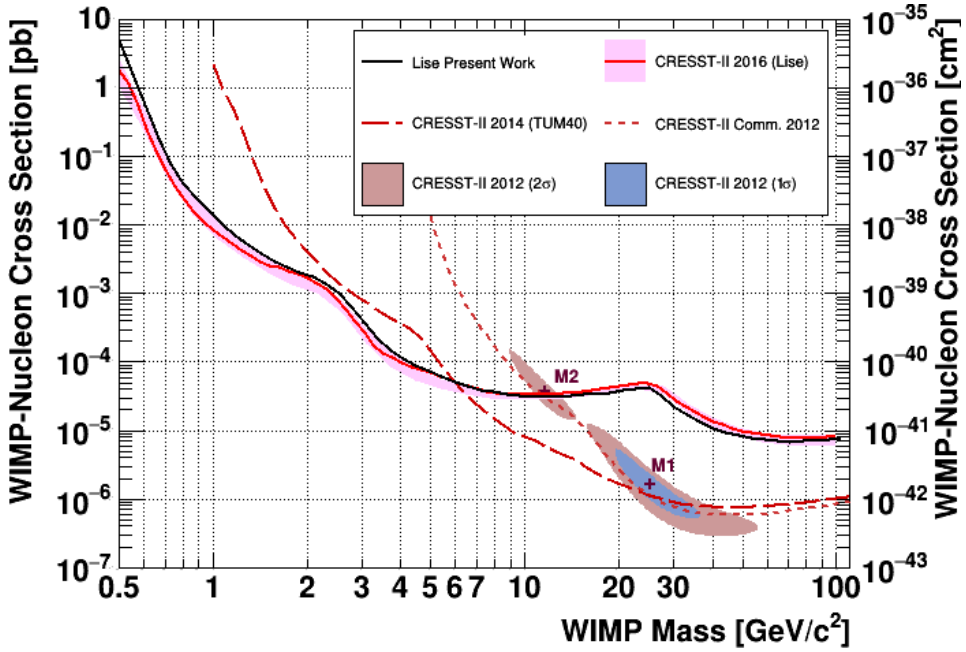

Figure 9.5: *Parameter space for elastic spin-independent WIMP-nucleon scattering containing several CRESST-II results. The favoured parameter space of CRESST-II phase 1 with the two likelihood maxima M1 and M2 is drawn as the shaded islands [107]. All drawn curves are 90 % C.L. exclusion limits of several other data sets of CRESST-II. The red dashed line is the result of the re-analysis of the commissioning run of CRESST-II [160]. The two published results of CRESST-II phase 2 are also drawn: the result of the training set of TUM40 (red long-dashed curve) [127] as well as the result of the blind data set of Lise (red solid curve) [159]. The light red band is the expected sensitivity for Lise based on an empirical background model. The black solid curve is the result of the present analysis of the blind data set of Lise. Within the expected statistical fluctuations both Lise results of the blind data set agree well. The present analysis results in a slightly worse exclusion limit compared to the published curve at low WIMP masses ($\lesssim 4\,\mathrm{GeV/c^2}$), while at higher masses ($\gtrsim 10\,\mathrm{GeV/c^2}$) a slightly better exclusion limit is obtained.*

dashed line [160]. The favoured parameter space of CRESST-II phase 1 with the two likelihood maxima M1 and M2 is drawn as the shaded islands [107] (see section 3.4 for more details).

As mentioned earlier in this section, the present analysis of the blind data set of Lise agrees well with the published result. At low WIMP masses ($\lesssim 4\,\mathrm{GeV}/c^2$) the published result is slightly better while at higher WIMP masses ($\gtrsim 10\,\mathrm{GeV}/c^2$) the present analysis performs marginally better. However, the deviations are in the order of the expected sensitivity fluctuations based on the empirical background model.

Due to the assumed A^2-dependency of the cross-section, heavy WIMPs are expected to mainly scatter off tungsten. However, for small WIMP masses the energy transferred to the tungsten nucleus drops below the energy threshold of the detector and, therefore, the dominant scattering partner changes (for more details see [123,159]). In both exclusion curves of Lise at a mass of $\sim 2.5\,\mathrm{GeV}/c^2$ the transition from tungsten (higher masses) to oxygen (lower masses) leads to a visible kink in the exclusion curve[47].

Compared to the exclusion limit obtained from the training set of TUM40 (red long-dashed line in figure 9.5) Lise does not have a competitive sensitivity at high WIMP masses. In particular in the mass range from 5–30 GeV/c^2 the curve obtained from Lise is almost flat due to the accidental illumination with the ^{55}Fe-source. Above $30\,\mathrm{GeV}/c^2$ the curve drops again since the optimum interval is found at energies above $\sim 6.5\,\mathrm{keV}$ and, thus, an enhancement in the sensitivity is achieved. At the highest WIMP masses drawn the exposure is already the limiting factor leading to a minimum of the exclusion limit at $\sim 70\,\mathrm{GeV}/c^2$. However, for light masses below $\sim 6\,\mathrm{GeV}/c^2$ new parameter space is excluded by this curve compared to TUM40. This improvement is mainly caused by the flat background down to the threshold of 308 eV observed in Lise. In case of the training set result of TUM40 the threshold is 603 eV and a rise at low energies ($\leq 1\,\mathrm{keV}$) is observed limiting the achievable sensitivity [127]. In section 9.8 the published limit of Lise (which is in agreement with the curve obtained in the present analysis) is compared to recent results of other direct Dark Matter search experiments.

9.2 Module TUM40/Michael

The module TUM40/Michael is the best overall performing module of CRESST-II phase 2. It is of the alternative module design, where the phonon detector is held by $CaWO_4$ sticks (see section 3.5.4) and, thus, features only scintillating or active surfaces inside the module housing. Furthermore, the trigger threshold of TUM40 is determined to be 609 eV in the blind and complete data set. In a subset of the blind data the threshold could be even lowered to 409 eV.

[47] Being related to the energy threshold the location of this transition point depends on the detector. In the exclusion curve of the training set of TUM40 (red long-dashed curve in figure 9.5) a kink is observed at $\sim 4.5\,\mathrm{GeV}/c^2$ [127].

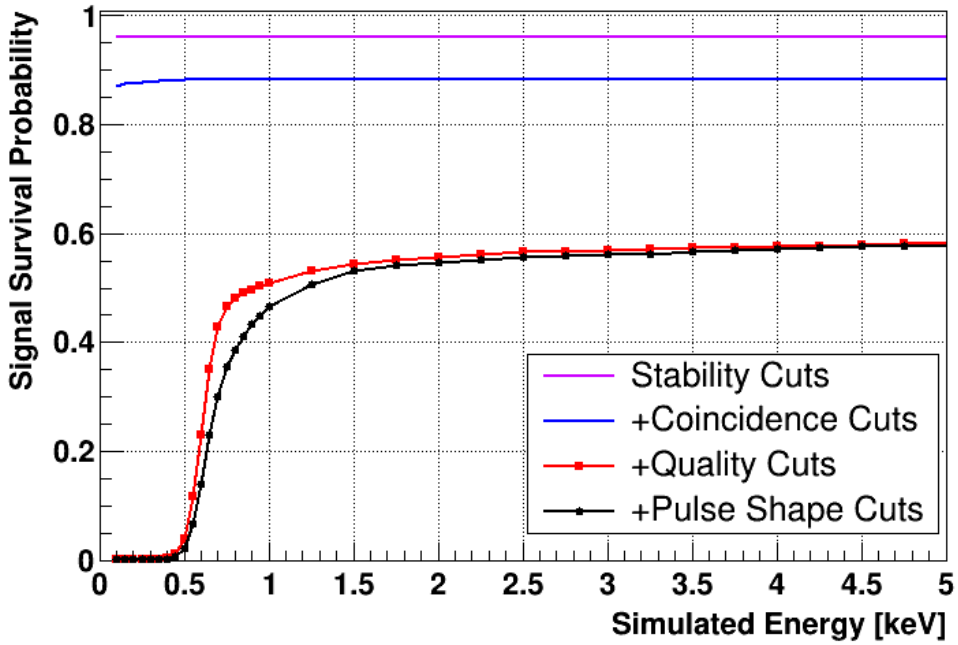

Figure 9.6: *Signal survival probabilities of the blind data-set of the module TUM40/Michael after successive application of the selection criteria. The largest fraction of events is removed by the data quality cuts (red solid line). Besides the sharp cut-off at the trigger threshold of 609 eV a second energy-dependency is observed at low energies starting already at* $\sim$ *1.5 keV. At the same energy also the pulse shape cuts remove a significant fraction of signal events resulting in the final cut efficiency curve (black solid line). Due to this considerable reduction only* $\sim$ *15 % of all events survive the complete cut series at the threshold.*

9.2.1 Results of the Blind Data Set

As for the module Lise/Enrico, also for TUM40/Michael a low-threshold analysis is performed. The results of this analysis are presented in the following.

Signal Survival Probability

For the module TUM40/Michael the signal survival probabilities after successive application of the selection criteria are depicted in figure 9.6. Compared to the curve obtained for Lise (see figure 9.1) in TUM40 the stability cuts (purple line, consisting of the rate and stability cuts) remove a lower fraction of events. The majority of the events removed by the coincidence cuts (blue curve) is caused by random coincidences. Thus, in TUM40 and Lise basically the same fraction of events is removed by this criterion. The data quality cuts (red line) ensure that the energy calibration of the pulses is valid and remove the largest fraction of events. Besides the cut-off at the trigger threshold also a slight energy dependency is introduced by this series of selection criteria (see section 5.4.1). The final cut acceptance (black curve) is obtained after application of the pulse shape cuts. Due to the large efforts performed in the present work only below $\sim$ 1.5 keV a considerable fraction of events is removed. Compared to

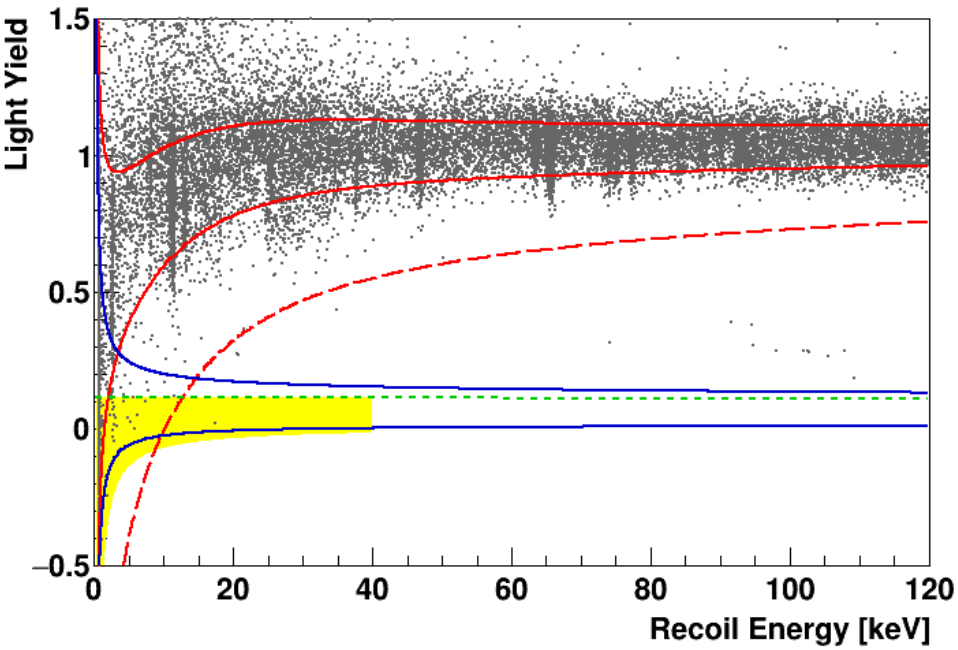

Figure 9.7: *Light yield - energy plot of the blind data set of the module TUM40/Michael. In red different limits of the e^-/γ-band are drawn: The solid lines restrict the central 80 % e^-/γ-band and correspond to its 90 % upper and lower limit, while the red dashed line is its lower 5 σ boundary. The blue solid lines mark the nuclear recoil band, where the upper line is the 90 % upper limit of the oxygen band and the lower line the lower 90 % limit of the tungsten band. The region of interest used for the Dark Matter analysis is highlighted in yellow. In energy, it ranges from the energy threshold of 609 eV up to 40 keV. In the light yield coordinate it is restricted from the mean of the oxygen band (green dashed line) down to the lower 99.5 % limit of the tungsten band. All events in this region are considered as potential WIMP events in the one-dimensional Yellin optimum interval method applied.*

the analysis performed in [127] this is a large improvement of the signal survival probability below $\sim$ 5 keV. For TUM40 a final signal survival probability of $\sim$ 15 % is achieved at the threshold energy of 609 eV, which is 2.5 times the fraction obtained for Lise in the present work. Compared to the final value stated in the published result of the training set of TUM40 a similarly large enhancement factor of 2.5 is found [127].

Light Yield - Energy Plane

The resulting scatter plot of the blind data set of TUM40 is depicted in figure 9.7. As for the plot of Lise also for TUM40 different light-yield bands are drawn: The red solid lines are the 90 % upper and lower limit of the e^-/γ-band, while the red dashed line is the 5 σ lower limit. The blue solid lines mark the nuclear recoil bands and correspond to the 90 % upper limit of the oxygen band and the 90 % lower limit of the tungsten band, respectively. As for Lise the yellow shaded area is the region of interest for the Dark Matter analysis. In the energy coordinate it expands from the threshold of the detector (609 eV) up to 40 keV. In the light-

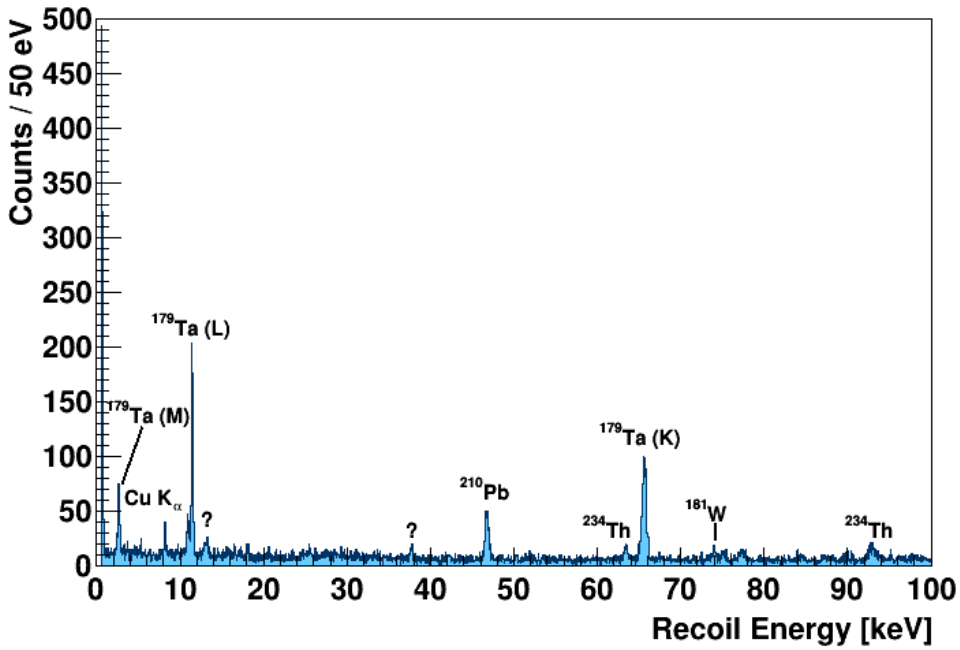

Figure 9.8: *Recoil-energy spectrum of all events below* 100 *keV in the blind data set of TUM40. The majority of all events is located inside the* e^-/γ*-band and, therefore, several* γ*-lines are observable. The origins of these lines are discussed in section 9.7. For TUM40 the overall background level in the energy region between* 1 *keV up to* 40 *keV is found to be* 3.74 ± 0.04 *counts/(keV kg day).*

yield coordinate a compromise between expected background leakage and maximal signal has to be chosen. Therefore, the upper limit is the central line of the oxygen band (green dashed line) while the lower limit corresponds to the 99.5 % lower limit of the tungsten band.

At energies of $\sim$ 100 keV (and slightly below) several events are observed between the nuclear recoil and the e^-/γ-band. These events are most probably caused by a decay of ^{210}Po on an inner surface (e.g. crystal or scintillating foil) inside the module housing. The resulting ^{206}Pb daughter nucleus can hit the detector and deposit its energy. The maximal recoil energy is 103 keV and, therefore, the events are clustered around this energy. The α-particle emitted in this decay might deposit part of its energy also in the phonon channel (e.g. while leaving the crystal). However, the majority of the energy is converted into light when the α-particle hits a scintillating inner surface. This results in a larger light yield of these events and due to this additional scintillation light these events are shifted out of the nuclear recoil band. However, this results in a slightly different pulse shape observed in the light detector and, thus, the majority of this kind of background events is removed by the cut on the RMS of the light detector. Nonetheless, as these events are in both coordinates, energy and light yield, well above the ROI they render no problem for Dark Matter searches. They are a direct prove that the veto for surface-background events works as intended by the module design.

Several line features are observable in the e^-/γ-band in figure 9.7 as well as in the energy spectrum below 100 keV as depicted in figure 9.8. The origins of these lines and their activities are discussed in detail in section 9.7. The overall background level in the energy region

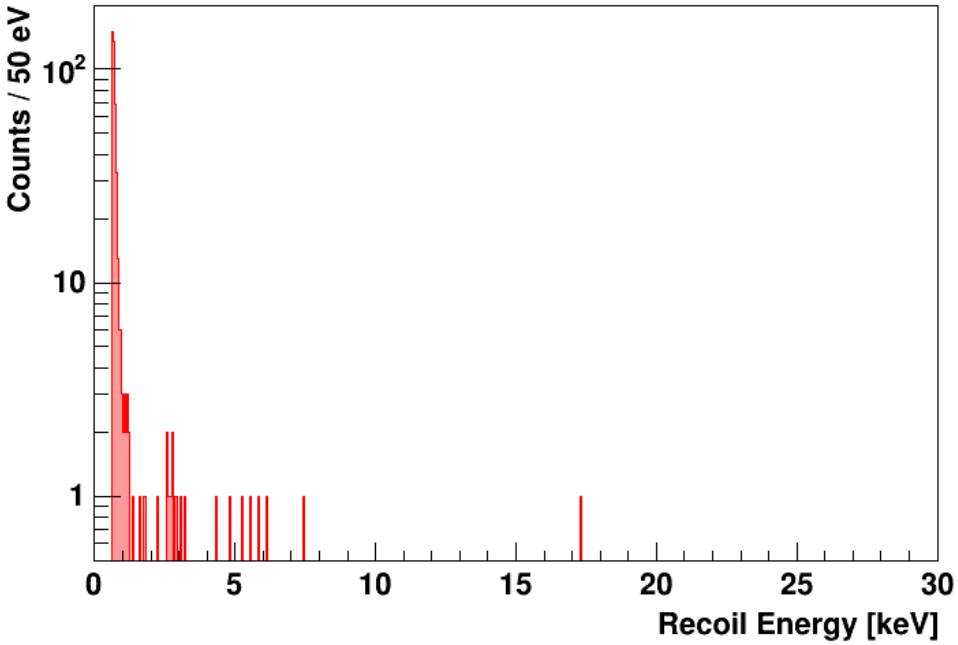

Figure 9.9: *Recoil-energy spectrum of all accepted events in the blind data set of the module TUM40/Michael. In total 450 events are located in the ROI for the Dark Matter search (yellow shaded area in figure 9.7). The spectrum strongly rises with decreasing energy. The few events clustered around an energy of 2.6 keV might be a hint for a leakage of e^-/γ-events into the ROI as at this energy a γ-line is observed. In the one-dimensional application of Yellin's optimum interval method all these events are treated conservatively as WIMP induced events and an 90 % C.L. exclusion limit on the WIMP-nucleon cross section is obtained.*

between 1 keV and 40 keV is found to be 3.74 ± 0.04 counts/(keV kg day) which is slightly higher compared to the value of 3.51 ± 0.09 counts/(keV kg day) obtained in [131].

Exclusion Limit of the Blind Data Set

In figure 9.9 the energy spectrum of all accepted events in the blind data set of TUM40 is depicted. With an exposure of 97.99 kg days in total 450 events are found in the ROI for Dark Matter search. The number of accepted events strongly increases for low energies near the trigger threshold of 609 eV. The few events clustered around an energy of 2.6 keV might be due to e^-/γ-leakage into the ROI as at this energy a γ-line is observed (see table 9.2 in section 9.7). In the one-dimensional application of Yellin's optimum interval method all accepted events are treated conservatively as WIMP-induced events and a 90 % C.L. exclusion limit on the WIMP-nucleon cross section is obtained.

In figure 9.10 the parameter space for elastic spin-independent WIMP-nucleon scattering is drawn including the resulting curve of TUM40 (black solid line). Several other 90 % C.L. exclusion limits of CRESST-II are also depicted: Most important here is the result of the training set of TUM40 drawn as red long-dashed curve. The re-analysis of the CRESST-II commissioning run [160] results in the red dashed line. The published result of the blind data

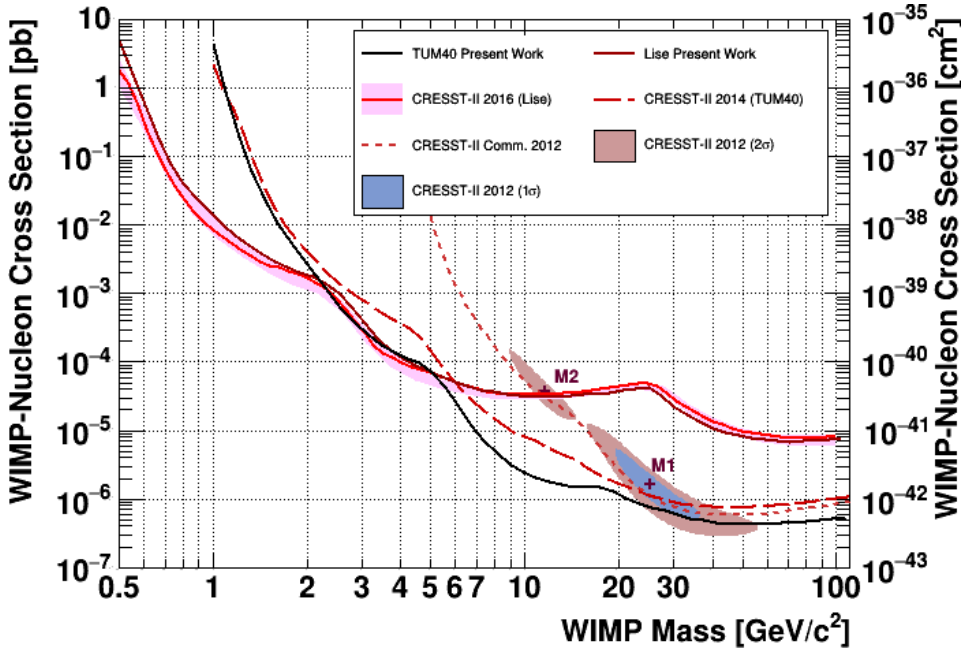

Figure 9.10: *Parameter space for elastic spin-independent WIMP-nucleon scattering containing several CRESST-II results. All drawn curves are 90 % C.L. exclusion limits. The result of the present analysis of TUM40 is drawn as black line. Due to the larger exposure of 97.99 kg days an enhanced sensitivity compared to the result of the training set of TUM40 (29.35 kg days, red long-dashed curve) [127] is achieved for almost all WIMP masses. The red dashed line is the result of the re-analysis of the commissioning run of CRESST-II [160]. The published result of the blind data set of Lise (red solid curve) [159] as well as the curve for Lise (dark-red line) of the present work are drawn. Finally, also the favoured parameter space of CRESST-II phase 1 with the two likelihood maxima M1 and M2 is drawn as the shaded islands [107].*

set of Lise (red solid curve) [159] as well as the curve for Lise (dark-red line) of the present work are also drawn. Finally, the favoured parameter space of CRESST-II phase 1 is marked by the shaded islands [107].

Due to the exposure of 97.99 kg days the result of the blind data set is for all WIMP masses considerable lower than the published curve of the training set of TUM40 (red long-dashed curve, exposure 29.35 kg days). As already explained for Lise, due to the energy threshold of the detector the dominant scattering nucleus changes at a certain WIMP mass. Therefore, a kink in the exclusion limit near $\sim 4\,\mathrm{GeV}/c^2$ is observed. A saddle point above $\sim 14\,\mathrm{GeV}/c^2$ is observed and in [123] it is shown, that removing the accepted event with the highest recoil energy of $\sim 17.3\,\mathrm{keV}$ artificially improves the exclusion limit at higher masses but does not remove the saddle point. Thus, it is concluded that the saddle point is caused by more accepted events than this one.

With the data of only this single detector it is possible to restrict a significant part of the favoured parameter space of CRESST-II phase 1 (labeled CRESST-II 2012 in figure 9.10) [107]. While the M2 solution (light Dark Matter particles) is completely excluded by at least one order of magnitude, for the heavier M1 solution some parameter space remains.

9.2.2 Origin of TES-Carrier Pulses

As the number of events containing TES-carrier-like pulses is surprisingly large in the training set of TUM40 the origin of this kind of background is investigated in detail. For the following discussion the complete data set of TUM40 is considered containing all the pulses of the training set as well as of the blind data set. First the time dependency of the TES-carrier rate is discussed and, afterwards, the number of events containing unidentified TES-carrier pulses is estimated.

Time Dependency of the TES-Carrier Rate

In figure 9.11 the number of events per 1 h live time interval is depicted for the complete data set of TUM40. All events before the application of the pulse shape cuts are depicted as red data points, the events surviving the application of the pulse shape cuts are the magenta data points. Finally, the black data points represent all events surviving the complete series of selection criteria applied. There are two separated phases in the data taking period as can be clearly seen, in particular, for the count rate before the application of the pulse shape cuts (red data points): while the count rate is exponentially decaying in the first part of the data set (real time $\lesssim 9\,000\,\mathrm{h}$), large fluctuations are observed later. At a real time of $\sim 8\,866\,\mathrm{h}$ the trigger threshold of TUM40 has been lowered from 609 eV down to 409 eV resulting in unstable time periods before application of the cuts. However, the pulse shape cuts seem to remove the events which feature an exponential decay rate completely (magenta data points). The majority of the fluctuations after the trigger threshold reduction are already rejected by the cut on the rise-time parameter. After application of all selection criteria, the surviving events (black data points) show an almost constant count rate per 1 h live time interval throughout the complete real time period of $\sim 16\,000\,\mathrm{h}$.

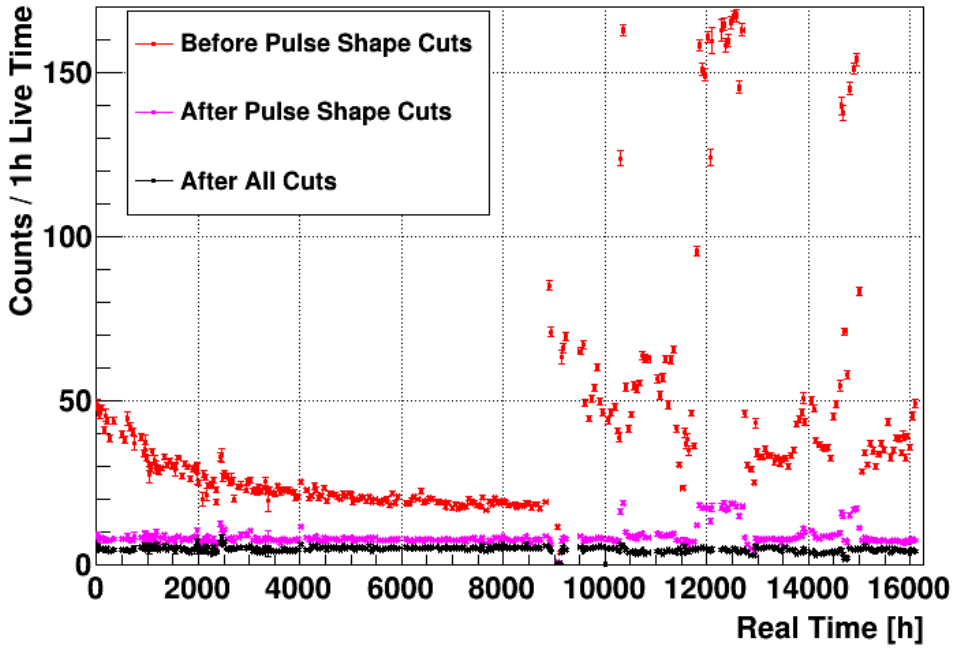

Figure 9.11: *Count rate per* 1 *h live time as a function of the real time for different event lists. The red data points are all events before any pulse shape cut is applied, while the magenta data points show the rate after the pulse shape cut. After application of the remaining cuts, in particular the RMS-cut, the final rate (black data points) is obtained. Two different time periods are clearly distinguishable and, in particular, visible in the rate before any pulse shape cut is applied. After a real time of 8 866 h the trigger threshold of TUM40 was lowered. Before this change in the first* $\sim$ 9 000 *h the rate is exponentially decreasing, while afterwards unstable running conditions are observed. Nonetheless, for the final event rate after all cuts a stable result is achieved throughout the complete data taking period of* $\sim$ 16 000 *h real time.*

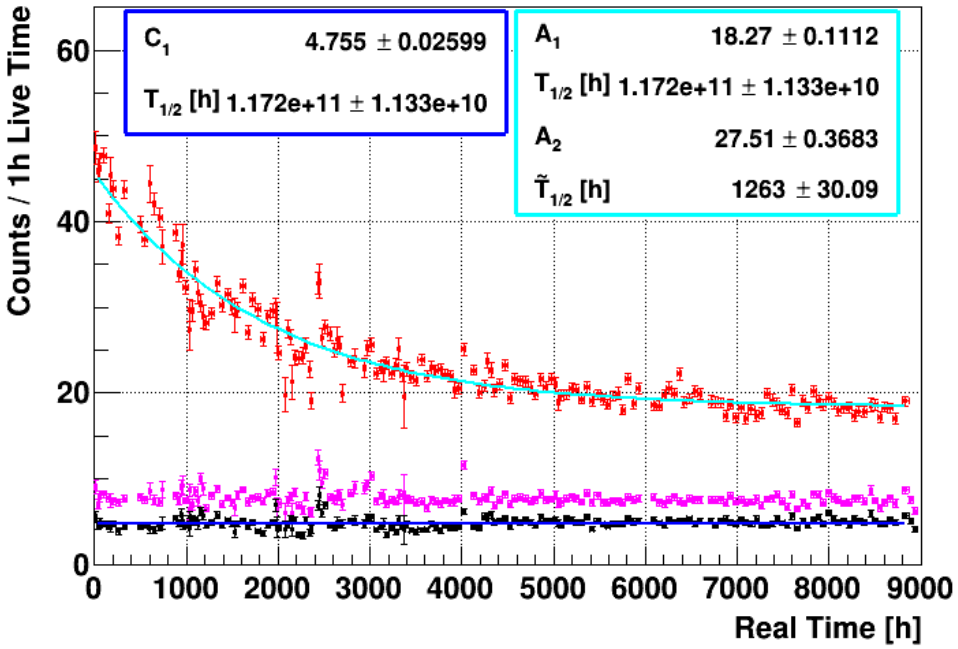

Figure 9.12: *Zoom into the first 9 000 h before lowering the trigger threshold. For different data sets the count rate per 1 h live time as a function of the real time is depicted. As in figure 9.11 the red data points correspond to the number of events before any pulse shape cut is applied, while the magenta data points are the events surviving the pulse shape cuts. The black data points are the final event rate after application of all cuts. Also drawn is the result of a combined fit of the final rate (one exponential function) and the event rate before any pulse shape cut is applied (two exponential functions) as dark and light blue solid line, respectively. For more details see text.*

In figure 9.12 a zoom into the first 9000 h real time is depicted. Also drawn are the results of a combined fit of the final rate (black) and the event rate before application of a pulse-shape cut (red) with one (dark blue line) and two (light blue line) exponential functions, respectively. Thereby, one of the two half-life parameters ($T_{1/2}$) is common for both data sets while the other parameters are individual for each set. This is done, as the final event rate is only a subset of the event rate before application of a pulse-shape cut. Thus, the time dependency of the former should also be present in the latter set. For the final event rate a large half life $T_{1/2} = (\sim 1.2 \pm 0.1) \cdot 10^{11}$ h compatible with a constant count rate is obtained. For the second half-life a value of $\tilde{T}_{1/2} = 1263 \pm 30$ h is determined corresponding to ~ 53 d.

At the beginning of CRESST-II phase 2 the ratio between constant and decaying count rate in the data set before any pulse-shape cut is applied is $\frac{A_2}{A_1} = 1.51 \pm 0.01$. Thus, at that time the number of events containing TES-carrier like pulses is dominating in TUM40. However, as the rate is decaying with a half-life of ~ 53 d after $\sim 5\,000$ h (corresponding to ~ 208 d) an almost constant count rate is observed. This result is not expected for the TES-carrier event rate and, thus, is a hint towards another background contribution. There are two possibilities which might create the observed time dependency: Firstly, a radioactive isotope only present in the TES-carrier and decaying with a half-life of ~ 53 d might be the origin. Thus, all isotopes which have a half-life within the $\pm 5\,\sigma$ error range of the fit value are identified. The only isotope, which is not discarded by a first glance is ^{89}Sr, since strontium belongs to the same periodic family as calcium and, thus, might be present in the $CaWO_4$ crystals. However, a closer look reveals that all mother isotopes of ^{89}Sr are very short-lived. The first isotope of this decay chain containing ^{89}Sr is ^{89}Se produced in a neutron capture and subsequent fission of ^{235}U. Therefore, it seems to be unlikely that ^{89}Sr is present in the carrier of TUM40.

Secondly, the events with decaying rate might be caused by stress relaxation, e.g., induced by the glue used to assemble the TES-carrier and the absorber crystal. In a physics run of CRESST-II performed in 2008 events with no light and decreasing rate have been observed in the low temperature detectors [161,162]. At that time the most probable origin of these events was stress relaxation at the contact surface between metal clamps and crystal. In particular, in the clamps covered with a plastic layer more events of this type have been observed.

In figure 9.13 a plot similar to the light - energy plane is depicted, with the difference that the x-axis contains the pulse height and not the energy measured in the phonon detector. Included are all events which are rejected by the pulse-shape analysis and which are not due to noise triggers. While (a) shows the complete light-energy range, in (b) a zoom into the low-energetic region is depicted. Two clearly separated populations are observable: Only 32.6 % of all events rejected by the pulse-shape analysis are accompanied by a light signal, while the remaining 67.4 % are phonon-only events without corresponding light.

The events which are accompanied by a light signal are most probably caused by a physical interaction in the $CaWO_4$ stick, which produces – besides a number of phonons – a simultaneous light signal. The phonons have to be transmitted into the main absorber before they are measured in the phonon detector and, therefore, a distorted pulse shape in the phonon detector is observed compared to direct absorber events. The amount of energy detected by the light detector depends on the amount of scintillation light created and the position of the stick relative to the light detector. Therefore, in (a) bands with different slopes are observable.

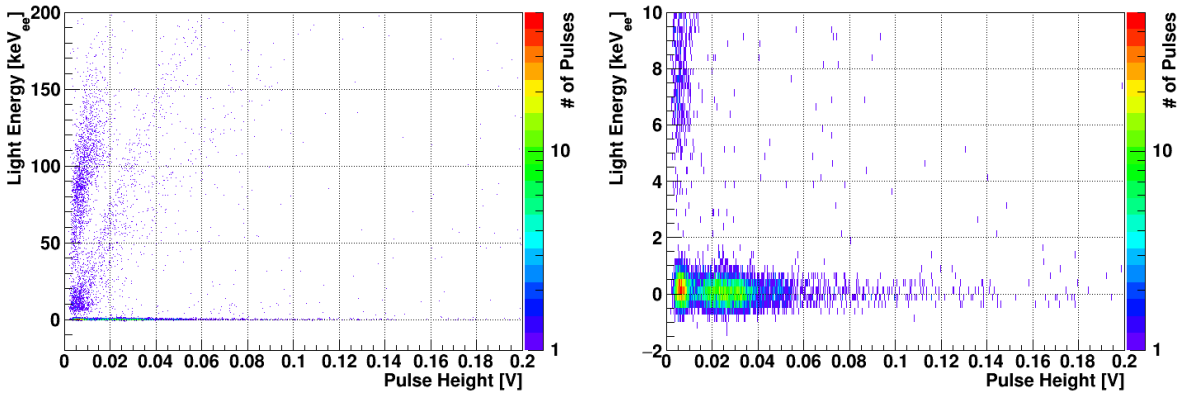

(a) Complete Light-Energy Region *(b) Zoom into Low Light-Energy Region*

Figure 9.13: *Energy measured in the light detector vs. pulse height measured in the phonon detector for all events of the complete data set of TUM40 which are rejected by the pulse-shape analysis and which are not due to noise triggers. While (a) shows the light-energy region below 200 keV_{ee}, in (b) a zoom into the low-energetic light region is depicted. As can be seen, the events can be clearly separated into two populations: one without and one with a light signal. The events accompanied by a light signal (32.6 %) are most probably due to a physical interaction inside the $CaWO_4$ holding sticks, where the light energy measured depends on the position of the stick relatively to the light detector. Only in the population without light (67.4 %) the previously-discussed decrease of the count rate is observable. The origin of these events might be stress relaxation either at the contact area where the stick presses onto the absorber crystal or induced by the glue used to assemble the TES-carrier and the absorber crystal.*

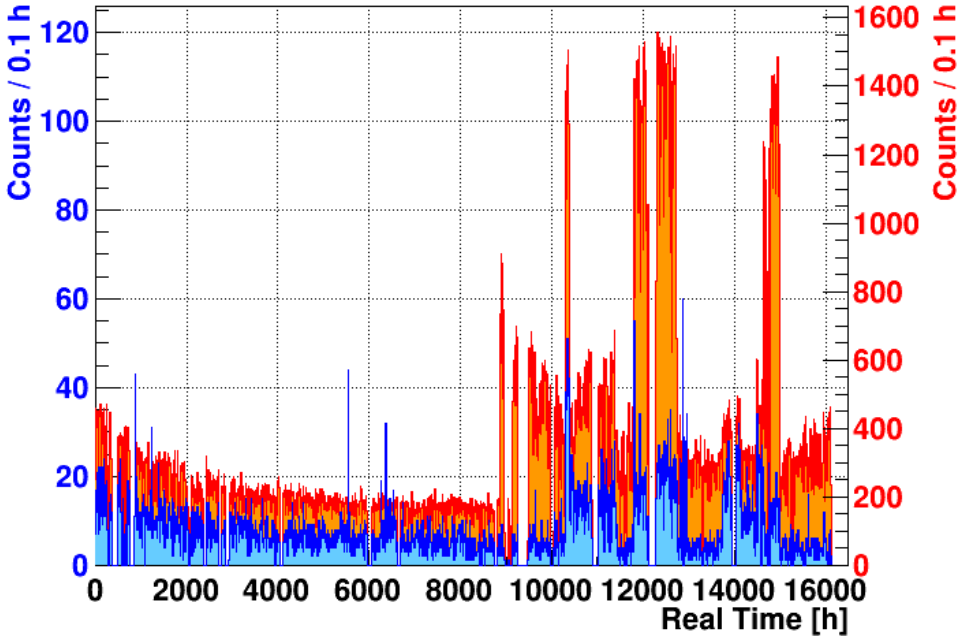

Figure 9.14: *Number of counts observed per 0.1 h real time for the phonon-only events with distorted pulse shape (blue histogram, left y-axis) as a function of the real time. Also depicted is the number of events observed per 0.1 h real time before any pulse shape cut is applied (red histogram, right y-axis). A clear correlation between both rates is observed. This might be another hint for stress relaxation as origin for the phonon-only events with distorted pulse shape. Most probably the noise increases from time to time due to mechanical vibrations which are coupled into the experimental setup. These vibrations might also affect the strength the sticks are pressed onto the crystal surface and trigger stress relaxation events.*

Only the events with distorted pulse shape that are not accompanied by a light signal show the decreasing rate with respect to the measurement time. These phonon-only events might be caused by relaxations to release stress induced either by the $CaWO_4$ sticks holding the crystal and, therefore, pressing onto the absorber crystal or by the glue used to assemble the TES-carrier and the absorber crystal.

In figure 9.14 the counts observed per 0.1 h real time are displayed for the phonon-only events with distorted pulse shape (blue histogram, left y-axis) as a function of the real time. Also depicted is the number of events observed per 0.1 h real time before any pulse shape cut is applied (red histogram, right y-axis). A clear correlation between both event populations is visible. On a first glance this is surprising, as the increase in the rate of all events is mainly caused by noise triggers while the blue histogram shows the rate of physical events. The increased level of the noise is most probably due to mechanical vibrations which are coupled into the experimental setup whereby the coupling strength seems to be related to some external variable (e.g. the liquid helium level in the dewar). In case of stress relaxation induced by the sticks as origin for the phonon-only events with distorted pulse shape, these mechanical vibrations might also affect the strength the stick is pressed onto the absorber surface and trigger stress relaxation events.

Number of Unidentified TES-Carrier Pulses

In principle it is possible to estimate the number of unidentified TES-carrier pulses in the complete data set of TUM40. The first input required is the survival probability of a TES-carrier pulse. From the independent validation data set mentioned in section 6.4.4 where no simulated TES-carrier pulse survived the selection criteria only an upper limit for this quantity can be estimated. For zero events observed in a Poisson process the 90 % C.L. upper limit on the expected number of events is 2.3. In total 11 929 TES-carrier pulses are simulated and, therefore, an upper limit on the survival probability $p_s < \frac{2.3}{11929} = 1.93 \cdot 10^{-4}$ is obtained.

Next it is important to know the fraction of TES-carrier pulses relatively to the total number of triggers in a given time interval. From the discussion above it is clear that this fraction is time dependent. For the first $\sim 9\,000$ h of real time during CRESST-II phase 2 an exponential decay of the rate is observed in TUM40, while at later times no constant conditions are obtained anymore due to the lower trigger threshold of TUM40. In the first $T_{\text{meas}} = 8\,866$ h (before the trigger threshold of TUM40 has been lowered) the total live time is $T_{\text{live}} = 7\,038$ h and, thus, the detector was operational in 79.38 % of the measurement time. To obtain the number of TES-carrier pulses $N_{\text{TES-carrier}}$ expected in this time period the exponentially decaying count rate is integrated. Afterwards the resulting number of events has to be scaled with the fraction of live time to real time $\frac{T_{\text{live}}}{T_{\text{meas}}}$ to obtain an estimation for the number of TES-carrier events. This rather complex procedure is required as the rate decreases with real time but the number of events only scales with the live time. Putting everything together results in

$$N_{\text{TES-carrier}} = \int_0^{T_{\text{meas}}} A_2 \cdot \exp\left(-\frac{\ln(2)}{\tilde{T}_{1/2}} \cdot t_{\text{real}}\right) dt_{\text{real}} \cdot \frac{T_{\text{live}}}{T_{\text{meas}}} = 49\,740 \cdot 0.7938 \approx 39\,483, \quad (9.1)$$

where t_{real} is the real time and A_2 as well as $\tilde{T}_{1/2}$ are the parameter values obtained from the fit (see figure 9.12). The estimation for the number of events containing an unidentified TES-carrier pulse N_{ui} is obtained by multiplying the upper limit of the survival probability p_s with the number of events:

$$N_{\text{ui}} = p_s \cdot N_{\text{TES-carrier}} = 7.62. \quad (9.2)$$

Therefore, the 90 % upper limit for the number of events containing unidentified TES-carrier pulses in the first $\sim 9\,000$ h of measurement time is ~ 8 events. All pulses with an energy value $\lesssim 20$ keV are checked by eye and no TES-carrier like pulse is clearly identified. Thus, it might be well possible that the given upper limit is very conservative. For the complete data set the estimation can not be performed, as the event rate is not stable with time throughout the complete measurement period.

9.3 Module TUM38/Petrus

In this section the results of the module TUM38/Petrus are discussed. TUM38 is a crystal with a big carrier crystal and is mounted together with a standard light detector in a module housing (see section 3.5.4). In the present section first the small non-blind adjustments of the RMS cut of Petrus, in particular with respect to the binning of the energy slices, are discussed.

These modifications are required for the complete data set to ensure the convergence of the fit in each energy slice. Afterwards, the results of the complete data set of TUM38 are discussed.

9.3.1 Non-blind Adjustments of the RMS Cut of Petrus

As discussed in section 5.3.8 for the RMS cut the complete energy region is split into several slices. In each of these slices the RMS distribution observed is fitted with an empirical model. Based on this fit result the actual cut limits are obtained. In the training set the binning parameters for the RMS cut are set and applied without change to the blind data set during un-blinding. However, in the complete data set the fit does not converge for Petrus in several slices. Convergence of all fits is reestablished when the binning is slightly increased from 15 keV bin width to 20 keV. As the adjustments are performed before the light yield - energy plot has been created for the first time it is not known whether events are located inside the ROI and a bias is almost excluded. Furthermore, as the majority of events is due to background contributions it is not expected that nuclear recoil events would have a strong influence on the resulting fit limit. Nonetheless, the influence of this change is tested, by performing the fit with the increased bin width of 20 keV once for all data and once only for the events inside the 80 % e^-/γ-band.

In figure 9.15a the resulting RMS distribution of Petrus after application of the final RMS cut is depicted (color-coded histogram). The black data points with error bars show the cut limits obtained from the fit of the events inside the 80 % e^-/γ-band. If these cut limits would have been applied to the data set 864 events would have been removed additionally. The light yield - energy plot of these 864 events is depicted in figure 9.15b showing that out of these 864 events only one is located inside the nuclear recoil band slightly above the mean of the oxygen band. Thus, zero of these 864 events rejected by the cut solely based on the e^-/γ-events, are located inside the ROI for Dark Matter search. Therefore, it is concluded that changing the bin width parameter in Petrus after un-blinding results in, if at all, no large bias for this detector.

9.3.2 Results of the Complete Data Set

For the module TUM38/Petrus the complete data set contains pulses recorded in an exposure of 158.87 kg days. Throughout the complete data taking period a trigger threshold of better than $\sim$ 3 keV is achieved in TUM38 (see appendix D.1). In the following, first the signal survival probabilities and the light yield - energy plot are discussed. Afterwards the energy spectrum of the accepted events is shown, while the discussion of these events is performed in section 9.6 together with the results of the other modules analysed.

Signal Survival Probability

The resulting signal survival probabilities after successive application of the different selection criteria are depicted in figure 9.16. Compared to the survival probabilities of Lise (see figure 9.1) and TUM40 (see figure 9.6) in particular the data quality cuts remove a considerably lower fraction of events. Therefore, the resulting signal survival probability after application of the data quality cuts as well as of the pulse shape cuts is significantly higher in TUM38 for

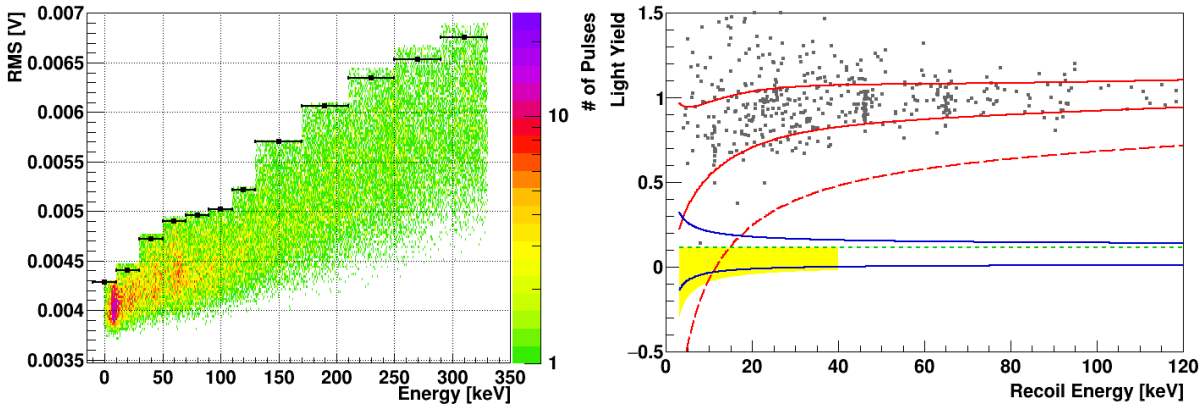

(a) *RMS distribution* ***(b)*** *Light yield - energy plane*

Figure 9.15: *Test of the influence of events outside the e^-/γ-band on the RMS cut limit of Petrus. In (a) the RMS distribution observed in Petrus after application of the final RMS-cut is depicted. By design, the cut limit is slightly different in each energy slice. The bin width is 20 keV for a mean energy below 120 keV and 40 keV above. The black data points with error bars are the result from the fit of only the events located inside the 80 % e^-/γ-band. As can be seen the obtained cut limits are slightly lower in a few energy bins. In total 864 events are found which would be removed by this more stringent cut. In (b) the relevant part of the light yield - energy plot is depicted for all events which would be removed by the e^-/γ-band based RMS-cut (black error bars in (a)). Only one event is located inside the nuclear recoil band (blue lines) slightly above the central line of the oxygen band (green dashed line). Thus, none of the accepted events would be removed by this modified cut. Therefore, it is concluded that, if at all, no large bias is introduced by changing the binning of the RMS-cut of Petrus after un-blinding of the complete data set.*

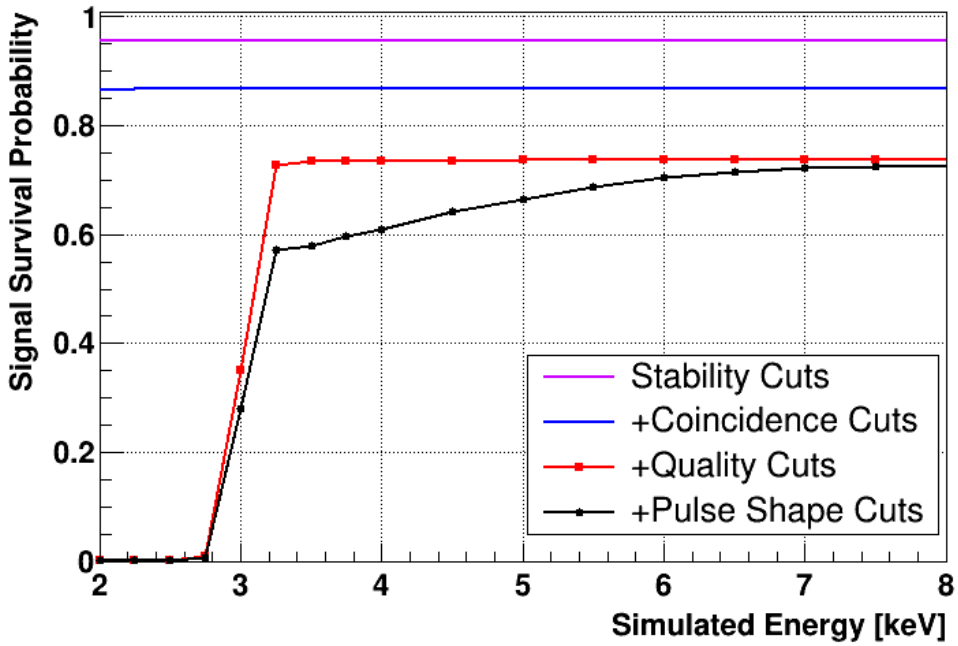

Figure 9.16: *Signal survival probabilities after successive application of different selection criteria to pulses of the complete data set of the module TUM38/Petrus. Besides the drop-off at the trigger threshold of* ~ 3 *keV no significant energy dependency is observed for the data quality cuts (red line). However, the pulse shape cuts lead to an energy dependent final signal survival probability (black line) below* ~ 7 *keV. Nonetheless, at the threshold still* ~ 28 *% of all events survive all cuts.*

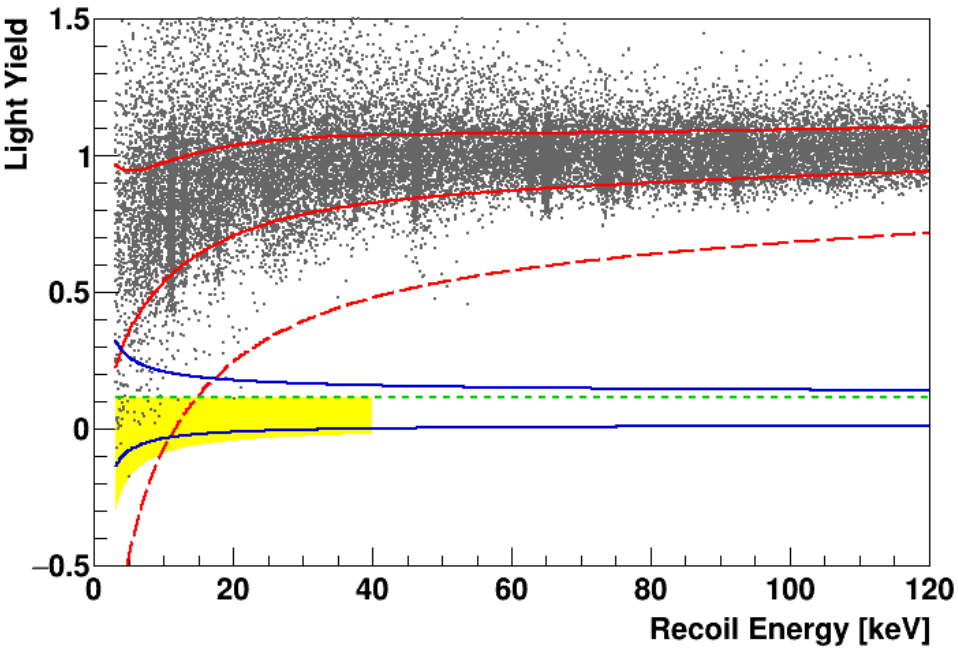

Figure 9.17: *Light yield - energy plot of the complete data set of TUM38. In red different limits of the e^-/γ-band are drawn: The solid lines restrict the central 80 % e^-/γ-band and correspond to its 90 % upper and lower limit, while the red dashed line is its lower 5 σ boundary. The blue lines mark the nuclear recoil band, where the upper line is the 90 % upper limit of the oxygen band and the lower blue solid line the lower 90 % limit of the tungsten band. The region of interest used for the Dark Matter analysis is highlighted in yellow. In energy it ranges from the energy threshold of $\sim$ 3 keV up to 40 keV. In the light-yield coordinate it is restricted from the mean of the oxygen band (green dashed line) down to the lower 99.5 % limit of the tungsten band. A few events are located inside the ROI. Possible origins are discussed later in section 9.6.*

all energies. In the low energetic region an energy dependency is observed which is mainly caused by the pulse shape cuts ($\gtrsim$ 3.2 keV) and a cut-off due to the trigger efficiency. The final signal survival probability at the trigger threshold with a value of $\sim$ 28 % is high compared to the results of Lise ($\sim$ 6 %) or TUM40 ($\sim$ 15 %).

Light Yield - Energy Plane

The light yield - energy plot for the pulses surviving all selection criteria in the complete data set of the module TUM38/Petrus is depicted in figure 9.17. The various lines mark different limits for the light yield bands: the solid red lines enclose the central 80 % e^-/γ-band. The solid-blue lines are the boundaries of the nuclear recoil band, where the upper curve is the 90 % upper limit of the oxygen band and the lower curve is the 90 % lower limit of the tungsten band. The yellow shaded area is the respective ROI for this detector ranging in energy from the threshold of $\sim$ 3 keV up to 40 keV. In the light yield coordinate the ROI expands from the 99.5 % lower limit of the tungsten band up to the mean line of the oxygen band (green dashed

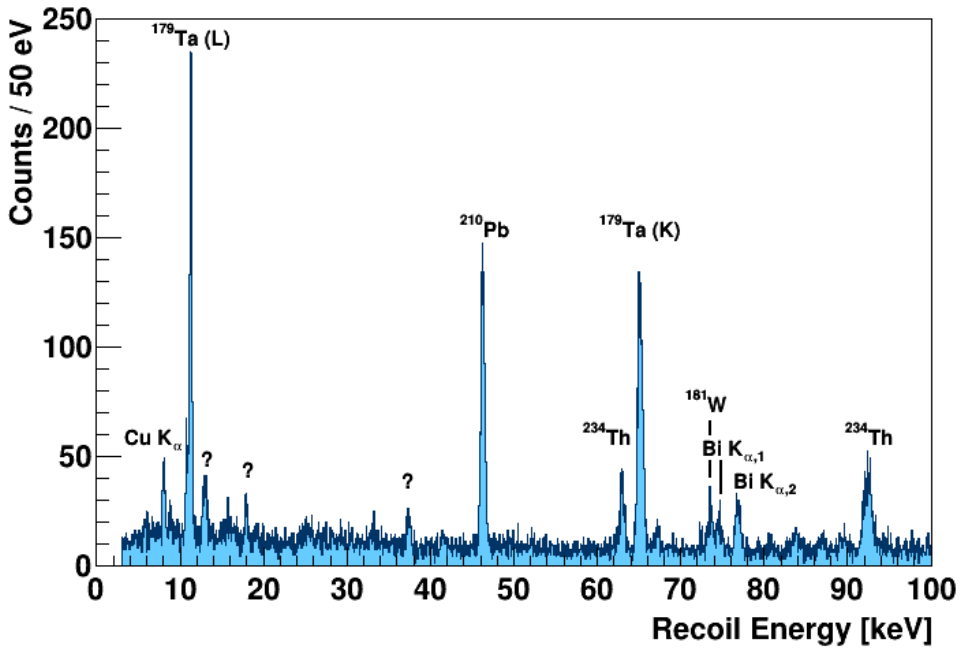

Figure 9.18: *Recoil-energy spectrum of all events below* 100 *keV in the complete data set of TUM38. The majority of all events is located inside the* e^-/γ*-band and, therefore, several* γ*-lines are observable. The origins of these lines are discussed in section 9.7. For TUM38 the overall background level in the energy region from* 3 *keV up to* 40 *keV is found to be* 2.77 ± 0.03 *counts/(keV kg day).*

line). The dashed-red line is the 5 σ lower boundary of the e^-/γ-band. There are several events located between this line and the 90 % lower limit of e^-/γ-band (lower red solid line). The possible origins for these events, in particular in the ROI, are discussed later in section 9.6.

In figure 9.18 the recoil-energy spectrum below 100 keV of all events in the complete data set of TUM38 is depicted. Several γ-lines are observable and their origins are discussed in section 9.7. The overall background level in the energy interval starting at the threshold of TUM38 ($\sim$ 3 keV) up to 40 keV is calculated. A value of 2.77 ± 0.03 counts/(keV kg day) is found, which is drastically lower than that of Lise. Also in comparison to TUM40 a lower overall background rate is found in TUM38. However, it should be kept in mind that these numbers are hardly comparable, as they assume a flat background in the complete energy range considered. As the background is dominated by γ-lines, the non-consideration of the energy range between 1 keV and 3 keV due to the high threshold in TUM38 might result in a lower value, in particular, if a prominent γ-line is observed in the neglected region, as is the case for TUM40. Nonetheless, the TUM-grown crystals feature an unprecedentedly low background level compared to all commercially available crystals [131].

Accepted Events

In figure 9.19 the energy spectrum of all accepted events in the complete data set of TUM38 is depicted. In an exposure of 158.87 kg days before cuts, in total 33 events are found inside the

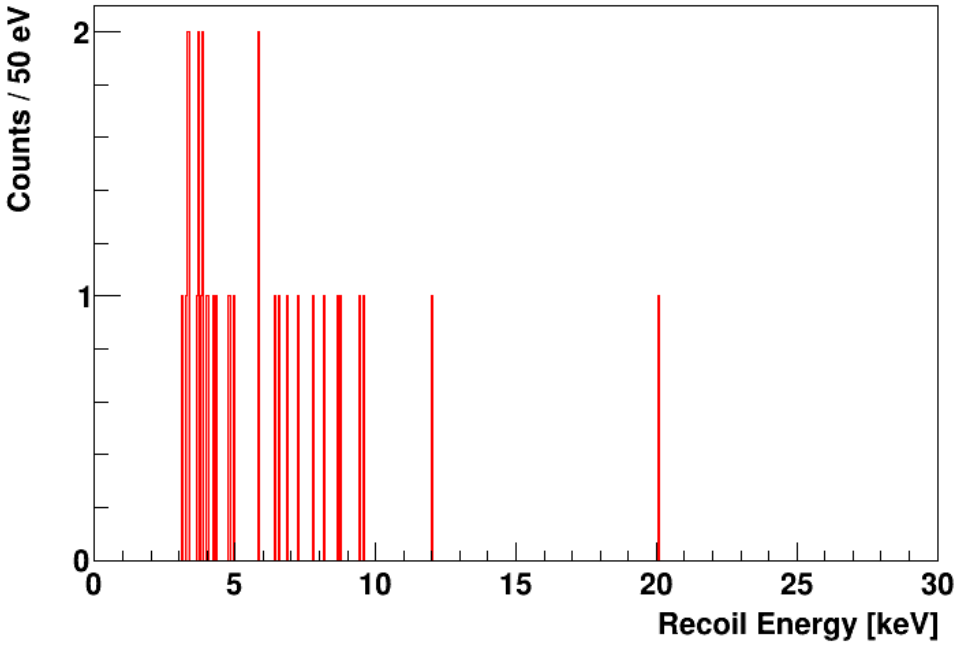

Figure 9.19: *Energy spectrum of the accepted events in the complete data set of TUM38. The trigger threshold of the phonon detector is* ~ 3 *keV. In an exposure of 158.87 kg days in total 33 events are located inside the ROI for Dark Matter search (yellow shaded area in figure 9.17).*

ROI for Dark Matter search (yellow shaded area in figure 9.17). In section 9.6 this number is compared to the expectation based on the background leakage. Furthermore, several possible sources for these events are also discussed there.

9.4 Module VK27/Diogenes

The module VK27/Diogenes is one of the two alternative modules with a silicon beaker as light detector. The trigger threshold of the phonon detector VK27 is 11.25 keV, i.e. relatively high. In total an exposure of 102.36 kg days is obtained in the complete measurement-time period considered here.

9.4.1 Signal Survival Probability

The signal survival probabilities after application of several selection criteria are depicted in figure 9.20. Due to the high threshold no significant energy dependency besides the drop-off at the threshold is observed for the data quality cuts (red line). As mentioned in section 6.8 it is not easy to train a neural network efficiently to remove the TES-carrier pulses of this module. This is also reflected by the final signal survival probability of the pulse shape cuts (black line). At the threshold of 11.25 keV only $\sim 6\,\%$ of all events survive the complete cut sequence. However, with increasing energy an almost linear increase until ~ 20 keV is

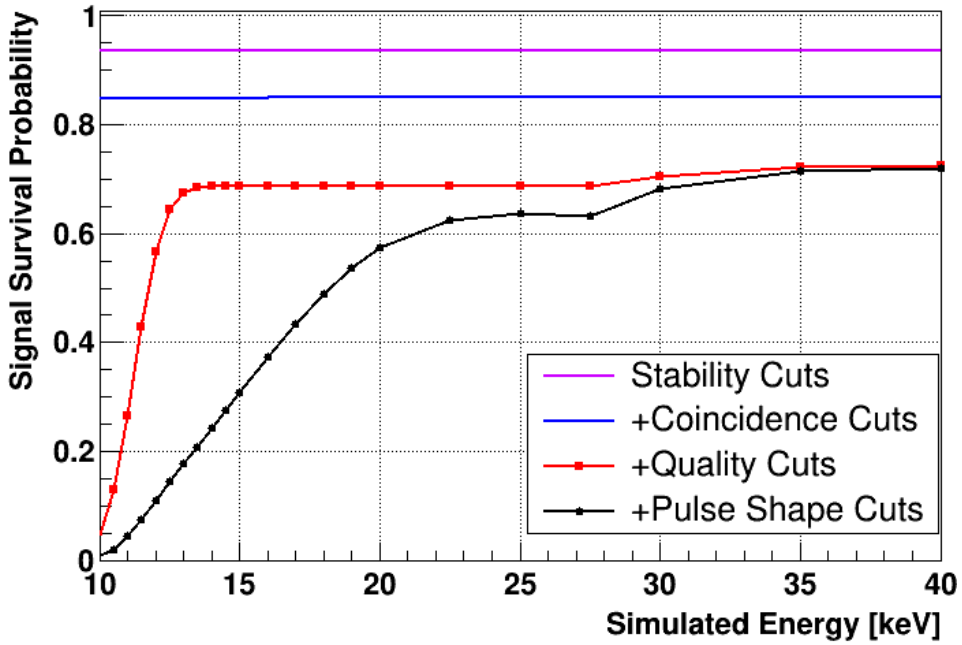

Figure 9.20: *Signal survival probabilities of the complete data set for the module VK27/Diogenes after successive application of the selection criteria. Due to the (high) trigger threshold of* 11.25 *keV the signal survival probability of the data quality cuts (red line) drops off at this energy. As the signal height in VK27 is unusually small it is hard to train a neural network that efficiently removes all TES-carrier pulses. The resulting final curve (black line) increases almost linearly from a value of* $\sim$ 6 *% at the threshold up to a value of* $\sim$ 57 *% at* $\sim$ 20 *keV. At energies higher than* $\sim$ 35 *keV it approaches the curve of the data quality cuts.*

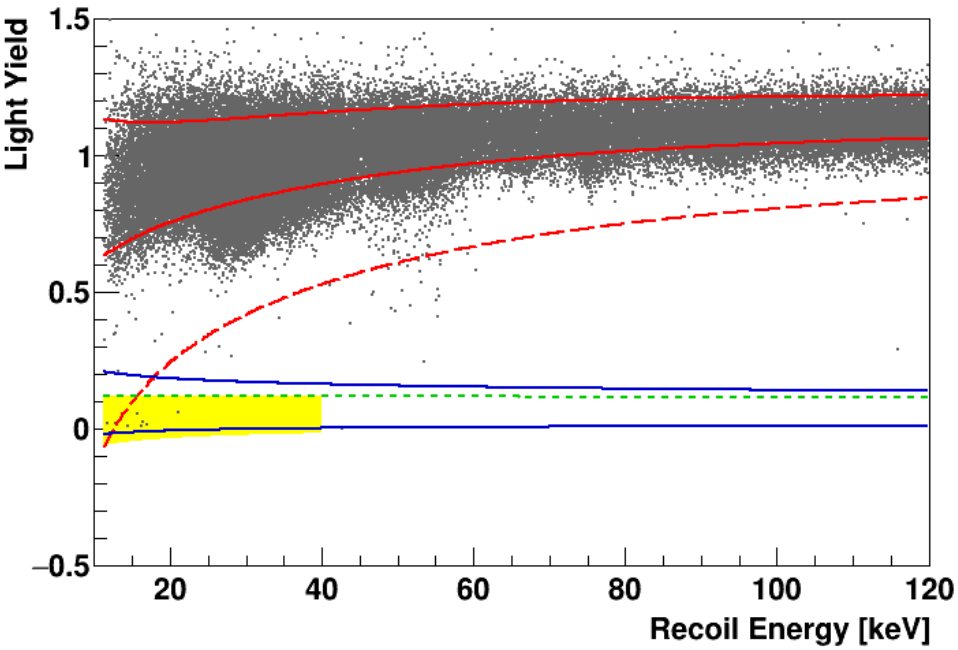

Figure 9.21: *Light yield - energy plot of the complete data set of VK27. In red different limits of the e^-/γ-band are drawn: The solid lines restrict the central 80 % e^-/γ-band, while the red dashed line is its lower 5 σ boundary. The blue lines mark the nuclear recoil band, where the upper line is the 90 % upper limit of the oxygen band and the lower blue line the lower 90 % limit of the tungsten band. The region of interest used for the Dark Matter analysis is highlighted in yellow. In energy it ranges from the energy threshold of 11.25 keV up to 40 keV. In the light yield coordinate it reaches from the mean of the oxygen band (green dashed line) down to the lower 99.5 % line of the tungsten band. In total 9 events are observed inside the ROI and possible origins of these events are discussed in section 9.6.*

observed and at even higher energies the final signal survival probability approaches more and more the curve of the data quality cuts.

9.4.2 Light Yield - Energy Plane

In figure 9.21 the resulting light yield - energy plane of VK27 is depicted together with the central 80 % e^-/γ-band (red solid lines). The nuclear recoil band (90 % upper limit of the oxygen band and 90 % lower limit of the tungsten band) is drawn as blue lines. As for the modules discussed before also the 5 σ lower boundary of the e^-/γ-band is shown as red dashed line. Starting at $\sim$ 24 keV a β-spectrum is observable, which is due to an intrinsic ^{227}Ac contamination. At higher energies of $\sim$ 46.5 keV another β-spectrum is visible caused by an intrinsic ^{210}Pb contamination. Both spectra are discussed later in more detail in section 9.5 for the similar crystal VK28. It has to be noted, that for a few events of these two spectral features a considerably reduced light output is observed. Therefore, these events leak down towards the nuclear recoil band, whereby the origin of this effect is not known up to now. Besides the several outliers most probably caused by this fact, the light-yield region between the electron

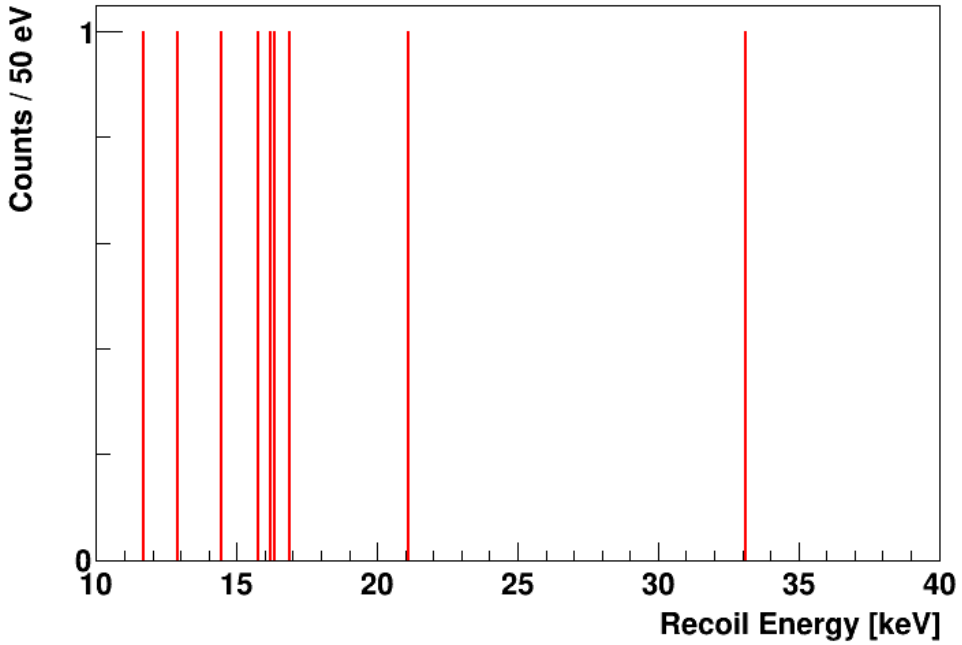

Figure 9.22: *Energy spectrum of the accepted events in the complete data set of the module VK27/Diogenes. The trigger threshold of the phonon detector (VK27) is* 11.25 *keV. In an exposure of 102.36 kg days in total 9 events are located inside the ROI for Dark Matter search (yellow shaded area in figure 9.21).*

and the nuclear recoil band is completely free of events.

9.4.3 Accepted Events

The region of interest (ROI) for the Dark Matter search is highlighted in yellow in figure 9.21. As for all other modules, it expands in the light yield from the mean line of the oxygen band down to the 99.5 % lower limit of the tungsten band. In energy the ROI starts at the rather high threshold of 11.25 keV and extends up to 40 keV. In total 9 events are observed in the ROI and their energy spectrum is depicted in figure 9.22. As for TUM38 these events are discussed in more detail in section 9.6.

9.5 Module VK28/Zam

The second module with a silicon beaker as light detector is VK28/Zam. The trigger threshold of the phonon detector VK28 is ~ 2 keV and in total an exposure of 100.65 kg days has been collected during the complete data taking phase.

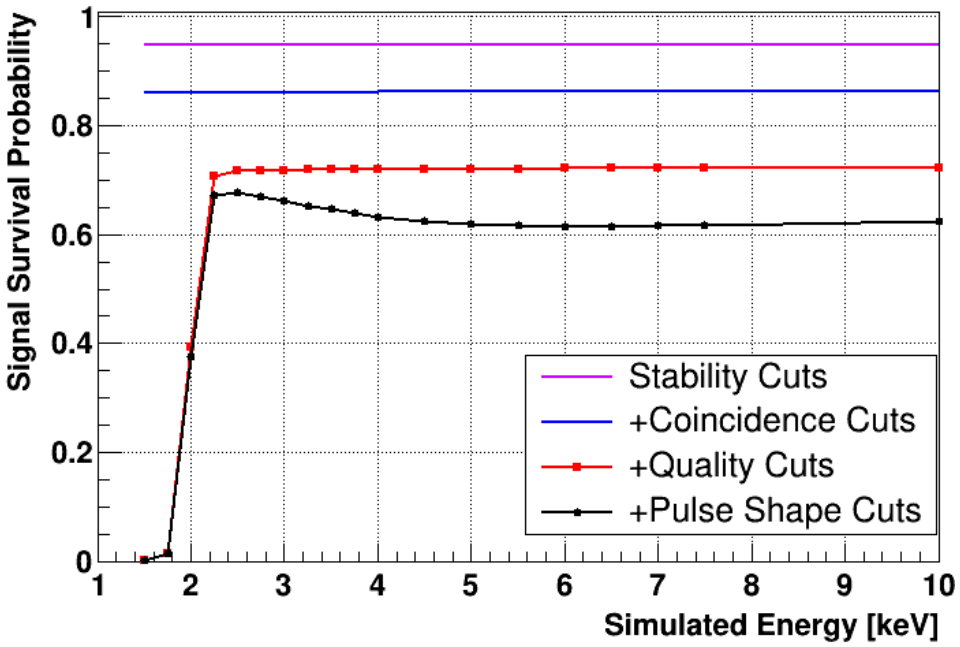

Figure 9.23: *Signal survival probability of the complete data-set of the module VK28/Zam after successive application of the selection criteria. Besides the sharp drop-off at the trigger threshold of $\sim 2\,keV$ no significant energy-dependency is observed for the data quality cuts (red line). However, the pulse shape cuts (black line) introduce such a dependency, as for energies of $\lesssim 5\,keV$ an increase of the final signal survival probability is observed. This reflects the rise of the output of the neural network trained for the TES-carrier pulse rejection (see figure 9.29 on page 240.) At the threshold of the detector the final signal survival probability yields an excellent value of $\sim 38\,\%$.*

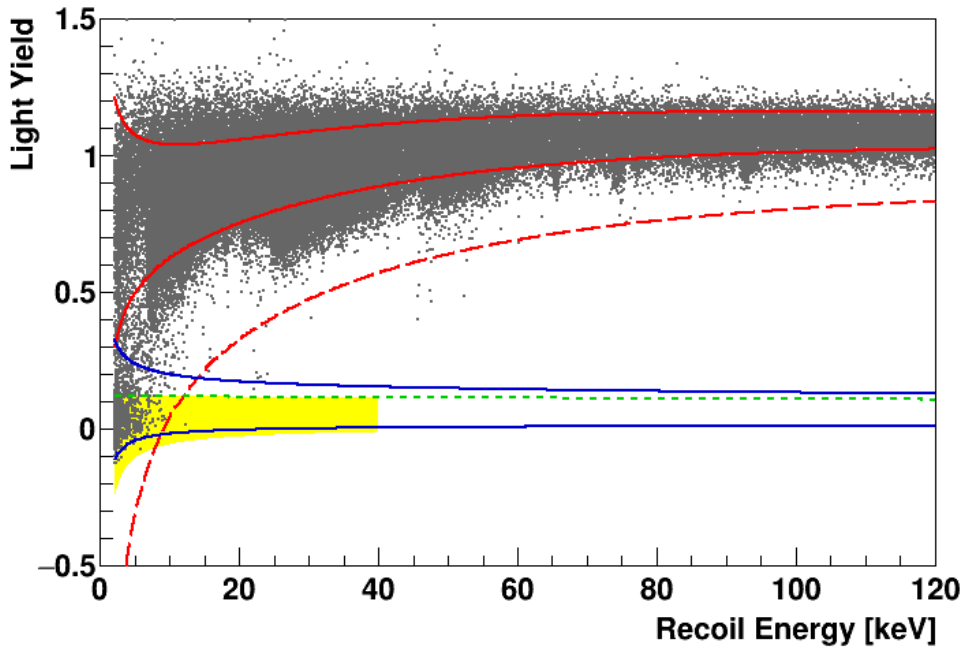

Figure 9.24: *Light yield - energy plot of the complete data set of VK28/Zam. In red different limits of the e^-/γ-band are drawn. The solid lines restrict the central 80 % e^-/γ-band, while the red dashed line is its lower $5\,\sigma$ boundary. The blue lines mark the nuclear recoil band, where the upper line is the 90 % upper limit of the oxygen band and the lower blue solid line the lower 90 % limit of the tungsten band. The region of interest used for the Dark Matter analysis is highlighted in yellow. In energy it ranges from the energy threshold of ~ 2 keV up to 40 keV. In the light yield coordinate it is restricted by the mean of the oxygen band (green dashed line) and by the lower 99.5 % limit of the tungsten band. A considerable number of 593 events is located inside the ROI and possible origins of these events are discussed in section 9.6.*

9.5.1 Signal Survival Probability

The signal survival probabilities after application of different selection criteria are depicted in figure 9.23. No significant energy dependency is observed in the data quality cuts (red line) besides the drop-off at the trigger threshold. The final signal survival probability (black line) is obtained after application of the pulse shape cuts, which efficiently remove the TES-carrier pulses. At higher energies $\gtrsim 5$ keV a fraction of ~ 10 % of all pulses is removed by this cut. At lower energies a rise of the survival probability is observed towards the trigger threshold which reflects the rise of the output values of one neural network used for the discrimination (see figure 9.29 on page 240). At the threshold of the detector (~ 2 keV) the final signal survival probability yields an excellent value of ~ 38 %.

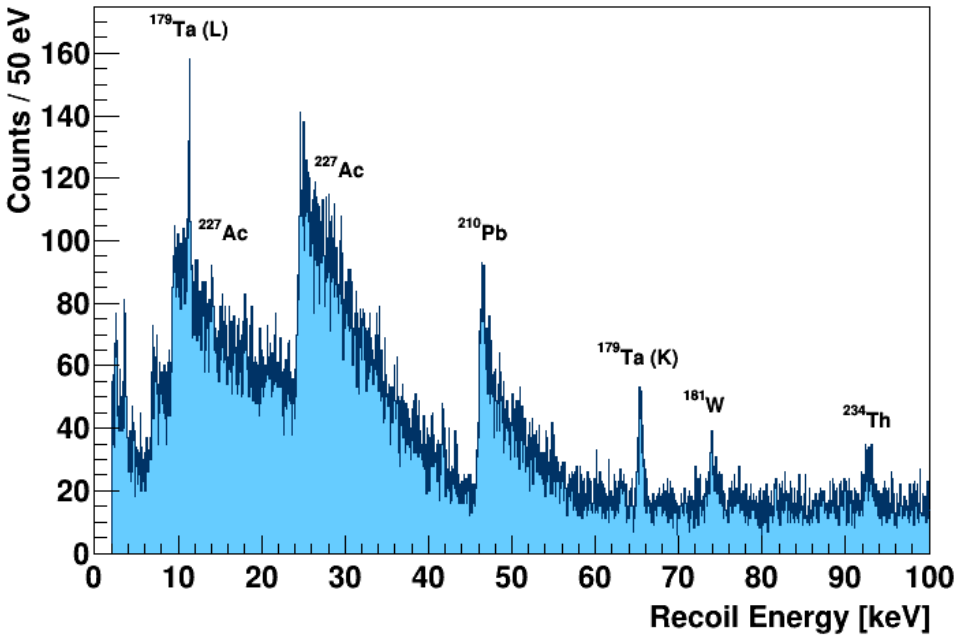

Figure 9.25: *Recoil-energy spectrum of all events below* 100 *keV in the complete data set of VK28. The spectrum at high energies (*$\gtrsim$ 60 *keV) is dominated by three* γ*-lines, while at low energies three* β*-spectra are observed. The two spectra starting at* 9.3 *keV and* 24.5 *keV are due to an intrinsic contamination of the crystal with* ^{227}*Ac. The* β*-spectrum starting at* 46.5 *keV originates from intrinsic* ^{210}*Pb decays. Also visible on top of the underlying* β*-spectrum is a double peak at* $\sim$ 11 *keV caused by* ^{179}*Ta-decay created via cosmogenic activation of tungsten.*

9.5.2 Light Yield - Energy Plane

In figure 9.24 the light yield - energy plot of the module VK28/Zam is depicted. As for the other modules also here the red solid lines limit the central 80 % e^-/γ-band, while the red dashed line is its lower 5 σ boundary. The limits of the nuclear recoil bands are drawn as blue solid lines, whereby the upper one corresponds to the 90 % upper limit of the oxygen band and the lower one to the 90 % lower limit of the tungsten band. The green dashed line marks the central line of the oxygen band, which is the upper boundary of the ROI for Dark Matter search (yellow shaded area) in the light-yield coordinate. The lower boundary is the 99.5 % lower limit of the tungsten band. In energy the ROI spans from the threshold of the detector of 2 keV up to 40 keV. In the complete data set of VK28 in total 593 events are observed in the ROI. Possible origins of these events are discussed in section 9.6.

The recoil-energy spectrum below 100 keV for the detector VK28[48] is depicted in figure 9.25. At low energies three β-spectra starting at 9.3 keV, 24.5 keV and 46.5 keV are observed. The first two are due to an intrinsic contamination of the crystal with the isotope ^{227}Ac while an intrinsic contamination of the crystal with ^{210}Pb-atoms results in the observed feature

[48] As mentioned in section 9.4, the recoil spectrum of VK27 is very similar to the one of VK28 depicted here. Therefore, in the present work only the spectrum of the detector with the lower threshold is shown.

starting at 46.5 keV.

^{227}Ac is part of the natural decay chain of ^{235}U and has a half-life of 21.773 a [90]. In 98.62 % of the time the isotope decays via the emission of a β^--particle into ^{227}Th, whereby three different states are possible. In $\sim$ 54 % of all β-decays the ground state is reached, resulting in a β-spectrum ranging up towards the Q-value of 44.8 keV. Secondly, in $\sim$ 35 % of all β-decays an excited state in ^{227}Th is reached. As this excitation is released via the emission of a γ-ray with 9.3 keV shortly after the initial decay, in the slow cryogenic detectors both processes are indistinguishable. Therefore, a β-spectrum starting at the γ-energy up to the Q-value is expected. Thirdly, in $\sim$ 10 % of all β-decays an even higher excited state in ^{227}Th is populated. This state results in a β-spectrum starting at 24.5 keV. All three features are observable in VK28 and partly in VK27 and, therefore, confirm that both crystals are intrinsically contaminated with ^{227}Ac.

In figure 9.25 also a few γ-lines are observed: The double peak observed at $\sim$ 11 keV and the peak at $\sim$ 65 keV are due to ^{179}Ta isotopes decaying via electron capture. These isotopes are created via cosmogenic activation of tungsten isotopes and are discussed in more detail in section 9.7.3. The peak observed at $\sim$ 75 keV is due to the decay of ^{181}W, another isotope created via cosmogenic activation. Finally, at $\sim$ 92 keV an external contamination with ^{234}Th results in a sharp γ-peak.

9.5.3 TES-Carrier Band

In figure 9.26 the amplitude spectrum obtained from the fit with the TES-carrier template is shown for all rejected TES-carrier-like events of VK28. Compared to the recoil-energy spectrum depicted in figure 9.25 a similar result is obtained. As no sharp line feature is observable in figure 9.26 an energy calibration is more complex. However, the starting point of the β-spectra could be used to obtain a rough calibration. For the energy axis on top the events in the rising part of the highest β-spectrum are set to 46.5 keV. This rough calibration validates the assumption that the other two β-spectra are caused by an intrinsic ^{227}Ac contamination, as the starting points agree with the expected values. If required, for a proper energy calibration of the big carrier crystals a similar scheme as for the main absorber could be applied (see section 4.4).

9.5.4 Accepted Events

The region of interest for Direct Dark Matter search is highlighted in yellow in figure 9.24. As for the other modules, it expands from the trigger threshold of the phonon detector of $\sim$ 2 keV up to 40 keV. In the light yield coordinate all events located between the central line of the oxygen band (green dashed line) and the 99.5 % lower limit of the tungsten band are accepted. In the exposure of 100.65 kg days of the complete data set of VK28 in total 593 events are found inside the ROI. The energy spectrum is depicted in figure 9.27 while possible sources for these events are discussed in section 9.6.

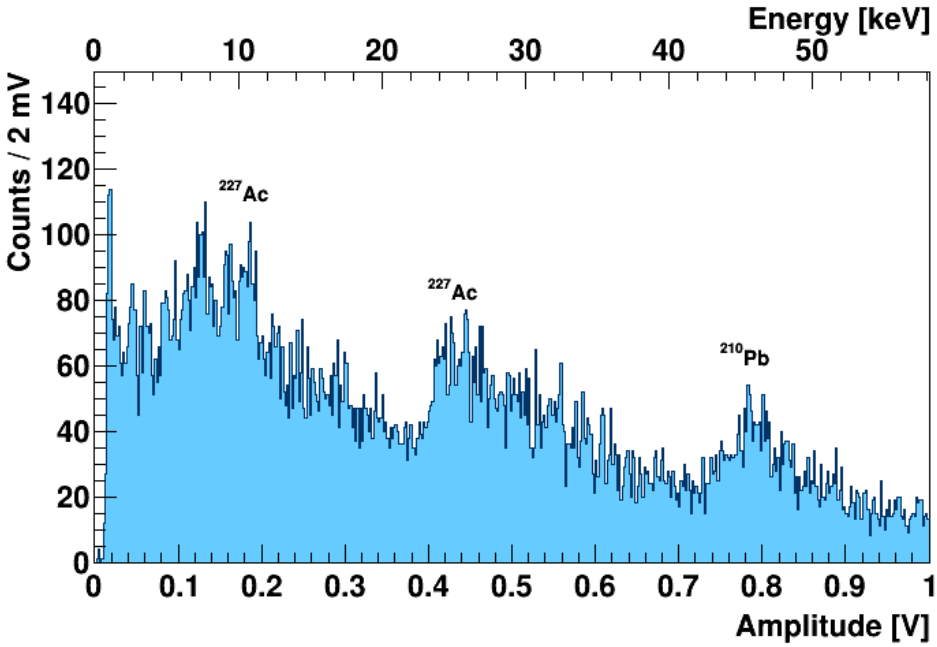

Figure 9.26: *Amplitude spectrum of the TES-carrier events observed in the complete data set of VK28. The amplitude is obtained from the fit with the TES-carrier template. No sharp γ-lines are observable and, thus, energy calibration is not trivial. However, the spectrum is similar to the one of the main absorber (see figure 9.25). Therefore, the β-spectra could be identified. Based on the ^{210}Pb β-spectrum starting at 46.5 keV a rough energy calibration is performed (second x-axis on top). Thus, the assumption for the origin of the two lower spectra to be due to an intrinsic ^{227}Ac contamination is confirmed and the energy calibration validated.*

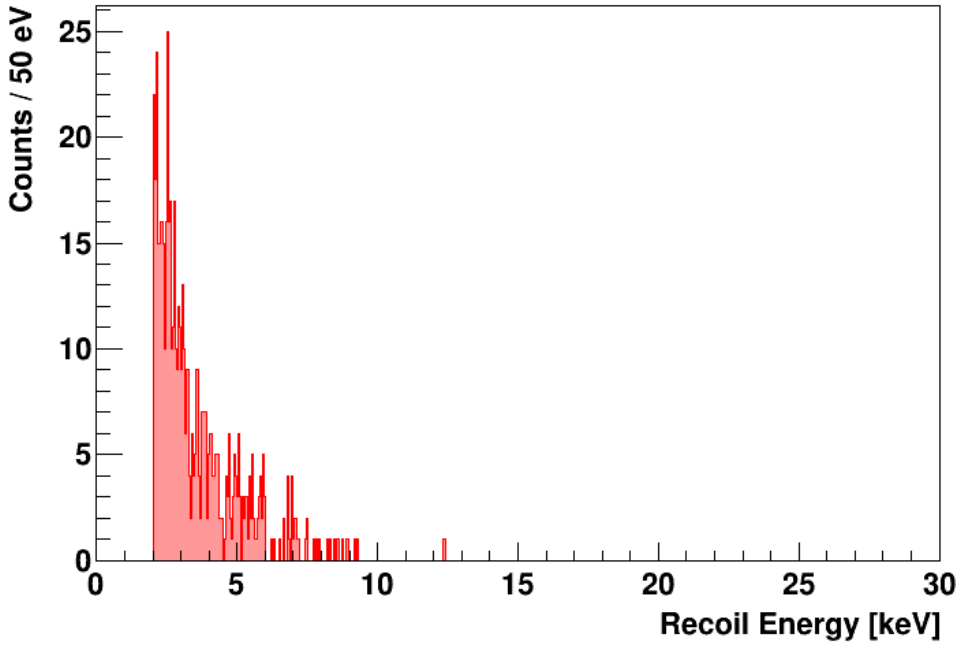

Figure 9.27: *Energy spectrum of the accepted events in the complete data set of the module VK28/Zam. The trigger threshold of the phonon detector (VK28) is* ~ 2 *keV. In an exposure of 100.65 kg days in total 593 events are located inside the ROI for Dark Matter search (yellow shaded area in figure 9.24).*

9.6 Events with Low Light Yields

The scatter plots of all modules analysed in the present work are shown in the previous sections of the present chapter. In all detectors a considerable amount of events is located inside the ROI for Dark Matter search. In the present section these events are discussed in more detail.

9.6.1 e^-/γ-Leakage

In order to quantify the leakage from the e^-/γ-band into the ROI for Dark Matter search the following scheme is used. First, the recoil-energy spectrum of the observed events inside the 80 % e^-/γ-band is determined. This spectrum is used for the density in the recoil energy parameter of the expected e^-/γ-band (see section 8.3.2). For the light-yield density the Gaussian band description as discussed in chapter 7 is applied. For this expected e^-/γ-band the leakage into the ROI is obtained via integration of the parameter space covered by the acceptance region.

It has to be mentioned here, that for the band fit performed in the present work the effect of a slightly different light yield for γ-events compared to e^--events is neglected [103, 145, 147]. While this is unimportant for the exclusion limit calculation performed, this approximation might be crucial for the leakage calculation[49]. Due to this fact the number of expected leakage

[49] As Yellin's optimum interval method is used to determine the respective exclusion limit on the WIMP-nucleon

events obtained might considerably be too low in particular if a low energetic γ-line is observed in the respective detector.

detector	accepted events	expected leakage events	probability
Lise	1318	1304.21	0.35
TUM38	33	8.43	$1.2 \cdot 10^{-10}$
TUM40	450	375.62	$6.2 \cdot 10^{-5}$
VK27	9	0.08	$3.0 \cdot 10^{-16}$
VK28	593	24.49	$3.7 \cdot 10^{-7}$

Table 9.1: *Number of accepted and expected leakage events per detector. Also given is the probability to observe the number of accepted events given the expected leakage. For all detectors more events than expected are accepted and, therefore, the probabilities to obtain an equal or higher number than the accepted events are given. Thereby, for an expected number of ≤ 50 leakage events the Poisson distribution is directly evaluated, while for higher values the latter is approximated by a Gaussian function.*

In table 9.1 the number of expected leakage events is given and compared to the number of accepted events for all five modules analysed. The probability to observe the number of accepted events when the number of leakage events is expected, is also calculated and included in the last column. Thereby, for an expected number of ≤ 50 leakage events the Poisson distribution is directly evaluated, while for higher expected values the latter is approximated by a Gaussian function. In all detectors more events than expected are observed. Therefore, the given values in the last column are the probabilities to observe an equal or higher number of events than actually accepted. The probabilities to observe such a number of events are very low in all detectors except in Lise, rendering a direct hint towards an excess of events in the ROI for Dark Matter searches. Thereby, it is important to state that for the following discussion Lise is neglected, as no excess of events is observed. For TUM40 the above-mentioned underestimation of the leakage events might relax the tension between expected and observed events most, as in this detector also the non-proportionality effect of the light output is very pronounced resulting in a large drop of the mean line of the e^-/γ-band.

9.6.2 Possible Explanations

As can be observed from the light yield - energy plots of all detectors analysed, in particular of the modules with big carrier design (see figure 9.17 (TUM38), figure 9.21 (VK27) and figure 9.24 (VK28)), the accepted events are located mainly at low energies and inside

cross section, all accepted events are considered as potential WIMP signals (see section 8.2). Therefore, a higher e^-/γ-leakage might lead, if at all, to a more conservative exclusion limit. Otherwise, considering this effect does not harm Yellin's methods and is strongly beneficial for a likelihood method, where the background contribution needs to be known as precisely as possible. Therefore, for the future it is planned to consider this effect. However, this is beyond the scope of the present work.

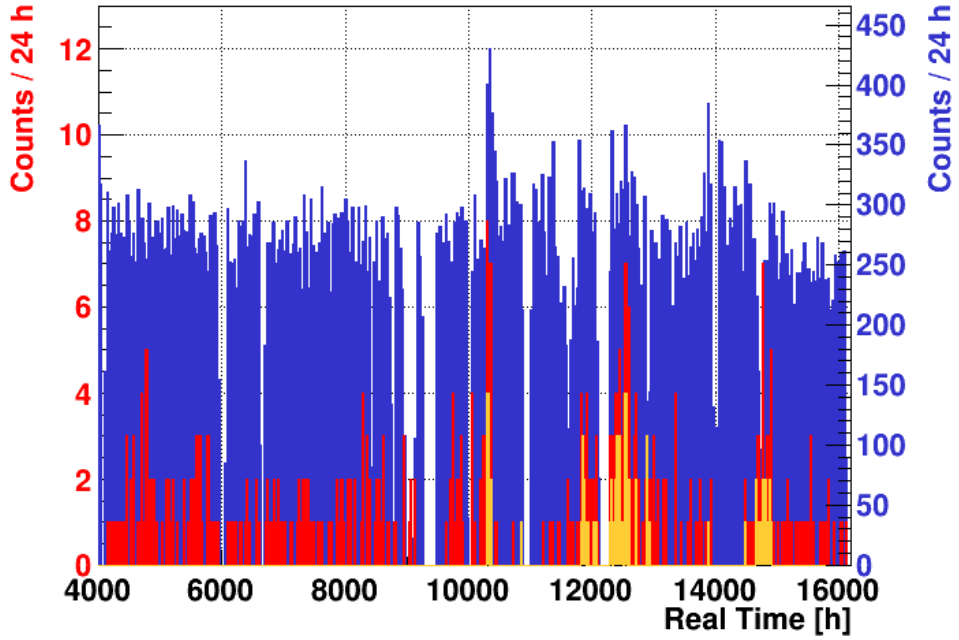

Figure 9.28: *Time distribution of all accepted events in the blind data set of TUM40 (red histogram, left y-axis). Highlighted in orange are the 65 events which are identified by eye as probable noise triggers (left y-axis). These potential background events occurred only after the trigger threshold of TUM40 had been lowered (∼ 9 000 h). For comparison, also the scaled time distribution of all events before any pulse-shape cut is applied is shown as blue histogram (right y-axis). The fact that potential noise triggers are found in coincidence with a high number of events before any pulse-shape cut is applied supports the conclusion that these events are unidentified invalid events.*

the nuclear recoil bands. There are several possible explanations for these events which are discussed in the following.

Unidentified Invalid Events

First of all, it might be possible that some of the events are invalid events, not identified by the applied selection criteria. To exclude this, the parameter distribution of the accepted events is compared to the distribution of all events. It is investigated whether or not some events are suspicious in one parameter which is used to identify invalid pulses (see section 5.3). However, no distinctive feature (e.g. that a large fraction of pulses shows a parameter value close to the cut limit) is found.

Furthermore, for all five modules analysed, all accepted events are checked by eye whether or not they are valid pulses. Only in TUM40 65 pulses are found which are most likely not identified noise triggers[50]. In figure 9.28 the time distribution of all accepted events of TUM40 (red histogram, left y-axis) is depicted whereby the subset of the noise-trigger events

[50] If there is any influence of these not identified noise triggers on the resulting exclusion limit, a more conservative result is obtained.

– identified by eye – is highlighted as orange histogram (left y-axis). For comparison also the time distribution of all events before any pulse shape cut is applied (blue histogram, right y-axis) is drawn in figure 9.28[51].

It has to be noted, that no noise-trigger events are observed before the lowering of the trigger threshold of TUM40 ($\sim 9\,000$ h), in particular, not in the training set. The fact that the accepted events identified by eye as potential noise triggers are clustered in time when also a large number of events before any pulse shape cuts are observed supports the conclusion of their origin.

Compared to the 454 accepted events in TUM40 these possible invalid events are still less than 15 %, however, the number is comparable to the potential excess. Therefore, in the following discussion TUM40 is not considered anymore[52].

For the other modules (TUM38, VK27 and VK28) it is excluded that a large fraction of unidentified invalid events is present. In these modules, also the time distribution of all accepted events shows no peculiar clustering at certain time periods.

Unidentified TES-carrier Events

Another explanation might be to assign the excess of events to a contribution of unidentified TES-carrier events, despite the large efforts performed in the present work to reject this type of background events. As the majority of the accepted events is observed at low energies, the outputs of the neural networks applied are checked. As the largest number of counts is observed in VK28 only this detector is discussed here. However, also for the other two modules VK27 and TUM38 it is investigated if the accepted events contain unidentified TES-carrier pulses.

In figure 9.29 the neural network output (trained with the stochastic minimization algorithm, see chapter 6) is depicted as a function of the pulse height for VK28. The black data points are all events with a pulse height of ≤ 0.15 V that survive the complete series of selection criteria, while the red data points are the subset of all accepted events for Dark Matter search. As can be seen, the distribution of both event sets are not significantly different and, therefore, no hint for unidentified TES-carrier pulses is found. The same is true for the second neural network parameter of VK28. Also for TUM38 and VK27 no suspicious differences between the parameter distribution of accepted and all events surviving the raw data analysis are found.

In the following, the events which are removed by the pulse shape cuts are investigated further. Therefore, a list is created which contains all events which are removed either by the rise-time cut, by the RMS-ratio cuts or by the two neural network based cuts.

In figure 9.30 the light yield - energy plot of these rejected events with energies below

[51] In this plot only data from the blind data set of TUM40 is depicted. Therefore, the x-axis starts at $\sim 4\,000$ h real time and the exponential decay of the rate is hardly visible (see figure 9.14). Due to the low number of accepted events also the bin width is significantly larger here. As a consequence, the rather short noise periods are not as distinctly visible as in figure 9.14. Nonetheless, a clear clustering of the accepted events at these periods is observed.

[52] The probability to observe 389 events when 375.62 events are expected is ~ 24.5 %. Furthermore, only the pulses which are clearly identified as noise-triggers are counted in this analysis. Thus, it is possible that the remaining events still contain a few unidentified noise triggers.

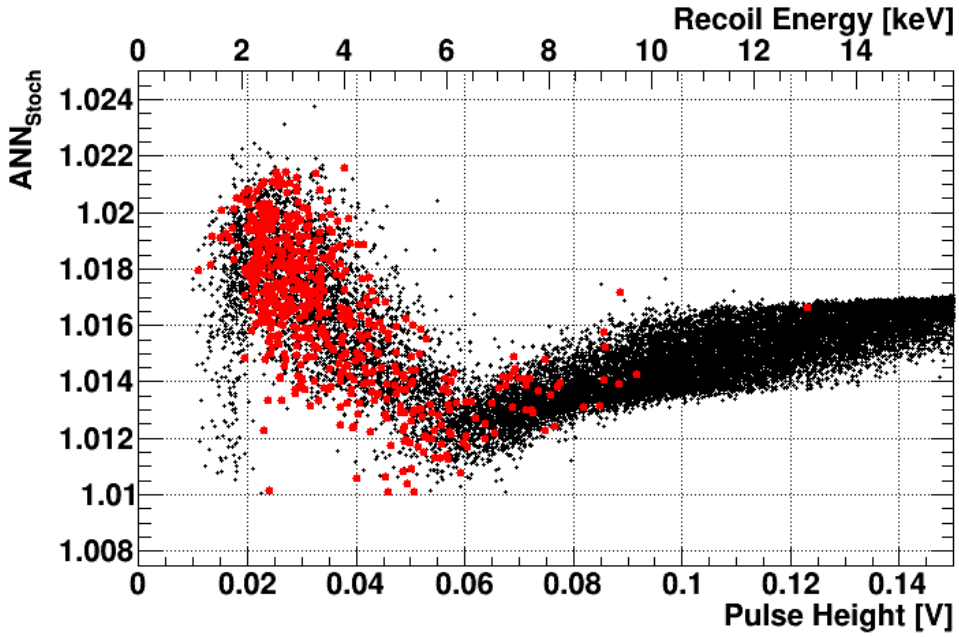

Figure 9.29: *Neural network output (trained with the stochastic minimization algorithm) as a function of the pulse height for different sets of events of VK28. The black data points are all events that survive the complete series of selection criteria, while the slightly larger red data points are the subset of all accepted events for Dark Matter search. No significant deviation between both populations is observed. Therefore, it is unlikely that the accepted events are spoiled by a large number of events containing unidentified TES-carrier phonon-detector pulses.*

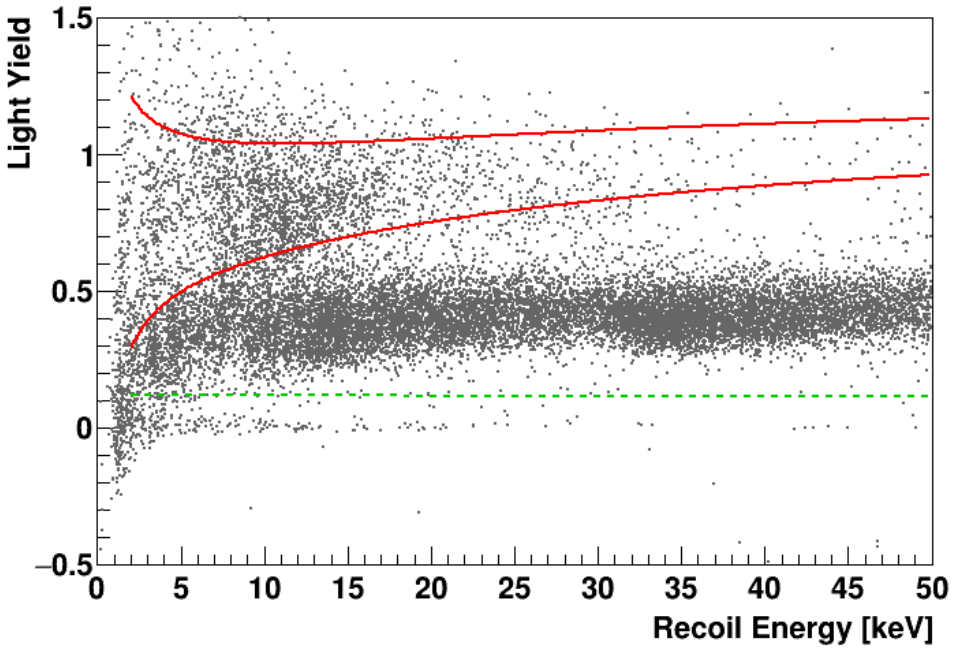

Figure 9.30: *Light yield - energy plane for recoil energies below* 50 *keV including the events rejected by the pulse-shape cuts of VK28*[53]*. The majority of these events is located below the* 80 *% e^-/γ-band (red solid lines) and above the central line of the oxygen band (green dashed line). The latter is the upper light-yield limit of the chosen ROI for Dark Matter search. In a band centered at a light yield of zero direct thermometer hits are observed and rejected. This is remarkable, as the neural networks have never been trained with pulses of this type but are still able to recognize them*[54]*. Although the networks are trained with both, absorber and TES-carrier pulses, the stringent cuts applied rely only on the fact that the pulse shape of absorber pulses is exactly known.*

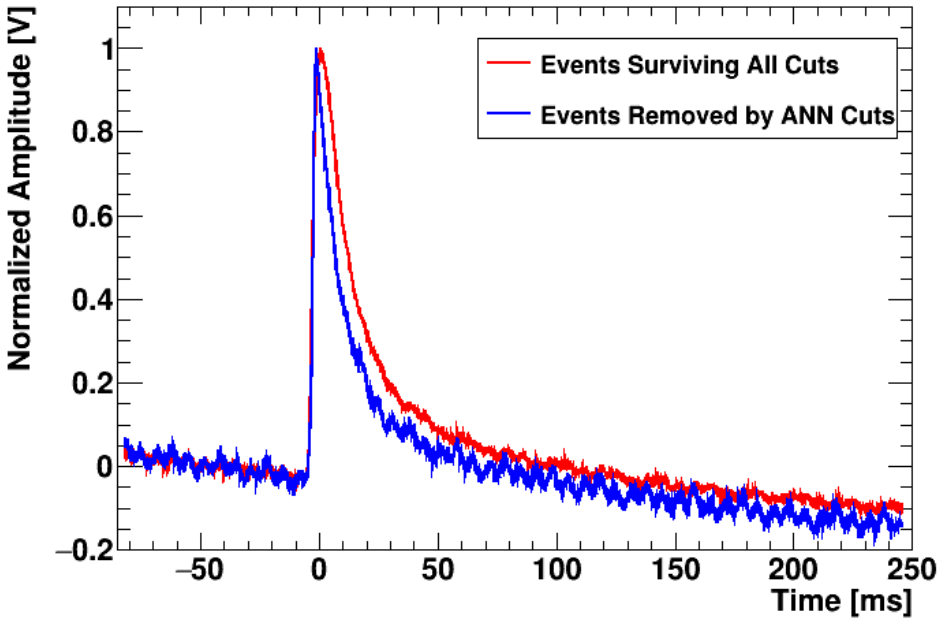

Figure 9.31: *Comparison of the templates of low light-yield events observed in VK28. The same cut limits are applied to two different sets of events. While the red template is created from pulses which survive the complete cut series in VK28, the blue one is made out of pulses which are rejected by the ANN-based pulse-shape cuts. As can be seen there is a clear difference in the pulse shape, which is exploited by the ANN to discriminate the respective events.*

$\sim 50\,\mathrm{keV}$ is depicted[53]. As can be seen the majority of all rejected events is not located inside the 80 % e^-/γ-band (red solid lines) but in a distinct band at a lower light yield but still above the central line of the oxygen band (green dashed line) which is the upper limit of the chosen acceptance region for Dark Matter search.

In addition, below the central line of the oxygen band in figure 9.30 the no-light band centered at a light yield of zero is visible. This band contains direct hits of the thermometer resulting in pulses with even faster rise and decay times than for TES-carrier pulses. For these interactions no corresponding light signal is expected. They are also rejected by the ANN-based cuts, which is remarkable, as the neural networks have never been trained with pulses of this type[54]. However, as explained in section 6.6 the networks know precisely what an absorber pulse looks like. Due to the chosen cut limits all pulses which do not feature the known absorber shape are rejected.

As discussed in section 4.3, template pulses are a proxy for the typical pulse shape of the different pulse classes with reduced noise contributions. From the pulses located in the

[53] Please note that at this stage no energy cut is applied (see section 5.3.11). Thus, it is possible that events are reconstructed below the energy threshold of $\gtrsim 2\,\mathrm{keV}$ (compare section 5.3.10).

[54] Technically, these pulses are removed by the cut on the rise-time parameter. However, it is checked that for low-energetic pulses the ANN-output value is ~ 0 and, thus, inside the parameter space dismissed. For higher energies the RMS-ratio parameter of these pulses is below the chosen cut limit.

nuclear-recoil band, templates are created as depicted in figure 9.31. This is done for both, the pulses which are removed by the ANN-based cuts (blue) as well as for the ones surviving all cuts (red template). Thereby, the same two-dimensional cut in the light yield - energy region is performed for both types. By doing so, it is possible to decide whether or not the two low-energetic pulse classes differ. Although the baseline of the pulses is slightly tilted, it can clearly be seen, that there is a distinct difference between both templates. The rise time and, in particular, the decay time of the blue template are slightly faster and for the ANNs applied this difference is large enough to separate both pulse classes.

In summary, it is very unlikely that a large fraction of unidentified TES-carrier pulses is present in the resulting event list. No significant difference in the parameter distribution of the accepted events compared to all events is observed. Furthermore, the majority of the events containing a TES-carrier pulse is located in a distinct band between the e^-/γ-band and the nuclear recoil band, while the accepted events are located in the lower part of the nuclear recoil band. Finally, the pulse shape of the phonon pulses in the events which are removed by the ANN-based cuts is clearly different from the pulse shape of the surviving pulses.

Unconsidered Module Design Related Background

As already mentioned above the excess is mainly observed in the three modules TUM38, VK27 and VK28. In total only five modules are analysed and in the mentioned modules the phonon detector is equipped with a large TES-carrier crystal. This might be just a pure coincidence due to the fact that the majority of all modules analysed is of this design type. However, it is also possible that the observed events are due to a module design related background. Up to now, such a background has not been observed for these modules, as in CRESST-II phase 2 modules of this design are operated for the first time successfully for a long measurement period[55].

In figure 9.32 the templates of e^-/γ-events and low light-yield events in VK28 are compared for the Dark Matter data set (a) and the neutron calibration (b). For both plots shown the two templates depicted are created from pulses of the low-energetic region. In order to select only nuclear recoils in the neutron calibration the respective template is created from pulses with energies in the range from 10 keV to 15 keV. Judging from the light yield - energy plot of the complete data set of VK28 (see figure 9.24) this region is well above the unknown event contribution, which might be also present in the neutron calibration data set. Consequently, also the corresponding template for electron recoils is created from this energy range.

In the Dark Matter data set (a) a slight difference between the two templates might be observable in the decay of the pulse. It seems that the low light-yield events (red pulse) exhibit a slightly larger decay time with respect to the e^-/γ template (black pulse). However, in the neutron calibration data (b) this is not observed for nuclear recoils (red pulse) and electron recoils (black pulse) of this detector. Thus, this might be a hint that the events observed in VK28 are not nuclear recoils and, therefore, might be induced by an unknown background source. Furthermore, if this is true it might be possible to train ANNs with these two templates and use them to discriminate the two pulse classes.

[55] In CRESST-II phase 1 another module of the big carrier crystal design has been installed. However, the corresponding light detector could not be operated and, thus, no such analysis is possible.

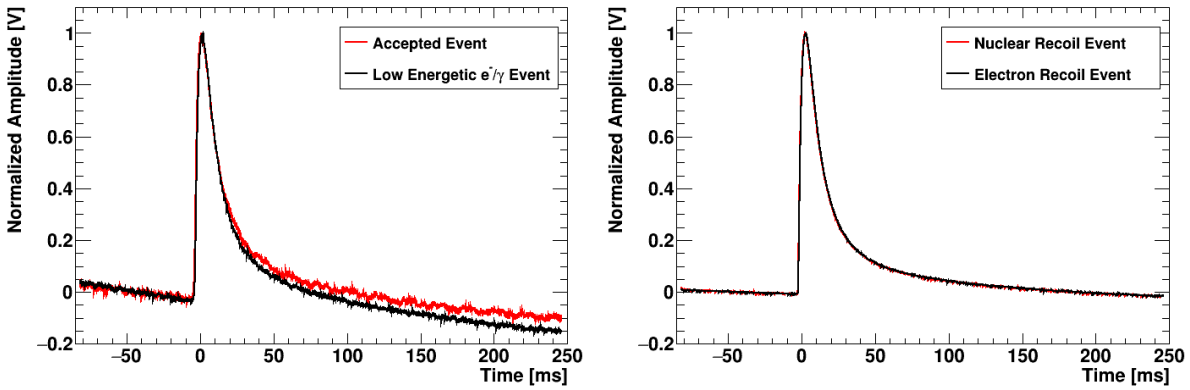

(a) Dark Matter Data Set *(b) Neutron Calibration Data*

Figure 9.32: *Comparison of templates of VK28 obtained in the Dark Matter (a) and in the neutron calibration data set (b). In both plots the black template is created from pulses of the e^-/γ-band, while the red template is built from low light-yield events. For the Dark Matter data set the template is created from the low light-yield events observed. The decay time for these pulses seems to be in average slightly longer compared to electron recoils. This is not observed for the nuclear recoils of the neutron calibration, where no difference between both templates can be seen. This might be a hint that the events observed at low light yields in VK28 are not nuclear recoils but instead caused by an unknown background source. Further investigations of this topic are required but this is beyond the scope of the present work.*

In figure 9.33 a zoom into the low-energy and low light-yield region of the light yield - energy plane of VK28 is depicted. In addition to the band limits already drawn in figure 9.24, this time also the central 80 % no-light band is marked by the magenta solid lines. Although there is a significant overlap with the nuclear recoil bands it seems that the majority of the events accepted is well inside this band. Thus, it might be possible that the majority of the events accepted are not accompanied by a light signal which is expected for stress-relaxation events.

Signal Contribution

Although it seems to be unlikely it is possible that the excess of events at low energies and low light yields might be caused by a signal contribution. In order to clarify the situation a method inherently able to decide whether an exclusion limit or a signal claim is supported by the observed data is required. Based on the numbers given in table 9.1 and the observation of unidentified invalid pulses in TUM40 it is concluded that an excess of events is, if at all, not pronounced in Lise and TUM40. However, in the other three modules the excess is distinct whereas for Dark Matter induced events the same amplitude is expected in all modules. Therefore, it seems to be unlikely that the events are induced by Dark Matter particles. Furthermore, it is not clear whether or not the number of excess events observed in TUM38, VK27 and VK28 are consistent with a signal contribution of the same strength.

In such a situation a signal fit could help to clarify the origin. If the combined fit of Lise,

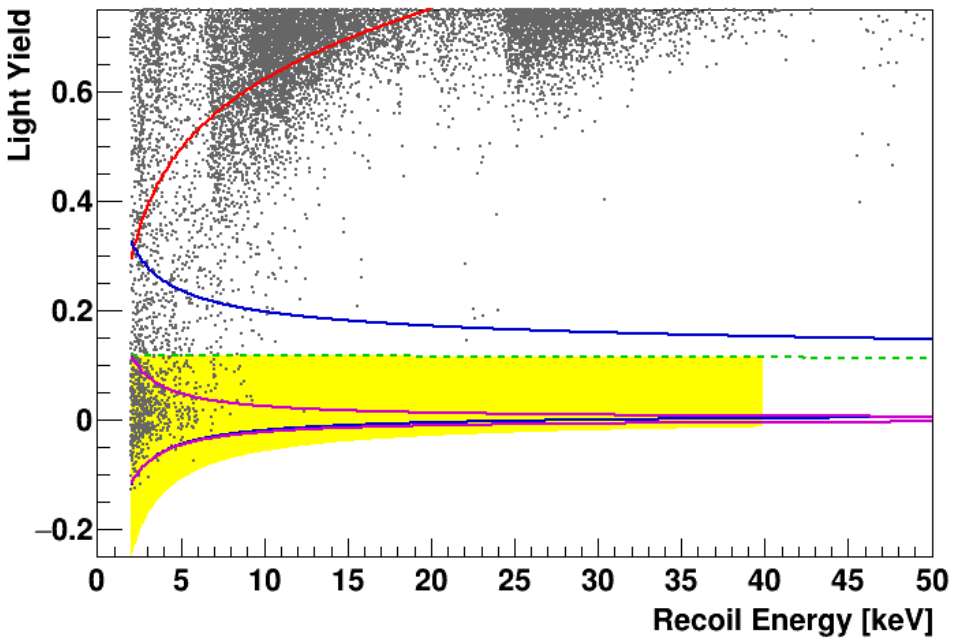

Figure 9.33: *Zoom into the low energy and low light-yield region of the light yield - energy plane of VK28. Besides the 90 % lower limit of the e^-/γ-band (red solid line) and the nuclear recoil band (blue solid lines) also the no-light band is depicted (magenta solid lines). The majority of the accepted events is located inside this no-light band. However, a strong overlap with the nuclear recoil bands is observed. Therefore, no clear statement is possible. Nonetheless, it might be a hint that the majority of the accepted events is not accompanied by a light signal which is expected for stress-relaxation events.*

TUM40, TUM38, VK27 and VK28 would result in a positive result this would strengthen the believe in a signal claim. The fit can also result in a rejection of the signal hypothesis as Lise and TUM40 are constraining the allowed maximal amplitude. Up to now the latter case seems to be more likely.

However, to perform such an analysis the background contributions need to be known precisely. As explained in section 3.1.2 neutrons are the ultimate background as they are scattering off nuclei much as expected for WIMPS. Therefore, they are indistinguishable from Dark Matter induced signal events. The number of neutron induced events could be constrained from an observed single-to-multiple scatter ratio (e.g. from the neutron calibration data set) [107]. The number of observed multiple-scatter neutron events in the data set could be used to restrict the number of expected single scatters induced by neutrons.

As explained in section 3.5 during the preparation for CRESST-II phase 2 an inner neutron shield, consisting of polyethylene pieces, has been installed. Therefore, the neutron background is drastically reduced in the current phase and based only on the five detectors analysed not well constrained in the fit. An analysis of all 18 modules installed might reveal a considerable number of events in the nuclear recoil band which are either coincident in time with the muon veto or other cryogenic detectors. Based on this number an upper limit for the neutron background might be obtained, however, this is beyond the scope of the present work.

Summary

In the present work five modules are analysed and in all of them events at low light yields are observed. In Lise the number of accepted events is compatible with the expectations from the e^-/γ-leakage, as the deviation is well inside the expected statistical fluctuation. In the other four modules an excess of events compared to the expectation based on the e^-/γ-leakage is found. As the slightly different light yield of γ-lines is not considered in the leakage calculation it might be well possible that the excess of events is not as large as stated here. In the following, the previous discussion of potential explanations of the observed excess of events is summarized.

For TUM40 a number of unidentified noise-trigger events is found which might explain the slight excess in this detector. For the other modules (TUM38, VK27 and VK28) no unidentified invalid pulses are found. Therefore, it is concluded that, if at all, only a small number of such events is present in the data sets.

Afterwards, it is investigated whether or not unidentified TES-carrier pulses might explain the observed excess. Also this explanation is very unlikely as the pulse shape in the phonon detector of the events in question is very similar to the expected pulse shape of absorber pulses. Furthermore, TES-carrier events are typically located in a band between nuclear and electron recoils.

Therefore, the two remaining explanations are either WIMP induced events or an unknown background source, most likely only present in the phonon detector design with a big carrier crystal. Up to now it is not clear which of these two explanations is true, however, the fact that the excess is only observed in the modules of this special phonon detector design might be suspicious. There are further indications hinting towards an unknown background contribution as origin of the excess events. Further investigations are required but this is well beyond

the scope of the present work. In particular data from CRESST-III, which is the next stage of CRESST, might help to clarify the origin of the excess events observed. Any kind of background related to the TES-carrier crystals is avoided as in the majority of the modules installed the phonon-detector TES is evaporated directly onto the absorber crystal.

9.7 Radioactive Contamination of TUM-grown Crystals

Based on the analysis of TUM38 and TUM40 the e^-/γ-background of these two TUM-grown crystals can be compared to obtain information about their radioactive contamination. To do this, the recoil-energy spectra of the complete data sets of both detectors are used. All peaks visible in the e^-/γ-band are fitted by the sum of a Gaussian function and a linear background. In case of two or more lines close to each other (distance of the means $\lesssim 2\,\text{keV}$) a corresponding number of Gaussian functions with a combined width parameter is fitted to the energy spectrum. The lines are identified based on their mean energy and the respective activity is determined by the fit. The signal survival probability $\varepsilon(E)$ (compare figure 9.6 and figure 9.16) is evaluated at the corresponding mean energy[56]. Thus, the final activity A of a specific line is given by:

$$A = \frac{n_{\text{obs}}}{t_{\text{live}} \cdot m \cdot \varepsilon(E)}, \tag{9.3}$$

where t_{live} is the live time, m the mass of the detector, $\varepsilon(E)$ the signal survival probability obtained at the mean energy E of the corresponding line and n_{obs} the number of counts observed in the respective line. The latter is determined by integration of the Gaussian function constrained by the fit:

$$n_{\text{obs}} = \int_{-\infty}^{\infty} C \cdot \exp\left(-\frac{(E-\mu)^2}{2\sigma^2}\right) dE = C \cdot \sqrt{2\pi}\sigma, \tag{9.4}$$

where C is the height of the Gaussian function, μ the mean and σ the width.

The radioactive contamination of the two TUM-grown crystals TUM38 and TUM40 is compared in table 9.2. In the cases, where in both detectors peaks are observed with nearby energies (with only a small deviation due to the different energy calibrations) the resulting γ-lines are listed[57]. The only exception from this is the M1 line of the ^{179}Ta decay with an energy of $\sim 2.6\,\text{keV}$, which is below the trigger threshold of TUM38 and, thus, not observable. For all identified γ-lines observed the corresponding literature energy E_{lit} is given in the second column [90]. In case of the γ-lines observed in both detectors at $\sim 13\,\text{keV}$ and $\sim 37.5\,\text{keV}$, the origin could not be identified. Therefore, for both lines also no literature energy could be given in table 9.2. The fitted mean energy E_{fit} of the Gaussian function and the corresponding activity A determined as described in equation 9.3 are given for both detectors[58]. In the remaining

[56] For energies $\geq 40\,\text{keV}$ it is assumed that the signal survival probability is constant. At these high energies no energy dependencies of the selection criteria applied is expected. In most of the modules analysed the signal survival probability is already flat at lower energies and, thus, this assumption seems to be valid.

[57] Two γ-lines at $\sim 18\,\text{keV}$ and $\sim 271\,\text{keV}$ are observed only in TUM38. As the origin of both of these lines is not identified they are neglected here.

[58] The complete list of all parameter values obtained from the fit are listed in appendix F.

origin	E_{lit} [keV]	TUM38		TUM40	
		E_{fit} [keV]	A [µBq / kg]	E_{fit} [keV]	A [µBq / kg]
^{179} Ta (M1)	2.601	-	-	2.637 ± 0.007	61.17 ± 4.31
Cu K_α (ext.)	8.048	8.038 ± 0.013	20.22 ± 2.96	8.185 ± 0.012	26.43 ± 3.04
^{179} Ta (L2)	10.739	10.790 ± 0.014	28.07 ± 2.53	10.928 ± 0.012	25.69 ± 2.03
^{179} Ta (L1)	11.271	11.270 ± 0.004	140.06 ± 6.21	11.439 ± 0.003	177.24 ± 5.59
?	?	12.968 ± 0.024	27.33 ± 4.08	13.138 ± 0.034	23.68 ± 3.28
?	?	37.367 ± 0.028	17.41 ± 3.20	37.751 ± 0.031	14.77 ± 2.89
^{210}Pb (ext.)	46.539	46.280 ± 0.007	161.13 ± 6.49	46.798 ± 0.013	75.26 ± 4.73
^{234}Th (ext.)	63.29	62.940 ± 0.019	45.28 ± 2.72	63.446 ± 0.034	18.03 ± 1.88
^{179}Ta (K)	65.351	65.156 ± 0.008	192.47 ± 6.63	65.657 ± 0.008	207.71 ± 6.57
^{181}W	73.6	73.538 ± 0.033	120.19 ± 20.47(a)	74.002 ± 0.038	107.67 ± 19.77(a)
Bi $K_{\alpha,1}$ (*)	74.815	74.602 ± 0.039	19.58 ± 2.62	75.016 ± 0.068	13.35 ± 2.09
Bi $K_{\alpha,2}$ (*)	77.107	76.869 ± 0.024	36.74 ± 3.73	77.428 ± 0.052	18.91 ± 3.43
Rn $K_{\alpha,1}$ (*)	83.787	83.822 ± 0.083	17.21 ± 4.88	84.475 ± 0.090	9.42 ± 2.49
Bi $K_{\beta,1}$ (*)	87.349	86.937 ± 0.082	8.30 ± 2.61	87.549 ± 0.150	10.76 ± 3.54
^{234}Th (ext.)	92.59	92.432 ± 0.024	84.94 ± 5.60	92.973 ± 0.046	39.15 ± 4.59
^{226}Ra (ext.)	186.211	185.445 ± 0.029	73.02 ± 4.82	186.109 ± 0.042	65.28 ± 4.73
^{212}Pb (ext.)	238.632	238.684 ± 0.021	135.35 ± 6.48	239.950 ± 0.042	119.10 ± 6.69

Table 9.2: *Radioactive contamination observed in the complete data set of TUM38 and TUM40. As the threshold achieved for TUM38 is ~ 3 keV all lines with mean energies below are not observable in this detector. In all other cases only lines which are observed in both detectors are listed here. The origin of the lines is given in the first column, whereby all lines caused by external decays are additionally marked by (ext.). The X-ray lines marked by $(*)$ are most probably also externally produced (for details see section 9.7.4) The literature energies E_{lit} given in the second column are taken from [90]. The origin and the corresponding literature energies of the two lines observed at ~ 13 keV and ~ 37.5 keV in both detectors could not be identified. Finally, the mean energy E_{fit} and the mean activity A of all lines are included for both detectors. For the values marked by (a) the exponential decay of the count rate with time is observable within the exposure. Therefore, the given numbers correspond to the start activity A_0 of this respective decay. For more details see text.*

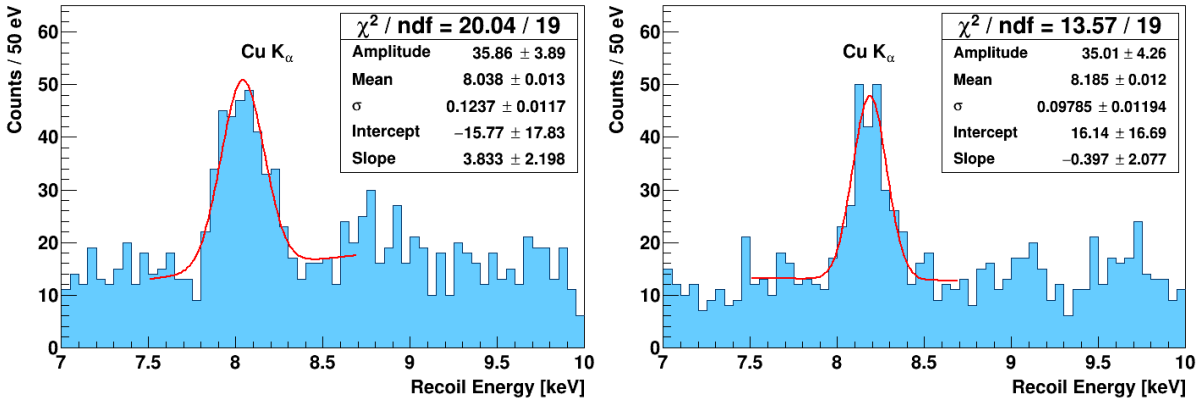

(a) *TUM38* ***(b)*** *TUM40*

Figure 9.34: *Recoil-energy spectrum around the copper fluorescence line observed in TUM38 (a) and TUM40 (b). The red line shows the fit function consisting of a Gaussian peak and a linear background function (intercept and slope parameter). The fit parameters are also depicted together with the corresponding statistical errors. A good agreement of the fitted mean energy and the literature value of* $E_{lit} = 8.04\,keV$ *[90] is observed. Furthermore, the fit yields with* $124 \pm 12\,eV$ *in TUM38 and* $98 \pm 12\,eV$ *in TUM40 an excellent* 1σ *energy resolution at this energy.*

part of the present section, the different observed γ-lines and their origins are discussed in more detail.

9.7.1 Copper Fluorescence and External Lines

As depicted in figure 9.34 in both detectors the copper K_α-line with a literature value of $E_{lit} = 8.05\,keV$ [90] is observed. This peak is attributed to the copper fluorescence, where γ-rays hit the copper in the vicinity of the detectors and interact via photoeffect with a copper atom. Thereby, an electron is excited and the resulting vacancy in the electron shell is re-filled by an electron of an outer shell under emission of a characteristic X-ray photon. The copper K_β-line ($E_{lit} = 8.91\,keV$) is expected only with a fraction of 12 % and, thus, is in both spectra not visible above the background level.

The energy calibration based on the response to test pulses assigns to the events of the line an energy very close to the literature value (see section 4.4 for more details). In TUM40 the deviation of the mean of the line, as determined from the fit, from E_{lit} is only 1.70 %, while in TUM38 an even better precision is achieved (0.12 % deviation). In both detectors excellent 1σ energy resolutions of $98 \pm 12\,eV$ (TUM40) and $124 \pm 12\,eV$ (TUM38) are obtained. The corresponding activities in the copper fluorescence line of both detectors agree well within the given statistical errors. As the activity is solely determined by the amount of copper in the vicinity of the detectors this does not have to be necessarily the case but can be expected as the module housing and the support structure are very similar for both module designs.

In figure 9.35 the recoil-energy spectra in the range of 40–70 keV are depicted for TUM38 in (a) and for TUM40 in (b). In both TUM-grown crystals a sharp γ-peak at 46.5 keV is

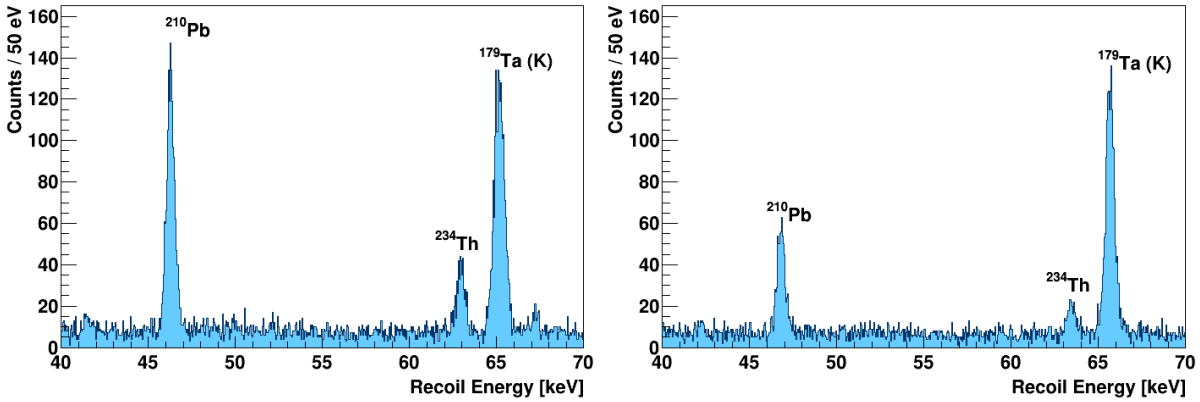

(a) TUM38 *(b) TUM40*

Figure 9.35: *Measured recoil-energy spectrum ranging from 40–70 keV for TUM38 (a) and for TUM40 (b). Three distinct γ-lines are observed in both detectors. The peak at ∼ 65.4 keV originates from activated tungsten isotopes decaying into ^{179}Ta, which in turn decays via electron capture. In the cryogenic detectors operated in CRESST-II this process results in a sharp γ-line at the binding energy of the daughter nucleus (here ^{179}Hf). The two other peaks observed are due to an external contamination with ^{210}Pb (∼ 46.5 keV) and ^{234}Th (∼ 63 keV). Both isotopes decay via the emission of a β-particle and, thus, in case of an intrinsic contamination a subsequent β-spectrum would be observed (e.g. for ^{210}Pb up to 63.5 keV). However, the background levels before and after the corresponding γ-peaks are flat and equally high. This supports the conclusion that TUM-grown crystals are not intrinsically contaminated with these two isotopes. In TUM38 larger peaks are observed compared to TUM40 and the resulting activities are given in table 9.2.*

observed and assigned to the ^{210}Pb decay. As explained in section 9.1.2, ^{210}Pb is transformed via a β-decay into ^{210}Bi with a half-life of 22.3 a. Thereby, mostly an excited state of bismuth is reached which relaxes with a half-life of < 3 ns via emission of a γ-ray. Thus, in the slow cryogenic detectors operated in CRESST-II an intrinsic contamination of ^{210}Pb would result in a γ-peak at 46.5 keV and a subsequent β-spectrum up to 63.5 keV (as observed for Lise in figure 9.3).

In both spectra of the TUM-grown crystals there is no hint for a subsequent β-spectrum, as the background levels before and after the γ-peak are flat and equally high. This observation supports the conclusion that the TUM-grown crystals are not intrinsically contaminated with ^{210}Pb but rather their direct vicinity (e.g. module housing and/or experimental volume). As ^{210}Pb is part of the uranium decay chain an exposure of the materials in the direct vicinity to radon (e.g. present in ambient air) is enough to explain this observed line. For TUM38 the resulting ^{210}Pb activity of $161.13 \pm 6.49\,\mu\text{Bq}/\text{kg}$ is twice as high compared to TUM40 ($75.26 \pm 4.73\,\mu\text{Bq}/\text{kg}$).

For two other unstable isotopes which undergo a β-decay (^{234}Th, ^{212}Pb) also only the γ-peaks without a hint of a subsequent β-spectrum are observed in both detectors. Therefore, these two lines are also marked as external in table 9.2. The argumentation for ^{226}Ra is different, as this isotope decays via emission of an α-particle into an excited state of ^{222}Rn [90].

The daughter nucleus relaxes with a half-life of 9 ns to the ground state via emission of a γ-ray of 238.6 keV. Thus, in the cryogenic detectors of CRESST an internal decay of ^{226}Ra would always include the α-decay together with the corresponding γ-ray. As the γ-line is observed, it has to be concluded that the preceding α-decay happened outside of the detector and, thus, this line is also caused by an external contamination.

9.7.2 ^{234}Th Lines

There are two γ-peaks, at ~ 63.4 keV (see figure 9.35) and at ~ 92.6 keV (see figure 9.37) which are visible in both spectra and are attributed to the external decay of ^{234}Th in table 9.2. According to the decay scheme of ^{234}Th there exists a γ-line at 63.29 keV with an intensity of 4.8 % [90]. Furthermore, there are two γ-rays close in energy, at 92.38 keV and at 92.80 keV with similar intensities of 2.81 % and 2.77 %, respectively. For these two lines the mean energies only differ by a value which is of the order of the respective energy resolution at this energy. Thus, within the given statistics no double-line feature but rather a broad single peak is expected to be observed in the energy spectrum. Indeed, the fit with a Gaussian peak above a linear background shows that the width of the Gaussian function is 462 ± 23 eV at a mean energy of 92.432 ± 0.024 keV in TUM38 and 411 ± 49 eV at 92.973 ± 0.046 keV in TUM40, respectively. This is rather broad compared to the width of 281 ± 23 eV and 281 ± 30 eV obtained for the ^{181}W decay at ~ 73.5 keV. Thus, in the following it is assumed that both theoretical lines are indistinguishable with the current detector performance. The literature energy of 92.588 keV given in table 9.2 is the intensity weighted mean of both γ-lines. The two intensities of the individual peaks have to be summed to obtain the expected fraction for the observed γ-peak.

For the two ^{234}Th lines observed at ~ 63 keV and ~ 92 keV (see table 9.2), based on the known intensities the expected activity of one of the two lines can be calculated with the measured activity of the other γ-line. However, the measured activities of the line at 63.3 keV of 45.28 ± 2.72 µBq / kg in TUM38 and 18.03 ± 1.88 µBq / kg in TUM40 do not match the expected values based on the ~ 92 keV line. In TUM38 an activity of 73.07 ± 4.82 µBq / kg and in TUM40 an activity of 33.68 ± 3.95 µBq / kg is expected. Therefore, only ~ 62 % and ~ 54 % of the expectation values, respectively, are actually observed.

This deviation can be explained with absorption of γ-rays passing through matter on their way to the respective detector. The start intensity I_0 of γ-rays with an energy E is reduced to an intensity value $I(d)$ after passing a distance d through a material of density ρ. This intensity is determined by the energy dependent absorption coefficient $\mu_{\text{abs}}(E)$ via:

$$I(d) = I_0 \cdot \exp\left(-\mu_{\text{abs}}(E) \cdot d\right). \tag{9.5}$$

The absorption coefficient $\mu_{\text{abs}}(E)$ is given by:

$$\mu_{\text{abs}}(E) = \rho \cdot \sigma_{\text{att}}(E), \tag{9.6}$$

where $\sigma_{\text{att}}(E)$ is the total attenuation coefficient of the respective material.

As explained in chapter 3, the majority of the parts surrounding the detectors is made of copper, which is a good absorber for γ-rays. The values for the total attenuation coefficient

$\sigma_{\text{att}}(E)$ are obtained from [163] for copper at the two energies of interest and are listed in table 9.3 together with the calculated absorption coefficients $\mu_{\text{abs}}(E)$. For the density of copper a value of $\rho = 8.96\,\text{g / cm}^3$ is used [164].

E [keV]	$\sigma_{\text{att}}(E)$ [cm^2 / g]	$\mu_{\text{abs}}(E)$ [1 / cm]
63.29	1.382	12.383
92.59	0.543	4.865

Table 9.3: *Attenuation coefficients $\sigma_{att}(E)$ for copper at the given energies E together with the respective absorption coefficients $\mu_{abs}(E) = \rho \cdot \sigma_{att}(E)$. For the density ρ of copper a value of 8.96 g / cm^3 is used [164]. The values for the attenuation coefficient are taken from [163].*

The thickness d required to explain the activity ratio between the two ^{234}Th lines observed in both detectors is obtained by:

$$d = \frac{\ln(\frac{\varepsilon_2}{\varepsilon_1} \cdot \frac{A_1}{A_2})}{\mu_{\text{abs},2} - \mu_{\text{abs},1}}, \tag{9.7}$$

where ε is the expected intensity, A the measured activity and μ_{abs} the absorption coefficient. The subscripts 1 and 2 denote the parameters for the two respective mean energies.

From Gaussian error propagation it follows for the error of the thickness Δd:

$$\Delta d = \sqrt{(\Delta A_1)^2 \cdot \left(\frac{1}{A_1 \cdot (\mu_{\text{abs},2} - \mu_{\text{abs},1})}\right)^2 + (\Delta A_2)^2 \cdot \left(\frac{1}{A_2 \cdot (\mu_{\text{abs},2} - \mu_{\text{abs},1})}\right)^2}. \tag{9.8}$$

To explain the measured activity ratios the γ-rays have to pass through copper of the thickness of only $d = 0.63 \pm 0.12$ mm for TUM38 and of $d = 1.51 \pm 0.17$ mm for TUM40. These numbers are reasonable in sight of the dimensions of the experimental volume and the amount of copper available.

9.7.3 Cosmogenic Activation of Tungsten

Due to cosmogenic activation of tungsten isotopes and their subsequent decay, γ-lines might be created and several lines originating from these isotopes can be seen in the detectors. Already with an exposure of a few weeks two decays have been observed in [103], namely the electron capture of ^{179}Ta and the electron capture of ^{181}W. The cleaner TUM-grown crystals operated in CRESST-II phase 2 allowed to identify further lines of these decays [127, 131]. Based on the large statistics of the complete data sets of TUM38 and TUM40 these decays are studied in more detail in the following.

^{179}Ta decay

A proton reaction of the form (p,α) on ^{182}W results in ^{179}Ta which in turn decays via an electron capture into ^{179}Hf. It is expected that ^{179}Ta is present in the crystals due to the cosmogenic activation of either the raw materials the crystals are grown from or due to activation

of the crystals themselves. As the half-life of the ^{179}Ta decay is $T_{1/2} = 665$ d such a cosmogenic activation is present as background for a long time in the corresponding crystals. In case of a ^{179}Ta decay in the crystal, the energy of the decay is released as kinetic energy of the neutrino. Subsequently, the remaining ^{179}Hf-atom lacks an electron in an inner shell, whereby this vacancy is quickly filled in an electron cascade. The calorimetric measurement performed by CRESST results in a peak at the corresponding binding energy of the ^{179}Hf-atom for the captured electron. The resulting energies for the capture of a K, L and M-shell electron are given in table 9.4.

electron shell	**binding energy [keV]**
M1	2.601
L2	10.739
L1	11.271
K	65.351

Table 9.4: *Binding energies of the different electron shells in the ^{179}Hf-atom [90]. ^{179}Ta produced via cosmogenic activation of ^{182}W decays via electron capture into ^{179}Hf. In the calorimetric measurement performed by the CRESST detectors the complete electron cascade of the decay is observed resulting in a measurement of the binding energy of the captured electron.*

In TUM40 all of these four lines are observed and well distinguishable, while in TUM38 the M-line could not be observed due to the high trigger threshold of ~ 3 keV. As the measurement in CRESST-II phase 2 lasted more than two years the exponential decay of the different lines might be observable. If the determined half-life corresponds to the expectation of the ^{179}Ta decay, this would strengthen the above-proposed origin.

Therefore, the events of the three different lines (M, L and K) are selected and their count rate per one hour of live time is drawn as a function of the real time in figure 9.36 [59]. The blue data points are for the events observed at the binding energy of the K-shell, the red ones for the L-shell and the black ones for the M-shell. Please note that the latter line is not observable in TUM38 due to the trigger threshold of ~ 3 keV. The corresponding errors (error bars in y-direction in figure 9.36) assume Gaussian distributed values. This assumption is always fulfilled due to the large bin width of 75 d (real time) and the large activities of all three lines. In both lines (L and K) observed in TUM38 as well as in the L-line observed in TUM40 it seems that the count rate is first increasing and decaying afterwards. This behavior is not expected and might be a hint for a further contamination first building up at these energies. However, as this is not understood up to now the respective bins are neglected in the fit. Changing the fit range affects the amplitude parameters more than the half-life. Therefore, in table 9.2 not the start activities, determined from the half-life fit, are listed but rather the mean activity is included. The latter is determined from the fit of a Gaussian function (above a linear background) to the energy spectrum.

[59] Within the given energy resolution of the detectors the L1 and L2 lines are well separated. However, the L2 line is less intensive than the L1 line and, thus, both L lines are investigated here together.

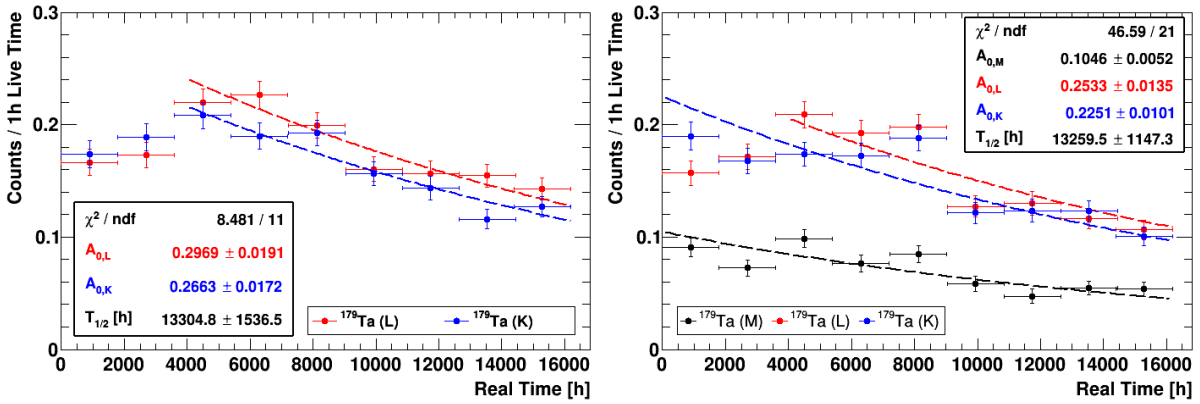

(a) TUM38 *(b) TUM40*

Figure 9.36: *Counts per one hour live time as a function of the real time in the ^{179}Ta K (blue), L (red) and M-shell (black) line observed in TUM38 (a) and TUM40 (b). In TUM38 the M-shell line with an energy of 2.6 keV is below the trigger threshold and, therefore, not observable. Also shown are exponential decays, whereby the parameters are obtained from a combined fit per detector. The start activities $A_{0,x}$ ($x \in \{M,L,K\}$) are individual parameters while the half-life is a combined parameter. The half-life of the ^{179}Ta decay is 665 d (15 960 h) and, thus, compatible with the given statistical error range.*

Also drawn in figure 9.36 are two and three exponential decays, respectively, whereby the parameters are determined in a combined fit for each detector. The start activities $A_{0,x}$, where x is M, L or K for the respective line, are individual parameters while the half-life $T_{1/2}$ is a combined parameter for all decays. The resulting values are also shown in the insets of figure 9.36. The start activities A_0,x are not used further due to the large systematic uncertainties mentioned above. For TUM38 a half-life of $13\,304.8 \pm 1\,536.5$ d and for TUM40 a comparable value of $13\,295.5 \pm 1\,147.3$ d are determined. Despite the fact of the unexpected behavior at the beginning of the measurement, both values are in good agreement with the expected half-life of 665 d (15 960 h) within the given statistical errors [90]. Thus, this result supports the reasonable assumption of the decay product of ^{179}Ta as origin for these three γ-lines.

As the observed activity is directly proportional to the capture rate of the different electrons in the electron capture decay this quantity is directly measured in the CRESST-II detectors. Based on the mean activities listed in table 9.2 the L/K-capture ratio is determined to be 0.87 ± 0.05 for TUM38 and 0.98 ± 0.04 for TUM40. In [165] two published values are listed: firstly, a value of 1.4 ± 0.4 for this decay is found in [166] and, secondly, a value of 0.63 ± 0.06 for the L/K-capture ratio is given in [167]. The values found in the present analysis are in good agreement with the first one while a slight disagreement with the second published value is observed. Nonetheless, in summary all three facts together, i.e. mean energies of the lines, half-life of the decay and capture rate, confirm the assumption for the origin of these three γ-lines.

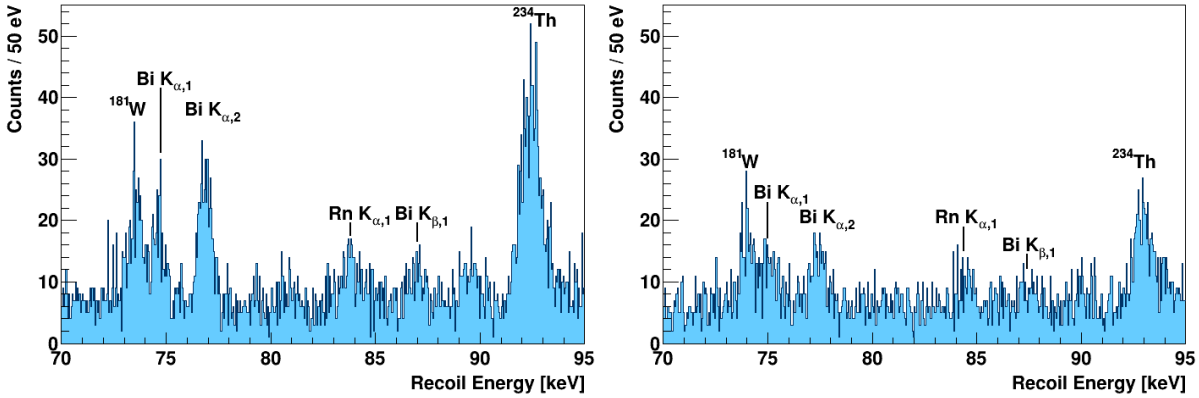

(a) TUM38 *(b) TUM40*

Figure 9.37: *Recoil-energy spectrum ranging from 70–95 keV for TUM38 (a) and for TUM40 (b). Several γ-lines are observed in this region. The largest peak at ∼ 93 keV is due to an external contamination of ^{234}Th. Several X-ray lines of bismuth are also observable. The peak at ∼ 74 keV is due to the electron capture decay of ^{181}W, created by cosmogenic activation of tungsten.*

^{181}W decay

^{181}W is present in the $CaWO_4$ crystals as it is created through the reaction ^{183}W(p,t)^{181}W [168]. It then decays via electron capture with a half-life of $T_{1/2} = 121.2$ d into ^{181}Ta, whereby in 76 % of all decays an excited state is reached [90]. As for the s-wave electron (K-shell) the probability is largest to be inside the nucleus, in the electron capture of ^{181}W mostly a K-shell electron with a binding energy of 67.4 keV is captured. The excited ^{181}Ta state is released via emission of a γ-ray of 6.2 keV. As this happens with a half-life of 6.05 µs the electron capture process and the emission of a γ-ray can not be resolved with the cryogenic detectors used. Therefore, the resulting peak of the ^{181}W decay is expected to be observed at the summed energy of 73.6 keV.

In figure 9.37 the recoil-energy spectrum ranging from 70–95 keV is depicted for the complete data sets of TUM38 (a) and TUM40 (b). Besides several other γ-lines observable in both spectra, there is also a clear peak at ∼ 73.7 keV. As mentioned in section 3.5, the complete measurement time of CRESST-II phase 2 lasted longer than two years and, thus, contains several half-life periods of this decay. Therefore, to determine the corresponding activity the radioactive decay has to be taken into account. Furthermore, a time analysis resulting in a half-life in agreement with the expected value of $T_{1/2} = 121.2$ d would strengthen the idea of the origin of this line.

In figure 9.38 the number of counts per one hour live time in the energy region around the ^{181}W γ-line is depicted as a function of the real time for TUM38 in (a) and for TUM40 in (b). The time dependency of all events in the energy region centered around the signal peak is depicted as black data points. This region contains the majority of the ^{181}W events but also a background distribution. While for the former an exponential decay is expected the latter is assumed to be constant in time. To be able to fit this constant background properly also a pure

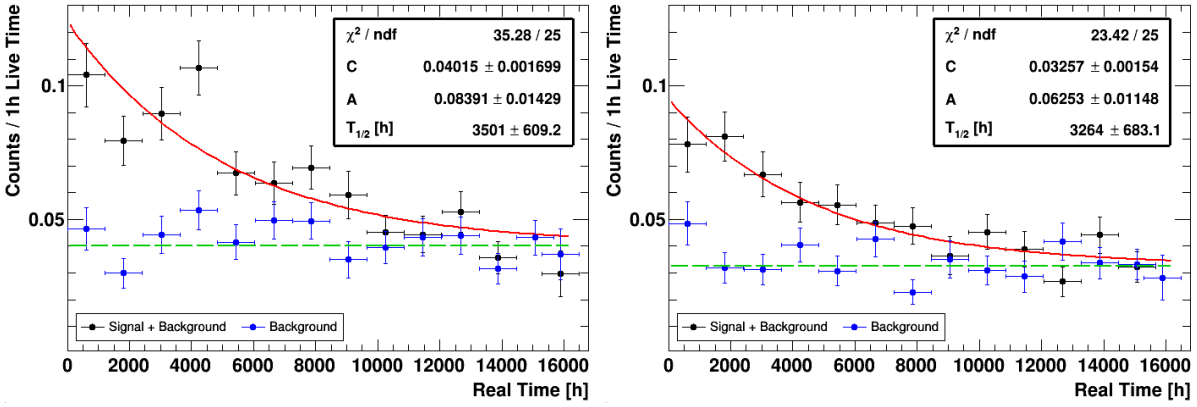

(a) *TUM38* ***(b)*** *TUM40*

Figure 9.38: *Time distribution of all events centered around the ^{181}W peak (black data points) as well as a background control region (blue data points). The former region contains the majority of the signal events. In order to result in an equal background rate in both data samples, the background peak caused by Bi $K_{\alpha,1}$ is split at the fitted mean: The low-energetic part leaking into the signal region is contained in this sample, while the high-energetic part contributes to the background region. For the ^{181}W-events an exponential decay with a half-life of $T_{1/2} = 121.2$ d (~ 2909 h) is expected while for the background-region events no time dependency should occur. These expectations are confirmed in both detectors by the observed data. For both detectors the fitted half-life agrees within the errors with the expected half-life of ^{181}W. This confirms the proposal of cosmogenically activated tungsten being present in the $CaWO_4$ crystals.*

background region of the same width is used and depicted as blue data points. The biggest problem for this approach is the close-by background peak caused by Bi $K_{\alpha,1}$. Therefore, the signal region contains the low-energetic part of the peak (up to the fitted mean), while the high-energetic part (above the fitted mean) is attributed to the background region. By doing so in a first approximation the same number of background events caused by this external contamination is included in both data samples.

The error bars are the statistical errors corresponding to the square root of the number of counts in the respective time bin. While the assumption of Gaussian distributed errors might be true in both detectors for the first time bins where a considerable fraction of signal events is still present, this is not the case for the later ones. This results in a reduced χ^2 that is smaller than one, indicating an overestimation of the corresponding errors. However, enlarging the time bins is not possible since the rate per time bin is not stable for ^{181}W due to the short expected half-life of only $T_{1/2} = 121.2\,\mathrm{d}$. For the chosen bin width of $\Delta t_{\mathrm{real}} = 50\,\mathrm{d}$ the expected activity drop ΔA from the beginning to the end of the time bin is

$$\Delta A = 1 - \exp\left(-\frac{\ln(2)}{T_{1/2}} \cdot \Delta t_{\mathrm{real}}\right) = 1 - \exp\left(-\frac{\ln(2)}{121.2\,\mathrm{d}} \cdot 50\,\mathrm{d}\right) \approx 0.25. \tag{9.9}$$

Therefore, the chosen bin width is a good compromise between these two effects mentioned above.

The solid-red line depicted in figure 9.38 is an exponential decay over a constant background. The parameters are obtained by a fit of the following form:

$$A_0 \cdot \exp\left(-\frac{\ln(2)}{T_{1/2}} \cdot t_{\mathrm{real}}\right) + C, \tag{9.10}$$

where t_{real} is the real time depicted on the abscissa, $T_{1/2}$ the half-life and A_0 the corresponding start activity. The constant background C (green dashed line in figure 9.38) is further restricted by an additional fit to the background sample (blue data points), whereby both fits are performed as a combination sharing the same constant background parameter. The resulting fit parameters are visible inside the boxes in figure 9.38.

The half-life is obtained as $T_{1/2} = 145.88 \pm 25.38\,\mathrm{d}$ for TUM38 and $T_{1/2} = 136.00 \pm 28.46\,\mathrm{d}$ for TUM40. Therefore, in both detectors good agreement with the expected half-life of $T_{1/2} = 121.2\,\mathrm{d}$ for the ^{181}W-decay is observed. Furthermore, the start activity A_0 is obtained to be $120.19 \pm 20.47\,\mu\mathrm{Bq/kg}$ for TUM38 and $107.67 \pm 19.77\,\mu\mathrm{Bq/kg}$ for TUM40.

9.7.4 Bismuth and Radium X-ray Lines

Besides the ^{181}W-peak at $\sim 74\,\mathrm{keV}$ and the ^{234}Th-peak at $\sim 93\,\mathrm{keV}$, both discussed above, there are several other peaks clearly visible in figure 9.37. These peaks are identified as the $K_{\alpha,1}$ ($\sim 74.815\,\mathrm{keV}$) and the $K_{\alpha,2}$ ($\sim 77.1\,\mathrm{keV}$) X-ray lines of bismuth [90]. The intensity per 100 K-shell vacancies of these two lines is 27.8 and 46.8, respectively. Based on the activity measured for one peak (here Bi $K_{\alpha,1}$) the expected activity of the second peak could be calculated resulting in an expectation of $32.96 \pm 4.41\,\mu\mathrm{Bq/kg}$ (TUM38) and

$22.47 \pm 3.52\,\mu Bq/kg$ (TUM40) for the Bi $K_{\alpha,2}$ line in the respective detector. In both detectors these values are in good agreement within the statistical errors with the actually measured activities of $36.74 \pm 3.73\,\mu Bq/kg$ (TUM38) and $18.91 \pm 3.43\,\mu Bq/kg$ (TUM40). Furthermore, the Bismuth $K_{\beta,1}$ and $K_{\beta,2}$ lines are expected at energies of 87.349 keV and 89.784 keV, respectively. Indeed, in both spectra there are either observable peaks at these energies ($K_{\beta,1}$) or at least hints for an excess of events. This supports the conclusion about the origin of the γ-lines being created from X-rays of bismuth.

Due to fluorescence induced by high-energetic γ-rays or muons these X-rays could be created. At least for the crystal TUM40 it is known from a dedicated α-analysis, that there is a considerable amount of bismuth inside the crystal [131]. As TUM38 and TUM40 are grown from the same batch of raw materials it is expected that also in TUM38 a bismuth contamination is present [169]. However, the radiation is most probably produced externally in the vicinity of the detectors as otherwise the excitation process would be detected as a single event. In the latter case it would be very unlikely to observe only the X-ray of bismuth and no further energy contribution of the exciting particle.

For bismuth there are more X-ray lines with reduced intensities which might be observed in the energy spectrum of both detectors. However, more statistics are required to clarify this situation. Also L-lines of bismuth at 10.839 keV and 13.023 keV might contribute to the low-energetic e^-/γ-background. The calculation of the expected intensities is not trivial since L-lines result from both K and L-shell vacancies. Therefore, for the expected intensities the different yields for the creation of a K and a L-shell vacancy have to be known. At ~ 13 keV there is a rather broad unidentified peak in both crystals which might be partly assigned to a bismuth contamination (compare figure 9.8 and figure 9.18). However, at ~ 11 keV there is the double-peak feature created by the cosmogenic activation of tungsten (^{179}Ta (L1) and ^{179}Ta (L2)) which hinders the clear observation of such a bismuth X-ray line.

Besides the bismuth X-ray lines there is also a peak at ~ 84 keV visible in both detectors, which might be assigned to a radon X-ray line. The literature energy of this $K_{\alpha,1}$ line is at 83.787 keV and it occurs in 46.5 % of the K-shell vacancies. The next prominent X-ray line of this element with an intensity of 28.0 % is the $K_{\alpha,2}$ line at 81.069 keV. At least in TUM38 there seems to be a peak at this energy with an activity of $10.95 \pm 3.84\,\mu Bq/kg$. Based on the measured activity of the line at ~ 84 keV and the intensities of the two X-ray lines this is in good agreement with the expected value of $10.36 \pm 2.94\,\mu Bq/kg$. Therefore, the ~ 84 keV line is assigned to be the Rn $K_{\alpha,1}$ X-ray line in table 9.2 without a confirmation of this effect in the second crystal TUM40. There already the peak most probably caused by the $K_{\alpha,1}$ line of radon at ~ 84 keV is hardly visible and, thus, the $K_{\alpha,2}$ could definitively not be observed above the background level.

9.7.5 Unidentified Peaks

In both energy spectra of the TUM-grown crystals TUM38 and TUM40 two γ-peaks are observed, where the origin can not be identified free of doubt. The first line has a mean energy of ~ 13 keV and might to some extend be explained by the bismuth X-rays discussed above. However, as the peak is very broad compared to the lines close-by in energy this fact supports the idea of at least two and maybe even more contributions. This line is also observed in

measurements performed in the test cryostat of the CRESST experiment which is also located underground in LNGS [108]. This observation supports the idea of an external contamination as origin for this line. The origin of the second line observed at $\sim 37.5\,\mathrm{keV}$ is totally unknown.

To summarize this section, there are several γ-lines observed and identified in the data set. In the complete data set of TUM40 as well as in TUM38 there is no hint of a β-decay spectrum in the e^-/γ-band below $\sim 300\,\mathrm{keV}$. In order to obtain more information about the intrinsic contamination of the TUM-grown crystals a dedicated α-analysis would be beneficial. For TUM40 [131] and several crystals installed in CRESST-II phase 1 [115, 132] this analysis has already been performed. However, for the other (TUM-grown) crystals installed in CRESST-II phase 2 this is beyond the scope of the present work [116].

9.8 Current Dark Matter Landscape

As already mentioned in section 2.2, there is a huge variety of experiments searching directly for Dark Matter and these experiments use several different approaches. To conclude this chapter about the results of the cryogenic modules analysed in the present work the current Dark Matter landscape is depicted in figure 9.39. All drawn lines correspond to exclusion limits of 90 % confidence level. The results of several liquid noble gas experiments are depicted as blue lines [54, 172–174], while the experiments based on silicon or germanium are shown in green [70, 80, 175–177]. The violet dashed line corresponds to the exclusion limit obtained from the PICO experiment [76], while the result of the KIMS experiment is included as orange solid line [178]. Furthermore, also the favored parameter spaces of CRESST-II phase 1 [107], CDMS-Si [170], CoGeNT [71] and DAMA/LIBRA [171] are drawn as shaded regions in figure 9.39. Finally, the published limits of CRESST-II phase 2 are included as red lines [127, 159, 160]. The gray shaded area is the region, where coherent neutrino-nucleus scattering, dominantly from solar neutrinos, will be an irreducible source of background for $CaWO_4$ based Dark Matter search experiments [179].

As mentioned in section 2.2, liquid noble gas experiments are leading in the search for high-mass Dark Matter particles. Consequently, the world leading limit above $\sim 6\,\mathrm{GeV}/c^2$ is achieved by the LUX experiment [54]. In this region the sensitivity is at least ~ 2 orders of magnitudes better than the best experiments not using liquid noble gases as target material.

However, at $\sim 6\,\mathrm{GeV}/c^2$ the enhanced detector performance of cryogenic detectors, in particular the lower threshold compared to liquid noble gas experiments, pays out resulting in drastically better sensitivities for experiments of this approach. The relatively low threshold of CDMS combined with the large exposure results in a world leading limit between $\sim 1.7\,\mathrm{GeV}/c^2$ and $\sim 6\,\mathrm{GeV}/c^2$ [175].

As can be seen in the low WIMP mass regime the sensitivity of the CRESST-II phase 2 result extends for the first time in direct Dark Matter searches down to $0.5\,\mathrm{GeV}/c^2$ [159][60]. Furthermore, the exclusion limit is world-leading below $\sim 1.7\,\mathrm{GeV}/c^2$ supporting the fact that low energy thresholds are the crucial requirement for studying the light Dark Matter regime. Consequently, for the next stage of CRESST a novel module design has been developed to achieve, in particular, very low thresholds. First prototypes have successfully been tested and

[60] Please note that here the term WIMP is used generically and not only for thermally produced WIMPs.

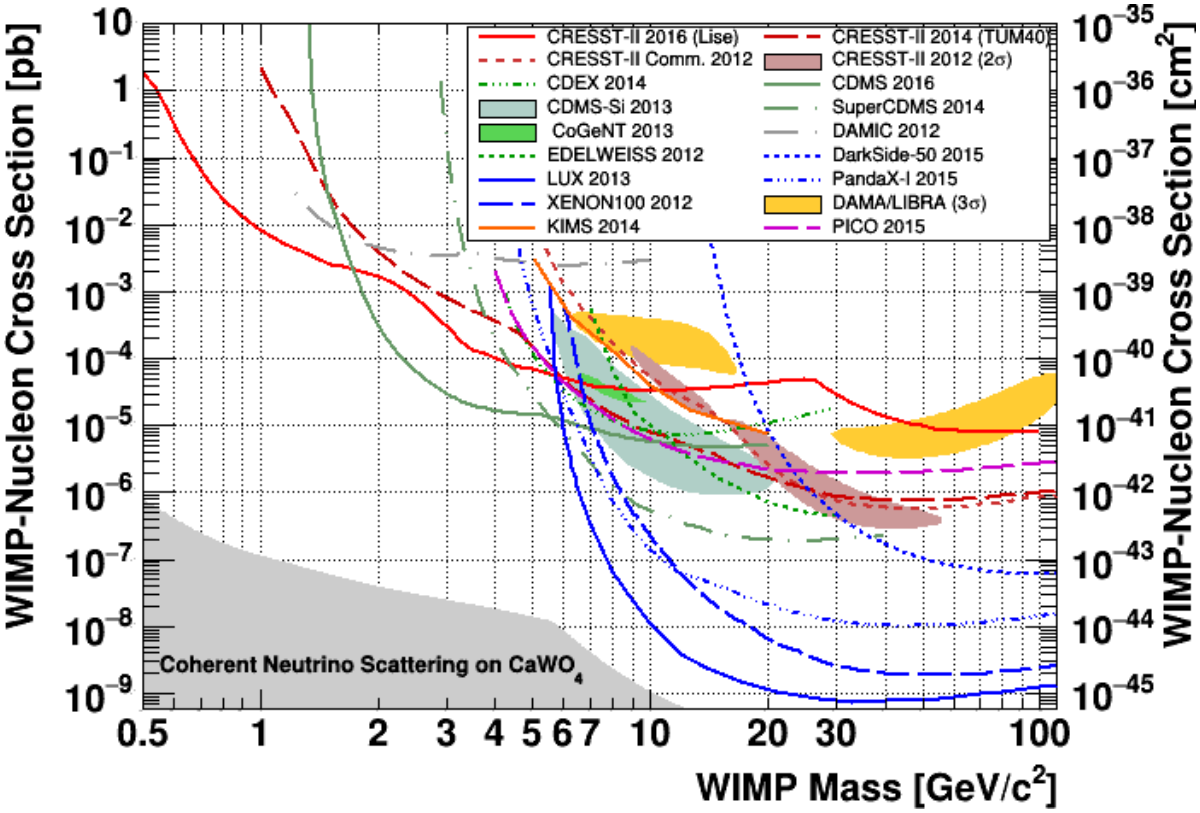

Figure 9.39: *Parameter space for elastic spin-independent WIMP-nucleon scattering[60]. The red lines correspond to exclusion limits (90 % C.L.) of CRESST-II [127, 159, 160]. For comparison also the favored parameter spaces of CRESST-II phase 1 [107], CDMS-Si [170], CoGeNT [71] and DAMA/LIBRA [171] are drawn as shaded regions. The exclusion limits (90 % C.L.) of the liquid noble gas experiments are drawn as blue lines [54, 172–174], of silicon and germanium based experiments in green [70, 80, 175–177]. The results of KIMS [178] (orange solid line) and PICO [76] (violet dashed line) are also included. In the gray area coherent neutrino nucleus scattering, dominantly from solar neutrinos, will be an irreducible background for $CaWO_4$-based Dark Matter search experiments [179].*

at the moment of writing already ten of these novel modules are installed in the experimental setup of CRESST (see section 11).

Part IV

Conclusion and Outlook

10 Conclusion

Despite large efforts performed in the last decade, the origin of Dark Matter remains one of the biggest puzzles in modern physics. There exist several observations on different astronomical length and time scales which are only explainable by the existence of Dark Matter. In chapter 1 several of these evidences are discussed and only the most striking one should be mentioned here. Since the precise measurement of the cosmic microwave background by the Planck satellite it is clear that only 4.9 % of the energy content in the universe is due to the well-known baryonic matter, 68.5 % consists of the totally unknown Dark Energy and 26.6 % is made up by cold Dark Matter. However, the particles that contribute to the Dark Matter content are unknown up to now.

There exist several theories for Dark Matter candidates (see section 1.2). The only Dark Matter candidate present in the standard model of particle physics is the neutrino, however, due to its small mass it has been relativistic during the freeze-out. Thus, neutrinos are hot Dark Matter and, therefore, excluded to be the dominant Dark Matter candidate by the observed structure formation in the universe. As a consequence of this, all astronomical evidences for Dark Matter are simultaneously a hint for physics beyond the standard model of particle physics.

A well motivated Dark Matter candidate is the Weakly Interacting Massive Particle (WIMP) which gained large interest due to the so-called *WIMP miracle*. Interestingly, the relic density of Dark Matter observed today is also obtained for the thermal freeze-out of particles with a mass of $\gtrsim 30\,\mathrm{GeV}/c^2$ and a cross-section in the order of the electroweak scale. The best-known theory which predicts WIMP candidates is the supersymmetric extension of the standard model of particle physics. However, also other theories give rise to WIMP-like Dark Matter candidates with masses of $\mathcal{O}\left(\mathrm{GeV}/c^2\right)$.

In chapter 2 the different experimental approaches to detect Dark Matter particles are listed. Three different scenarios exist to detect Dark Matter: Firstly, it could be produced directly in collisions of SM particles (e.g. at the LHC). The smoking gun signature of the production of a Dark Matter particle would be an event with a large amount of missing energy corresponding to the mass of the Dark Matter particle. Secondly, indirect search experiments try to detect standard model particles which are created in the annihilation or decay of Dark Matter particles. The most crucial and difficult task of such experiments is to exclude an astrophysical origin of the observed particles. The third scenario is the so-called direct detection of Dark Matter particles via their interaction with the nuclei in a target volume. All three scenarios provide complementary information about Dark Matter, however, in the present work only the direct approach is discussed further.

In section 2.1 the expected count rates induced by WIMP interactions in a direct detection experiment is deduced. WIMPs are expected to (elastically) scatter off nuclei and transfer only a small amount of energy. The latter depends on the masses of the WIMP and the nuclei

of the target material of the detector. However, in all cases it is a featureless exponentially decaying energy spectrum constrained at low energies ($\mathcal{O}$(keV)). The expected count rates depend on the scattering cross-section between Dark Matter particle and nucleus. However, as these particles are not observed up to now the cross section has to be small if these particles exist at all.

This implies some experimental challenges for the direct detection of Dark Matter particles. The different experimental approaches towards a direct detection are discussed in section 2.2. There exist several ideas and techniques and all of them have strengths and weaknesses. The currently leading experiments are liquid noble gas detectors (LUX) or cryogenic detectors (SuperCDMS and CRESST). The former ones are easier to scale to large detector masses and, thus, large exposures. Simultaneously, a very low radioactive contamination is achieved due to self-shielding of the target material and a fiducial volume. Therefore, at high WIMP masses $\gtrsim 10\,\mathrm{GeV}/c^2$ this technique plays the leading role. However, in these detectors a worse energy resolution and energy threshold is achieved compared to cryogenic detectors. Therefore, at low WIMP masses $\lesssim 10\,\mathrm{GeV}/c^2$ experiments of this approach achieve the highest sensitivities.

The present work is performed in the framework of the Cryogenic Rare Event Search with Superconducting Thermometers (CRESST) experiment. CRESST is a direct detection experiment based on cryogenic detectors operated at millikelvin temperatures. The experimental setup is located underground in the LNGS in Italy. The majority of the setup consists of a large amount of shielding material around the actual detectors (see chapter 3). The large effort to shield all background sources is required in order to be able to reduce the external radioactivity to a level where WIMP interactions might be observable.

CRESST-II uses scintillating $CaWO_4$ single crystals each equipped with a sensitive thermometer, a so-called *Transition Edge Sensor* (TES) as target material (see section 3.2). In a particle interaction the majority of the energy is converted into heat, warming up the absorber crystal and detected by the TES. Besides the heat signal a small amount of energy is converted into scintillation light. The actual ratio between both signals – the light yield – depends on the kind of interacting particle. Therefore, the $CaWO_4$ crystal is mounted together with a light detector in a reflective module housing in order to detect as much as possible of the scintillation light. The light signal recorded allows to discriminate signal (nuclear recoils) and background events (electron recoils) on an event-by-event basis.

The data analysed in the present work has been obtained during the second extensive physics run of CRESST-II also denoted CRESST-II phase 2. It lasted for more than two years and featured several calibration measurements including two neutron calibrations. However, the majority of the data is used to search for Dark Matter induced interactions.

In the present work, data of five modules starting from the raw pulses of phonon (heat) and light detector are analysed. The different steps required to obtain the relevant parameters in the raw data analysis of the recorded pulses are discussed in chapter 4. Thereby, the amplitude of the pulse, which is directly related to the energy deposited and, therefore, used for the energy calibration, is reconstructed by a so-called template fit. All time periods where one or both detectors of a module were not fully operational have to be rejected. Furthermore, all pulses where the template fit fails, mainly due to artifacts on the pulse trace, have to be rejected. The different methods and selection criteria applied are explained and discussed in chapter 5. In the template fit the Root Mean Square (RMS) deviation of the scaled template from the

actual pulse samples is determined for each pulse. This parameter is the most generic and, simultaneously, the most powerful measure against any kind of background. In the present work a method is developed and applied to determine the cut limit on the RMS parameter dynamically based on the observed data set.

The main part of the work is denoted to the development of artificial neural networks used to efficiently discriminate pulses with a different pulse shape down to the energy thresholds of the detectors (see chapter 6). This is the first time that these machine-learning algorithms are applied for a pulse-shape analysis in CRESST. In the evaporation process of the tungsten film used for the TES, the crystal has to be heated up. This results in oxygen vacancies and, therefore, a reduced light output. In order to avoid a reduction of the light output a composite detector design has been developed, whereby the TES is evaporated onto a $CaWO_4$ substrate (also called TES-carrier) which is then glued onto the main absorber crystal. Interactions in the TES-carrier result in pulses with different shapes compared to absorber pulses. This difference is exploited by specially trained multilayer perceptrons to discriminate these events. Such a multilayer perceptron uses the weighted (non-linear) sum of its input parameters to output a decision variable. In order to learn which values of the input variables are special for the different pulse classes, the network has to be trained with pulses of known type. Therefore, also a pulse simulation method has been developed and applied in the present work. Based on these artificial data various discrimination parameters have been studied. The usage of a multilayer perceptron allows to combine all of these parameters and obtain a decisive output variable. The combination of two of these networks trained slightly differently is able to discriminate the different pulse classes in both, simulation as well as real data. This process has been applied to all five modules analysed in the present work.

The main result of the raw data analysis is the so-called light yield - energy plot, where the different event populations show up in different (roughly) horizontal bands (see chapter 7). It is used further in the high level analysis also performed in the present work to obtain ideally new information on the WIMP-nucleon cross section. The majority of all events is observed in the e^-/γ-band while Dark Matter particles are expected to scatter off nuclei. To describe the form of the nuclear-recoil bands (oxygen, calcium and tungsten) properly the e^-/γ-band is fitted and extrapolated to lower light yields by the usage of so-called quenching factors. These have been determined in a dedicated external setup and, therefore, the approach has been validated with neutron calibration data.

An acceptance region for Dark Matter particles is defined, where the signal probability is high and, simultaneously, a low background contribution is expected (see chapter 8). Based on the observed events inside this region for two modules an exclusion limit on the WIMP-nucleon scattering cross-section has been obtained. Therefore, the frequentist approach of Yellin's one-dimensional optimum interval method has been used to obtain curves with a 90 % confidence level.

Finally, in chapter 9 the results of the high-level analysis are discussed. The exclusion curves obtained in a low-threshold analysis for the modules Lise/Enrico and TUM40/Michael are shown in section 9.1 and 9.2. For the other three modules analysed (TUM38/Petrus, VK27/Diogenes and VK28/Zam) an excess of events inside the ROI is observed (see sections 9.3 – 9.5). In section 9.6 several possibilities for the origin of these events with low light yields are discussed. The most likely scenario is that these events are caused by an unknown

background related to the phonon detector design with a big carrier crystal. In order to clarify this, in the majority of the modules installed in the next stage of CRESST (denoted by CRESST-III) the TES-carrier is omitted by direct evaporation of the TES onto the absorber crystal.

The radioactive contamination of the TUM-grown crystals, analysed in the present work, is compared in section 9.7. Several lines, observed in the e^-/γ-band, are discussed and their activity is determined. Thereby, it is found that the majority of the observed contamination is not intrinsic but external.

The excellent results obtained by a low-threshold analysis of the module featuring the phonon detector with the lowest trigger threshold (Lise) are compared to other experiments in section 9.8. The analysis of this module performed in the present work is in good agreement with the published results discussed there. For the first time in the Dark Matter community a sensitivity down to $0.5\,\mathrm{GeV}/c^2$ is achieved and, simultaneously, for Dark Matter particles masses smaller than $\sim 1.7\,\mathrm{GeV}/c^2$ the world leading exclusion limit is obtained. This shows the great potential of low-threshold detectors for low-mass Dark Matter search.

11 Outlook

In this chapter, various steps which might be performed in the future to improve some aspects of the present work are further described. These aspects span from better analysis techniques for the limit calculation to new data analysis of various physical topics. In addition, there exist several ideas to further improve the excellent performance of the pulse-shape analysis and to use neural networks for the event selection of the complete data analysis.

Likelihood and Bayesian Analysis

The consequent next step for the limit calculation is the development of enhanced statistic methods to obtain the best possible result from the measured data. These methods should not only consider the energy distribution of the events but also the light-yield information since in the latter parameter the signal and the majority of backgrounds deviate significantly. One key requirement for such analyses is the existence of a valid background model describing the energy as well as the light-yield distribution of the main background sources. As already explained, in CRESST-II phase 2 large improvements in using Monte Carlo simulations to predict these distributions have been achieved [131]. By now, the predictions based on the identified internal and external radioactive contamination can explain $\sim 70\,\%$ of the background level observed in TUM40.

In addition to Yellin's one-dimensional optimum interval method, also a one-dimensional likelihood limit is calculated for TUM40 and Lise in [123] using a data-driven model to describe the energy distribution. This background model is considered in the total likelihood and promising results are obtained. For the future also a Bayesian analysis of the data is favorable, as from a technical point of view both methods do not differ significantly while the statistical interpretations obtained from both methods do. Furthermore, the full two-dimensional information should be used in order to separate signal and background efficiently.

Alternative Physics Studies

Besides the WIMP scenario there exist other theories to generate the Dark Matter content observed in the universe. The data gathered by CRESST-II could be used to proof, constrain or exclude parameter space predicted by these theories. In particular the low energy threshold of the cryogenic detectors allows to explore previously inaccessible regions in such parameter spaces. An analysis similar to the one performed in [180] could constrain the parameter space for Dark Photon Dark Matter. First results of such an analysis seem to be very promising and

due to the low threshold of cryogenic detectors the obtained limits extend to lower dark photon masses [181].

Another example which should explicitly be mentioned here is a possible indication of a positive signal based on momentum dependent Dark Matter. According to [182] the existence of an asymmetric Dark Matter particle (see section 1.2.5) is able to explain the discrepancy between helioseismological observables and the predictions from solar models. By using the low-threshold data obtained with Lise [159] and the non-observation of a signal contribution, the CRESST collaboration is able to exclude this signal claim [183].

However, CRESST can not only contribute with results to the Dark Matter community but also in other fields of astroparticle physics. Since $CaWO_4$ contains some amount of the isotope ^{48}Ca, also an analysis searching for the neutrinoless double beta decay could be performed with the gathered data. Furthermore, it might be possible to improve the limits on the half-life for double electron capture processes. At the time of writing of the present work a dedicated paper on this topic is in preparation for the two isotopes ^{40}Ca and ^{180}W using data obtained in CRESST-II phase 1 [184]. However, the same analysis could be applied to the data gathered in CRESST-II phase 2 and analysed in the present work.

CRESST-III

Since major upgrades of the detectors are foreseen with the upcoming next phase the experiment is renamed as CRESST-III [185]. The volume of the target crystal is drastically reduced, resulting in a reduction of the crystal mass of an individual module from $\sim 300\,\mathrm{g}$ down to $\sim 25\,\mathrm{g}$. This leads to a decreased energy threshold and, simultaneously, the module housing as well as the detector layouts are optimized for the new specifications. All measures together are expected to result in a substantial gain of sensitivity for low Dark Matter masses.

In figure 11.1 a schematic drawing as well as a picture of a newly developed and optimized module design for light Dark Matter searches are depicted. The optimized detector design as well as results of measurements performed with the prototype module are presented in [186].

Similar to the stick design described in section 3.5.4, the absorber crystal is held by in total three $CaWO_4$ sticks. However, for the first time also the light detector is held by three $CaWO_4$ sticks. The majority of all modules of CRESST-III is equipped with TUM-grown crystals, due to their lower overall radioactive contamination. The TES is directly evaporated onto the absorber crystal to avoid the creation of pulses with distorted pulse shape due to gluing of the TES-carrier onto the crystal. Finally, to veto stick events down to the low energy threshold of the phonon detector, also the sticks holding the absorber crystal are equipped with TESs to provide a veto signal. Therefore, in figure 11.1 the stick holding the phonon detector is denoted by *iStick* (instrumented stick). These signals are read out in parallel by a single SQUID and, thus, in total three channels are required for a single module.

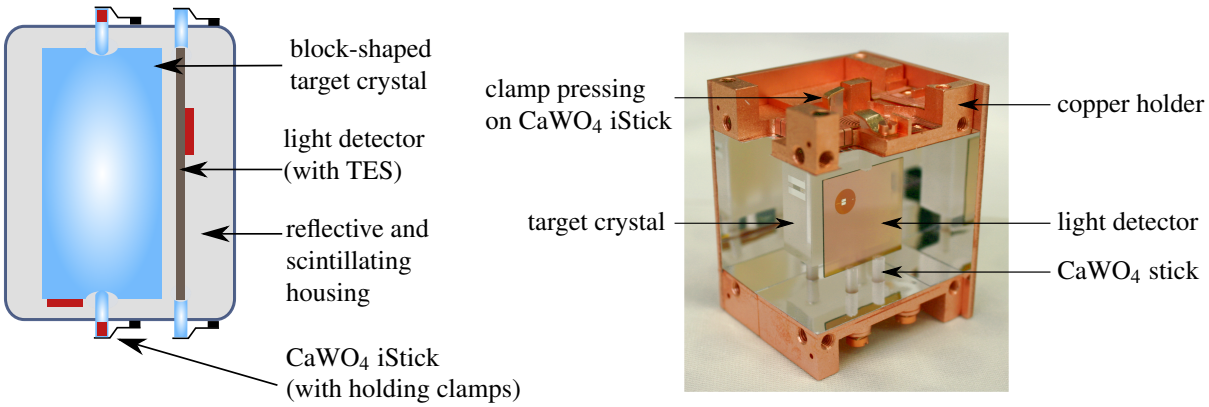

Figure 11.1: *Schematic drawing (left) and realization(right) of the optimized module design for light Dark Matter searches. The volume of the absorber crystal is drastically sized down, corresponding to a mass of* $\sim 25\,g$*. In CRESST-III the majority of the absorber crystals installed are grown at TUM due to the lower radioactive contamination. The absorber crystal as well as the light detector are each held by three* $CaWO_4$ *sticks, whereby the three phonon detector sticks are instrumented with a TES (denoted by iStick). Images adapted from [186].*

Improvements of Pulse-Shape Analysis

The fact that in the small modules of CRESST-III the $CaWO_4$ sticks holding the phonon detector are equipped with a separate TES is a great opportunity to directly measure the rejection probability for stick events of an ANN-based pulse-shape analysis. Therefore, ANNs have to be trained with templates of absorber and stick pulses of the phonon detector and an pulse-shape analysis similar to the one applied in the present work has to be performed. Furthermore, in an independent analysis based on the signal measured in the iSticks also stick events are selectable. By comparing the number of events rejected in both methods the rejection efficiency of the ANN-based analysis could be directly determined as a function of the energy.

If the performance of the ANN-based analysis is not good enough and needs to be improved one possibility is to not use derived pulse parameters describing the pulse but rather to use the pulse samples directly as input for an ANN. Ideally this ANN is a deep neural network and learns the relevant features of the different classes directly from the raw data. The latter fact is one of the key aspects of deep learning and the reason for the large success of this type of networks in many fields [187]. Recently, a team of researches of the Google Brain Team released an open source software library for machine learning called TensorFlow™ [188]. This software might be a good starting point for studies including a deep neural-network analysis.

The biggest issue of this approach – known up to know – might be that the simulation of empty baselines results in slightly different parameter distributions compared to the original data set (see appendix E). However, for deep neural networks a large number of labeled data is required in order to train it successfully. Thus, before using the empty baseline simulation it has to be investigated whether or not these deviations are significantly important for the generalization capability of the resulting ANN. If this is the case, further investigations in the

simulation part are required. For CRESST-III, besides the read-out explained in the present work, in addition also a continuous read-out of the data is planned. In that case the number of recorded empty baselines might not be limited anymore and the problem of simulating baselines vanishes.

Furthermore, ANN based pulse shape analysis might be also applied to light detector signals and help to reject different background processes efficiently. One example are the excess light events (see section 7.1.3) which might be removable due to an observed difference of the shape of the light detector signal.

ANN-based Data Analysis

Another application of artificial neural networks might be to dominantly base the event selection on the output of the neural network. A similar approach based on Boosted Decision Trees (BDTs) – another machine learning algorithm – is discussed in [189] for a cryogenic detector of the EDELWEISS experiment. Only stability cuts are applied to the data to remove invalid events. A blind analysis is performed, however, the background events observed in side bands, i.e. regions where only background and no signal events are observable, are used to determine the parameter distribution and to derive an empirical background model. For the WIMP signal contribution nuclear recoils are created, whereby the model is similar to the one outlined in section 2.1. Just like an ANN also a BDT learns in the training phase how to separate signal from background events. An optimum cut value is determined and, simultaneously, an expectation for the number of background events is obtained. This cut is applied to the actually measured data set in the ROI for Dark Matter search and the number of observed events is compared to the number of expected events.

The same procedure might be adopted to the cryogenic detectors of CRESST but it is also possible to train neural networks for this task. Again the biggest issue known up to now, is the simulation of empty baselines used for the creation of artificial pulses of known type.

With this approach it is possible to train several networks for different WIMP masses. This allows to apply optimal cuts on the background contributions tailored for a specific WIMP mass. For example, for light Dark Matter particles it might be required to efficiently remove low-energetic background events by a cut which simultaneously removes a considerable fraction of potential signal events in the complete energy range. However, for heavier Dark Matter particles it might be a better choice to release this specific cut resulting in more background events at low energies but simultaneously in a large fraction of surviving potential signal events.

Part V

Appendix

A Muon Veto Calibration

As explained in section 3.1.2 the CRESST experimental setup is enclosed by 20 plastic scintillator panels each read out by a single photomultiplier tube (PMT). The signal output of the latter is transferred via a BNC cable to an optical system, which allows to transmit the signal out of the Faraday cage to a QDC module. There the pulse is integrated for a predefined time window and the charge is converted to a digital number. This is done for all 20 panels as well as for the analog sum of these individual channels. Thus, in total 21 QDC values are stored for the offline analysis. The signal of these 21 channels is not only fed into QDC modules but also into a hardware trigger. As for the cryogenic detectors, also for the muon-veto system a threshold trigger unit is used.

A typical QDC spectrum of one channel irradiated with a radioactive source is shown in figure A.1a. Three distinct features are visible in the spectrum: The so-called *pedestal peak* at the lowest channel numbers corresponds to the QDC value readout when no input signal is present in the complete integration time window. At the highest channel numbers shown a typical Compton spectrum is visible, which is induced by the radioactive source. Finally, between these two features a peak-like structure is observed and denoted by trigger effect in figure A.1a. The main part is due to internal and external radioactive contamination of the PMT and of the panel. The drop-off at the left-side of this structure is due to the influence of the trigger threshold, as can be seen in in figure A.1b. There the influence of different trigger thresholds on this structure is depicted, whereby the spectra are scaled in such a way that the number of counts measured in the interval ranging from channel 300 up to 600 is the same for all threshold values. With increasing threshold the pedestal peak vanishes and the QDC spectrum is cut at larger channel numbers. Due to this strong effect a small deviation of the trigger threshold can result in a significant change in the trigger rate observed for the muon veto.

A.1 Gain of the Optical System

One parameter which can be adjusted in the electronics of the muon-veto system is the gain of the optical transmitter system. In order to set a similar gain for each readout channel a pulse (-200 mV pulse height and 80 ns width) is created by a tail pulser and injected into the system. This results in a spectrum, where at low QDC channel numbers the pedestal peak is observed, while at higher QDC channels a sharp peak corresponding to the injected pulse height is visible. The gain of each transmitter channel is adjusted such, that the difference between the two mean positions of the peaks is 3 080 channels.

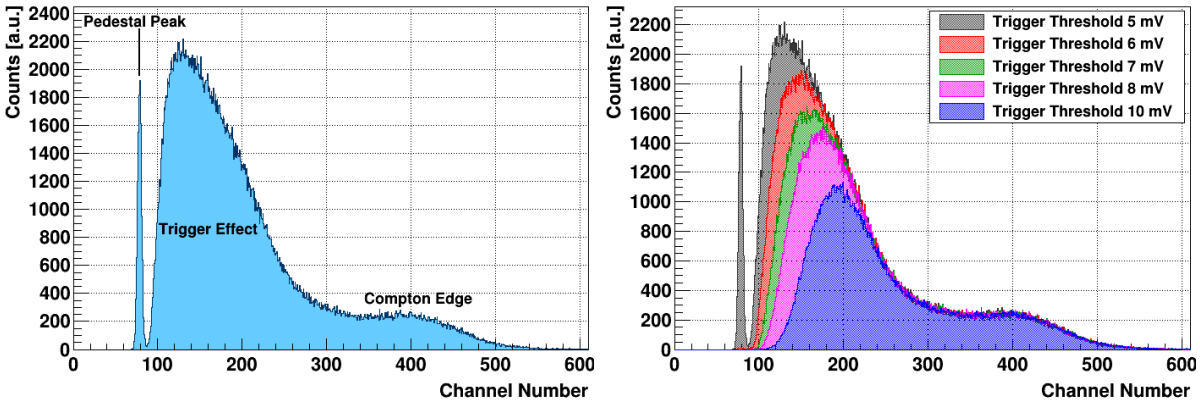

(a) Typical QDC Spectrum *(b) Influence of the Trigger Threshold*

Figure A.1: *In (a) a typical QDC spectrum induced by a radioactive source is depicted. Three different features are visible. At low channel numbers the so-called pedestal peak is observed which corresponds to the QDC value readout, when no input signal is present in the complete integration time window. At high channel numbers the Compton spectrum induced by the radioactive source is measured. The peak-like structure between these two features is caused by the influence of the trigger unit as depicted in more detail in (b). The spectra are scaled such, that the number of counts between channel 300 and 600 is the same for all threshold values. With increasing threshold the cut-off in the QDC spectrum is observed at higher channel numbers.*

A.2 Thorium Calibration

After the gains of the optical system have been adjusted a radioactive source is required for the actual calibration. Here, a thorium source (consisting of a welding rod containing $\sim 4\,\%$ thorium) is used to set the operational voltage of each PMT individually which is discussed in the following.

A.2.1 Thorium Source

In figure A.2 the thorium source used for the calibration is shown. The welding rod is depicted in figure A.2a, while the corresponding energy spectrum measured by a germanium detector is shown in figure A.2b [190]. The highest observable γ-line is caused by ^{208}Tl with an energy of 2.6 MeV [90]. The total activity in the ^{208}Tl γ-peak is measured to be $\sim 6\,$kBq [190].

A.2.2 PMT Voltage

In the plastic scintillator panels this γ-line at 2.6 MeV creates a Compton edge, whereby the exact position depends on the operational voltage of the PMT. Thus, it is possible to adjust the voltage in such a way that for all PMTs the Compton edge is measured in almost the same channel.

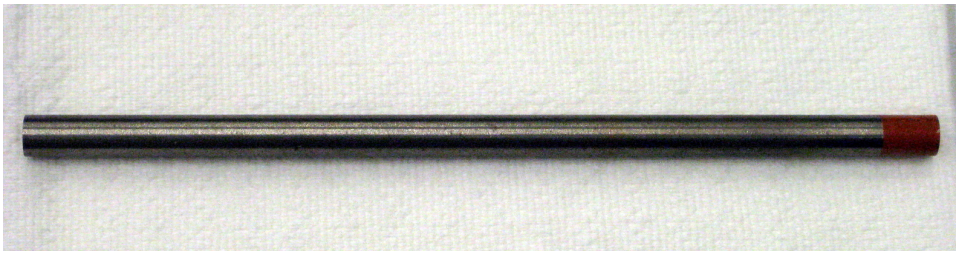

(a) Thorium welding rod

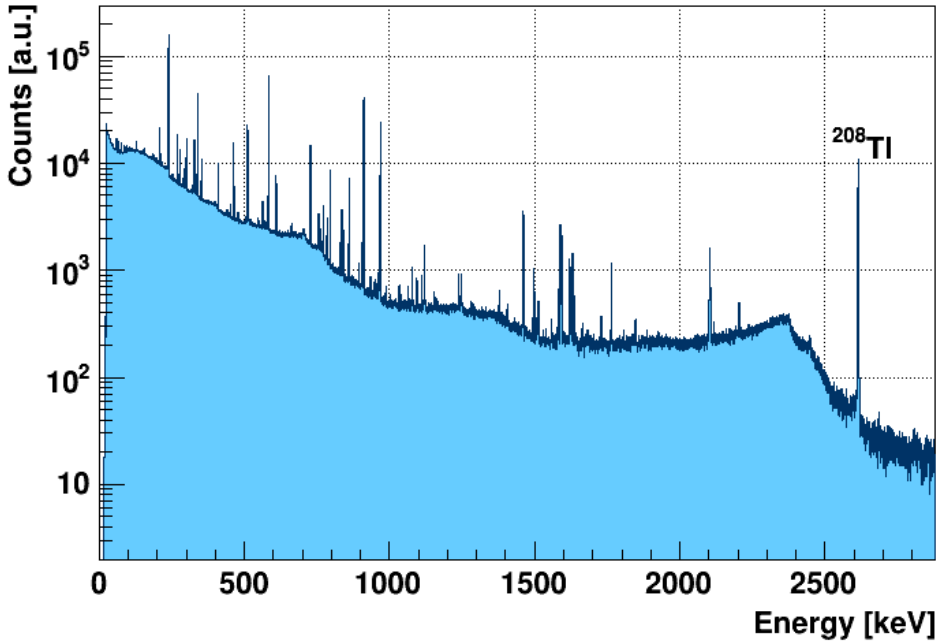

(b) Energy spectrum of rod (measured by a germanium detector) [190]

Figure A.2: *In (a) a picture of the thorium welding rod used for the calibration of the muon panels is shown. The corresponding energy spectrum measured by a germanium detector is depicted in (b). For the latter, the data is provided by [190]. For the muon veto calibration only the* ^{208}Tl *γ-line at* $\sim 2.6\,MeV$ *is used [90]. The activity in this line is measured to be* $\sim 6\,kBq$*.*

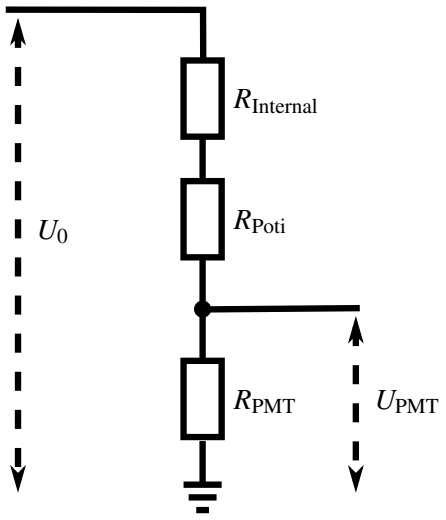

Figure A.3: *Schematic drawing of the wiring for a single PMT of the CRESST muon veto system. A common voltage supply U_0 is used for all 20 PMTs together. The serial connection of an internal resistance $R_{Internal}$ and an adjustable potentiometer R_{Poti} allows to control the operational voltage U_{PMT} of the individual PMT. Also important is the resistance R_{PMT} of the voltage divider of the PMT.*

The schematic drawing of the wiring for a single PMT is depicted in figure A.3. In CRESST a common voltage supply U_0 is used for all PMTs and the individual operational voltage U_{PMT} is obtained by a serial connection of an internal resistance R_{Internal} and an adjustable potentiometer R_{Poti}. The resistance of the voltage divider of the PMT is denoted by R_{PMT}. This value can be directly measured and is used together with the other values to calculate the operational voltage U_{PMT} of each PMT according to the following equation:

$$U_{\text{PMT}} = (1 - \frac{R_{\text{Internal}} + R_{\text{Poti}}}{R_{\text{Internal}} + R_{\text{Poti}} + R_{\text{PMT}}}) \cdot U_0 \tag{A.1}$$

A.2.3 Calibration

The gain of the PMT is related to the applied voltage and, thus, by varying the individual voltage the PMTs can be calibrated as illustrated in figure A.4. To obtain this spectrum the source is placed in the middle of the plastic scintillator panels and the induced pulses are recorded. The height of the plateau N before the observed Compton edge is measured.

Next the channel C_0 is determined, which is the channel where the spectrum has dropped to $N/2$. The voltage and, thus, the gain of the PMT is adjusted in such a way that for each PMT C_0 corresponds to the same channel number.

In table A.1 the resulting operational voltages are listed. Also the resistances of the PMTs, the internal resistances, and the potentiometer values are included.

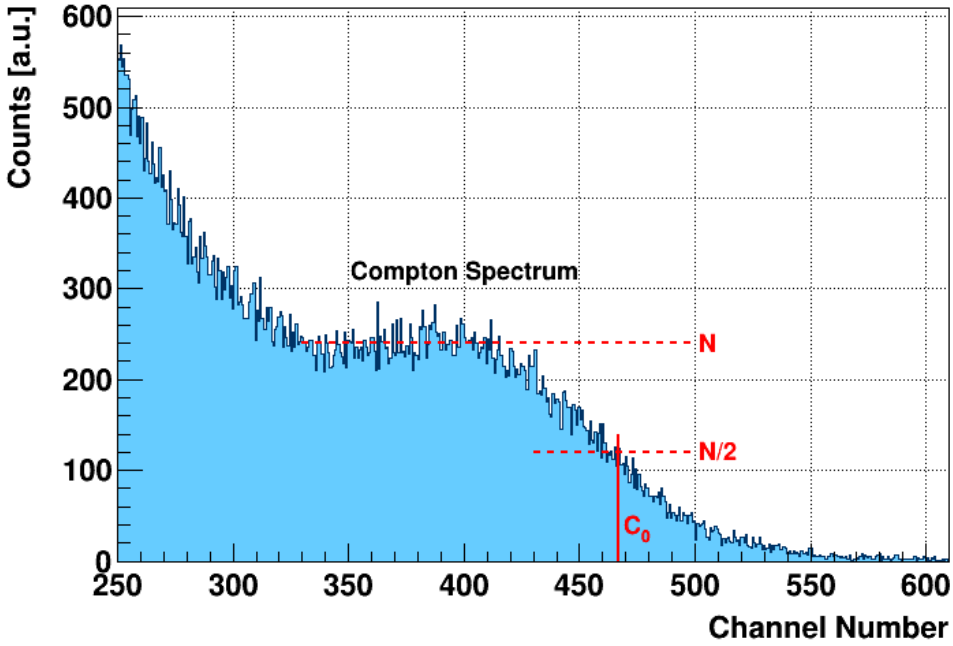

Figure A.4: *Applied calibration scheme for each PMT of the CRESST muon-veto system. A thorium source is placed in the center of the respective plastic scintillator panel. The level of the plateau N before the resulting Compton edge is measured. The channel C_0, where the spectrum has dropped to $N/2$ is determined. By varying the operational voltage C_0 is set to the same channel number for each PMT.*

A.3 Cross-Check of the Calibration

In order to cross-check the muon-veto calibration the spectrum between channel 350 and 600 is fitted by the following function:

$$f_{\text{fit}}(x) = C + A \cdot \textbf{erfc}\left(\frac{x-\mu}{\sqrt{2}\cdot\sigma}\right), \tag{A.2}$$

where **erfc** is the complementary error function.

In table A.2 the fitted values of the position μ are listed for all 20 muon-veto channels. In the last row the calculated mean and RMS value are also included. The standard deviation is $\lesssim 7$ channels and, thus, only $\sim 0.84\,\%$. This very good result is also confirmed by the small span between the minimum and maximum of the fitted positions μ: a value of $\lesssim 25$ QDC channels is found.

panel PI-	channel	PMT resistance [MΩ]	internal resistance [kΩ]	potentiometer value	voltage [V]
108	1	4.330	390	4.50	802
109	2	4.320	750 (2 x 1500 parallel)	3.50	741
110	3	4.333	220	5.50	839
111	4	4.320	330	7.50	837
112	5	4.320	509 (470 & 39 serial)	4.60	784
113	6	4.335	517 (470 & 47 serial)	3.50	775
114	7	4.339	330	6.46	828
115	8	4.360	750 (2 x 1500 parallel)	6.50	763
116	9	4.350	300	4.00	813
117	10	4.341	470	3.00	778
118	11	4.330	0	4.40	869
119	12	4.325	900 (2 x 1800 parallel)	3.20	719
120	13	4.273	390	2.40	784
121	14	4.346	599 (560 & 39 serial)	4.70	772
122	15	4.360	560	9.95	819
123	16	4.350	0	5.50	880
124	17	4.320	820	2.00	721
125	18	4.336	526 (470 & 56 serial)	5.90	792
126	19	4.326	330	5.00	816
127	20	4.351	0	3.50	861

Table A.1: *List of the PMT resistances, the internal resistances and the potentiometer values for the different channels of the muon-veto system. The voltage applied for each PMT (last column) is calculated with formula A.1 and a common voltage $U_0 = 925$ V. The values given in parenthesis are the actual resistor values in kΩ connected either in series or parallel.*

channel	**position μ [QDC ch.]**	**channel**	**position μ [QDC ch.]**
1	772.3	11	771.7
2	786.0	12	772.3
3	770.8	13	775.2
4	766.1	14	771.7
5	783.7	15	771.2
6	776.5	16	768.4
7	763.5	17	781.6
8	783.3	18	760.1
9	775.2	19	780.2
10	778.7	20	780.5
mean	**774.4**	**RMS**	**6.78**

Table A.2: *Fitted positions of the Compton edge of the thorium source for all channels. The standard deviation of only ~ 0.84 % is very small and even the span between minimum and maximum position is only ~ 25 QDC channels. If an energy of the Compton edge of 2.381 MeV is assumed, each panel can be energy calibrated.*

B Energy Calibration Parameters

detector	deviation factor	max. fraction [%]	CPE order	CPE factor [$\frac{\text{keV}}{\text{V}}$]
Lise	4	22.5	4	199.07
Enrico	4	20.0	6	208.237
TUM40	4	25.0	3	204.978
Michael	4	22.5	5	221.331
TUM38	4	22.5	3	197.835
Petrus	4	22.5	5	207.260
VK27	4	20.0	6	209.435
Diogenes	4	20.0	5	212.969
VK28	4	22.5	3	185.417
Zam	4	20.0	5	195.773

Table B.1: *Required parameters for the energy calibration of the different detectors.*

In table B.1 the different parameters required for the energy calibration of all investigated modules are listed. In section 4.4.3 it is described, that outlying test pulses which have a pulse height too far away from the mean of their population are removed. The deviation factor is given in units of σ, i.e. the width of the distribution, and, thus, all test pulses which deviate more than the given factor are removed. In case that by this method more pulses than the allowed maximum fraction of test pulses is removed for a specific spline, the automatic removal is stopped and the user is informed.

As described in section 4.4.2 the response to the test pulses is fitted by a low-order polynomial. This order is called CPE-order in table B.1. The linear conversion factor to transform the equivalent test pulse amplitude to the actual energy value is given as CPE-factor.

The latter is determined during the calibration of the heater system with radioactive sources. In figure B.1 a schematic drawing explains how the CPE-factor is calculated. For a mono-energetic line of known energy E_{lit} the corresponding amplitude A_{pp} is observed in the detector (red star). The two test pulses, which produce the closest amplitude below and above the mono-energetic line, are identified. Their test pulse amplitude, i.e. the injected energy amount, is denoted as TPA_{low} and TPA_{high}, while the resulting amplitudes are given as $A_{\text{tp,low}}$ and $A_{\text{tp,high}}$ respectively. Now one can derive the linear equation connecting the observed and the

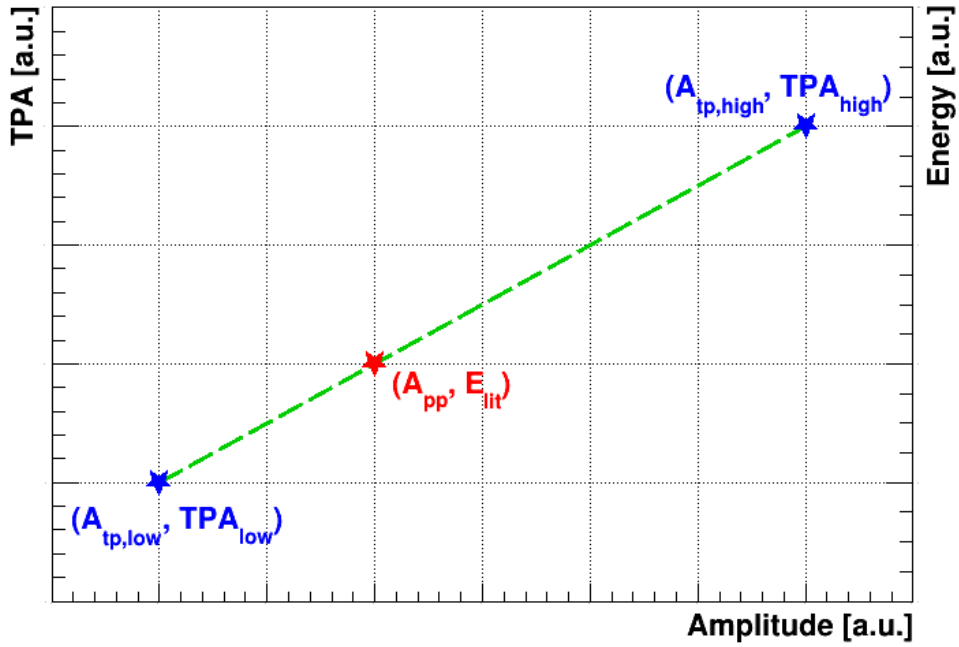

Figure B.1: *Schematic drawing of the calculation scheme of the CPE-factor. See text on previous page for more details.*

injected amplitudes of test pulses (green dashed line in figure B.1):

$$\mathrm{TPA}\,(A) = \frac{\mathrm{TPA_{low}} - \mathrm{TPA_{high}}}{A_{\mathrm{tp,low}} - A_{\mathrm{tp,high}}} \cdot A + \frac{\mathrm{TPA_{high}} \cdot A_{\mathrm{tp,low}} - \mathrm{TPA_{low}} \cdot A_{\mathrm{tp,high}}}{A_{\mathrm{tp,low}} - A_{\mathrm{tp,high}}} \tag{B.1}$$

As explained to obtain the energy scale just a linear transformation of the injected test pulse amplitude is performed. Thus, the CPE-factor is calculated with the following formula:

$$\mathrm{CPE} = \frac{E_{\mathrm{lit}}}{\mathrm{TPA}\left(A_{\mathrm{pp}}\right)}. \tag{B.2}$$

C File Lists

In table C.1 for all detectors analysed, the respective data set types as well as the different start and end files are listed. In addition, the total number of files in the respective data set is given in the last column. In total 303 files, recorded between May 2013 and August 2015, have been analysed, the file list of the Dark Matter data set is shown in table C.2. All files which are included in table C.2 and which feature a number between the start file number and the end file number of a respective data set (see table C.1) are contained in that data set. For the respective exposure and the energy threshold of the different detectors see table 5.1 on page 93.

detector	**data set type**	**start file**	**end file**	**# of files**
All	training set	bck_001	bck_105	87
TUM38, VK27, VK28	blind data set	bck_106	bck_353	216
TUM40	blind data set 1	bck_106	bck_207	91
	low-threshold supplement	bck_208	bck_214	6
	blind data set 2	bck_215	bck_353	119
Lise	blind data set 1	bck_106	bck_226	109
	low-threshold supplement	bck_227	bck_241	12
	blind data set 2	bck_242	bck_353	95

Table C.1: *For the different detectors analysed the start and end files of the respective data set with the given type (second column) are listed. In the last column also the total number of files contained in the sets are listed.*

file list							
bck_001	bck_048	bck_095	bck_133	bck_176	bck_221	bck_267	bck_314
bck_002	bck_049	bck_096	bck_134	bck_177	bck_222	bck_268	bck_315
bck_003	bck_050	bck_097	bck_135	bck_178	bck_223	bck_273	bck_316
bck_004	bck_051	bck_098	bck_136	bck_179	bck_224	bck_274	bck_317
bck_005	bck_052	bck_099	bck_137	bck_180	bck_225	bck_275	bck_318
bck_006	bck_053	bck_100	bck_138	bck_183	bck_226	bck_276	bck_319
bck_007	bck_054	bck_101	bck_139	bck_184	bck_227	bck_277	bck_320
bck_008	bck_056	bck_102	bck_140	bck_185	bck_228	bck_278	bck_323
bck_010	bck_057	bck_103	bck_141	bck_186	bck_229	bck_279	bck_324
bck_013	bck_058	bck_104	bck_142	bck_187	bck_230	bck_281	bck_325
bck_014	bck_059	bck_105	bck_143	bck_188	bck_231	bck_282	bck_326
bck_016	bck_060	bck_106	bck_144	bck_189	bck_232	bck_283	bck_327
bck_018	bck_061	bck_107	bck_148	bck_190	bck_234	bck_284	bck_328
bck_020	bck_062	bck_108	bck_149	bck_191	bck_235	bck_285	bck_329
bck_021	bck_063	bck_109	bck_150	bck_192	bck_236	bck_286	bck_330
bck_025	bck_065	bck_110	bck_151	bck_194	bck_237	bck_287	bck_331
bck_026	bck_066	bck_111	bck_152	bck_195	bck_238	bck_288	bck_332
bck_027	bck_070	bck_112	bck_153	bck_196	bck_241	bck_289	bck_333
bck_028	bck_071	bck_113	bck_154	bck_197	bck_242	bck_290	bck_334
bck_029	bck_072	bck_114	bck_155	bck_198	bck_243	bck_291	bck_335
bck_030	bck_073	bck_115	bck_156	bck_199	bck_244	bck_292	bck_336
bck_031	bck_074	bck_116	bck_157	bck_201	bck_245	bck_293	bck_338
bck_032	bck_075	bck_117	bck_160	bck_202	bck_247	bck_294	bck_339
bck_033	bck_077	bck_118	bck_161	bck_203	bck_248	bck_295	bck_340
bck_034	bck_078	bck_119	bck_162	bck_206	bck_249	bck_296	bck_341
bck_035	bck_079	bck_120	bck_163	bck_207	bck_250	bck_297	bck_342
bck_036	bck_082	bck_121	bck_164	bck_208	bck_251	bck_298	bck_343
bck_037	bck_083	bck_122	bck_165	bck_209	bck_252	bck_299	bck_344
bck_038	bck_085	bck_123	bck_166	bck_211	bck_254	bck_300	bck_345
bck_039	bck_086	bck_124	bck_167	bck_212	bck_256	bck_301	bck_346
bck_040	bck_087	bck_125	bck_168	bck_213	bck_258	bck_302	bck_347
bck_041	bck_088	bck_126	bck_169	bck_214	bck_260	bck_303	bck_348
bck_042	bck_089	bck_127	bck_170	bck_215	bck_261	bck_304	bck_349
bck_043	bck_090	bck_128	bck_171	bck_216	bck_262	bck_305	bck_350
bck_044	bck_091	bck_129	bck_172	bck_217	bck_263	bck_306	bck_351
bck_045	bck_092	bck_130	bck_173	bck_218	bck_264	bck_311	bck_352
bck_046	bck_093	bck_131	bck_174	bck_219	bck_265	bck_312	bck_353
bck_047	bck_094	bck_132	bck_175	bck_220	bck_266	bck_313	

Table C.2: *File list of all 303 analysed data files of the Dark Matter data set. The data was obtained during CRESST-II phase 2 lasting from May 2013 until August 2015.*

D Trigger Threshold and Cut Values

D.1 Trigger Threshold

In section 4.8 the method to measure the trigger threshold of a detector with low-energetic test pulses is explained. During CRESST-II phase 2 several dedicated measurement campaigns to determine the thresholds of the detectors were carried out.

In figure D.1 the threshold measurements of all detectors analysed are depicted. For TUM40 and Lise the threshold could be lowered during the data taking period and, thus, for both detectors measurements of the higher and of the lower thresholds have been performed. The lowest trigger threshold of 308 eV could be obtained for Lise, while for TUM40 a value of 409 keV has been measured. Before lowering the threshold a value of 901 eV for Lise and 609 eV for TUM40 had been obtained. Due to small signal heights caused by a problem in the cabling of the detector [142], for VK27 a rather high value of 11.25 keV is determined. For TUM38 and VK28 the trigger threshold can not be determined precisely since there are not enough test pulses sampled in the transition region of these detectors. Thus, for the threshold values only upper limits of 3 keV for TUM38 and 2 keV for VK28 have been determined.

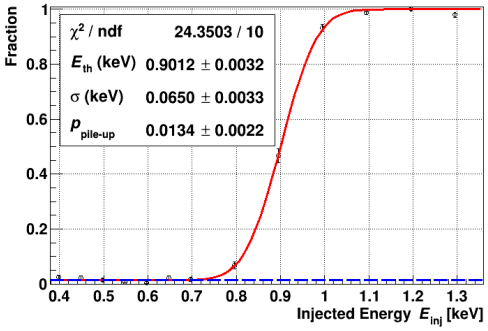

(a) High-Threshold Measurement of Lise

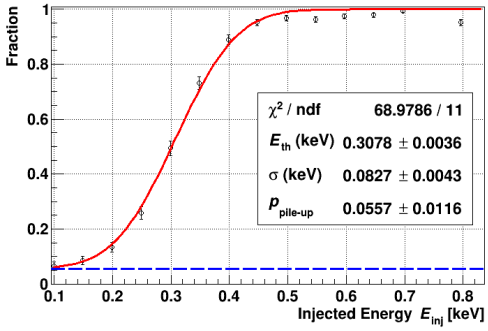

(b) Low-Threshold Measurement of Lise

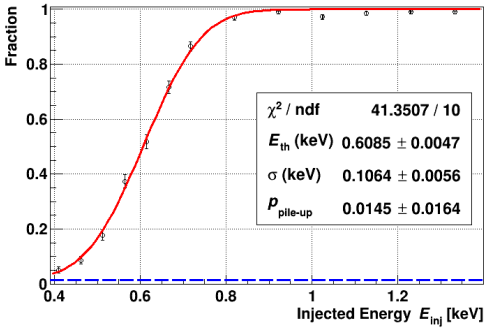

(c) High-Threshold Measurement of TUM40

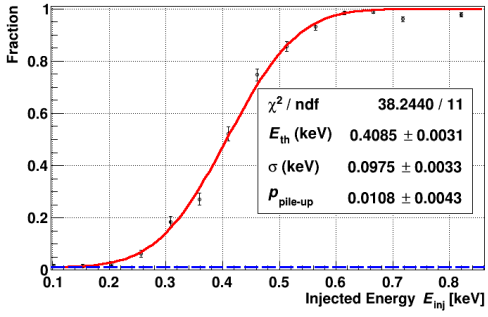

(d) Low-Threshold Measurement of TUM40

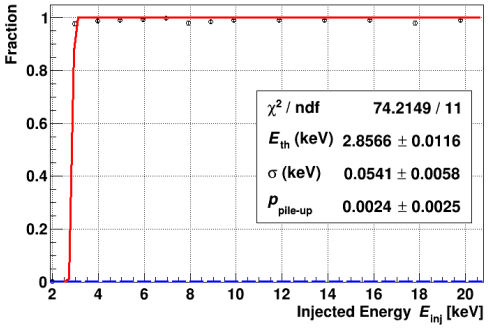

(e) Threshold Measurement of TUM38

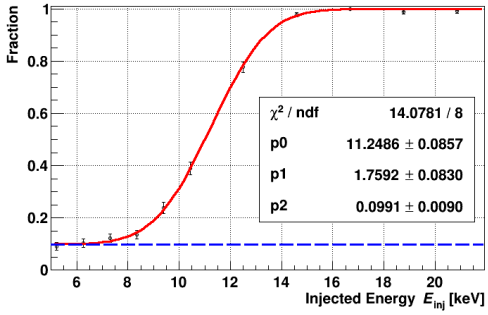

(f) Threshold Measurement of VK27

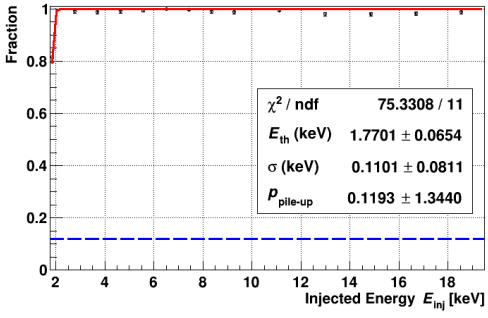

(g) Threshold Measurement of VK28

Figure D.1: *Threshold measurements of all detectors investigated. For Lise and TUM40 both measurements, the one with high as well as the one with low threshold, are shown. For TUM38 and VK28 not enough test pulses have been sampled in the transition region and, thus, only upper limits are obtained for the thresholds of both detectors. The threshold of VK27 is rather high due to a small signal height caused by a problem in the cabling of the detector [142].*

D.2 Precise Cut Values

In section 5.3 the different selection criteria used to reject the various types of invalid pulses are qualitatively described. The actual cut values for the analysed modules are listed in the following.

D.2.1 One-dimensional Cuts

In table D.1 the precise cut values of the one-dimensional cuts are listed for all detectors investigated. If the respective parameter value is within the given range the event survives the cut otherwise it is rejected. In case a selection criterion is not applied for the respective detector it is marked by *n.a.* in the table.

D.2.2 Two-dimensional Cuts

The parameter distributions as well as the cut limits of the three two-dimensional cuts applied are drawn. Furthermore the supporting points of the two-dimensional cut functions are also given. Between these points a linear interpolation is applied.

RMS Cut

In section 5.3.8 the method to determine the cut limits for the generic RMS cut is explained. The complete energy range is divided into several energy slices and the cut limits are determined in each slice individually by a fit with an empirical model. The relevant parameters for the creation of the two-dimensional RMS-energy histogram are listed in table D.2 and the parameters used for the slice generation are listed in table D.3.

By combining the different limits obtained from the individual slices the total RMS cut is created. In the figures D.2 - D.7 the different results are depicted for all five modules analysed.

Shift Difference Cut

The cut on the shift-difference parameter is performed only for the detectors Lise, TUM40 and VK28. It is only applied to pulses below the truncation limit of the respective detector, as for higher pulse heights the parameter is not well-defined anymore. There, typically a systematical shift to later times is observed for the fit with the TES-carrier template as the decaying part of the pulse is fitted.

In figure D.8 the parameter distributions as a function of the pulse height are shown for all three detectors. The red lines indicate the cut limits and the numerical values of the supporting points are listed in the corresponding tables.

ANN based Cut

The limits for the cuts performed on the output variable of the two multilayer perceptrons are listed in table D.4.

detector	CP Range [V]	Rate [trig. / 0.1 h]	Amplitude A [V]	Trigger Delay [ms]
Lise	$7.177 \leq \mathrm{CP} \leq 7.543$	≤ 50	$-1 \leq \mathrm{A} \leq 8$	> -2496
Enrico	$0.122 \leq \mathrm{CP} \leq 0.134$		$\lvert\mathrm{A}\rvert \leq 0.1$	n.a.
TUM40	$8.735 \leq \mathrm{CP} \leq 9.085$	≤ 26.5	$-1 \leq \mathrm{A} \leq 8$	> -2496
Michael	$2.864 \leq \mathrm{CP} \leq 2.957$		$\lvert\mathrm{A}\rvert \leq 4.5$	n.a.
TUM38	$8.608 \leq \mathrm{CP} \leq 8.912$	≤ 50	$-1 \leq \mathrm{A} \leq 7$	> -2496
Petrus	$2.864 \leq \mathrm{CP} \leq 2.957$		$\lvert\mathrm{A}\rvert \leq 2$	n.a.
VK27	$0.778 \leq \mathrm{CP} \leq 0.8556$	≤ 60	$-1 \leq \mathrm{A} \leq 0.5$	> -2496
Diogenes	$3.527 \leq \mathrm{CP} \leq 3.593$		$\lvert\mathrm{A}\rvert \leq 2.1$	n.a.
VK28	$8.644 \leq \mathrm{CP} \leq 8.776$	≤ 50	$-1 \leq \mathrm{A} \leq 6.2$	> -2496
Zam	$4.411 \leq \mathrm{CP} \leq 4.449$		$\lvert\mathrm{A}\rvert \leq 2.1$	n.a.

detector	Delta Voltage/RMS δ	Peak Position μ_P [ms]	Shift μ_S [ms]
Lise	$-7.370 \leq \delta \leq 0.195$	$66.523 \leq \mu_\mathrm{P} \leq 211.554$	$-18.870 \leq \mu_\mathrm{S} \leq 123.251$
Enrico	$-1.823 \leq \delta \leq 0.091$	n.a.	n.a.
TUM40	$-6.836 \leq \delta \leq 0.226$	$66.523 \leq \mu_\mathrm{P} \leq 211.672$	$-18.356 \leq \mu_\mathrm{S} \leq 124.994$
Michael	$-6.543 \leq \delta \leq 0.164$	n.a.	n.a.
TUM38	$-6.920 \leq \delta \leq 0.226$	$67.575 \leq \mu_\mathrm{P} \leq 213.776$	$-17.080 \leq \mu_\mathrm{S} \leq 124.301$
Petrus	$-7.038 \leq \delta \leq 0.319$	n.a.	n.a.
VK27	$-2.872 \leq \delta \leq 0.195$	$66.523 \leq \mu_\mathrm{P} \leq 209.568$	$-29.608 \leq \mu_\mathrm{S} \leq 126.091$
Diogenes	$-7.735 \leq \delta \leq 0.319$	n.a.	n.a.
VK28	$-9.128 \leq \delta \leq 0.195$	$60.212 \leq \mu_\mathrm{P} \leq 208.673$	$-21.852 \leq \mu_\mathrm{S} \leq 124.358$
Zam	$-7.394 \leq \delta \leq 0.226$	n.a.	n.a.

detector	Right−Left Baseline RLB [V]	Rise Time [ms]	RMS ratio	Reconstructed Energy [keV]
Lise	$-0.750 \leq \mathrm{RLB} \leq 0.250$	> 1.5	> -0.01	> 0.308
Enrico	$-0.100 \leq \mathrm{RLB} \leq 0.050$	n.a.	n.a.	n.a.
TUM40	$-1.079 \leq \mathrm{RLB} \leq 10$	> 1.5	> -0.05	> 0.609
Michael	$-0.506 \leq \mathrm{RLB} \leq 10$	n.a.	n.a.	n.a.
TUM38	$-0.600 \leq \mathrm{RLB} \leq 0.400$	> 1.5	> -0.05	> 3.000
Petrus	$-0.504 \leq \mathrm{RLB} \leq 0.086$	n.a.	n.a.	n.a.
VK27	$-0.650 \leq \mathrm{RLB} \leq 0.028$	> 1.5	> -0.05	> 11.250
Diogenes	$-0.430 \leq \mathrm{RLB} \leq 0.220$	n.a.	n.a.	n.a.
VK28	$-0.405 \leq \mathrm{RLB} \leq 0.333$	> 1.5	> -0.05	> 2.000
Zam	$-0.294 \leq \mathrm{RLB} \leq 0.164$	n.a.	n.a.	n.a.

Table D.1: *Cut values of all one-dimensional cuts applied to the detectors investigated. In case a cut is not performed the corresponding cut value is marked by n.a. in the respective cell. Pulses with parameter values within the given range survive the cut. Whenever a pulse of the phonon or light detector is rejected by a cut, the complete event is dismissed.*

detector	$\mathbf{nBins}_E$	$\boldsymbol{E}_{\mathbf{min}}$ [keV]	$\boldsymbol{E}_{\mathbf{max}}$ [keV]	$\mathbf{nBins}_{\mathbf{RMS}}$	$\mathbf{RMS}_{\mathbf{min}}$ [V]	$\mathbf{RMS}_{\mathbf{max}}$ [V]
Lise	1400	-50	300	1000	0.00	0.05
Enrico	1400	-50	300	2000	0.00	0.10
TUM38	3200	0	800	2000	0.00	0.10
Petrus	1600	-50	350	2000	0.00	0.10
TUM40	3400	-50	800	200	0.00	0.01
Michael	3400	-50	800	2000	0.00	0.10
VK27	2800	-50	650	1000	0.00	0.05
Diogenes	2800	-50	650	2000	0.00	0.10
VK28	2000	-50	450	2000	0.00	0.10
Zam	1800	-50	400	2000	0.00	0.10

Table D.2: *Parameters used for the generation of the two-dimensional histograms (RMS vs. reconstructed energy) of the given detector. The number of bins ($nBins_x$) and the minimum and maximum values of the respective parameters x are given.*

detector	$\boldsymbol{\Delta_E}$ [keV]	$\boldsymbol{E}_{\mathbf{limit}}$ [keV]	$\boldsymbol{E}_{\mathbf{max}}$ [keV]	Fit-Model
Lise	20	200	210	empirical
Enrico	20	180	230	empirical
TUM38	15	120	320	empirical
Petrus	20	120	320	empirical
TUM40	10	100	700	empirical
Michael	50	350	700	empirical
VK27	20	100	580	Gaussian + pol1
Diogenes	250	100	450	empirical
VK28	25	100	375	empirical
Zam	15	150	400	empirical

Table D.3: *Parameters used for the creation of the individual energy slices as well as for the fit. Up to the energy limit E_{limit} slices with a bin width Δ_E are created. For higher energies the bin width is doubled until the maximal energy E_{max} is included in a slice. Afterwards the given model is fitted to the resulting distribution, whereby the empirical model corresponds to the model described in section 5.3.8. For VK27 an easier model consisting of the sum of a Gaussian function and a first-order polynomial is used.*

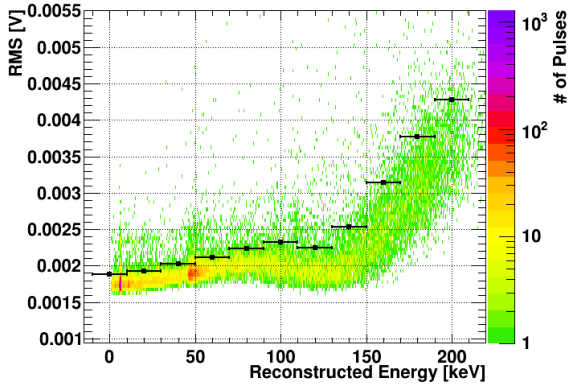

(a) RMS Distribution - Lise

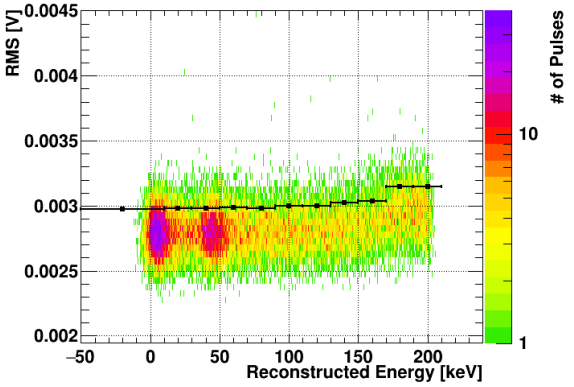

(b) RMS Distribution - Enrico

Energy E	RMS_{cut} [V]
$-10 \leq E < 10$	0.001883
$10 \leq E < 30$	0.001927
$30 \leq E < 50$	0.002023
$50 \leq E < 70$	0.002114
$70 \leq E < 90$	0.002242
$90 \leq E < 110$	0.002322
$110 \leq E < 130$	0.002249
$130 \leq E < 150$	0.002531
$150 \leq E < 170$	0.003145
$170 \leq E < 190$	0.003768
$190 \leq E < 210$	0.004284

(c) 2D Cut Values - Lise

Energy E	RMS_{cut} [V]
$-50 \leq E < 10$	0.002974
$10 \leq E < 30$	0.002979
$30 \leq E < 50$	0.002979
$50 \leq E < 70$	0.002985
$70 \leq E < 90$	0.002982
$90 \leq E < 110$	0.002997
$110 \leq E < 130$	0.002998
$130 \leq E < 150$	0.003022
$150 \leq E < 170$	0.003033
$170 \leq E < 190$	0.003146
$190 \leq E < 210$	0.003148

(d) 2D Cut Values - Enrico

Figure D.2: *RMS distributions of all pulses of the training set of Lise (left) and Enrico (right). The RMS-parameter values are obtained from the fit with the absorber template. The resulting limits of the RMS cut are given in the tables below the respective distributions.*

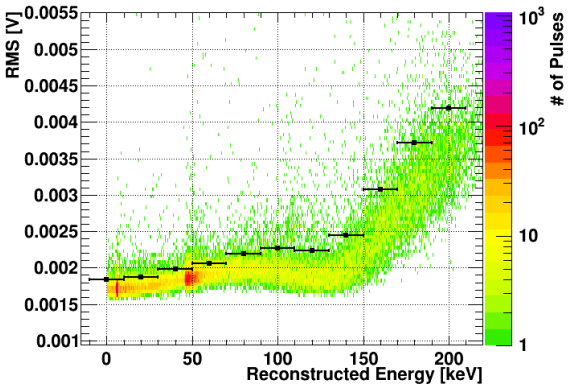

(a) RMS Distribution - Lise

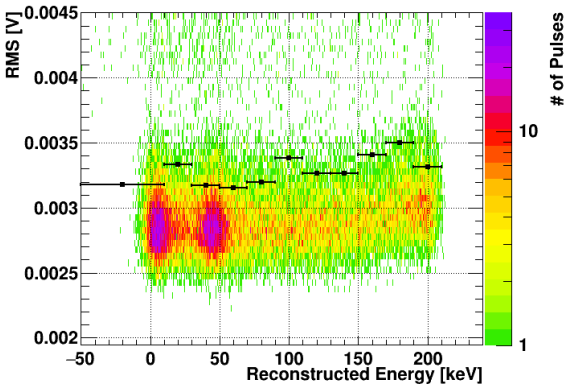

(b) RMS Distribution - Enrico

Energy E	RMS_{cut} [V]
$-10 \leq E < 10$	0.001838
$10 \leq E < 30$	0.001869
$30 \leq E < 50$	0.001981
$50 \leq E < 70$	0.002061
$70 \leq E < 90$	0.002189
$90 \leq E < 110$	0.002274
$110 \leq E < 130$	0.002234
$130 \leq E < 150$	0.002450
$150 \leq E < 170$	0.003080
$170 \leq E < 190$	0.003720
$190 \leq E < 210$	0.004187

(c) 2D Cut Values - Lise

Energy E	RMS_{cut} [V]
$-50 \leq E < 10$	0.003177
$10 \leq E < 30$	0.003335
$30 \leq E < 50$	0.003175
$50 \leq E < 70$	0.003152
$70 \leq E < 90$	0.003199
$90 \leq E < 110$	0.003382
$110 \leq E < 130$	0.003266
$130 \leq E < 150$	0.003267
$150 \leq E < 170$	0.003406
$170 \leq E < 190$	0.003499
$190 \leq E < 210$	0.003314

(d) 2D Cut Values - Enrico

Figure D.3: *RMS distributions of all pulses of the blind data set of Lise (left) and Enrico (right). The RMS-parameter values are obtained from the fit with the absorber template. The resulting limits of the RMS cut are given in the tables below the respective distributions.*

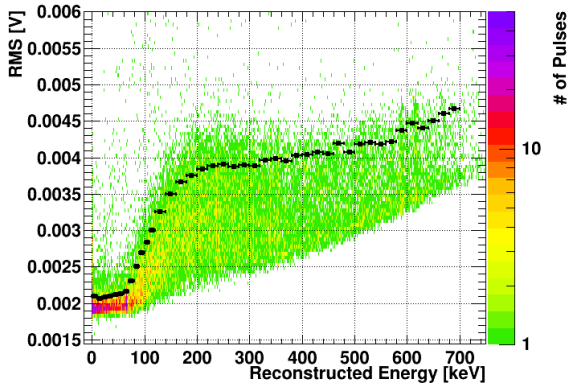

(a) RMS Distribution - TUM40

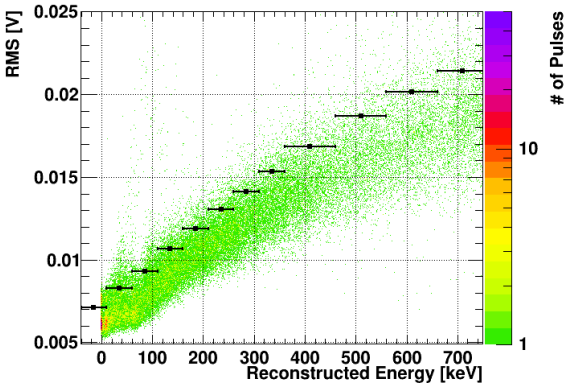

(b) RMS Distribution - Michael

Energy E	RMS_{cut} [V]
$0 \leq E < 10$	0.002096
$10 \leq E < 20$	0.002059
$20 \leq E < 30$	0.002089
$30 \leq E < 40$	0.002092
$40 \leq E < 50$	0.002117
$50 \leq E < 60$	0.002132
$60 \leq E < 70$	0.002157
$70 \leq E < 80$	0.002304
$80 \leq E < 90$	0.002509
$90 \leq E < 100$	0.002693
$100 \leq E < 110$	0.002840
$110 \leq E < 120$	0.003004
$120 \leq E < 140$	0.003252
$140 \leq E < 160$	0.003500
$160 \leq E < 180$	0.003664
$180 \leq E < 200$	0.003758
$200 \leq E < 220$	0.003838
$220 \leq E < 240$	0.003884
$240 \leq E < 260$	0.003908
$260 \leq E < 280$	0.003876
$280 \leq E < 300$	0.003901

Energy E	RMS_{cut} [V]
$300 \leq E < 320$	0.003887
$320 \leq E < 340$	0.003965
$340 \leq E < 360$	0.003983
$360 \leq E < 380$	0.003953
$380 \leq E < 400$	0.004032
$400 \leq E < 420$	0.004036
$420 \leq E < 440$	0.004076
$440 \leq E < 460$	0.004047
$460 \leq E < 480$	0.004191
$480 \leq E < 500$	0.004074
$500 \leq E < 520$	0.004178
$520 \leq E < 540$	0.004208
$540 \leq E < 560$	0.004182
$560 \leq E < 580$	0.004216
$580 \leq E < 600$	0.004369
$600 \leq E < 620$	0.004474
$620 \leq E < 640$	0.004400
$640 \leq E < 660$	0.004503
$660 \leq E < 680$	0.004607
$680 \leq E < 700$	0.004673

(c) 2D Cut Values - TUM40

Energy E	RMS_{cut} [V]
$-40 \leq E < 10$	0.007129
$10 \leq E < 60$	0.008307
$60 \leq E < 110$	0.009319
$110 \leq E < 160$	0.01065
$160 \leq E < 210$	0.01188
$210 \leq E < 260$	0.01303
$260 \leq E < 310$	0.01410
$310 \leq E < 360$	0.01532
$360 \leq E < 460$	0.01682
$460 \leq E < 560$	0.01870
$560 \leq E < 660$	0.02017
$660 \leq E < 760$	0.02145

(d) 2D Cut Values - Michael

Figure D.4: *RMS distributions of all pulses of the blind data set for the phonon detector TUM40 (left) and the corresponding light detector Michael (right). The RMS-parameter values are obtained from the fit with the absorber template. The resulting limits of the RMS cut are given in the tables below the respective distributions.*

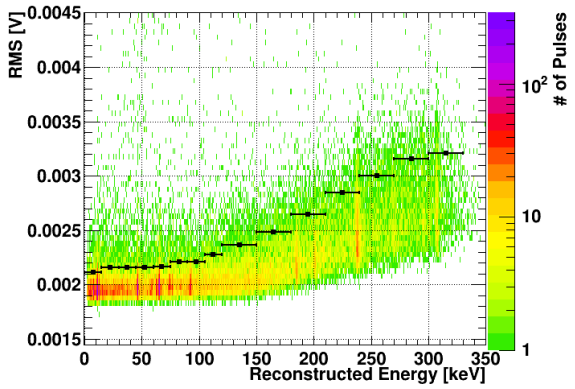

(a) RMS Distribution - TUM38

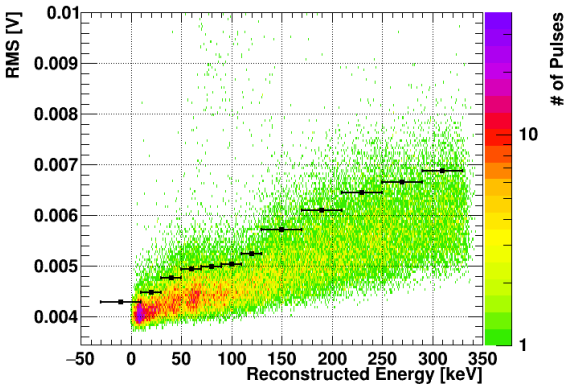

(b) RMS Distribution - Petrus

Energy E	RMS_{cut} [V]
$0 \leq E < 15$	0.002115
$15 \leq E < 30$	0.002159
$30 \leq E < 45$	0.002160
$45 \leq E < 60$	0.002155
$60 \leq E < 75$	0.002167
$75 \leq E < 90$	0.002208
$90 \leq E < 105$	0.002212
$105 \leq E < 120$	0.002276
$120 \leq E < 150$	0.002361
$150 \leq E < 180$	0.002486
$180 \leq E < 210$	0.002644
$210 \leq E < 240$	0.002844
$240 \leq E < 270$	0.003000
$270 \leq E < 300$	0.003154
$300 \leq E < 330$	0.003206

(c) 2D Cut Values - TUM38

Energy E	RMS_{cut} [V]
$-30 \leq E < 10$	0.004293
$10 \leq E < 30$	0.004475
$30 \leq E < 50$	0.004769
$50 \leq E < 70$	0.004932
$70 \leq E < 90$	0.004980
$90 \leq E < 110$	0.005025
$110 \leq E < 130$	0.005238
$130 \leq E < 170$	0.005723
$170 \leq E < 210$	0.006095
$210 \leq E < 250$	0.006442
$250 \leq E < 290$	0.006652
$290 \leq E < 330$	0.006882

(d) 2D Cut Values - Petrus

Figure D.5: *RMS distributions of all pulses of the complete data set for the phonon detector TUM38 (left) and the corresponding light detector Petrus (right). The RMS-parameter values are obtained from the fit with the absorber template. The resulting limits of the RMS cut are given in the tables below the respective distributions.*

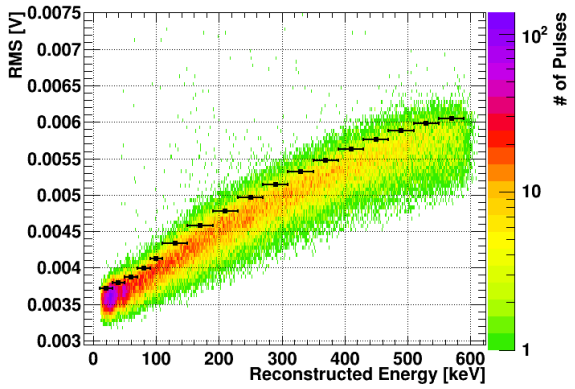

(a) RMS Distribution - VK27

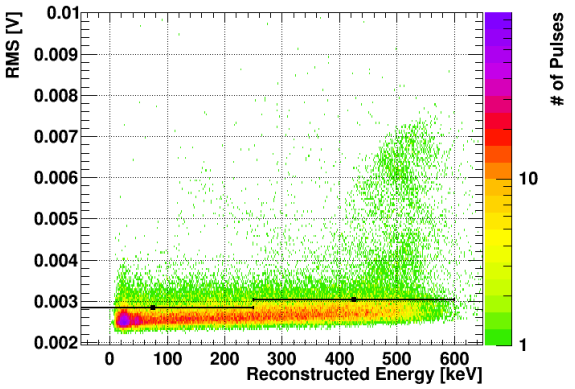

(b) RMS Distribution - Diogenes

Energy E	RMS_{cut} [V]
$10 \leq E < 30$	0.003723
$30 \leq E < 50$	0.003794
$50 \leq E < 70$	0.003875
$70 \leq E < 90$	0.003996
$90 \leq E < 110$	0.004124
$110 \leq E < 150$	0.004337
$150 \leq E < 190$	0.004580
$190 \leq E < 230$	0.004783
$230 \leq E < 270$	0.004970
$270 \leq E < 310$	0.005145
$310 \leq E < 350$	0.005317
$350 \leq E < 390$	0.005477
$390 \leq E < 430$	0.005627
$430 \leq E < 470$	0.005758
$470 \leq E < 510$	0.005884
$510 \leq E < 550$	0.005983
$550 \leq E < 590$	0.006043

(c) 2D Cut Values - VK27

Energy E	RMS_{cut} [V]
$-50 \leq E < 250$	0.002837
$250 \leq E < 650$	0.003044

(d) 2D Cut Values - Diogenes

Figure D.6: *RMS distributions of all pulses of the complete data set for the phonon detector VK27 (left) and the corresponding light detector Diogenes (right). The RMS-parameter values are obtained from the fit with the absorber template. The resulting limits of the RMS cut are given in the tables below the respective distributions.*

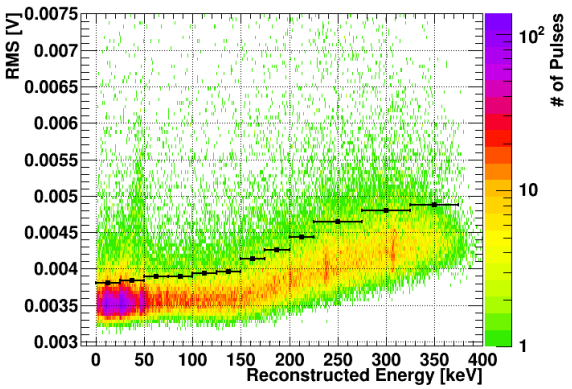

(a) RMS Distribution - VK28

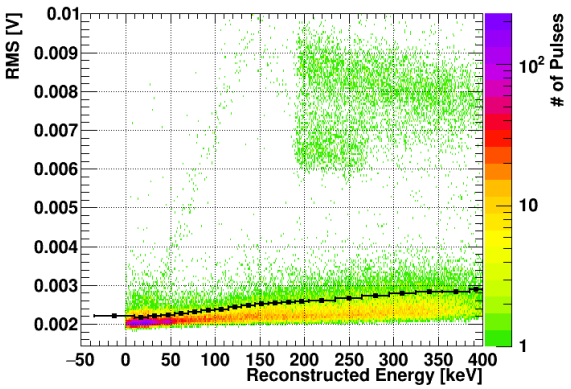

(b) RMS Distribution - Zam

Energy E	RMS_{cut} [V]
$0 \leq E < 25$	0.003811
$25 \leq E < 50$	0.003837
$50 \leq E < 75$	0.003892
$75 \leq E < 100$	0.003899
$100 \leq E < 125$	0.003934
$125 \leq E < 150$	0.003960
$150 \leq E < 175$	0.004138
$175 \leq E < 200$	0.004264
$200 \leq E < 225$	0.004437
$225 \leq E < 275$	0.004640
$275 \leq E < 325$	0.004796
$325 \leq E < 375$	0.004879

(c) 2D Cut Values - VK28

Energy E	RMS_{cut} [V]
$-35 \leq E < 10$	0.002200
$10 \leq E < 25$	0.002175
$25 \leq E < 40.$	0.002204
$40 \leq E < 55$	0.002232
$55 \leq E < 70$	0.002277
$70 \leq E < 85$	0.002322
$85 \leq E < 100$	0.002346
$100 \leq E < 115$	0.002381
$115 \leq E < 130$	0.002428
$130 \leq E < 145$	0.002474
$145 \leq E < 160$	0.002512

Energy E	RMS_{cut} [V]
$160 \leq E < 175$	0.002537
$175 \leq E < 190$	0.002554
$190 \leq E < 205$	0.002585
$205 \leq E < 235$	0.002604
$235 \leq E < 265$	0.002672
$265 \leq E < 295$	0.002727
$295 \leq E < 325$	0.002789
$325 \leq E < 355$	0.002839
$355 \leq E < 385$	0.002839
$385 \leq E < 400$	0.002901

(d) 2D Cut Values - Zam

Figure D.7: *RMS distributions of all pulses of the complete data set for the phonon detector VK28 (left) and the corresponding light detector Zam (right). The RMS-parameter values are obtained from the fit with the absorber template. The resulting limits of the RMS cut are given in the tables below the respective distributions.*

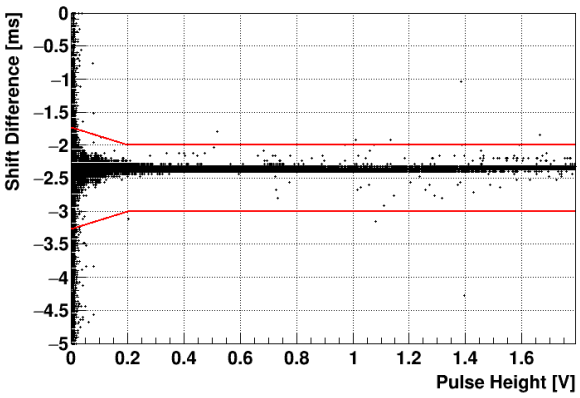

pulse height [V]	allowed parameter range
-0.10	$-3.40 \leq S \leq -1.60$
0.20	$-3.00 \leq S \leq -2.00$
1.80	$-3.00 \leq S \leq -2.00$

(a) Lise

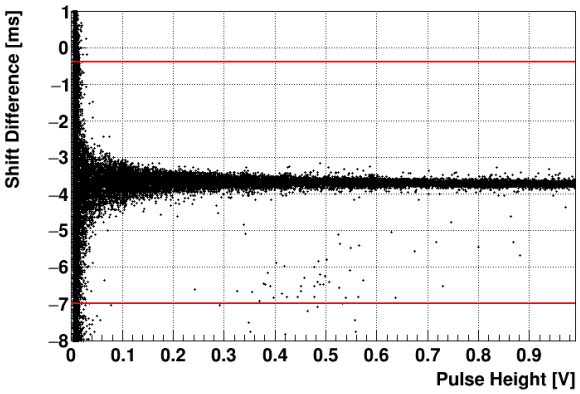

pulse height [V]	allowed parameter range
-0.20	$-7.00 \leq S \leq -0.40$
1.00	$-7.00 \leq S \leq -0.40$

(b) TUM40

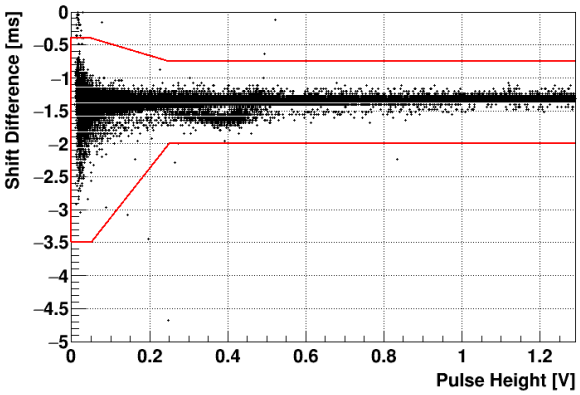

pulse height [V]	allowed parameter range
0.00	$-3.50 \leq S \leq -0.40$
0.05	$-3.50 \leq S \leq -0.40$
0.25	$-2.00 \leq S \leq -0.75$
1.30	$-2.00 \leq S \leq -0.75$

(c) VK28

Figure D.8: *Shift difference (S) parameter distributions as a function of the pulse height of the respective detector. The red lines correspond to the respective cut limits. The tables contain the supporting points of the two-dimensional cut functions. Between these points linear interpolations are applied. For pulses larger than the maximal given pulse-height values the cut is not applied.*

detector	Training method	Pulse Height [V]	Cut Limit
Lise	Stochastic	≤ 0.150	> 0.9950
	BFGS	≤ 0.080	> 0.9930
TUM38	Stochastic	≤ 0.100	> 0.9970
	BFGS	≤ 0.100	> 0.9980
TUM40	Stochastic	≤ 0.075	> 0.9991
		$0.075 < PH \leq 0.100$	> 0.9980
	BFGS	≤ 0.030	> 0.9825
VK27	Stochastic	≤ 0.050	> 0.9800
	BFGS	≤ 0.040	> 0.9960
		$0.040 < PH \leq 0.060$	> 0.9000
VK28	Stochastic	≤ 0.100	> 1.0100
	BFGS	≤ 0.100	> 0.9950

Table D.4: *Cut limits applied to the output of the respective MLPs trained with the given algorithm for all detectors. In most cases a single cut limit (last column) is applied for all pulses below a certain pulse height (given in the third column).*

E Simulation of Baselines

In [118] a method to simulate baselines based on the noise distributions measured is explained. This method involves a Fourier transformation of the record i to obtain the Fourier coefficient $F_i\left(\nu_j\right)$ for each frequency ν_j. Thus, when several records $i = 1,\ldots,N$ are transformed, the distribution $f_j\left(\nu_j\right)$ for each Fourier coefficient is obtained. In the next step for all frequencies ν_j Fourier coefficients $\tilde{F}_i\left(\nu_j\right)$ are sampled from the corresponding distributions $f_j\left(\nu_j\right)$ and a simulated Fourier transform is created. The inverse Fourier transformation of this simulated Fourier transform results in a simulated baseline.

In [118] the distributions are described either by Gaussian functions in both, the real and the imaginary part, or in case of a discrete noise frequency by a Gaussian function in the modulus and a uniform distribution in the phase parameter. For each frequency both models are fitted to the coefficient distribution $f_j\left(\nu_j\right)$ and the best fit is found based on the respective χ^2-parameter. Finally, the Fourier coefficients are simulated based on the best fitting model for this frequency. However, in the present work the actual coefficient distributions $f_j\left(\nu_j\right)$ are stored and directly used to generate the simulated Fourier transform.

The amplitude spectral densities (ASD) of measured (blue) and simulated (red) empty baselines (EBLs) are depicted in figure E.1. For clarity, the spectral density of the simulated baselines is artificially scaled by a factor of ten. At discrete frequencies distinct peaks are observed in both spectral densities corresponding to discrete noise contributions. Between both densities no significant deviation is observed supporting the simulation method.

Based on this method, simulated empty baselines are created and compared to measured empty baseline as depicted in figure E.2. While figure E.2a shows an example of a measured baseline of TUM40, figure E.2b contains a simulated one. On a first glance no significant deviation between both types of empty baselines is observable by eye.

However, when parameter distributions are compared as depicted in figure E.3 significant differences between both data sets are visible. In figure E.3a the distribution of the pulse height parameter is depicted for simulated (red) and measured (blue) baselines. In order to represent the same number of pulses the measured distributions are artificially scaled down.

For the simulated baselines less records with large pulse heights ($\gtrsim 0.025\,\mathrm{V}$) are created while simultaneously the distribution at small pulse heights is broader compared to the measured one. For the FWHM of baseline parameter shown in figure E.3b the mode of the simulated distribution is shifted to slightly higher values and, simultaneously, the width of the distribution is increased.

To investigate the origin of this behavior, the simulation is performed first with measured baselines as inputs. Afterwards, these resulting simulated baselines are used as inputs for a second simulation. In this case equivalent parameter distributions for the input and output simulated baselines are obtained. Thus, it is concluded that the simulation is self-consistent.

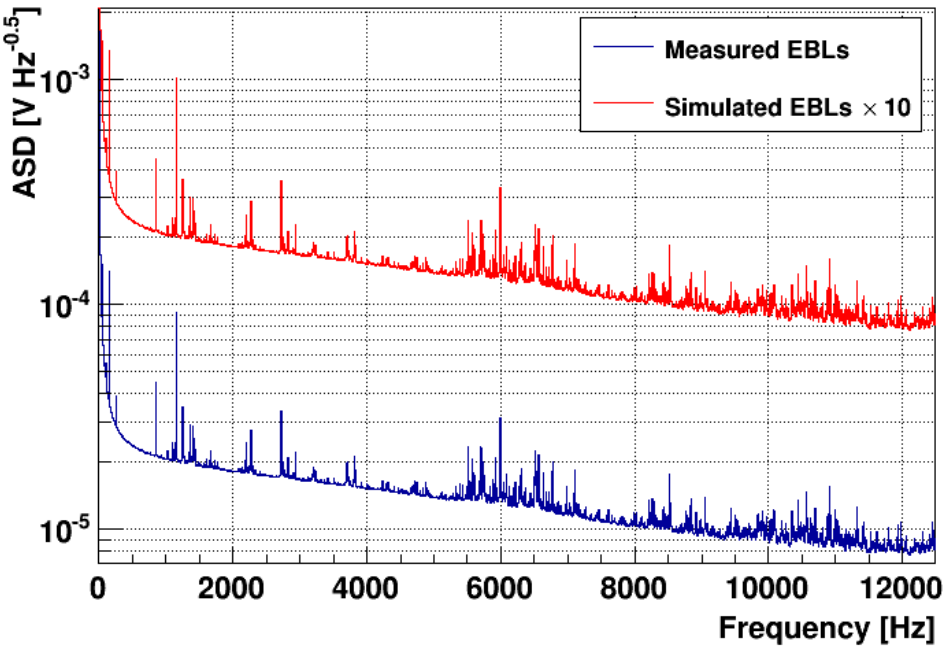

Figure E.1: *Simulated and measured amplitude spectral densities (ASD) of empty baselines (EBLs) for the phonon detector TUM40. For clarity, the spectral density for simulated EBLs is artificially scaled by a factor of ten. No significant difference between both spectra is observed. For the simulation of EBLs, a list of pre-cleaned records i, containing ideally only pure noise samples, is Fourier transformed and the distributions $f_j\left(\nu_j\right)$ of the Fourier coefficient $F_i\left(\nu_j\right)$ are obtained for each frequency ν_j. Based on these distributions simulated Fourier coefficients $\tilde{F}_i\left(\nu_j\right)$ are created and the inverse Fourier transformation results in a simulated EBL.*

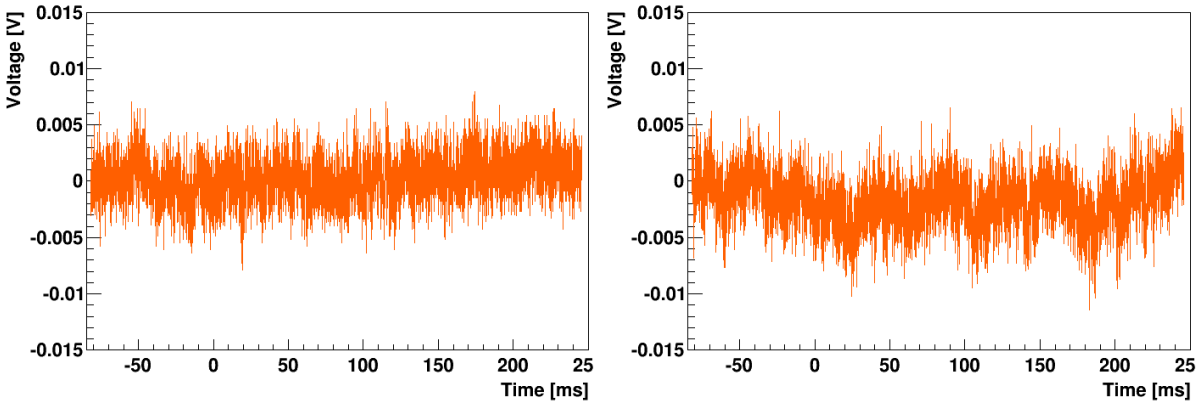

(a) *Measured Empty Baseline* ***(b)*** *Simulated Empty Baseline*

Figure E.2: *Comparison of a measured (a) and a simulated (b) empty baseline of TUM40. On a first glance no relevant difference between both exemplary baselines is observable by eye.*

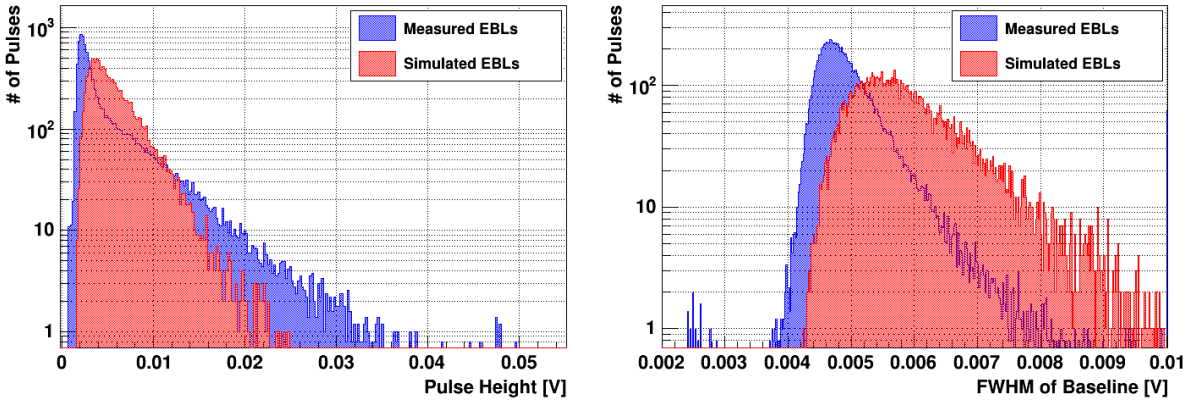

(a) Pulse Height *(b) FWHM of Baseline*

Figure E.3: *Comparison of two parameter distributions of simulated (red) and measured (blue) empty baselines (EBLs) of TUM40. The pulse height as well as the FWHM of baseline parameter are depicted in (a) and (b), respectively. Despite no significant deviation is visible by eye in the records (compare figure E.2), a clear deviation between both data sets is observed for these two parameter distributions. Whether these deviations are relevant for the performance of ANNs has to be checked before simulated baselines are used for the training task.*

Consequently, the origin of the deviation has to be present in the measured baselines but is lost during the simulation. Therefore, the deviation is most probably due to correlations in the measured data which are neglected by the simulation. For example, when a noise contribution at a distinct frequency is observed it is very likely that also harmonics of this frequency are present. However, in the simulation scheme described above these correlations are neglected.

In order to judge whether or not these deviations have a relevance for the performance of the ANN, a dedicated test has to be performed once with measured and once with simulated baselines. However, in the present thesis the number of measured baselines is sufficient and, thus, no simulated baselines are used.

F Fit of γ-Lines

The tables F.1 and F.2 list the parameter values obtained from the fits of the γ-lines observed in the recoil-energy spectra of TUM38 and TUM40, respectively.

TUM38					
E_{fit} [keV]	**Amplitude**	**σ [eV]**	**Intercept**	**Slope**	**Counts**
8.04 ± 0.01	34.31 ± 3.91	117 ± 11	-14.42 ± 8.49	3.89 ± 1.08	201.14 ± 29.47
10.79 ± 0.01	43.17 ± 3.71	131 ± 4	6.66 ± 11.91	0.69 ± 1.09	284.00 ± 25.59
11.27 ± 0.00	215.41 ± 7.57				1417.11 ± 62.86
12.97 ± 0.02	24.62 ± 2.57	224 ± 23	10.60 ± 12.67	0.23 ± 0.97	276.55 ± 40.62
17.90 ± 0.02	17.71 ± 2.91	143 ± 27	-12.04 ± 16.40	1.24 ± 0.91	127.02 ± 31.50
37.37 ± 0.03	15.32 ± 2.17	202 ± 30	36.13 ± 35.55	-0.73 ± 0.02	154.97 ± 31.83
46.28 ± 0.01	122.74 ± 4.34	233 ± 6	36.13 ± 0.00	-0.60 ± 0.01	1434.53 ± 64.56
62.94 ± 0.02	28.63 ± 1.83	281 ± 7	-8.13 ± 7.75	0.25 ± 0.12	403.14 ± 27.50
65.16 ± 0.01	121.67 ± 3.82				1713.49 ± 67.07
73.54 ± 0.03	17.10 ± 1.73	282 ± 23	12.39 ± 11.43	-0.06 ± 0.16	241.73 ± 31.47
12.33 ± 1.58	74.60 ± 0.04				174.28 ± 26.47
76.87 ± 0.02	22.03 ± 1.86	296 ± 22	44.75 ± 13.36	-0.50 ± 0.17	327.04 ± 37.15
83.82 ± 0.08	6.69 ± 1.05	510 ± 120	-17.27 ± 10.55	0.28 ± 0.12	171.15 ± 48.50
86.94 ± 0.08	5.10 ± 1.19	329 ± 66	13.09 ± 10.21	-0.07 ± 0.12	83.98 ± 25.96
89.52 ± 0.09	5.97 ± 1.20	380 ± 102	15.39 ± 32.01	-0.10 ± 0.36	113.59 ± 38.16
92.43 ± 0.02	32.66 ± 1.77	462 ± 23	-35.50 ± 10.18	0.47 ± 0.11	756.20 ± 55.74
185.45 ± 0.03	23.75 ± 1.34	546 ± 26	14.75 ± 6.08	-0.05 ± 0.03	650.10 ± 47.90
238.68 ± 0.02	42.30 ± 1.72	568 ± 20	-177.25 ± 11.04	0.77 ± 0.05	1205.01 ± 64.46
271.07 ± 0.12	9.61 ± 1.03	1102 ± 120	-2.75 ± 8.82	0.03 ± 0.03	265.47 ± 40.51
301.30 ± 0.11	6.95 ± 1.51	544 ± 197	-22.63 ± 8.56	0.09 ± 0.03	94.85 ± 40.01

Table F.1: *Fit results of the γ-lines observed in the recoil spectrum of the complete data set of TUM38. The lines are fitted by a sum of a Gaussian function (first three columns) and a linear background model (intercept and slope). In case of two lines close to each other the sum of two Gaussian functions with a combined width parameter and a linear background model is fitted. In this case the respective cells are merged in the table. Concerning the origin as well as the corresponding activity of the various γ-lines see table 9.2 on page 248. The given counts are the result of the integration of the Gaussian function according to equation 9.4.*

TUM40					
E_{fit} [keV]	Amplitude	σ [eV]	Intercept	Slope	Counts
2.64 ± 0.01	78.95 ± 6.16	96 ± 8	23.29 ± 6.79	-2.22 ± 2.57	381.67 ± 42.88
8.19 ± 0.01	35.09 ± 4.23	100 ± 12	24.84 ± 19.01	-1.50 ± 2.28	175.44 ± 30.27
10.93 ± 0.01	41.23 ± 3.73	105 ± 3	6.52 ± 0.42	0.61 ± 0.04	216.91 ± 20.50
11.44 ± 0.00	233.62 ± 8.66				1223.79 ± 56.57
13.14 ± 0.03	14.77 ± 2.16	221 ± 30	17.99 ± 7.20	-0.44 ± 0.52	163.50 ± 32.62
37.75 ± 0.03	12.23 ± 2.08	176 ± 36	48.67 ± 15.33	-1.11 ± 0.41	107.94 ± 28.75
46.80 ± 0.01	49.34 ± 3.03	222 ± 13	-26.64 ± 14.76	0.73 ± 0.32	549.48 ± 47.05
63.45 ± 0.03	12.55 ± 1.44	255 ± 7	-7.12 ± 6.76	0.23 ± 0.11	160.95 ± 19.00
65.66 ± 0.01	118.28 ± 4.06				1516.51 ± 66.49
74.00 ± 0.04	12.22 ± 1.56	281 ± 30	21.93 ± 7.04	0.39 ± 0.10	172.39 ± 28.73
75.02 ± 0.07	6.91 ± 1.31				97.47 ± 21.19
77.43 ± 0.05	8.70 ± 1.41	317 ± 59	21.79 ± 22.31	-0.20 ± 0.28	138.09 ± 34.09
84.47 ± 0.09	4.40 ± 1.18	312 ± 75	-3.53 ± 11.88	0.12 ± 0.14	68.81 ± 24.77
87.55 ± 0.15	3.50 ± 1.01	449 ± 154	48.99 ± 36.41	-0.49 ± 0.42	78.59 ± 35.26
92.97 ± 0.05	13.89 ± 1.47	411 ± 49	-17.69 ± 8.20	0.27 ± 0.09	285.85 ± 45.71
186.11 ± 0.04	15.57 ± 1.11	611 ± 42	38.16 ± 6.48	-0.18 ± 0.03	476.61 ± 47.05
239.95 ± 0.04	19.97 ± 1.05	868 ± 48	43.47 ± 0.13	-0.16 ± 0.00	869.51 ± 66.55
342.45 ± 0.12	4.74 ± 0.46	1294 ± 111	5.45 ± 7.06	-0.01 ± 0.02	307.48 ± 39.61
356.27 ± 0.24	3.05 ± 0.39	1661 ± 255	3.80 ± 18.62	-0.01 ± 0.05	254.21 ± 50.92
597.92 ± 0.38	4.12 ± 0.29	3031 ± 453	40.09 ± 1.86	-0.07 ± 0.00	626.62 ± 103.69

Table F.2: *Fit results of the γ-lines observed in the recoil spectrum of the complete data set of TUM38. The lines are fitted by a sum of a Gaussian function (first three columns) and a linear background model (intercept and slope). In case of two lines close to each other the sum of two Gaussian functions with a combined width parameter and a linear background model is fitted. In this case the respective cells are merged in the table. Concerning the origin as well as the corresponding activity of the various γ-lines see table 9.2 on page 248. The given counts are the result of the integration of the Gaussian function according to equation 9.4.*

Bibliography

[1] F. Zwicky, Helv. Phys. Acta **6**, 110 (1933).

[2] J. C. Kapteyn, ApJ**55**, 302 (1922).

[3] R. B. Tully and J. R. Fisher, A&A**54**, 661 (1977).

[4] P. R. Hague and M. I. Wilkinson, ApJ**800**, 15 (2015), arXiv:1408.4452, ©AAS. Reproduced with permission.

[5] ESO/Digitized Sky Survey 2 Acknowledgement: Davide De Martin, Triangulum Galaxy Snapped by VST, Press Release, 2014, Credit: ESO/Digitized Sky Survey 2. Acknowledgement: Davide De Martin. Retrieved from `http://www.eso.org/public/news/eso1424/`.

[6] E. Corbelli, D. Thilker, S. Zibetti, C. Giovanardi, and P. Salucci, A&A**572**, A23 (2014), arXiv:1409.2665.

[7] I. D. Karachentsev, V. E. Karachentseva, W. K. Huchtmeier, and D. I. Makarov, AJ**127**, 2031 (2004).

[8] M. Milgrom, AIP Conf Proc **1241**, 139 (2010), arXiv:0912.2678.

[9] F. W. Dyson, A. S. Eddington, and C. Davidson, Phil. Trans. RSA **220**, 291 (1920).

[10] NASA, ESA, A. Fruchter and the ERO Team (STScI, ST-ECF), Gravitational lens helps Hubble and Keck discover galaxy building block, Press Release, 2001, Retrieved from `http://www.spacetelescope.org/news/heic0113/`.

[11] A. Einstein, Science **84**, 506 (1936).

[12] D. Clowe *et al.*, ApJ**648**, L109 (2006), arXiv:astro-ph/0608407, ©AAS. Reproduced with permission.

[13] D. Clowe, A. Gonzalez, and M. Markevitch, ApJ**604**, 596 (2004), arXiv:astro-ph/0312273.

[14] S. W. Allen, R. W. Schmidt, and A. C. Fabian, MNRAS**334**, L11 (2002), arXiv:astro-ph/0205007, and references therein.

[15] D. Clowe *et al.*, ApJ**758**, 128 (2012), arXiv:1209.2143.

[16] A. Mahdavi, H. Hoekstra, A. Babul, D. D. Balam, and P. L. Capak, ApJ**668**, 806 (2007), arXiv:0706.3048.

[17] A. A. Penzias and R. W. Wilson, ApJ**142**, 419 (1965).

[18] ESA and the Planck Collaboration, P. A. R. Ade *et al.*, A&A**571**, A1 (2014), arXiv:1303.5062, reproduced with permission ©ESO.

[19] ESA and the Planck Collaboration, P. A. R. Ade *et al.*, A&A**571**, A16 (2014), arXiv:1303.5076.

[20] SDSS, D. G. York *et al.*, AJ**120**, 1579 (2000), arXiv:astro-ph/0006396.

[21] T. Padmanabhan, *Structure formation in the universe* (Cambridge University Press, Cambridge, 1993).

[22] A. Klypin, G. Yepes, S. Gottlöber, F. Prada, and S. Heß, MNRAS(2016), arXiv:1411.4001.

[23] A. A. Klypin, S. Trujillo-Gomez, and J. Primack, ApJ**740**, 102 (2011), arXiv:1002.3660.

[24] K. Riebe *et al.*, Astro. Nachr. **334**, 691 (2013), arXiv:1109.0003.

[25] N. McCurdy, 2015, Retrieved from `http://www.sci.utah.edu/~nmccurdy/images/medialibrary/SDSSBolshoiMpc_USE_THIS_ONE-copy.jpg`, Sources: Nina McCurdy/University of California, Santa Cruz; Ralf Kaehler and Risa Wechsler/Stanford University; Sloan Digital Sky Survey; Michael Busha/University of Zurich; J. R. Primack and T. E. Bell, Sky & Telescope **07**, 28 (2012), Retrieved from `http://hipacc.ucsc.edu/Bolshoi/S&TFeature2012.html`.

[26] C. Alcock *et al.*, ApJ**542**, 281 (2000), arXiv:astro-ph/0001272.

[27] EROS-2 Collaboration, P. Tisserand *et al.*, A&A**469**, 387 (2007), arXiv:astro-ph/0607207.

[28] G. Bertone, D. Hooper, and J. Silk, Phys. Rep.**405**, 279 (2005), arXiv:hep-ph/0404175.

[29] J. L. Feng, ARA&A**48**, 495 (2010), arXiv:1003.0904.

[30] R. Adhikari *et al.*, ArXiv e-prints (2016), arXiv:1602.04816.

[31] C. A. Baker *et al.*, Phys. Rev. Lett.**97**, 131801 (2006), arXiv:hep-ex/0602020.

[32] R. D. Peccei and H. R. Quinn, Phys. Rev. Lett.**38**, 1440 (1977).

[33] G. Jungman, M. Kamionkowski, and K. Griest, Phys. Rep.**267**, 195 (1996), arXiv:hep-ph/9506380.

[34] B. W. Lee and S. Weinberg, Phys. Rev. Lett.**39**, 165 (1977).

[35] K. Petraki and R. R. Volkas, Int. J. Mod. Phys. A **28**, 30028 (2013), arXiv:1305.4939.

[36] ATLAS Collaboration, G. Aad *et al.*, Eur. Phys. J. C **75**, 299 (2015), arXiv:1502.01518, and erratum: ibid., 408.

[37] CMS Collaboration, V. Khachatryan *et al.*, Physics Letters B **755**, 102 (2016), arXiv:1410.8812.

[38] M. CIRELLI, Pramana **79**, 1021 (2012), arXiv:1202.1454.

[39] R. Kappl and M. W. Winkler, Nucl. Phys. B **850**, 505 (2011), arXiv:1104.0679.

[40] IceCube Collaboration, M. G. Aartsen *et al.*, Phys. Rev. Lett.**110**, 131302 (2013), arXiv:1212.4097.

[41] A. Ibarra, M. Totzauer, and S. Wild, J. Cosmology Astropart. Phys.**2014**, 012 (2014), arXiv:1402.4375.

[42] J. Conrad, ArXiv eprints (2014), arXiv:1411.1925.

[43] M. Klasen, M. Pohl, and G. Sigl, Prog. Part. Nucl. Phys. **85**, 1 (2015), arXiv:1507.03800.

[44] J. Schmaler, *The CRESST Dark Matter Search – New Analysis Methods and Recent Results*, PhD thesis, Technische Universität München, 2010.

[45] J. D. Lewin and P. F. Smith, Astropart. Phys. **6**, 87 (1996).

[46] R. H. Helm, Phys. Rev. **104**, 1466 (1956).

[47] J. Engel, Phys. Lett. B **264**, 114 (1991).

[48] F. Donato, N. Fornengo, and S. Scopel, Astropart. Phys. **9**, 247 (1998), arXiv:hep-ph/9803295.

[49] F. J. Kerr and D. Lynden-Bell, MNRAS**221**, 1023 (1986).

[50] M. C. Smith *et al.*, MNRAS**379**, 755 (2007), arXiv:astro-ph/0611671.

[51] J. I. Read, J. Phys. G **41**, 063101 (2014), arXiv:1404.1938.

[52] M. Weber and W. de Boer, A&A**509**, A25 (2010), arXiv:0910.4272.

[53] J. Bovy and S. Tremaine, ApJ**756**, 89 (2012), arXiv:1205.4033.

[54] LUX Collaboration, D. S. Akerib *et al.*, Phys. Rev. Lett.**112**, 091303 (2014), arXiv:1310.8214.

[55] K. D. Abbhyankar, *Astrophysics of the Solar System* (Universities Press, 1999).

[56] K. Griest, Phys. Rev. D**37**, 2703 (1988).

[57] A. K. Drukier, K. Freese, and D. N. Spergel, Phys. Rev. D**33**, 3495 (1986).

[58] K. Freese, J. Frieman, and A. Gould, Phys. Rev. D**37**, 3388 (1988).

[59] DEAP Collaboration, M. G. Boulay, JPCS **375**, 012027 (2012), arXiv:1203.0604.

[60] K. Rielage *et al.*, Phys. Procedia **61**, 144 (2015), arXiv:1403.4842.

[61] K. Abe *et al.*, Nucl. Instrum. Meth. A **716**, 78 (2013), arXiv:1301.2815.

[62] C. E. Aalseth *et al.*, Adv. High Energy Phys. **2015**, 541362 (2015).

[63] D. Akerib *et al.*, Nucl. Instrum. Meth. A **704**, 111 (2013), arXiv:1211.3788.

[64] X. Cao *et al.*, Science China Physics, Mechanics & Astronomy **57**, 1476 (2014), arXiv:1405.2882.

[65] XENON100 Collaboration, E. Aprile *et al.*, Astropart. Phys. **35**, 573 (2012), arXiv:1107.2155.

[66] CDMS II Collaboration, Z. Ahmed *et al.*, Science **327**, 1619 (2010), arXiv:0912.3592.

[67] EDELWEISS Collaboration, E. Armengaud *et al.*, Phys. Rev. B**702**, 329 (2011), arXiv:1103.4070.

[68] Edelweiss Collaboration, V. Kozlov, JPCS **259**, 012037 (2010), arXiv:1010.5947.

[69] K. Ke-Jun *et al.*, Chinese Phys. C **37**, 126002 (2013), arXiv:1305.0401.

[70] CDEX Collaboration, Q. Yue *et al.*, Phys. Rev. D**90**, 091701 (2014), arXiv:1404.4946.

[71] CoGeNT Collaboration, C. E. Aalseth *et al.*, Phys. Rev. D**88**, 012002 (2013), arXiv:1208.5737.

[72] C. E. Aalseth *et al.*, ArXiv e-prints (2014), arXiv:1401.3295.

[73] C. E. Aalseth *et al.*, ArXiv e-prints (2014), arXiv:1401.6234.

[74] COUPP Collaboration, E. Behnke *et al.*, Phys. Rev. Lett.**106**, 021303 (2011), arXiv:1008.3518.

[75] S. Archambault *et al.*, Phys. Rev. B**682**, 185 (2009), arXiv:0907.0307.

[76] PICO Collaboration, C. Amole *et al.*, Phys. Rev. Lett.**114**, 231302 (2015).

[77] T. Saab, An Introduction to Dark Matter Direct Detection Searches & Techniques, in *The Dark Secrets of the Terascale (TASI 2011) - Proceedings of the 2011 Theoretical Advanced Study Institute in Elementary Particle Physics. Edited by Matchev Konstantin et al. Published by World Scientific Publishing Co. Pte. Ltd., 2013. ISBN 9789814390163, pp. 711-738*, edited by K. Matchev et al., pp. 711–738, 2013, arXiv:1203.2566.

[78] E. Behnke *et al.*, Science **319**, 933 (2008), arXiv:0804.2886.

[79] F. Aubin *et al.*, New J. Phys. **10**, 103017 (2008), arXiv:0807.1536.

[80] J. Barreto *et al.*, Phys. Lett. B **711**, 264 (2012), arXiv:1105.5191.

[81] R. Bernabei *et al.*, Eur. Phys. J. C **73**, 2648 (2013), arXiv:1308.5109.

[82] KIMS Collaboration, S. C. Kim *et al.*, Phys. Rev. Lett.**108**, 181301 (2012), arXiv:1204.2646.

[83] J. Amaré *et al.*, Phys. Procedia **61**, 157 (2015).

[84] DM-Ice Collaboration, J. Cherwinka *et al.*, Phys. Rev. D**90**, 092005 (2014), arXiv:1401.4804.

[85] K. Fushimi *et al.*, Phys. Procedia **61**, 67 (2015), arXiv:1407.3542.

[86] K. Kim *et al.*, Astropart. Phys. **62**, 249 (2015), arXiv:1407.1586.

[87] E. Shields, J. Xu, and F. Calaprice, Phys. Procedia **61**, 169 (2015).

[88] CUORE Collaboration, D. R. Artusa *et al.*, Adv. High Energy Phys. **2015**, 879871 (2015), arXiv:1402.6072.

[89] LVD Collaboration, M. Aglietta *et al.*, Phys. Rev. D**58**, 092005 (1998), arXiv:hep-ex/9806001.

[90] R. B. Firestone, C. Baglin, and S. Y. F. Chu, *Table of isotopes: 1998 update with CD-ROM* (Wiley, New York, NY, 1998); S. Y. F. Chu, L. P. Ekström, and R. B. Firestone, WWW Table of Radioactive Isotopes, database version 1999-02-28, retrieved from `http://nucleardata.nuclear.lu.se/nucleardata/toi/`.

[91] M. Berglund and M. E. Wieser, Pure Appl. Chem. **82**, 397 (2011).

[92] C. Arpesella, Nucl. Phys. B-Proc. Sup. **28**, 420 (1992).

[93] P. Belli *et al.*, Il Nuovo Cimento A (1965-1970) **101**, 959 (1989).

[94] H. Wulandari, J. Jochum, W. Rau, and F. von Feilitzsch, Astropart. Phys. **22**, 313 (2004), arXiv:hep-ex/0312050.

[95] M. Kiefer *et al.*, Nucl. Instrum. Meth. A **821**, 116 (2016), arXiv:1503.07806.

[96] Y. Zdesenko *et al.*, Nucl. Instrum. Meth. A **538**, 657 (2005).

[97] M. von Sivers, *Scintillating $CaWO_4$ Crystals for the Direct Dark Matter Search Experiments CRESST and EURECA*, PhD thesis, Technische Universität München, 2014.

[98] F. Pröbst *et al.*, J. Low Temp. Phys. **100**, 69 (1995).

[99] A. Tanzke, 2011, private communication.

[100] J. Ninkovic, *Investigation of $CaWO_4$ Crystals for Simultaneous Phonon-Light Detection in the CRESST Dark Matter Search*, PhD thesis, Technische Universität München, 2005.

[101] J.-C. Lanfranchi, *Development of a New Composite Cryogenic Detection Concept for a Radiochemical Solar Neutrino Experiment*, PhD thesis, Technische Universität München, 2005.

[102] M. Kiefer, *Improving the Light Channel of the CRESST-II Dark Matter Detectors*, PhD thesis, Technische Universität München, 2012.

[103] R. F. Lang, *Search for Dark Matter with the CRESST Experiment*, PhD thesis, Technische Universität München, 2008.

[104] S. Henry, *The 66-channel readout for the CRESST dark matter search*, PhD thesis, University of Oxford, 2003.

[105] S. Henry *et al.*, J. Instrum. **2**, P11003 (2007).

[106] R. C. Jaklevic, J. Lambe, A. H. Silver, and J. E. Mercereau, Phys. Rev. Lett.**12**, 159 (1964).

[107] G. Angloher *et al.*, Eur. Phys. J. C **72**, 1971 (2012), arXiv:1109.0702.

[108] K. Schäffner, *Study of Backgrounds in the CRESST Dark Matter Search*, PhD thesis, Technische Universität München, 2013.

[109] M. Kuźniak, M. Boulay, and T. Pollmann, Astropart. Phys. **36**, 77 (2012), arXiv:1203.1576.

[110] S. M. Scholl, *Neutron Background Simulation for the CRESST-II Experiment*, PhD thesis, University of Tübingen, 2011.

[111] S. Scholl, private communication, 2015.

[112] R. Strauss *et al.*, Eur. Phys. J. C **75**, 352 (2015), arXiv:1410.1753.

[113] C. Ciemniak *et al.*, EAS Publications Series **36**, 269 (2009).

[114] A. Erb and J.-C. Lanfranchi, CrystEngComm **15**, 2301 (2013).

[115] A. Münster *et al.*, J. Cosmology Astropart. Phys.**5**, 18 (2014), arXiv:1403.5114.

[116] A. Münster, PhD thesis, Technische Universität München, in preparation.

[117] R. Strauss, *Energy-Dependent Quenching Factor Measurements of CaWO4 Crystals at mK Temperatures and Detector Prototypes for Direct Dark Matter Search with CRESST*, PhD thesis, Technische Universität München, 2013.

[118] R. M^{c}Gowan, *Data Analysis and Results of the Upgraded CRESST Dark Matter Search*, PhD thesis, University of Oxford, 2008.

[119] A. Brown, *Analysis and Modelling for CRESST-II*, PhD thesis, University of Oxford, 2012.

[120] R. Brun and F. Rademakers, Nucl. Instrum. Meth. A **389**, 81 (1997), ROOT 5.28 or higher.

[121] F. Pröbst, private communication, 2015.

[122] C. de Boor, *A Practical Guide to Splines (Applied Mathematical Sciences)* (Springer, 1994).

[123] F. Reindl, *Exploring Light Dark Matter With CRESST-II Low-Threshold Detectors*, PhD thesis, Technische Universität München, in preparation.

[124] F. Reindl, Analysis of CRESST Dark Matter Search Data, Diploma thesis, Technische Universität München, 2011.

[125] R. Strauss *et al.*, Eur. Phys. J. C **74**, 2957 (2014), arXiv:1401.3332.

[126] C. Arnaboldi *et al.*, Astropart. Phys. **34**, 143 (2010), arXiv:1005.1239.

[127] G. Angloher *et al.*, Eur. Phys. J. C **74**, 3184 (2014), arXiv:1407.3146.

[128] F. Pröbst, private communication, 2016.

[129] J. Amaré *et al.*, Appl. Phys. Lett. **87**, 264102 (2005).

[130] J. R. Klein and A. Roodman, Annu. Rev. Nucl. Sci **55**, 141 (2005).

[131] R. Strauss *et al.*, J. Cosmology Astropart. Phys.**2015**, 030 (2015), arXiv:1410.4188.

[132] A. Münster, Absolute α-Radioactivity Determination of Scintillating $CaWO_4$ Crystals for Direct Dark Matter Search, Diploma thesis, Technische Universität München, 2013.

[133] S. E. Pfister, *Suche nach Dunkler Materie mit dem CRESST-II-Experiment*, PhD thesis, Technische Universität München, 2010.

[134] G. E. P. Box, W. G. Hunter, and J. S. Hunter, *Statistics for experimenters : an introduction to design, data analysis, and model building* Wiley series in probability and mathematical statistics (J. Wiley & Sons, New York, Chichester, Brisbane, 1978).

[135] C. M. Bishop, *Pattern Recognition and Machine Learning* Information Science and Statistics (Springer-Verlag New York, Inc., Secaucus, NJ, USA, 2006).

[136] Nature Insight: Machine Intelligence, Nature **521**, 435-482 (2015).

[137] A. Hoecker *et al.*, PoS **ACAT**, 040 (2007), arXiv:physics/0703039, TMVA Release: 4.1.4.

[138] F. Hitzler, Artificial Neural Network for Pulse Shape Analysis in Rare Event Searches, Master's thesis, Technische Universität München, 2015.

[139] H. Robbins and S. Monro, Ann. Math. Statist. **22**, 400 (1951).

[140] C. G. BROYDEN, IMA J. Appl. Math. **6**, 76 (1970); R. Fletcher, Comput. J. **13**, 317 (1970); D. Goldfarb, Math. Comp. **24**, 23 (1970); D. F. Shanno, Math. Comp. **24**, 647 (1970).

[141] J. Nocedal and S. J. Wright, *Numerical Optimization* Springer Series in Operations Research and Financial Engineering (Springer New York, 2006).

[142] F. Pröbst, 2016, private communication.

[143] W. Moses, S. Payne, W.-S. Choong, G. Hull, and B. Reutter, IEEE Trans. Nucl. Sci. **55**, 1049 (2008).

[144] S. Payne *et al.*, IEEE Trans. Nucl. Sci. **56**, 2506 (2009).

[145] S. Roth, *The Potential of Naganov-Luke Amplified Cryogenic Light Detectors and the Scintillation-Light Quenching Mechanism in $CaWO_4$ Single Crystals in the Context of the Dark Matter Search Experiment CRESST-II*, PhD thesis, Technische Universität München, 2013.

[146] T. Förster, Ann. Phys. **437**, 55 (1948).

[147] R. F. Lang *et al.*, ArXiv e-prints (2009), arXiv:0910.4414.

[148] C. Isaila, *Development of Cryogenic Light Detectors with Neganov-Luke Amplification for the Dark Matter Experiments CRESST and EURECA*, PhD thesis, Technische Universität München, 2010.

[149] C. Ciemniak, *Setup of a Neutron Scattering Facility for the Measurement of Scintillation Light Quenching Factors of Low-Temperature Detectors Used in the Direct Dark Matter Search Experiments CRESST and EURECA*, PhD thesis, Technische Universität München, 2011.

[150] F. Reindl, private communication, 2015.

[151] F. Pröbst, private communication, 2015.

[152] T. Marrodán Undagoitia and L. Rauch, J. Phys. G **43**, 013001 (2016), arXiv:1509.08767, and references therein. ©IOP Publishing. Reproduced with permission. All rights reserved..

[153] J. Conrad, Astropart. Phys. **62**, 165 (2015), arXiv:1407.6617.

[154] G. J. Feldman and R. D. Cousins, Phys. Rev. D**57**, 3873 (1998), arXiv:physics/9711021.

[155] S. Yellin, Phys. Rev. D**66**, 032005 (2002), arXiv:physics/0203002.

[156] XENON100 Collaboration, E. Aprile *et al.*, Phys. Rev. D**84**, 052003 (2011), arXiv:1103.0303.

[157] C. Arina, Physics of the Dark Universe **5–6**, 1 (2014), arXiv:1310.5718.

[158] S. Yellin, ArXiv e-prints (2007), arXiv:0709.2701.

[159] CRESST Collaboration, Angloher, G. *et al.*, Eur. Phys. J. C **76**, 25 (2016), arXiv:1509.01515.

[160] A. Brown, S. Henry, H. Kraus, and C. McCabe, Phys. Rev. D**85**, 021301 (2012), arXiv:1109.2589.

[161] F. Pröbst, CRESST - Talk for MPI Project Review, 2008, Retrieved from `https://indico.mpp.mpg.de/getFile.py/access?contribId=9&sessionId=3&resId=0&materialId=slides&confId=384`.

[162] J. Schmaler, CRESST - Talk for MPI Project Review, 2009, Retrieved from `https://indico.mpp.mpg.de/getFile.py/access?contribId=7&sessionId=2&resId=0&materialId=slides&confId=660`.

[163] M. J. Berger *et al.*, XCOM: Photon Cross Section Database (version 1.5), 2010.

[164] W. M. Haynes, *CRC Handbook of Chemistry and Physics*, 95th ed. (CRC Press, 2014).

[165] W. Bambynek *et al.*, Rev. Mod. Phys. **49**, 77 (1977), and erratum: ibid., 961.

[166] A. Bisi, L. Zappa, and E. Zimmer, Il Nuovo Cimento (1955-1965) **4**, 307 (2008).

[167] R. C. Jopson, H. Mark, C. D. Swift, and J. H. Zenger, Phys. Rev. **124**, 157 (1961).

[168] M. H. Mortensen, R. R. Betts, and C. K. Bockelman, Phys. Rev. C **21**, 2288 (1980).

[169] A. Münster, 2016, private communication.

[170] CDMS Collaboration, R. Agnese *et al.*, Phys. Rev. Lett.**111**, 251301 (2013), arXiv:1304.4279.

[171] C. Savage, G. Gelmini, P. Gondolo, and K. Freese, J. Cosmology Astropart. Phys.**2009**, 010 (2009), arXiv:0808.3607.

[172] P. Agnes *et al.*, Phys. Lett. B **743**, 456 (2015), arXiv:1410.0653.

[173] PandaX Collaboration, X. Xiao *et al.*, Phys. Rev. D**92**, 052004 (2015), arXiv:1505.00771.

[174] XENON100 Collaboration, E. Aprile *et al.*, Phys. Rev. Lett.**109**, 181301 (2012), arXiv:1207.5988.

[175] SuperCDMS Collaboration, R. Agnese *et al.*, Phys. Rev. Lett.**116**, 071301 (2016).

[176] SuperCDMS Collaboration, R. Agnese *et al.*, Phys. Rev. Lett.**112**, 241302 (2014), arXiv:1402.7137.

[177] EDELWEISS Collaboration, E. Armengaud *et al.*, Phys. Rev. D**86**, 051701 (2012), arXiv:1207.1815.

[178] KIMS Collaboration, H. S. Lee *et al.*, Phys. Rev. D**90**, 052006 (2014), arXiv:1404.3443.

[179] A. Gütlein *et al.*, Astropart. Phys. **69**, 44 (2015), arXiv:1408.2357.

[180] H. An, M. Pospelov, J. Pradler, and A. Ritz, Phys. Lett. B **747**, 331 (2015), arXiv:1412.8378.

[181] CRESST Collaboration, A. Gütlein *et al.*, to be published.

[182] A. C. Vincent, P. Scott, and A. Serenelli, Phys. Rev. Lett.**114**, 081302 (2015), arXiv:1411.6626.

[183] G. Angloher *et al.*, ArXiv e-prints (2016), arXiv:1601.04447.

[184] CRESST Collaboration, M. von Sivers *et al.*, to be published.

[185] CRESST Collaboration, G. Angloher *et al.*, ArXiv e-prints (2015), arXiv:1503.08065.

[186] A. Tanzke, PhD thesis, Technische Universität München, in preparation.

[187] Y. LeCun, Y. Bengio, and G. Hinton, Nature**521**, 436 .

[188] M. Abadi *et al.*, TensorFlow: Large-scale machine learning on heterogeneous systems, 2015, Software available from tensorflow.org.

[189] EDELWEISS Collaboration, T. de Boissière, ArXiv e-prints (2015), arXiv:1504.00820.

[190] J. Janicsko, 2013, private communication.

Danksagung

Am Ende jeder Arbeit steht eine Liste von Menschen ohne die so ein Doktorarbeits-Projekt nicht zu meistern wäre.

Zuallererst möchte ich mich bei Prof. Dr. Stefan Schönert für die Möglichkeit zur Anfertigung einer Doktorarbeit am Lehrstuhl für Experimentalphysik und Astroteilchenphysik bedanken. Dein Interesse an CRESST und unseren Resultaten war für mich sehr erfreulich. Meinem Doktorvater Prof. Dr. Lothar Oberauer gilt mein besonderer Dank für das entgegengebrachte Interesse an meiner Arbeit insbesondere an den künstlichen neuronalen Netzen.

Bei Dr. Walter Potzel möchte ich mich aus tiefstem Herzen bedanken - dein konstanter Zuspruch und die sehr interessanten Diskussionen waren trotz mancher Widrigkeiten immer eine Motivation weiter zu machen und nicht zu verzagen. Auch bei Dr. Jean-Côme Lanfranchi möchte ich mich für das entgegengebrachte Vertrauen und den konstanten Zuspruch bedanken. Danke für das Organisieren der Korsika-Fahrt der Kryogruppe, auf der du uns nicht nur deine Heimat sondern mir auch gezeigt hast wie sehr du meine Arbeit wertschätzt.

Bei Dr. Franz Pröbst möchte ich mich für die vielen interessanten Gespräche, die schöne gemeinsame Zeit am Gran Sasso und die guten Inputs für meine Arbeit bedanken. Dein nahezu unerschöpfliches Wissen zu CRESST, Elektronik und Fragen der Datenanalysen waren für mich immer hilfreich. Auch dich Florian habe ich nicht vergessen - danke für das Beantworten all meiner Fragen und für die vielen Stunden die wir uns mit dem einen oder anderen Problem um die Ohren geschlagen haben. Auch Danke für die viele Shiften und das Organisieren so mancher privater Aktivitäten.

Mein besonderer Dank gilt auch dir Andrea - du warst meine erste Diplomandin und trotz allem gehörst du für mich immer noch zur Analysegruppe :-P. Danke für die vielen Diskussionen über meine Arbeit, insbesondere für das Korrekturlesen und die vielen Inputs dabei.

Bei Vincenz und den anderen (Anton, Thurid, Paul, Ferdinand) die mit mir in einem Büro saßen möchte ich mich für das gute Arbeitsklima bedanken. Danke auch an Dominik für dein offenes Ohr für all meine Fragen und die vielen Diskussion dazu. Dein unglaubliches Wissen über ROOT, C++ oder Physik hat mir immer weiter geholfen.

Auch wenn wir nur kurz zusammengearbeitet haben hast du doch einen prägenden Eindruck hinterlassen; deshalb einen großen Dank an Sebastian für das Anlernen in das Thema der Datenanalyse. Auch Jens hat mit seinen vielen Oxrop-Makros, die er uns überlassen hat, viel zum Erfolg der Arbeit beigetragen. Danke auch an Achim und Sabine, für die vielen Diskussionen über CRESST, meine Arbeit oder sonstige Dinge. Ihr habt euch dafür immer Zeit genommen und mir dadurch sehr geholfen.

Bei Herrn Hagn möchte ich mich insbesondere für unseren gemeinsamen Gran Sasso Aufenthalt bedanken, wo durch Ihre Arbeit das Kalibrieren des Muon Veto Systems erst möglich wurde.

Bei unseren Sekretärinnen (insbesondere Maria und Sabine K.) möchte ich mich für die

Hilfe bei allen verwaltungstechnischen Fragen bedanken. Ohne euch wäre der alltägliche Bürokratiewahnsinn sicherlich nicht zu bewältigen gewesen.

Bei allen aktiven und ehemaligen Mitgliedern der CRESST-Familie möchte ich mich auch bedanken. Dabei müssen Karo und Marco, die mit ihren vielen Arbeitsstunden direkt am Gran Sasso alles am Laufen halten, besonders hervorgehoben werden. Ohne die vielen Leute die auf Shift am Experiment gewesen sind, wären keine Daten aufgezeichnet worden und das Analysieren der Daten gar nicht erst möglich gewesen. Deshalb auch hier noch einmal mein Dank an alle Beteiligten. Danke an Marc, dass du mit mir die Geduld hattest um die eine oder andere Bergtour am Gran Sasso zu unternehmen.

Danke an alle Mitglieder der Kryogruppe von E15 für die vielen Diskussionen über unsere gemeinsamen Arbeiten. Insbesondere der Korsika-Workshop wird mir lange in Erinnerung bleiben, da er uns zu einer Gruppe zusammen geschweißt hat. Bei allen aktiven und ehemaligen Mitgliedern von E15 möchte ich mich für den außergewöhnlichen kollegialen Zusammenhalt bedanken. Es hat immer Spaß gemacht an den Lehrstuhl zu kommen, zu arbeiten oder doch auch einfach mal nur zu ratschen. Danke insbesondere an Patrick für die schöne Werkstudententätigkeit, wodurch ich ein Teil der E15-Familie wurde :) Danke auch an Prof. Dr. Franz von Feilitzsch für des rege Interesse an meiner Arbeit und die interessanten Diskussion über alle möglichen Dinge wenn Sie zu einem Besuch an ihrem ehemaligen Lehrstuhl vorbeigekommen sind.

Danke an Sebastian Skambraks vom MPI für die nette und kompetente Einführung in Neuronale Netze und die späteren Diskussionen zu meiner Arbeit.

Bei Achim, Christian, Nils, Timo und Tobias möchte ich mich für die vielen Stunden Freizeitaktivität bedanken. Das Abtauchen in fremde Welten und auf andere Kontinente erlaubt es mir immer wieder zu entspannen und den Arbeitsstress zu verdrängen.

Thanks to the family D'Archivio for your great hospitality and, in particular, for the very delicious pizza e pasta. Despite the large number of days I spend at Gran Sasso it was always a pleasure to come back into your hotel. Grazie di tutto e alla prossima!

Zu guter Letzt kommen die Menschen die für den Erfolg so einer Arbeit unerlässlich sind. Sie helfen einem durch die anstrengendsten Zeiten und bekommen manchmal den ganzen Frust ab. Dafür dass ihr mir dennoch die ganze Zeit zur Seite standet gebührt euch, Bernhard, Heidrun, Angela und Maria mein großer Dank. Auch bei meinen Großeltern (insbesondere Maria und Otto) möchte ich mich für den steten Zuspruch und die konstante Unterstützung bedanken. Danke auch an Anja für deine großartige Unterstützung, das Korrigieren der kompletten Arbeit und dass du mich vor allem während der Schreibphase ertragen hast.